

General Disclaimer

One or more of the Following Statements may affect this Document

- This document has been reproduced from the best copy furnished by the organizational source. It is being released in the interest of making available as much information as possible.
- This document may contain data, which exceeds the sheet parameters. It was furnished in this condition by the organizational source and is the best copy available.
- This document may contain tone-on-tone or color graphs, charts and/or pictures, which have been reproduced in black and white.
- This document is paginated as submitted by the original source.
- Portions of this document are not fully legible due to the historical nature of some of the material. However, it is the best reproduction available from the original submission.

CR 137952

SHUTTLE INFRARED TELESCOPE FACILITY (SIRTF)

PRELIMINARY DESIGN STUDY

FINAL REPORT

(Data Item I.D. - 9)

AUGUST 1976

(NASA-CR-137952) SHUTTLE INFRARED TELESCOPE
FACILITY (SIRTF) PRELIMINARY DESIGN STUDY
Final Report (Hughes Aircraft Co.) 416 p HC
\$11.00 CSCL 20F

N76-33013

Unclassified
G3/74 05871

Distribution of this report is provided in the interest of information
exchange. Responsibility for the contents resides in the author or
organization that prepared it.

Prepared under Contract No. NAS2-8494 by

Hughes Aircraft Company

Culver City, California

for

Ames Research Center

National Aeronautics and Space Administration



Errata Sheet
for
HAC-SIRTF Preliminary Design Study
Final Report

<u>Page</u>	<u>Location</u>	<u>Present</u>	<u>Correct</u>
3-35	Title Fig. 3-26.	"Pin 6"	"Scan"
4-12	Next to last line	"20 arc sec"	"20 microradians"
4-30	Line 3	"on-axis"	"in the right position"
	Line 6	"on-axis"	"in the right position"
4-33	Line 5	"W/ H z"	"W"

CR-137952

SHUTTLE INFRARED TELESCOPE FACILITY (SIRTF)
PRELIMINARY DESIGN STUDY
FINAL REPORT

(Data Item I. D. -9)

August 1976

Prepared for
Ames Research Center
National Aeronautics and Space Administration
Moffett Field, California 94035



Hughes Aircraft Company
Electro-Optical Division
Culver City, California 90230

CONTENTS

1.	INTRODUCTION	1-1
1.1	Background	1-1
1.1.1	History	1-1
1.1.2	Scope of the Study	1-2
1.1.3	Related Activities	1-4
1.2	Advantages of IR Telescopes in Space	1-5
1.3	Alternative IR Facilities	1-6
1.4	Plans	1-8
1.5	Organization of the Report	1-9
2.	SIRTF SYSTEM	2-1
2.1	SIRTF Facility	2-2
2.2	SIRTF/Spacelab/Shuttle: Mechanical Definition	2-9
2.2.1	Mechanical Interfaces	2-9
2.2.2	System Definition and Requirements	2-21
2.3	SIRTF/Spacelab/Shuttle: Control and Data Management	2-31
2.3.1	MIC Instruments	2-31
2.3.2	Command and Data Management	2-32
2.3.3	Spacelab/Shuttle Command and Data Management	2-54
2.3.4	Utilization of Command and Data Support Systems for SIRTF	2-62
2.4	Power Requirements	2-70
2.5	Ground Support	2-70
2.5.1	Cryogenic Servicing Equipment	2-72
2.5.2	Ground Support Equipment	2-75

CONTENTS (Continued)

3.	SIRTF TELESCOPE	3-1
3.1	General Telescope Configuration	3-1
3.2	Optical Design and Performance Analysis	3-5
3.2.1	Data IR Telescope Design and Performance	3-5
3.2.2	Description of the Star Tracker Optics	3-14
3.2.3	Infrared and Visible Transmittance of the SIRTF Telescope	3-24
3.2.4	Out-of-Field Source Rejection	3-30
3.2.5	Effects of Contamination	3-38
3.2.6	Optical Engineering	3-44
3.3	Mechanical Subsystems	3-59
3.3.1	Mechanical Structure of the Telescope	3-59
3.3.2	Approximate Thickness of SIRTF Mirrors	3-78
3.3.3	Mechanical Environment Studies	3-84
3.3.4	SIRTF Telescope Mass Properties	3-98
3.4	Thermal Analysis	3-109
3.4.1	Thermal Model	3-110
3.4.2	Aperture Load	3-114
3.4.3	Results	3-119
3.4.4	Conclusions	3-119
3.5	Acquisition, Stabilization and Pointing	3-124
3.5.1	SIRTF-IPS System Concept	3-124
3.5.2	SIRTF-IPS Operational Sequence	3-132
3.5.3	Subsystem Studies	3-135
3.6	SIRTF Telescope Performance	3-144
3.6.1	Spatial Performance Parameters	3-144
3.6.2	Radiometric Performance	3-150
3.6.3	Zodiacal Emission Model	3-155
3.6.4	Radiation Effects on Detectors	3-167

CONTENTS (Continued)

4.	MAJOR SYSTEM TRADES	4-1
4.1	Gregorian Vs Cassegrainian Telescope	4-2
4.1.1	Optical Performance	4-2
4.1.2	Off-Axis Rejection	4-13
4.1.3	Conclusions	4-18
4.2	Aperture Diameter	4-20
4.3	CCD Vs. Video Star Tracker	4-25
4.4	SIRTF Vs. Large Ambient IR Telescope	4-27
4.5	Dedicated Gimbal Vs. IPS	4-35
4.6	Cryogen Transfer	4-37
5.	SIRTF OPERATIONS	5-1
5.1	Integration and Launch Support	5-1
5.2	Cryogen Servicing	5-8
5.2.1	General Approach	5-8
5.2.2	Cryogenic Servicing Timeline	5-9
5.3	Flight Operations	5-13
5.3.1	Flight Crew Duties	5-13
5.3.2	POCC Operations	5-16
5.3.3	Mission Philosophy for Partial Malfunctions	5-21
5.4	Post-Flight Operations	5-25
6.	SIRTF DEVELOPMENT PLAN	6-1
6.1	Basis of Plans and Estimates	6-1
6.1.1	Subsystems and Components	6-3
6.1.2	Documentation	6-3
6.1.3	Qualification	6-6
6.1.4	Quality	6-7
6.1.5	Reliability	6-7
6.2	SIRTF Development Schedule and Cost	6-7
6.3	Cost Drivers	6-10
6.4	Cost Reduction Options	6-11
6.5	SIRTF Technology Development	6-12
6.6	Large Ambient Telescope Development	6-13

CONTENTS (Continued)

APPENDICES

A	UNIFORMLY LOADED ANNULAR PLATE SIMPLY SUPPORTED ALONG THE OUTER DIAMETER	A-1
B	UNIFORMLY LOADED ANNULAR PLATE SIMPLY SUPPORTED AT THREE EQUALLY SPACED POINTS ON THE OUTER DIAMETER	B-1
C	THERMAL ANALYSIS MODEL	C-1
D	DEDICATED GIMBAL ASSEMBLY FOR SIRTF	D-1

BIBLIOGRAPHY

LIST OF ILLUSTRATIONS

Figure		Page
1-1	Shuttle Infrared Telescope Facility — Conceptual View	facing 1-1
2-1	Shuttle IR Telescope Facility	2-3
2-2	SIRTF and Related Spacelab and Shuttle Subsystems	2-5
2-3A	SIRTF Telescope (Isometric View)	2-8
2-3B	SIRTF Telescope Layout (Stowed Sunshield)	2-8
2-3C	SIRTF Telescope Layout (Deployed Sunshield)	2-9
2-4	SIRTF 7-Day Mission — General Arrangement of Equipment	2-11
2-5	SIRTF 30-Day Mission — General Arrangement of Equipment	2-13
2-6	SIRTF to Orbiter/Spacelab Interface and Details	2-19
2-7	Schematic MIC Layout: Cross Section	2-34
2-8	Schematic MIC Layout: End View	2-35
2-9	IR Field of View	2-52
2-10	Data 1 Display for the Michelson Interferometer	2-53
2-11	Data 2 Display for the Michelson Interferometer	2-53
2-12	Status 1 Display	2-53
2-13	New Star Standard Format	2-53
2-14	Spacelab-Orbiter Combined Avionics Systems	2-55
2-15	SIRTF Command and Data Management Interface with Spacelab and Shuttle	2-63
2-16	IPS Gimbal Slaving	2-67
2-17	Basic SIRTF Cryogenic Tanks Servicing Schematic	2-74
3-1	Telescope Schematic	3-1
3-2	SIRTF Telescope	3-2
3-3	Optical Layout of the SIRTF Optical System	3-7

LIST OF ILLUSTRATIONS (Continued)

Figure		Page
3-4	On-Axis Point Spread Function, $\lambda = 5$ Micrometers	3-9
3-5	On-Axis Physical Modulation Transfer Function	3-9
3-6	On-Axis Physical Optics Radial Energy Distribution	3-10
3-7	Convolution of the On-Axis PSF with a 1.0 and 2.17 Arc Second Square Detector	3-10
3-8	Convolution of the On-Axis PSF with Gaussian Jitter Function for $\lambda = 1, 2, 5, 10$ and 20 Microradian Jitter	3-11
3-9	Jitter Analysis Physical Optics Radial Energy Distributions	3-11
3-10	Profiles of Point Spread Functions for Different Field Positions and Chop Mirror Displacement Angles	3-12
3-11	Image Degradation Introduced by Tilting the Secondary Mirror	3-13
3-12	Optical Layout of Star Tracker Relay	3-14
3-13	Refractive Index Change with Temperature for B&L 523-586 Glass	3-16
3-14	Knife-Edge Scans in X Direction for the Star Tracker Optical System	3-18
3-15	Knife-Edge Scans in Y Direction for the Star Tracker Optical System	3-18
3-16	Geometrical Spot Diagram, On-Axis	3-19
3-17	Geometrical Radial Energy Distribution, On-Axis	3-20
3-18	Geometrical Knife-Edge Scans, On-Axis	3-21
3-19	Unfolded Optical Schematic of Star Tracker	3-22
3-20	Reflectance as a Function of Wavelength of the OCLI Protected Silver Mirror	3-26
3-21	Transmittance and Reflectance as a Function of Wavelength of the OCLI Indium Oxide Beamsplitter Coating	3-27
3-22	Reflectance per Surface as a Function of Wavelength for OCLI Extended HEA on 522-595 Glass (Schott K5)	3-29
3-23	Telescope Definition for Out-of-Field Source Rejection Calculation	3-31
3-24	Bi-Directional Reflectance Distribution Function for Bare Beryllium	3-32

LIST OF ILLUSTRATIONS (Continued)

Figure		Page
3-25	Focal Plan Irradiance due to Out-of-Field Sources	3-33
3-26	Change in Focal Plane Flux due to Space Chop	3-35
3-27	Sky Radiance from Zodiacal Emission	3-36
3-28	Path Difference due to a Rough Surface	3-39
3-29	Path Difference due to a Rough Layer	3-40
3-30	Temporal Stability Test Results	3-47
3-31	α and ΔL for Beryllium	3-49
3-32	Scattering of Single-Point Diamond Turned Aluminum Mirror Samples Compared to Bare Beryllium	3-53
3-33A	SIRTF Telescope Layout - Identification of Subsystems and Components	3-61
3-33B	SIRTF Telescope Layout - Dimensions	3-63
3-34	Primary Mirror Mount	3-66
3-35	Mirror Mount Schematic Concept	3-67
3-36	Mirror Mount Set Schematic Concept and Equivalent . .	3-68
3-37	First Folding Mirror Mount and Drive	3-71
3-38	MIC Selector	3-72
3-39	MIC Installation	3-74
3-40	SIRTF Cover and Support Structure	3-75
3-41	Telescope Barrel Construction (Configuration C)	3-86
3-42	Mathematical Model Idealization	3-87
3-43	Mode No. 1 - Primary Mirror Mode	3-90
3-44	Mode No. 2 - Vacuum Housing Mode	3-90
3-45	Mode No. 3 - Second Folding Mirror Mode	3-90
3-46	Mode No. 4 - Combined Mode Primary Mirror and Second Folding Mirror Out of Phase	3-91
3-47	Mode No. 5 - Combined Mode First Folding Mirror and Second Folding Mirror Out of Phase	3-91
3-48	Finite Element Model	3-93
3-49	Internal Spatial Averaged Sound Pressure Level	3-94
3-50	First Shell Mode Shape - Axial View	3-96

LIST OF ILLUSTRATIONS (Continued)

Figure		Page
3-51	Second Shell Mode Shape - Axial View	3-96
3-52	Third Shell Mode Shape - Axial View	3-97
3-53	Radial Acceleration Spectrum - Vacuum Housing Thermal Isolator Interface, $\theta = 0^\circ$	3-99
3-54	Axial Acceleration Spectrum - Vacuum Housing Thermal Isolator Interface, $\theta = 0^\circ$	3-100
3-55	Radial Acceleration Spectrum - Vacuum Housing Thermal Isolator Interface, $\theta = 90^\circ$	3-101
3-56	Axial Acceleration Spectrum - Vacuum Housing Thermal Isolator Interface, $\theta = 90^\circ$	3-102
3-57	Radial Acceleration Spectrum - Vacuum Housing Thermal Isolator Interface, $\theta = 180^\circ$	3-103
3-58	Axial Acceleration Spectrum - Vacuum Housing Thermal Isolator Interface, $\theta = 180^\circ$	3-104
3-59	Radial Acceleration Spectrum - Vacuum Housing Thermal Isolator Interface, $\theta = 270^\circ$	3-105
3-60	Axial Acceleration Spectrum - Vacuum Housing Thermal Isolator Interface, $\theta = 270^\circ$	3-106
3-61	RMS Radial Acceleration Level at Interface	3-107
3-62	Proposed Helium Flow-Path in SIRTF Cryogenic System	3-111
3-63	Node Locations	3-113
3-64	Scattering Data	3-115
3-65	Solar Aperture Load	3-116
3-66	Schematic of SIRTF Cooling and Vacuum System	3-123
3-67	IPS Gimbal Configuration	3-125
3-68	IPS Angular Coverage	3-127
3-69	IPS Gimbal Suspension Configuration	3-127
3-70	Optical Stabilization Loop Using CCD Array Detector	3-129
3-71	Optical Stabilization Loop Using Chopping Bypass Mirror and Quadrant Detector	3-129
3-72	IPS Gimbal Slave Loop Configuration	3-131
3-73	Four-Field Readout of CCD Star Tracker	3-137
3-74	Reactionless Two-Axis Drive for Second Folding Mirror	3-138

LIST OF ILLUSTRATIONS (Continued)

Figure		Page
3-75	Space Chopping Waveform	3-139
3-76	SIRTF Chopping Mirror Performance - 10 mW	3-141
3-77	SIRTF Chopping Mirror Performance - 30 mW	3-142
3-78	SIRTF Chopping Mirror Performance - 100 mW	3-142
3-79	SIRTF Chopping Mirror Performance - 500 mW	3-143
3-80	On-Axis Point Spread Function, $\lambda = 5$ Micrometers . .	3-145
3-81	SIRTF Telescope Field-of-View Coverage	3-146
3-82	SIRTF Chopping Power Requirements - 100 mw	3-147
3-83	Example Scan Fields Using Second Folding Mirror Scanning	3-150
3-84	Photon Fluctuation Noise in the SIRTF Focal Plane Caused by Emission of Atmospheric Gases	3-152
3-85	Radiant Power on the 1 arc minute SIRTF Detector due to Water and Carbon Dioxide Released by the Shuttle	3-153
3-86	Water Vapor Rotation Band Radiation (20-30 μ) and SIRTF NEP	3-154
3-87	Particle Size Distribution	3-157
3-88	Geometry of Integration Scheme	3-158
3-89	Visible Zodiacal Radiance for Assumptions of only a Refracted and only a Reflected Component	3-163
3-90	Infrared Zodiacal Radiance in the Plane of Ecliptic at 90° Elongation	3-164
3-91	Infrared Zodiacal Radiance for Five Elongations for Curve B in Figure 3-90	3-165
3-92	Infrared Zodiacal Radiance as a Function of Elongation for Curves b and d in Figure 3-90 at a Wavelength of 15 μ m	3-166
3-93	Detector Event Rate as a Function of Detector Size . .	3-170
3-94	Comparison of Detector Event Rates (Peak) as a Function of Detector Size	3-171
3-95	Comparison of Detector Event Rates (Peak) as a Function of Detector Size	3-172
3-96	Comparison of Detector Event Rates (Peak) as a Function of Detector Size	3-173

LIST OF ILLUSTRATIONS (Continued)

Figure		Page
3-97	Comparison of Detector Event Rates (Peak) as a Function of Detector Size	3-174
4-1	Variation of Radial Energy Distribution with Field of View Displacement for Different Percent Encircled Energies	4-4
4-2	Variation of 80-percent Blur Diameters (Centered on Centroid) as a Function of Primary f-number and Secondary Magnification for the Telescopes Summarized in Table 4-3 for the Point in the Center of the Displaced FOV	4-6
4-3	Image Points at which the Telescopes are Evaluated ..	4-7
4-4	The Measure of Coma used in the Evaluation of Figure 4-5	4-8
4-5	Variation in Coma as a Function of Displacement Angle, θ , for Different Values of the Primary Mirror Conic Constant, K	4-9
4-6	Effects of Defocus at the Image Plane due to Tilting the Scan Mirror Through an Angle, α	4-11
4-7	Through-Focus Variation in Blur Radius for 70, 80 and 90 percent Energies, and for Field Angles, θ , of 0 and 7.5 arc minutes	4-12
4-8	Cassegrainian Systems	4-14
4-9	Double-Folded Gregorian Systems	4-15
4-10	Steady-State Photon Flux in Focal Plane with Space Chopping Mirror Centered	4-17
4-11	Variation in Photon Flux on Detector (Scan Modulation). ,	4-19
4-12	Diffraction Blur Parameters as a Function of Primary Mirror Diameter	4-21
4-13	Total SIRTF System Weight as a Function of Primary Mirror Diameter	4-21
4-14	Pallet Train Load as a Function of Primary Mirror Diameter	4-22
4-15	Moment of Inertia of SIRTF Telescope as a Function of Primary Mirror Diameter	4-24
4-16	LIRTS Sensor - Hughes Conceptual Layout	4-29
4-17	Typical LIRTS Performance Curves	4-32

LIST OF ILLUSTRATIONS (Continued)

Figure		Page
4-18	SIRTF and LIRTS NEP Comparison	4-33
4-19	SIRTF and LIRTS NEFD Comparison	4-34
4-20	Cryogen Supply Trade Study Approaches	4-38
5-1	SIRTF Launch Site Integration Flow	5-3
5-2	Payload and Mission Specialist SIRTF Duties	5-17
5-3	Ground-Based Scientist SIRTF Duties	5-19
5-4	SIRTF On-Orbit Operations	5-20
5-5	SIRTF Malfunction Decision Tree	5-23
6-1	SIRTF Hardware Development Program Schedule	6-8
6-2	SIRTF Hardware Development Program Cost Estimate	6-8
6-3	Ambient Telescope Hardware Development Program Cost Estimate	6-19

LIST OF TABLES

Table		Page
2-1	SIRTF System Parameters	2-7
2-2	7-Day Mission: Interface Tabulation	2-23
2-3	30-Day Mission: Interface Tabulation	2-25
2-4A	SIRTF Mass Properties: 7-Day Mission	2-27
2-4B	SIRTF Mass Properties: 30-Day Mission	2-27
2-5	SIRTF Mass Properties: 7-Day Mission Baseline Masses	2-28
2-6	SIRTF Mass Properties: 30-Day Mission Baseline Masses	2-29
2-7	Spacelab Subsystem Mass Detail	2-30
2-8	MIC Instrument Summary	2-33
2-9	Data Rate Based on SIRTF Instruments	2-36
2-10	Data Rate Based on SIRTF Detectors	2-37
2-11	Summary of SIRTF Science Data Generation Rates	2-38
2-12	SIRTF Control Functions	2-41
2-13	Memory Requirements Estimates	2-45
2-14	Typical Operator Commands	2-51
2-15	Execution Time Estimates	2-69
2-16	SIRTF Power Requirements	2-71
3-1	SIRTF IR Telescope Optical Characteristics	3-6
3-2	Boresight Sensitivity and Image Degradation Analysis Summary	3-13
3-3	Temperature Coefficients of Schott K5 (522-595) Glass (Spectral Band in Star Tracker Channel: 650 to 950 nm)	3-16

LIST OF TABLES (Continued)

Table		Page
3-4	SIRTF Star Tracker Optical Characteristics (Including the IR Telescope)	3-17
3-5	Distortion of the Star Tracker Optics	3-23
3-6	Coating Material Tradeoff	3-25
3-7	Change in Detector Irradiance with Scan	3-37
3-8	Number of Mono-Layers in 2.5 μ m	3-42
3-9	Cryo-Contaminants Measured for Scattering	3-43
3-10	LALOS Scan Mirror Preliminary Data	3-50
3-11	Thermal Expansion Comparison	3-54
3-12	Definitions of Symbols	3-82
3-13	Mirror Dimensions and Deflections	3-83
3-14	Vacuum Housing Configurations	3-86
3-15	Deflections and Rotations of Optical Elements	3-88
3-16	First Six Natural Frequencies	3-89
3-17	Shell Natural Frequencies	3-95
3-18	SIRTF Telescope Mass Properties	3-108
3-19	Material Properties	3-113
3-20	Aperture Loads Due to IR Emission from Shade	3-118
3-21	Aperture Loads (W)	3-118
3-22	Model Results (Temperatures in °K)	3-120
3-23	Heat Balance Nominal Case SIRTF	3-121
3-24	SIRTF-IPS Stabilization Performance	3-133
3-25	Star Acquisition Element Characteristics	3-136
3-26	Second Folding Mirror Drive Specifications	3-139
3-27	Chopping Performance Requirements	3-141
3-28	SIRTF Focal Plane Linear and Angular Dimensions . . .	3-145
3-29	Chopping Performance Requirements	3-148
3-30	SIRTF Stabilization System Error Estimates	3-149
3-31	SIRTF Radiometric Performance Specification	3-151

LIST OF TABLES (Continued)

Table		Page
4-1	SIRTF Optical Performance Requirements	4-3
4-2	Classical Cassegrainian Telescope Parameters	4-4
4-3	Optical Characteristics of Three Cassegrainian Telescopes	4-5
4-4	Ritchey-Chretien Telescope Optical Characteristics ..	4-7
4-5	Dimensional Data for Systems Considered	4-16
4-6	Comparison of Star Tracker Sensors	4-26
4-7	LIRTS Parameter Summary	4-28
4-8	LIRTS Primary Mirror Trade	4-31
4-9	Low Temperature Mirror Trade	4-31
4-10	Crogen Supply Trade Results	4-39
5-1	List of Acronyms for Figure 5-1	5-2
5-2	SIRTF Cryogenic Helium Servicing Time Line	5-10
6-1	SIRTF Subsystems, Assemblies and Major Components	6-4
6-2	SIRTF Technology Development Program	6-14

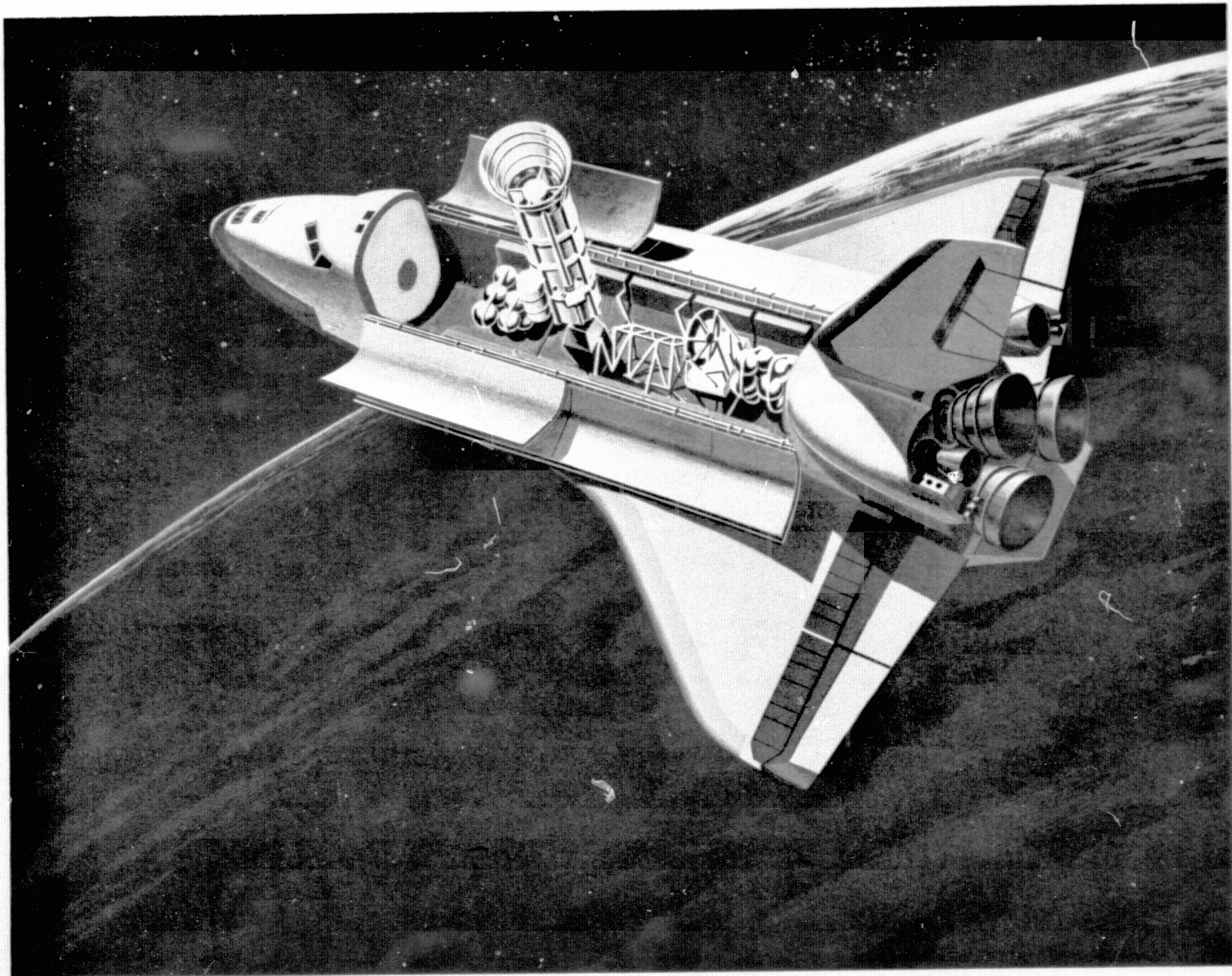


Figure 1-1. Shuttle Infrared Telescope Facility – conceptual view.

1. INTRODUCTION

1.1 BACKGROUND

1.1.1 History

Concepts for cooled infrared telescopes have been discussed in the literature for over a decade. However, until the early 1970's interest had not been high in exploiting the space environment to utilize such an instrument. Probably the main reason was that, because infrared astronomy is a relatively new branch of the science, the astronomers were busy with the discoveries they were making with ground-based, balloon-borne, and aircraft telescopes within the limits set by atmospheric absorption and emission and by the balloon and aircraft performance. A contributing factor also was the unavailability of infrared detectors that would be sensitive enough to benefit from a cooled telescope. At about the same time that the astronomers began to feel it was worthwhile to consider more sensitive facilities, they were also finding out that the technology for making very sensitive detectors and cooled telescopes, developed by the military, could be made available to them.

The design of SIRTF (Figure 1-1) was guided by a number of preceding and concurrent studies which defined goals for infrared astronomy and indicated how these goals might be accomplished using the Shuttle. In May 1971, investigators at the Ames Research Center described possible plans for developing a large cooled telescope for the Space Shuttle; preliminary studies were funded and carried out through 1973 (Ref. 1-1). In 1972, at the Space Shuttle Sortie Workshop (Ref. 1-2), the IR Astronomy Working Group proposed that a 1-meter cooled telescope be developed. Subsequently, NASA Headquarters formed an Astronomy Working Group which recommended a somewhat larger instrument (Ref. 1-3). Later, the 1973 Woods Hole Summer

Study recommended that NASA undertake a design study of a 1-meter cooled IR telescope to establish its feasibility on the Space Shuttle (Ref. 1-4). The Space Science Board Infrared and Submillimeter Study (Ref. 1-5) further defined astronomy goals and identified a cooled 1-meter telescope of the SIRTF type as the first priority Shuttle payload.

Ames and NASA Headquarters invited a group of infrared astronomers to serve as advisors on the study. This group, called the Shuttle Infrared Telescope Science Accommodations Group (SIRTSAG), first met in February 1974. Chairman was Dr. David M. Rank of the University of California at Santa Cruz, and the members were: Dr. Eric E. Becklin, of the California Institute of Technology; Dr. Fred C. Gillett, of Kitt Peak National Observatory; Dr. D. A. Harper, Jr., of Yerkes Observatory; Dr. William F. Hoffmann, of the University of Arizona; Dr. Frank J. Low, of the University of Arizona; Dr. Russell G. Walker, who was at that time at the Air Force Cambridge Research Laboratory and is now at Ames Research Center; and Dr. Fred C. Witteborn, of Ames Research Center.

It was decided by NASA that a major study effort should be performed by an industrial firm that had experience with similar, albeit smaller, space projects. A request for proposal (RFP) for the SIRTF Preliminary Design Study was issued in February 1974, with a modification that incorporated the final SIRTSAG inputs. Six company teams responded, and after evaluation by Ames and the SIRTSAG with NASA Headquarters, NASA Marshall Space Flight Center and USAF personnel assistance, the contract was awarded to Hughes Aircraft Company in July 1974. Grumman Aerospace Corporation, as a subcontractor to Hughes, provided assistance in the area of the SIRTF-Shuttle interface.

1.1.2 Scope of the Study

The basic requirement at the outset of the study was to define a SIRTF concept, determine its feasibility for the Space Shuttle/Spacelab, and perform tradeoffs to define the best and most economical set of characteristics and interfaces. Also, requisite technology development was to be identified. It became apparent during proposal evaluation that there would be little or no

question about the feasibility, and so the study was directed to concentrate on the preliminary design and tradeoffs. The focal plane instruments and their removable Multiple Instrument Chamber (MIC) were not included in the study, but were tentatively defined by NASA and the SIRTSAG. The contractor was required to define a substitute MIC (SUBMIC) for testing purposes.

The modularity inherent in the use of Shuttle support and Spacelab components has allowed rather flexible design ranges to be considered. This reduced the amount of effort that was required to "fit" the SIRTF into the Space Transportation System (STS), and allowed additional effort to be applied to the design definition. As a result, except in the areas of scientific instruments and some interfaces, the output of the study could form the basis for proceeding almost immediately to the hardware phase.

Several additions to the study were made as a result of SIRTSAG, Ames and NASA Headquarters requests. First, Hughes was required to compare the performance of a Ritchey-Chretien (Cassegrain) optical layout with that of the folded Gregorian that had been proposed. Several special investigations of scan noise sources were requested. The Instrument Pointing System (IPS) was proposed as a new item of Spacelab common-use equipment after the study had begun, and Hughes was required to incorporate the IPS into the design and to report on a tradeoff between the IPS and the dedicated gimbal that was required by the contract. After NASA defined the Video Inertial Pointing (VIP) system (Ref. 1-6), Hughes was tasked to incorporate the VIP focal plane sensor in the design and to coordinate with the sensor development at Ames and JPL. Contamination prediction was deleted from the contract requirements and a requirement to use the NASA contaminant radiation and absorption model was substituted. A special study of the effects of hard radiation on detectors at the SIRTF focal plane was added. Finally, a requirement to compare SIRTF performance and cost to a larger, ambient-temperature telescope (based on Reference 1-7) was added.

This report describes the preliminary design of SIRTF based on the Shuttle and Spacelab definitions available as of December 1975. The tradeoffs and special studies that were performed to arrive at the design are described, and the estimated cost for the facility is presented. A complete list of the reports issued during the study is included in the bibliography.

1.1.3 Related Activities

An important activity that has paralleled the Hughes work is a contamination assessment performed by NASA-Ames. Based on the predictions of the Orbiter contaminant sources and densities given by References 1-8 and 1-9, Dr. Janet P. Simpson and Dr. Fred Witteborn at Ames predicted the background that would be seen by a sensitive telescope (Ref. 1-10). Also, all data that were available on particulates seen during space flights, including Skylab and one military vehicle, were reviewed and studied. The results are also reported in Reference 1-10, and are used herein. Work on contaminant background is continuing at Ames, and now includes development of an infrared radiometer to fly on early Shuttle flights to measure the background (Ref. 1-11). Ames has also performed tests to determine the number of dust particles ejected from Orbiter heat protection tiles, and plans an investigation of the dust velocity distributions for simulated leaks from pressure vessels.

Dr. Simpson at Ames has also predicted the natural infrared background from residual atmosphere at orbital altitudes (Ref. 1-12). To this must be added the zodiacal emission; the estimate that was used in this study was derived by Hughes personnel, and is reported herein.

Some technology development needs were identified during the study and these are being pursued by Ames. One is the demonstration of performance of a Joule-Thomson expansion valve for cooling the focal plane instruments to very low temperatures without inducing excessive thermal or acoustic noise. Development of the VIP system (Ref. 1-6) as a candidate for common use by Spacelab astronomy payloads has been closely coordinated with the SIRTF study. The VIP focal plane sensor, a charge-coupled-device (CCD) array, is being developed by JPL with Ames' cooperation.

Ongoing facility operations, such as the 91-cm IR telescope on the Kuiper Airborne Observatory (C-141) at Ames, have contributed to the background of this study. Similar study efforts of other proposed facilities, such as the Large Infrared Telescope on Spacelab (LIRTS) described in Reference 1-7, have been followed closely to avoid duplication of effort. An attempt has been made to coordinate with later studies such as the Infrared Astronomy Satellite

(IRAS) being carried out jointly by the Netherlands, United Kingdom and USA, to provide SIRTF results for their use.

Finally, NASA-Ames has maintained liaison with the USAF so that technology developments of mutual interest have been identified and realistic predictions of technology requirements are being made.

1.2 ADVANTAGES OF IR TELESCOPES IN SPACE

A distinguishing characteristic of infrared astronomy is the set of special techniques that it requires. Only a tiny amount of infrared energy reaches the focal plane of a telescope from an astronomical source. For ground-based telescopes, only energy in certain wavelengths escapes absorption by the atmosphere. The energy that finally reaches the telescope is superimposed on, and often hidden by, the much larger background radiating from the earth's atmosphere and the telescope. Earth-based infrared astronomers have developed a technique of spatial chopping to differentiate the source from some of the background. In this method, one of the mirrors in the optical path is oscillated so that the detector alternately sees the source plus the background, then the background only. The difference in signal should therefore be from the source itself. This technique works well in practice for strong sources, but fluctuations in the background or temperature gradients in the telescope often provide too much noise to allow detection of faint objects. Repetitive measurements and additional techniques are required in order to determine the spectral characteristics of the objects, making most investigations very time-consuming.

If the capability to do infrared astronomy is to be enhanced, it is clear that the infrared background must be reduced. A large improvement can be achieved by lifting the telescope above the earth's atmosphere; the very strong variable emission and almost complete absorption at many wavelengths are thereby avoided.

A second major improvement results from cooling the telescope so that its emission is reduced below the level that will interfere with the signal. Cooling to very low temperature is necessary, but this method of improving performance can only be applied outside the atmosphere where atmosphere

constituents will not condense on the cooled surfaces. Cooling of the optics allows the most sensitive detectors to be used with a wide field of view and large spectral bandwidths.

The advent of the Space Shuttle, with the Spacelab support equipment, will allow large, cooled infrared telescopes to be placed and operated in space and returned to earth for refurbishment. The large weight and size allowances for payloads will make it possible to build advanced scientific facilities without the extreme effort or compromise necessary to fit into less capable means of space transportation. Automatic protection against all possible malfunctions (except safety-of-flight items) is not required of the designer, because the trained operators on board can respond to nearly all unforeseen occurrences. Important cost savings will accrue from use of standard Orbiter and Spacelab components.

The preceding are a few of the advantages of using the Space Transportation System as a base for infrared astronomy. More discussion of these can be found in References 1-13 and 1-14. During the study effort, much more emphasis was placed on identifying areas where the STS might be deficient so that, through NASA-Ames, changes could be suggested during the development of the STS. The only serious concern, contamination from the Shuttle itself, was suggested by infrared astronomers at the beginning of the study. An extensive study of the sources of contaminants and their effects on the telescope performance has been carried out by NASA-Ames with help from some of the scientists. The results are reported in Reference 1-10. Contamination avoidance and prevention have been included in the SIRTF functional and operational design.

1.3 ALTERNATIVE IR FACILITIES

Space Shuttle operations allow several kinds of IR facilities to be considered besides the large cooled attached telescope. Large free-flying telescopes could be launched and retrieved by Shuttle. Some investigations require very high spatial resolution, and therefore require either a very large-aperture telescope or a long-baseline interferometer. Also, some special investigations might conveniently be carried out using relatively

small cooled infrared telescopes that can be flown as parts of an integrated astronomy payload.

Some alternate facilities have been compared from an engineering viewpoint during the work reported on herein. The limitation on kinds of IR facilities that should be considered for the early Shuttle era is mainly that of cost. Most are technically feasible; but wherever the design will require application of technology that has not been demonstrated, the cost estimate must include the projected cost of the technology development. Based on past experience, this can be very high.

The initial and operational cost of a free-flying, large, cooled infrared telescope is seen as significantly higher than for the same size telescope in the sortie mode. This results partly because to take full advantage of the mission, very long durations will be desired, and because greater reliability will be required during such missions. Also, the free-flying observatory cannot take advantage of Shuttle/Spacelab power, data handling, computation, pointing, and other subsystems. These, therefore, must be specially designed or at least specially assembled and integrated from standard components.

Some infrared astronomy objectives would benefit from the increased resolution that could be achieved by a very large ($\geq 3\text{m}$) aperture telescope in space. A cooled telescope of this size will require mirror material development. Specially-processed beryllium is the most suitable material; but this processing technology has only been demonstrated, and the requisite tooling developed, for mirrors of up to 1.6-m diameter.

A 3-m telescope with ambient temperature optics has also been suggested for the sortie mode (Ref. 1-7). Such a telescope would have 2 to 3 times the resolving power of SIRTF, but much poorer sensitivity, especially in the important 5- to 30- μm band.

For a telescope of this type, the mirrors could be made of one of the proven ceramics. However, unless some active means is developed to control the thermal gradients in the mirrors, the very low thermal conductivity of such material will cause gradients that will give rise to excessive noise during spatial chopping. The weight of mirrors made from ceramic is also relatively high, and this begins to become a design driver that forces cost

up. The smaller SIRTF (1.2-m) cooled telescope, which will be 100 times more sensitive at most wavelengths, can be built for about the same cost as a 2.4-m ambient telescope. Some of the objectives that might be best satisfied by a large ambient telescope will be accomplished by instruments planned for the focal plane of the Space Telescope (ST). Although the ST optics will not be cooled, it will be able to provide high resolving power and long integration times.

This study did not consider any other facilities; when the astronomers indicate an interest in pursuing advanced developments, it is assumed that NASA will direct such efforts. It is worthwhile to note that the 1.2-m diameter and 5.1-m length arrived at for SIRTF could be compatible with carrying two telescopes in the Shuttle for simultaneous use as a long-baseline interferometer; later missions of this sort could exceed the resolving power of a very large single telescope, without sacrificing sensitivity.

1.4 PLANS

Most of the areas covered by this study could be adequately investigated and defined with the information available. However, it is apparent that the Shuttle and Spacelab interfaces are still being developed and will continue to change for at least another year. NASA-Ames has therefore required that Hughes update the interfaces described herein as better information becomes available. The areas of most concern are the IPS, the command and data handling subsystem (including computation), multi-mission support equipment, and operations. The STS program is also generating more information about payload acoustic and thermal environments and about on-orbit stabilization capability that may need to be factored into the preliminary design.

One area of telescope design that NASA feels should receive additional attention is that of the image-motion-compensation control loop. Analysis will be performed and the results provided to NASA for inclusion in the VIP/SIRTF simulations at Ames and Stanford University.

As the results of the IRAS study become available, they will be reviewed to see if their proposed approaches (such as use of superfluid helium technology) should be traded off against the SIRTF baseline.

Besides the Shuttle/Spacelab interfaces, the area that most needs additional definition is that of the scientific instruments. NASA plans to obtain assistance from infrared scientists in this activity, and it is anticipated that it will result in a better definition of the internal interfaces of the SIRTF.

1.5 ORGANIZATION OF THE REPORT

Following this introduction, Section 2 of this report presents an overall picture of SIRTF as a system: telescope, focal plane instruments, cryogen supply, and Shuttle and Spacelab support subsystems. Individual subsections deal with a brief definition of MIC instruments; mechanical and data interfaces with Spacelab and Shuttle; ground support equipment; and lists of required hardware, mass properties, power, and data requirements.

Section 3 concentrates on the telescope and its performance. Optical performance analysis, optical engineering, and off-axis rejection are treated first. The second subsection describes the mechanical design and mechanical environment studies that were made. The thermal design and thermal modeling are discussed next, followed by a description of the SIRTF internal stabilization subsystem and its interface with the IPS. The section closes with an evaluation of the expected performance in the Shuttle environment.

Several major tradeoffs were conducted during the study. These are described in Section 4 and include the Gregorian versus Cassegrain telescope evaluation, aperture diameter tradeoff, CCD versus image dissector for the SIRTF star tracker, the large (2.4 to 3.0 m) ambient telescope versus SIRTF, and a dedicated gimbal versus IPS.

Section 5 discusses SIRTF operations from integration through launch and recovery. Definitions of functions for the flight crew and an initial flight operations profile are presented.

Section 6 presents the SIRTF development plan. Technology items required for development are discussed. Estimates of SIRTF procurement and program costs are presented, and the methods of deriving the costs and the inherent assumptions are described.

During the course of the study, Hughes issued some 25 reports on a variety of subjects (e.g., optical design, SIRTF stabilization).* In some cases these reports have been incorporated into the text of the final report. Where additional detail is supplied in the individual reports, this fact is noted in the appropriate section of the final report. Copies of specific reports can be obtained by interested parties from NASA-Ames.

* A complete list is given in the Bibliography, at the end of this report.

REFERENCES FOR SECTION 1

- 1-1. Study to Compile Available Information for a Space Shuttle Mounted Infrared Telescope. Martin Marietta Corporation, Denver, CO, and Honeywell Radiation Center, Lexington, MA, May 1973.
- 1-2. Proceedings of the Space Shuttle Sortie Workshop. NASA Goddard Space Flight Center, Greenbelt, MD, July 31 - August 4, 1972.
- 1-3. Final Report of the Payload Planning Working Groups, Vol. I, Astronomy. NASA Goddard Space Flight Center, Greenbelt, MD, May 1973.
- 1-4. Scientific Uses of the Space Shuttle, National Academy of Sciences, Washington, D.C., 1974.
- 1-5. Report of the Space Science Board Summer Study on Infrared and Sub-millimeter Astronomy, August 1975. Publication pending, National Academy of Sciences, Washington, D.C.
- 1-6. Lorell, K. R., Murphy, J. P., and Swift, C. D., A Computer-Aided Telescope Pointing System Utilizing a Video Star Tracker. NASA TM X-62, 505, 1976.
- 1-7. Large Infrared Telescope on Spacelab (LIRTS), Report on the Mission Definition Study. European Space Research Organization, MS(74)24, Neuilly, France, December 1974.
- 1-8. Bareiss, L. E., Rantanen, R. O. and Ress, E. B., Payload/Orbiter Contamination Control Requirement Study Final Report. Martin-Marietta Aerospace Corporation, Denver, CO, 1974.
- 1-9. Rantanen, R. O., and Ress, E. B., Payload/Orbiter Contamination Control Assessment Support Final Report. MCR 75-3, Martin-Marietta Aerospace Corporation, Denver, CO, 1975.
- 1-10. Simpson, J. P. and Witteborn, F. C., The Effect of the Shuttle Contaminant Environment on a Sensitive Infrared Telescope. To be published 1976, NASA Ames Research Center, Moffett Field, CA.
- 1-11. Witteborn, F. C., Simpson, J. P., Young, L. S., Swift, C. D., and Melugin, R. K., A Radiometer for Monitoring Column Densities of Infrared-Active Molecules. Proceedings 8th Conference on Space Simulation, NASA SP-379, 1975.
- 1-12. Simpson, J. P., Infrared Emission from the Atmosphere Above 200 km. NASA TND-8138, October 1975.

- 1-13. Witteborn, F. C., and Young, L.S., A Cooled Infrared Telescope for the Space Shuttle - The Spacelab Infrared Telescope Facility (SIRTF). AIAA Paper 76-174, presented at the 14th Aerospace Sciences Meeting, Washington, D.C., January 1976.
- 1-14. McCarthy, Stephen G., Young, Lou S., and Witteborn, Fred C., A Large Cooled Infrared Telescope Facility for Spacelab. AAS 75-234, presented at the 21st Annual Meeting, Denver, CO, August 1975.

2. SIRTF SYSTEM

This section presents the SIRTF system concept and preliminary design as it was developed during the study. Section 2.1 is an overview of the system, identifying the major subsystems and their functions and the major system-level parameters.

Section 2.2 covers the mechanical aspects of the SIRTF system and its mechanical interfaces with Spacelab and the Shuttle. Mounting of the telescope, cryogen tanks, electrical power kits, and water storage tanks are dealt with. Tables defining major SIRTF subsystems and SIRTF-supporting Spacelab subsystems give location in the payload bay, dimensions, and mass properties. Shuttle center-of-gravity restrictions are shown to be met.

Section 2.3 deals with all aspects of command, control, and data handling. The instruments in the focal plane are the source of science data and are briefly described. SIRTF needs for data handling are derived. SIRTF command requirements are tabulated, and various modes of operation (automatic, semi-automatic, and manual) are described. The combined Spacelab-Shuttle command and data management system is synthesized in a single block diagram. The section concludes with a block diagram showing the integration of SIRTF into the Spacelab/Shuttle system.

Section 2.4 presents power requirements. Section 2.5 provides a list of ground support equipment and describes the supercritical helium loading equipment.

Where reference is made in this report to "Requirements", these requirements have been taken from NASA-Ames Specification 2-24483, "Performance Requirements for Space Shuttle Infrared Telescope Facility (SIRTF)", dated July 15, 1974. This document will be referred to herein as the "SIRTF Specification". Where a design criterion has been derived from these requirements, the derivation will be described.

2.1 SIRTF FACILITY

Figure 2-1 shows a conceptual drawing of SIRTF in a 7-day flight configuration. Compatible astronomy payloads, payloads of other disciplines, or free flyers can share the mission. For example, additional instruments mounted on the Small Instrument Pointing System (SIPS) might be involved in parallel measurements of sources. Another possibility is the use of a second IR telescope at the front of the bay to provide a 15-meter-baseline interferometer.

The SIRTF telescope is mounted on the ESA-developed Instrument Pointing System (IPS), which in turn is mounted on a platform above the floor of the standard Spacelab pallet. This configuration allows SIRTF to utilize the full 60° half-angle cone capability of the IPS. Although the telescope itself is only 1.6m in diameter, the cryogen supply tanks mounted on the telescope and the requirement to rotate the telescope ±90° about its line of sight for polarization measurements results in utilization of almost the full 4.6m (15-foot) diameter of the payload bay, and produces interference at the extreme angles. Use of the platform eliminates the need for raising the IPS after arrival in orbit. A special tie-down fixture to handle launch and re-entry loads will be required, in lieu of the standard IPS fixture.

The telescope is equipped with a retractable sun shield to reduce scattered infrared radiation from the sun and earth which would otherwise reduce SIRTF sensitivity by increasing the background; the shield also reduces the heat load which must be absorbed by the cryogenic cooling system, and thus reduces the quantity of cryogen which must be carried.

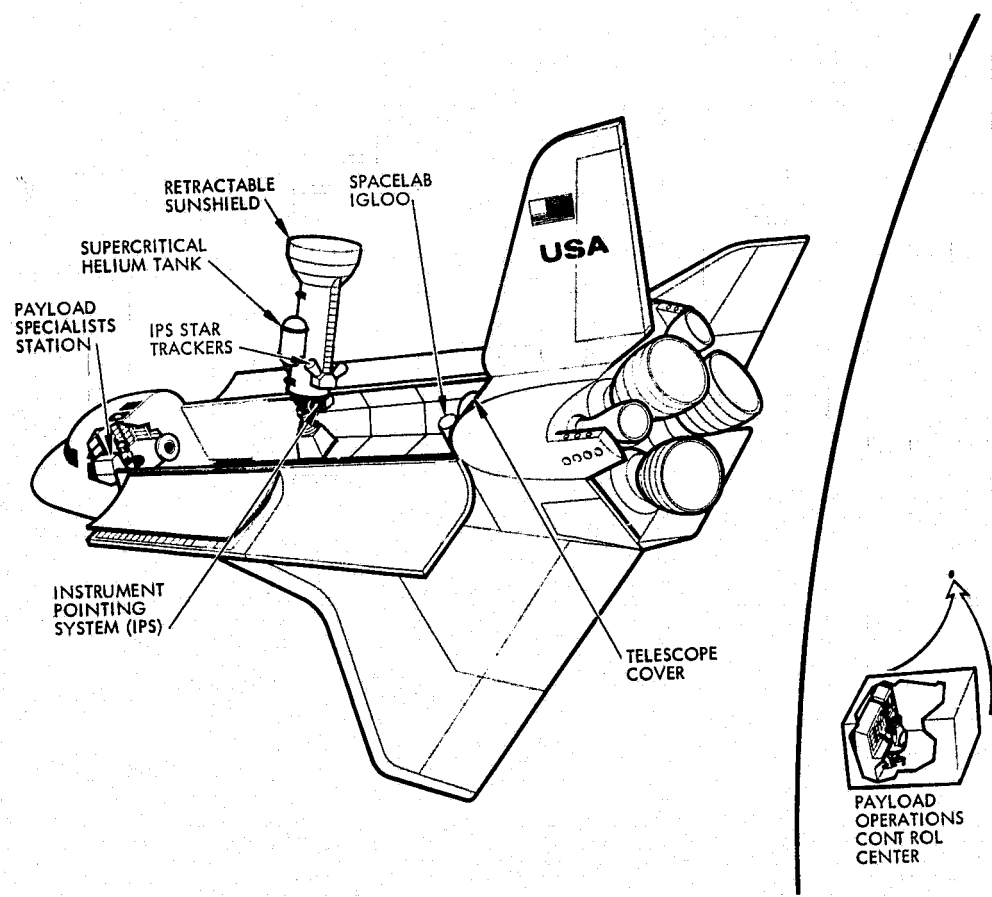


Figure 2-1. Shuttle IR telescope facility.

Two supercritical helium tanks, each of 1300 liters (45 cu ft) capacity, will provide sufficient cooling for missions up to 30 days; one tank will suffice for 14-day and shorter missions. The current favored configuration is to mount the cryogen tanks on the telescope; this eliminates the heat losses, pointing errors, and technical risks in transferring the cryogen from pallet-mounted tanks. The telescope will be covered and sealed during ascent and re-entry. The cover is mounted on a standard pallet, with fuel cell excess water storage kits also mounted on that pallet.

Besides requiring a second cryogen tank, the 30-day SIRTF mission will require additional fuel cell reactant kits and water storage tanks as shown conceptually in Figure 1-1. These kits will have a major effect on weight and center of gravity location.

Figure 2-2 is a top-level block diagram of the SIRTF system and related systems supplied by the Shuttle and Spacelab. The Multiple Instrument Chamber (MIC) is a unit which contains up to six infrared astronomical instruments such as single- or multiple-detector radiometers or photometers, polarimeters, grating spectrometers, and interferometer spectrometers. The MIC provides a separate mechanical, thermal and electrical integration structure for the instruments. These instruments will be supplied by infrared astronomers, either built in university laboratories or built by industrial firms to astronomers' specification. A selector mirror near the focal plane of the SIRTF telescope will direct the beam into one of these instruments; when a given observation is completed, the same source can be observed with another instrument or the telescope can be slewed to observe a new source. For telescope testing purposes, a substitute MIC (SUBMIC) that has the same kinds of interfaces as the MIC but only contains a single detector array has been defined.

The science data will be digitized in the MIC and transmitted through the Remote Acquisition Units to the Spacelab experiment computer for monitoring and, if necessary, further processing. The data is then transferred to the Orbiter data system for selected display at the Payload Specialist's Station and transmission to the ground. It is expected that the Tracking and Data Relay Satellite System (TDRSS) will be used whenever available to provide nearly continuous data transmission and occasional updating of command and control. Direct relay of data to the Orbiter Ground Station (OGS) is also available as a backup. Science data will be re-transmitted to the IR Astronomy Ground Station at Ames Research Center.

Onboard data reduction and display to the payload specialist will provide him with real-time evaluation of the status of the observations. The science data will be transmitted to the ground via TDRSS. During periods when the TDRSS is not available, the data must be stored temporarily. The expected science data generation rate during the early 1980's ranges up to 250 kilobits per second, and grows to 30 megabits per second in the post-1985 time frame. It thus remains within the Spacelab data rate capability of 50 megabits per second.

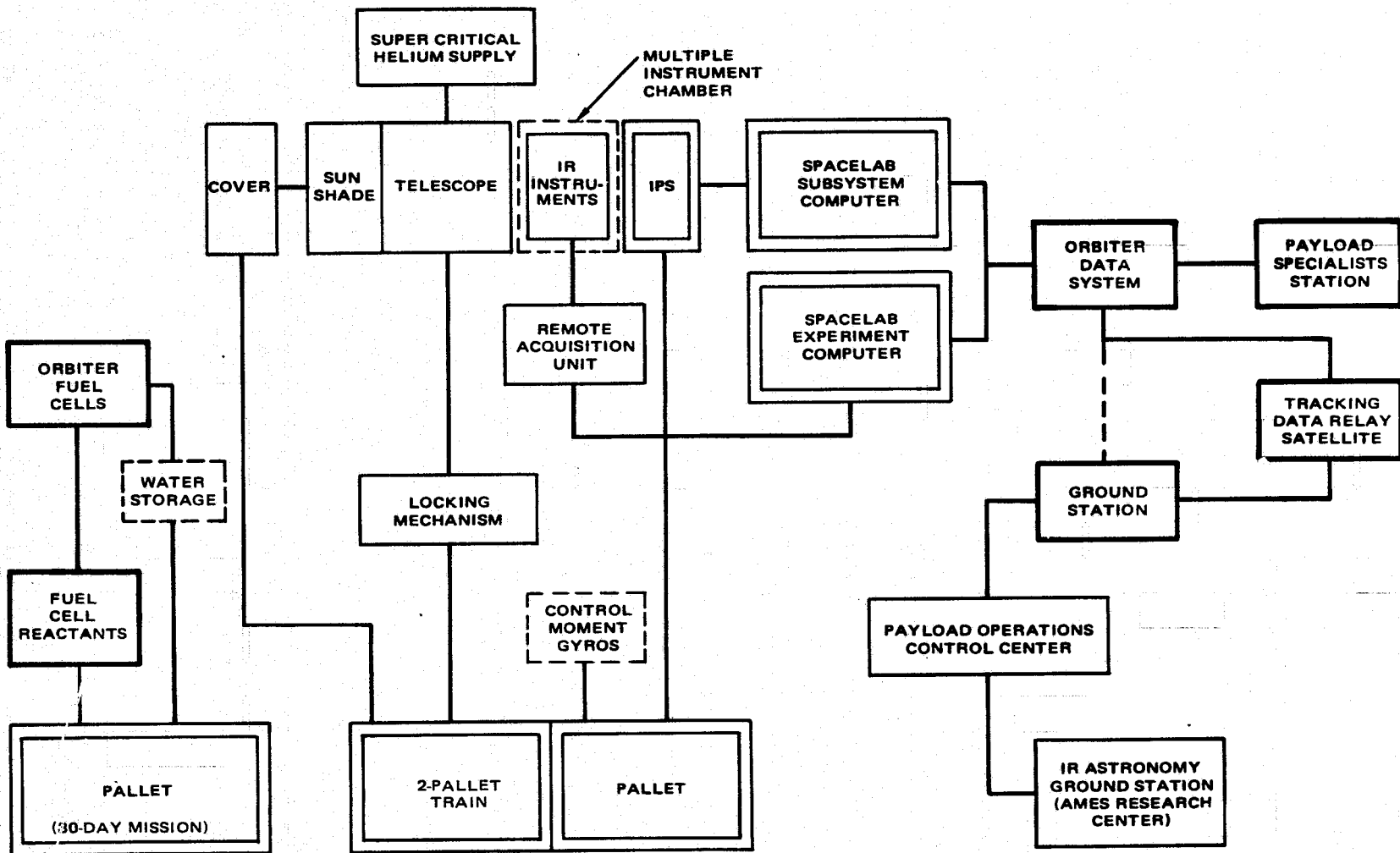


Figure 2-2. SIRTF and related Spacelab and Shuttle subsystems.

The command system follows, in reverse direction, the same onboard path as the science data flow. Although it is expected that the observing program will be stored in the Spacelab experiment computer prior to flight, modifications and updating of the observing program can be made by the payload specialist on board or by the astronomers on the ground working through the Shuttle command system. In addition to commanding the MIC instruments, the ground-based astronomers and the astronomer-astronaut will be able to command the IPS for pointing corrections, raster scans, etc.

Table 2-1 lists the major SIRTF system parameters. Figure 2-3A is an isometric of the SIRTF telescope, and Figures 2-3B and 2-3C are layouts of the telescope. The telescope selected for the study is a Gregorian configuration (discussed in more detail in Section 3); the aperture diameter was chosen to provide a collecting area equal to that of a 1-meter diameter unobscured aperture. The telescope provides diffraction-limited (at 5 μm) performance over its full 15 arc minute diameter field of view for all positions of the chop mirror. To provide high sensitivity observations of infrared sources, the telescope is cooled to between 12°K and 30°K, depending on the needs of the specific experiment.

Power consumption for SIRTF will be up to 3kW, as shown in Table 2-1. In addition to the items listed, power is required for Orbiter operation and for the mission-independent Spacelab functions. The SIRTF component category includes a maximum of 110 W for MIC instrument drives, and an allowance for science requirements not presently defined by the SIRTF Specification.

SIRTF-peculiar mass totals 8,836 to 19,229 kg. In addition to the SIRTF telescope, Spacelab subsystems, EPS kits for Orbiter and Spacelab, water storage tanks, etc., must be added. The total SIRTF-chargeable weight, including some ballast that may eventually not be required (see Sect. 2.2.1) for a 30-day mission, is at the landing limit of 14,500 kg; thus a combined attached payload is possible only for shorter missions.

TABLE 2-1. SIRTF SYSTEM PARAMETERS

Telescope	
Aperture diameter	1.16m
Field of view diameter	15 arc min
Space chopping throw	7.5 arc min
Resolution	diffraction-limited at $\lambda = 5 \mu\text{m}$ (3.5 arc sec dia)
Temperature	12 to 30°K
Sensitivity (NEP) (10 μm band width)	
5 μm to 30 μm (1 arc min FOV)	$1 \times 10^{-17} \text{ W}/\sqrt{\text{Hz}}$
5 μm to 30 μm (diffraction-limited FOV)	$1 \times 10^{-18} \text{ W}/\sqrt{\text{Hz}}$
30 μm to 200 μm (1 arc min FOV)	$1 \times 10^{-16} \text{ W}/\sqrt{\text{Hz}}$
Supercritical helium supply	
Open cycle (1300-liter tanks)	
7-14 day mission	1 tank
14-28 day mission	2 tanks
Data rate	250 kbps
Power consumption (total maximum)	3 kW
SIRTF components	1 kW
Spacelab electronics	1 kW
IPS	1 kW
Mass	
7-day mission	
Launch	8,836 kg
Landing	7,912 kg
30-day mission	
Launch	19,229 kg
Landing	14,494 kg

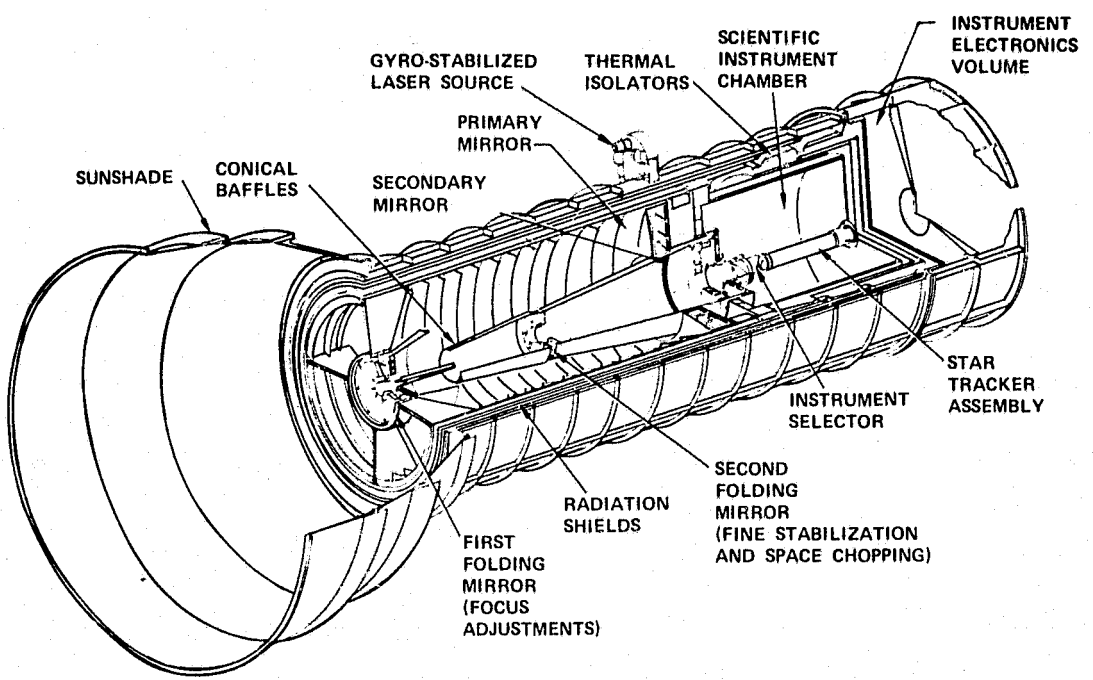


Figure 2-3A. SIRTF telescope (isometric view).

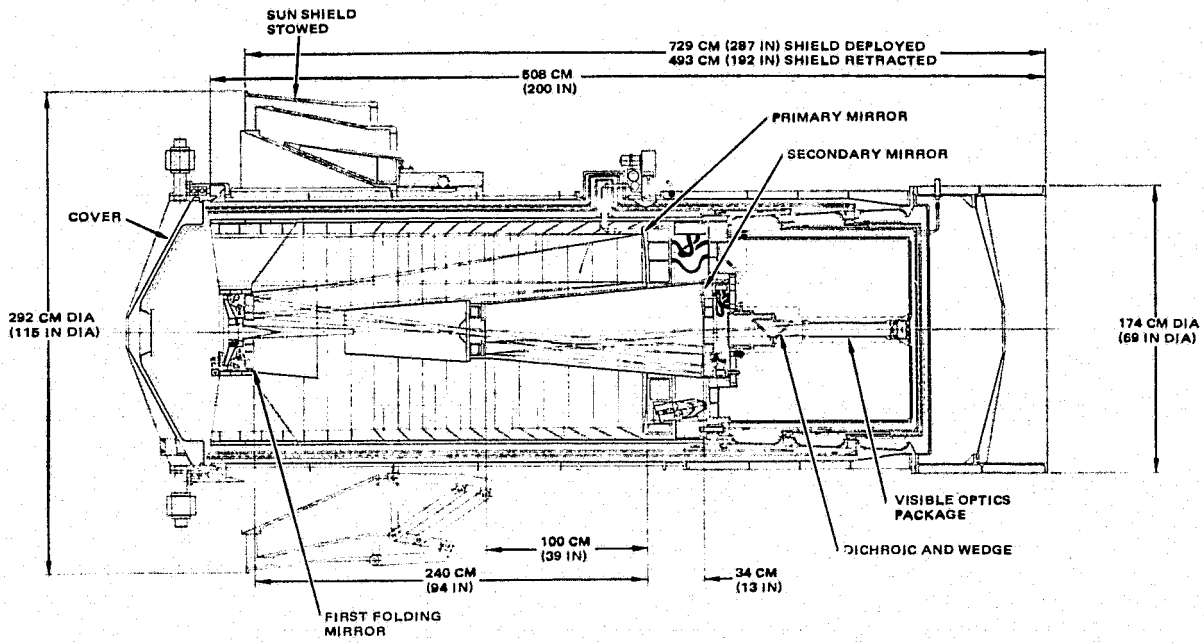


Figure 2-3B. SIRTF telescope layout (stowed sunshield).

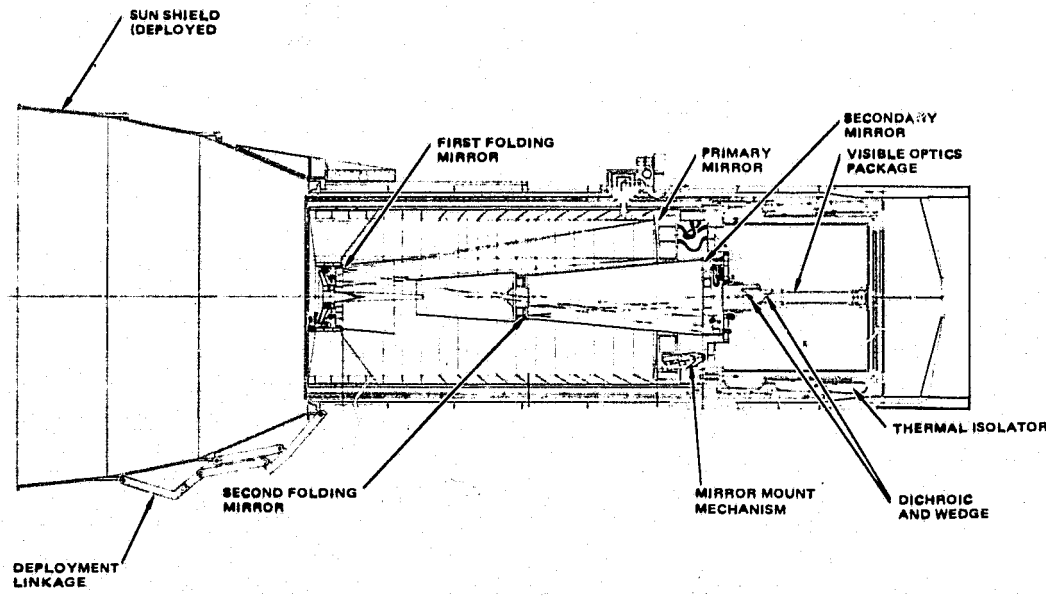


Figure 2-3C. SIRTF telescope layout (deployed sunshield).

2.2 SIRTF/SPACELAB/SHUTTLE: MECHANICAL DEFINITION

This section describes the SIRTF system, including those subsystems of Spacelab and the Shuttle that function as subsystems to SIRTF. Interfaces among these subsystems are defined. Layouts of the SIRTF system elements in the payload bay are presented for both 7-day and 30-day missions. General layouts of cables and cryogen lines are provided. A tabulation listing each SIRTF and Spacelab element and its location in the payload bay is given, as well as mass properties lists and center of gravity locations for launch and landing conditions for both 7- and 30-day missions.

2.2.1 Mechanical Interfaces

In selecting a mounting position and orientation for SIRTF in the Orbiter cargo bay, a number of constraints and requirements had to be met. The major ones are:

1. Keep within the Orbiter total load and c. g. limits.
2. Use standard Spacelab pallets for mounting, and keep within the load and c. g. limits of the pallets. Pallets may be connected.

3. Use the IPS for telescope pointing, and keep within the load and c.g. limits of the IPS gimbal.
4. Provide viewing over a 60° half-angle cone except in the region near the Orbiter tail.
5. Allow for $\pm 90^{\circ}$ rotation of the telescope about the optical axis for polarization experiments.

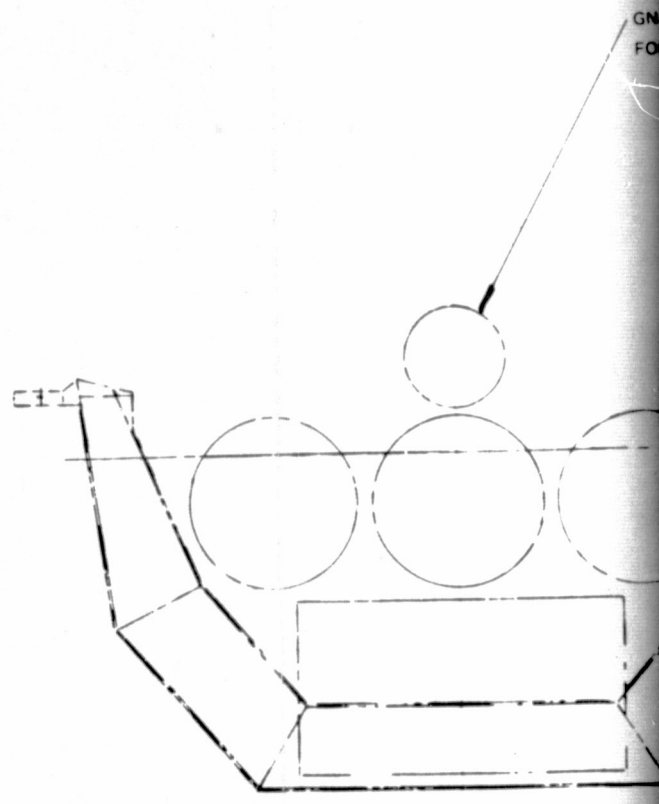
Of these, the first is a requirement for Shuttle safety, while the second and third are ground rules which were imposed on the study. The fourth and fifth can be relaxed as long as a large viewing solid angle is maintained. Reference 2-1 discusses the limitations imposed by use of the standard pallets and the advantages of dedicated pallets. Reference 2-2 discusses the design of a dedicated gimbal developed prior to the decision to baseline the IPS and is summarized in Section 4.

Those items to be located in the Orbiter cargo bay are shown on Figures 2-4 and 2-5, for the 7-day and 30-day missions, respectively. Three pallets are needed to support SIRTF for both missions, but the 30-day mission requires two more pallet segments to mount the electric power kits required by the Shuttle. These segments, together with the Igloo, occupy almost the entire length of the cargo bay for the 30-day mission. There is a clear 1.5m (5 ft) of cargo bay length, with an additional 0.9m (3 ft) of length above the Igloo, available as a minimum at the forward end of the bay for EVA ingress/egress of the crew from the cabin air lock.

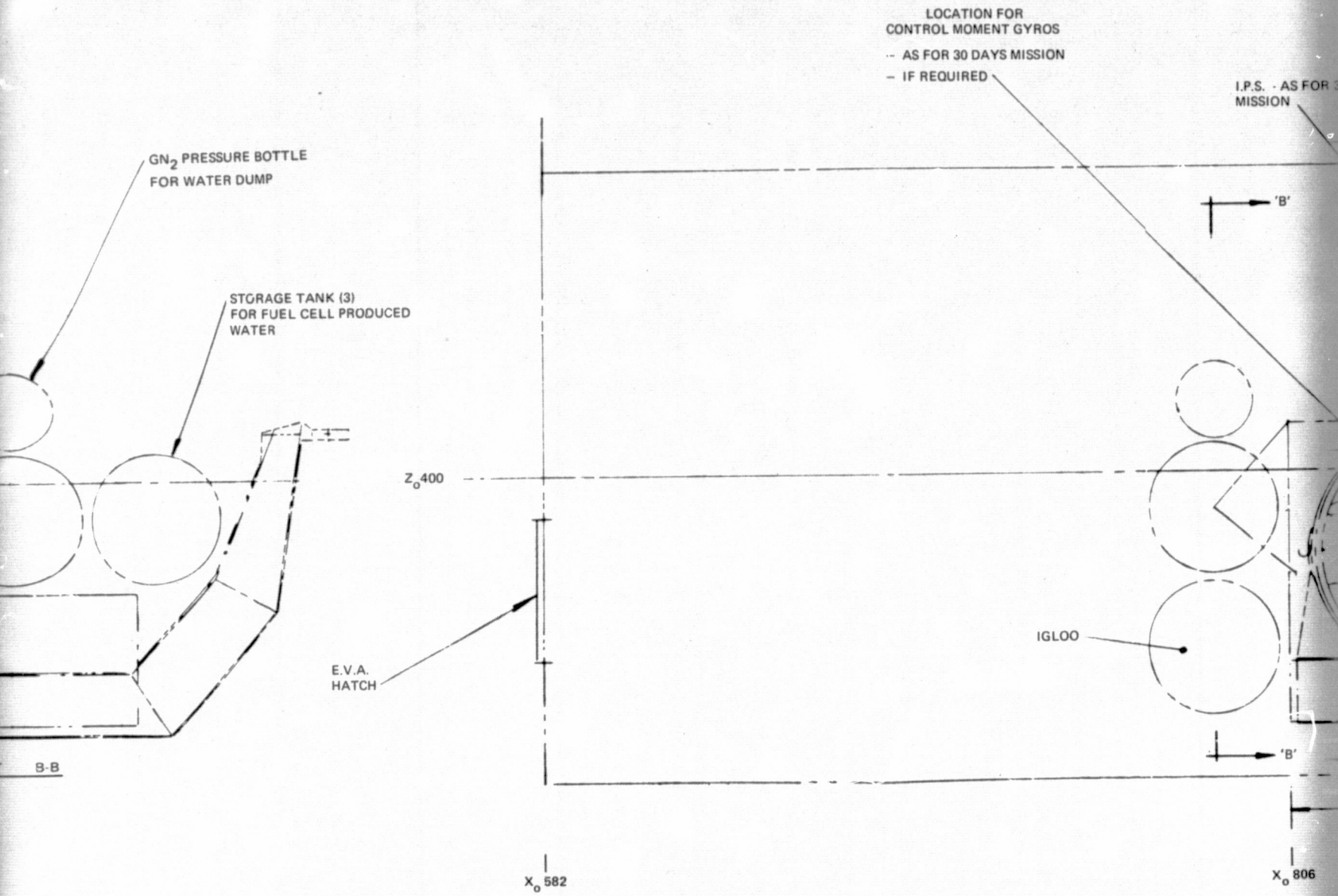
The attachment points of the pallets to the Orbiter are all at 1.5m (59 in.) pitch, or multiples thereof, and are at locations defined in Volume XIV (Reference 2-3).

The arrangement of equipment on the pallets is such that:

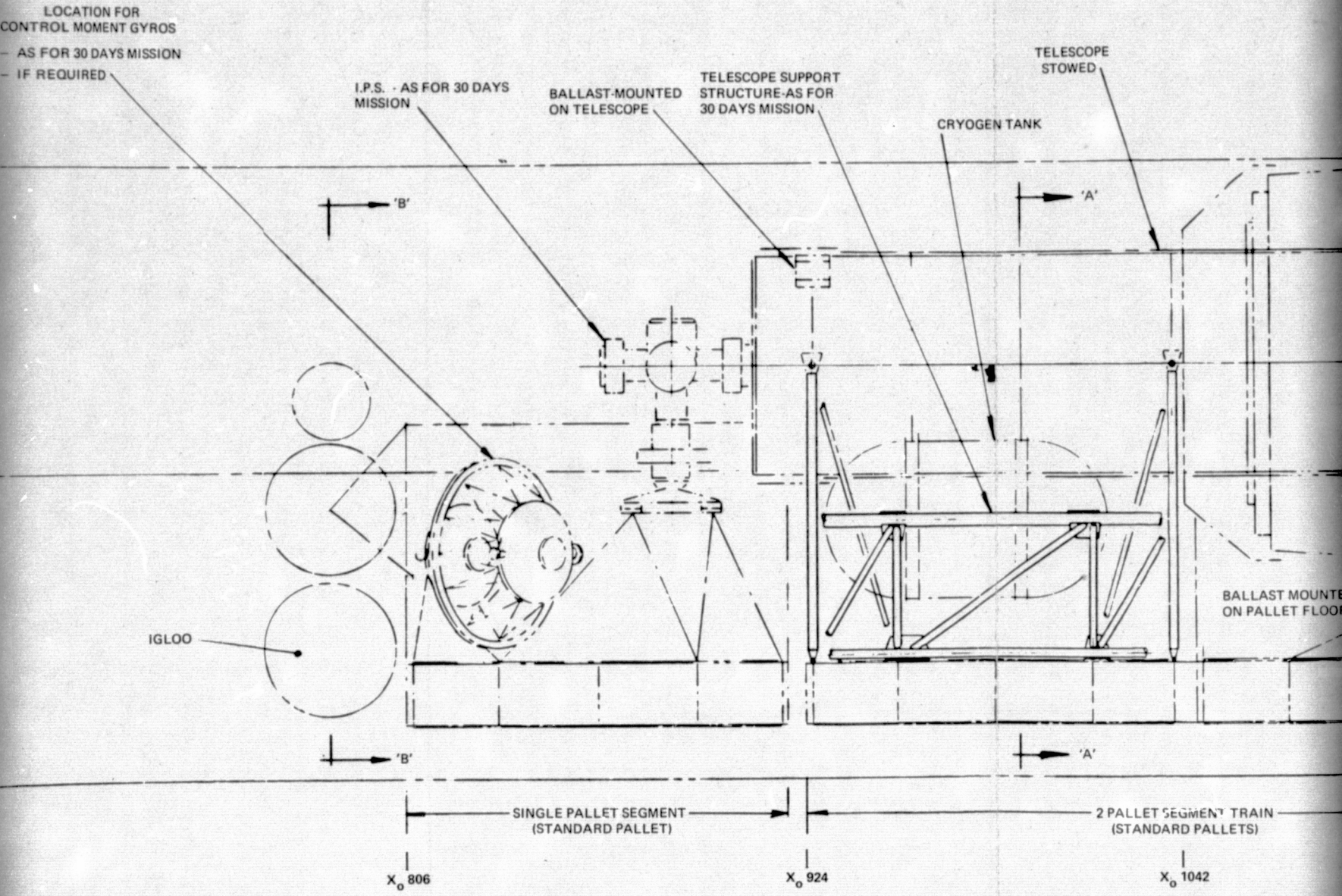
- Operational requirements are met.
- Orbiter payload c.g. limitations are not violated.
- Pallet load-carrying capabilities, to the extent that they are given in Reference 2-4, are not exceeded.
- Orbiter/pallet structural attachment capabilities are not exceeded.

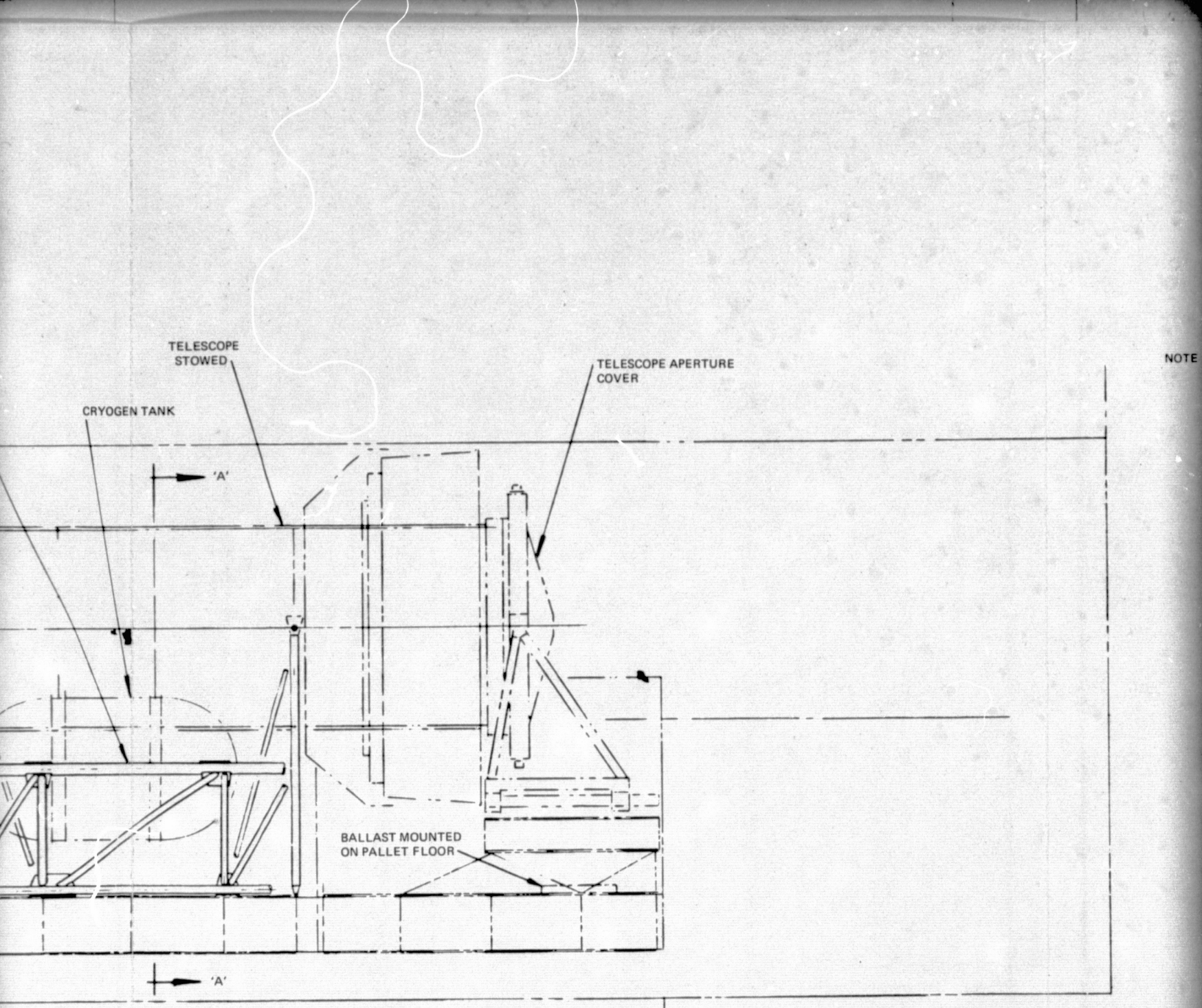


FOLDOUT FRAME |



FOLDOUT FRAME 2





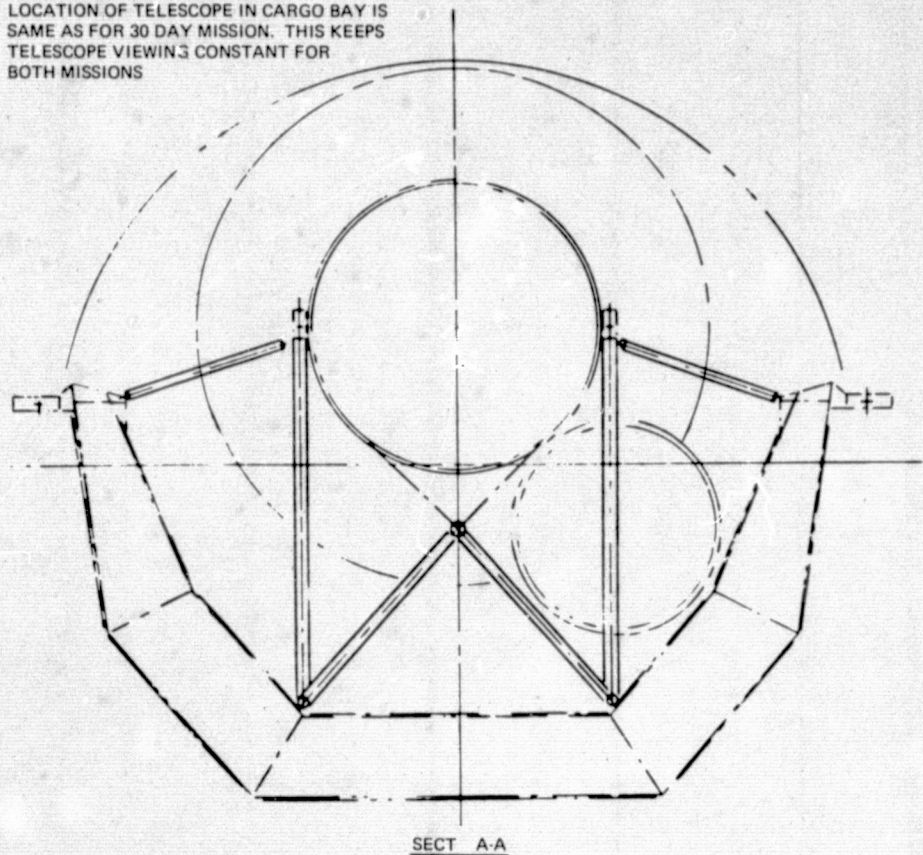
X₀ 1042

X₀ 1302

FOLDOUT FRAME 4

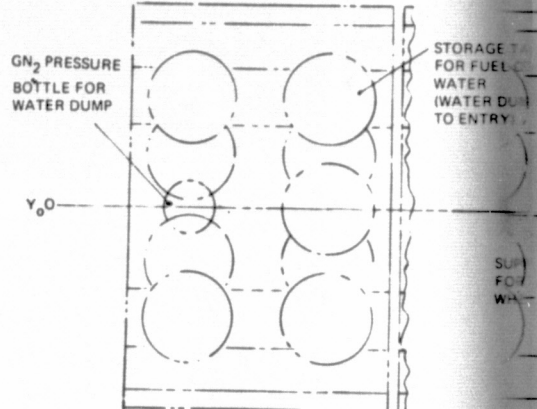
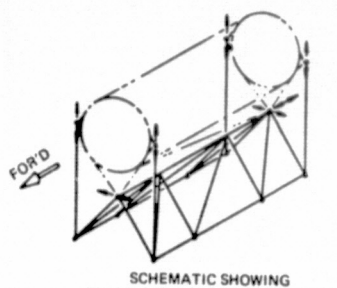
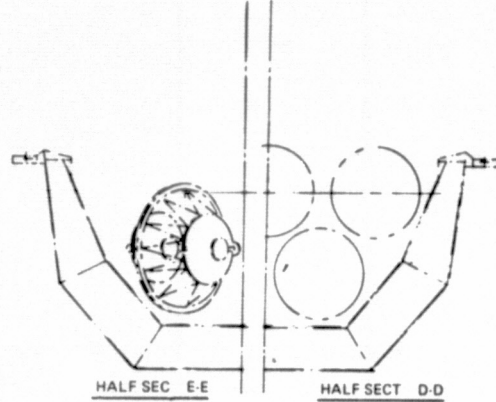
NOTE

NOTE - FOR FURTHER INFORMATION, SEE
GENERAL ARRANGEMENT FOR 30 DAYS
MISSION - FIGURE 2-5
- LOCATION OF TELESCOPE IN CARGO BAY IS
SAME AS FOR 30 DAY MISSION. THIS KEEPS
TELESCOPE VIEWING CONSTANT FOR
BOTH MISSIONS



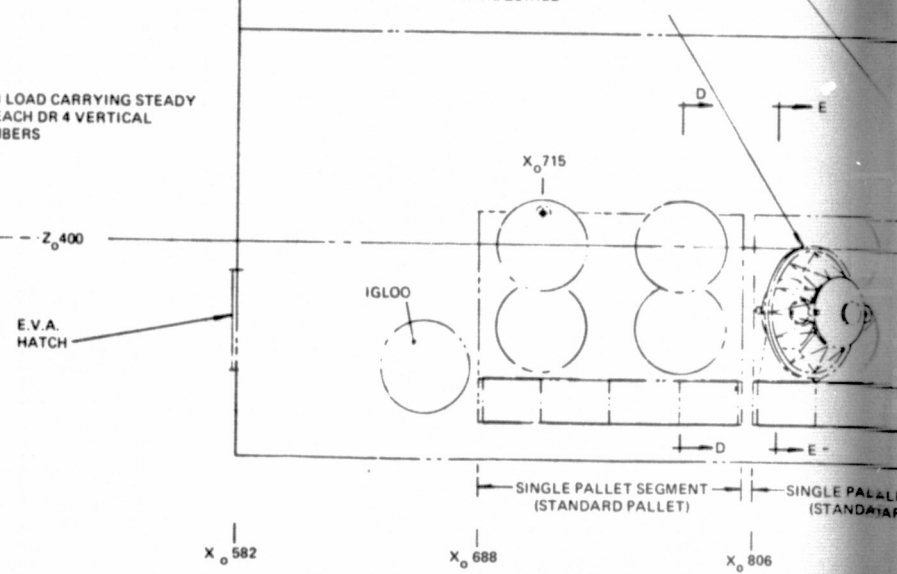
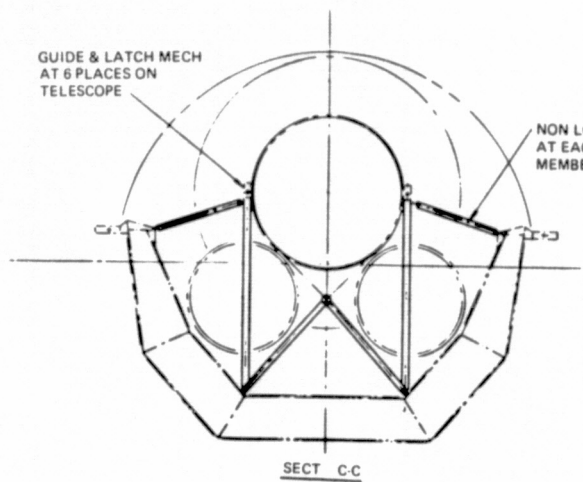
X₀ 1302

Figure 2-4. SIRTF 7-day mission -
general arrangement of equipment.



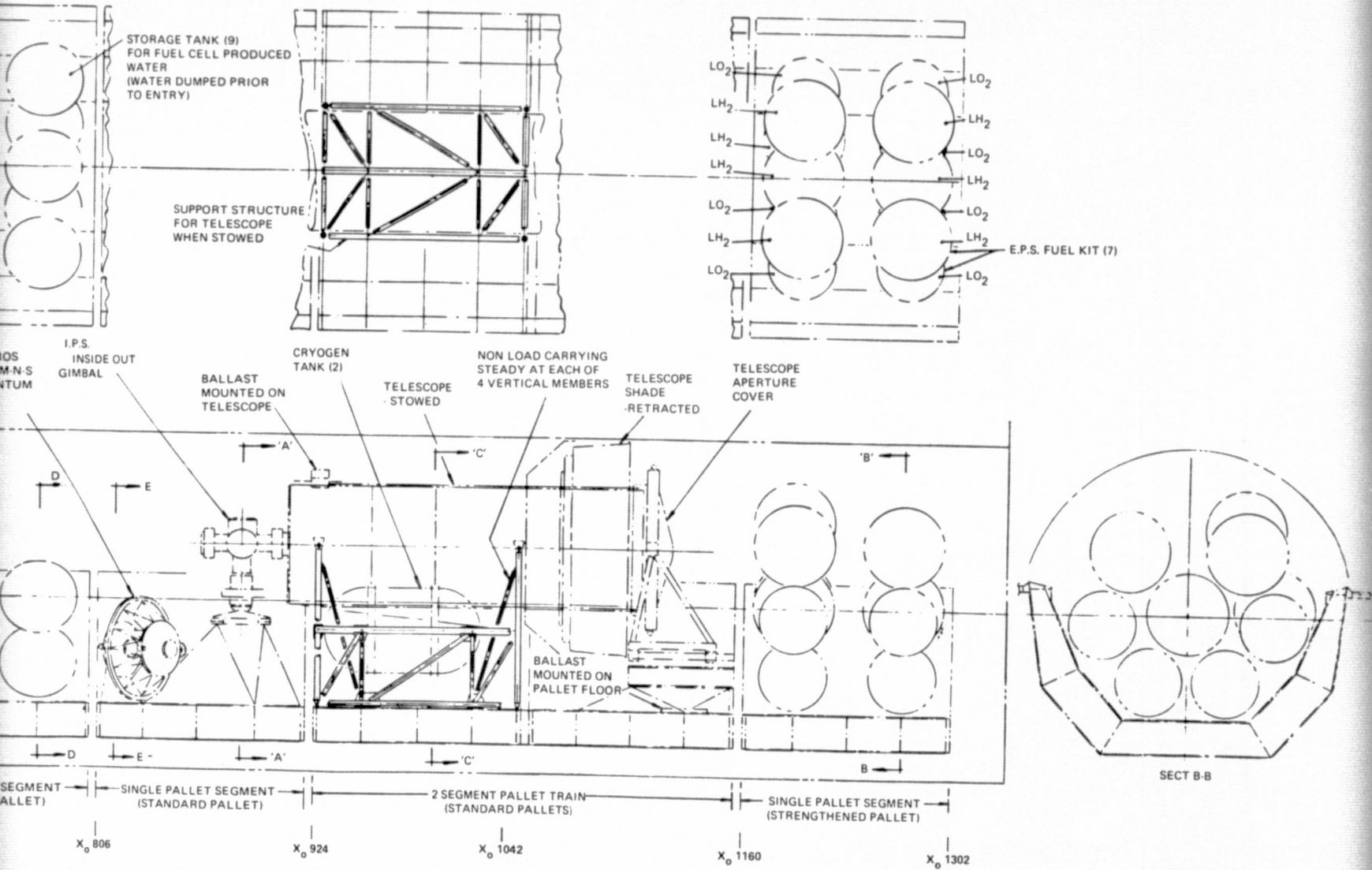
LOCATION FOR CONTROL MOMENT GYROS
-4 SINGLE GIMBAL 2712 M-N-S
(2000 FT-LB-SEC) MOMENTUM
-IF REQUIRED

I.P.S.
INSIDE OUT
GIMBAL



PRECEDING PAGE BLANK NOT FILMED

FOLDOUT FRAME



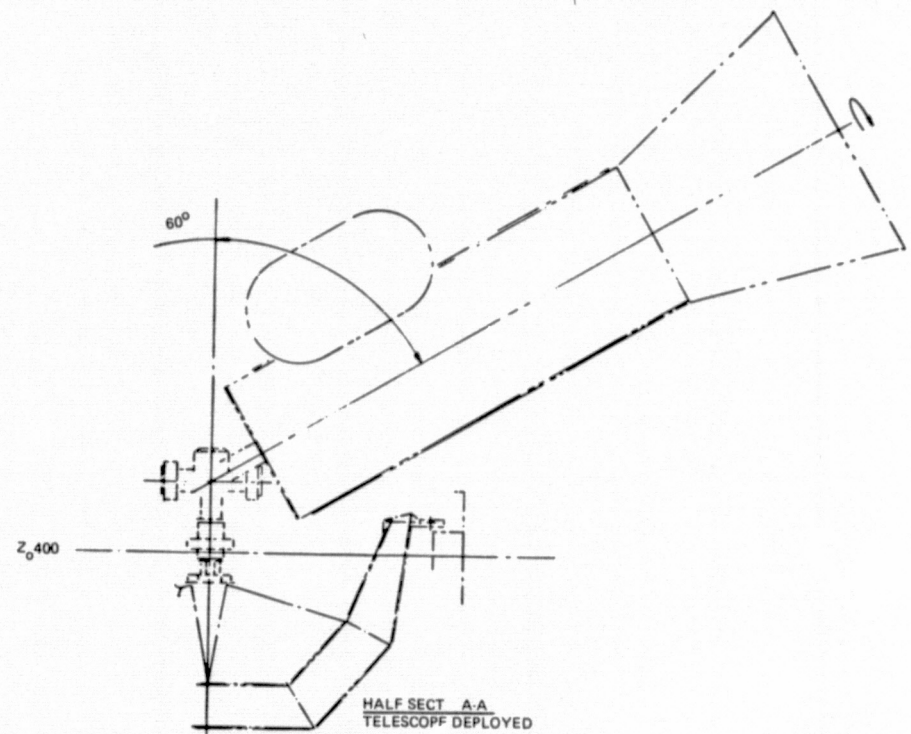
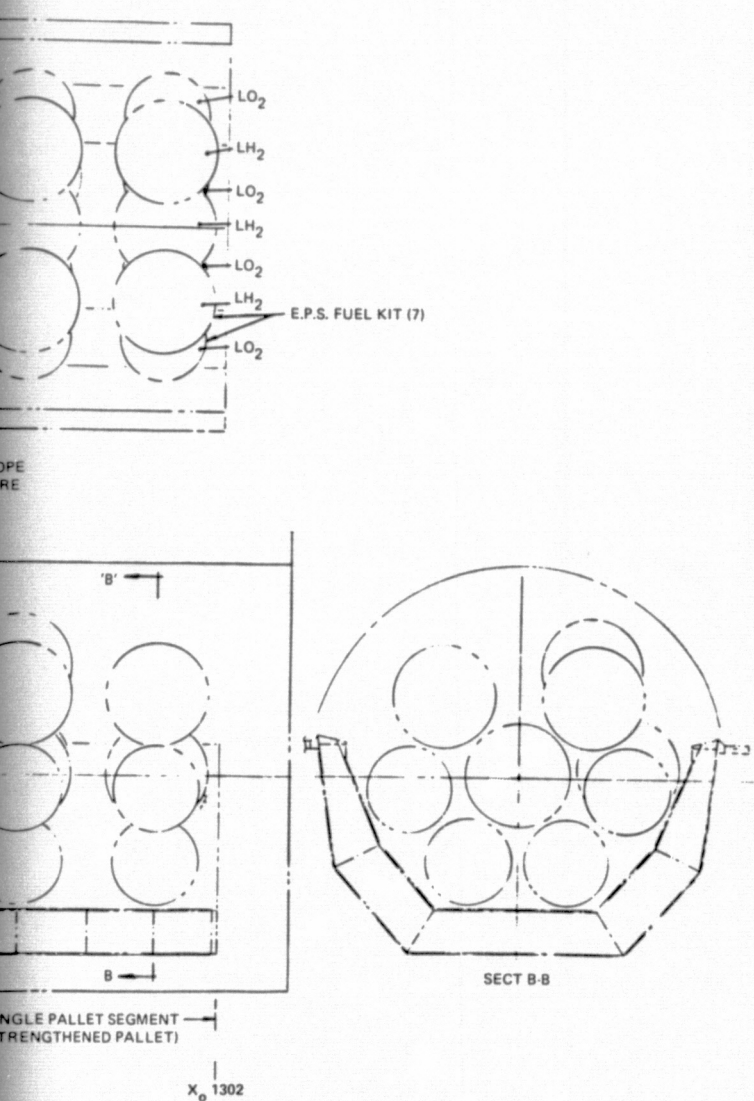


Figure 2-5. SIRTF 30-day mission – general arrangement of equipment.

7-Day Mission Arrangement

Referring to Figure 2-4, the 7-day mission configuration uses three normal-duty pallets to mount the equipment. (These are the three center pallets, with some modification, of the 30-day mission configuration.) The pallets are shown occupying the same positions in the cargo bay for both missions, which provides telescope viewing commonality. If another payload is to be flown with SIRTF on the 7-day mission, the telescope can be relocated, and it can be stowed looking forward (as illustrated in Figure 2-1). The addition of another payload is also discussed in the section on Mass Properties (Section 2.2.2).

The first pallet mounts the Instrument Pointing System. The gimbal is mounted on structure above the pallet to elevate the telescope as much as possible and thus improve its viewing capabilities. The Igloo and Forward Utility Bridge are mounted off the front of this pallet. Additionally, three storage tanks for fuel-cell-produced water are mounted off the front of this pallet, above the Igloo. A $6 \times 10^6 \text{ N/m}^2$ (1000 psi) pressure gaseous nitrogen bottle of 0.62 m (24 in) inside diameter, is mounted with the water tanks, for dumping accumulated water before entry. The vertical Igloo configuration, introduced too late for inclusion in this study, will necessitate some modification in the arrangement of water tanks. Provision is also made to mount four single-gimbal control moment gyros, of 2700 m-N-s (2000 ft-lb-sec) momentum each, should they be required for attitude control in place of the RCS. This pallet may be attached to the next two to form a three-pallet train if this proves easier for ground checkout; however, it approaches the pallet load limitation for such a train. It is not mechanically necessary for the IPS to be mounted on the same pallet as the telescope since it is not rigidly connected to the telescope during launch and landing.

Next, two normal duty pallets are connected to form a train which mounts the telescope assembly and its aperture cover. The cryogen tank is mounted on the telescope with its location determined by necessary

clearance from the pallet with the telescope stowed. The Spacelab Payload Accommodations Handbook* (Reference 2-4) defines c.g. limitations for an IPS payload of 2000 kg (4409 lb), but quotes an IPS payload mass limitation of 3000 kg (6614 lb). SIRTF equipment to be supported by the IPS amounts to 2348 kg (5176 lb), including 176 kg (388 lb) of ballast, and is therefore within the mass limitation. The ballast is mounted on the telescope to bring the c. g. of that assembly to within limits. The limits adhered to are those for the 2000 kg mass, since none are quoted for a larger mass. Another pallet-generated requirement which has been complied with is that the c. g. of a pallet payload should lie between the $Z_o = 400$ axis and 250mm (9.8 in.) above the pallet floor (Reference 2-4). It required 857 kg (1889 lb) of ballast located on the pallet floor to bring the c.g. of the items mounted on this pallet train to below the $Z_o = 400$ axis. The purpose of this requirement should be re-examined since, as it is stated, even a very small payload mounted on a pallet above the $Z_o = 400$ axis required ballast to bring the combined c.g. within limits.

There are many deployable/stowable sortie payloads similar to the telescope that will be carried by the Orbiter; therefore, it is assumed that a standard guide and latch mechanism will be designed and provided as GFE to hold such payloads, release them, and guide them in and out of the mounts. Hence, no design effort has been expended in this area. The supporting arms will have to be specially designed, however. The telescope aperture cover, with its retraction mechanism, is mounted off the pallet floor and aligned with the telescope. The telescope cover is mounted in a limited freedom gimbal to avoid loads due to flexing of the Orbiter that may cause misalignment of the pallets.

*Reference 2-5 states that the IPS limitations are based on loads on the clamps which hold the payload in the stowed position. These limitations in turn are based on assumptions about the load-carrying limitations of the pallet structure, which have not been defined yet. It is believed that the assumptions are conservative and that in all probability, the ballast will not be required.

Generally, the telescope can be gimballed $\pm 60^\circ$ from the vertical in any plane and can rotate $\pm 90^\circ$ around its axis from a fixed position. In the Orbiter lateral plane there is adequate clearance from the fixed structure forming the side of the fuselage, but geometries of the cargo bay door hinges and remote manipulator system supports are not provided (Reference 2-3) and may represent a local reduction in telescope viewing capability.

Two Orbiter standard EPS fuel cell kits are mounted under the cargo bay floor in addition to the two permanent kits.

Five storage tanks, two for water and three for waste water, are located forward of the cargo bay. Also in that area is the additional equipment at the Payload Specialist Station.

30-Day Mission Arrangement

The 30-day mission requires five pallets, the center three of which are the same as the three for the 7-day mission, with some modifications. The first pallet is a normal duty segment and mounts the storage tanks for fuel-cell produced water, together with a $2 \times 10^7 \text{ N/m}^2$ (3000 psi) pressure gaseous nitrogen bottle, 0.62 m (24 in.) inside diameter, for dumping the accumulated water before entry. There are nine storage tanks, each 1 m (39 in.) in diameter and sized to contain 477 kg (1050 lb) of water produced during the experiment operational phase of the mission. The Igloo is mounted off the front of the first pallet and contains such items as the star observation program, I/O units, and computers. The forward utility bridge routes services between the Spacelab and the Orbiter.

The second pallet is the IPS mounting pallet, identical to that of the 7-day mission.

The two-pallet train mounting the telescope assembly and the telescope aperture cover is the same as for the 7-day mission with the exception that two cryogen tanks, loaded to liquid helium density, are required for this mission. This affects the weight of ballast to be mounted on the telescope and, in turn, the weight of ballast mounted on the pallet floor. Support structures for the telescope and the aperture cover are unchanged.

The most aft pallet is a single-segment heavy duty unit that supports nearly double the standard pallet load. Seven Orbiter standard EPS fuel kits are mounted on this pallet. Since there probably will be many Orbiter payloads requiring these kits in varying quantities, it is assumed that a standard dedicated structure designed to support them will be available as a kit instead of the standard configuration pallet. Thus, the standard pallet weight has been used in the weight lists.

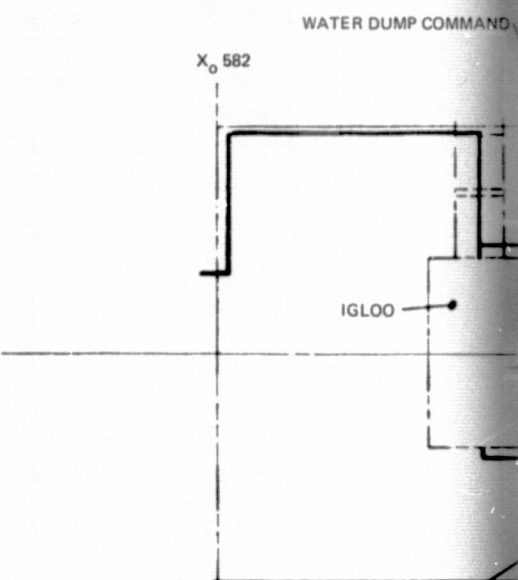
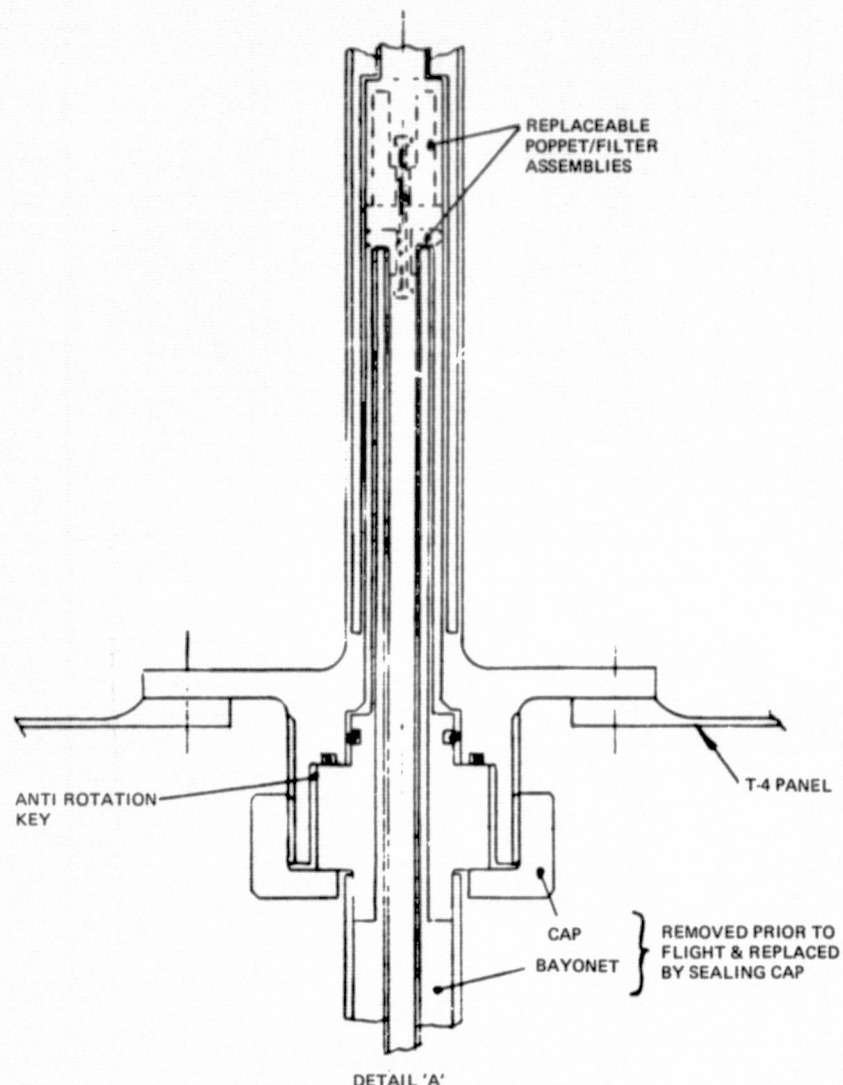
Another five Orbiter standard EPS fuel cell kits are mounted under the cargo bay floor at locations defined in the JSC Mission Kit Summary (Reference 2-6). These are in addition to the two kits permanently located there, which are not chargeable to SIRTF.

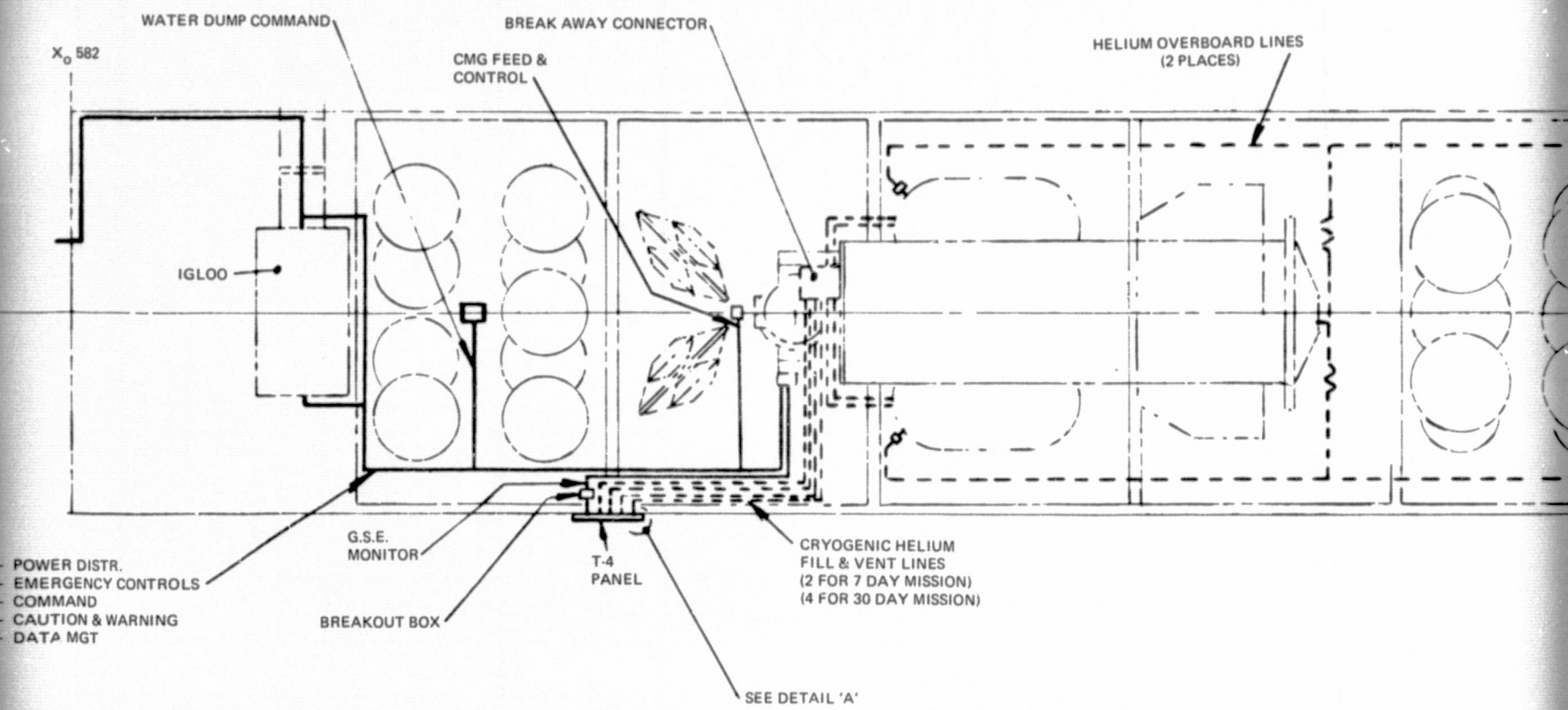
Five Orbiter standard waste storage tanks are located under the floor. These tanks are empty during ascent but contain waste during descent. Five additional storage tanks are located forward of the cargo bay, two for fresh water and three for waste water. Life support supplies for four men for 30 days are stored in the crew compartment. Additional equipment, such as video presentation and controls, are mounted in the aft flight deck.

Cables and Cryogen Lines

Figure 2-6 shows interfaces between the SIRTF and the Orbiter and the Spacelab.

The helium system lines are shown dotted to make them easily discernible. The entire flight system is checked out before installation in the Orbiter and then capped. After installation in the cargo bay, the fill and vent lines are hooked up to the T-4 panel. Flexible sections are provided in these lines to facilitate the hook-up. The caps are removed from the helium fill and vent lines at the T-4 panel, helium purge is initiated, and the lines connected to the cryogen GSE system. Helium loading is described in Section 5.9 and in References 2-7 and 2-8. When loaded, the lines are disconnected from the GSE and the flight-half poppet valves and checked for leakage and internal disconnect. Sealing caps are then placed over the flight fill and vent lines and lock-wired. The effluent helium line, which discharges overboard, is mated to a thrust neutralizer, possibly through the T-0 panel.





FOLDOUT FRAME 2

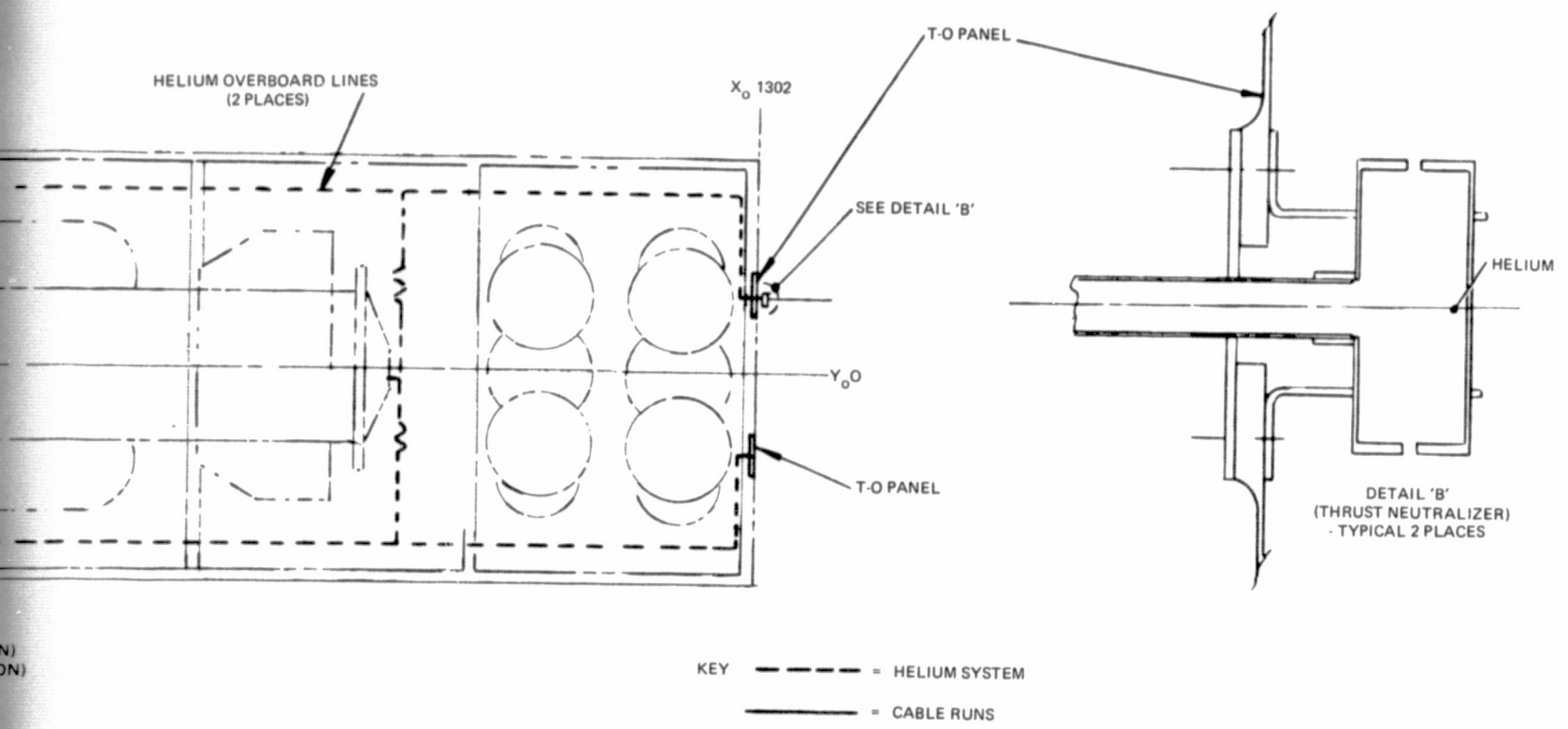


Figure 2-6. SIRTF to Orbiter/Spacelab interface and details.

The heavy, continuous lines show the wiring interfaces. Power electronics and data distribution boxes are located near the IPS gimbal. From these boxes, cables run to and from the Igloo and the crew cabin. These cables carry the following functions:

- Power Distribution
- Video to PS Star Map Display
- Scientific Data to PS Console
- Housekeeping Data to PS
- Commands to Telescope, Drive, MIC, Water Tank Dump and, if carried, CMGs
- Caution and Warning System
- Emergency Controls

GSE cables run from the power electronics box to the T-4 panel via a break-out box.

2.2.2 System Definition and Requirements

This section defines the SIRTF system described above by providing lists of equipment for the 7-day and 30-day missions including size, capacity, location, etc. The mass properties of the subsystems, and of the SIRTF system as a whole, are given. Power and data handling requirements are also given.

SIRTF Hardware Lists

Tables 2-2 and 2-3 define the SIRTF/Orbiter and SIRTF/Spacelab interfaces for both the 7-day and 30-day SIRTF missions. Sufficient details are incorporated in these tabulations to assure compatibility of SIRTF with the Spacelab and Orbiter.

Sources of the component characteristics used in the tabulations are included; where estimates were used due to lack of information, the respective items are so identified.

Mass Properties

Tables 2-4A and 2-4B summarize the launch and landing weights, with their related centers-of-gravity positions, for the 7-day and 30-day missions. The weights include all items which are weight-chargeable to the SIRTF mission. They are broken down into the pallet assemblies in the Orbiter cargo bay, the "under the cargo bay floor" installation, and the crew compartment installation. The centers-of-gravity for launch and landing of each mission are within the acceptable limits for Orbiter payloads (JSC 07700 Volume XIV Reference 2-3) and are shown graphically.

With the 7-day mission, volume and weight are available for a payload to be flown with SIRTF. The SIRTF can be positioned at various locations in the payload bay. Companion sortie payloads must have landed weights less than 6600 kg (14,535 lb). Assuming the c.g. of the additional payload to be at its midpoint, the combined c.g. of SIRTF and this payload falls within the allowable limits, as shown on the plot in Table 2-4A. There could be some limitation of the SIRTF telescope viewing due to its change in position.

Since, in general, additional payloads will not be exactly 6600 kg mass and will not have their c. g.'s at their midpoints, each must be examined individually. Further, if the CMGs are not needed, the water tanks and pressure bottle can be stored on the IPS pallet.

Tables 2-5 and 2-6 give further breakdown on the masses quoted in Tables 2-4A and 2-4B. The control moment gyros are an alternate to RCS control, and until a decision is made to use them, are not included as a baseline mass. The majority of items have given masses. It is assumed that appropriate contingencies have already been included in these masses. Table 2-7 provides detail on Spacelab subsystem masses.

Where it was necessary to estimate masses for items not given, a 10-percent contingency has been included. No contingencies have been added for water, cryogen, power storage and reactants.

ITEM NO.	QTY	ITEM DESCRIPTION ^[1]	LOCATION (ORBITER COORDINATES) ^[2]						ENVIRONMENT (LOCATION) NOTE ^[1]	F		
			X		Y		Z					
			MM	IN.	MM	IN.	MM	IN.				
1	(3)	STANDARD PALLET										
1.1	3	- NORMAL DUTY #1	21869	861	0	0	9119	359	P/L BAY	MECHANICAL		
		#2	24841	978	0	0	9119	359	P/L BAY	MECHANICAL		
		#3	27838	1096	0	0	9119	359	P/L BAY	MECHANICAL		
1.2	1	- INTERPALLET STRUCTURE	26340	1037	0	0	9119	359	P/L BAY	MECHANICAL		
2	1	IGLOO	19863	782	0	0	8865	349	P/L BAY	PROVIDED		
2.1	1	FORWARD UTILITY BRIDGE	19863	782	1600	63	8865	349	P/L BAY	SERVICE		
3	1	TELESCOPE ^[4]	25222	993	0	0	10947	431	P/L BAY	SCIENTIFIC		
3.1	1	TELESCOPE COVER WITH MOUNT	28219	1111	0	0	10439	411	P/L BAY	EVACUATE		
3.2	1	COVER SUPPORT STRUCTURE	28473	1121	0	0	9220	363	P/L BAY	CONTAMINANT		
4	1	INSIDE OUT GIMBAL IPS	22454	884	0	0	10846	427	P/L BAY	SUPPORT		
5	(2)	BALLAST										
5.1	1	- ON TELESCOPE ^[4]	23520	926	584	23	11836	466	P/L BAY	LOG IPS C		
5.2	1	- ON PALLET	28600	1126	0	0	8484	334	P/L BAY	PALLET		
6	1	TELESCOPE MOUNT STRUCTURE	24867	979	0	0	9398	370	P/L BAY	STOWED		
7	1	CRYOGEN TANK	24663	971	-889	-35	9771	385	P/L BAY	TELESCOPE		
7.1	1	FILL LINE FROM/TO	29955/24226	825/953	-2743/-914	-108/-36	8890/9779	350/385	P/L BAY	CRYOTA		
7.2	1	VENT LINE FROM/TO	29955/24226	825/953	-2743/-914	-108/-36	8894/9779	350/385	P/L BAY	CRYOTA		
7.3	1	EMERGENCY DUMP LINE FROM/TO	29370/29226	958/1130	-1720/-1605	-59/-75	9779/9398	385/370	P/L BAY	OVERPRESSURE		
7.4	1	OPERATIONAL VENT FROM/TO	29370/29226	1147/1307	-127/-889	-35/-35	10922/9017	430/355	P/L BAY	OPERATOR		
8	3	WATER RETENTION TANK ^[5]	19863	782	0	0	9881	389	P/L BAY	CONTAMINANT		
8.1	1	DUMP LINE FROM/TO	19863/19118	782/1307	0/-1778	0/-60	10693/9017	421/355	P/L BAY	DUMPLINE		
8.2	1	GAS PRESSURE TANK	19863	782	0	0	10160	400	P/L BAY	RE-ENTRY		
8.3	1	- RE-ENTRY LINE								LANDING		
9	(2)	ELECTRIC POWER REACTANT KIT										
9.1	2	- KITS OUTSIDE P/L										
		ENVELOPE ^[5]	26568	1046	0	0	7620	300	BELLOW P/L BAY	REACTANT		
10	1	P/L SPECIALIST (PS) PANEL	13208	520	0	0	7620	300	CABIN, ORBITER	PAYOUT		
11	2	TAPE RECORDER	13208	520	0	0	7620	300	CABIN, ORBITER	DATA STORE		
12	-	CABLES	-	-	-	-	-	-	UTILITY TUNNELS	DATA & POWER		

Notes:

- [1] - P/L = Payload
- [2] - Without Igloo. Deduct 500 Kg (1101 lb) on pallet which carries the Igloo
- [3] - Reflects either estimated cg location of components, or, end points of line
- [4] - With telescope in stowed configuration
- [5] - Location reflects the combined cg of the multitude of components
- [6] - Designed for 200 atm for 30-day mission

TABLE 2-2. 7-DAY MISSION:
INTERFACE TABULATION

LOCATION (ORBITER COORDINATES) ^[1]						ENVIRONMENT (LOCATION) NOTE ^[1]	FUNCTION	S=SIZE, OR C=CAPACITY PER UNIT		REMARKS
X	Y	Z	MM	IN.	MM	IN.		METRIC UNITS	BRITISH UNITS	
21869	861	0	0	9119	359	P/L BAY	MECHANICAL SUPPORT	C:3500 KG ^[2]	C:7709 LB ^[2]	
24841	978	0	0	9119	359	P/L BAY	MECHANICAL SUPPORT	C:3500 KG ^[2]	C:7709 LB ^[2]	
27838	1056	0	0	9119	359	P/L BAY	MECHANICAL SUPPORT	C:3500 KG ^[2]	C:7709 LB ^[2]	
26340	1037	0	0	9119	359	P/L BAY	MECHANICAL SUPPORT	-	-	
19863	782	0	0	8865	349	P/L BAY	PROVIDE PRESSURIZED VOLUME SERVICE DUCT	S:L = 188 CM, D = 95 CM	S:L = 74 IN., D = 37.4 IN.	
19863	782	1600	63	8865	349	P/L BAY		-	-	
25222	993	0	0	10947	431	P/L BAY	SCIENTIFIC OBSERVATION	S:L = 508 CM; D = 174 CM	S:L = 200 IN.; D = 69 IN.	SIZE WITHOUT SHADE
28219	1111	0	0	10439	411	P/L BAY	EVACUATION/CALIBRATION/ CONTAMINATION AVOIDANCE	-	-	
28473	1121	0	0	9220	363	P/L BAY	SUPPORT	-	-	
22454	884	0	0	10846	427	P/L BAY	TELESCOPE POINTING	C:3000 KG	C:6608 LB	DATA FROM REF. 2-4
23520	926	584	23	11836	466	P/L BAY	I0G IPS CG CONSTRAINT	-	-	CALCULATED
28600	1126	0	0	8484	334	P/L BAY	PALLET CG CONSTRAINT	-	-	CALCULATED
24867	979	0	0	9398	370	P/L BAY	STOWED TELESCOPE SUPPORT	C:2348 KG	C:5172 LB	CAPACITY FOR 30-DAY MISSION
24663	971	-889	-35	9779	385	P/L BAY	TELESCOPE COOLING	C:1.274 M ³	C:45 CF	ELMS DESIGN DERIVATIVE
22955/22956/22957/22958/22959/22960	953/-2743/953/-2743/953/-2743/953/-2743/953/-2743/953/-2743/	974/36/36/36/36/36/36/	-108/108/108/108/108/108/108/	8899/8899/8899/8899/8899/8899/8899/	359/359/359/359/359/359/359/	P/L BAY	CRYOTANK LOADING	S:12.7 MM ID	S:5 IN. ID	VACUUM JACKETED
22955/22956/22957/22958/22959/22960	953/-2743/953/-2743/953/-2743/953/-2743/953/-2743/953/-2743/	974/36/36/36/36/36/36/	-108/108/108/108/108/108/108/	8899/8899/8899/8899/8899/8899/8899/	359/359/359/359/359/359/359/	P/L BAY	CRYOTANK LOADING	S:15.9 MM ID	S:63 IN. ID	VACUUM JACKETED
22955/22956/22957/22958/22959/22960	953/-2743/953/-2743/953/-2743/953/-2743/953/-2743/953/-2743/	974/36/36/36/36/36/36/	-108/108/108/108/108/108/108/	8899/8899/8899/8899/8899/8899/8899/	359/359/359/359/359/359/359/	P/L BAY	OVERPRESSURE PROTECT'N	S:12.7 MM ID	S:5 IN. ID	EXTERNALLY INSULATED
22955/22956/22957/22958/22959/22960	953/-2743/953/-2743/953/-2743/953/-2743/953/-2743/953/-2743/	974/36/36/36/36/36/36/	-108/108/108/108/108/108/108/	8899/8899/8899/8899/8899/8899/8899/	359/359/359/359/359/359/359/	P/L BAY	OPERATIONAL REQUIRE'MT	S:12.7 MM ID	S:5 IN. ID	EXTERNALLY INSULATED
33148	1137	-122/-889	-35	10822	430	P/L BAY	CONTAMINATION AVOIDANCE	C:477 KG	C:1050 LB	SELECTED CAPACITY
19863	782	0	0	9881	389	P/L BAY	DUMP BEFORE RE-ENTRY TO REDUCE LANDING WEIGHT	S:29.2 MM ID	S:1.15 IN. ID	
19863/19863/19863	782/782/782	0/0/0	%/%/%	10693/9617/9617	421/355/355/	P/L BAY		C: .123 M ³	C:4.35 CF	CHARGED TO 70 ATM ^[6] N ₂
19863	782	0	0	10160	400	P/L BAY				1 EA LH ₂ & LO ₂ TANK
26568	1046	0	0	7620	300	BELLOW P/L BAY	REACTANTS FOR EL. POWER	C: per kit - 41.8 KG LH ₂ 354.6 KG LO ₂	C: per kit - 92 LB LH ₂ 781 LB LO ₂	AS FOR PHASE I
13208	520	0	0	7620	300	CABIN, ORBITER	PAYOUT MEAS. & CONTR.	-	-	ADDED TO STD ORBITER
13208	520	0	0	7620	300	CABIN, ORBITER	DATA STORAGE	-	-	
-	-	-	-	-	-	UTILITY TUNNELS	DATA & COMMAND LINES	-	-	

10 Kg (1101 lb) on pallet which carries the Igloo
cg location of components, or, end points of line
configuration
combined cg of the multitude of components
30-day mission

ITEM NO.	QTY	ITEM DESCRIPTION ^[1]	LOCATION (ORBITER COORDINATES) ^[2]						ENVIRONMENTAL (LOCATION) ^[3] NOTE ^[4]	
			X		Y		Z			
			MM	IN.	MM	IN.	MM	IN.		
1		STANDARD PALLET								
1.1	4	— NORMAL DUTY #1	18872	743	0	0	9119	359	P/L BAY	
		— #2	21869	861	0	0	9119	359	P/L BAY	
		— #3	24841	978	0	0	9119	359	P/L BAY	
		— #4	27538	1096	0	0	9119	359	P/L BAY	
1.2	1	— HEAVY DUTY	30835	1214	0	0	9119	359	P/L BAY	
1.3	1	— INTER PALLET STRUCTURE	26340	1037	0	0	9119	359	P/L BAY	
2	1	IGLOO	16866	664	0	0	8865	349	P/L BAY	
2.1	1	FORWARD UTILITY BRIDGE	16866	664	1600	63	8865	349	P/L BAY	
3	1	TELESCOPE ^[4]	25222	993	0	0	10947	431	P/L BAY	
3.1	1	TELESCOPE COVER WITH MOUNT	28219	1111	0	0	10439	411	P/L BAY	
3.2	1	COVER SUPPORT STRUCTURE	28473	1121	0	0	9220	363	P/L BAY	
4	1	INSIDE OUT GIMBAL IPS	22454	884	0	0	10846	427	P/L BAY	
5	(2)	BALLAST								
5.1	1	— ON TELESCOPE ^[4]	23520	926	0	0	11862	467	P/L BAY	
5.2	1	— ON PALLET	28600	1126	0	0	8484	334	P/L BAY	
6	1	TELESCOPE MOUNT STRUCTURE	24867	979	0	0	9398	370	P/L BAY	
7	2	CRYOGEN TANK ^{[4], [5]}	24663	971	0	0	9779	385	P/L BAY	
7.1	2	FILL LINE FROM/TO	20852/ 24208	823/ 914	-2743/ -36	-108/ 36	8999/ 8999/ 385/ 385/		P/L BAY	
7.2	2	VENT LINE FROM/TO	20852/ 24208	823/ 914	-2743/ -36	-108/ 36	8999/ 8999/ 385/ 385/		P/L BAY	
7.3	2	EMERGENCY DUMP LINE FROM/TO	24332/ 29210	996/ 1196	-1270/ -1905	-150/ -150	9768/ 9368/ 385/ 385/		P/L BAY	
7.4	2	OPERATIONAL VENT FROM/TO	20932/ 33148	1133/ 1307	-127/ -889	-150/ -35	10982/ 9017/ 385/ 385/		P/L BAY	
8	9	WATER RETENTION TANK ^[3]	18974	747	0	0	9804	386	P/L BAY	
8.1	1	DUMP LINE FROM/TO	18172/ 18161	730/ 715	0	0	8804/ 10160	385/ 400	P/L BAY	
8.2	1	GAS PRESSURANT TANK	18161	715	0	0	10160	400	P/L BAY	
9	(12)	ELECTRIC POWER REACTANT KIT								
9.1	5	— KITS OUTSIDE P/L ENVELOPE ^[5]	27508	1083	0	0	7620	300	BELOW P/L	
9.2	7	— KITS WITHIN P/L ENVELOPE ^[5]	30988	1220	0	0	9474	373	P/L BAY	
10	(5)	WASTE WATER TANK								
10.1	5	— WASTE WATER OUTSIDE P/L BAY ^[5]	26416	1040	0	0	7620	300	BELOW P/L	
11	1	P/L SPECIALIST (PS) PANEL	13208	520	0	0	7620	300	CABIN, ORB	
12	2	TAPE RECORDER	13208	520	0	0	7620	300	CABIN, ORB	
13	—	CABLES	—	—	—	—	—	—	UTILITY TUBES	

Notes:

- [1] — P/L = Payload
- [2] — Without Igloo. Deduct 500 Kg (1101 lb) on pallet which carries the Igloo.
- [3] — Reflects either estimated cg location of components, or, end points of lines.
- [4] — With telescope in stowed configuration
- [5] — Location reflects the combined cg of the multitude of components

PRECEDING PAGE BLANK NOT FILMED

FOLDOUT FRAME

TABLE 2-3. 30-DAY MISSION:
INTERFACE TABULATION

STRUCTURE	LOCATION (ORBITER COORDINATES) ⁽¹⁾						ENVIRONMENT (LOCATION) NOTE ⁽¹⁾	FUNCTION	S-SIZE, OR C-CAPACITY PER UNIT		REMARKS			
	X		Y		Z				METRIC UNITS					
	MM	IN.	MM	IN.	MM	IN.			C:3500 KG ⁽²⁾	C:7709 LB ⁽²⁾				
STRUCTURE	18872	743	0	0	9119	359	P/L BAY	MECHANICAL SUPPORT	C:3500 KG ⁽²⁾	C:7709 LB ⁽²⁾				
	21869	861	0	0	9119	359	P/L BAY	MECHANICAL SUPPORT	C:3500 KG ⁽²⁾	C:7709 LB ⁽²⁾				
	24841	978	0	0	9119	359	P/L BAY	MECHANICAL SUPPORT	C:3500 KG ⁽²⁾	C:7709 LB ⁽²⁾				
	27838	1096	0	0	9119	359	P/L BAY	MECHANICAL SUPPORT	C:3500 KG ⁽²⁾	C:7709 LB ⁽²⁾				
	30835	1214	0	0	9119	359	P/L BAY	MECHANICAL SUPPORT	C:6000 KG ⁽²⁾	C:13216 LB ⁽²⁾				
	26340	1037	0	0	9119	359	P/L BAY	MECHANICAL SUPPORT	-	-				
	16866	664	0	0	8865	349	P/L BAY	PROVIDE PRESSURIZED VOLUME	S:L=188 CM; D=95 CM	S:L=74 IN.; D=37.4 IN.				
	16866	664	1600	63	8865	349	P/L BAY	SERVICE DUCT	-	-				
	25222	993	0	0	10947	431	P/L BAY	SCIENTIFIC OBSERVATION	S:L=508 CM; D=174 CM	S:L=200 IN.; D=69 IN.				
	28219	1111	0	0	10439	411	P/L BAY	EVACUATION/CALIBRATION/CONTAMINATOR AVOIDANCE	-	-	SIZE WITHOUT SHADE. DATA FROM REF.			
STRUCTURE	28473	1121	0	0	9220	363	P/L BAY	SUPPORT	-	-				
	22454	884	0	0	10846	427	P/L BAY	TELESCOPE POINTING	C:3000 KG	C:6608 LB	DATA FROM REF. 2-4			
	23520	926	0	0	11862	467	P/L BAY	IOG IPS CG CONSTRAINT	-	-				
	28600	1126	0	0	8484	334	P/L BAY	PALLET CG CONSTRAINT	-	-				
	24867	979	0	0	9398	370	P/L BAY	STOWED TELESCOPE SUPPORT	C:2348 KG	C:5172 LB	STRUCTURE DESIGNED			
	24663	971	0	0	9779	385	P/L BAY	TELESCOPE COOLING	C:1.274 M ³	C:45 CF	ELMS DESIGN DERIVATIVE			
	20955/24206	823/953	-2743/974	-108/36	8899/8799	388/388	P/L BAY	CRYOTANK LOADING	S:12.7 MM ID	S:.5 IN. ID	VACUUM JACKETED			
	20955/24206	823/953	-2743/974	-108/36	8899/8799	388/388	P/L BAY	CRYOTANK LOADING	S:15.9 MM ID	S: 63 IN. ID	VACUUM JACKETED			
	24273/24274	9550/11437	-1370/1389	-75/35	9279/9017	388/388	P/L BAY	OVERPRESSURE PROTECTION	S:12.7 MM ID	S:.5 IN. ID	EXTERNALLY INSULATED			
	39023/39148	11437/11437	-1389/1389	-75/35	10922/9017	388/388	P/L BAY	OPERATIONAL REQUIREMENT	S:12.7 MM ID	S:.5 IN. ID	EXTERNALLY INSULATED			
STRUCTURE	18974	747	0	0	9804	386	P/L BAY	CONTAMINATION AVOIDANCE	C:477 KG	C:1050 LB	SELECTED CAPACITY			
	18974/39198	747/1377	0	%	9804/9817	386/385	P/L BAY	DUMP BEFORE RE-ENTRY	S:292 MM ID	S:1.15 IN. ID				
	18161	715	0	0	10160	400	P/L BAY	TO REDUCE LANDING WEIGHT	C:123 M ³	C:4.35 CF	CHARGED TO 200 ATM N ₂			
	27508	1083	0	0	7620	300	BELOW P/L BAY	REACTANTS FOR EL. POWER	C:PER KIT- 41.8 KG LH ₂	C:PER KIT- 92 LB LH ₂	1 EA LH ₂ & LO ₂ TANK			
STRUCTURE	30988	1220	0	0	9474	373	P/L BAY	REACTANTS FOR EL. POWER	354.6 KG LO ₂	781 LB LO ₂				
	26416	1040	0	0	7620	300	BELOW P/L BAY	WASTE WATER STORAGE	C:74.9 KG	C:165 LB	REFERENCE 2-5			
	13208	520	0	0	7620	300	CABIN, ORBITER	PAYOUT MEAS & CONTROL	-	-	AS FOR PHASE I			
	13208	520	0	0	7620	300	CABIN, ORBITER	DATA STORAGE	-	-	ADDED TO STD ORBITER			
STRUCTURE	-	-	-	-	-	-	UTILITY TUNNELS	DATA & COMMAND LINES	-	-	-			

ject 500 Kg (1101 lb) on pallet which carries the Igloo.

ated cg location of components, or, end points of lines.

ved configuration

combined cg of the multitude of components

TABLE 2-4A. SIRTF MASS PROPERTIES: 7-DAY MISSION

	Mass		Center of Gravity (Orbiter Locations)		
	KG	LB	X	Y	Z
LAUNCH					
IPS pallet	2463	5428	843.1	0	383
Telescope pallet train	4767	10511	1041.9	2.2	389
Equipment under cargo bay floor	1449	3194	1046.3	0	300
Orbiter aft flight deck	157	346	520	0	300
Total/combined CG	8836	19479	968.9	1.1	370
LANDING					
IPS pallet	2460	5422	843.1	0	383
Telescope pallet train	4612	10169	1044.4	2.2	389
Equipment under cargo bay floor	683	1506	1005.2	0	300
Orbiter aft flight deck	157	346	520	0	300
Total/combined CG	7912	17443	944.5	1.6	375
<p>The graph plots weight (WT, KLB) on the Y-axis (0 to 60) against cargo bay length (FT) on the X-axis (0 to 60). Two curves are shown: one for SIRTF CG AT LANDING (solid line with 'X' marker) and one for SIRTF CG AT LAUNCH (solid line with 'XX' marker). A third curve, labeled 'LANDED CG WITH SIRTF FORWARD AND MAX WEIGHT ADDITIONAL PAYLOAD AFT', is shown as a dashed line starting at approximately 40 ft length and 55 lb weight.</p>					

TABLE 2-4B. SIRTF MASS PROPERTIES: 30-DAY MISSION

	Mass		Center of Gravity (Orbiter Locations)		
	KG	LB	X	Y	Z
LAUNCH					
Water storage pallet	1995	4397	718.5	0	364
IPS pallet	1469	3238	875.2	0	391
Telescope pallet train	5220	11508	1034.9	0	389
EPS kit pallet	5747	12670	1220	-7.0	403
Equipment under cargo bay floor	3748	8263	1082	6.8	300
Orbiter aft flight deck	1050	2315	520	0	300
Total/combined CG	19229	42391	1024.7	0	368
LANDING					
Water storage pallet	1980	4365	718.5	0	364
IPS pallet	1469	3238	875.2	0	391
Telescope pallet train	4886	10772	1039.5	0	388
EPS kit pallet	2975	6359	1216	2.3	393
Equipment under cargo bay floor	2207	4865	1042.6	0	300
Orbiter aft flight deck	977	2154	520	0	300
Total/combined CG	14494	31953	966.7	0	366
<p>The graph plots weight (WT, KLB) on the Y-axis (0 to 60) against cargo bay length (FT) on the X-axis (0 to 60). Two curves are shown: one for SIRTF CG AT LANDING (solid line with 'X' marker) and one for SIRTF CG AT LAUNCH (solid line with 'XX' marker).</p>					

**TABLE 2-5. SIRTF MASS PROPERTIES: 7-DAY
MISSION BASELINE MASSES**

	Mass Launched		Mass Landed		Notes
	KG	LB	KG	LB	
IPS PALLET	(2463)	(5428)	(2460)	(5421)	
Instrument pointing system	750	1653	750	1653	1
Gimbal support structure	50	110	50	110	2
Water storage tanks (3)	154	339	154	339	
Pressurization	48	106	45	99	
Tanks support	22	48	22	48	2
Igloo	552	1216	552	1216	
Forward utility bridge	218	481	218	481	1
Pallet	669	1475	669	1475	3
TELESCOPE PALLET TRAIN	(4767)	(10511)	(4613)	(10169)	
Telescope	1392	3069	1392	3069	
Telescope support structure	40	88	40	88	2
Aperture cover assy	585	1290	585	1290	
Cover support structure	35	77	35	77	2
Cryogen tank	163	359	163	359	
Plumbing	59	130	59	130	
Cryogen	155	342	—	—	
Ballast on telescope	125	276	125	276	
Ballast on pallet floor	858	1892	858	1892	4
Pallet train (2)	1341	2957	1341	2957	4
Pallets bridge	14	31	14	31	1
EQUIPMENT UNDER CARGO BAY FLOOR	(1449)	(3194)	(683)	(1506)	
EPS kit no. 1	709	1563	326	719	3
EPS kit no. 2	740	1631	357	787	3
ORBITER AFT FLIGHT DECK	(157)	(346)	(157)	(346)	1
Total	8836	19479	7912	17434	

1. See Table 2-7 for detail.
 2. These items include 10% contingency since they are estimated weights. All other hardware items are given weights and assumed to contain any necessary contingencies. No contingencies are allowed for water, cryogen, power storage, and reactants.
 3. Reference: "Spacelab Element Mass Properties", Marshall Space Flight Center, (No Date).
 4. Spacelab Handbook (Ref 2-4) implies but does not share ballast requirement. Note 2 also applies.

**TABLE 2-6. SIRTF MASS PROPERTIES: 30-DAY
MISSION BASELINE MASSES**

	Mass Launched		Mass Landed		Notes
	KG	LB	KG	LB	
WATER STORAGE PALLET	(1995)	(.4397)	(1980)	(4365)	
Water storage tanks (9)	461	1016	461	1016	
Pressurization	68	150	53	117	
Tanks support	35	77	35	77	2
Igloo	552	1216	552	1217	1
Forward utility bridge	218	418	218	481	3
Pallet and hard points (8)	661	1457	661	1457	3
IPS PALLET	(1469)	(3238)	(1469)	(3238)	
Instrument pointing system	750	1653	750	1653	1
Gimbal support structure	50	110	50	110	2
Pallet	669	1475	669	1475	1
TELESCOPE PALLET TRAIN	(5220)	(11508)	(4886)	(10772)	
Telescope	1392	3069	1392	3069	
Telescope support structure	40	88	40	88	2
Aperture cover assy	585	1290	585	1290	
Cover support structure	35	77	35	77	2
Cryogen tanks (2)	327	721	327	721	
Plumbing	118	260	119	262	
Cryogen	335	738	—	—	
Ballast on telescope	176	388	176	388	4
Ballast on pallet floor	857	1889	857	1889	4
Pallet train (2)	1341	2957	1341	2957	
Pallets bridge	14	31	14	31	1
EPS PALLET	(5747)	(12670)	(2975)	(6559)	
Fuel cell reactant kits (7)	5093	11228	2321	5117	
Pallet	654	1442	654	1442	3
EQUIPMENT UNDER CARGO BAY FLOOR	(3748)	(8263)	(2207)	(4865)	
EPS kit no. 1	709	1563	326	719	3
EPS kit no. 2 - 5	2960	6526	1428	3148	3
Waste storage tanks (5)	79	174	79	174	
Water	—	—	374	824	
EQUIPMENT IN CREW COMPARTMENT	(1050)	(2315)	(977)	(2154)	
Life support	893	1969	820	1808	3
Orbiter aft flight deck	157	346	157	346	1
	19229	43291	14494	31953	

(See Notes Table 2-5)

TABLE 2-7. SPACELAB SUBSYSTEM MASS DETAIL

	Mass		References
	KG	LBS	
INSTRUMENT POINTING SYSTEM	<u>750</u>	<u>1654</u>	a
Gimbal	256	564	a
Drives	126	278	a
Thermal	10	22	a
Clamps	144	317	a
Attitude measurement	57	126	a
Power electronics	27	60	a
Data electronics	24	53	a
Contingency	106	234	a
IGLOO	<u>552</u>	<u>1216</u>	
Structure/subsystems	387	853	b
Experiment computer	29	64	c
I/O unit	17	37	c
Display & symbol generator	29	64	c
Inverter 400 Hz	32	70	c
Inverter 60 Hz	58	128	c
ORBITER AFT FLIGHT DECK	<u>157</u>	<u>346</u>	
Basic installation	99	218	c
High bit rate recorder	49	108	c
Recording/communication control	6	13	c
Time display	3	7	c
PALLET (IPS MOUNT)	<u>669</u>	<u>1475</u>	
Pallet	654	1442	c
Hard points (6)	5	11	c
Experiment RAU's (2)	4	9	c
Coldplate/standoff	6	13	c
PALLET TRAIN (TELESCOPE MOUNT)	<u>1341</u>	<u>2957</u>	
Pallets (2)	1308	2884	c
Hard points (10)	8	18	c
Pallet retention mechanism	25	55	c

a. "IPS Presentation to NASA Headquarters" ESRO, 6 February 1976.
 b. "Spacelab Mass Properties Status Report," ERNO, December 1975.
 c. "Spacelab Element Mass Properties," Marshall Space Flight Center
 (no date, circa Oct. 1975).

Regarding the 30-day mission, two mass reduction possibilities are (a) the reduction in the number of water storage tanks with the consequent elimination of one pallet and (b) a dedicated structure in place of a strengthened pallet to support fuel cell reactant kits in the Orbiter cargo bay. The necessity for predicted power level is discussed in Section 2.4.

2.3 SIRTF /SPACELAB/SHUTTLE: CONTROL AND DATA MANAGEMENT

The control and data management functions for SIRTF rely heavily on the facilities provided by Spacelab and by the Shuttle as well as Shuttle support systems (Tracking Data Relay Satellite, Payload Operations Control Center). This section defines the SIRTF command and data management requirements, and describes how Spacelab and Shuttle subsystems will be utilized.

The SIRTF scientific data originates in the focal plane instruments located in the Multiple Instrument Chamber (MIC). These instruments (photometers, interferometers, spectrometers, etc.) in general generate low-voltage analog signals which are amplified and converted to digital bit streams in a processor at the MIC. The first subsection below describes some typical MIC instruments. The following sections develop the command and data needs for SIRTF and particularly for the MIC, and explain how the Spacelab and Shuttle facilities will be utilized.

2.3.1 MIC Instruments

Preliminary design of MIC instruments was not a part of the SIRTF contract. Conceptual designs for five MIC instruments were developed by the SIRTF Science Accommodations Group and Ames personnel. They are briefly described here to give an idea of the types of instruments which will be used in SIRTF.

The instruments covered include a grating spectrograph, photometer camera, lamellar grating interferometer, Michelson interferometer and a polarimeter. The nominal SIRTF complement is six instruments. Of these, four or five will typically be photometers, and the other one or two will be spectrometers of one type or another. The photometers will cover a variety

of spectral bands and will vary in complexity from simple photometers with a few detector elements to arrays of several hundred elements. As both the knowledge of IR astronomy and detector technology matures, spectrometers will be used more widely, and the complexity of the photometer arrays will increase to the level of thousands of elements by utilizing charge-coupled device technology.

Table 2-8 lists the major parameters which affect the SIRTF preliminary design. The data supplied by the SIRTSAG and Ames has been modified by Hughes as follows:

- Detector heat load is not less than 0.5 mW per detector element.
- At least one electrical feedthrough per detector element is provided. One is a minimum for transimpedance amplifiers and two are required for best performance.
- Standby heat load includes at least 0.1 mW per electrical feedthrough at $10^{\circ} - 20^{\circ}\text{K}$.

The far right columns are an attempt to bound the requirements for SIRTF. Two cases are considered: the five instruments listed, and a typical complement of four photometers and two spectrometers. The values for detector heat load and number of electrical feedthroughs are somewhat higher than would actually occur, due to the fact that it is unlikely that four photometer cameras of the high density type will be used on the same flight.

Figures 2-7 and 2-8 show outline schematics of how the five instruments may be mounted in the MIC. Further definition of the instruments is required before more detailed preliminary design of the MIC can be undertaken.

2.3.2 Command and Data Management

This section is divided into three main subsections; science data, telescope control, and engineering design of control functions. Section 2.3.3 deals with the Spacelab/Orbiter support capabilities according to the same categories.

TABLE 2-8. MIC INSTRUMENT SUMMARY

	Grating Spectrograph	Photometer Camera	Lamellar Grating Interferometer	Michelson Interferometer	Polarimeter	Totals	
						Five Instruments	Four Photometers and Two Spectrometers
Size (meters)	0.5 x 0.3 x 0.1	0 x 5 x 0.3 x 0.1	0.3 x 0.3 x 1.0	0.6 x 0.4 x 0.3*	0.1 x 0.1 x 0.1	—	—
Weight (kg)	20	10	10	16	4	60	76
Power (watts at 300°K)							
Operating	10	10	3	110	3	3.5 to 110	3.5 to 110
Standby	0.1	0.1	0.1	0.1	0.1		
Heat Load (watts at 10-20°K)							
Operating	0.4	0.4	0.4	0.4	0.2	0.75 to 1.05	1.4 to 1.6
Standby	0.2	0.25	0.06	0.06	0.16		
Momentary	1	1	—	10	1	10	10
No. Detectors	200	256/36/36	3	25	2	—	—
Det. Temp. (°K)	4	4/1.2/1.2	0.1	4	4	—	—
Det. Heat Load (mW)	100	128/18/18	2	13	2	2 to 164	2 to 164
Feedthroughs							
Mechanical	3-4	0	1	1	3	8-9	6-7
Electrical	200	328	10	60	8	600	2500
Optical	0	0	0	1	0	1	1
FOV (arc minute)	<1	>5	5	5	0.33 - 2	—	—
Data Rate (KBPS)	10	25	1	25	0.1	0.1 to 25	0.1 to 25
Special Calibration Sources	Blackbody Spectral	Blackbody	Blackbody Spectral	Blackbody Spectral	Blackbody	—	—
Venting	No	Yes	Yes	No	No	—	—

*Plus 0.2 x 0.2 x 0.3 outside MIC for a motor drive.

INSTRUMENTS SHOWN:
MICHELSON INTERFEROMETER
10-200 μ CAMERA

DIMENSION IN CM

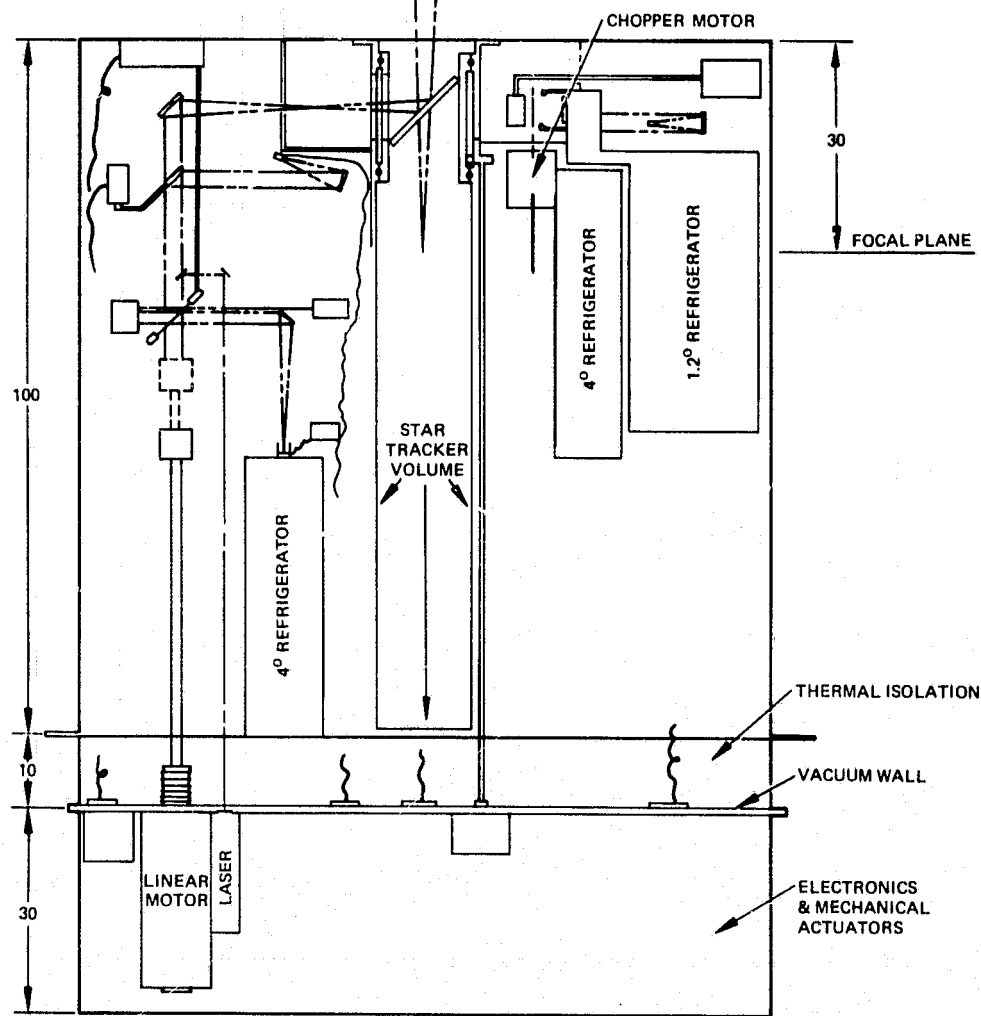


Figure 2-7. Schematic MIC layout: cross section.

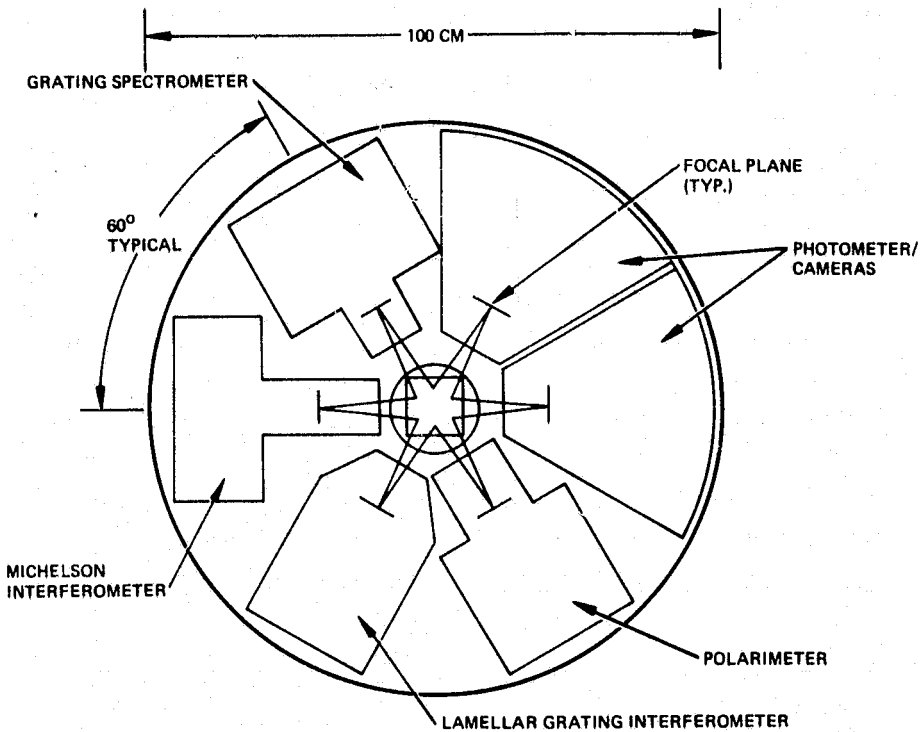


Figure 2-8. Schematic MIC layout: end view.

2.3.2.1 Science Data

Science Data Generation Rates. Estimates of the science data magnitude for SIRTF are derived from three sources: (1) conceptual designs of instruments (based largely on current ground-based instrument designs); (2) data rates and focal plane densities of current and near-term conventional detector arrays; and (3) data rates and densities of charge-coupled device (CCD) focal planes that are currently under development and are expected to be readily available in the SIRTF time frame.

The data rates are intended to be maximum realistic values, and are computed in order to evaluate the capabilities of the Spacelab/Orbiter data system as compared to SIRTF needs. It is recognized that most instruments will employ fewer detectors, lower data rates, and fewer quantization levels than the maximum values cited here.

Table 2-9 summarizes the pertinent data based on the conceptual designs of five focal plane instruments described previously. It is immediately evident that the maximum rate is 25 kbps. (Only one instrument operates at a given time.)

Discrete detector types were selected for analysis, based on their being the most likely candidates in each of the broad spectral bands that are to be covered. The response times of the detector element and of the preamplifier circuit are listed in Table 2-10. Maximum data rates for each type of detector are, of course, limited by the slower of the two response times. The sample rate values are computed on the basis of six samples per cycle, which is needed to accurately reproduce pulse shapes for narrow pulse widths.

In determining the data rate, the density of detectors in the focal plane must also be considered. For detectors in an advanced state of development (Ge:Hg, Si:As, Si:Sb, and Hg CdTe), arrays of hundreds of detectors will be available to SIRTF. The less advanced detectors will be limited to arrays of 10 to 100 unless very ambitious development programs are undertaken.

The third factor in determining data rate is the number of quantization levels. Typically, infrared detectors have dynamic ranges of 10^6 or less, and the uniformity of response limits the measurement accuracy to the order of 5 percent. Logarithmic encoding requires 8 bits to obtain 2.7×10^5 dynamic range or 9 bits for 7.1×10^{10} .

TABLE 2-9. DATA RATE BASED ON SIRTF INSTRUMENTS

Instrument	Grating Spectrograph	Photometer Camera	Lamellar Grating Interferometer	Michelson Interferometer	Polarimeter
Number of Detectors	200	328	3	25	2
Data Rate (kbps)	10	25	1	25	0.1

TABLE 2-10. DATA RATE BASED ON SIRTF DETECTORS

Detector	Ge:Hg Si:As Si:Sb	Ge:Ga	HgCdTe	InSb	Si or Ge Bolometer
Detector Response Time Constant (second)	3×10^{-8}	4×10^{-8}	1.0×10^0	2×10^{-7}	10^{-2} to 10^{-4}
Circuit Response Time Constant (second)	5×10^{-3}	2×10^{-4}	6×10^{-10}	$<< 1 \times 10^{-7}$	$<< 10^{-4}$
Sample Rate (second ⁻¹)	1.2×10^3	5×10^3	6×10^0	5×10^6	1×10^4

Alternatively, in astronomical terms, using an 8-bit word and logarithmic quantization, the star amplitude can be quantized to 0.1 magnitude (9.5 percent) over a range of 25 magnitudes, or to 0.01 magnitude (0.93 percent) over a range of 2.5 magnitudes. It appears that most experiments will be accommodated by these ranges of quantization levels so that 8-bit data words will be sufficient.

For highest sensitivity, a small region of space will be scanned repeatedly and the results co-added to lift signals out of the noise. When operating in this mode, the quantization levels will be set lower than 5 percent, but the maximum signal amplitude will be much less than the dynamic range of the detectors. Hence 8 bits appear to be adequate for quantization of most signals.

The data rate is the product of the sample rate, number of detectors, and quantization word length. For a 300-detector array of Ge:Hg detectors, the data rate is just under 3 Mbps.

Charge-coupled devices are presently being developed incorporating extrinsic silicon detector arrays. Based on results to date, high sensitivity arrays can be expected to be available in the 1980's. A typical present-day

development chip contains an array of 32×32 (1024) detector elements, and is sampled at rates of 250 ksp (samples per second) to 2.5Msps. Goals for dynamic range are 60 to 80 dB, so that an 11-bit word will be required to quantize signals to 0.01 magnitude. If it is assumed that about ten chips are grouped in the focal plane, the data rate will be on the order of 3×10^7 bps.

Table 2-11 summarizes the SIRTF data generation rates corresponding to the above discussion.

Science Data Computing Requirements. The SIRTF operating concept calls for the Payload Specialist (or Mission Specialist) to monitor telescope performance and data quality so that adjustments in pointing, chopping characteristics, scan patterns, etc. may be made as the need arises. Among other things, this operating mode calls for routine reduction of the telescope output data in near real time. Where the data rates are very high, reduction of samples of the data will be acceptable.

Processing of scans from the Michelson interferometer was chosen as representing the highest on board computing requirements both in terms of memory and of operations. A 4096-point transform was selected as representing the largest output that might be processed on board the Shuttle; it provides e.g., $1/4 \text{ cm}^{-1}$ resolution over the $5\mu\text{m}$ to $10\mu\text{m}$ band. Higher resolution scans can be processed on the ground.

TABLE 2-11. SUMMARY OF SIRTF SCIENCE DATA GENERATION RATES (kbps)

	Initial Configuration	Post-1985
Required	25	250
Maximum	250	30,000

The program requires approximately 400 16-bit words of program storage and 12,300 32-bit words of data storage. The computation time is

$$\tau \frac{N}{2} \log_2 N$$

where τ is the computer time required to perform the operation

$$A \pm (B \times C)$$

where A and B are complex data and C is a complex number. Thus, the time required is $2.5 \times 10^4 \tau$ seconds; this should be comparable to the data acquisition rate, presumably on the order of 1 second.

Science Data Transmission. SIRTF operating plans call for transmission of all data to the ground in unreduced form during flight. Methods for accomplishing the transmission will vary depending on the data rate of the experiment and the availability of TDRSS (Tracking Data Relay Satellite System) and ground stations. Unreduced data will be stored on board between ground contacts. Assuming 80-85 percent contact time, the transmission data rates are essentially the same as the generation rates discussed above.

An alternate approach, which was explored during the study, involved recording all data and retaining it on board until error-free receipt on the ground had been certified. This alternative was finally rejected for two reasons: (1) the specified TDRSS error rate is $\leq 1 \times 10^{-5}$ so that the degree of contamination in transmission is very low; and (2) an additional tape recorder (not part of Spacelab equipment) would be required, with attendant substantial power and heat rejection requirements.

2.3.2.2 Telescope Control

Overall control of SIRTF can be divided into three major categories: control of the SIRTF system, control of the IPS and its subsystems, and control of the SIRTF-related portions of the Spacelab Command and Data

Management System (CDMS). Table 2-12 lists the major command and control functions required to operate SIRTF and the IPS. While the list of Table 2-12 will grow as the SIRTF system is more fully defined, it appears that on the order of 10 to 20 on-off type commands will be required, and only a few kbps of discrete command capability will be required. The columns list the function controlled, the active component or subsystem, the component or subsystem that monitors the function, the nature of the control function (whether it occurs at a specific time, intermittently, or continuously), and finally the predominant mode of control: manual, automatic as part of the pre-programmed observation plan, or servo-controlled.

In general, servo-controlled functions will be hardwired in the SIRTF system, and commands will not be transferred through the Spacelab CDMS. In contrast, the manual and observation program command and control will be exercised through the CDMS; commands will be transferred from the keyboard, dedicated controls, and/or Spacelab experiment computer via the experiment data bus to the experiment. The degree of operator involvement is defined at three levels: Automatic, Semi-automatic, and Manual.

Automatic. As the name implies, in the Automatic Mode SIRTF will gather data from a number of stars using a number of instruments without operator intervention. An automatic observing sequence for SIRTF requires a Shuttle flight program (presumably also automatic) which is beyond the scope of the current study. However, the general procedure can be formulated: The crew will check that all Shuttle, Spacelab and SIRTF systems are ready to start the observing program. The pilot will initiate the Shuttle pre-programmed flight plan, the mission specialist will enable the Spacelab subsystems, and the payload specialist will enable SIRTF. The Shuttle flight plan will orient the Shuttle and, upon verification of correct Shuttle orientation, issue a proceed command to the Spacelab subsystem computer. The subsystem computer will excite a series of commands such as pointing the telescope using the IPS, and loading the data processing routine into the

TABLE 2-12. SIRTF CONTROL FUNCTIONS

*Observing program may be overridden at any time by commands from the PSS/MSS keyboards or dedicated controls.
**BOS: Bright Object Sensor

**BOS: Bright Object Sensor

experiment computer. The subsystem computer will issue a proceed command to the experiment computer, and the experiment computer will command functions such as: orient the MIC selector mirror to the proper focal plane instrument, acquire and track guide star(s) in the focal plane star tracker, and initiate space chopping at the programmed amplitude and frequency. When all three computers indicate that their subsystems are ready, data-taking starts. Data-taking is terminated after a fixed period of time or when the star can no longer be tracked due to its proximity to the earth's horizon. If the same target is to be measured with a second focal plane instrument, the subsystem and experiment computers make the appropriate changes and data-taking is resumed. If a new target is to be acquired, the Shuttle orientation is changed as necessary and the subsystem and experiment computers make the necessary changes. This mode continues until the pre-planned program is complete or is terminated by operator intervention.

The steps involved in control of the telescope are as follows for the Automatic Mode Sequence:

1. Obtain next star and initiate pointing logic
2. Load program for first instrument data processing
3. Wait for "bad transmission" recovery logic to be completed
4. Output star identification
5. Send instrument selection command to the MIC selector
6. Load timer for observation
7. Initiate data acquisition; select data format for CRT display
8. Transfer control to instrument data processing; data collection continues to the end of the specified time period
9. Stop data acquisition
10. If more instruments are to be used on this star observation, load program for next instrument data processing. Repeat steps 5-10 for each instrument
11. Initiate "bad data transmission" recovery logic
12. Loop back to step 1.

Semi-automatic. The operator (Payload Specialist or operator at the POCC) initiates the pointing to the next star on the star list. The operator verifies the correct pointing of the telescope; he may modify the pointing angle with a console joystick. The program collects data from each specified instrument for the current star. Several options exist for division of duties.

One potential Semi-automatic Mode Sequence is:

1. When operator is ready to commence next observation, he commands the computer to do steps 1-5 of Automatic sequence.
2. When operator has verified correct pointing of telescope, he commands the computer to do steps 6-11 of Automatic sequence.
3. Loop back to step 1.

Manual. The Payload Specialist or POCC operator inputs the angular coordinates to which the telescope is to be pointed. The program points the telescope. The operator verifies (and may modify with the joystick) the pointing angle. The operator selects the instrument. The program collects the data.

The Manual Mode Sequence is:

1. The operator inputs the angular coordinates of the star through the keyboard.
2. The computer initiates abbreviated pointing logic.
3. The computer waits for "bad data transmission" logic to terminate.
4. The computer informs the operator that the pointing is complete.
5. The operator verifies correct pointing.
6. The operator requests instrument and time.
7. The computer loads data processing program for specified instrument.

8. The computer executes steps 4-9 of Automatic Mode sequence.
Return to step 6 or continue.
9. Initiate "bad data transmission" recovery logic.
10. Return to step 1.

2.3.2.3 Engineering Design of Control Functions

Further definition of the functions used in the Modes described in Section 2.3.2.2 are contained herein. The functions are grouped by type: time-driven functions, cyclic functions, and event-driven functions. The program and data memory estimates for each function are given in Table 2-13. The estimates are based on the parameters discussed here, and on experience in the design and development of similar control systems.

Time-Driven Functions. Some functions will be invoked periodically (i.e., as a function of time). These functions are described below.

Status Input and Update

Frequency: Twice per second

Read housekeeping status signals

Update display on status panel

Object Avoidance

Frequency: Once per second

Compute position of sun, moon, and earth with respect to the telescope (assume sun and moon scribe circular planar orbits around the earth)

If not in telescope pointing process:

- read angle of telescope

If telescope is pointing into an avoidance area:

- break lock
- drive telescope away from area
- inform system
- inform operator

TABLE 2-13. MEMORY REQUIREMENTS ESTIMATES

	<u>Program and Data Memory (number of 16-bit words)</u>
Automatic Mode Sequence	
Semi-Automatic Mode Sequence	800
Manual Mode Sequence	
Status Input and Update	250
Object Avoidance	500
Obtain Next Star	200
Pointing Process	
Coordinate Conversion	200
Pattern Matching	1,500
Other Functions	600
Instrument Data Processing (Fast Fourier Transform)	
Program Memory	400
Data Memory (12,300 32-bit Words)	24,600
Instrument Data Processing for Additional (Undefined) Experiments	2,500
Bad Transmission Recovery Logic	400
Data Acquisition/Distribution	400
Data Recording	400
Bad Record Message Receiver	200
Display Formatter	1,500
Operator Interface Routine	750
New Star Routine	500
Inter-Computer Communication Control	350
Diagnostic Processor	500
Total	36,550

If telescope is pointing near an avoidance area:

- inform operator

(If the system is in the telescope pointing process, the pointing logic assumes the object avoidance task.)

It is assumed that the IPS logic contains provision for avoiding contact with the Orbiter structure, backed up by limit sensors.

Cyclic Functions. These functions are invoked during the process of sequencing through any of the three operational modes. The next star to be observed is obtained from the preloaded observing program, or the POCC operator or Payload Specialist queue. A data set for an observation includes the following star data:

1. Angular coordinates of the IR LOS. 21 bits each will specify coordinates to units of arc seconds.
2. Magnitude of star on IR LOS, or
3. Offset of guide star LOS from IR star LOS, Δ angular coordinates, units of arc seconds. This will require 10 bits each (FOV is 15 arc minutes).
4. Angular coordinates and magnitudes of up to 12 visual stars (four for each IPS star sensor) for pattern matching.
5. Angular coordinates and magnitudes of up to four stars for CCD star tracker pattern matching. The angular coordinates can be expressed as Δ angles from the IR LOS.
6. An ordered list of instruments to be used for the observation, associated time that instrument is to be used, and instrument parameters (if any) for the observation.

The cyclic functions are listed and described below:

Point Telescope

Input:

1. Position in ECI (earth-centered inertial - probably right ascension and declination) coordinate system and magnitude of three stars.
2. Star map consisting of four stars for each FOV (position and magnitude) for pattern matching.
3. Orbiter state vector containing at least angles of rotation between Orbiter and ECI coordinate systems.
4. Time-GMT

Functions:

1. Convert star coordinates from ECI to Orbiter coordinate system. The pointing process is sufficiently rapid that change of the pointing process will not introduce a significant error.
2. Determine if final position of telescope is in an avoidance area; if so, abort the pointing process.
3. Compute telescope slew path and determine if it will intercept an avoidance area; if so, develop a new slew path.
4. Compute vector between two CCD sensor guide stars. From this, compute roll angle (ρ) of telescope.
5. Output angular position of IPS star track lines of sight and guide stars to the IPS and wait for response of IPS in angle.
6. If a multi-segment slew path, repeat step 5 for all remaining segments.
7. Output magnitudes of guide stars to IPS and wait for confirmation of acquisition.
8. If IPS reports no acquisition, abort pointing process.
9. Perform pattern matching on visual CCD guide stars (if required):
 - acquire CCD sensor FOV
 - determine if correct star is on LOS; if not, compute angles,
 - output new angular positions, and repeat from step 7.
10. Output magnitude of telescope LOS IR star and wait for confirmation of acquisition.
11. If CCD star tracker reports no acquisition, abort pointing process and signal operator.
12. Send track command to CCD star tracker electronics.
13. Report successful lock to payload specialist's station.

Output:

1. Notification that the telescope is locked onto the specified star, or
2. An indication that the telescope cannot lock onto the star because:
 - star too close to a warm object (avoidance area),
 - the telescope cannot acquire the guide stars, or
 - the pattern matching process was not successful.

Section 3.5.2 (page 3-132) and Table 3-24 (page 3-133) provide additional material on the pointing process.

Load Program. The preloaded observing program also contains the list of instruments to be used and how long (time) they are to be used for this star.

The operating system is requested to load the data processing program for the instrument, and appropriate instrument and/or data processing parameters. The identification of the current instrument is placed in memory for use by the data transmission logic.

Output Star ID. A short record that identifies the current star under observation is output. This record contains:

- star coordinates in ECI
- GMT
- attitude of Orbiter
- pointing angles of telescope

Initiate Data Acquisition. The operating system is requested to read data from the MIC in blocks. The acquisition of a data block causes the Instrument Data Processing function to be scheduled. The data is simultaneously transmitted to the ground or read onto magnetic tape.

Instrument Data Processing. The example function for study purposes is the Fast Fourier Transform (FFT). The time required to do an FFT is given by

$$\tau \frac{N}{2} \log_2 N$$

where τ is the computer time required to do

$A \pm (BXC)$ (A and B are complex data and C is a complex number)

Assuming a 4096-word input as described earlier, the program requires approximately 400 (16 bit) words of program storage and 12300 (32 bit) words of data storage.

Further discussion on Instrument Data Processing is found in the section on Event Driven Functions below.

Bad Transmission Recovery Logic (BTRL). Normal operational mode is to transmit data to the ground in real time using TDRSS. During TDRSS outages, the data will be recorded on magnetic tape, and transmitted during the next ground contact.

During or following transmission, the ground sends up messages indicating the records that were received in error. The record numbers are stored and the BTRL sequences through the list of bad records and retransmits (from the tape) the requested records. This process continues until all records are received with sufficiently low error.

Event Driven Functions. The following functions are invoked by the occurrence of some event, usually the presence of data.

Fine Acquisition. Upon initial acquisition of the IR star by the selected MIC instrument, the computer commands the stabilization mirror to execute a small amplitude dither about its nominal position until the instrument output is maximized. When the maximum is found, signals are transmitted to the SIRTF star tracker to establish this position as the guiding position for this observation.

Data Acquisition/Distribution. When the operating system has acquired a block of data from the MIC, the Data Acquisition/Distribution function is invoked.

The Data Acquisition/Distribution function distributes the data to the Instrument Data Processing function, and also to the Data Recording function. The recorded data includes an identification header (instrument name, parameters, time).

Instrument Data Processing. The instrument data processing is invoked by the occurrence of a 512-word data block. The processing is divided into two parts, viz., data collection and data processing.

Data Collection. A number, n , of data blocks are collected. If n is greater than 1, the data blocks are written in mass storage. When n data blocks have been collected, the data processing part is invoked (for the Michelson Interferometer, n is 8).

Data Processing. The n data blocks are input from mass store, and the processing function ensues. The output of the processing function is sent to the Display Formatter in the Orbiter computer.

Bad Record Message Receiver. The Bad Record Message Receiver receives messages from the ground and stores these messages for the Bad Data Transmission Recovery Logic. These messages contain record numbers of those records which were not received correctly on the ground.

Display Formatter. The Display Formatter receives data from the Instrument Data Processing function and builds the appropriate display(s) in the computer memory. The Display Formatter will be instrument dependent.

Operator Interface Routine. The Operator Interface Processor is invoked when the Payload Specialist or POCC operator inserts a command on the computer keyboard.

Typical commands that are available and their functions are listed in Table 2-14.

TABLE 2-14. TYPICAL OPERATOR COMMANDS

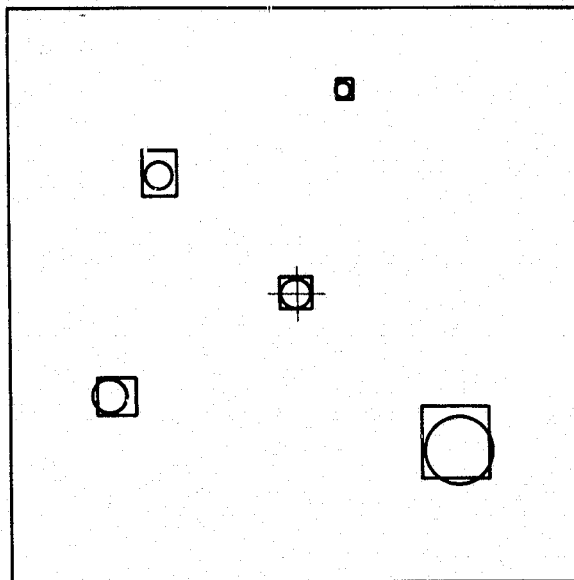
<u>Command</u>	<u>Function</u>
Di (i=1, n)	Causes the ith data display for the current instrument to be displayed.
Si (i=1, n)	Causes the ith status display to be displayed.
SI	Causes the program to stop acquiring data from the current instrument and to sequence to the next instrument for the current star.
SS	Causes the program to stop the observation of the current star and to sequence to the next star on the ground/airborne operator queue or the preloaded observing program.
SU	Causes the program to go to a suspended state at the end of the current star observation, i.e., further star observations are not commanded.
CO	Causes the program to continue execution in the current mode.
SN	Causes the program to read the contents of the CRT screen.
RS	Causes the program to restart at step 1 of the current mode.
NS	Causes the boilerplate format for new star entry to be displayed.

In addition to these keyboard commands, the operator has three function keys which define the three modes (automatic, semi-automatic, manual). There is also a suspended state light. When the software is in a suspended state, the operator may activate the program by entering either a continue, CO, or restart, RS, command. In addition there is a red emergency halt button which stops all software processing, including object avoidance. The suggested display formats are shown in Figures 2-9 through 2-13.

New Star Routine. The New Star Routine is invoked when the Payload Specialist enters a new star observation request or a new star observation is commanded by the POCC.

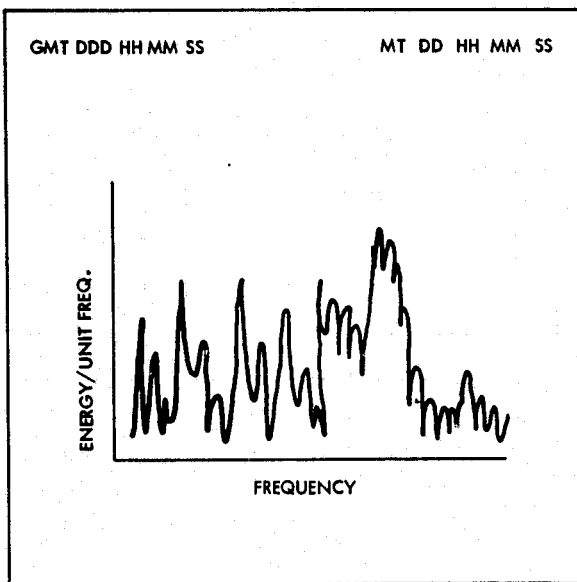
If pattern matching is requested, a request for star maps is sent to the computer mass memory or to the POCC.

The information from the display is built into a format similar to the preloaded star list and placed in the queue.



THE CENTER OF THE DISPLAY IS THE IR LOS. THE VISIBLE STARS AS SEEN BY THE TELESCOPE ARE SYMBOLICALLY DISPLAYED BY CIRCLES; THE SIZE OF THE CIRCLE INDICATES THE VISIBLE MAGNITUDE. THE KNOWN STARS - EXPECTED FOV - ARE SYMBOLICALLY DISPLAYED BY SQUARES; THE SIZE OF THE SQUARE INDICATES THE KNOWN MAGNITUDE.

Figure 2-9. IR field of view.



EXPERIMENT DATA DISPLAY IS ON THE CRT WHICH IS CONNECTED TO THE ORBITER COMPUTER.

Figure 2-10. Data 1 display for the Michelson interferometer.

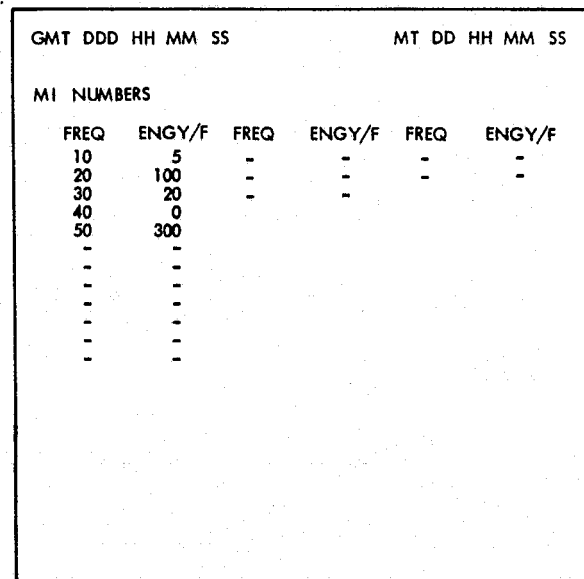


Figure 2-11. Data 2 display for the Michelson interferometer.

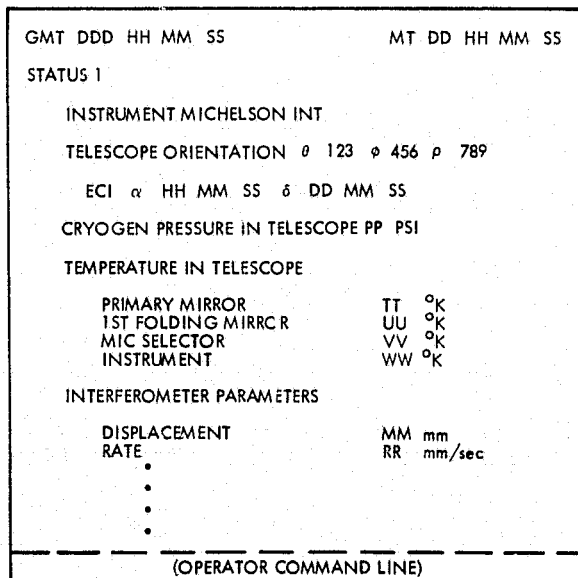
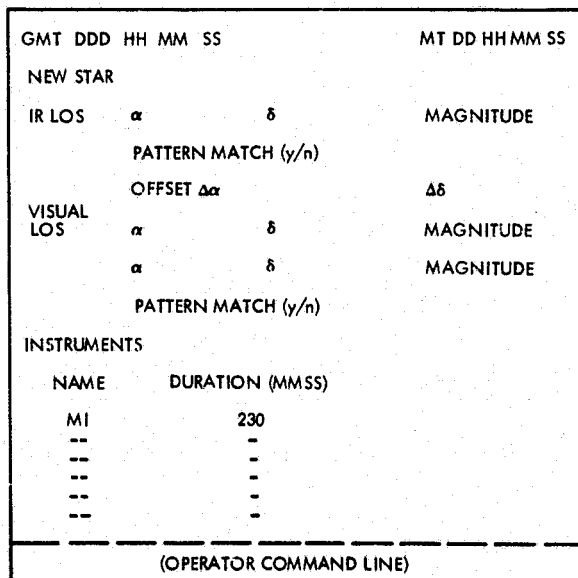


Figure 2-12. Status 1 display.



IF A PATTERN MATCH IS REQUESTED, A STAR MAP (S) IS REQUESTED FROM THE ON-BOARD MEMORY OR FROM THE GROUND. THE NEW STAR IS NOT PLACED ON THE GROUND/AIRBORNE OPERATOR QUEUE UNTIL THE STAR MAP (S) HAVE BEEN RECEIVED.

Figure 2-13. New star standard format.

POCC Telemetry Receiver. The POCC Telemetry Receiver is invoked when a message is received from the ground. The message may command any function commandable by the payload specialists, except fine pointing, because the data transmission lag will make fine pointing very difficult from the ground.

The correct (or incorrect) receipt of the message is acknowledged. The message type is decoded and sent to the appropriate processor.

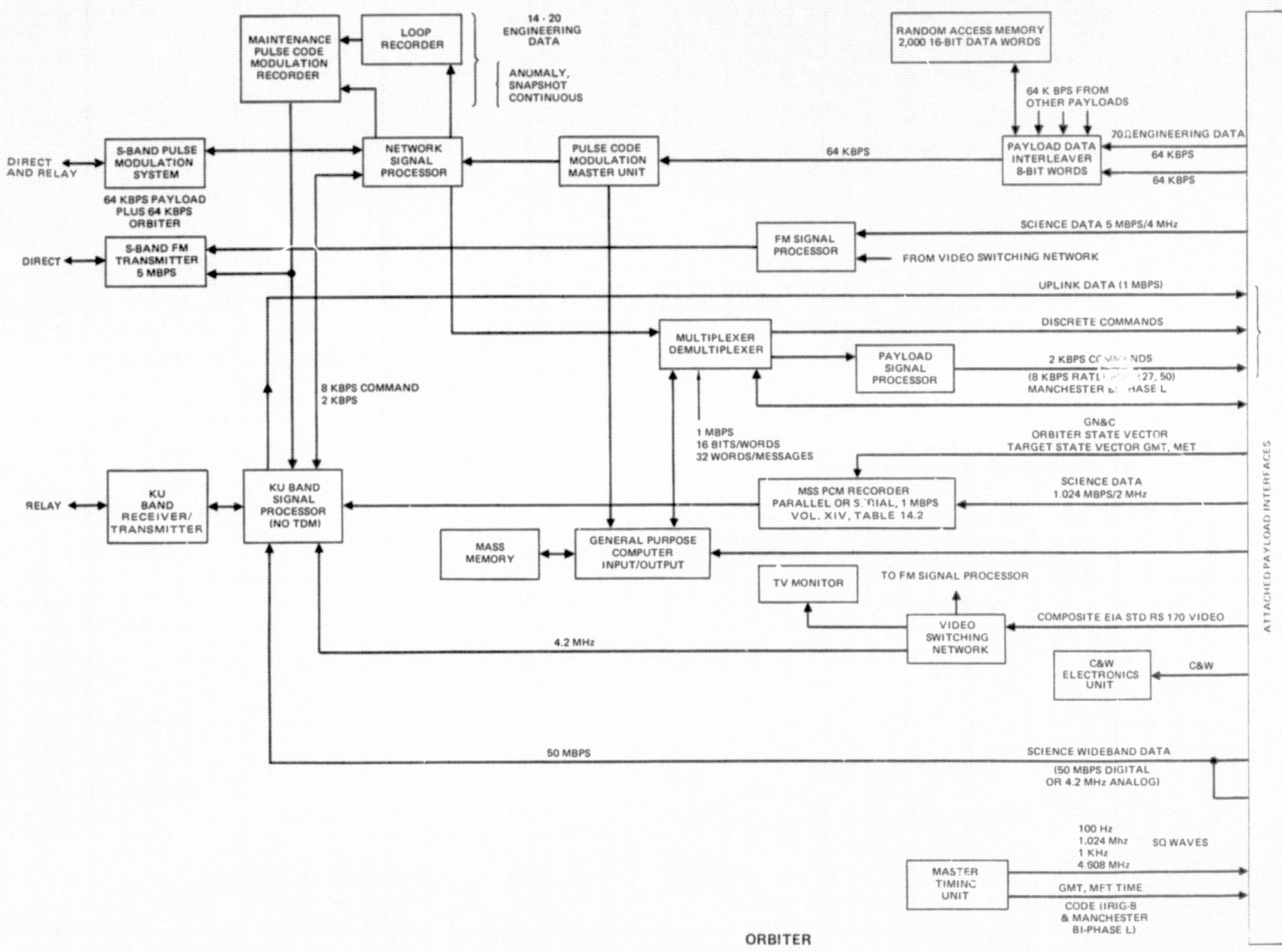
2.3.3 Spacelab/Shuttle Command and Data Management

This section and the one which follows discuss the planned methods for utilizing the Spacelab Command and Data Management System and the Orbiter Avionics System to perform the command and data support functions. Supplementary equipment which will be required is identified.

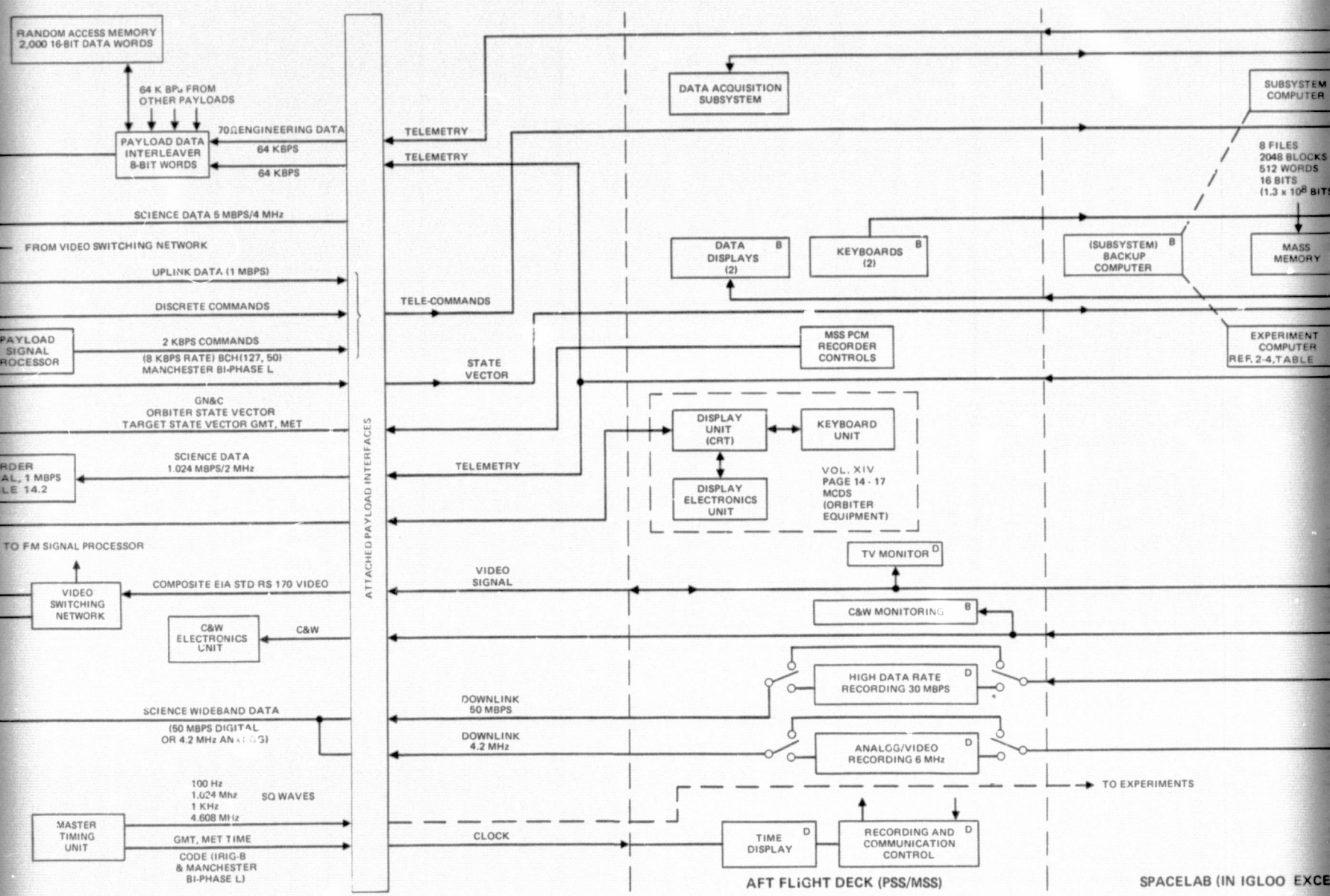
Because a combined Spacelab-Orbiter avionics system has not yet been defined in the various payload accommodation documents, a block diagram of the combined system as developed from material in References 2-3 and 2-4 is presented first. Uncertainties and/or apparent inconsistencies which affect SIRTF support functions are identified. Section 2.3.4 describes the way the support functions will be allocated among the Spacelab and Orbiter equipment, and evaluates the adequacy of the subsystem for the assigned tasks.

Spacelab-Orbiter Avionics

Figure 2-14 is a block diagram of the combined avionics systems of the Orbiter and Spacelab. The portion to the right of the Attached Payload Interfaces block is based on Figure 4-23 of Reference 2-4, with added details taken from other parts of Section 4.4. The portion to the left of the Attached Payload Interfaces block is based on Figure 14-2 of Reference 2-3, with added details taken from other parts of Section 14. The two exceptions are



FOLDOUT FRAME



FOLDOUT FRAME 2

SPACELAB (IN IGLOO EXCE

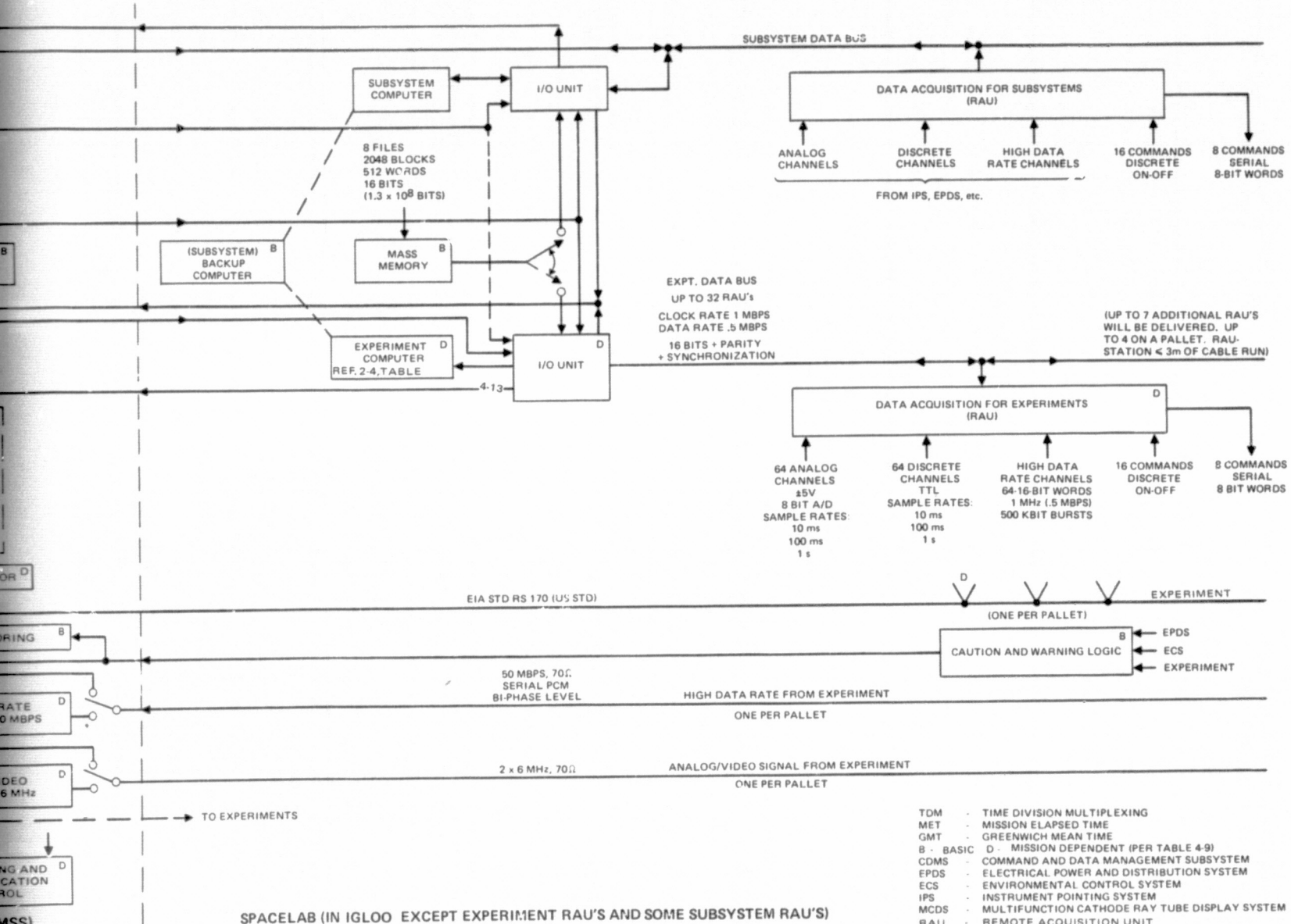


Figure 2-14. Spacelab-Orbiter combined avionics systems.

the MSS PCM recorder controls and MCDS, which are Orbiter equipment but are located in the aft flight deck. Some items from the Orbiter block diagram which do not relate directly to SIRTF or IPS operation have been omitted in order to avoid unnecessary complication. The command portion of the system will be explained first, then the data retrieval portion.

Commands

Commands originate at the Spacelab keyboard, at the Orbiter MCDS, or at the POCC. POCC-initiated commands are transmitted up through the S-band PM link or the Ku-band relay. Commands from the Spacelab keyboards feed directly to the Spacelab experiment computer through the I/O unit, and then out on the experiment data bus to the experiment RAU. The command lines leaving the RAUs are connected to the appropriate inputs on experiments and Spacelab subsystems.

Commands originating at the MCDS, which is the Orbiter command and display unit, are fed to the Orbiter general purpose computer, and then to the modulator-demodulator (MDM). Discrete commands pass directly to the Attached Payload Interface; serial commands are fed to the Payload Signal Processor prior to transfer to the Attached Payload Interface. It is assumed (not specifically stated in References 2-3 or 2-4) that these commands enter the Spacelab avionics system on the Telecommand line, which feeds them to the experiment I/O unit (Reference 2-4, page 4-42, not shown on Figure 4-23) and hence to the experiment along the same route as the keyboard-originated commands.

It is not clear from either reference whether one of the two control keyboards will be at the Payload Specialists Station and the other at the Mission Specialists Station, or whether it is intended to have redundant keyboards.

Commands originating from the ground are transmitted via the S-band PM system to the Network Signal Processor, MDM, Payload Signal Processor, and finally the Telecommand line in Spacelab. The Ku-band system can also receive the 9 kbps command data (when the S-band system is powered down). It feeds the command to the Network Signal Processor and from there the commands proceed along the same route as S-band-received commands.

In addition, the Ku-band system can supply data to the payload directly at a rate of up to 1 Mbps. It is assumed that this data also enters the Spacelab avionics system on the Telecommand line. This facility will be used to provide updated or revised observing programs.

In addition to direct on-board or ground operator control, the experiment can be commanded by programs stored in the Spacelab mass memory. Commands enter the experiment computer through the I/O unit and are transferred to the experiment along the experiment data bus. Due to the fact that the portion of the mass memory which can be assigned to experiments is TBD in Reference 2-4, the size of the observing program which can be stored and the frequency of observing program update required cannot be estimated.

The command modes that have been described for the experiment are also used for the Spacelab subsystem, notably the IPS. There is a separate computer I/O unit, and one or more RAUs for the subsystem. All other equipment is used in common with the experiment. The function of the Data Acquisition Subsystem located on the aft flight deck is not defined in Reference 2-4.

Data

Orbiter state vector, target state vector, time, and standard frequencies are fed to the Spacelab subsystems and experiments as needed on the state vector and clock lines. How the clock lines tie into the experiments is not defined at this time.

Data generated by experiments is separated into two general categories: science data, and engineering data. According to Reference 2-3, Page 10-5, engineering data facilities not required for engineering data can be used for science data transmission and processing.

Engineering data is collected through the RAU, and transferred on the subsystem or experiment data bus to the I/O units of the respective computers, and to the Telemetry interface. It is assumed that the Telemetry interface ties into the Orbiter 64 kbps engineering data lines, one (or more) lines for the Spacelab subsystems, and a separate line for the experiment engineering data. The engineering data lines feed the data into the Payload Data

interleaver, which decommutes the incoming data and reformats it as required for telemetry. The data then moves through the PCM master unit, and the network signal processor to the S-Band pulse modulation system and the ground. In parallel, it is fed to the general purpose computer (GPC). GPC programs provide automatic performance monitoring, checkout and display of engineering data on the MCDS. This completes the manual control loop, since the Payload Specialist can initiate corrective action through the keyboard on the MCDS or special purpose controls.

The route of the science data through the Spacelab and Orbiter data system will depend on the character of the instrument in use at the time and of the data it produces. It is expected that the high data rate channel through the RAU will provide the needed capability for most experiments. Alternatively, the discrete channels will be used for experiments with sufficiently low sample rates. It is expected that the experiments or the MIC micro-processor will include appropriate A/D conversion for the SIRTF experiments so that the use of the RAU analog channel will be small.

Science data proceeds from the RAU via the experiment data bus to the experiment computer where it is processed according to the instructions of the observing program. All or selected portions of the data are fed to the data displays and the payload specialist can modify instrument parameters or program parameters to optimize the performance. The data is simultaneously recorded by the MSS PCM recorder. During POCC contact periods, the data is read off the MSS PCM recorder and transmitted to the ground through the Ku-band subsystem. During the transmission period, new data will be stored in the Spacelab computer mass memory, or on the high data rate digital recorder.

C&W and clock lines are indicated on the block diagram, but are not of major concern at this point in the SIRTF system definition.

For the higher data rates discussed in Section 2.3.2, the data will be fed out the 50 Mbps high data rate line independent of the RAUs. It will then be recorded and transmitted to the ground on the science wideband data line through the Ku-band signal processor. Monitoring of the high rate data will be accomplished by sending samples of the data through the high data rate channel of the RAU. The MIC micro-processor will perform the sampling.

Video signals developed by the experiment will be distributed on the internal video signal line to the closed circuit TV system. Selected portions of the video presentation can be transmitted to the ground via the FM signal processor and the S-band FM transmitter. Alternatively, experiment-originated video can be recorded on the analog/video recorder for later transmission to the ground via Ku-band.

Assumptions

There are some inconsistencies within the References 2-3 and 2-4 data and uncertainties as to how the two avionics systems will interact. These are listed below, and the assumptions made in the discussions above are stated explicitly.

1. Reference 2-4:

- Figure 4-23 (page 4-41) shows a High Digital Rate Recorder in the Block Diagram of the Pallet-only Mode.
- Section 4.4.6.1 (page 4-53, 2nd paragraph) states "At present no high data rate recording is foreseen for the pallet-only mode."
- It has been assumed that the block diagram is correct, and that a high digital rate recorder will be available in the pallet-only mode. If it is not, it will have to be provided for high data rate experiments.

2. Reference 2-4:

- Figure 4-23 (page 4-41) shows no connection from the Telecommand uplink to the Experiment Input/Output Unit (only to the Subsystem Input/Output Unit).
- Section 4.4.1 (page 4-42, paragraph 1) states "An Orbiter provided uplink allows commands to be sent to Spacelab experiments from the ground."
- Section 4.4.7 (page 4-54, last line) "The RAUs deliver signals to the experiments for telecommand control from the ground".
- It has been assumed that the telecommand line is connected to both the subsystem and the Experiment Input/Output units. If it is not, commanding from the ground as required by the SIRTF specification will not be possible.

3. Reference 2-4:

- Page 4-45 (Section 4.4.2.1, 4th paragraph on page) states "The serial digital input will essentially allow ... to transfer digital data at the data bus clock rate (1 Mbps, paragraph immediately preceding) in a programmed sequence (500 to 600 kbps bursts)."
- Page 4-46 (Table 4-11, line 5 under "High Rate Digital"), states "equivalent data rate 102.4 kbps".
- It has been assumed that the 500-600 kbps rate is the maximum. This affects only which experiments are treated as high data rate experiments.

4. Reference 2-3:

- Section 14.2.13 (page 14-113) refers to a Payload Wideband Recorder. No other mention is made of it; it does not appear in any block diagram.
- This recorder has not been included in the SIRTF study; if it is to be available, it may be useful as a backup or as a replacement for the recorder discussed under assumption 1.

5. Reference 2-4:

- Section 4.4.7 (page 4-54, 2nd paragraph from bottom) states "the data are ... transmitted to the ground via the 64 kbps downlink as programmed."
- This downlink is not mentioned anywhere else in the section.
- This downlink has not been included in the SIRTF study; there seems to be adequate downlink capacity, so there is no immediate impact.

6. References 2-3 and 2-4:

- Are the CRT and keyboard shown located in the Aft Flight Deck the same as the Orbiter MCDS CRT and keyboard or are they separate units?
- Although shown separately on the block diagrams, an integrated display system would be advantageous for the payload and mission specialists.

2.3.4 Utilization of Command and Data Support Systems for SIRTF

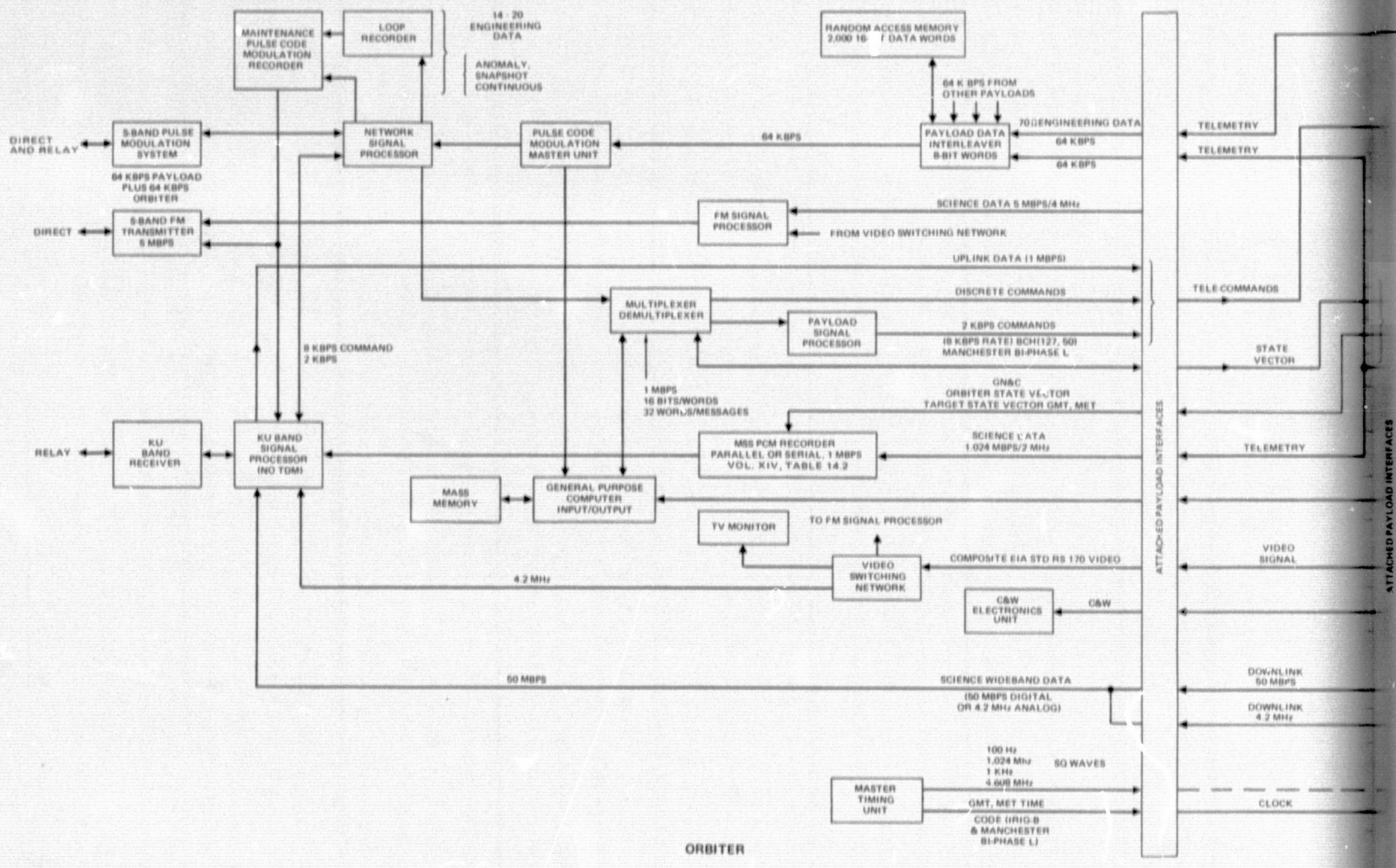
Figure 2-15 shows the SIRTF subsystem block diagram and how it will tie into a Spacelab RAU and the direct transmission lines. The IPS command and data lines are also shown.

The SIRTF interface unit provides functions such as: routing and buffering of commands; digitizing, interleaving, and formatting of engineering data; status checking; and initiating of caution and warning signals.

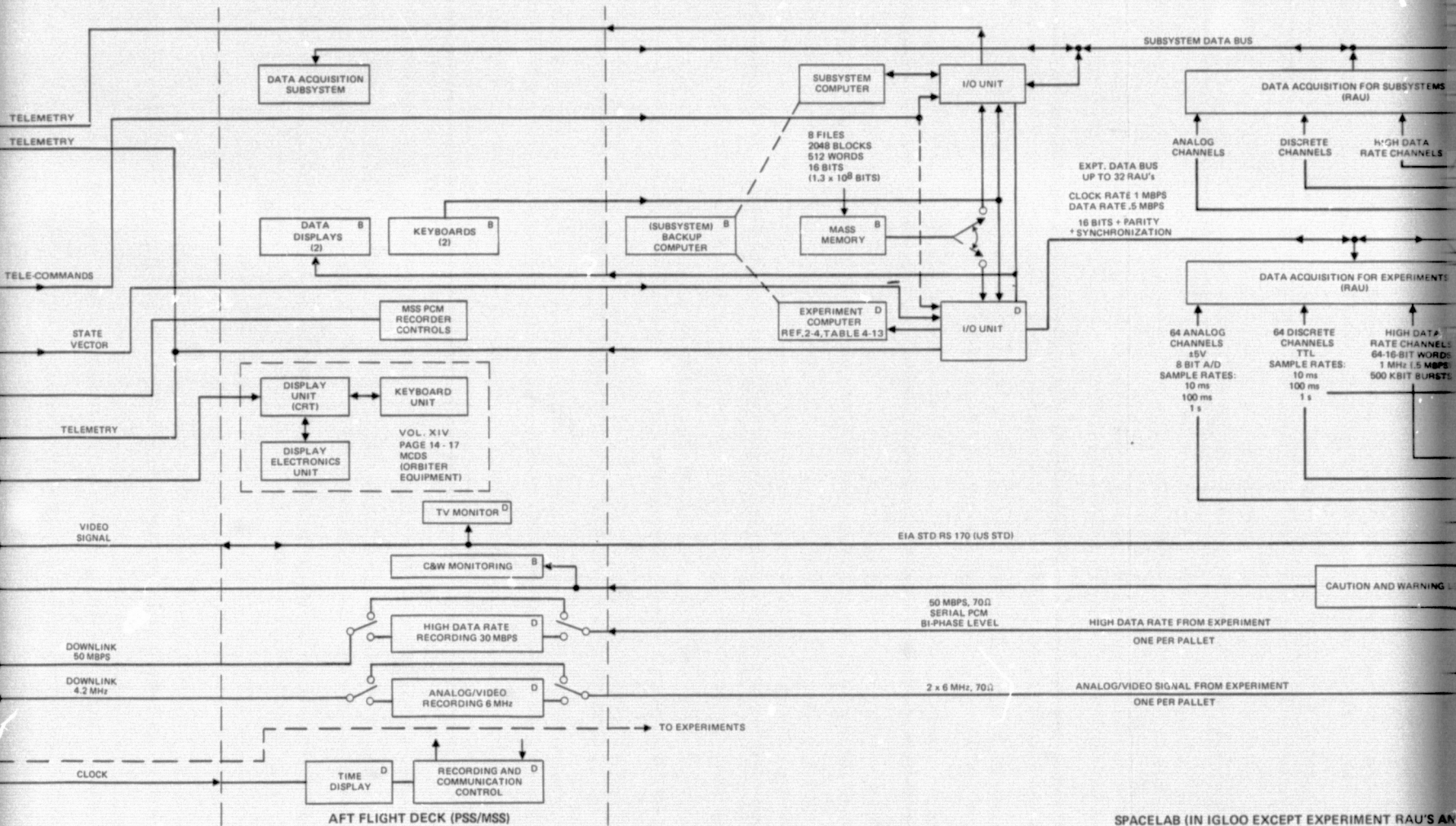
The MIC interface unit's chief function is the processing of science data from the MIC. A Spacelab micro-processor may be used for part or all of this function, depending on the extent of the processing required. Processing includes analog-to-digital conversion, formatting, and buffering. In the case of high rate data which must be transmitted to the ground on the high data rate line, the MIC interface unit samples the data and transfers the sampled data to the experiment computer via the RAU. The experiment computer further processes the data and displays it on the Spacelab display unit.

The MIC interface unit also collects and formats housekeeping data from the MIC, transfers it to the SIRTF interface unit, and feeds commands to the MIC.

The command route through the SIRTF interface unit to the MIC interface unit and SIRTF telescope was selected as providing the simplest interface for final integration of SIRTF into Spacelab. In a typical integration sequence, the MIC and MIC interface unit will be tested and checked out independent of SIRTF, with the MIC interface unit tied directly to the test console. The MIC and MIC interface unit will then be integrated with SIRTF and the SIRTF interface unit. All commands will then enter the SIRTF system through the SIRTF interface unit, and all engineering data will leave through the SIRTF interface unit. Science data, which is not processed in the SIRTF interface unit, is transferred directly from the MIC data processor to the RAU, high data rate, or video lines.



PRINTOUT FRAME



FOLDOUT FRAME

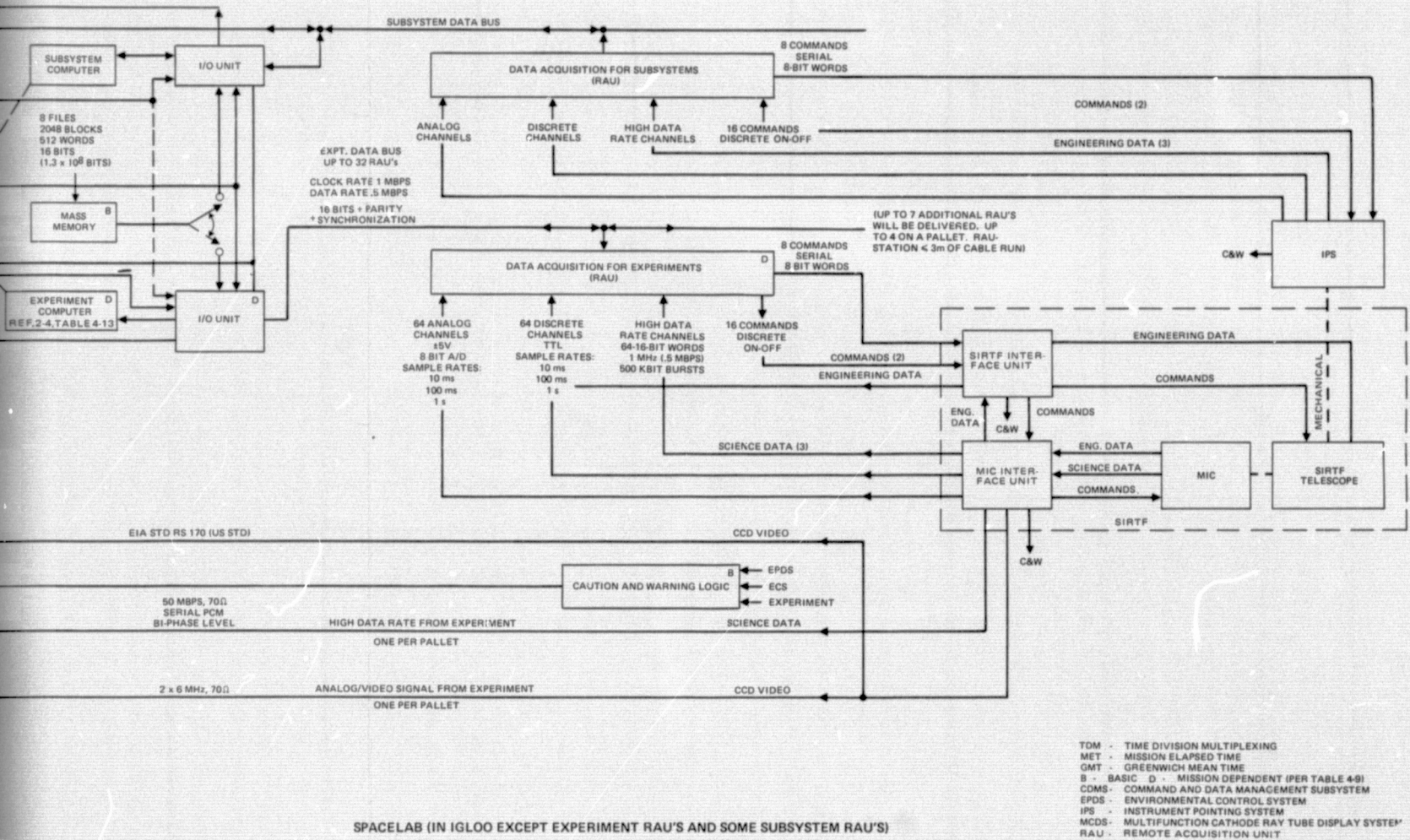


Figure 2-15. SIRTF command and data management interface with Spacelab and Shuttle.

Commands

The command lines from one experiment RAU appear to have sufficient capability for SIRTF control. The 16 discrete commands will be used for power control to the overall system and the major subsystems; the serial digital command lines will be used for all multiple and parametric output commands (e.g., MIC selector mirror, interferometer sweep rate). No data rate for the serial command lines is given in Reference 2-4; however, if they match the 2 kbps command rate in the Orbiter, they will be sufficient to control SIRTF functions.

The IPS receives commands from, and transfers engineering data to, the subsystem computer via the subsystem RAU. Only mechanical connections exist directly between the IPS and the SIRTF and MIC; all electrical connections are made through the Spacelab subsystem and experiment computers. There is concern that pointing control cannot be exercised adequately in this manner, and that a direct SIRTF-IPS electrical link is needed.

In order to understand the need for the direct link, it must be noted that control of the SIRTF LOS involves several operations that are not apparent from the block diagram of Figure 2-15. Briefly stated, the initial processor for target acquisition is as follows:

1. Prepare the telescope for observation by releasing the telescope hold-down clamps that lock the telescope to the Shuttle pallet, operate the mechanism that attaches the telescope to the IPS integration plate, and release the telescope cover.
2. Rotate the telescope out of the Shuttle bay and extend the sunshade.
3. Slew the IPS gimbals to an initial position commanded by the subsystem computer. The slewing is accomplished by means of the IPS gimbal position servos.
4. Transmit prestored guide star coordinates and magnitude data to the IPS wide-angle star trackers ($8^{\circ} \times 8^{\circ}$ FOV), and command the star trackers to acquire the first set of guide stars.
5. Align the telescope with the desired guide stars using information derived from the IPS star trackers. The alignment is accomplished using the IPS gimbal servos.
6. Transmit prestored guide star coordinates and magnitudes to the SIRTF internal star tracker (30 arc minutes FOV) and command the star tracker to acquire the guide stars.

After the SIRTF internal star tracker has acquired the desired guide stars, the control of the SIRTF LOS is transferred to the internal star tracker. At this point the IPS gimbals are no longer commanded but are instead slaved to the gyro-stabilized platform mounted on the telescope. The LOS control then involves the following operations:

1. The platform gyros are updated by information from the SIRTF internal star tracker.
2. The SIRTF autoalignment system holds the telescope LOS in alignment with the platform.
3. The IPS gimbals are slaved to the platform.

A detailed discussion of the above LOS control operations is given in Reference 2-9. The slaving of the IPS gimbals to the platform is accomplished by using the platform deflection angles (relative to the telescope) as error signals to drive the IPS gimbal servos. The deflection angles are measured with position transducers and sent directly to the IPS servos. Therefore, no computer processing of IPS commands is required.

During slave mode operation, the SIRTF platform gyros rather than the IPS gyros are used for stabilization purposes. The IPS gyros can then be caged and used as highly accurate angular rate transducers for implementing a rate loop within each gimbal position loop. The dynamic performance and static accuracy of the slaving system are thereby improved.

The right side of Figure 2-15 can be modified as shown in Figure 2-16 to show the IPS gimbal slaving operation. The transfer of IPS control from the subsystem computer to the SIRTF occurs just before the beginning of an active viewing period. Further definition of the IPS is required to insure that this slaving can be accomplished.

Data

The engineering data rate will be sufficient for collection of SIRTF engineering data.

It is expected that the bulk of the science data will be transferred to the RAU on its high data rate channel. Most experiments will produce data at rates from 10 kbps to 250 kbps. Higher data rate experiments will use the high data rate line which bypasses the RAU. As mentioned above,

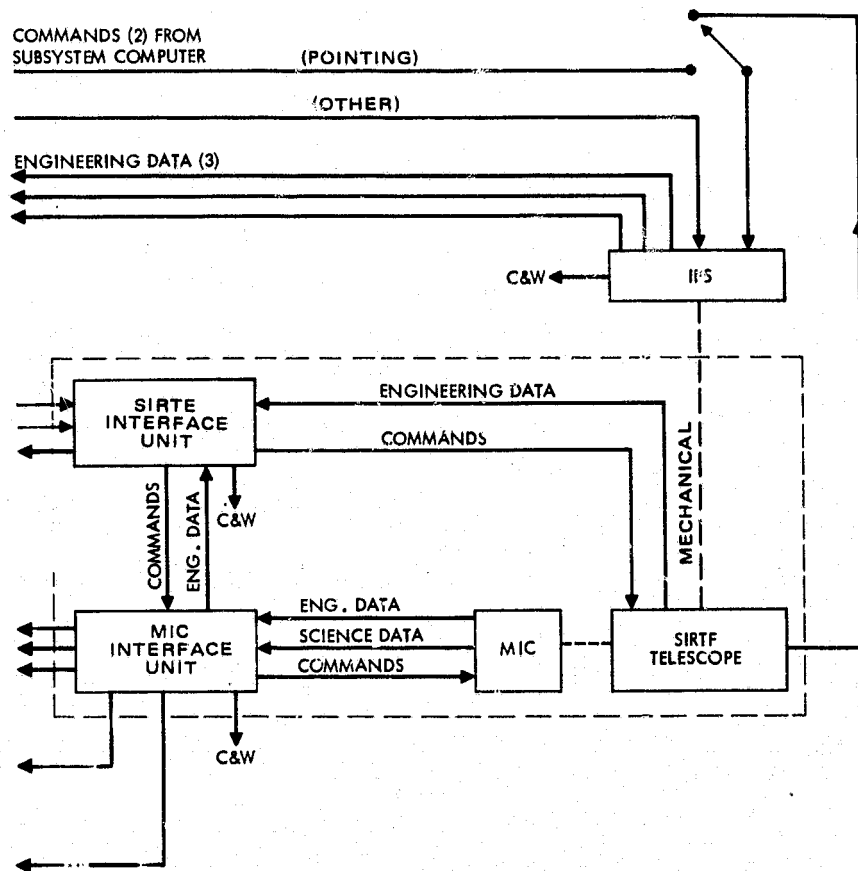


Figure 2-16. IPS gimbal slaving.

samples of the data at a rate within the capability of the RAU and experiment data bus will be transferred to the experiment computer and to the data displays. Science data is also shown being transferred via the RAU discrete channel inputs. This appears to be a possible, although rarely useful, alternative.

CCD star tracker data will be transferred out on engineering data lines. The data can be reconstructed into a SIRTF field of view presentation either on-board or at the POCC.

The conclusions based on the preceding discussions are that the data channels provided by Spacelab have the capacity required by SIRTF; however, there may be problems in pointing control if the IPS and SIRTF control subsystems remain independent.

Recording

Recording of science data will be required only during periods when SIRTF is not in contact with a ground station directly or through the TDRSS. The out-of-contact period is estimated at 20 percent. Recording will be done on the MSS PCM recorder or on the high data rate recorder.

The MSS PCM recorder is very flexible, with recording times and data rates ranging from 18.6 hours at 51 kbps to 0.9 hour at 1 Mbps. Thus, accommodation of varying data rates and outage periods can be made. At present, the high data rate recorder is very inflexible, recording for 0.3 hour at 30 Mbps only. A more flexible recorder is being considered. If the present high data rate recorder is selected and must be used, a substantial buffer will be required in the MIC interface unit so that TDRSS outage times longer than 0.3 hour can be accepted.

Addition of a second recorder in parallel with the MSS PCM recorder provides full flexibility: all data can then be recorded and retained until error-free transmission to the POCC is verified. The penalties are cost, weight, and most importantly, power on board. This does not appear to be an attractive alternative.

The conclusion is, thus, that either the MSS PCM recorder or the high data rate recorder will be used for data recording during TDRSS and ground station outage periods.

Computer

Table 2-15 lists the estimated execution times for the functions also listed in Table 2-14, based on the computer description in Reference 2-4. The computer appears to be adequate for SIRTF needs.

TABLE 2-15. EXECUTION TIME ESTIMATES

<u>Operation</u>	<u>Execution Time</u>
Automatic Mode Sequence	1.7 ms
Semi-Automatic Mode Sequence	
Manual Mode Sequence	
Status Input and Update	0.6 ms
Object Avoidance	3.0 ms
Obtain Next Star	0.5 ms
Pointing Process	
Coordinate Conversion	2.0 ms
Pattern Matching	15.0 ms
Reminder	1.3 ms
Instrument Data Processing (Fast Fourier Transform)	1.2 sec/ 2^{12} points
Bad Transmission Recovery Logic	I/O Limited
Data Acquisition/Distribution	0.9 ms
Data Transmission/Recording	0.9 ms
Bad Record Message Receiver	0.5 ms
Display Formatter	3.5 ms
Operator Interface Processor	I/O Limited
Airborne New Star Processor	1.5 ms
Ground New Star Processor	1.0 ms
Ground Telemetry Receiver	0.5 ms
Inter Computer Communication Control	0.8 ms
Diagnostic Processor	1.0 ms

2.4 POWER REQUIREMENTS

Table 2-16 lists the estimated power requirements for SIRTF. A large contingency has been added due to the many uncertainties.

The power requirements have been grouped under SIRTF (telescope), MIC, and Spacelab Mission-Dependent Equipment headings.

The main power consumption in the SIRTF telescope is the internal stabilization loop. The estimates for the gyro-stabilized platform, laser, and servo electronics are based on the conceptual design work at Hughes. The CCD star tracker estimate is based on current JPL work on a similar device.

The MIC instrument power requirements were estimated as part of the MIC definition (Section 2.3.1). The MIC interface unit will include amplifiers, A/D Converters, buffers and short-term storage.

The Spacelab equipment power requirements are taken from reference 2-4, with the exception of the IPS for which a recent updated estimate was used.

The total power requirement is estimated at 1.3 to 2.2 kW. A 50 percent contingency is added to allow for estimating errors, design changes, and power condition equipment inefficiencies. The 1.9 to 3.3 kW total is well under the allowable 5.2 kW and 450 kWh for the 7-day mission. Hence, the SIRTF requirements are roughly equal to half the available power, so that flying a second payload with SIRTF is feasible in terms of electrical power. The cryogenic cooling system does not generate heat, so the heat rejection requirement of SIRTF is also on the order of 1.9 to 3.3 kW, substantially less than half of the 6.6 kW available in the pallet-only mode.

2.5 GROUND SUPPORT

The ground support portions of the overall SIRTF system include two major subsystems: the launch support equipment and the in-flight support. The latter includes the TDRSS, the Payload Operations Control Center (POCC) and the astronomers' remote station. Of the launch equipment, the cryogenic servicing equipment is the major large size, time critical item, and is discussed in most detail herein. The rest of the ground support equipment can be standard items.

TABLE 2-16. SIRTF POWER REQUIREMENTS

SIRTF		145
Gyro-Stabilized Platform	50	
Laser	30	
CCD Star Tracker Processor	25	
Servo Electronics and Mirror Drive	35	
Housekeeping (Buffer Amplifiers)	5	
MIC		55-160
Grating Spectrometer	10	
Photometer Camera	10	
Lamellar Grating Interferometer	3	
Michelson Interferometer	110	
Polarimeter	3	
Data Processor	50	
SPACELAB MISSION-DEPENDENT EQUIPMENT		
CDMS		745
Experiment Computer	310	
Experiment I/O Units (2)	90	
Remote Acquisition Unit	15	
High Bit Rate Recorder	200	
Recording and Communication Control Equipment	50	
TV Monitor	50	
Time Display	30	
IPS		320-1150
Total Listed		1265-2200
Contingency (50 percent)		635-1100
Total		1900-3300

The work reported here for this preliminary design study was aimed at defining requirements for command and control and data transfer. The result is in the nature of general requirements for the POCC and the astronomer remote station rather than detailed definition. The definition work has now begun at ARC in coordination with work by the JSC and MSFC; it will be reported later.

2.5.1 Cryogenic Servicing Equipment

There are two cryogenic servicing tasks to be performed at the launch site: one is to cool down and fill the storage tanks which supply cryogen to SIRTF in flight; the second is to cool down the SIRTF telescope itself. Because the tanks have a large capacity and small mass, their cool-down is achieved by filling them, allowing them to cold soak for about 24 hours, and finally filling and topping off as needed. The telescope, on the other hand, has a large mass to be cooled and a small cryogen capacity so that a continuous flow is required. A second difference is that the helium only will be used to cool down the tanks, whereas liquid nitrogen will be used to cool the telescope to about 80°F, a more rapid and less costly approach due to the higher heat capacity and lower cost of liquid nitrogen. Thus it is expected that the two cryogenic servicing systems will operate somewhat independently, and they are described separately here.

Storage Tanks

The cryogenic servicing approach for SIRTF is based directly on the cryogenic servicing equipment and procedures developed by Grumman for the LM (Lunar Module) propellant pressurization system. The modifications which will be required are a result of the larger capacity of the SIRTF tanks as compared to the LM tanks.

Among the features of the LM loading equipment is the ability to load to a range of loading densities from liquid into the supercritical regime. This provides the possibility of varying the total cooling available with a fixed number of tanks in order to meet individual mission requirements. Reference 2-7 describes the LM equipment and the modifications required in detail.

Figure 2-17 is a schematic of the SIRTF tanks cryogenic servicing equipment. The hardware elements are described below.

Flight Tank(s) To Be Loaded. The fill and vent couplings are mounted on lines leading to the tank(s). The couplings are mounted in the prelaunch payload service panel (T-4 umbilical). Both couplings are vacuum jacketed and sealed with a spring-loaded, central pin-operated poppet. Full engagement with the ground halves opens the poppet. Each coupling has, furthermore, a metallic filter and a dust cap capable of withstanding full operating pressure.

LHe Storage and Transfer Dewar. This will be one or more commercial dewars of large capacity; a unit which has been previously qualified for launch complex use will be selected; it will be equipped with the necessary pressurization and over-pressure protection means.

Conditioning Unit Subassembly. This subassembly provides high-pressure cold helium gas for the "top-off" cycle — that is, the activity when the liquid helium in the flight tank is being driven supercritical by means of mass addition. It contains, besides the necessary valving and instrumentation, the following key elements:

- A liquid nitrogen precooler for helium gas
- A high-efficiency gaseous helium-to-helium heat exchanger
- A liquid helium cooler (boiler)

All of these items are enclosed in a vacuum-jacketed housing.

In operation, high-pressure gaseous helium enters the liquid nitrogen boiler. Gaseous nitrogen boil-off is vented overboard.

The high-pressure helium leaving the heat exchanger enters the liquid helium boiler where it is cooled to approximately 5°K before it leaves the conditioning unit subassembly.

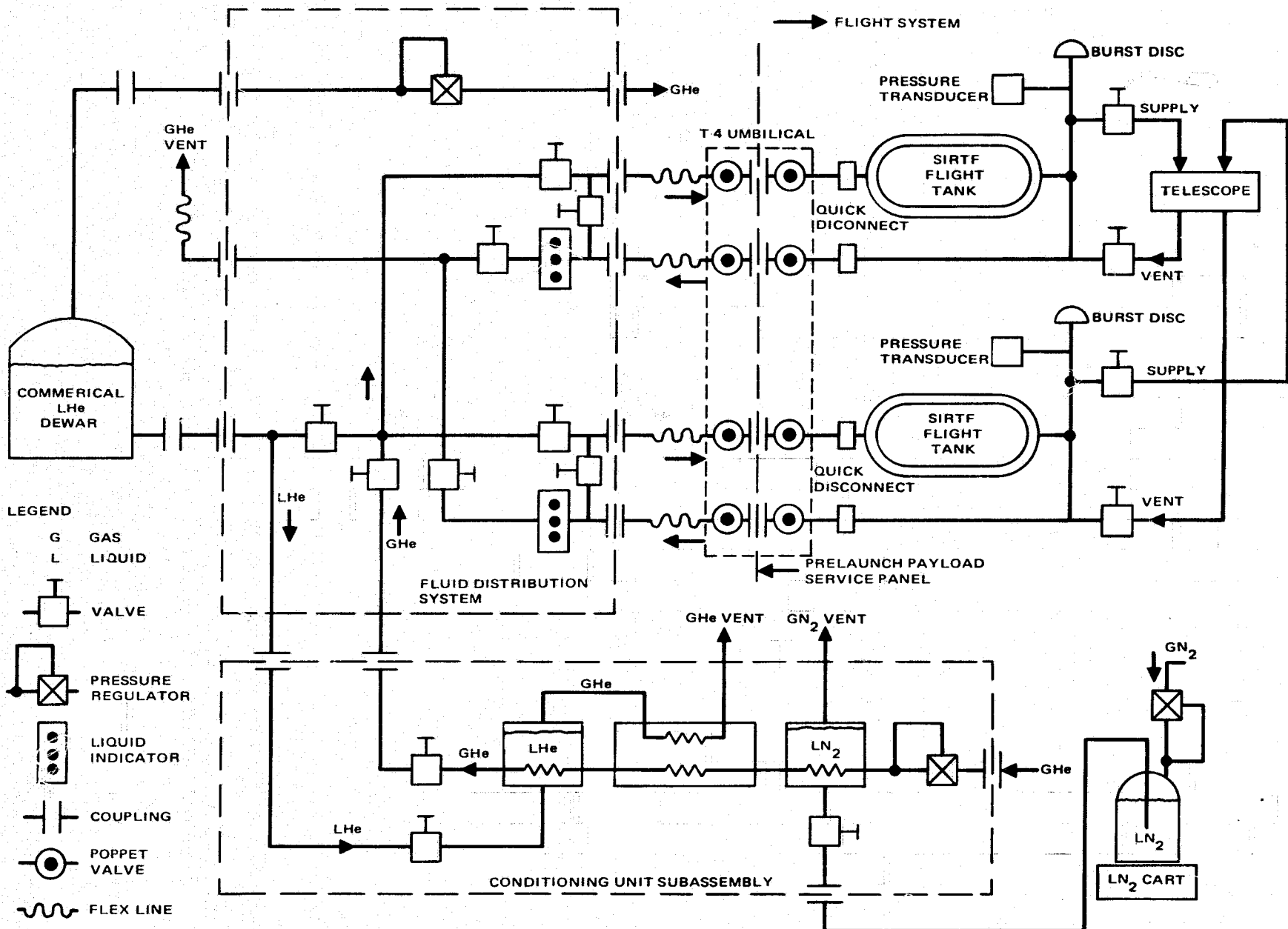


Figure 2-17. Basic SIRTF cryogenic tanks servicing schematic (the second flight tank is used only for missions of more than 14 days).

Fluid Distribution Unit Subassembly. This subassembly provides the necessary flow paths of helium to and from the flight tank(s). Furthermore, it possesses the capability to bypass the flight item for line prechill purposes. It is equipped with indicators which signal "tank full" condition by reacting to liquid being present in the vent line.

Liquid Nitrogen Supply Unit. This unit fills the liquid nitrogen boiler of the conditioning unit subassembly.

Other Hardware. Other hardware consists of vacuum-jacked inter-connect lines and high-vacuum maintenance units. The cryogenic supply lines (fill and vent lines) will be serviced through the Pre-launch Payload Service Panel (see Reference 2-7). This panel is configured to be replaced by special panels made for special missions. Connection of the helium fill and vent lines through this panel permits the application of mechanical caps over the flight coupling halves prior to launch - a practice successfully employed on the Apollo-LM vehicle. For this reason, cryogenic fill and vent lines through the T-O launch umbilicals are not recommended.

2.5.2 Ground Support Equipment

Ground support equipment for SIRTF consists of the following:

Cryogen Servicing Equipment

Cryogen Transfer Lines
(Servicing Equipment to Shuttle Umbilical)

Shuttle Umbilical Interface

Preflight Test Console

Flight Control Console (at KSC and ARC)

Ground Transportation and Handling Equipment

Control Console Simulator (at Ames Research Center)

Test Cover

The test cover will have twelve 8-cm diameter windows in two rows of six, 90 degrees apart; these make it possible to accurately inject visible energy into the system and verify focus and image quality in the MIC at operating temperature without building and qualifying a 1 meter class

cryogenic optical test facility. The windows will be coated to provide low emittance in the infrared region of the spectrum to minimize thermal loads during test.

REFERENCES FOR SECTION 2

- 2-1. Shuttle Infrared Telescope Facility, SIRTF/Orbiter/Spacelab Tradeoff Report, SIRTF Integration (Data Item ID1-4e) Grumman Aerospace Corporation/Hughes Aircraft Company, January 1976.
- 2-2. Shuttle Infrared Telescope Facility, Acquisition/Stabilization/Auto-Alignment Tradeoff Report, Part B: Dedicated Gimbal Assembly (Data Items ID1-1.c) Hughes Aircraft Company, May 1976.
- 2-3. Space Shuttle System Payload Accommodations, Level II Program Definition and Requirements, JSC 07700 Volume XIV Revision D, Johnson Space Center, 26 November 1975.
- 2-4. Spacelab Payload Accommodation Handbook, ESTEC Ref. No. SLP/2104, European Space Research Organization, May 1975.
- 2-5. Instrument Pointing System Project Technical Note: Design Definition at the IPS Structure and Clamps, IPS-TN-035-050, Dornier System 14 March 1975.
- 2-6. Mission Kit Summary, Johnson Space Center, 1975.
- 2-7. Shuttle Infrared Telescope Facility SIRTF Support Analysis Report, Cryogenic Servicing (Data Item ID1-2.f) Grumman Aerospace Corporation/Hughes Aircraft Company, May 1975.
- 2-8. Shuttle Infrared Telescope Facility Hardware Implementation Plan, SIR-RP-008 Grumman Aerospace Corporation/Hughes Aircraft Company, September 1975.
- 2-9. Shuttle Infrared Telescope Facility, Acquisition/Stabilization/Auto Alignment Tradeoff Report, Part A: IPS Mounted (Data Item ID1-1c) Hughes Aircraft Company, August 1975.

3. SIRTF TELESCOPE

The SIRTF telescope is described in this section. Additional material can be found in the various telescope subsystem reports which are referenced throughout the section. The sections herein cover the mechanical, optical, thermal, acquisition, pointing and stabilization subsystems in detail. The final subsection discusses performance predictions, including the effects of contamination on sensitivity.

3.1 GENERAL TELESCOPE CONFIGURATION

Figure 3-1 is a schematic of the SIRTF telescope. Major subsystems are the optics, baffles, star tracker, and cryogenic cooling system. Figure 3-2 is a cutaway view that gives a better idea of the actual appearance of

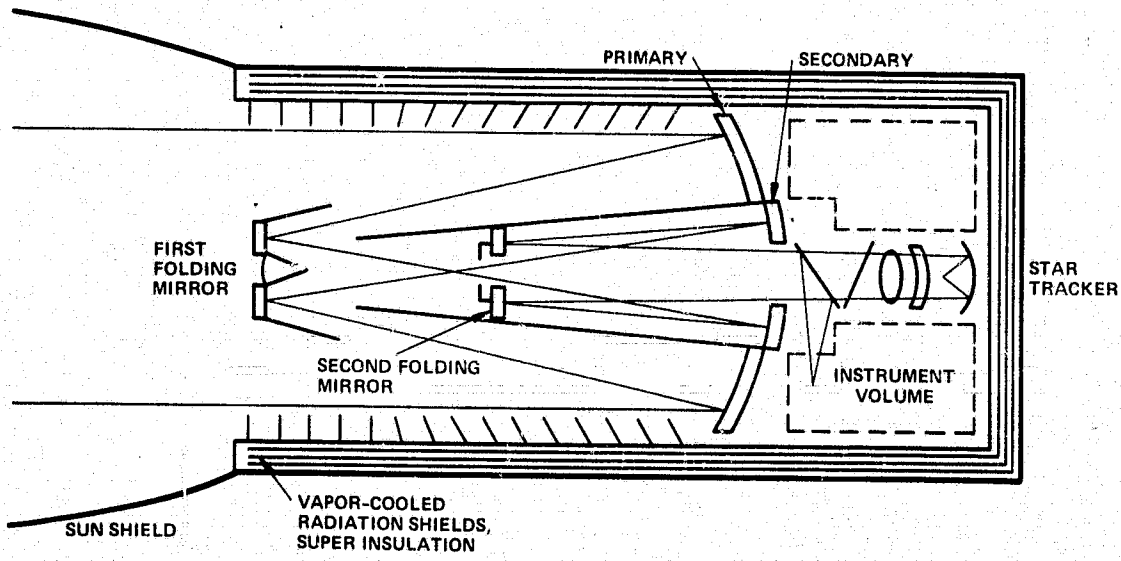


Figure 3-1. Telescope schematic.

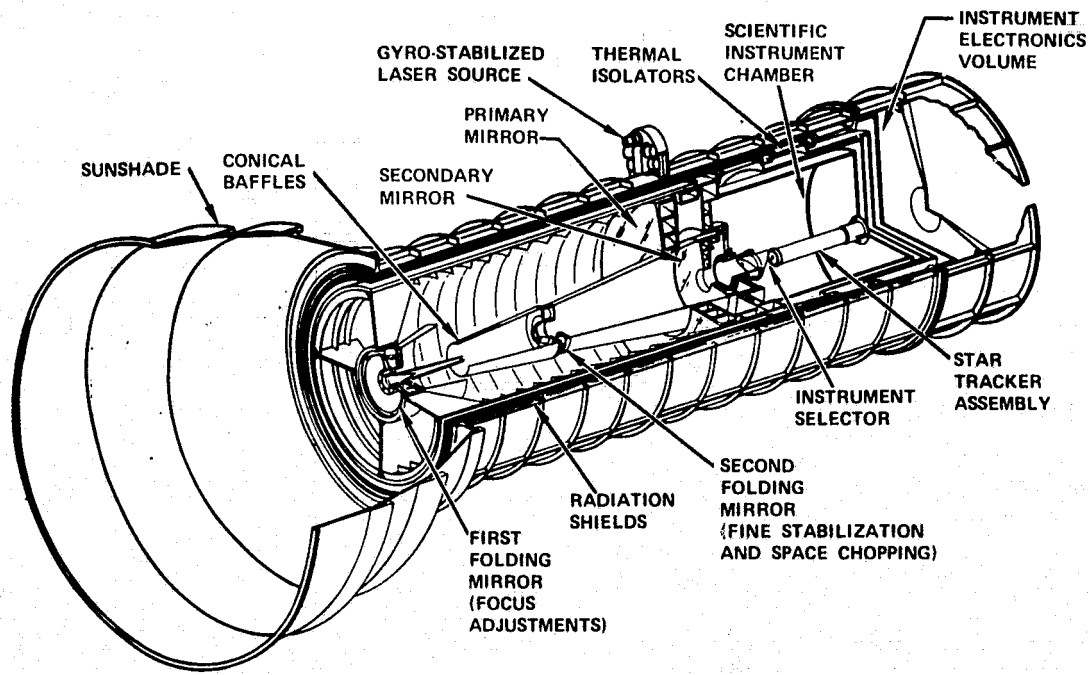


Figure 3-2. SIRTF telescope.

of the telescope. The main telescope collects and focuses both infrared and visible energy. The primary mirror of the Gregorian forms a real image of the field of view after reflection of the energy from the first folding mirror; a field stop at the first focal plane prevents energy from out-of-field sources from reaching the detectors. The beam diverges and the secondary mirror refocuses the energy at the focal plane of the telescope after reflection off the second folding mirror. A beamsplitter reflects the infrared energy into one of the astronomical instruments; the visible energy passes through the beamsplitter to the star tracker.

The telescope mirrors, which are made of beryllium, are mounted in an inner telescope barrel made of aluminum. The inner barrel is in turn mounted to the outer vacuum shell on a fiberglass cone which provides thermal isolation between the inner barrel and the outer shell. Vapor-cooled radiation shields and superinsulation reduce heat transfer rate from the outer shell to the barrel.

Astronomical data will be collected by each of six instruments located in the multiple instrument chamber (MIC). The instruments will range from

single-element photometers, with one or more filters to define spectral bands of interest, to multiplex spectrometers, such as a Michelson interferometer spectrometer which can generate high resolution spectra over wide bands. Other instruments may include multidetector, multifilter photometers, polarimeters, and grating spectrometers of various types. The instrument complement may be changed between flights as research interests progress.

The MIC will serve as the interface between SIRTF and the instruments. Instruments will be mounted, aligned, and tested in the MIC, and the MIC will then be installed in SIRTF and aligned with the telescope. Cooling, electrical connections, and preliminary data processing will be supplied to the instruments by the MIC. Design of the MIC and of the individual instruments was not a part of the SIRTF preliminary design study. Preliminary design of the MIC and instruments is planned as a future activity by NASA.

While the IPS will provide a high degree of stability and pointing accuracy, it is not sufficiently stable for telescopes requiring arc-second pointing. The SIRTF study has shown that an internal image stabilization system is necessary to realize the full potential of SIRTF. This is implemented by means of a focal plane star tracker operating in the visible region, and a servo drive on the second folding mirror. Once the star tracker has acquired the visible star (either on-axis or with a fixed offset), it generates error signals which are used to drive the second folding mirror and maintain pointing. For cases where there is no sufficiently bright star in the field of view, a gyro-stabilized laser provides an artificial star. More detail is provided in Section 3.5.

The modified, double-folded Gregorian optical design can be shown to have substantial advantages for the telescope. One important attribute of the folded Gregorian design is that the detectors are shielded from all extraneous radiation except energy which arrives, after scattering or diffraction, at the primary field stop within the FOV bundle. Energy radiated by the cone running between the secondary and the second folding mirror can also reach the detectors; however, the cone is kept cold enough so that this energy does not materially contribute to the background at the detector.

Another advantage of the Gregorian telescope over Cassegrain types is that space chopping and fine stabilization are achieved by moving the second (flat) folding mirror instead of moving the figured secondary. The secondary mirror of the Gregorian images the primary mirror precisely onto the second folding mirror so that the image of the primary at the second focal plane does not change as the mirror is tilted. By eliminating beam travel on the primary, scan modulation (or offset) due to scanning over condensed materials or dust is eliminated. The beam does travel on the first folding mirror and secondary but these are better protected from condensation than the primary so their levels of contamination will be lower. We will discuss contamination in a later section.

A third advantage of the Gregorian design is that there is no degradation of image quality over the field of view, even during space chopping. The aberration correction which can be obtained in the Gregorian is comparable to that obtained in a Ritchey-Chretien design; scanning of the second folding mirror introduces no aberration other than defocus, which for the present design is far smaller than the diffraction limit.

A fourth advantage is that the primary and secondary mirrors are located close to each other so that they are effectively both mounted to the same rigid structure, thus avoiding the problem of achieving and holding alignment (collimation) between the primary and secondary. Tilt of the first folding mirror has a minor effect on optical performance that can be corrected in flight.

Although the above advantages were considered important enough to warrant choice of the Gregorian as the baseline design, some astronomers have expressed concern about the lack of experience in dealing with the effects of the large central obscuration (0.50 diameter) and second folding mirror chopping on astronomical observations. A reduced-scale test of a folded Gregorian telescope is being planned to resolve these concerns. The results of this test will determine the final SIRTF telescope configuration.

The major subsystems (mechanical, optics, thermal, and stabilization) are discussed in the following subsections.

3.2 OPTICAL DESIGN AND PERFORMANCE ANALYSIS

The optical characteristics and performance evaluation of the SIRTF optical system are presented in this section. The double-folded Gregorian IR telescope is described and evaluated in Section 3.2.1 and the star tracker optical system is discussed in Section 3.2.2. Section 3.2.3 deals with the laser stabilization optics, and Section 3.2.4 rejection of energy from out-of-field sources. Section 3.2.5 covers the effects of condensed contamination on the telescope performance.

The design of the SIRTF IR telescope satisfies the optical performance criteria of being diffraction limited at 5 micrometers over its 15 arc minute field of view. The star tracker detecting element is still in the preliminary design stage and some minor additional optical design effort will be required to optimize the optical performance over its 30 arc minute field of view.

3.2.1 Data IR Telescope Design and Performance

The SIRTF IR telescope is a double-folded Gregorian configuration consisting of an f/3.15 ellipsoidal primary mirror and an ellipsoidal secondary mirror. The system aperture stop is located at the second folding mirror. An optical layout of this telescope is shown in Figure 3-3. In this telescope the first folding mirror is used to maintain focus and the second folding mirror is tilted to implement space chopping and image motion compensation. This mirror is controlled by a two-axis reactionless drive mechanism described in Section 3.5.1.

The main optical characteristics of the SIRTF IR telescope are summarized in Table 3-1.

Optical Performance

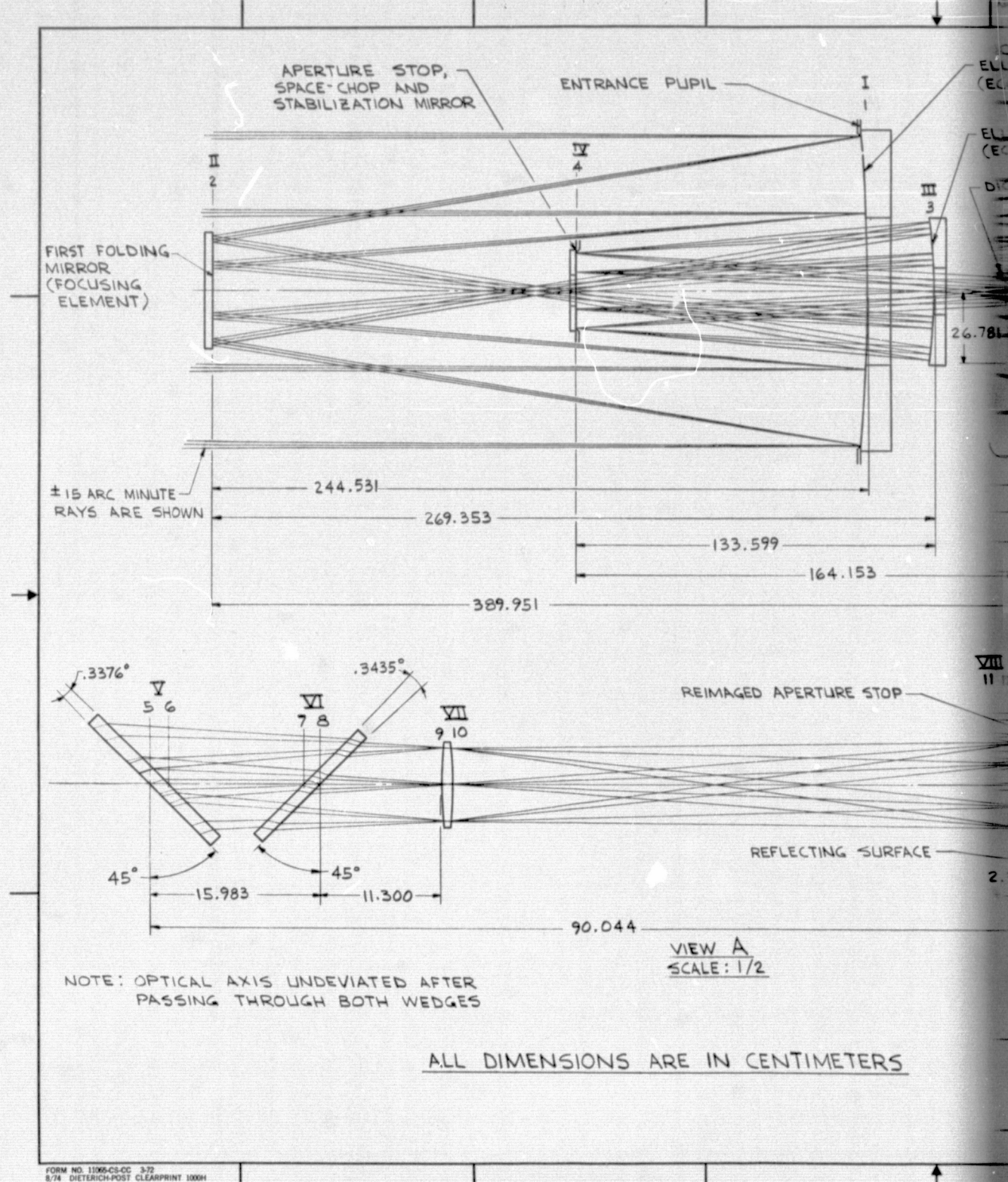
The optical performance of the SIRTF IR telescope was evaluated by two-dimensional Fourier analysis to generate point spread functions (PSF), physical modulation transfer function (MTF), physical optics radial energy distributions and spatial convolutions of the PSF with square detector elements.

TABLE 3-1. SIRTF IR TELESCOPE OPTICAL CHARACTERISTICS

<u>Parameter</u>	<u>Values</u>
Effective focal length, m.	7.97
Telescope f-number	6.87
Primary mirror f-number	3.15
Secondary magnification	2.18
Entrance pupil diameter, m.	1.16
Linear obscuration, %	50.0
Total field of view, arc-min.	15
Space chopping displacement angle, arc min.	± 7.5 in two perpendicular directions

The on-axis performance was examined in detail, and the other field positions were evaluated by calculating PSF and physical optics radial energy distributions. In particular, the on-axis performance at 5.0 micrometers was evaluated by generating the point spread function shown in Figure 3-4, by calculating the physical modulation transfer function shown in Figure 3-5, by calculating the physical optics radial energy distribution shown in Figure 3-6 and by convolving the PSF with a 1.0 arc second, and a 2.17 arc second (Airy disc diameter) square detector (Figure 3-7). A jitter analysis was completed by convolving the on-axis point spread function with a Gaussian jitter function and is shown in Figure 3-8. Physical optics radial energy distributions are presented in Figure 3-9.

The other field positions evaluated were +4.0 arc minute, +7.5 arc minute, on-axis with 4.0 arc minute displacement angle of the field of view and on-axis with 7.5 arc minute displacement angle. At each point in the field and at each displacement angle, point spread functions and physical optics radial energy distributions were calculated. Figure 3-10 illustrates profiles of the point spread functions for the different field positions and displacement angles. Since the physical optics radial energy distributions were almost identical to the on-axis case shown in Figure 3-6, they are not presented.



FOLDOUT FRAME

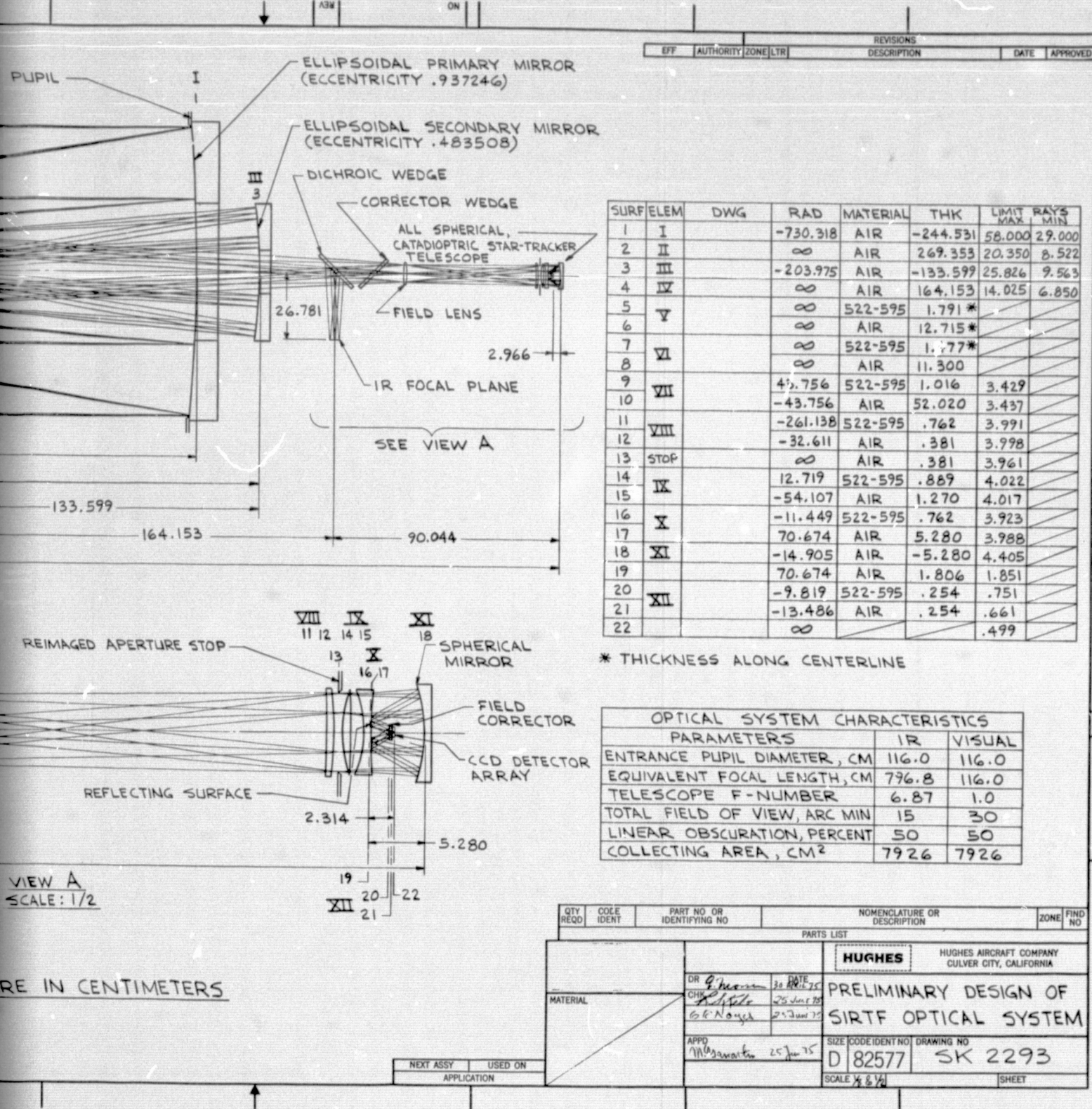


Figure 3-3. Optical layout of the SIRTF optical system.

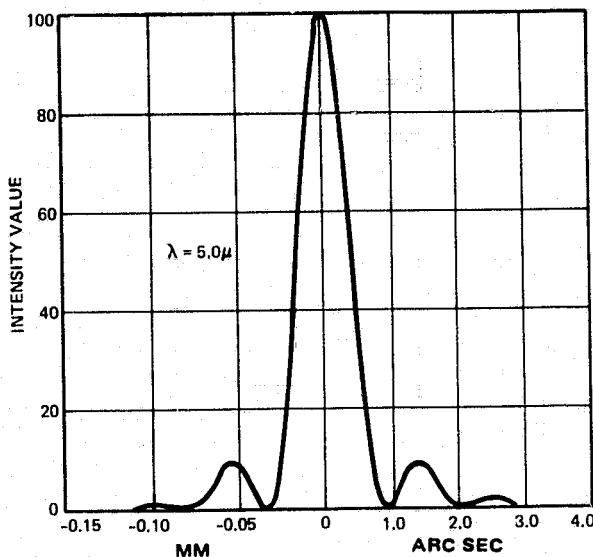
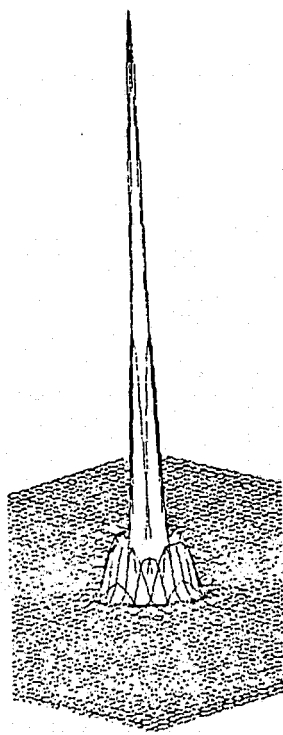


Figure 3-4. On-axis point spread function, $\lambda = 5$ micrometers.

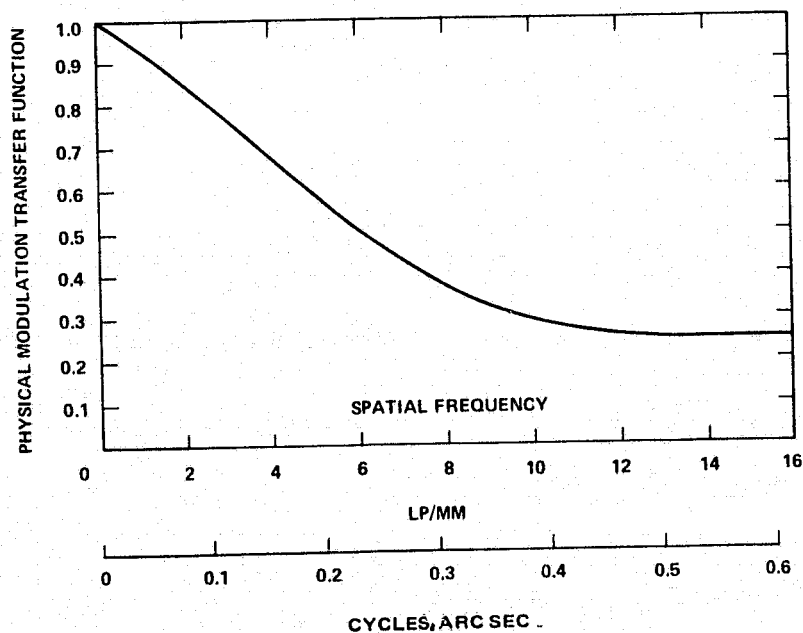


Figure 3-5. On-axis physical modulation transfer function.

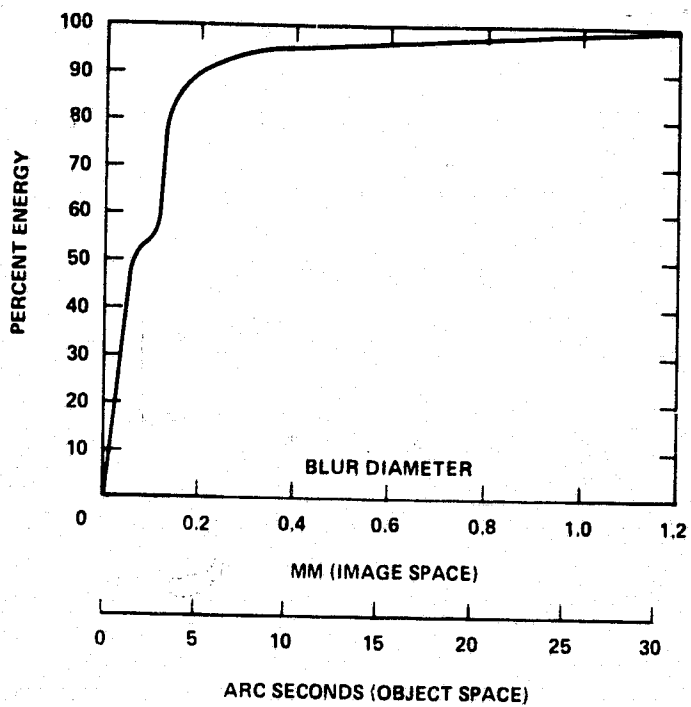


Figure 3-6. On-axis physical optics radial energy distribution.

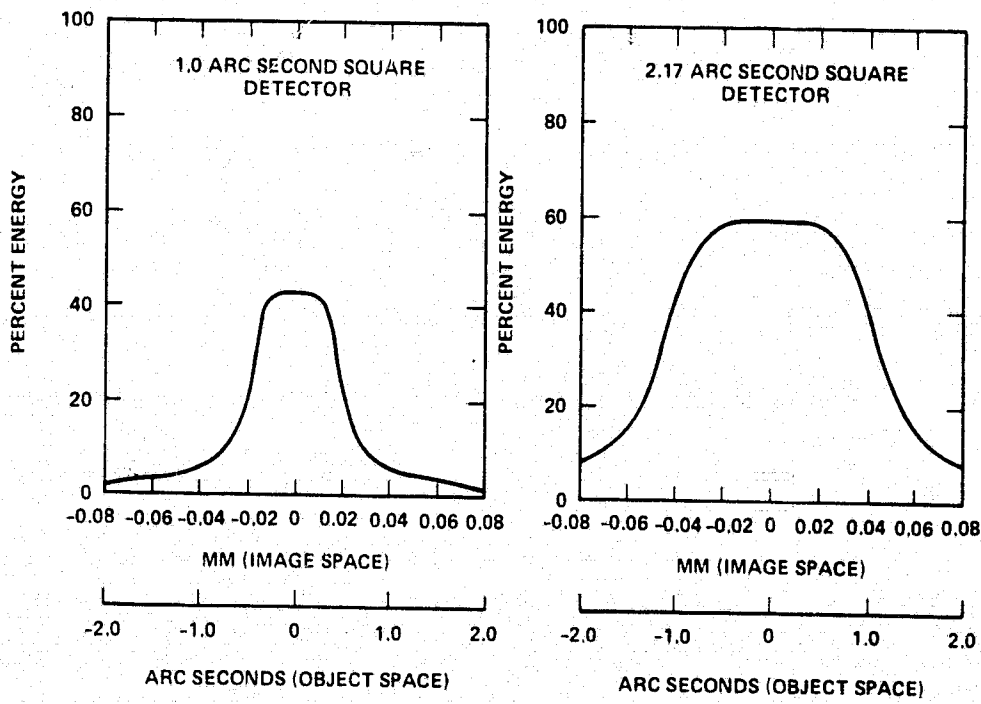


Figure 3-7. Convolution of the on-axis PSF with a 1.0 and 2.17 arc second square detector.

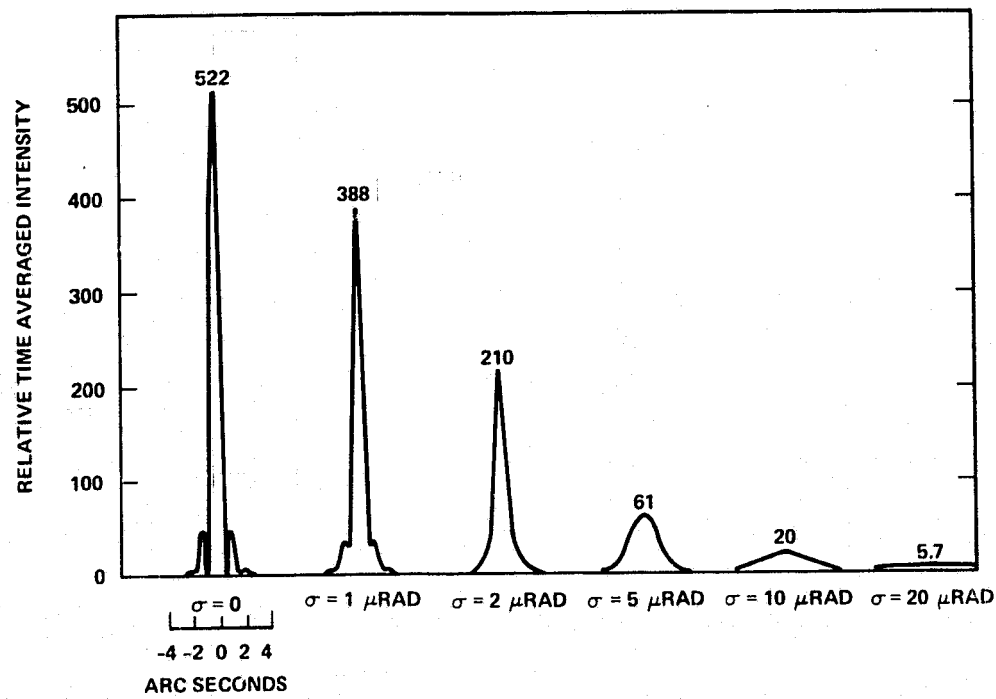


Figure 3-8. Convolution of the on-axis PSF with Gaussian jitter function for $\lambda = 1, 2, 5, 10$ and 20 microradian jitter.

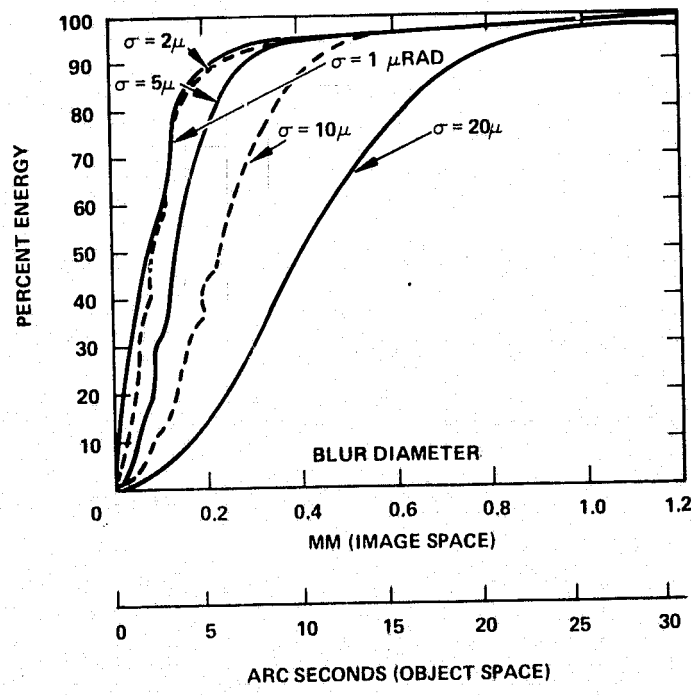


Figure 3-9. Jitter analysis physical optics radial energy distributions.

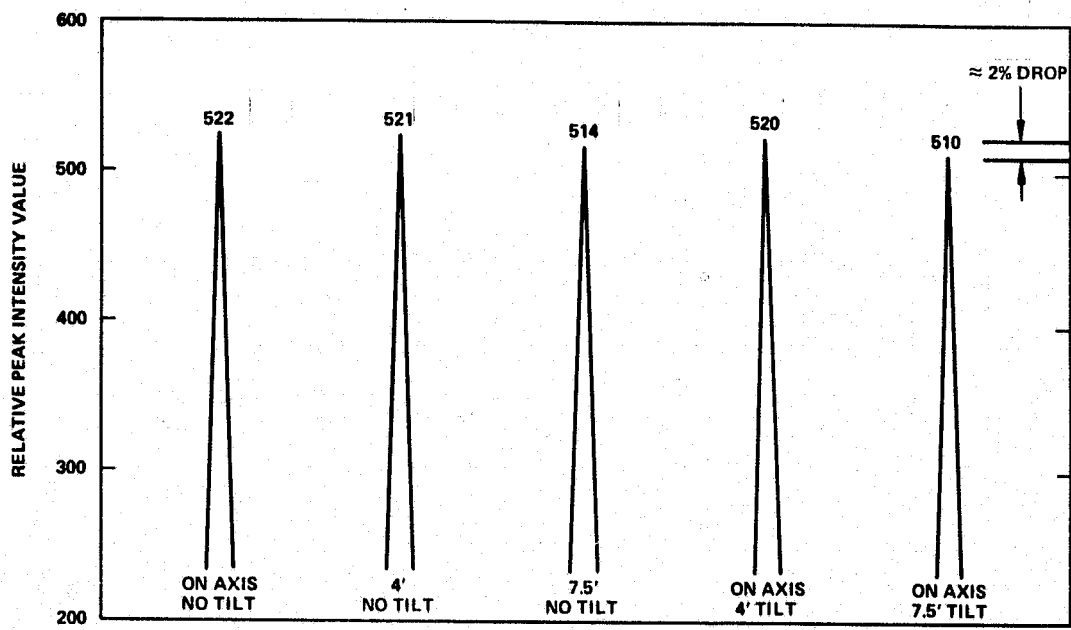


Figure 3-10. Profiles of point spread functions for different field positions and field of view displacement angles (tilt).

An examination of the point spread functions shown in Figure 3-10 indicates the optical performance of the SIRTF IR telescope is diffraction limited over the 15 arc minute field of view and also on-axis with a ± 7.5 arc minute space-chop displacement angle.

Boresight Sensitivity and Image Degradation Analysis

The boresight sensitivity of the SIRTF IR telescope was analyzed by individually tilting and decentering the primary and secondary mirrors and by tilting the first and second folding mirrors. In this calculation the mirrors were tilted by one arc minute and the primary and secondary were decentered by 0.5 millimeter. For each separate tilt or decenter, the change in boresight angle in object space was recorded and the image quality was examined by calculating a geometrical radial energy distribution from a 500-ray spot diagram. The results of this analysis are summarized in Table 3-2. This table contains the change in boresight angle for 1 arc minute of tilt, 0.5 millimeter decenter and the geometrical blur diameter containing 90 percent energy for each case.

TABLE 3-2. BORESIGHT SENSITIVITY AND IMAGE DEGRADATION ANALYSIS SUMMARY

Mirrors	1 Arc Minute Mirror Tilt		Decentration = 0.5 mm	
	Δ Boresight Angle, mrad	90% Energy Blur Diameter, mm	Δ Boresight Angle, mrad	90% Energy Blur Diameter, mm
Primary	0.58	0.035	-0.14	0.016
1st folding	-0.19	0.026	-	-
Secondary	-0.24	0.012	0.20	0.016
2nd folding	0.14	0.0036	-	-

The image degradation introduced by tilting the secondary mirror was examined in terms of geometrical radial energy distributions and the results are shown in Figure 3-11. For a 5 arc minute tilt of the secondary mirror, the geometrical blur diameter containing 90 percent of the energy is less

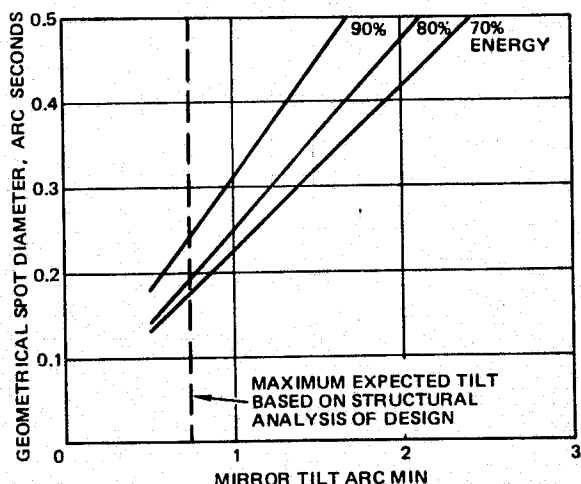


Figure 3-11. Image degradation introduced by tilting the secondary mirror.

than 1.42 arc second. Calculations based on the actual mechanical design indicate that the actual tilts will be in the range of 10 to 30 arc seconds; the effect on the blur will thus be negligible (see Section 3.4.1).

In summary, the SIRTF IR telescope has been designed to be diffraction limited at 5.0 micrometers over its 15 arc minute field of view and on axis with a ± 7.5 arc minute space chop displacement angle introduced by tilting the second folding mirror. Tilt and decenter introduced by mechanical and thermal effects will not affect performance.

3.2.2 Description of the Star Tracker Optics

The SIRTF star tracker consists of an optical system, a 400 by 400 element charge-coupled device (CCD) array, and associated signal processing electronics. The size of the CCD array makes it necessary to de-magnify the data telescope FOV before imaging on the CCD array. (See Section 3.5.2.) The SIRTF star tracker optics, preceded by the two tilted wedges of the dichroic beamsplitter in the converging beam of the IR telescope, consists of a relay lens (comprised of a field lens at the intermediate image plane, and an f/7.0 singlet element), and an f/1.0 catadioptric star tracker telescope. A layout of this optical system is illustrated in the lower portion of Figure 3-3 and also in Figure 3-12.

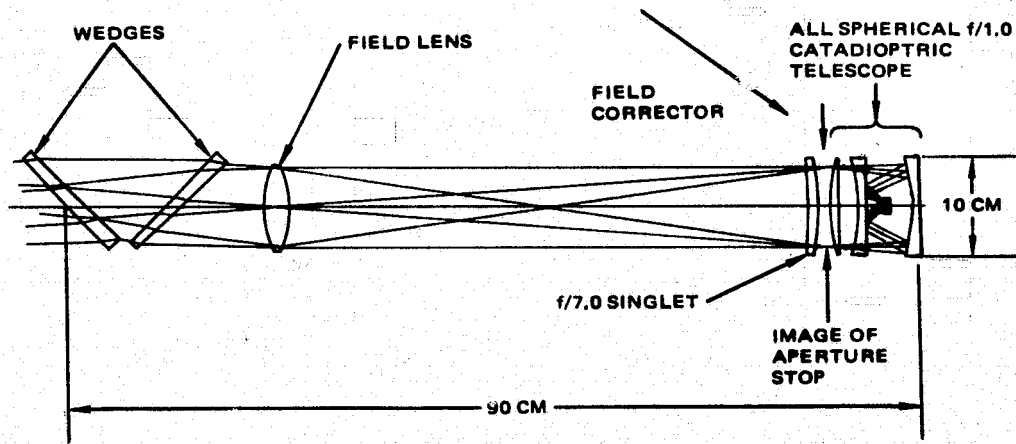


Figure 3-12. Optical layout of star tracker relay.

The first optical components in the diagram of the star tracker relay are a pair of wedges tilted at 45 degrees with respect to the optical axis. The front surface of the first wedge has a dichroic beamsplitter coating which reflects the IR radiation and transmits the visible radiation. The second surface of the wedge is not parallel to the first surface to correct the axial astigmatism introduced by having a tilted plate in a converging beam. The second tilted wedge is required to correct the residual axial astigmatism and coma introduced by the first wedge. The wedge angle and thickness of the second wedge are selected to restore the optical axis along the optical axis of the IR telescope. The star tracker relay optical axis must be coaxial with the IR optical axis in order to permit the dichroic wedge surface to rotate 360 degrees to select different MIC experiments.

The second component of the star tracker relay is a field lens at the intermediate image plane which redirects the off-axis radiation toward the entrance pupil of the catadioptric telescope. The third component is an f/7.0 singlet which collimates the radiation from the field lens into the telescope.

The final component is an f/1.0 catadioptric system which consists of two low-power corrector elements, a spherical primary mirror, a spherical secondary mirror (reflective coating on the rear surface of the second corrector element) and a field corrector lens.

Because the star tracker is located in the MIC where the ambient temperature is about 20°K, the performance of the star tracker optical system at low temperatures was studied. In this design, all the refractive elements were assumed to be made from Schott K5 glass (522-595) because of its low change of refractive index with temperature. Because of the lack of data at low temperatures on Schott K5, data on Bausch and Lomb 523-586 (a very similar glass) was also used. Table 3-3 gives refractive index change with temperature data in air and vacuum. The absolute index changes are 4 to 14 times less than those in air. Figure 3-13 shows lower temperature data for the B&L glass; this data is relative rather than absolute index change and at shorter wavelengths than the CCD band. Since the B&L glass change at low temperatures is much too small to cause image degradation, and the absolute refractive index change is smaller than the relative change,

TABLE 3-3. TEMPERATURE COEFFICIENTS OF SCHOTT K5 (522-595) GLASS (SPECTRAL BAND IN STAR TRACKER CHANNEL: 650 TO 950 nm)

Temperature Range (°C)	Temperature Coefficients $\frac{\Delta n}{\Delta T} \times 10^6 / {}^\circ C$ (Temperature of Glass and Ambient Air are Equal)			Temperature Coefficients of Absolute Refractive Index $\frac{dn}{dT} \times 10^6 / {}^\circ C$ (in vacuum)		
	643.8 nm	850 nm	1060 nm	643.8 nm	850 nm	1060 nm
0 to +20	1.8	1.4	1.5	0.2	-0.1	0.0
+20 to +40	1.8	1.4	1.5	0.5	0.1	0.2
+40 to +60	1.8	1.4	1.5	0.7	0.3	0.4

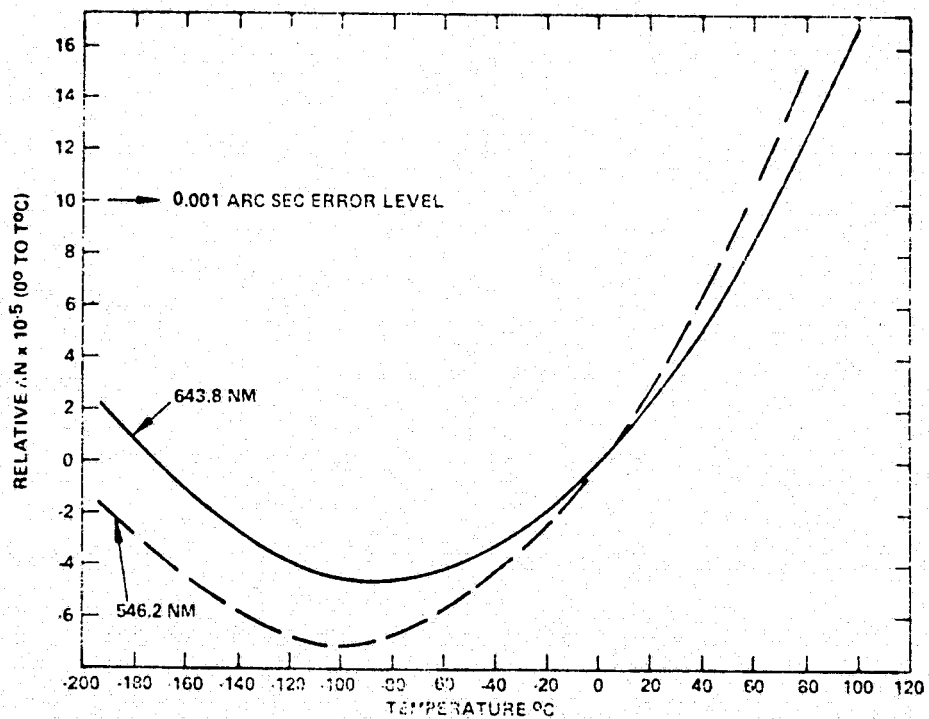


Figure 3-13. Refractive index change with temperature for B&L 523-586 glass.

and the coefficient change with temperature is smaller at longer wavelengths, there will be no image degradation due to index change at low temperatures.

The main characteristics of the star tracker optics combined with the SIRTF IR telescope are provided in Table 3-4.

TABLE 3-4. SIRTF STAR TRACKER OPTICAL CHARACTERISTICS
(INCLUDING THE IR TELESCOPE)

<u>Parameter</u>	<u>Values</u>
Effective focal length, m	1.16
Telescope f-number	1.00
Entrance pupil diameter, m	1.16
Linear obscuration, %	50.0
Total field of view, arc min.	30
Space chopping displacement angle, arc min.	± 7.5 in two perpendicular directions
Approximate transmittance, % (without obscuration)	60

Performance of the Star Tracker Optical System

The performance of the star tracker optical system combined with the SIRTF IR telescope and compensating wedges was evaluated by tracing spot diagrams and calculating knife-edge scans in the X and Y directions at the on-axis and +7.5 arc minute elevation field position. These knife-edge scans of the preliminary version of the star tracker optical system are shown in Figures 3-14 and 3-15 for the X and Y scan directions respectively. The +7.5 arc minute field position in azimuth and the -7.5 arc minute field position in elevation were also examined and the knife-edge results were found to be almost identical to the knife-edge scans at +7.5 arc minute in elevation. In addition, the diagonal field positions within a 7.5 arc minute radius were checked to verify the image quality through the pair of compensating wedges. These results were also almost identical to the knife-edge scans at 7.5 arc minute in elevation.

In actual practice, the star tracker optics may be used in a defocused mode to allow the image blur to cover at least 4 x 4 resolution elements of the 400 x 400 element CCD array. This defocusing improves the pointing accuracy. By computing the locations of the centroid of the blur (from the ratios of energy on the various elements) the centroid can be located to about 1/10 the resolution element dimension.

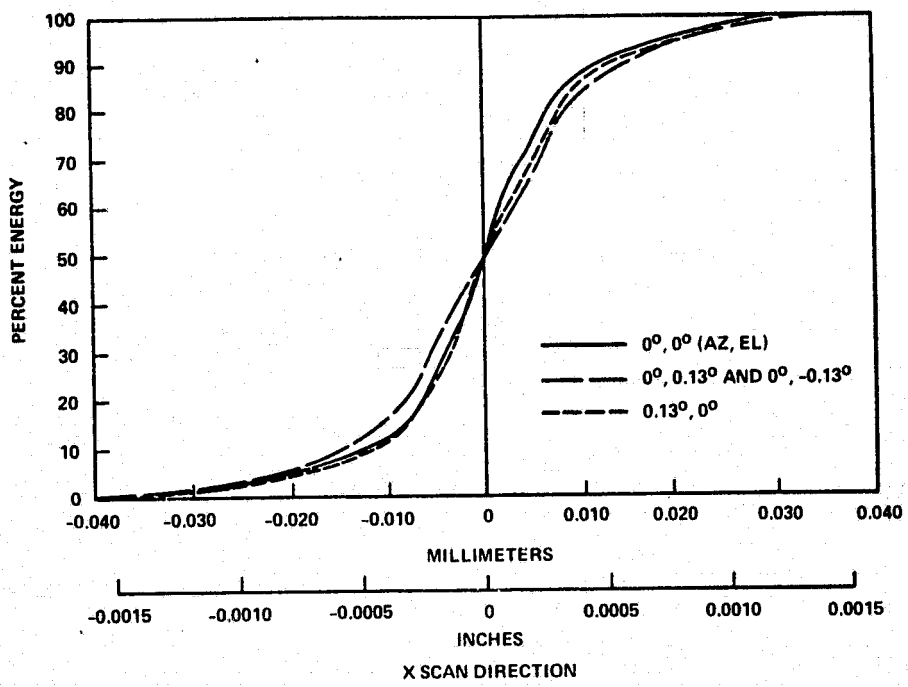


Figure 3-14. Knife-edge scans in X direction for the star tracker optical system.

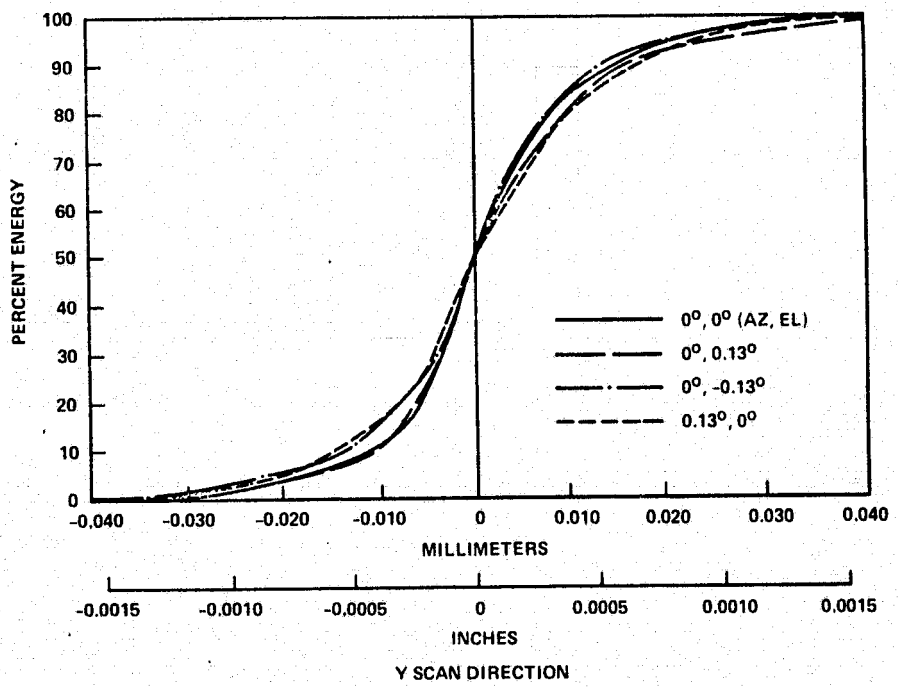


Figure 3-15. Knife-edge scans in Y direction for the star tracker optical system.

In order to evaluate the on-axis geometrical blur at a suitable defocused position, a spot diagram consisting of 300 rays at 0.78 micrometers, 150 rays at 0.65 micrometers and 150 rays at 0.93 micrometers was calculated for various defocus conditions until the 4×4 resolution elements were approximately covered. Figure 3-16 illustrates the spot diagram filling a 4×4 resolution element area.

In this spot diagram, the points indicated by 1 correspond to radiation at 0.78 micrometers. An examination of Figure 3-16 reveals that radiation at 0.78 micrometers is focused into an annular image. The points indicated by 2 correspond to radiation at 0.65 micrometers. Radiation at this wavelength is focused into a small area in the center of the image blur and tends

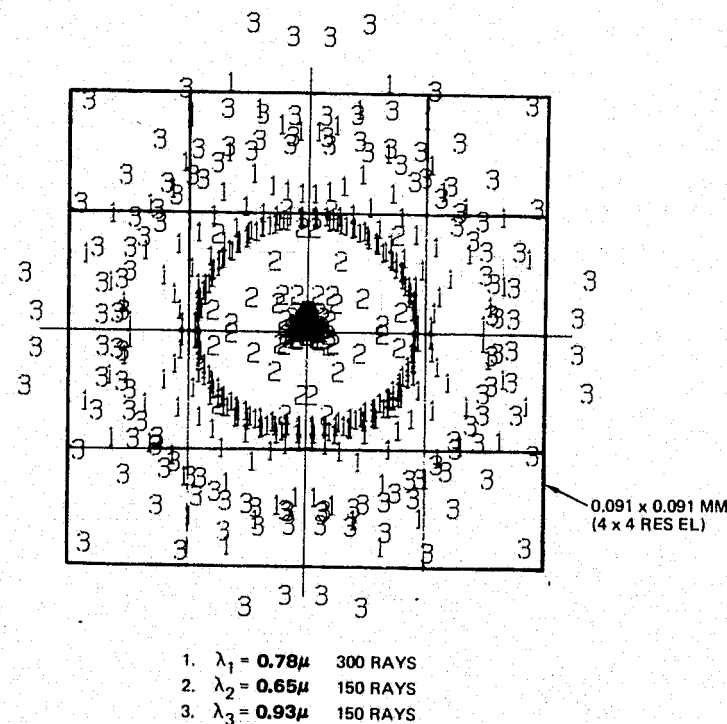


Figure 3-16. Geometrical spot diagram, on-axis.

to fill the hole in the annular image. The points indicated by 3 correspond to radiation at 0.93 micrometers. At this wavelength, the radiation is focused into a larger annular image.

It appears that radiation between 0.65 and 0.78 micrometers will be focused near the central portion of the image so that the image remains peaked at its center.

An on-axis radial distribution was calculated from this spot diagram and is shown in Figure 3-17. The irregular regions on this radial energy distribution are caused by the fact that only three wavelengths of radiation are traced in this spot diagram. If many wavelengths of radiation were traced to calculate a new spot diagram, the radial energy distribution would have the same magnitude but would be smoother in appearance.

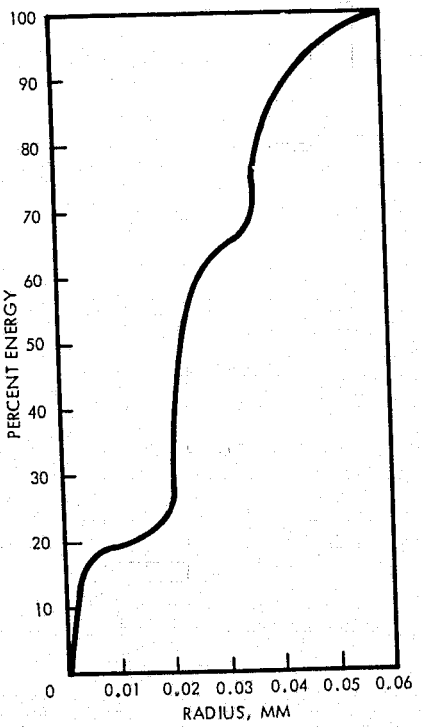


Figure 3-17. Geometrical radial energy distribution, on-axis.

Figure 3-18 represents knife-edge scans in X and Y directions of the defocused spot diagram shown in Figure 3-16. These knife-edge scans would also be smoother if many wavelengths of radiation between 0.65 and 0.93 micrometers were traced to calculate the spot diagram.

Another potential problem area in star tracker performance is the amount of anamorphic distortion introduced by the tilted beamsplitter wedge and compensating wedge in the star-tracker optics. This is analyzed here by tracing chief rays at various field positions in azimuth and plus and minus elevation. Figure 3-19 illustrates the optical schematic of the SIRTF star tracker and the orientation of image heights X, +Y and -Y with respect to the tilted wedges and field angle θ . (θ shown in the YZ plane for Y image heights.)

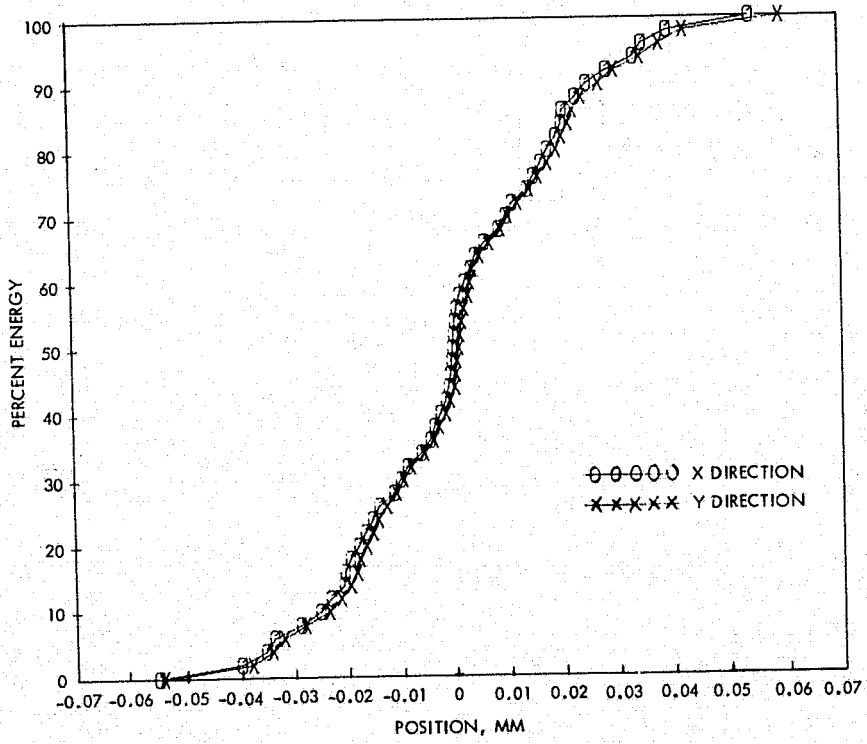


Figure 3-18. Geometrical knife-edge scans, on-axis.

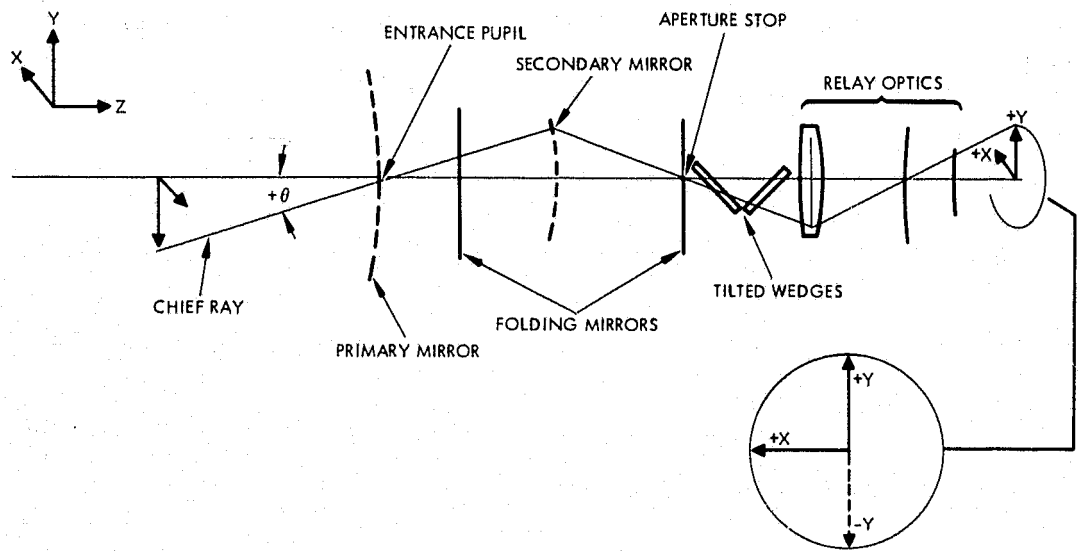


Figure 3-19. Unfolded optical schematic of star tracker.

Table 3-5A lists the paraxial image heights ($f \tan \theta$) and the actual image heights, H_{pr} , for +Y, -Y and $\pm X$ directions in the paraxial image plane for various semi-field angles θ . (Note: a negative semi-field angle θ corresponds to the negative image heights in the -Y direction.) Table 3-5B lists the angular distortion calculated from the expression:

$$\text{Angular Distortion(arc sec)} = (H_{pr} - f \tan \theta) \times (177.8 \frac{\text{arc sec}}{\text{mm}})$$

The anamorphic distortion introduced by the tilted wedges causes the image heights along the Y axis to be reduced by approximately 1.5 percent throughout the elevation field of view. The image heights along the X axis are relatively unchanged from the paraxial image heights. Since this results in fixed position errors of up to 14 arc second, the star tracker data processor will have to initiate this fixed correction (as a function of field angle) when guiding on an off-axis star. Since the distortion is fixed, this will not increase the random error in off-axis guiding.

Thus, the preliminary version of the star tracker optics provides a uniform geometrical blur over 15 arc minutes of its 30 arc minute field of view.

TABLE 3-5. DISTORTION OF THE STAR TRACKER OPTICS

A. SUMMARY OF PARAXIAL AND ACTUAL IMAGE HEIGHTS
FOR VARIOUS VALUES OF θ (mm)

(Distortion = $H_{pr} - f \tan \theta$, $f = 1160$ mm)

θ°	$f \tan \theta$	$H_{pr} (+Y)$	$H_{pr} (-Y)$	$H_{pr} (\pm X)$
0.05	1.0122912	0.997674	-0.997666	1.01399
0.10	2.0245838	1.99506	-1.99501	2.02765
0.15	3.0368797	2.99184	-2.99172	3.04065
0.20	4.0491802	3.98768	-3.98747	4.05265
0.25	5.061487	4.98224	-4.98190	5.06326

B. ANGULAR DISTORTION AS A FUNCTION OF
SEMI-FIELD ANGLE θ

θ°	Angular Distortion		
	+Y Direction (arc sec)	-Y Direction (arc sec)	$\pm X$ Direction (arc sec)
0.05	- 2.60	- 2.60	0.302
0.10	- 5.25	- 5.26	0.545
0.15	- 8.01	- 8.03	0.670
0.20	-10.93	-10.97	0.617
0.25	-14.09	-14.15	0.315

Further optimization of the star tracker optical system will improve the uniformity of the image throughout the entire 30 arc minute field of view. Having established that a high quality image can be produced for the star tracker further work must await details of the final configuration of the CCD chip, which is under development by Jet Propulsion Laboratory.

3.2.3 Infrared and Visible Transmittance of the SIRTF Telescope

Coatings for the mirrors and beamsplitter (MIC selector) are discussed, followed by computation of the transmission of the SIRTF telescope in the infrared, and of the star tracker optics.

Coatings

The coatings for the SIRTF telescope mirrors and beamsplitter were selected considering both optical and environmental requirements. A trade-off was made among bare beryllium, bare silver, silver with magnesium fluoride overcoat, electrolytic gold and vacuum deposited gold. Previous measurements of samples of each type of coating have been used to predict the transmittance of the telescope as a function of wavelength.

Characteristics of the mirror surfaces are listed in Table 3-6. The table shows that optically the best mirror coating for SIRTF is silver because its reflectance is the highest of any metal over the entire 0.5 to 1000 μm wavelength region. (High reflectance in the visible is needed to provide high signal levels to the star tracker.) Hughes' experience is that silver tarnishes quite easily so that it must be protected. Members of the SIRTSAG claimed that they have seen little tarnishing on silver astronomical mirrors. They are opposed to overcoating because overcoatings have one or more absorption bands in the infrared range. The question was not fully resolved; a coating without absorption bands has been tested since the final discussions took place and may represent a solution. In any case, final selection of the coating need not be made until shortly before the primary is actually coated, and a coating can be stripped off and replaced at any time if it proves to be unsatisfactory.

Figure 3-20 illustrates the performance of the coating initially suggested. The main features of this coating, which was developed by Optical Coating Laboratories, Inc. (OCLI), are its durability (i. e., resistance to abrasion, humidity, etc.), the protection it gives the silver, and its almost lack of absorption bands. Measurements shown in Figure 3-20 are for a coating on glass and the measurements were made after the MIL-M-13508 humidity, adhesion, and abrasion tests. Equally good performance is obtained coating on beryllium. Also shown is the reflectance raised to the fourth

TABLE 3-6. COATING MATERIAL TRADEOFF

A. Mirrors				
	IR Reflectivity	Visible Reflectivity	Durability	Degradation in Normal Use
Bare Be	97%	50%	Good	Slight amount
Bare Ag	>99%	>97%	Very poor	Tarnishes easily
Ag with OCLI dielectric	99%	97%	Excellent	Very slight amount
Electrolytic Au	96%	~50%	Fair	Very little
Vacuum deposited Au	>99%	~50%	Very soft	Very little

B. Beamsplitter				
	IR Reflection	Visible Transmission	Durability	Degradation in Normal Use
Bare Gold	95%	60%	Very poor	Slight
Overcoated Gold	90% but not uniform	65%	Good	Slight
Inconel	85%	50-70%	Very good	Slight
Chromium	85%	50-70%	Very good	Slight
Indium oxide	85%	78%	Excellent	Very slight

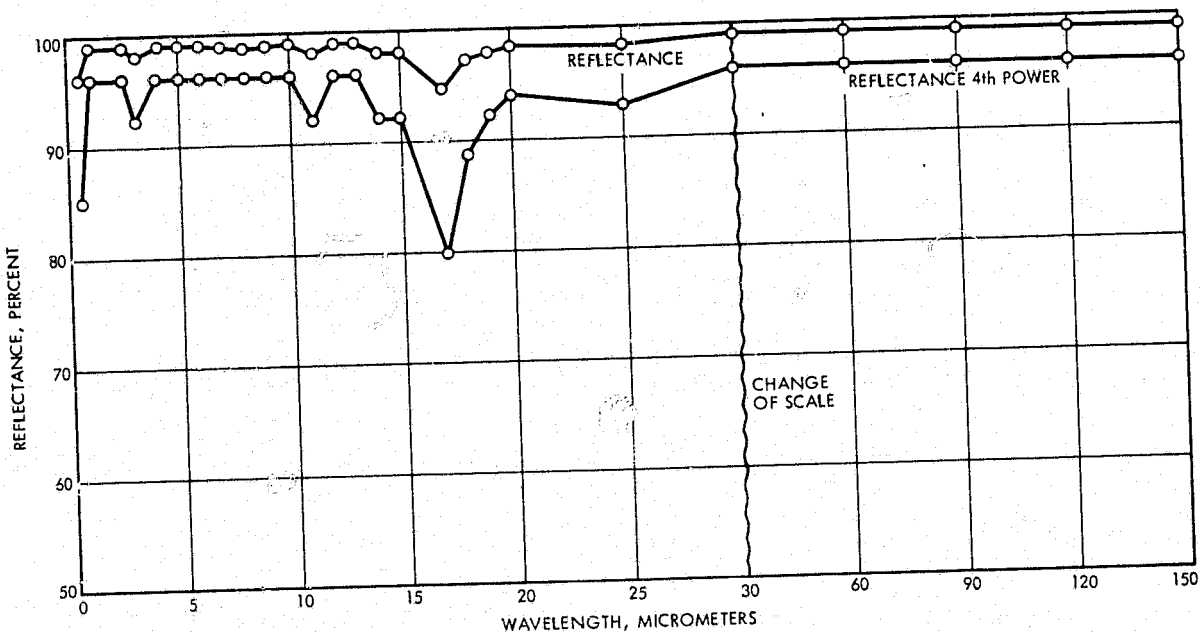


Figure 3-20. Reflectance as a function of wavelength of the OCLI protected silver mirror.

power. As can be seen from Figure 3-20 there are two small (1 percent) absorption bands at $3 \mu\text{m}$ and $11 \mu\text{m}$ and a larger absorption band (8 percent) at $17 \mu\text{m}$.

While the above coating avoids the undesirable absorption bands of silicon oxides near $9 \mu\text{m}$, a coating currently under development may be substantially better. This material, also an OCLI development, has been tested and shows the reflectance to be greater than 95 percent in the visible, coupled with no absorption bands in the infrared from 1 to $50 \mu\text{m}$. Because this overcoating is approximately $0.1 \mu\text{m}$ thick, it is expected that there will be no absorption bands beyond $50 \mu\text{m}$. The results are still preliminary and further testing will be required to fully establish the coating's performance.

The beamsplitter is used to separate the infrared ($\lambda > 1 \mu\text{m}$) from the visible energy (0.5 to $0.9 \mu\text{m}$) used by the star tracker. The coating will be applied to the front surface of a flat glass substrate to reflect the infrared and transmit the visible. As shown in Table 3-6B, several beamsplitter coatings were considered.

Gold was the first candidate, but has been eliminated because it requires an overcoating in order to be durable and to have acceptable visible

transmittance. When used at a 45° angle of incidence, the overcoating causes undesirable regions of spectral absorptance due to reststrahlen effects. The inconel and the chrome coatings are both durable, but do not give the required performance. Indium oxide was chosen because of its better spectral characteristics. (See Figure 3-21.) It should be noted that the values of Figure 3-21 can be traded off. That is, the infrared reflectance can be increased to say 95 percent, but this would lower the star tracker optics transmittance to approximately 5 percent.

Predicted Transmittance of the IR Telescope

The predicted transmittance of the telescope (neglecting obscuration) for all wavelengths from 1 to 1000 μm will be greater than

$$T = R_M^4 R_B = (0.92)^4 \cdot 0.85 = 60 \text{ percent}$$

where

R_M is the reflectance of a mirror surface

R_B is the reflectance of the beamsplitter

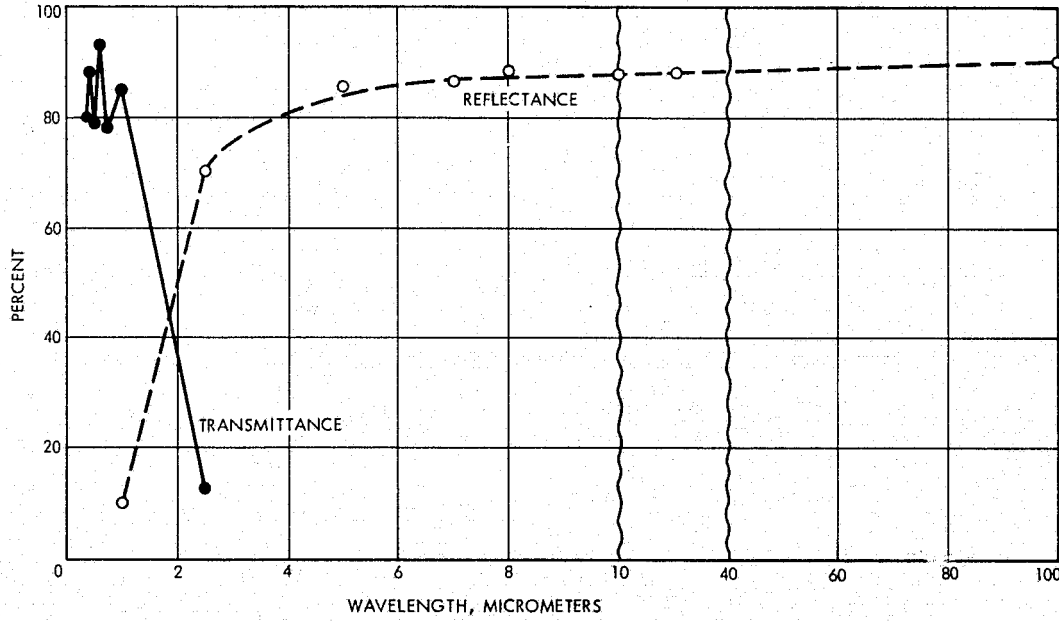


Figure 3-21. Transmittance and reflectance as a function of wavelength of the OCLI indium oxide beamsplitter coating.

Predicted Transmittance of the Star Tracker Telescope

Including glass absorption, the predicted transmittance of the visible portion of the SIRTF telescope is

$$T = R_M^6 T_B^{12} T_S^{2.78} T_g^{2.78} = (0.96)^6 0.78 (0.9925)^{12} (0.99)^{2.78} = 53 \text{ percent}$$

where

T_g = bulk transmittance of one cm of glass

T_B = average transmittance of the beamsplitter from 0.5 to 0.9 μm

T_S = average transmittance of the antireflection coated glass surfaces from 0.5 to 0.9 μm

Note that 0.0075 average reflectance per surface was used for the 0.5 to 0.9 μm region.

Predicted Transmittance of the Alignment Laser Energy

$$T = R_M^6 T_B^{12} T_L^{2.78} T_g^{2.78} = (0.96)^6 0.81 (0.9975)^{12} (0.99)^{2.78} = 59 \text{ percent}$$

where

T_B = transmittance of the beamsplitter at 6328 Å

T_L = transmittance of the coated glass surfaces at 6328 Å

Star Tracker Ghost Images

The use of a laser beam as part of the SIRTF stabilization system raises the question of whether ghost images of the laser beam can interface with tracking on a faint guide star. (The stabilization subsystem is discussed in detail in Section 3.5.)

The antireflection coatings on the refracting surfaces of the relay optics for the star tracker can be peaked for minimum reflectance at the laser wavelength, 0.6328 μm and at the same time have less than 1 percent reflectance from 0.5 to 0.9 μm . A reasonable value for the reflectance at 0.6328 μm is 0.25 percent (see Figure 3-22). Since a ghost requires at least

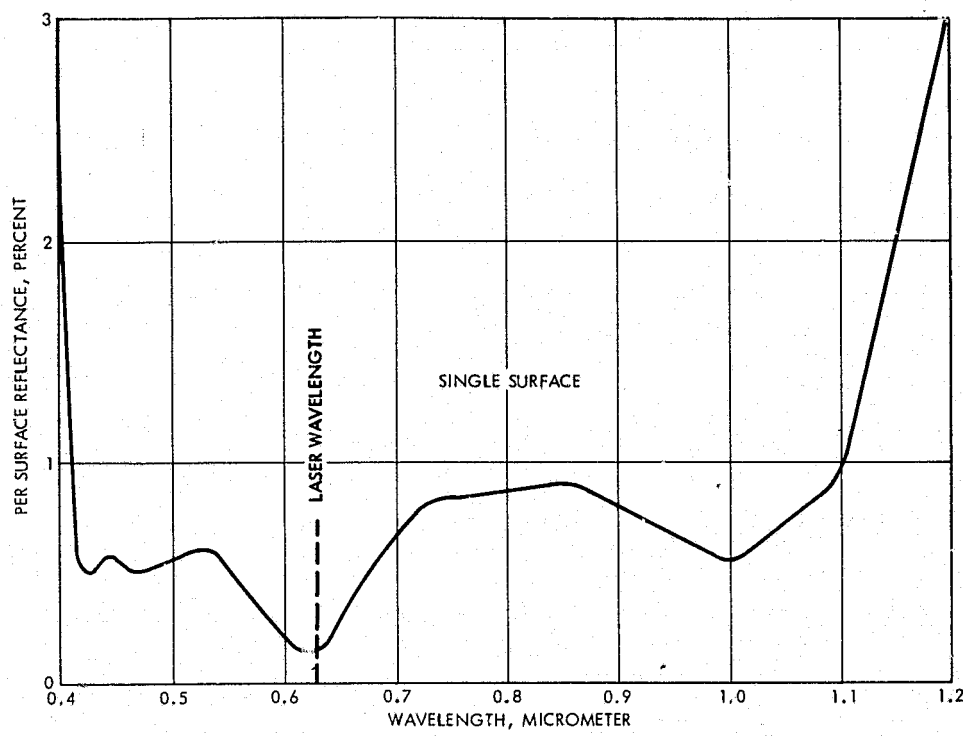


Figure 3-22. Reflectance per surface as a function of wavelength for OCLI extended HEA on 522-595 glass (Schott K5).

two reflections, using this coating will reduce any potential ghosts to at least 6×10^{-6} of that of the main beam. The minimum intensity guide star is fourteenth magnitude, and the maximum intensity for the laser beam is the equivalent of ninth magnitude. Thus, the ghost of the laser beam will be twenty-second magnitude. Therefore, the brightest ghost of the laser beam will be 1.6×10^{-3} of the minimum guide star and no interference from laser ghosts is anticipated.

On the other hand, if a single layer magnesium fluoride antireflection coating such as that of MIL-C-675, were used, the minimum reflectance would be approximately 1.75 percent. Thus the laser at the brightness of ninth magnitude would give a ghost approximately as bright as a seventeenth magnitude star. This is four visual magnitudes fainter than the star being tracked but the larger margin offered by the high efficiency anti-reflection (HEA) coating is preferred.

Summary

The values for reflectance and transmittance presented in this section are based on measured data using small witness samples. However, there should be no problem in coating the full size hardware with equally good coatings. In all cases the transmittance and reflectance values used in the calculations are not quite as good as the measured values. This allows for loss in performance due to handling during the manufacturing and testing phase of the program. During the detail design of SIRTF a trade-off study of the beam-splitter visible transmittance versus its infrared reflectance should be made. All of the coatings considered will withstand the entire environmental requirements of MIL-M-13508.

The environmental capabilities and the spectral performance of the above coatings can be achieved on flight hardware and meet the SIRTF requirements.

3.2.4 Out-of-Field Source Rejection

The sensitivity of the SIRTF telescope can be seriously degraded by the background generated by infrared energy that is diffracted or scattered into the field of view from sources (e.g., sun, moon, earth) outside the field of view. To reduce this background, several design approaches are used: (1) low-scatter mirrors are used to limit the scattering of out-of-field energy into the field of view; (2) high absorptivity cold baffles are placed so as to intercept the out-of-field energy; and (3) a sun shield is located at the front of the telescope. The sun shield serves the further purpose of limiting the thermal load on the telescope cryogen subsystem.

This section presents the estimated detector flux density for this telescope over an extended range of horizon angles, from 20 to 60 degrees. Scan modulation (flux density change) is presented over the same range. Photon flux from the sun and the moon are also presented over the full range of off-axis angles. The contribution of zodiacal emission is estimated, as well as the effect of scanning along the gradient of zodiacal emission. Finally, the effect of scanning the first folding mirror for stabilization purposes is investigated.

Telescope Definition

The configuration and pertinent dimensions of the SIRTF telescope are shown in Figure 3-23. The dimensions of the specular sunshade are such that the baffles are not directly illuminated at source angles equal to or greater than 45 degrees from the optical axis.

The scattering characteristics for the primary and first folding mirrors were assumed to be those of a bare beryllium surface. These characteristics are described by the BRDF (bidirectional reflectance distribution function) which is the relative power scattered per steradian as a function of angle from the specular beam. The measured BDRF for bare beryllium is given in Figure 3-24. The diffuse component of reflectance for the conical shield was assumed to be 1 percent, and the distribution was assumed to be Lambertian. The baffles and walls were assumed to have surfaces of Martin black, with a diffuse reflectance of 1 percent.

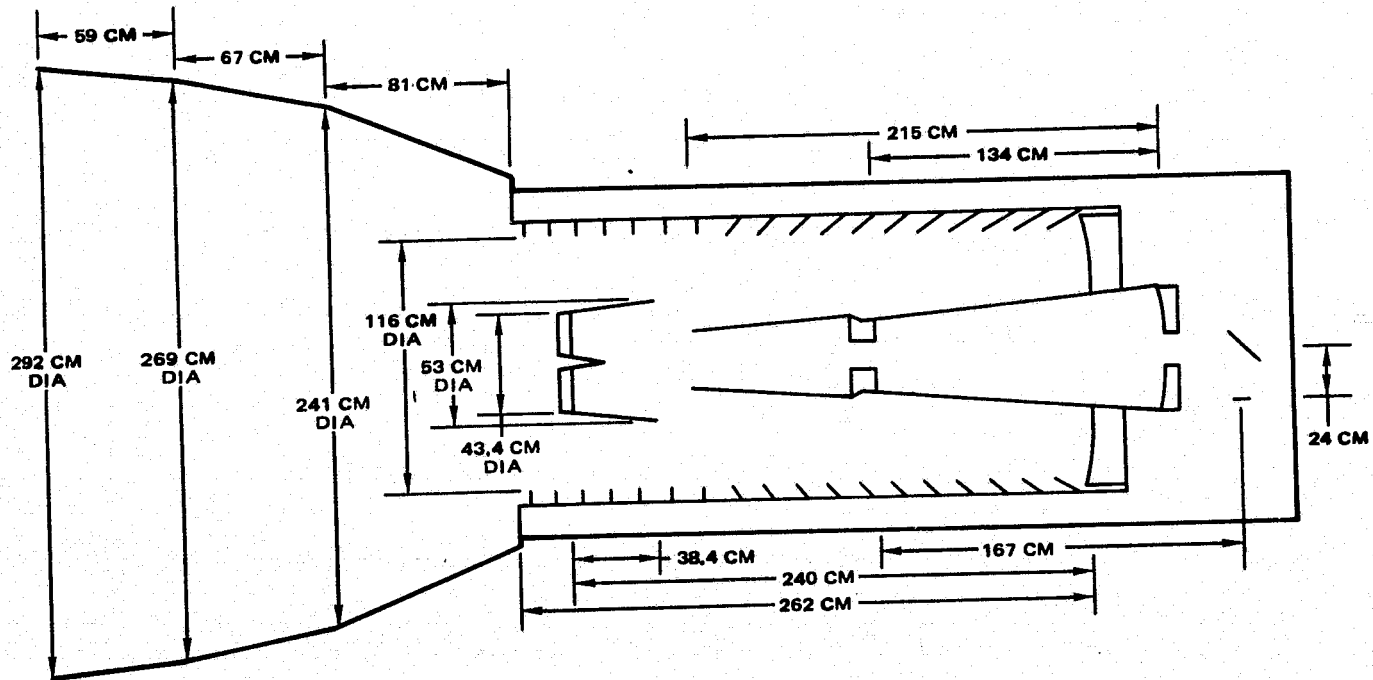


Figure 3-23. Telescope definition for out-of-field source rejection calculation.

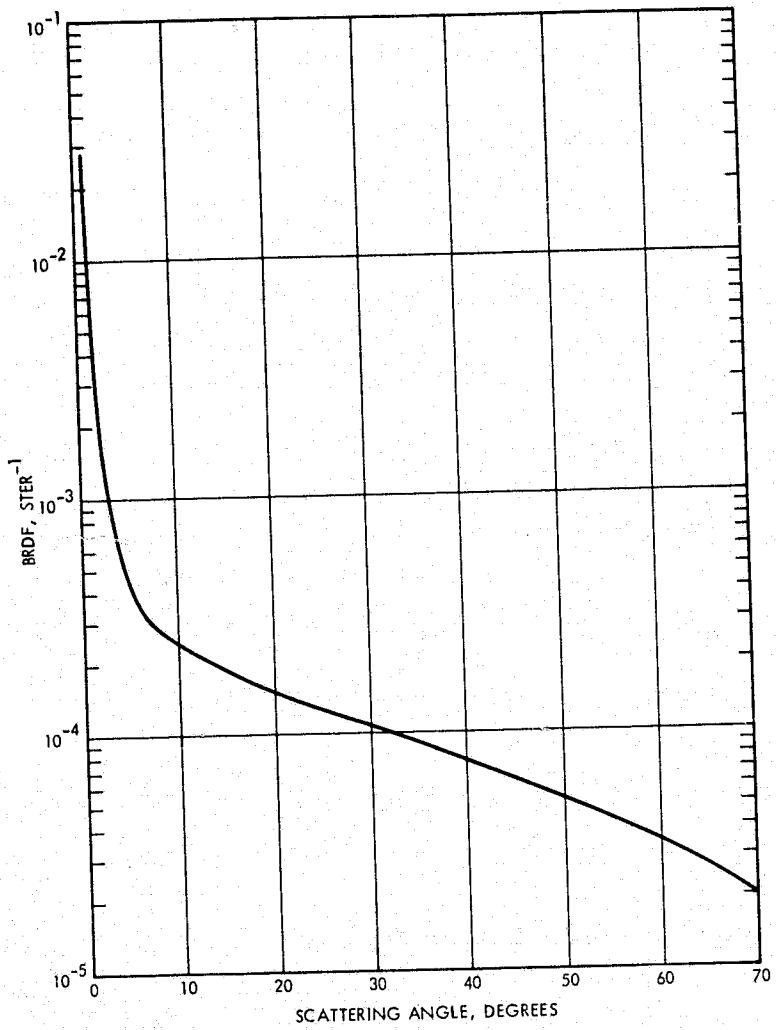


Figure 3-24. Bi-directional reflectance distribution function for bare beryllium.

Off-Axis Rejection

At source angles greater than 45 degrees from the optical axis, the only source of radiation entering the baffle tube is that which is scattered from the specular interior of the conical shield. At source angles less than 30 degrees from the optical axis, radiation could reflect directly from illuminated baffles to the folding mirror, and at source angles less than 15 degrees from the optical axis, the primary mirror would be directly illuminated, so angles of less than 30 degrees are to be avoided. The photon

flux at the center detector due to all scattering mechanisms is shown in Figure 3-25 for the spectral band between 5 and 15 micrometers. The contribution due to diffraction was calculated and found to be negligible compared to scattering.

The earth contribution is for a height of 400 km. The sun and moon were considered to be point sources (actually they subtend about 0.5 degree).

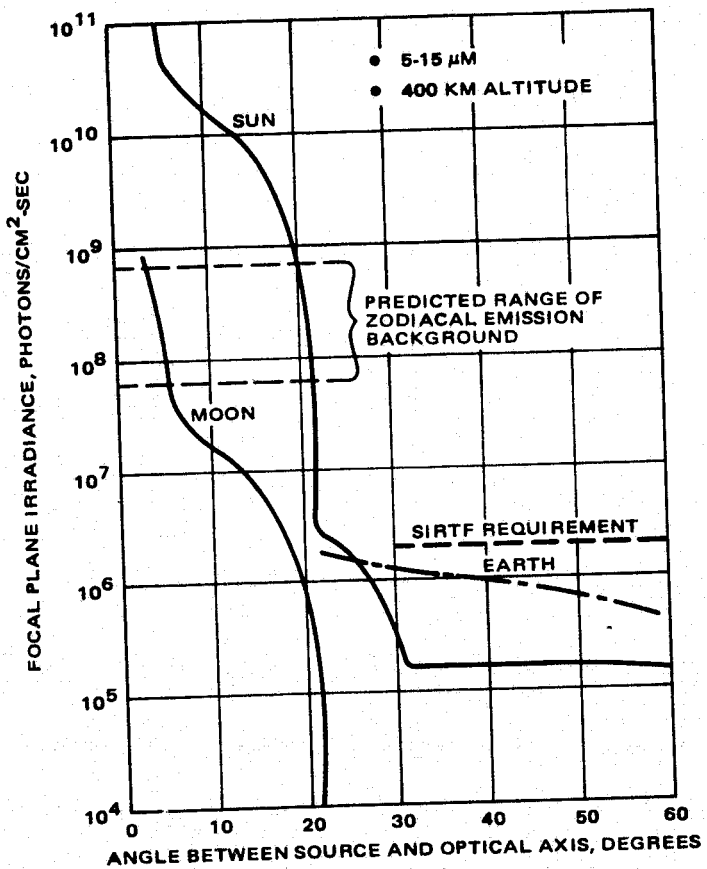


Figure 3-25. Focal plan irradiance due to out-of-field sources (5-15 μ m).

The emitted radiance from the full moon is several orders of magnitude higher than the radiance due to sunlight reflected from the moon. It was assumed that the moon was full and that the peak temperature (at the center) is 373°K. The average radiance of the moon was calculated by assuming that the energy received from the sun falls off as the cosine of the angle of incidence and that the 4th power of the temperature is proportional to this energy. The "requirement" in Figure 3-25 is that photon flux which will just allow the SIRTF telescope to meet its NEP requirements. It can be seen that SIRTF will meet the requirements for all angles greater than 30° off axis.

Offset (Scan Modulation)

The modulation due to scanning perpendicular to the earth horizon (offset) was calculated, and is presented in Figure 3-26. There is no modulation due to scanning parallel to the horizon. Values were calculated for both ends of a detector array 15 arc minutes long, and for the center. The number presented is the difference between the photon flux values received at each end of a 15 arc minute scan. The "+ end" of the array is the end farthest from the earth edge. At horizon angles greater than 40 degrees, the "- end" of the array receives the highest irradiance, while at horizon angles less than 40 degrees, the "+ end" receives the highest irradiance. At about 40 degrees, the two effects tend to offset each other, so an estimate of the variation caused by scanning is represented by the dotted lines.

The "requirement" in Figure 3-26 is set a factor of 10 below the static background requirement as shown in Figure 3-25, in order to avoid offset interference with short-integration observations. For long-integration observations, telescope wobbling must be employed to cancel the offset.

Zodiacal Emission

The effects of zodiacal emission on background photon flux were investigated. The zodiacal emission data were based on a Hughes model which has the average absorptance of the interplanetary dust equal to 0.6 and the emissivity equal to 0.9 at a wavelength of 13 micrometers. (Further discussion of zodiacal emission appears in Section 3.6.3.) This particular

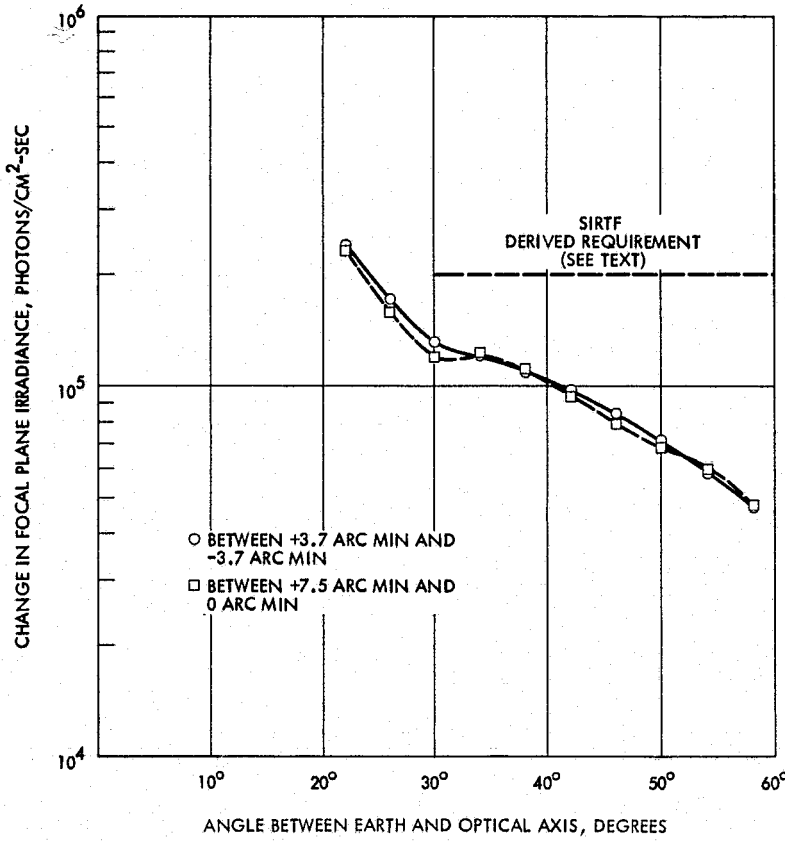


Figure 3-26. Change in focal plane flux due to space chop. Pin 6 perpendicular to the earth horizon (5 to 15 μ m).

case is shown in Figure 3-27 for the plane of the ecliptic. The estimated photon flux at the center detector is shown in Figure 3-25 for two elongation angles in the plane of the ecliptic - 45 degrees (the minimum angle required between SIRTF and the sun) and 180 degrees (the minimum value attained). The zodiacal emission value is in fact quite uniform throughout the entire anti-solar hemisphere.

The effect of scanning along the gradient of zodiacal emission in the plane of the ecliptic was investigated. The contribution to scan modulation comes from three sources: the changes in directly-viewed radiation as the field of view moves along the gradient, the change in zodiacal radiation scattered from the telescope, and the apparent change in collecting aperture

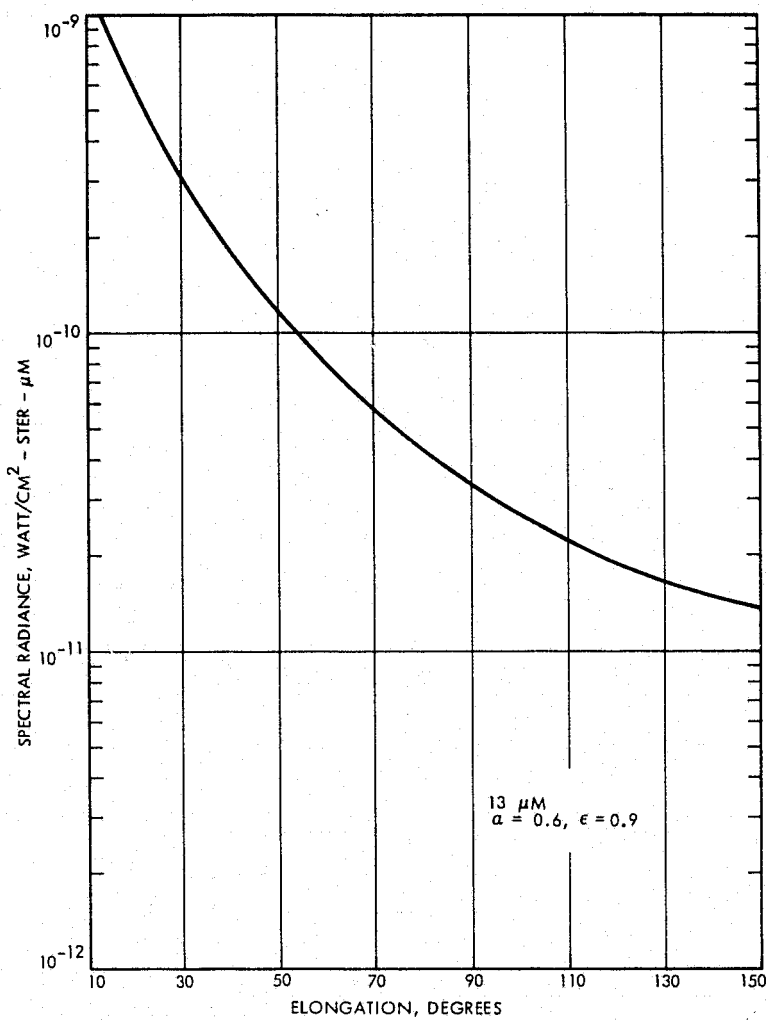


Figure 3-27. Sky radiance from zodiacal emission.

due to the tilting of the second folding mirror, which defines the aperture. The contributions from all three sources are presented in Table 3-7 for the case of three difference scan angles, when scanned at an elongation angle of 45 degrees in the plane of the ecliptic. As would be expected, the change in directly-viewed radiation is by far the largest source. The case of scanning perpendicular to the earth at a horizon angle of 30 degrees is presented for comparison. It is seen that this is over two orders of magnitude below the detector photon flux from scanning zodiacal emission.

TABLE 3-7. CHANGE IN DETECTOR IRRADIANCE WITH SCAN
(Values in photons/cm²-sec in the Focal Plane)

Source	Half Scan Angle		
	7.5 min	30 sec	2.5 sec
Zodiacal emission - 45° elongation			
change in directly viewed radiation	7.2×10^6	4.8×10^5	4.0×10^4
change in scattered radiation	2.3×10^4	1.5×10^3	1.3×10^2
effect of apparent aperture change	2.5×10^2	1.1×10^0	7.7×10^{-3}
Earth background			
30° horizon angle	2.5×10^4	1.6×10^3	1.3×10^2

Internal stabilization of the SIRTF image has been considered using either the first or second folding mirror. For stabilization, the only variation in the background flux is due to the change in zodiacal emission scattered from the optics, and as shown in Table 3-7, the effect is small if the stabilization is done by the second folding mirror. In the case of tilting the first folding mirror for stabilization control, the maximum mirror tilt possible before vignetting occurs is ± 3.95 arc minutes. This corresponds to a change in object space of ± 2.5 arc minutes. The change in detector photon flux if the first folding mirror tilts this amount along the gradient of zodiacal emission at an elongation angle of 45 degrees is 7.7×10^3 photons/cm²-sec, again well below the other effects, but in order to achieve larger correction angles and to enable use of the chopping drive for LOS stabilization (Section 3.5) second-folding-flat chopping is preferred.

Summary of Results

The steady state levels of background flux are all summarized in Figure 3-25 for the 5 to 15 micrometer band. It is seen that the contribution from the sun is equal to or higher than that from the earth, but never by more than an order of magnitude. The contribution from the moon is far less than that from either the earth or sun. The requirement for the maximum value

of background irradiance is shown, and the background for all three sources is below this requirement. The contribution from zodiacal emission is shown for two elongation angles, the second of which can be regarded as a minimum value. The values are shown as horizontal lines because they are independent of earth and moon angles. The background from zodiacal emission is considerably higher than the requirements for both cases, and much higher than the background from the sun or earth except at source angles below 15 degrees. Thus zodiacal emission will increase SIRTF NEFD in the new IR by 1/2 to 1 order of magnitude. (This is discussed fully in Subsection 3.6.2.) The modulation from scanning along the gradient of zodiacal emission, as shown in Table 3-7, is over two orders of magnitude higher than the modulation caused by scanning perpendicular to the earth at a horizon angle of 30 degrees. The modulation caused by adjusting the tilt of either the first or second folding mirror for stabilization, along the gradient of the zodiacal emission, is much lower than that caused by scanning perpendicular to the earth at 30 degrees, for the expected stabilization scan angles.

Summary

The analyzed design meets or exceeds the static off-axis requirements of the SIRTF specification for the off-axis earth, sun, and moon. In addition, it is also possible to meet the Hughes-generated requirement for scan modulation while implementing space chopping perpendicular to the earth at 30° from the horizon. Direct-viewed zodiacal emission may dominate all these effects, holding SIRTF performance in the ecliptic plane to a factor of 100 better than comparable ambient-temperature telescopes.

3.2.5 Effects of Contamination

The off-axis rejection analysis of the SIRTF telescope was made assuming clean optics. Contamination of the optical surfaces will reduce the rejection capability of the telescope. This section addresses the effects of cryo-contamination; i.e., condensation of such gases as O₂, N₂, CO₂ and water vapor on the cold (15-20°K) optics. The probability of occurrence of contamination and its overall effect on performance is discussed in Section 3.6.3.

Most of the work on cryo-contamination has been concerned with changes in emittance and reflectance (Reference 3-1, 3-2, 3-3). The work

that has been done on scattering has been so limited in scope that it can only be qualitatively applied to this study (References 3-4, 3-5). For this reason the study was done in two parts. First a worst case analysis was made based on a pessimistic assumption. In the second part of the study, the available measured data was compared with the worst case analysis.

Scattering from Rough Surface

To make the worst case estimate first consider scattering from a rough surface. For a qualitative approach, first formulated by Rayleigh, consider the two reflected rays in Figure 3-28. The path difference between the two rays is

$$\Delta d = 2h \cos \theta$$

and the phase difference is

$$\Delta \Phi = \frac{2\pi}{\lambda} \Delta d = \frac{4\pi h}{\lambda} \cos \theta \quad (3.2.5-1)$$

For $\Delta \Phi = \pi$, the two rays will destructively interfere and the scattering is complete. For $\Delta \Phi < \pi$ the scattering is partial. The scattering is thus shown to be a function of the distribution of phase of the reflected radiation (or equivalently the distribution of surface heights).

A more exact analysis (Reference 3-6) shows that the angular distribution of the scattered radiation is also dependent on the distribution of

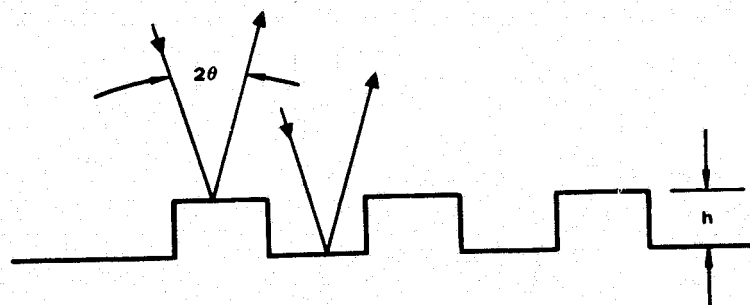


Figure 3-28. Path difference due to a rough surface.

slopes but the total scattering is only dependent on the rms surface roughness. The relation between total scatter and surface roughness is

$$S_T = (4\pi\sigma/\lambda)^2 R \cos\theta \quad (3.2.5-2)$$

where

S_T = total scatter

σ = rms surface roughness

R = surface reflectivity

θ = angle of incidence

There are several approximations which appear in the derivation of Eq. 3.2.5-2 but it is accurate enough for the worst case analysis.

Since the total scattering is only dependent on the phase shift of the reflected radiation the analysis may be extended to the rough transparent layer shown in Figure 3-29. The phase shift for these two rays (with $\theta = 0$) is

$$\Delta\Phi = 4\pi h (n-1)/\lambda \quad (3.2.5-3)$$

where n is the index of refraction of the rough layer. Comparing the phase shifts in Eqs. (3.2.5-1) and (3.2.5-3) we can write an analogous expression to Eq. (3.2.5-2) for total scatter (again with $\theta = 0$).

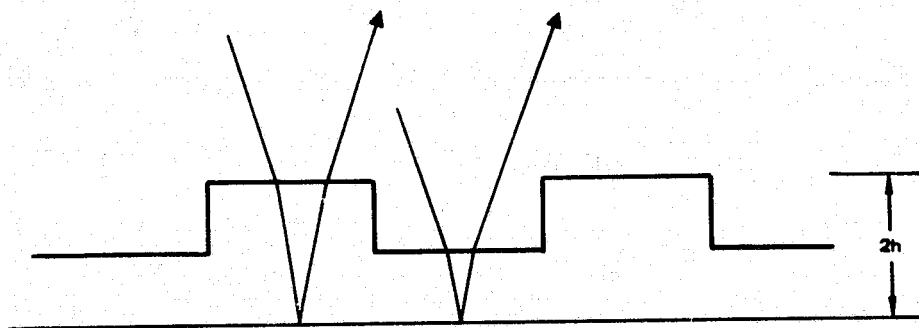


Figure 3-29. Path difference due to a rough layer.

$$S_T = [(4\pi \sigma (n-1)/\lambda)]^2 R \quad (3.2.5-4)$$

The situation is complicated by the fact that the amplitude of the scattered wave is the sum of the amplitudes of the radiation scattered from the top of the layer and the radiation scattered by passage through the layer. Since the indices of refraction of most of the cryo-deposits considered here are low, the surface contribution may be ignored and Eq. (3.2.5-4) used.

Worst Case Analysis

Assume that at the very worst, a cryo-layer of average thickness h is completely rough. For a uniform distribution of maximum height $2h$ the rms roughness

$$\sigma = h/\sqrt{3} \quad (3.2.5-5)$$

From Eqs. (3.2.5-4) and (3.2.5-5) (assuming $R = 1$) the maximum allowable cryo-deposit thickness as a function of wavelength and cryo-deposit refractive index is obtained:

$$h \leq \frac{\lambda}{4\pi(n-1)} \sqrt{3S_T} \quad (3.2.5-6)$$

The off-axis rejection analysis can be used to calculate the allowable total scatter. The predicted scattering at 45° is about a factor of 10^3 below the specification. This analysis was made assuming a mirror with a total scatter obtained from Reference 3-7 of 3×10^{-4} . Thus if the total scatter is increased by a factor of 10^3 to 0.3,

$$h \leq 0.075 \lambda/(n-1) \quad (3.2.5-7)$$

For $n \approx 1.3$ and $\lambda = 10 \mu\text{m}$ (the earth limb peaks strongly at this wavelength) the maximum allowable cryo-deposit thickness is

$$h \leq 2.5 \mu\text{m} \quad (3.2.5-8)$$

The number of corresponding mono-layers is shown in Table 3-8.

Empirical Results

Scattering measurements on cryogenically cooled surface are quite difficult and very little data exists. The visible scattering measurements by Viehmann et. al. (Reference 3-4) and 10.6 μm scattering measurements by Young (Reference 3-5) do confirm that the previous analysis is pessimistic.

The key is the manner in which the contaminants are deposited. If they form lamellar layers (homogenous films of uniform thickness) then they will scatter very little. For example Young found no significant increase in scattering for layers of N_2 as thick as 25 μm . This is of particular significance since Young used a state-of-the-art low scatter mirror. Viehmann reported little change in visible light scattering for film thicknesses below 2 μm . Table 3-9 lists the contaminants investigated.

If the film does not form a lamellar layer but fractures into diffusely reflecting fragments, the scattering will increase by orders of magnitude. The conditions under which fracture occurs are varied and not well understood. Arnold observed occasional fracturing of NH_3 layers and attributed it in part to previous contamination of the mirror by N_2 . He observed that H_2O deposition at 20°K took on a hazy appearance when the mirror was raised to 50°K. Some fracturing CO_2 layers were also observed. Young observed fracturing of cryo deposits when the mirror temperature changed after the

TABLE 3-8. NUMBER OF MONO-LAYERS IN 2.5 μm

Cryo-Deposit	Density*	Number of Layers
O_2	1.52 g/cm ²	7.6×10^3
N_2	0.93	6.8
NH_3	0.94	8.0
CO_2	1.67	7.1
H_2O	1.0	8.0

*Values from Reference 3-5

TABLE 3-9. CRYO-CONTAMINANTS MEASURED FOR SCATTERING

Investigator	Cryo-Contaminant	Visible Refractive Index*
Young	N ₂	1.24
	O ₂	1.31
	CO ₂	1.34
	CO	
	H ₂ O	1.32
	NH ₃	1.38
	60 percent N ₂ , 40 percent NH ₃	
	33 percent N ₂ , 67 percent NH ₃	
	Air	
Viehmann	Water	1.42
	Acetone	1.36
	Ethanol	1.36
	Methanol	1.32
	2-Propanol	1.33
	Toluene	1.53
	Silicon Oil (DC-200)	1.36
	Benzene	1.49
	Tricholoroethylene	1.48
	Carbon Dioxide	1.30

* The first set of refractive indices were determined by Arnold, the second set by Viehmann.

deposits had formed, possibly the result of thermal stress. Young also observed significant increase in scatter from a 6 μm deposit of N₂ after 3 μm had been evaporated. He noticed an even greater increase when an additional 3 μm of N₂ were deposited on top of the partially evaporated layer.

The above has covered only the increase in total scattering, saying nothing about the change in the angular distribution of the scattering.* It has been Hughes experience (verified by Young) that the scattering from contaminated mirrors increases faster at large angles than at small angles. For example, if the total scatter increases one order or magnitude, the BRDF at 60° might increase two orders of magnitude. The off axis rejection study has shown, however, that the main contribution comes from scattering angles on the optics between 5° and 20° . In this range the total scatter and the BRDF increase approximately proportionately.

Conclusions

The results of this study give an estimate of the cryo deposit scattering problem. The worst case analysis indicates a maximum allowable deposit thickness of about $2.5 \mu\text{m}$. This analysis is pessimistic, however, and the available measured data indicates that deposits of an order of magnitude thicker cause no degradation in scattering performance. In addition the results of Section 3.6.3 indicate that deposited or condensed contaminants are unlikely to occur.

3.2.6 Optical Engineering

This section covers the development of the SIRTF optical design from a purely mathematical solution into physically realizable hardware. This includes material selection, opto-mechanical tolerancing, mirror design and analysis, mirror mounting methods, and alignment and test procedures. For SIRTF the dominant constraints are maintaining the specified resolution in the thermal and mechanical environment at minimum cost. The telescope must attain its performance requirements under zero gravity conditions with 20K optics which were manufactured, aligned, and tested at 300K under full earth gravity.

*Usually presented in terms of the bidirectional reflectance distribution function (BRDF), a measure of the scattering per steradian in a particular direction.

Material Selection

There are two basic approaches for designing optical systems which must be built and tested at room temperature and used at cryogenic temperatures. The first is to build the mirrors and critical mirror support structure out of a single material or out of two materials whose coefficients of thermal expansion closely track each other over the temperature range. Cooling the telescope from room temperature to cryogenic temperature then causes the entire telescope to contract uniformly, so that it remains aligned and in focus.

The second approach is to select materials for the mirrors and for the structure independently, the mirror material being chosen on the basis of good optical and thermal properties, and the structural material on the basis of structural and thermal properties, and cost. It is then necessary to design mirror mounts which will not transmit stresses to the mirror as the temperature changes, and to provide a focusing adjustment.

Both approaches were studied for SIRTF. For the first (single material) approach, beryllium is the only material which combines all the necessary properties. Glass, pyrex, and silica mirrors (for which there are structural metals with closely matching coefficients) are ruled out because of their low thermal conductivity which results in long cool-down and warm-up times, large thermally-induced stresses, and slow diffusion of thermal gradients. Aluminum is an excellent structural material, but is not sufficiently stable for use as a material for a 1-meter primary mirror where diffraction-limited performance at $5 \mu\text{m}$ is required. Performance of beryllium and aluminum as optical materials is discussed in the immediately following subsection.

The selected approach for SIRTF is beryllium mirrors and an aluminum structure. The choice of aluminum as the structural material and the design of the mirror mounts with the required characteristics are discussed under mechanical design (Section 3.3.1).

Optical Materials

The selection of a material for the primary mirror is based on considerations of achievable optical surface quality, and temporal and thermal stability. Surface quality can be improved by application of electroless nickel plating over the mirror substrate material; however, as will be discussed below, the bimetallic thermal stresses induced over the temperature range of the SIRTF mirror will degrade the mirror's figure. Beryllium properties will be discussed first, followed by a discussion of aluminum.

Beryllium technology for optical applications has developed extensively over the past several years. As recently as 1970, total integrated scatter of 0.1 percent of the incident energy outside a 1-degree specular cone was considered a state-of-the-art polish. Since that time, the basic material has improved and changes in polishing techniques have given further reduction in surface scatter. The two best current grades of beryllium for bare optics in the sizes required are HP-81 for Kawecki-Berlyco, and I-70A by Brush-Wellman. These are fine grain, low oxide, high density, hot pressed block materials. Current size capacity has been demonstrated for mirrors up to approximately 1.6 meters in diameter.

Due to the well baffled characteristics of the double folded Gregorian design it is possible to meet the background requirements using currently achievable scattering from conventionally polished HP-81 or I-70A. It is not necessary to rely on the successful development of current experimental low scatter techniques such as chemical-mechanical polishing or sputtering of an amorphous beryllium surface layer on hot pressed block.

The temporal stability of properly machined beryllium has been well established. In 1969 Hughes designed a 20 μ rad resolution space sensor with a 33 cm diameter f/1.5 primary mirror. Two beryllium temporal stability test mirrors were fabricated to better than $\lambda/8$ (peak to peak) at 0.5896 μ m.

These mirrors were processed carefully and fully stress relieved to arrive at a very stable condition and then periodically examined over the following four years. One mirror was bare beryllium and the other was electroless nickel plated. The results of those measurements are given in Figure 3-30 where the rms figure change is plotted as a function of time. The basic precision of the measurement equipment is $\approx 0.02\lambda$ rms at 0.6328 μ m.

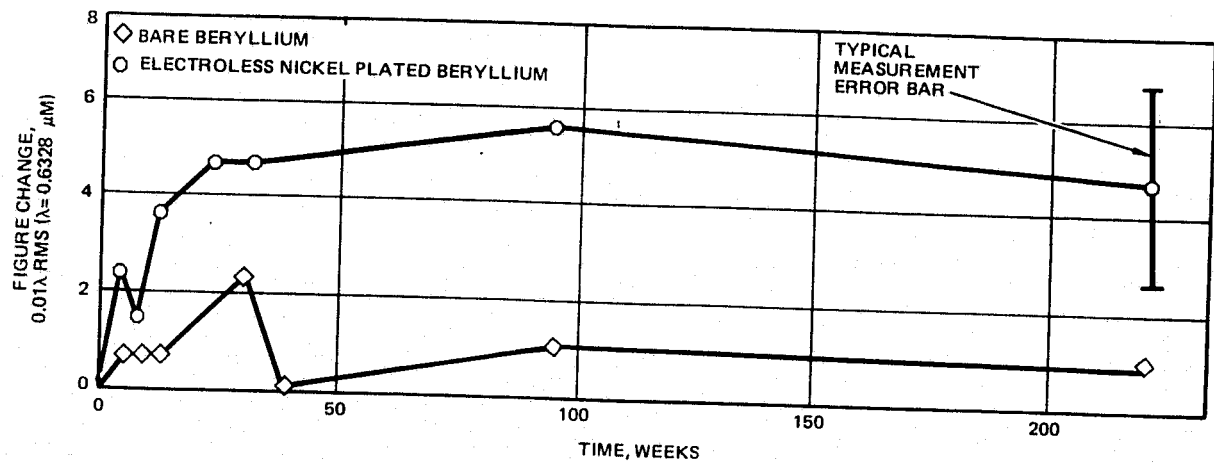


Figure 3-30. Temporal stability test results.

These mirrors continue to exhibit extremely good temporal stability. Over 3.8 years of surface change is on the order of 0.01μ rms for both the bare beryllium and electroless nickel plated mirrors. This level of temporal stability significantly exceeds that required for the SIRTF optical system.

The above test indicates that, with proper processing and stress relieving, very stable beryllium mirrors can be obtained. However, with improper processing, a poorly relieved mirror will warp two orders of magnitude more than the test mirrors cited above, i.e., on the order of 5 wavelengths at $6328 \mu m$. This would seriously degrade the SIRTF performance at the short wavelength end of its operating region. Detailed fabrication drawings and careful material and machining specification can ensure fabrication of mirrors with the necessary temporal stability.

Processing of the beryllium is extremely important because elastic thermal strains can be imposed on the mirror figure by a uniform temperature change acting on the inherently anisotropic material. The coefficient of thermal expansion of beryllium perpendicular to the C-axis ($10.6 \times 10^{-6}^{\circ}K^{-1}$) is approximately 38 percent larger than the coefficient parallel to the C-axis ($7.7 \times 10^{-6}^{\circ}K^{-1}$). The standard grades of commercially available beryllium used for mirrors for the past ten years randomize the basic powder mix well enough that the residual anisotropy is usually less than 8 percent. However, the new optical grades of material (HP-81 or I-70A) use improved powder processing techniques and achieve uniform expansion in all directions to within 1 percent.

The powder used for compaction is impact ground to give small chunky pieces rather than the normally used spherical powder. X-ray diffraction studies show the crystal orientation to be very random, and coefficient of thermal expansion measurements on both laboratory and production pressings show uniform expansion. Interferometric measurements at Hughes on a 33 cm diameter f/1.5 I-70A beryllium mirror at cryogenic temperature verifies the greatly improved thermal stability of this new optical grade material.

Limited published data (Reference 3-10) indicate a residual thermal instability on the order of $0.18 \times 10^{-3} \lambda$ rms/ $^{\circ}\text{K}$ for two I-70A mirrors, 13 cm (5 inches) in diameter, and one 43 cm (17 inches) in diameter. This was obtained over an approximate thermal range of 85°C to -60°C .

If one assumes that elastic thermal instability is directly related to the thermal coefficient of expansion, then the anisotropic expansion errors should not continue to grow at this rate all the way down to 20°K since the coefficient of expansion drops rapidly below 100°K . Figure 3-31 is a plot of α and $\Delta L/L$ for beryllium (Reference 3-11). In going from room temperature (293°K) to -60°C approximately 60 percent of the total shrinkage has been experienced while going through only 27 percent of the temperature range. If one assumes that 60 percent of the anisotropic errors have been introduced when 60 percent of the basic shrinkage occurs, then the total shrinkage from room temperature to 20°K should be in the range of:

$$(0.18 \times 10^{-3} \lambda \text{ rms}/^{\circ}\text{K}) (80^{\circ}\text{K}) (\frac{1}{0.60}) = 0.024 \lambda \text{ rms}$$

to

$$(0.36 \times 10^{-3} \lambda \text{ rms}/^{\circ}\text{K}) (80^{\circ}\text{K}) (\frac{1}{0.60}) = 0.048 \lambda \text{ rms}$$

$$(\lambda = 0.6328 \mu\text{m})$$

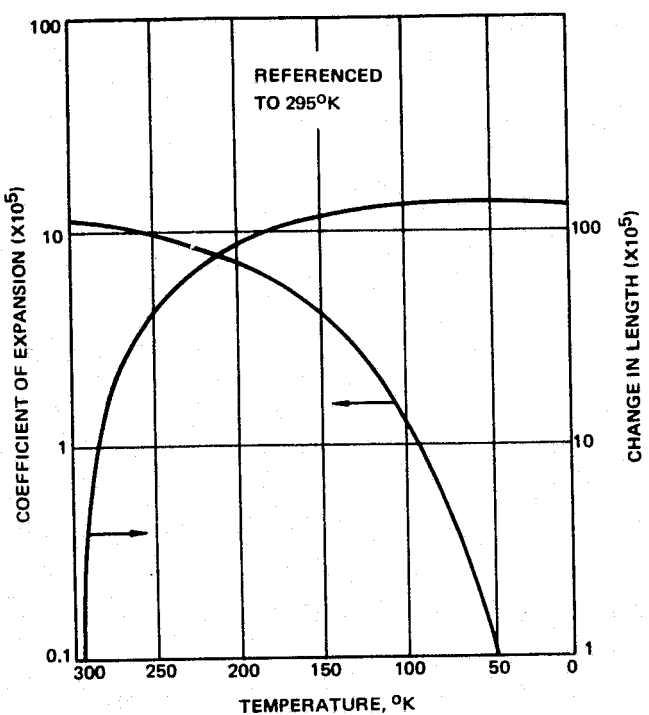


Figure 3-31. α .and ΔL for beryllium.

If the 0.048λ rms represented a true worst-case prediction, then the residual errors would be $\lambda/66$ rms at $5 \mu\text{m}$, and less at all longer wavelengths, which is truly insignificant. Unfortunately this predicted range is from only two small samples tested over a limited temperature range.

The largest beryllium mirror tested to date over substantial temperature range is the $86 \times 81 \text{ cm}$ (34×32 inches) LALOS (Large Aperture Light-weight Optical System) scan mirror machined by Speedring from a I-70A billet. The design, optical fabrication, and test was performed by Perkin-Elmer, Norwalk, Connecticut. There are larger elements in the system, but they have not been completely fabricated. Speedring has completed the machining of a $165 \times 102 \text{ cm}$ (65×40 inches) f/0.67 secondary mirror, but Perkin-Elmer has not done any optical fabrication. The mirror design and test methods have been described (Reference 3-12) but the actual test results were not formally reported. A summary of the first look data reduction given informally is presented in Table 3-10.

TABLE 3-10. LALOS SCAN MIRROR PRELIMINARY DATA

Temperature (°K)	Residual Error (λ RMS)	Change (λ RMS)	$\frac{E_T - E_{300}}{\Delta T}$ (λ RMS/°K)	$\frac{E_T - E_{T+20}}{20}$ (λ RMS/°K)
300	0.064	0	0	0
280	0.10	0.036	0.0018	0.0018
260	0.17	0.106	0.0026	0.0035
240	0.25	0.186	0.0031	0.0040
220	0.30	0.236	0.0030	0.0025
150	--	No Reduced Data	--	--
300	0.057	0.007	--	--

($\lambda = 0.6328 \mu\text{m}$)

The mirror has been cycled to 150°K, but the errors were large enough that the automatic fringe scanner could not reduce the interferograms. That data is being reduced by hand, but no results are currently available. The 300°K point at the bottom of the table represents the mirror after the thermal cycle. This indicates that the errors were all elastic since the 0.007 λ rms deviation from the pre-cycle condition is well below the 0.02 λ rms test accuracy. The fact that the errors are all elastic implies that the mirror was well machined, has been well stress relieved, and should have excellent temporal stability.

The next to last column of Table 3-10 ($E_T - E_{300}/\Delta T$) is a measure of the average error introduced in going from 300°K to T. The last column ($E_T - E_{T+20}/20$) is the rate of anisotropic error generation during only the last 20 degrees prior to reaching temperature T. The first thing one notices is that the error rate is approximately an order of magnitude larger than previously reported for I-70A mirrors. As a matter of fact, the error rate is larger than for several mirrors of less random material. Even more surprising is the fact that the error rate grows with decreasing temperature to 240°K before starting to fall off. This is not consistent with behavior of

the coefficient of expansion, but may be consistent with a mismatch to the titanium mount. Based on examination of the interferograms taken at reduced temperature, it appears that the mirror may be bending slightly in addition to experiencing some random irregularity.

In light of the preliminary nature of the data as well as the large errors and possible bending, it would be prudent to treat the data with some reservation. However, using $0.0030 \lambda \text{ rms}/{}^\circ\text{K}$ (the average error rate from 300°K to 220°K) the extrapolation to 20°K is

$$(0.0030 \lambda \text{ rms}/{}^\circ\text{K}) (80^\circ\text{K}) (\sim \frac{1}{0.60}) = 0.40 \lambda \text{ rms}$$

At $5 \mu\text{m}$ this corresponds to $\lambda/8 \text{ rms}$ which is good, but not insignificant with respect to diffraction limited operation. It may be that examination of the overall test program will uncover some unexpected problems which lead to the relatively large errors experienced. Of course it might be determined that the mirror in a free state would have better performance and this data represents what can be obtained in a mounted mirror (or this particular mirror, or that particular mount). However, even if the behavior of a large mounted beryllium mirror will be no better than reported here, the mirror can still be made suitable for SIRTF, since only a few iterations of room temperature polishing using interferograms obtained at cryogenic temperatures will suffice to reduce the residual $\lambda/8 \text{ rms}$ at $5 \mu\text{m}$ to negligible levels.

In order to demonstrate conclusively the suitability of beryllium for SIRTF use at $5 \mu\text{m}$, several tasks should be accomplished. First, final data should be obtained to replace the preliminary data shown there. The data presented in Table 3-10 should be extended down at least to 80°K , and preferably to 20°K to determine if the anisotropic errors truly fall off as α does. As one part of that verification, the two 33 cm f/1.5 test spherical mirrors currently at Hughes could be measured at cryogenic temperature. One mirror is HP-81, and the other is I-70A. Comparison between them, and with the LALOS mirror is advisable. It would also be desirable to figure the large unfinished LALOS secondary mirror to a good sphere and test it at cryogenic temperature. This is valuable both because it is approximately the same size as the SIRTF primary, and because it is not a flat. The Table 3-10 data is for

a smaller flat mirror, and anisotropy out of the plane may be worse for a curved surface.

In addition to any basic beryllium performance questions it is necessary to demonstrate performance of a mounted (constrained) mirror at cryogenic temperature. The modified Sarrut's mechanisms appear to be an excellent approach to providing low stress, low moment coupling between a beryllium mirror and aluminum structure over the large temperature range required. If successful, this concept will provide a significant cost savings by using the weight carrying capability of Shuttle to allow aluminum structure instead of beryllium. It is absolutely essential that this design be modeled and tested prior to detailed design of the telescope in order to determine if this two-material design concept will truly give adequate performance.

Aluminum as a mirror material for cyrogenic applications is deficient compared to beryllium in both surface quality and stability. Aluminum cannot be polished to an optical quality surface using standard optical polishing techniques. The current effort to produce high quality aluminum mirrors is based on single-point diamond turning, and useful mirrors of moderate size are being fabricated for applications where low scattering is not a requirement. Figure 3-32 shows BRDF's for two small (3.8 cm dia - 1.5 in dia) mirrors produced by diamond turning at Lawrence Livermore Laboratories and measured at Hughes. The BRDF is seen to average an order of magnitude higher for scattering perpendicular to the machining grooves and to range between an order of magnitude higher to equal for scattering parallel to the grooves. The Lawrence Livermore capability is currently limited to about 46 cm (18 in). Union Carbide-Oak Ridge has the capability for turning mirrors up to 2 meters (80 in) diameter with surface accuracy to 7.5 μ m. No scattering data on these mirrors is known. Diamond-point turning is in an active state of development so that substantial improvements may be expected in the next few years.

The usual approach with aluminum mirrors is to deposit an electroless nickel coating on the figured surface, and to form the final figure and polish on the nickel. This approach works well in applications where the mirror experiences only small temperature changes, or the minimum wavelength of interest is relatively long, so that the diffraction blur is large, and mirror figure is not critical.

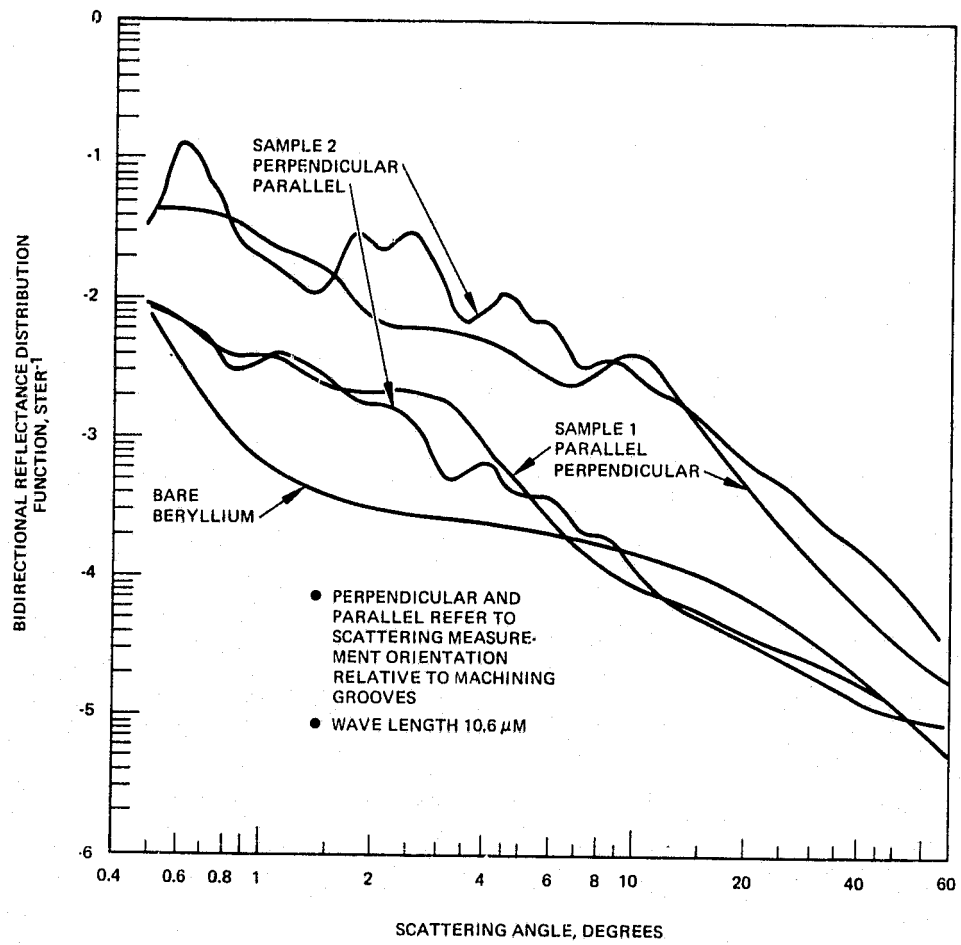


Figure 3-32. Scattering of single-point diamond turned aluminum mirror samples compared to bare beryllium.

Due to lack of data on large nickel-plated aluminum mirrors, the problems with this approach must be approached via beryllium (Reference 3-12A). Nickel-plated beryllium mirrors exhibit a surface figure degradation an order of magnitude worse than the acceptable value for SIRTF. Since the same mirrors are temporally stable when not temperature cycled, the degradation is attributed to bi-metallic thermal stress. The thermal mismatch between aluminum and nickel is eight times worse than that between beryllium and nickel (see Table 3-11).

Thus nickel plating is not a solution to the surface quality problem of aluminum.

TABLE 3-11. THERMAL EXPANSION COMPARISON

	Coefficient of Thermal Expansion, $\alpha(K^{-1} \times 10^6)$	$\alpha - \alpha_{Ni}(K^{-1} \times 10^6)$
Aluminum	23.9	10.9
Beryllium	11.7	-1.3
Nickel	13.0	—

In addition to its surface finish problems, aluminum does not have good dimensional stability. Precision heat treatment and machining processes have been developed for tooling and other precision applications, but these do not supply the precision required for the SIRTF primary mirror. In the absence of published material on aluminum mirrors, the following organizations were contacted to provide corroboration of the above:

- Applied Optics Center
- University of Arizona, Optical Sciences Center
- North American Rockwell
- Aerospace Corporation
- AVCO
- Honeywell
- Lawrence Livermore Laboratory
- Perkin-Elmer

All agreed that aluminum should not be used for large mirrors which were to be cooled to cryogenic temperatures. Rockwell and Aerospace cited experience indicating acceptable performance at 0.1 mr (~20 arc sec) for mirrors up to 58 cm (23 inches) cooled to 4K. Honeywell measured 3 fringes (visible) shift on a 20 cm (12 inches) mirror cooled to 4K; a 63 cm (25 inches) mirror changed a larger, unknown amount. The University of Arizona 1 meter aluminum mirror operates satisfactorily at the 29 km balloon float altitude (220-230K). Although telescope data is not known, the minimum detector size used is 30 arc sec diameter. Hence none of these mirrors can provide a basis for design and fabrication of the SIRTF primary mirror.

Optical Fabrication

The optical elements which make up the preliminary design of the SIRTF optical system are all well within the current manufacturing state of the art. Allowing $\lambda/2$ of irregularity in the visible does not unduly tax the capability of several good optical fabrication suppliers, yet would give approximately $\lambda/20$ peak to peak allowance for static figuring errors at 5 μm . This gives essentially perfect optical elements and reserves the maximum tolerance possible for alignment and thermal distortion of the mirrors.

Preliminary mirror thicknesses were assigned using engineering judgement in order to get adequate space allocations into the optomechanical layout. These thicknesses were then evaluated on the basis of self-weight deflection when loaded to 1-g while being supported at the three mounting points. For first cut performance criteria 1/4 arc second maximum slope errors and $\lambda/10$ maximum deflection at 5 μm ($\approx 20 \times 10^{-6}$ inches) were assigned as reasonable limits to show adequacy of the design concept. These are roughly equivalent numbers when compared to the diffraction Airy disc size, and to first order result in essentially undegraded imagery at 5 μm . Reference 3-13 describes the analysis in detail. To summarize that report, the primary is slightly thin based on the above criteria, since the maximum slope was actually 0.29 arc seconds rather than 0.25 arc seconds. The maximum deflection was 17.6×10^{-6} inches. The other three mirrors are all thicker than required. When the mirrors are actually designed in detail a set of Zernike polynomials will be fitted to the surface deformation calculated in Reference 3-13. These are then used to calculate total system performance including diffraction, system aberrations, and the deformations. The mirror design will be optimized based on the results of that analysis. However, the work to date clearly indicates that the preliminary optomechanical design is capable of giving adequate performance, and design practices well in hand will lead to an optimized design during the design phase of the program.

The basic alignment philosophy of the double-folded Gregorian is well suited to the size and environmental requirements of the SIRTF system. The primary mirror is mounted to the structure with adjustment in tilt to adjust the axis of the ellipse parallel to the telescope structure. Axial adjustment is provided to relax focal length tolerances on the mirror and mechanical tolerances on the structure. The first folding mirror is adjusted in angle until perpendicular to the primary optical axis, and axial adjustment is provided as well. The second folding mirror is adjusted in angle until parallel to the first folding mirror with the stabilization servo zeroed. Finally, the secondary mirror is adjusted in tilt until the ellipsoidal axis is parallel to the primary ellipsoidal axis. No centration capability is provided between the primary and secondary mirrors. (Analysis indicates the relative insensitivity to decentration of the elements. See Section 3.2.1, particularly Table 3-2.) Cost and reliability are both enhanced by eliminating a complex and unnecessary adjustment capability.

The telescope alignment and focus will be accomplished at room temperature. Focus and image quality will be checked in the visible portion of the spectrum. A full aperture test flat can be used in front of the system to allow double pass examination of the system performance at the focal plane. Alternately, a full aperture collimator can be used to provide a plane wave to the telescope. Either method is satisfactory; the autocollimation technique has size advantages; a smaller test laboratory can be used but the collimator approach is more direct and allows easier test interpretation at the expense of larger space requirements. In the one to two meter diameter size range there is no significant cost difference between a test quality flat or paraboloid. The determination will be made on the basis of desired tests and convenience.

After verification of warm focus and image quality the elements will be adjusted axially to compensate for the predicted differential expansion between the beryllium optics and aluminum structure. This setting will be made manually, with the mechanized focus adjust on the first folding mirror set in the middle of its range. Cold focus will be verified after sensor cool-down by viewing the focal plane through a permanently installed set of windows

in the sensor cover. These windows will be coated to provide low infrared emittance to minimize heat leaks while maintaining adequate visible transmittance for examination of the focal plane, through the optical system. By arranging the windows to act like the sampling holes of a Hartmann screen it is possible to verify focus and image quality at the MIC focal plane at operating temperature without building and qualifying a 1-2 meter or larger cryogenic optical test facility. The first folding mirror is mechanized and will be used to adjust focus, and if a significant fraction of its range is used to optimize focus during the first cryogenic cycle it will be reset to the center of its range and the whole unit adjusted axially to the corresponding distance when the sensor is brought back to room temperature.

Optical Surfaces

The mirrors will all have a vacuum deposited silver reflectance layer. The final decision whether or not to overcoat has not been made. Candidate coatings, as well as the beamsplitter and refractive element coatings, are described in Section 3.2.3. The mirror scattering properties require no development over that currently obtainable through careful conventional polishing of optical grade beryllium. The Bidirectional Reflectance Distribution Function (BRDF) used in the off-axis rejection analysis is shown in Figure 3-24.

The baffles are aluminum finished with the Martin-Marietta Optical Black Coating (a form of anodized aluminum). This coating was chosen for its excellent absorption over a wide spectral range. From 6 to 15 μm the reflectance is less than 1 percent, and from 15 to 120 μm the reflectance is approximately 1.5 percent.

Because the black surface is an optical surface, it is susceptible to contaminants which may be deposited on it. These can change its characteristics, because the contaminants, in effect, become the surface on which the light impinges. Also, much of the effectiveness of the Martin-Marietta black surface is due to the microscopic physical texture of the surface. Abrasion can change this microscopic texture. For these reasons, it is of prime importance to ensure that nothing solid is allowed to touch the surface after it is produced. To insure this, the baffle assembly is assembled and then the

Martin-Marietta anodize is applied. The entire baffle assembly can then be handled from the exterior, without touching the optical surfaces. If a local spot is damaged through abrasion, the reflectance is typically degraded to that of a normal aluminum black anodize, or approximately 10 percent. Due to the wide design margin in off-axis rejection, significant area degradation can be allowed without affecting system performance. The Martin-Marietta anodize is stable, and does not degrade with time as long as the above precautions are observed.

Summary

Preliminary optical engineering analysis and judgement based on experience indicate that it will be possible to realize the required SIRTF performance with hardware in space at 20°K. Currently available beryllium material and manufacturing technology allow adequate surface figure and BRDF to deliver adequate image quality at temperature, with sufficient off-axis rejection to meet the sensitivity requirements in the presence of the earth, sun, and moon. Preliminary mirror designs have been evaluated and provide acceptable stiffness with respect to one g-zero g distortion to maintain diffraction limited image quality. Mirror mount concepts have been developed which will allow use of aluminum structure with the beryllium optics. This takes advantage of Shuttle's weight carrying capacity to reduce SIRTF system cost.

The work to date has developed a preliminary design which shows performance adequate to meet the statement of work requirements. All of the optical components are within the current state of the art, however some performance verification tests are recommended prior to detailed design and fabrication of the SIRTF telescope. Specifically they are:

1. Further LALOS tests
2. Test of Hughes 33 cm mirrors
3. Breadboard and test of mirror mount concepts at cryogenic temperature

These tests do not represent technical obstacles which must be overcome. Rather schedule requirements dictate that these items should be investigated prior to detailed design and fabrication.

3.3 MECHANICAL SUBSYSTEMS

The mechanical and thermal subsystems of SIRTF are very closely integrated. The optical portion of the telescope, which is maintained at about 20°K, is mounted by a thermal isolator to the external vacuum shell which remains at ambient temperature. Radiation shields and superinsulation blankets mounted to the thermal isolator reduce the radiated heat loads. Within the cooled portion, mirror mounts and transition joints between dissimilar materials are designed to accommodate the differences in thermal contraction of the materials between room temperature and 20°K.

Section 3.3.1 is a description of the mechanical structure of the telescope. Section 3.3.2 is a discussion of mirror thickness requirements and the resulting stability of the mirrors. Environmental study results are presented in Section 3.3.3 including a structural analysis and an acoustic analysis. Mass properties of the telescope are summarized in Section 2.3, and 3.3.4.

Backup material is provided in Reference 3-15 (Mechanical Design Tradeoff Report). This consists of studies of methods of joining dissimilar materials, and tradeoffs of thermal isolator materials.

3.3.1 Mechanical Structure of the Telescope

The SIRTF telescope system, Figure 3-33 (A and B) is comprised of an outer vacuum housing, thermal isolator, optical assembly, cryogenic subsystem, removable cover assembly, and a deployable sun/earth shade assembly.

Outer Vacuum Housing

The outer vacuum housing is an aluminum structure which serves two primary functions. First, it serves as a vacuum housing around the cryogenically cooled internal telescope assemblies. A vacuum housing is a necessary component of the flight system because the system will be launched precooled, i.e., at operational temperature. Second, it is the structural load carrying member between the IPS (Instrument Pointing System) mount and the telescope thermal isolator and thus supports most of the system. It also performs the additional functions of mounting the earth/sun shield assembly, the laser/gyro

package, the cryogenic tankage, and it has provision for electrical and cryogenic feedthroughs. Thus, the basic design requirements of the housing are that it be vacuum tight and that it withstand all applied or induced loads without structural failure.

The vacuum integrity of the housing is achieved by design techniques and choice of housing materials. Elastomeric O-ring seals are used in all joints for three reasons: (1) they allow easy and rapid assembly/disassembly of a joint, (2) the required joint sealing forces are relatively small, thus allowing a lightweight joint design, and (3) they have been highly successful in past designs. The elastomeric seals do not display significant outgassing or otherwise contribute to contamination.

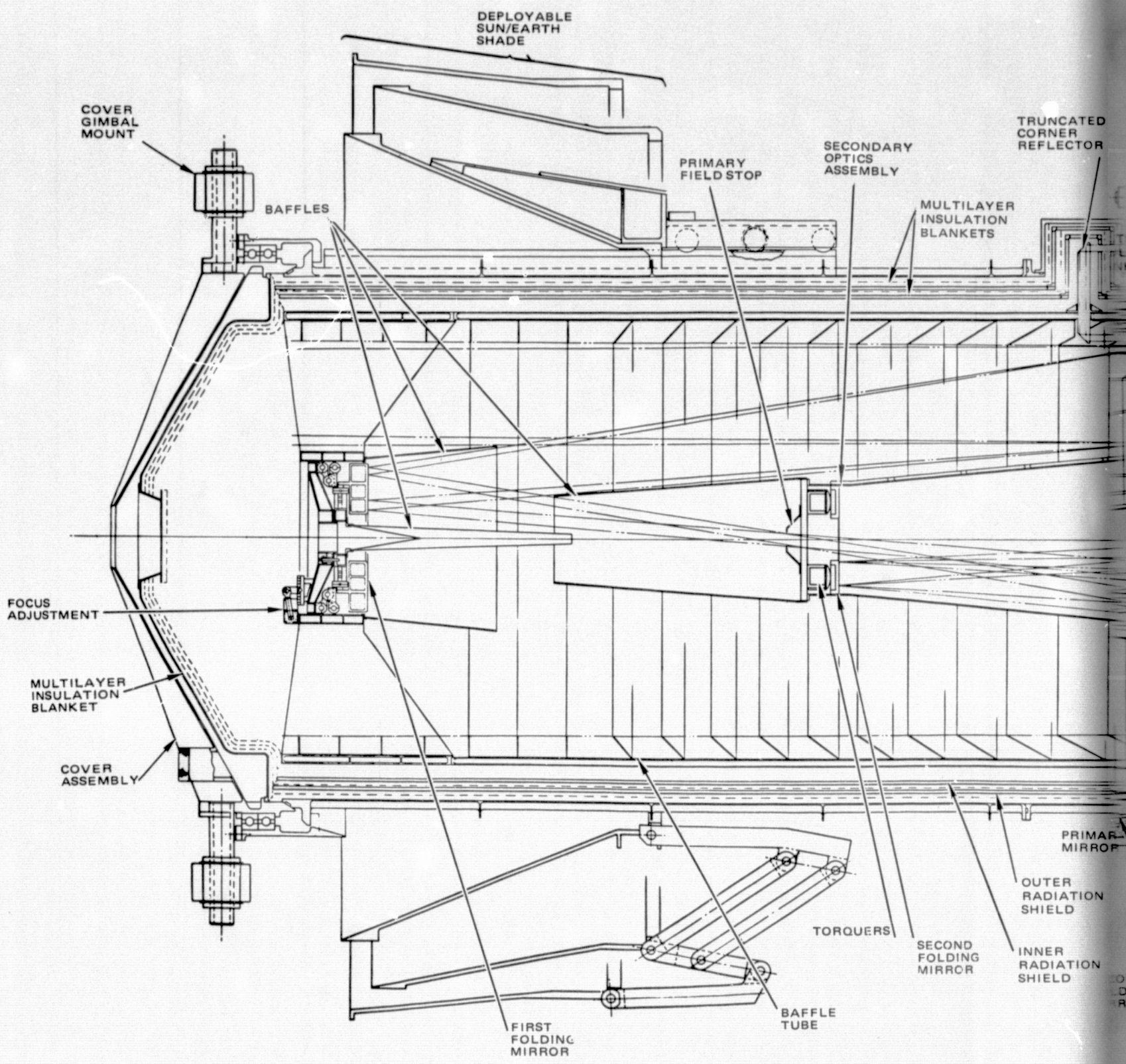
The housing material is 6061 aluminum. This material was selected because it has demonstrated success as a vacuum housing material, it has good structural properties combined with low weight, it is amenable to most manufacturing processes (e.g. machining, welding and forming), and it is readily available at economical cost. The structural sizing of the outer housing is described in Section 3.3.3. The selected approach is to use a cylindrical shell stiffened with rings and stringers. This provides a stiff structure with high natural frequencies and low weight.

An additional design requirement that was imposed upon the outer housing was that the multiple instrument chamber (MIC) have direct and easy access. This requirement is incorporated into the design through the inclusion of the rear cover plate.

It was also decided to subdivide the housing into several component parts to facilitate assembly and to alleviate fabrication problems with their associated costs by avoiding excessively large structures.

Thermal Isolator Subsystem

The thermal isolation subsystem is comprised of a thermal isolator, radiation shields, and multilayer insulation which covers the outer radiation shield. Its purpose is to provide thermal protection of the cryogenically cooled assemblies.



FOLDOUT FRAME

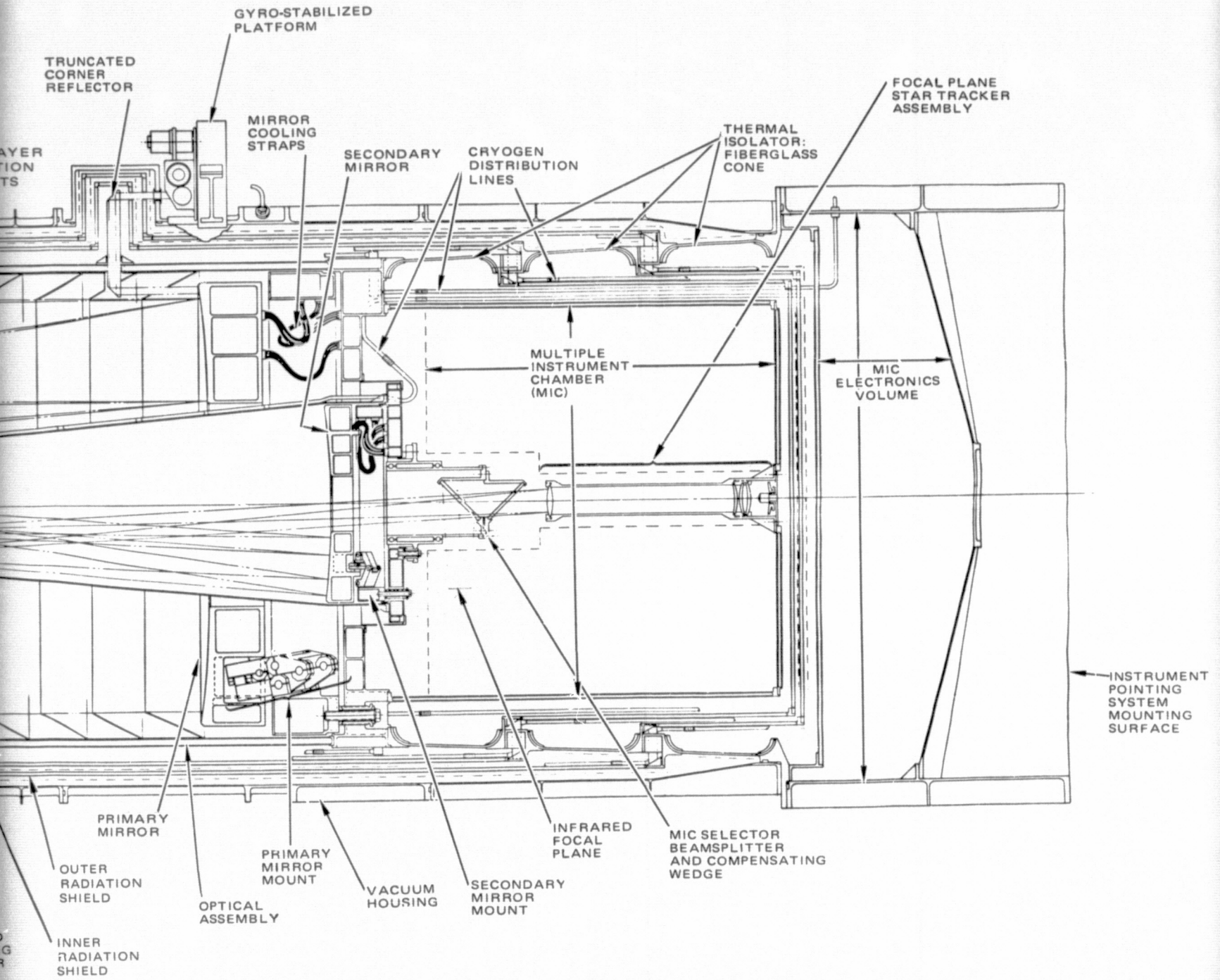
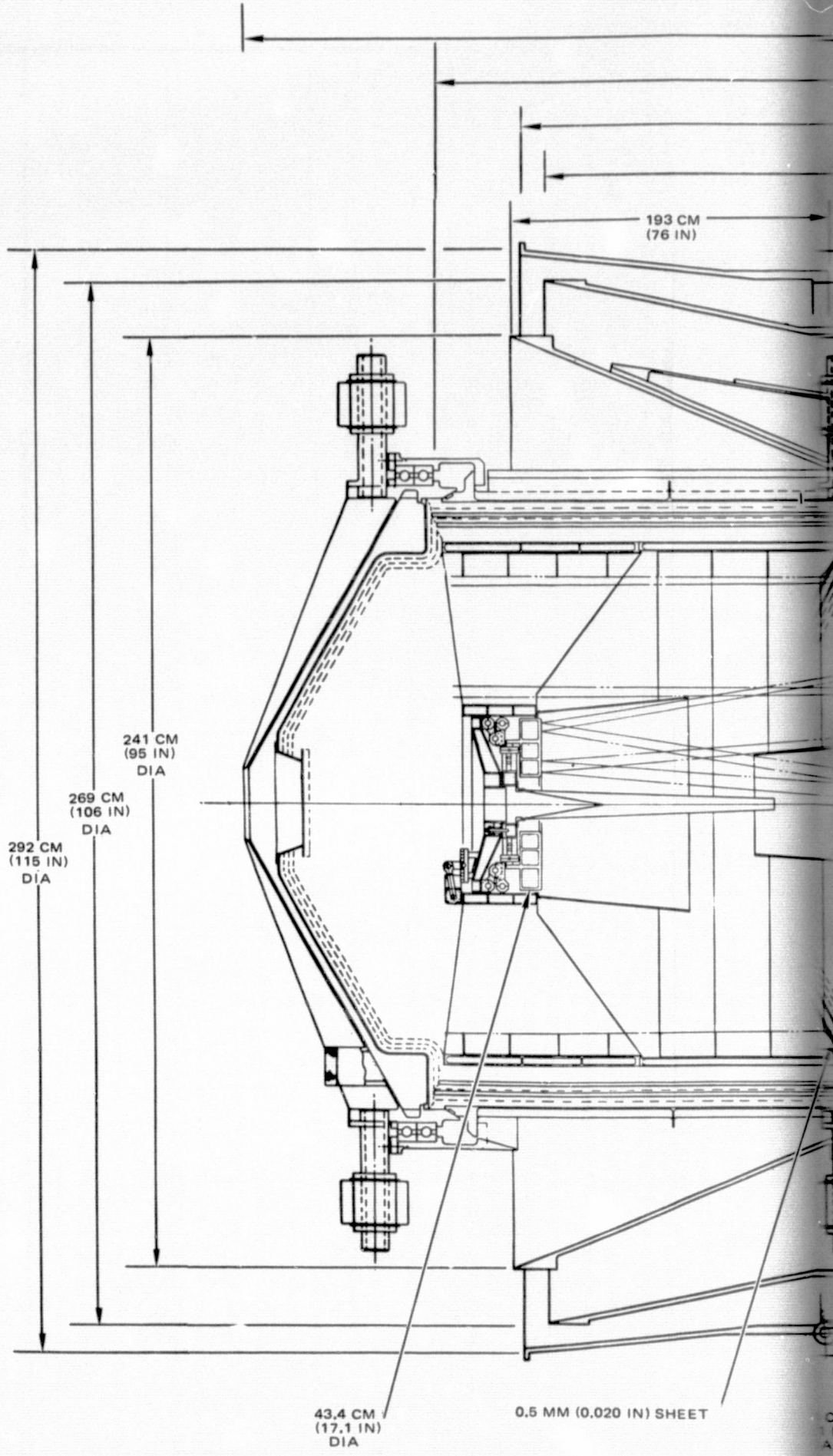
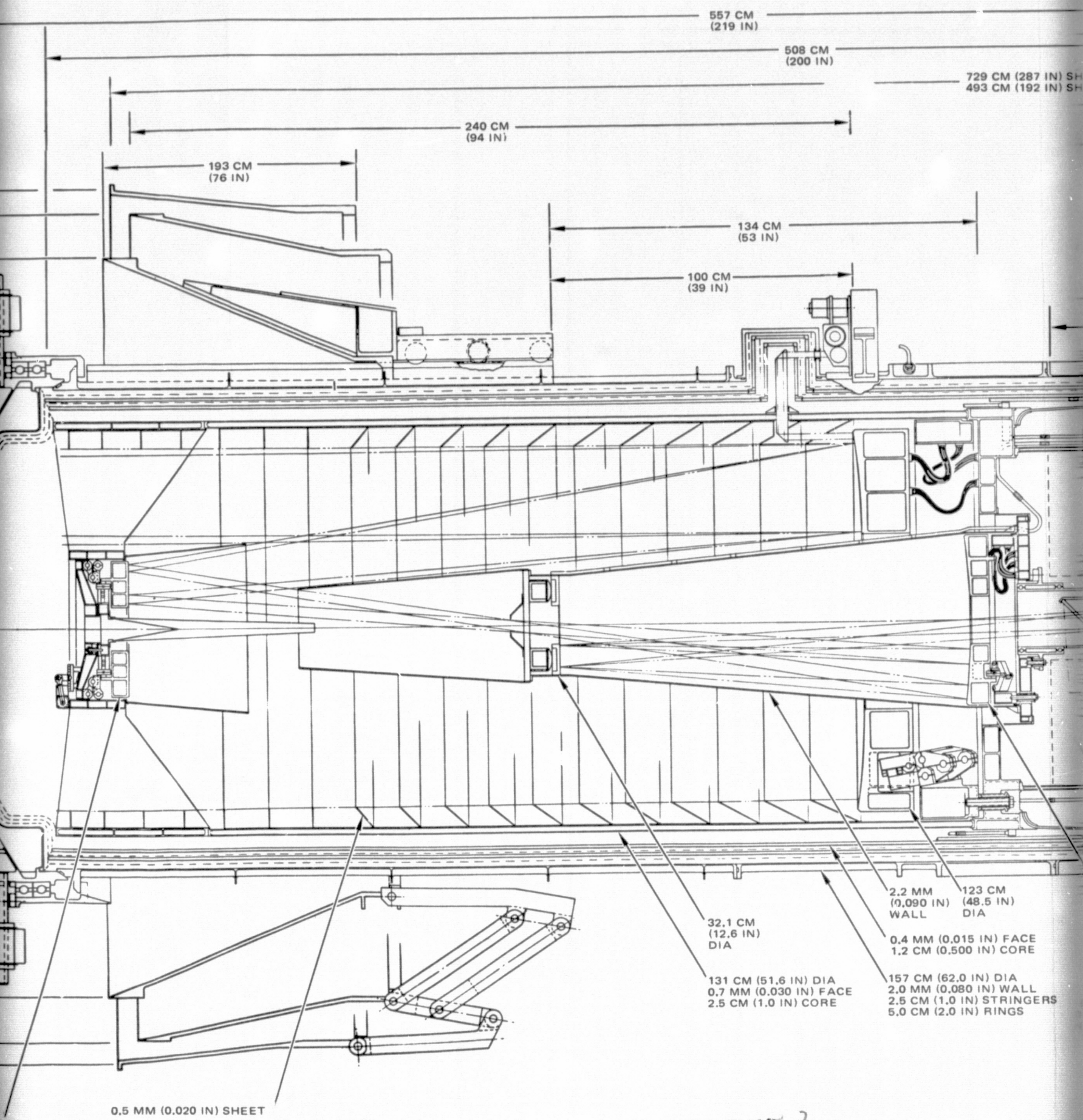


Figure 3-33A. SIRTF telescope layout — identification of subsystems and components.



FOLDOUT FRAME |



FOLDOUT FRAME 2

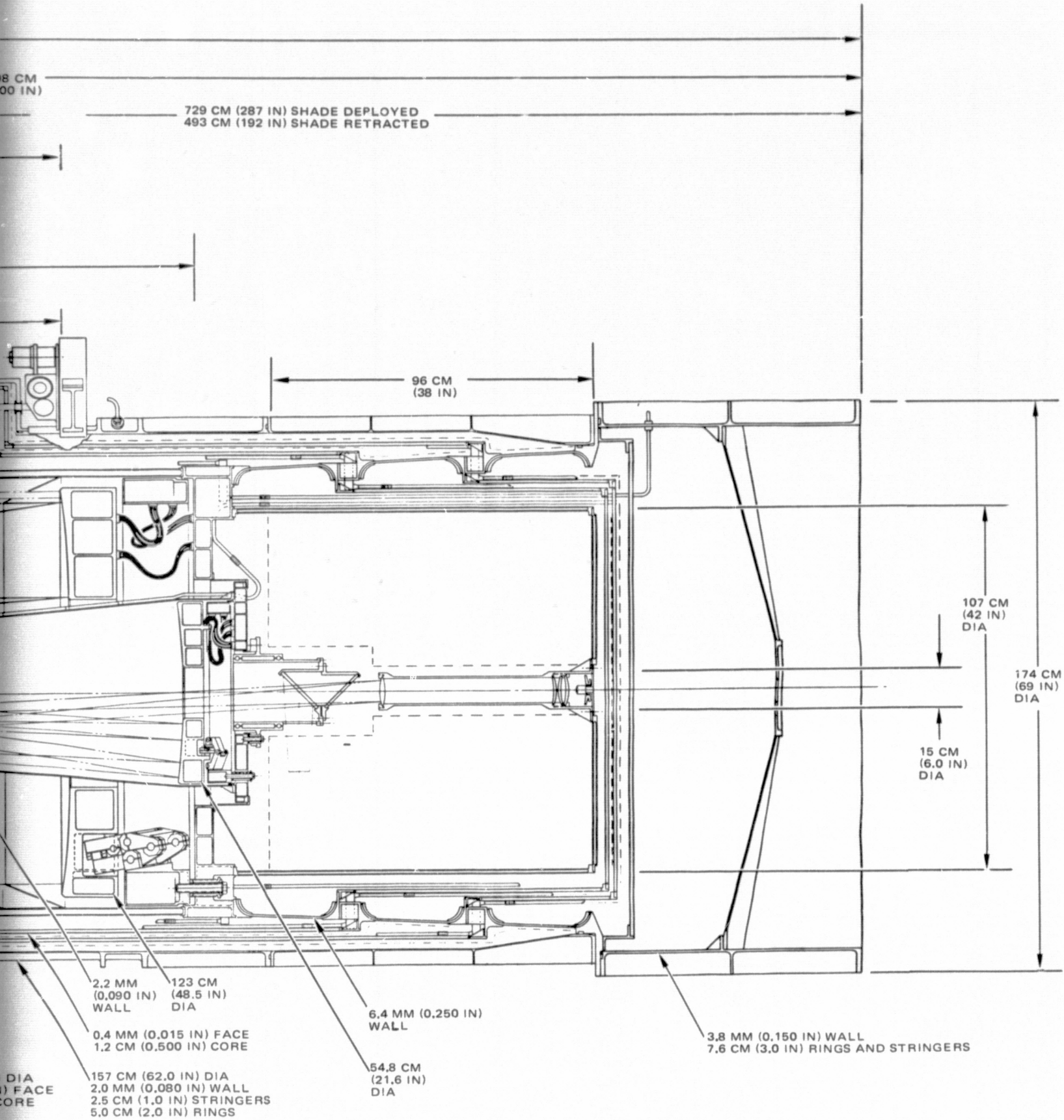


Figure 3-33B. SIRTF telescope layout - dimensions.

3-63

FOLDOUT FRAME 3

PRECEDING PAGE BLANK NOT FILED

The fiberglass/steel thermal isolator is attached to the outer vacuum housing and the main optics support. It serves to both thermally isolate the cryogenically cooled assemblies from the warm outer vacuum housing and structurally support all the cooled assemblies.

The isolator is comprised of three filament-wound, S-type fiberglass sections joined by steel retaining rings. The rings serve to mount the radiation shields and attach the isolator to the optics assembly and the outer vacuum housing.

Because of the conflicting structural and thermal design criteria placed on the isolator, material tradeoff studies were performed prior to selection of the S-type fiberglass. Briefly, S-type fiberglass was selected because the fiberglass isolator's required size, i. e., length and wall thickness, is more readily packaged than that of the other candidate, titanium. The study is presented in Reference 3-15.

The aluminum inner and outer radiation shields are attached to the middle rings of the thermal isolator. The function of the radiation shields is to shunt heat that enters through the insulation and is radiated between the shields by heat exchange with the cryogen. This is accomplished by routing the cryogen, after cooling the instruments and mirrors, through local heat exchangers located at selected points on each of the shields. In addition, the shields serve to shunt conducted heat through the isolator by virtue of their thermal contact to the thermal isolator.

The radiation shields are large cylindrical shells (except the MIC covers which are circular flat plates) which are of a honeycomb construction with 0.4 mm (0.015 inch) face sheets and 13 mm (0.50 inch) core thickness. Honeycomb was selected for two related reasons. First, its relatively low weight significantly alleviates the structural design of the thermal isolator because a significant portion of the isolator loading is attributable to the dynamic response of the radiation shields. The low weight structure also provides a smaller thermal conduction path and makes thermal design of the isolator somewhat easier. Second, the most probable failure mode of a lightweight radiation shield is local buckling. Honeycomb has inherently high resistance to local buckling compared to other types of structures of equal weight.

Optics Assembly

The optics assembly is attached to the thermal isolator and comprises all optical elements, their mounts, the interconnecting structure, the auto-focus mechanism, the MIC selector, and the MIC mount. The major structural element of the optics assembly is the main optical support.

The main optical support (Figure 3-34) is an aluminum, closed-cell composite structure which serves as the structural backbone of the optics assembly because all optical structure either directly or indirectly attaches to this member, which is itself directly attached to the thermal isolator. It mounts the primary mirror and mount assembly, the first folding mirror and autofocus mechanism through the spider assembly (four struts) and the main telescope barrel, the secondary optics assembly and the MIC selector, and the MIC mount.

A substantial portion of the design effort was devoted to developing a means for mounting the beryllium mirrors to an aluminum structure. This was an important objective because of the difficulties and costs associated with building the entire telescope barrel, a structure up to 140 cm (55 inches)

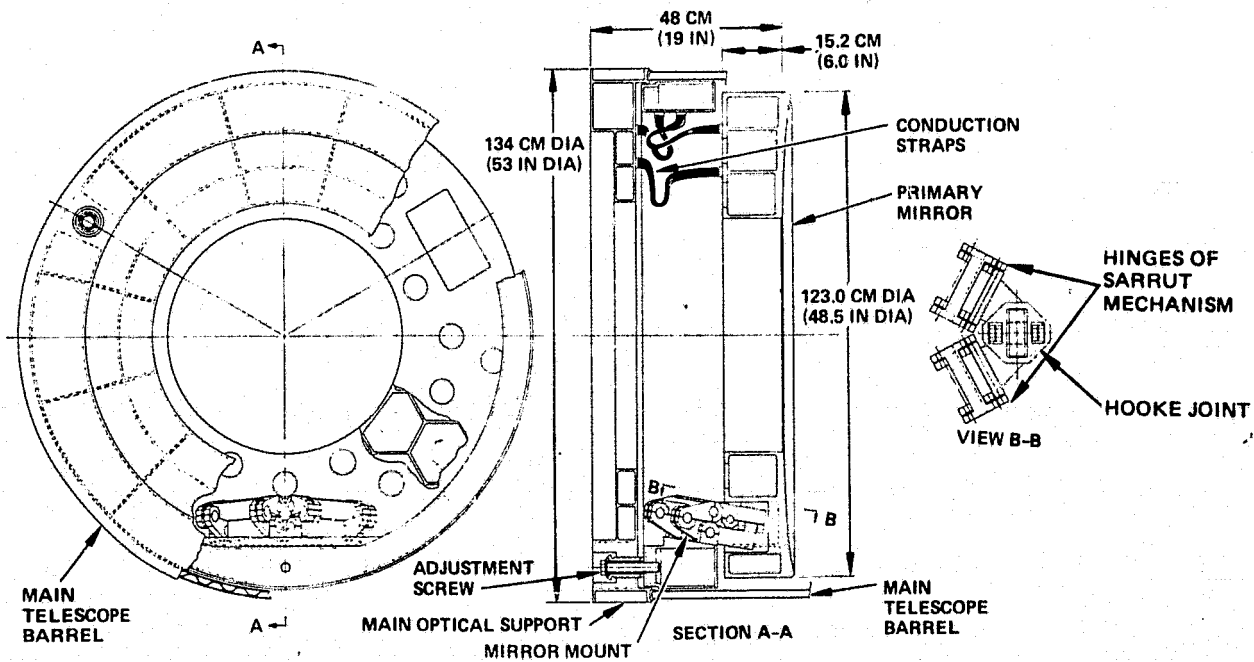


Figure 3-34. Primary mirror mount.

in diameter and 274 cm (108 inches) long, of beryllium. The additional weight of the aluminum structure, 150 lbs (70 kg) is not judged to be a significant drawback. Although it is practical to build some of the smaller structural components of beryllium, the chosen design approach was to restrict the use of beryllium to the mirrors only. This was accomplished through the use of three Hooke joint/Sarrut mechanisms to mount each mirror.

A schematic representation of a single mirror mount is shown in Figure 3-35, and of the mirror mount set in Figure 3-36. In essence the Sarrut mechanism is composed of two hinges, the axes of the hinges being non-parallel. Kinematically, it is a six-bar space mechanism composed of revolute pairs which produces pure straight line motion.

The mirror mount scheme is to utilize three Sarrut mechanisms so aligned that the line of action of each mechanism which passes through its point of mirror attachment intersects in a common point with similar lines of action of the other mechanisms. Under this condition the differential thermal expansions/contractions which occur between the mirror and the

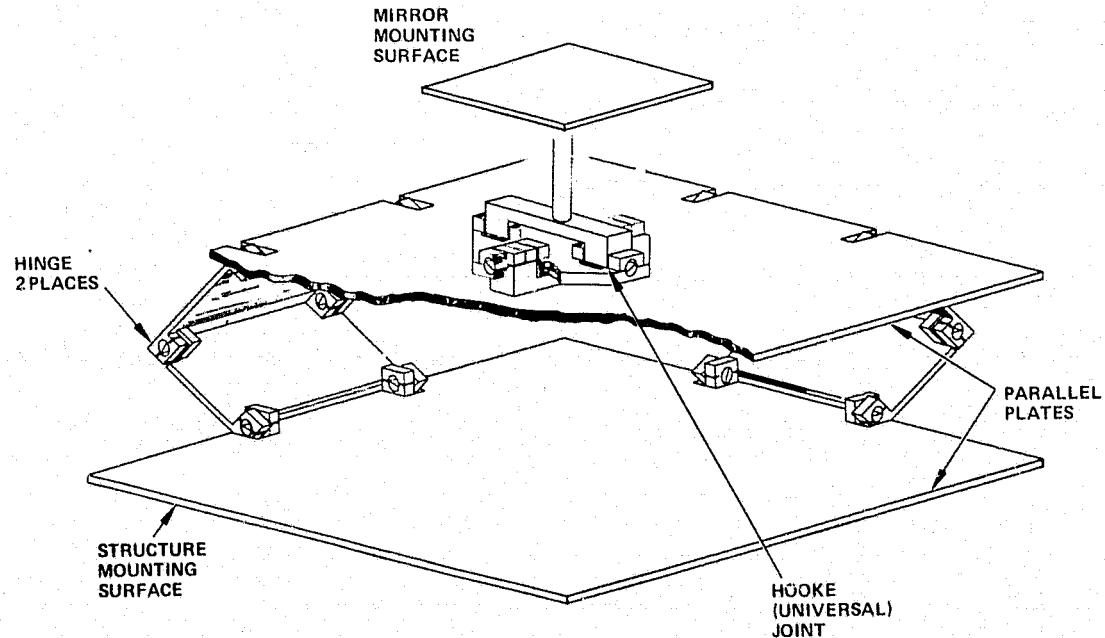
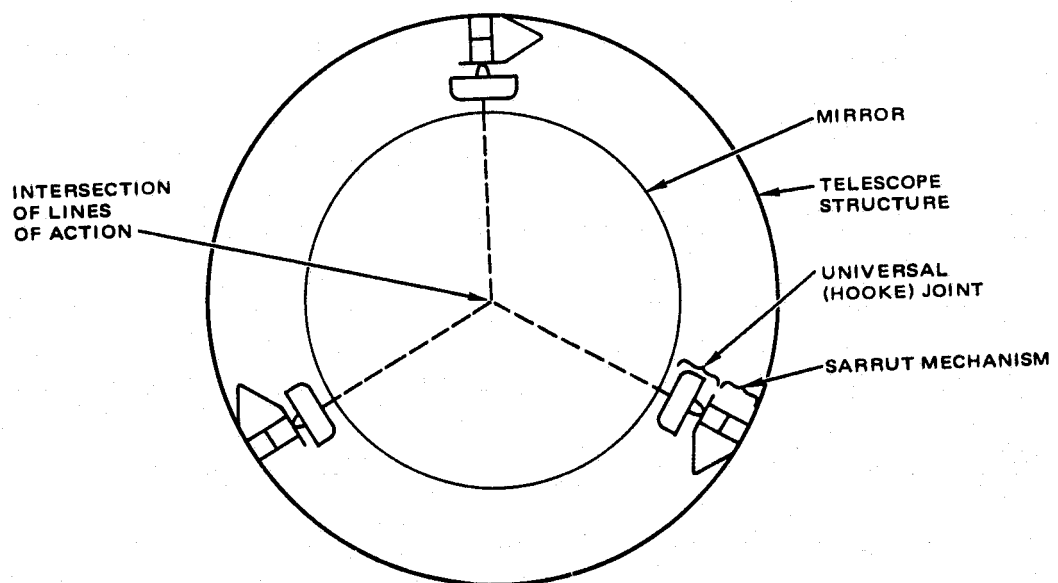
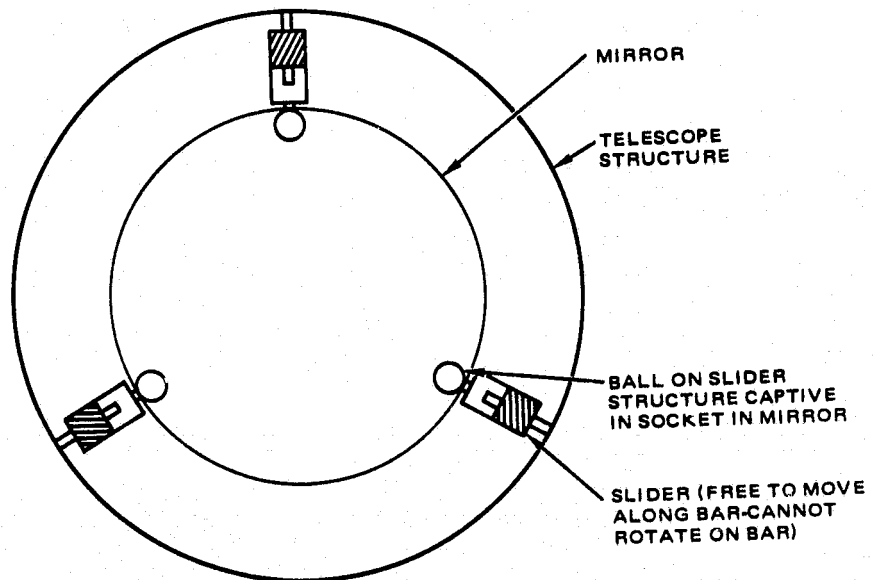


Figure 3-35. Mirror mount schematic concept.



A. MIRROR MOUNT SCHEMATIC



B. BALL AND SLIDER EQUIVALENT

Figure 3-36. Mirror mount set-schematic concept and equivalent.

mirror mounting ring, i.e., across each mechanism, are accommodated without translating or tilting the mirror.

However, if these lines of action are skewed, (e.g., due to manufacturing errors) then there will be accompanying translations and rotations whose magnitudes are dependent upon the degree of skew. The translations are inherently accommodated by each mechanism because they each possess that kinematic degree of freedom. However, the mechanism will not accommodate any rotation because they do not possess rotational degrees of freedom.

A Hooke joint (more commonly known as a U-joint) is incorporated between the mirror and each Sarrut mechanism to provide rotational degrees of freedom. The rotational degrees of freedom are necessary to accommodate the effects of fabrication and assembly tolerances on the skewness of each mechanism's line of action.

Although the Hooke joint provides only two rotational degrees of freedom, it is believed that the rotations about each mechanism's line of action are insignificant. Thus, the Hooke joint associated with each Sarrut mechanism is aligned so that it accommodates rotations about axes which are perpendicular to the line of action of the Sarrut mechanism.

In summary, the mirror mounting approach used for all mirrors (excepting the chopping mirror) is comprised of three Hooke joint/Sarrut mechanism sets which are aligned so that their respective lines of action intersect in a common point.

The Hooke joint/Sarrut mechanism unit is composed of titanium and employs flexures in all joints rather than bearings. Titanium was chosen because its thermal expansion properties closely match that of beryllium over the design temperature range. Flexures were selected because they are free of the play associated with bearings resulting from fits and internal clearance.

Each Hooke joint/Sarrut mechanism is attached both to the beryllium mirror and to the aluminum mirror mounting ring through double-piloted joints which allow differential thermal expansion and contraction to occur while attaining high positional accuracy and precision. These joints are described in Reference 3-15.

The mirror mounting ring is attached to the fixed optical structure through three adjustment screw assemblies which provide both focus and tilt adjustment (see Figure 3-35). Each adjustment screw assembly consists of spherical washers, an internal locking screw, and the adjustment screw and are so designed that there is no moment transfer across the assembly. Because this design requires a relatively large clearance between the internal locking screw and the adjustment screw, an aluminum mounting ring collar is incorporated in the design which permits focus and tilt adjustments, but precludes radial movement of the mirror mount assembly.

The mirror mounting technique described above is used to mount the primary mirror, the first folding mirror, and the secondary mirror. This is one of several possible approaches which have not been fully explored. It is believed that the described approach should be subjected to further study because the largest structural compliances of the telescope system occur in the mirror mounts.

The autofocus mechanism is located at the first folding mirror and consists of a large flexural type Sarrut mechanism which provides axial movement of the first folding mirror of approximately ± 1.0 cm (0.4 inch) for focus (see Figure 3-37). The mechanism drive is provided by a dc motor/gearhead/brake which drives a form of slider/crank linkage. In this case, the slider is replaced by the large flexural type Sarrut mechanism and the linkage incorporates flexures at all kinematic pairs. The brake is incorporated into the system to allow the system to be locked into position at all times that the motor is not engaged.

The linkage was synthesized to produce a linear relationship between crank angle and mirror displacement. A linearity of less than 0.05 percent (structural error) was obtained in the final design. This will probably result in a total estimated error of less than 1 percent in the actual hardware.

The autofocus mechanism (Figure 3-37) is mounted to the aluminum spider assembly which is comprised of an inner ring, four honeycomb struts, and an outer ring which attaches to the main telescope barrel. The construction is of composite closed cell construction for the rings and thinner honeycomb for the struts. This construction was selected to provide a relatively low weight structure with good stiffness and high resistance to buckling.

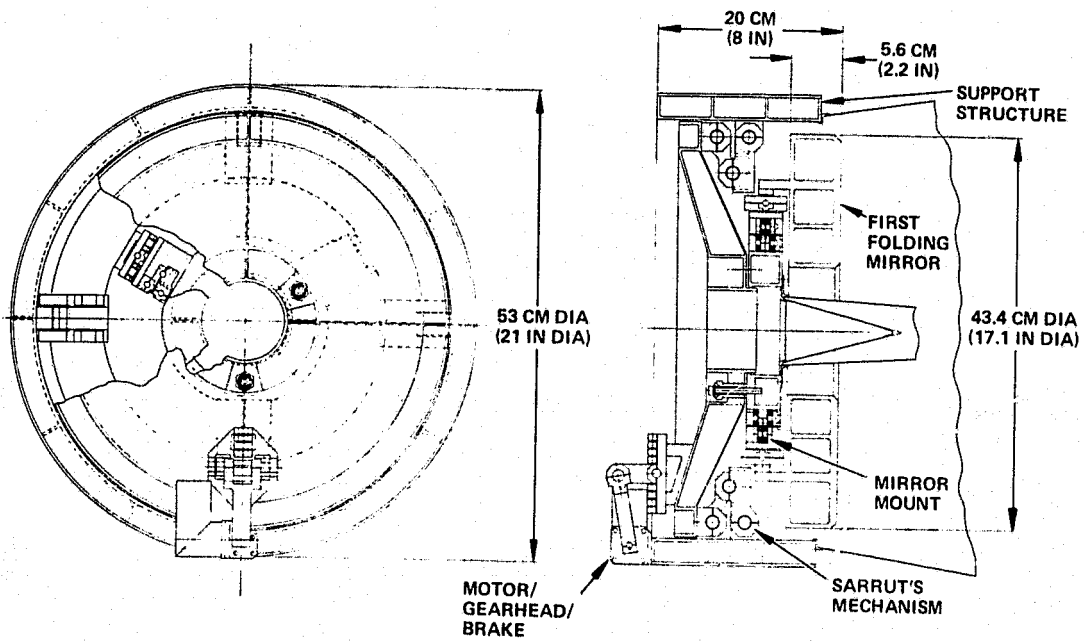


Figure 3-37. First folding mirror mount and drive.

The main telescope barrel is an aluminum sandwich section cylinder which serves to mount the baffles in addition to providing structural support of the first folding mirror and its related structure. The sandwich construction was selected because it is a more positive (i. e., it can be welded rather than brazed or bonded) structure than honeycomb.

The secondary optics assembly is comprised of the secondary and chopping mirrors and the conical baffle between them which serves as the supporting structure. It also mounts the MIC selector.

The secondary optics assembly is mounted as a unit to the main optical support. If later analysis shows that a thermal isolator is necessary, the study indicates that the assembly can be mounted on a titanium isolator with minor design impact.

MIC Selector

The MIC Selector consists of a dichroic window and a correcting wedge, a bearing assembly, latching pawls, a dc motor/clutch drive, and an induction potentiometer for position readout. The purpose of the MIC selector is to provide a means to optically switch the infrared energy from instrument

to instrument within the MIC. The dichroic window is provided to allow visible radiation to pass through to the star tracker. See Figure 3-38.

The wedges are both adjustable to each other and as a unit to the bearing. The bearing assembly is in turn adjustable in tilt, decenter, and axial position to the secondary optics and hence to the entire optics assembly.

The bearing assembly is a double row, angular contact bearing which is preloaded to eliminate axial and radial play that would adversely affect optical alignment. The bearing is of a custom design to minimize the effects of tolerance accumulations upon performance. Further, it is not anticipated that the bearing will require lubrication because of the relatively low number of revolutions (less than 5000) it will experience over its life.

A set of (spring loaded) latching pawls (with an engagement tooth) are provided for each of the six MIC selector locations. These provide a highly accurate repeatability of the selector location because one pawl acts as a stop and the other, which is flexure mounted, provides a highly repeatable latching force. Both the engagement tooth and the pawls for each location are adjustable so that the necessary angular accuracy of approximately 5 to 15 μ rad (1 to 3 arc second) can be achieved without unduly stringent tolerances.

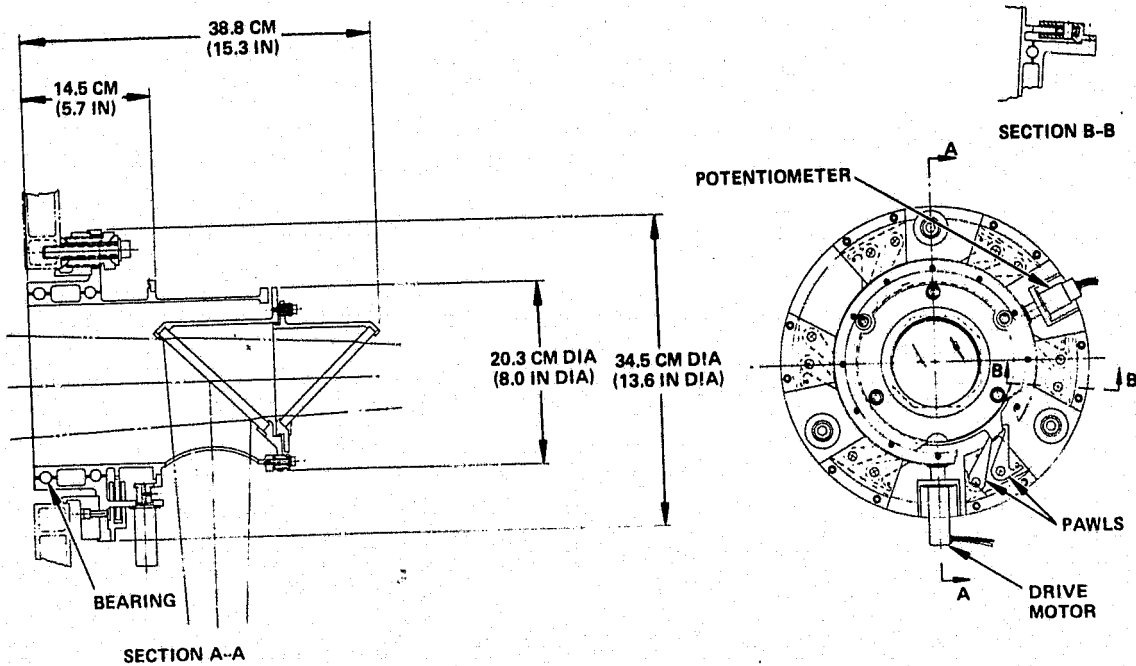


Figure 3-38. MIC selector.

The selector drive is provided by a dc motor/clutch which drives the bearing through bevel gearing (unlubricated). When the motor is engaged, the clutch is engaged thus allowing the motor to drive the bearing. When the motor is de-energized, the bearing assembly is free wheeling thus allowing the pawls to engage and lock the assembly. The potentiometer provides position readout so that the motor can be de-energized at a point where the pawls can cam the assembly to the lock position.

MIC Mounting

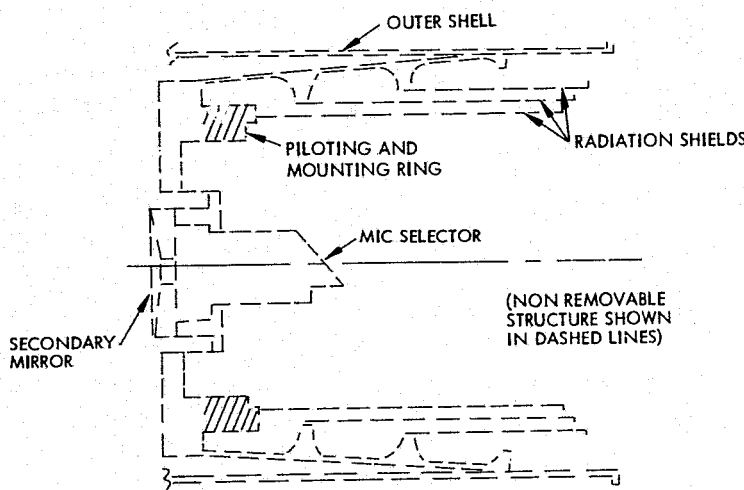
The MIC (Multiple Instrument Chamber) mounting is accomplished using pilots and bolts in the forward faceplate of the MIC. Figure 3-39 shows the various steps in the installation. Figure 3-39a shows the rear end of the telescope ready for MIC installation and Figure 3-39b shows the MIC with one of the standard size instruments installed. The MIC, which is prealigned and completely checked out, is inserted into SIRTF and the pilots and alignment pins engaged. Bolts are inserted between the mounting ring in the telescope and the edge of the MIC integration plate. Alignment is checked warm through one or more apertures in the rear plate.

Following warm alignment and installation of the rear plates of the radiation shields, and various helium fill connections and motor drives, the MIC is ready for cooldown and cold alignment and performance checks.

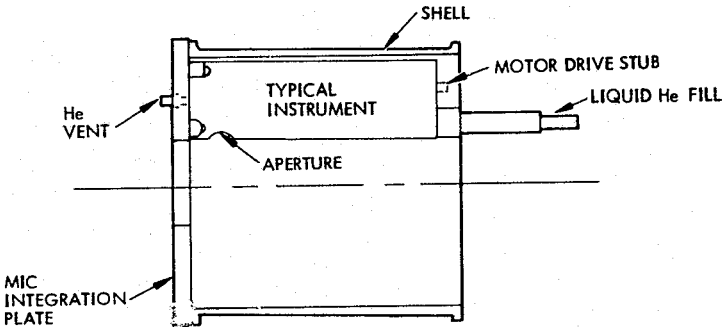
It is noted that the warm electronics/components assembly of the MIC has not been defined and that the allotted volume depicted in Figure 3-33 is arbitrary.

Sun-Earth Shade

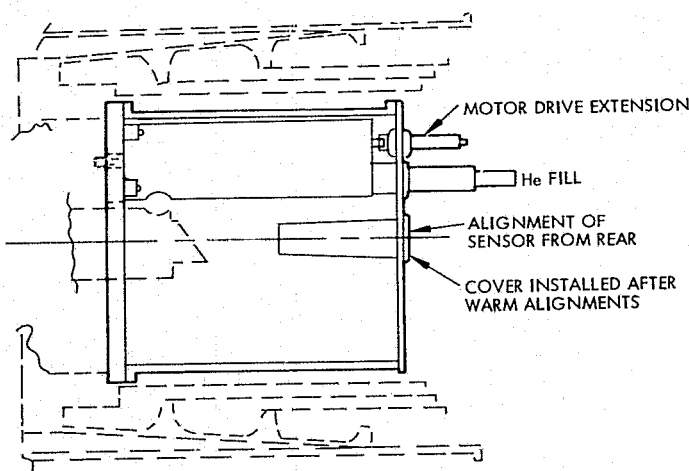
The deployable sun-earth shade assembly consists of three aluminum honeycomb cones and a mechanism and drive to deploy and retract the shields. The purpose of the assembly is to provide protection of the telescope aperture from radiation from the earth, sun and Shuttle. The design requirement was to shield the telescope aperture from incident radiation at angles greater than 0.79 rad (45 degrees) from the telescope line of sight.



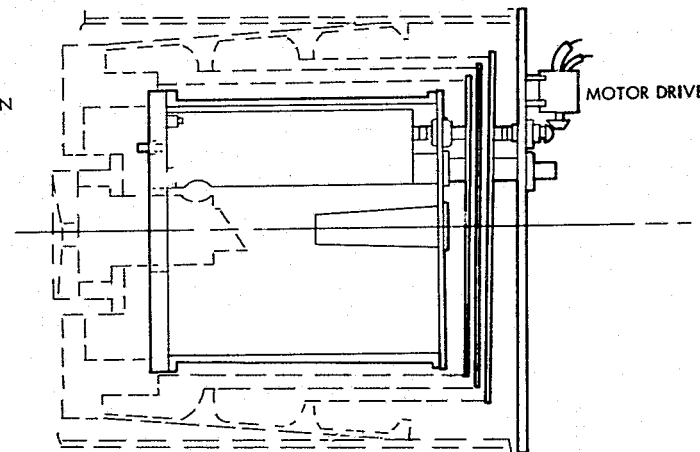
A. REAR END OF TELESCOPE READY FOR MIC INSTALLATION



B. MIC READY FOR INSTALLATION - ONE INSTRUMENT SHOWN. ROUGH ALIGNMENT HAS BEEN DONE



C. WARM ALIGNMENTS COMPLETE, FIRST COVER INSTALLED



D. READY FOR TELESCOPE COOL DOWN AND LIQUID HELIUM FILL

Figure 3-39. MIC installation.

The shade was divided into three sections to provide adequate room on the outer vacuum housing for the mounting of the cryogen tankage and associated structure. Each shade section is connected to the others through the deployment linkage which is basically a compounded or double Sarrut mechanism. One half of the linkage is shown in the lower portion of Figures 3-32 and 3-33.

The entire shade/linkage assembly mounts to the outer vacuum housing by means of three trucks which travel along corresponding rails which are attached to the housing. The drive concept is to use a dc motor driven rack and pinion arrangement to both roll the shield assembly forward and deploy the shields through a suitable slip clutch arrangement.

Cover Assembly

The removable cover assembly consists of the vacuum cover, rotating dog ring, dog ring motor drive, and associated structure and mechanism which provide the vacuum cover with five kinematic degrees of freedom with respect to the telescope. See Figure 3-40. The only degree of freedom which is not provided the cover is roll about the telescope line of sight. These five degrees

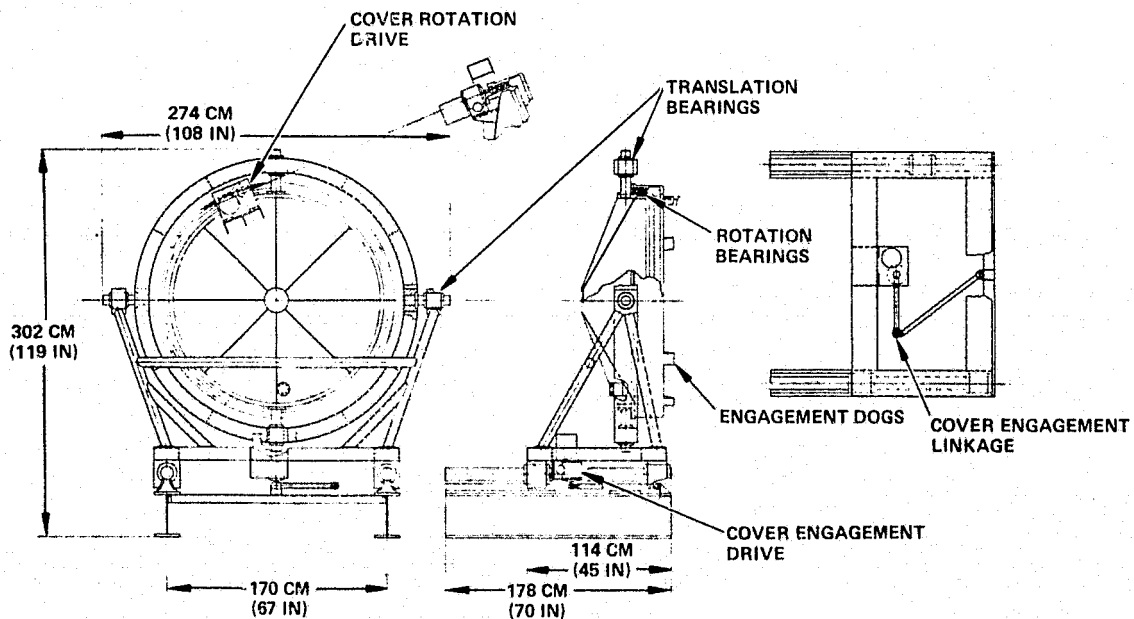


Figure 3-40. SIRTF cover and support structure.

of freedom are required to accommodate the misalignments which may occur between the cover assembly and the telescope over successive engagements and disengagements during the mission. These misalignments may for example be attributed to thermal distortions of the Shuttle and pallets or one-g to zero-g effects on the entire system.

The purpose of the cover assembly is to complete the vacuum envelope around the cooled assemblies for the cold ground testing and launch. In addition, it provides contamination protection of the telescope during the mission should the telescope's external environment be contaminated.

The vacuum cover is a cylindrical aluminum shell which has radial stiffening ribs to preclude buckling. It mounts a vacuum valve, vent and a lightweight shield which carries a multilayer insulation pack. The vent (on the helium tank-telescope system) leads to the T-O umbilical for prelaunch venting. The inner surface of the cover is cooled by conduction and radiation.

The cover also mounts the rotating dog ring by means of a preloaded pair of bearings and the dog ring drive. The function of the dog ring is to develop the necessary seal preload between the cover and the outer vacuum housing by a wedging action between the dogs on the rotating ring and a similar set of dogs on the outer vacuum housing. This action is very similar to that of a pressure cooker lid. This approach was selected because the necessary seal preload is developed only across the sealing surfaces. Thus there is no structural loading of the telescope outer vacuum housing, the pallet, or the cover structure and mechanism. The sealing surfaces are tapered to facilitate engagement and to allow a seal gland design which retains the seal when the cover is not engaged. The seal is a large cross section, 1.2 cm (0.5 inch), elastomeric O-ring seal.

The vacuum cover is attached to a two axis gimbal which provides both two angular and two translational degrees of freedom. This gimbal is in turn attached to another translational gimbal whose function is to either retract or engage the entire cover assembly with the telescope. This is accomplished by a linkage driven by a wormgear motor.

An open loop, unpowered design approach is used in the two axis gimbal. This approach was selected because it is believed that the potential misalignments between the cover and outer housing will not exceed ± 3 mrad (± 1 degree) and ± 5 cm (± 2 inches). Thus, the cover and dog ring can be made sufficiently oversized to accommodate these alignments and be such that the cover assembly is self aligning. This however requires further study because the amount of misalignment has not been established. Should the amount of misalignment become excessive, it would be necessary to resort to a closed loop powered system with a considerable increase in complexity.

Cryogenics Supply

The telescope cryogenic system is a long plumbing line with local heat exchangers at selected points to provide cooling of the structure. Bellows are incorporated into the design at selected points to preclude differential thermal expansion/contraction effects and to allow the use of a continuous single line free of interconnections and fittings. This approach is both feasible and highly desirable because it allows the plumbing to be leak checked prior to installation. Because there are no connections made during the telescope assembly, except at the interface to the outer vacuum housing, a high confidence is developed that the system is helium leak tight.

The cryogen line enters the outer vacuum housing and is routed directly through the radiation shield to the following sequence of heat exchangers:

- SIRTF-MIC interface
- Secondary optics assembly
 - Secondary mirror mount
 - Chopping mirror
- Main optics support
- First folding mirror spider
- Radiation shields
 - Inner
 - Outer

The aperture shield is not actively cooled; the telescope barrel is cooled by conductive coupling to the heat exchanger at the main optics support and the first folding mirror spider. The cryogen line final exit location will be within the main barrel, to provide a purge flow to prevent contaminant from entering the telescope. The exact locations, orientations and number of outlets have not been worked out.

The thermal design and results of the thermal analysis are discussed in more detail in Section 3.4.

3.3.2 Approximate Thickness of SIRTF Mirrors

The sizing of the thicknesses of the SIRTF mirrors is of twofold importance. First, the mirrors must have sufficient thickness to preclude excessive figure distortion arising from service loads. Secondly, the mirror thicknesses impact the allocation of space within the telescope and thus affect the configuration of the optical structure and the overall telescope mechanical design.

A highly accurate sizing of the mirror thicknesses (and hence mirror blank design) is a task requiring the construction of large and complex stress models and consequently numerous computer runs. This would be outside the scope of the present preliminary design study. The sizing of the mirror thicknesses for this study has been accomplished by a combination of extrapolation from existing mirror designs, approximate analytical methods, and judgement.

Development of Approach

From an analytical viewpoint, a reasonable starting point is to approximate the mirrors as annular flat plates, i.e., circular flat plates with a central hole. The inherent assumptions of this approximation are (Reference 3-16, Page 7):

1. The mirror is flat or the effect of power on geometry is negligible.
2. The plate is of uniform thickness and of homogeneous isotropic material.

3. The thickness is not more than about one-quarter of the least transverse dimension and the maximum deflection is not more than about one-half the thickness.
4. The plate is nowhere stressed beyond the elastic limit.

In the case of assumption (1), the greater the power of the mirror the greater the inaccuracy of the assumption and thus of the analysis. Fortunately, the SIRTF mirrors are either flat or of relatively low power ($f/\text{no} > 3$) and thus may be considered reasonably flat. It is noted that the thicknesses used in all subsequent analysis correspond to mean section thickness.

The SIRTF mirrors are lightweight mirror designs which will utilize either cored or eggcrate construction. Because mirrors of this type experience considerably less deflection than do solid mirrors (see for example Reference 3-17) the effect of assumption 2 is to yield conservative results, i.e., mirror thicknesses greater than required.

In the case of assumption 3, the thickness can exceed one-quarter of the least transverse dimension if the effects of direct shear are included (Reference 3-16, page 8). In this analysis, the effects of shear will be assumed negligible.

Assumption 4 is of no consequence in this analysis because the stress levels associated with mirror deflections are seldom greater than 10 percent of the material yield strength.

The basic loading for which the mirrors must be designed is the sagging of the mirror on its supports due to its own weight. That is, the mirror sag must not exceed a specified value to prevent excessive image aberrations in the transition from the one-g environment where it is fabricated and tested, to the zero-g environment where it is operated. From assumption 2, this loading can be reasonably approximated by the case of uniform loading over the surface of the plate.

All of the SIRTF mirrors utilize a three point mounting arrangement. The mounts are equally spaced on an intermediate diameter (i.e., not on a mirror boundary) which is concentric to the mirror axis. Unfortunately, there are no algebraic or numerical solutions for an annular plate with three point intermediate support. However, the case for three-point support on the outer diameter is readily derivable, provided the point supports are simple

supports. Thus, for analytical convenience the mirror supports are considered to be simple supports acting at the mirror outer diameter. It is of interest to consider the implications of this simplification. First, a uniformly loaded plate supported on its outer diameter would experience greater deflection and slopes than would a plate similarly loaded but supported at an intermediate diameter. Second, simple supports also would result in greater deflection and slope than fixed or elastic supports. Therefore, a mirror designed for three-point simple support on its outer diameter, but in reality supported at a proper intermediate diameter on elastic or fixed supports would experience less deflection and slope and the effect of the simplification is conservative.

It is noted that the local moments introduced at the supports by manufacturing and assembly errors, misalignments, and thermal effects are necessarily ignored because of the large uncertainty in their magnitude and because their inclusion would enormously complicate the task at hand. Although totally qualitative, the effects of the local moments will be somewhat compensated by the conservatism of assumption 2. That is, the assumption of a solid mirror rather than the actual lightweight design.

Derivations of the necessary equations for deflection and radial and tangential slope are given in Appendices 3-1 and 3-2. The deflection and slopes are given by Equations (19), (20) and (21) of Appendix 3-2.

Having established a means of analysis, it remains to establish a criteria for thickness selection. From an optical standpoint the mirror thickness must be sufficient to preclude excessive figure distortion. More precisely, the slope changes and deflections of the mirror figure resulting from loading must be of sufficiently small magnitude to attain the required optical performance.

The optical requirements on slope and deflection due to loading are derived and presented in Section 3.2.6 (Optical Fabrication).

1. The maximum slope change at any point shall not exceed 0.25 arc second ($0.12 \mu\text{rad}$).
2. The maximum deflection at any point shall not exceed $0.5 \mu\text{m}$ (20×10^{-6} inches).

It is noted that the above requirements are conservative approximations to the optical requirements and that much more sophisticated and precise evaluation techniques would be employed in the actual design of the mirrors (see Reference 3-18).

In the case of self weight deflection, the load intensity q is defined as the weight per unit area. For annular plates,

$$q = \frac{(a^2 - b^2) h\eta}{\pi (a^2 - b^2)} = h\eta$$

(See Table 3-12 for definitions.) The flexural rigidity of a plate is defined in Appendix 3-1 and is given by

$$D = \frac{Eh^3}{12(1-\nu^2)}$$

Substituting the above expressions into Equations (19), (20), and (21) of Appendix 3-2 yield

$$w = \frac{12\eta(1-\nu^2)a^4}{Eh^2} X_m \quad (1)$$

$$\theta_r = \frac{12\eta(1-\nu^2)a^3}{Eh^2} Y_m \quad (2)$$

$$\theta_t = \frac{12\eta(1-\nu^2)a^3}{Eh^2} X_m \quad (3)$$

where

$$w_{max} = 508 \mu m (20 \times 10^{-6} \text{ inches})$$

$$(\theta)_r \text{ max} = 0.25 \text{ arc second} (1.2 \mu \text{rad})$$

and Y_m , X_m are evaluated at $(\rho, \theta) = (1, 0)$ and $(\rho, \theta) = (t, \pi/3)$, respectively.

It is noted that the above requirements are conservative approximations to the optical requirements and that much more sophisticated and precise evaluation techniques would be employed in the actual design of the mirrors (see Reference 3-18).

In the case of self weight deflection, the load intensity q is defined as the weight per unit area. For annular plates,

$$q = \frac{(a^2 - b^2) hn}{\pi (a^2 - b^2)} = hn$$

(See Table 3-12 for definitions.) The flexural rigidity of a plate is defined in Appendix 3-1 and is given by

$$D = \frac{Eh^3}{12(1-\nu^2)}$$

Substituting the above expressions into Equations (19), (20), and (21) of Appendix 3-2 yield

$$w = \frac{12\eta(1-\nu^2)a^4}{Eh^2} X_m \quad (1)$$

$$\theta_r = \frac{12\eta(1-\nu^2)a^3}{Eh^2} Y_m \quad (2)$$

$$\theta_t = \frac{12\eta(1-\nu^2)a^3}{Eh^2} X_m \quad (3)$$

where

$$w_{max} = 508 \mu m (20 \times 10^{-6} \text{ inches})$$

$$(\theta)_r \text{ max} = 0.25 \text{ arc second} (1.2 \mu \text{rad})$$

and Y_m , X_m are evaluated at $(\rho, \theta) = (1, 0)$ and $(\rho, \theta) = (t, \pi/3)$, respectively.

TABLE 3-12. DEFINITIONS OF SYMBOLS

h	= plate thickness
η	= material density
a	= outer radius of plate
b	= inner radius of plate
D	= flexural rigidity of plate
E	= Elastic modulus
ν	= Poisson's ratio
w	= deflection of plate
ϕ_r	= radial slope
ϕ_t	= tangential slope
\bar{X}_m	= } normalized algebraic terms
\bar{Y}_m	= }
ρ	= radial coordinate (normalized)
θ	= angular coordinate (normalized)

It can be shown that the maximum deflection occurs on the inner boundary midway between the supports. Noting that the tangential slope is zero at a support point by reason of symmetry, and that the maximum value of radial slope (magnitude of gradient) occurs at the support point, then the magnitude of gradient equals the radial slope ϕ_r . Thus, Equations (2) and (3) above may be each solved for thickness to yield the following design equation

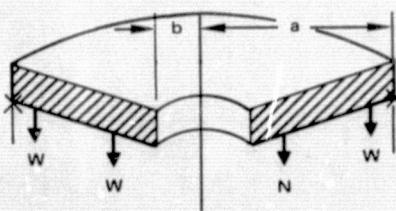
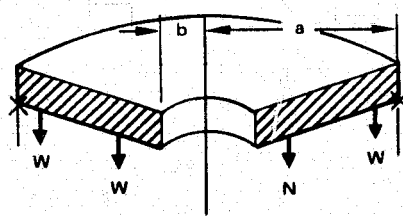


TABLE 3-12. DEFINITIONS OF SYMBOLS

h	= plate thickness
η	= material density
a	= outer radius of plate
b	= inner radius of plate
D	= flexural rigidity of plate
E	= Elastic modulus
ν	= Poisson's ratio
w	= deflection of plate
ϕ_r	= radial slope
ϕ_t	= tangential slope
$\frac{X_m}{Y_m}$	= } normalized algebraic terms
ρ	= radial coordinate (normalized)
θ	= angular coordinate (normalized)

It can be shown that the maximum deflection occurs on the inner boundary midway between the supports. Noting that the tangential slope is zero at a support point by reason of symmetry, and that the maximum value of radial slope (magnitude of gradient) occurs at the support point, then the magnitude of gradient equals the radial slope ϕ_r . Thus, Equations (2) and (3) above may be each solved for thickness to yield the following design equation



$$h_{\text{req}} = \text{greater of} \quad (4)$$

$$\left[\frac{12\eta(1-v^2)a^3}{E(\phi_r)_{\max}} Y_m \right]^{1/2}$$

$$\left[\frac{12\eta(1-v^2)a^4}{Ew_{\max}} X_m \right]^{1/2}$$

Discussion of Results

Table 3-13 presents a summary of the analysis that was performed on the SIR TF mirrors using the equations of the preceding section. It is noted that the thicknesses appearing in the table represent average thicknesses of each mirror cross section. In addition, the mirror thicknesses (those shown in the telescope layouts) were initially determined by engineering judgement, thus accounting for the differences between the thicknesses shown on the layouts (Figure 3-33) and the calculated thicknesses. Further, the second folding mirror (chopping mirror) was not analyzed because its loading is much more complex than that of this analysis.

TABLE 3-13. MIRROR DIMENSIONS AND DEFLECTIONS

Mirror	Outer Radius, mm (inches)	Inner Radius, mm (inches)	Layout Thickness, mm (inches)	Maximum Slope, μrad	Maximum Deflection, μm (mils)	Calculated Thickness* mm (inches)
Primary	614 (24.25)	295 (11.6)	157 (6.20)	1.49	44.7 (1.8)	175 (6.90)
First folding	217 (8.55)	70.1 (2.76)	55.9 (2.20)	0.55	61 (2.4)	37.6 (1.48)
Secondary	274 (10.80)	76.2 (3.00)	66.0 (2.6)	0.79	114 (4.5)	53.6 (2.11)
Material (All Cases) Beryllium						
$E = 29 \times 10^6 \text{ N/cm}^2 (42 \times 10^6 \text{ lb}_f/\text{in}^2)$						
$v = 0.07$						
$\eta = 1.85 \text{ g/cm}^3 (0.067 \text{ lb}_m/\text{in}^3)$						
*Calculated by Equation (4)						

$$\left[\frac{12\eta(1-v^2)a^3}{E(\phi_r)_{\max}} Y_m \right]^{1/2} \quad (4)$$

h_{req} = greater of

$$\left[\frac{12\eta(1-v^2)a^4}{Ew_{\max}} X_m \right]^{1/2}$$

Discussion of Results

Table 3-13 presents a summary of the analysis that was performed on the SIR TF mirrors using the equations of the preceding section. It is noted that the thicknesses appearing in the table represent average thicknesses of each mirror cross section. In addition, the mirror thicknesses (those shown in the telescope layouts) were initially determined by engineering judgement, thus accounting for the differences between the thicknesses shown on the layouts (Figure 3-33) and the calculated thicknesses. Further, the second folding mirror (chopping mirror) was not analyzed because its loading is much more complex than that of this analysis.

TABLE 3-13. MIRROR DIMENSIONS AND DEFLECTIONS

Mirror	Outer Radius, mm (inches)	Inner Radius, mm (inches)	Layout Thickness, mm (inches)	Maximum Slope, μrad	Maximum Deflection, μm (mils)	Calculated Thickness* mm (inches)
Primary	614 (24.25)	295 (11.6)	157 (6.20)	1.49	44.7 (1.8)	175 (6.90)
First folding	217 (8.55)	70.1 (2.76)	55.9 (2.20)	0.55	61 (2.4)	37.6 (1.48)
Secondary	274 (10.80)	76.2 (3.00)	66.0 (2.6)	0.79	114 (4.5)	53.6 (2.11)
Material (All Cases) Beryllium						
$E = 29 \times 10^6 \text{ N/cm}^2 (42 \times 10^6 \text{ lb}_f/\text{in}^2)$						
$v = 0.07$						
$\eta = 1.85 \text{ g/cm}^3 (0.067 \text{ lb}_m/\text{in}^3)$						
* Calculated by Equation (4)						

It can be seen from the table that with the exception of the primary mirror, the thicknesses shown in the telescope layouts are more than adequate to attain the required optical performance. In the case of the primary mirror, the required thickness is slightly greater than that shown in the telescope layout. It is judged that the computed maximum deflection and maximum slope will be of little or no consequence because the previously stated optical requirements are, by virtue of their simplicity, rather conservative approximations to the actual case. Thus, the thickness of the primary mirror shown in the layouts is reasonably close to that which might be expected for a final design.

It is noted that both the required thickness and the layout thickness of the primary mirror violate assumption (3) of the preceding section. That is, the effects of shear on deflection and slope are not truly negligible. However, the foregoing assumption of a solid plate is probably too conservative (see Reference 3-17 for comparisons between cored or eggcrated designs and solid designs), and that the layout design, or one similar, will meet the required optical performance when a more sophisticated analysis which includes both the true geometry and shear effects is conducted.

Conclusions

The thicknesses of the first folding mirror and the secondary mirror are adequate as shown in the layout. The thickness of the primary mirror (Figures 3-33 and 3-34) is expected to be adequate, however a more sophisticated analysis is required to accurately determine its required thickness.

3.3.3 Mechanical Environment Studies

Two studies of the effects of mechanical environment on SIRTF were made. A 32-node mathematical model was developed and the first six modes and frequencies of the major telescope components were determined. Due to substantial concern about the effects of the shuttle acoustic environment on large structures, an 800-element model was developed of the vacuum housing and its interface with the internal optics support structures. The first 20 natural frequencies of the outer shell were identified and power spectral density curves were generated.

It can be seen from the table that with the exception of the primary mirror, the thicknesses shown in the telescope layouts are more than adequate to attain the required optical performance. In the case of the primary mirror, the required thickness is slightly greater than that shown in the telescope layout. It is judged that the computed maximum deflection and maximum slope will be of little or no consequence because the previously stated optical requirements are, by virtue of their simplicity, rather conservative approximations to the actual case. Thus, the thickness of the primary mirror shown in the layouts is reasonably close to that which might be expected for a final design.

It is noted that both the required thickness and the layout thickness of the primary mirror violate assumption (3) of the preceding section. That is, the effects of shear on deflection and slope are not truly negligible. However, the foregoing assumption of a solid plate is probably too conservative (see Reference 3-17 for comparisons between cored or eggcrated designs and solid designs), and that the layout design, or one similar, will meet the required optical performance when a more sophisticated analysis which includes both the true geometry and shear effects is conducted.

Conclusions

The thicknesses of the first folding mirror and the secondary mirror are adequate as shown in the layout. The thickness of the primary mirror (Figures 3-33 and 3-34) is expected to be adequate, however a more sophisticated analysis is required to accurately determine its required thickness.

3.3.3 Mechanical Environment Studies

Two studies of the effects of mechanical environment on SIRTF were made. A 32-node mathematical model was developed and the first six modes and frequencies of the major telescope components were determined. Due to substantial concern about the effects of the shuttle acoustic environment on large structures, an 800-element model was developed of the vacuum housing and its interface with the internal optics support structures. The first 20 natural frequencies of the outer shell were identified and power spectral density curves were generated.

3.3.3.1 Structural Analysis

This section presents the results and essential features of a study of the structural characteristics of the SIRTF telescope barrel, vacuum housing, and related structural components. The purpose of the study was to determine the beam bending natural frequencies and mode shapes of the telescope, and to determine the structural deformations resulting in going from a 1 "g" environment to a zero "g" environment.

Introduction

A study was performed to determine the dynamic characteristics, modes and frequencies, of the SIRTF telescope barrel, vacuum housing, and related structural components. The deformations resulting from going to a zero "g" environment from a 1 "g" environment were also calculated. The stardyne computer program was used for the analysis. This is a finite element program that uses the direct stiffness method of analysis. Rudimentary techniques were used to determine the structural element sizing, except for the mirror mounts. Detailed analyses were performed to determine mirror mount stiffness. The structural elements and the mirror mount stiffnesses were incorporated into a math model. Subsequently, static and dynamic analyses were performed on the math model using the computer program. A discussion of the sizing of the structural elements, the math model, and the analytical results follows.

Structural Sizing

An acceleration of 20 "g's" applied independently along each axis was the basic load condition used to size the structural elements. In addition, an external pressure of 16 psi was applied simultaneously to the telescope vacuum housing.

The telescope housing was basically determined by the external pressure load, with the bending moment due to the acceleration load contributing approximately 20 percent of the stress. The basic mode of failure was considered to be shell buckling. Three configurations covering a range of shell thicknesses were analyzed; a summary of the configurations is shown in Table 3-14.

3.3.3.1 Structural Analysis

This section presents the results and essential features of a study of the structural characteristics of the SIRTF telescope barrel, vacuum housing, and related structural components. The purpose of the study was to determine the beam bending natural frequencies and mode shapes of the telescope, and to determine the structural deformations resulting in going from a 1 "g" environment to a zero "g" environment.

Introduction

A study was performed to determine the dynamic characteristics, modes and frequencies, of the SIRTF telescope barrel, vacuum housing, and related structural components. The deformations resulting from going to a zero "g" environment from a 1 "g" environment were also calculated. The stardyne computer program was used for the analysis. This is a finite element program that uses the direct stiffness method of analysis. Rudimentary techniques were used to determine the structural element sizing, except for the mirror mounts. Detailed analyses were performed to determine mirror mount stiffness. The structural elements and the mirror mount stiffnesses were incorporated into a math model. Subsequently, static and dynamic analyses were performed on the math model using the computer program. A discussion of the sizing of the structural elements, the math model, and the analytical results follows.

Structural Sizing

An acceleration of 20 "g's" applied independently along each axis was the basic load condition used to size the structural elements. In addition, an external pressure of 16 psi was applied simultaneously to the telescope vacuum housing.

The telescope housing was basically determined by the external pressure load, with the bending moment due to the acceleration load contributing approximately 20 percent of the stress. The basic mode of failure was considered to be shell buckling. Three configurations covering a range of shell thicknesses were analyzed; a summary of the configurations is shown in Table 3-14.

TABLE 3-14. VACUUM HOUSING CONFIGURATIONS

Configuration	Shell Thickness		Ring Spacing		Stress		Allowable Stress		Mass (Weight)	
	cm	in	cm	in	Pa ($\times 10^6$)	psi ($\times 10^3$)	Pa ($\times 10^6$)	psi ($\times 10^3$)	Kg	lbs
A	0.75	0.30	No rings		1.14	1.65	1.35	1.96	425	937
B	0.50	0.20	102	40	2.28	3.31	2.49	3.62	397	875
C	0.38	0.15	51	20	3.65	5.30	3.79	5.50	304	669

Configuration C was used as the baseline design for the mathematical model; being lowest weight and having a small stress margin, it is close to an optimum design. The sizing of the radiation shields and telescope barrel were accomplished in essentially the same manner. The maximum bending moment and subsequent stress due to acceleration load was calculated for several configurations. A standard type of honeycomb structure was used for the radiation shields. The face sheets of the honeycomb are 0.04 cm (0.015 inch) aluminum with a core thickness of 1.3 cm (0.5 inch). A sandwich type of structure was chosen for the telescope barrel. It consists of 0.08 cm (0.03 inch) face sheets and 0.08 cm (0.03 inch) corrugated shear web; a sketch is shown in Figure 3-41.

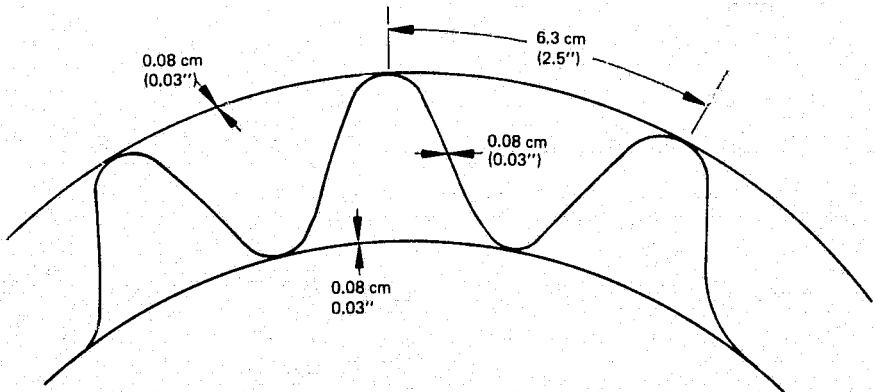


Figure 3-41. Telescope barrel construction.
(Configuration C)

The second folding mirror support structure was designed as a cone of constant wall thickness subjected to lateral acceleration loads. The lateral acceleration loads induce bending moment and stress into the structure. The basic mode of failure is buckling of the cone. The analysis resulted in an aluminum cone of 0.23 cm (0.09 inch) thick.

The sizing of the fiberglass thermal isolator is found in Reference 3-19.

Mathematical Model

A finite element mathematical model of the telescope was developed. Thirty-two mass points (nodes) were included in the model connected by massless elastic beam elements. A sketch of the model is shown in Figure 3-42. All masses and elastic elements were on the telescope center line, the branches are displayed for clarity. The model is fixed at mass point (node) 10, the gimbal attachpoint. The vacuum housing is represented by elements connecting nodes 1 through 10. The main fiberglass thermal isolator is represented by elements connecting nodes 10 through 13. The telescope barrel connects nodes 13, 15 through 20, and the secondary folding mirror support structure is represented by elements connecting nodes 22 through 27. The elastic elements connecting the above nodes have the stiffness characteristics of the structure described in the previous section.

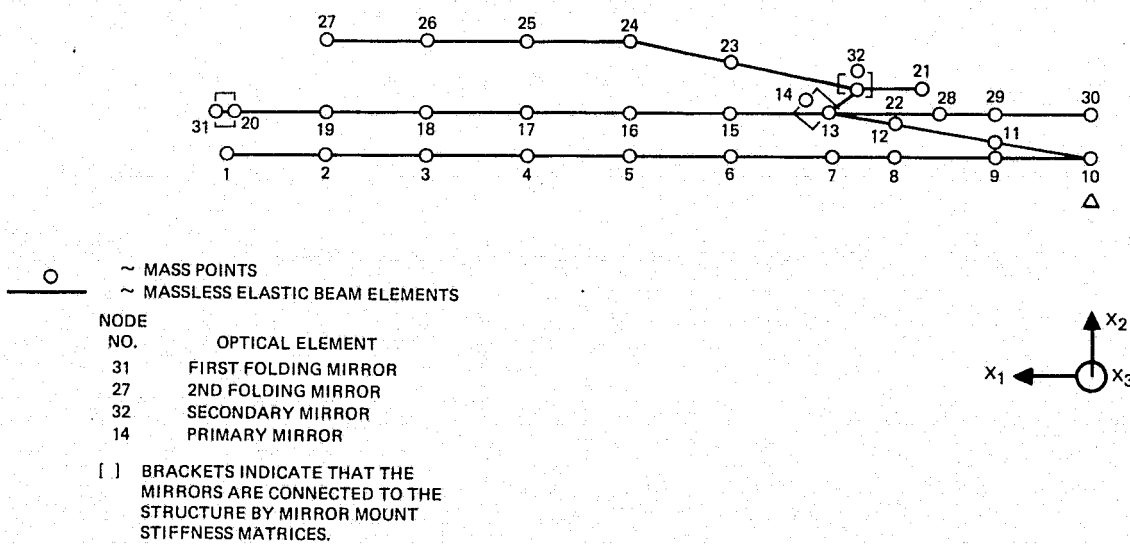


Figure 3-42. Mathematical model idealization.

Node 14 represents the primary mirror. Node 32 is the secondary mirror. The first and second folding mirrors are represented by nodes 31 and 27. The primary, secondary, and first folding mirror are connected to the telescope structure by stiffness matrices representing the mirror mounting structure. A stiffness matrix for the second folding mirror is not defined at present, and the second folding mirror is rigidly attached to its support structure.

Node 21 represents the beamsplitter and node 30 represents the MIC.

Listings of the model data are presented in Reference 3-19. It is noted that the model represents the telescope in its operational configuration.

Analytical Results

A "1 g" uniform acceleration was applied to the math model and the deflections and rotations of the structure were calculated. The deflections due to the application of a "1 g" acceleration are equivalent to the deflections of going from a "1 g" environment to a "0 g" environment. A summary of the deflections and rotations of the optical elements are given in Table 3-15 below.

The natural frequencies of the telescope were calculated using the mathematical model. The first six bending modes are presented in Table 3-16. The modes are strongly influenced by the mirrors and their mounts.

TABLE 3-15. DEFLECTIONS AND ROTATIONS OF OPTICAL ELEMENTS

Description	Node No.	Translation		Rotation radians
		cm	in	
Primary mirror	14	0.0204	0.00803	0.000176
Secondary mirror	32	0.0093	0.00365	0.000277
1st folding mirror	31	0.0209	0.00822	0.000277
2nd folding mirror	27	0.0184	0.00725	0.000079
MIC	30	0.0312	0.01228	-0.000005

TABLE 3-16. FIRST SIX NATURAL FREQUENCIES

Node No.	Frequency, Hz	Description
1	30.9	Combined in-phase motion of the primary mirror and the 2nd folding mirror on its support structure.
2	39.7	Vacuum Housing Bending Mode
3	40.9	2nd Folding Mirror on its support structure.
4	49.7	Combined out-of-phase motion of the primary mirror and the 2nd folding mirror on its support structure.
5	50.7	Combined out-of-phase motion of the 1st folding mirror and 2nd folding mirror on their support structures.
6	52.3	Secondary mirror on its support mounts.

Sketches of the mode shapes are shown in Figures 3-43 through 3-47.

Conclusions

The calculation of beam bending vibration modes are first order approximations of the dynamic characteristics of the SIRTF telescope. The modes and frequencies are most strongly influenced by the mirror mount stiffnesses, consequently further study of the selected approach and possibly other approaches is warranted.

3.3.3.2 Effects of Acoustic Environment

A structural dynamic analysis of SIRTF has been performed to determine its ability to survive a shuttle orbiter payload bay internal acoustic environment of 145 db (OAL). The basis for the analysis is a finite element

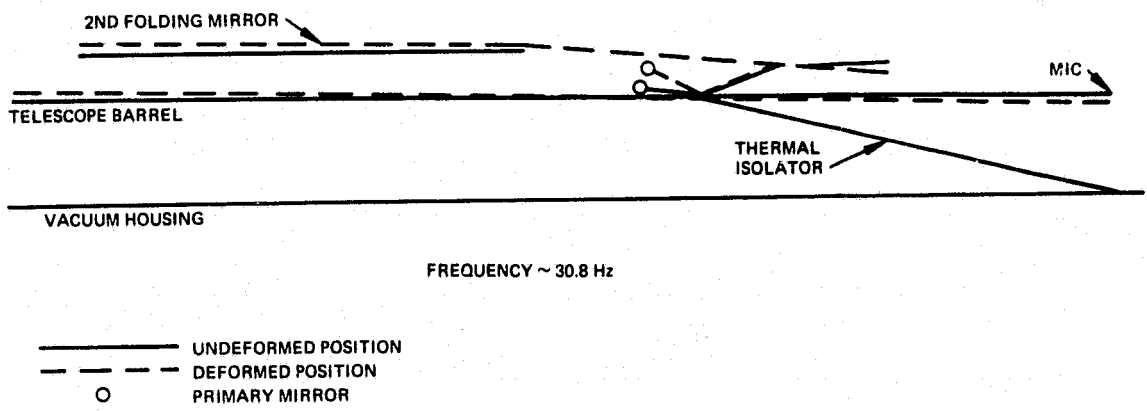


Figure 3-43. Mode No. 1 – Primary mirror mode.

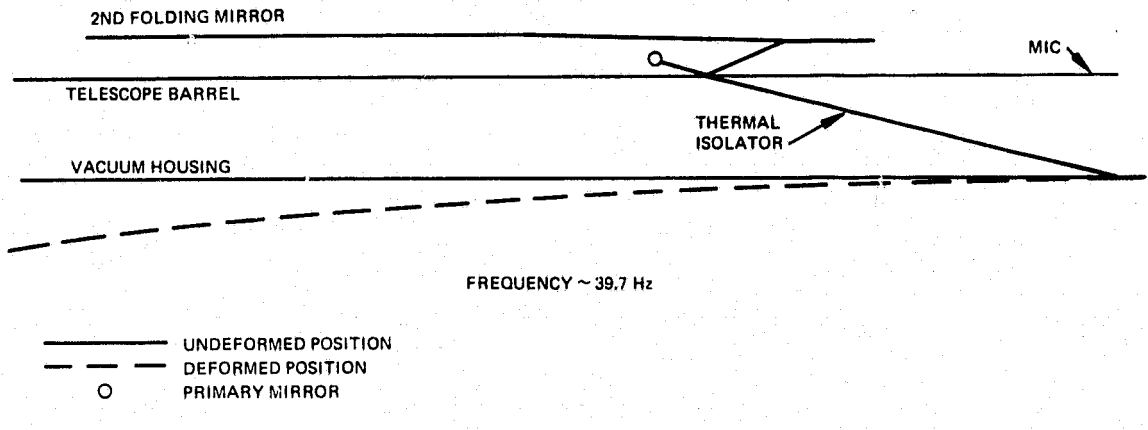


Figure 3-44. Mode No. 2 – Vacuum housing mode.

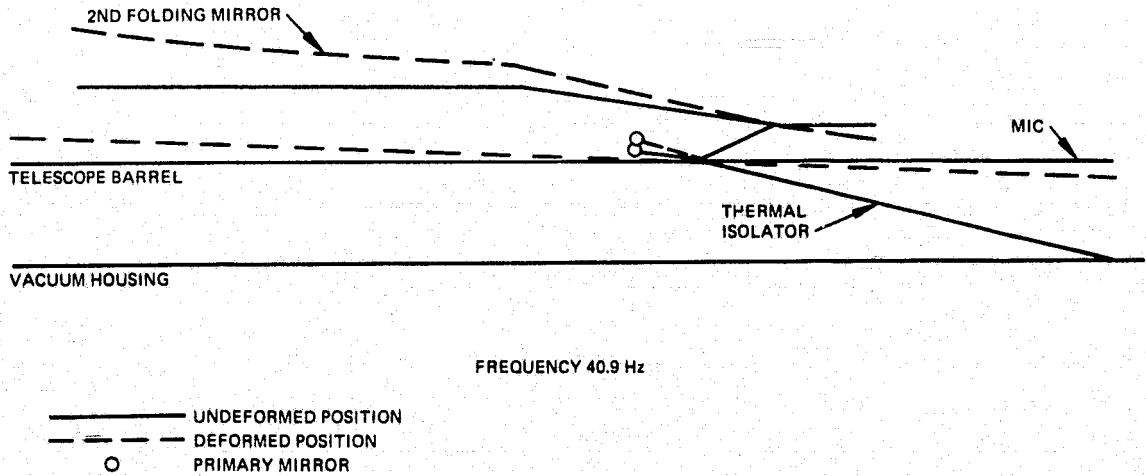


Figure 3-45. Mode No. 3 – Second folding mirror mode.

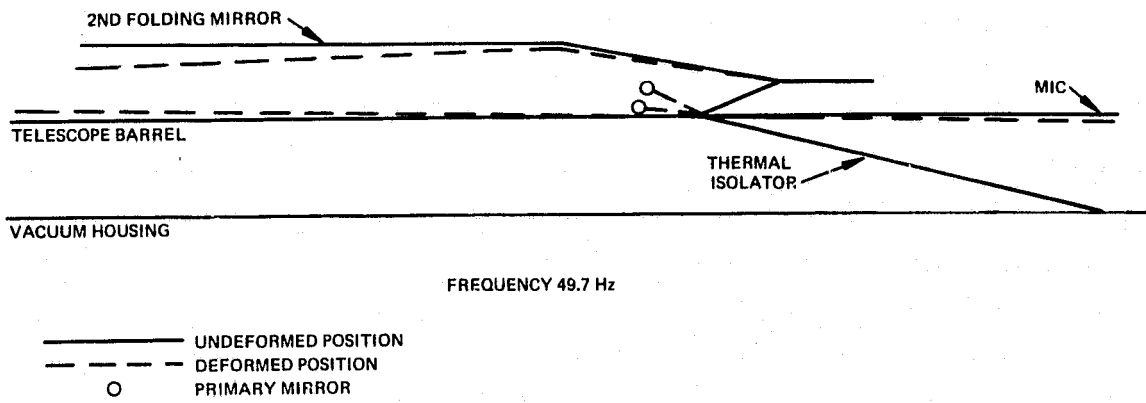


Figure 3-46. Mode No. 4 – Combined mode primary mirror and second folding mirror out of phase.

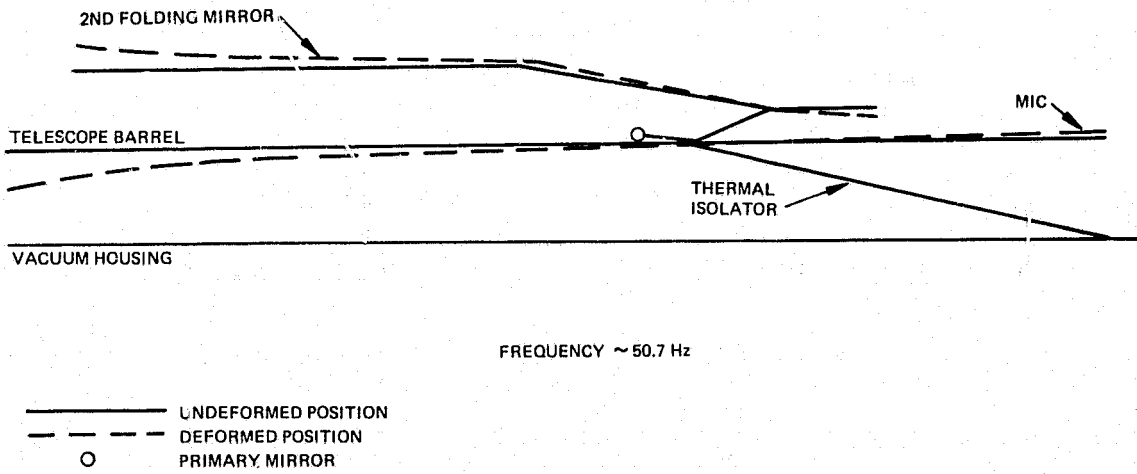


Figure 3-47. Mode No. 5 – Combined mode first folding mirror and second folding mirror out of phase.

mathematical model that represents the vacuum housing and its interface with the internal optics support structure. By analytically subjecting the model to the acoustic environment, the internal stresses throughout the rib-reinforced vacuum housing as well as the accelerations transmitted to the optics have been determined. Structural adequacy of the housing is demonstrated because the maximum stress level is calculated to be 7.03×10^6 Pa (1.02×10^3 psi) (rms) which is substantially below the fatigue endurance level for the material (aluminum). Furthermore, the maximum acceleration transmitted through

the vacuum housing to the optics support structure is calculated at 0.723G (rms), which is not considered to be a problem.

Analytical Procedure

A finite element model has been developed to represent both the rib-reinforced aluminum vacuum housing and the structural coupling of this housing to the optics support structure. The configuration is presented in Figure 3-33 and shows that the internal optics are connected to the vacuum housing through an axisymmetric thermal isolator. The vacuum housing is reinforced by 14 circumferential and 20 longitudinal ribs and is assumed to be fixed to a shear wall at its base. The detailed finite element model of the housing is comprised of an assemblage of 260 quadrilateral plate and 540 rectangular beam elements (see Figure 3-48). Stiffness matrices are utilized to define the housing/thermal isolator interface. Elements in these matrices are based on the solution of an edge-loaded cylinder and are required to obtain realistic values for the acceleration transmitted through the vacuum housing.

Several well founded structural analysis digital computer programs are available to perform random vibration analysis, the one utilized in this study is STARDYNE (see References 3-19 and 3-20). Having developed a model that is representative of the mass and flexibility distribution in the structure, the analytical procedure is to first compute the eigensolution. This gives a finite number of natural frequencies and mode shapes that describe the dynamic characteristics of the structure and that can be used to calculate structural response, i.e., displacements, accelerations, internal stress distribution, etc. The modal information is used in this effort to determine the structural response to a stationary-zero mean random vibration environment. This environment is defined in terms of payload bay dB levels at a set of octave band center frequencies that is tractable via the STARDYNE computer program. The particular acoustic spectrum utilized for this study is shown in Figure 3-49 and is based on a representative payload volume and payload-volume-to-surface-area ratio, and conservatively assumes a reverberant sound field (see Reference 3-21, Figure 28). Although several spectrum

X2 VIEW ROTATED AXES

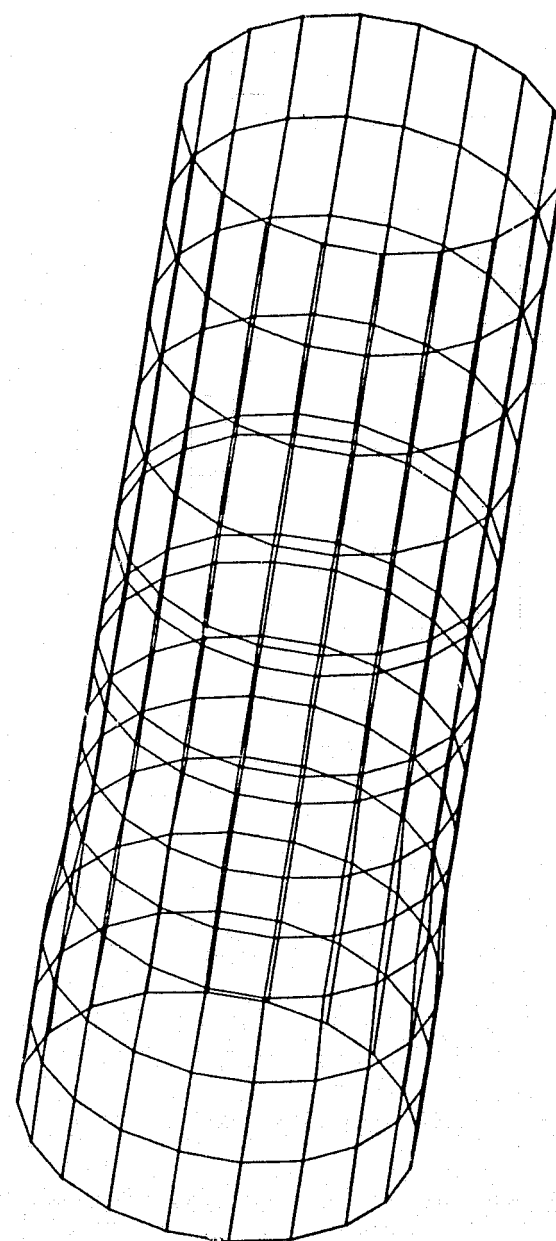


Figure 3-48. Finite element model.

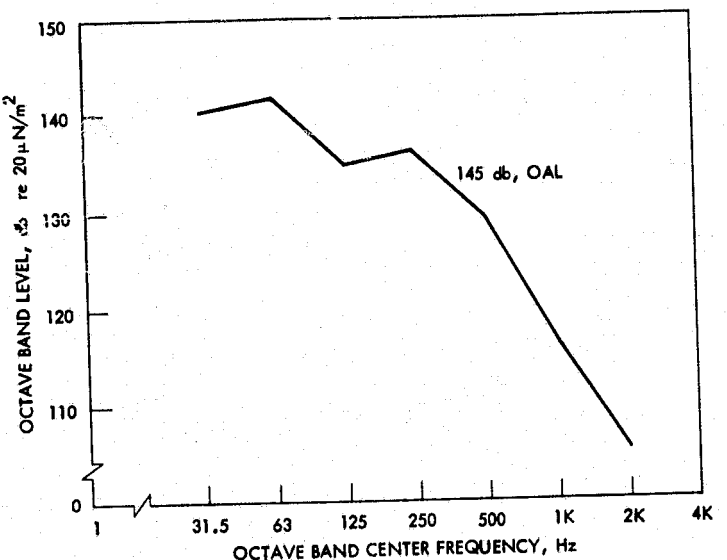


Figure 3-49. Internal spatial averaged sound pressure level.

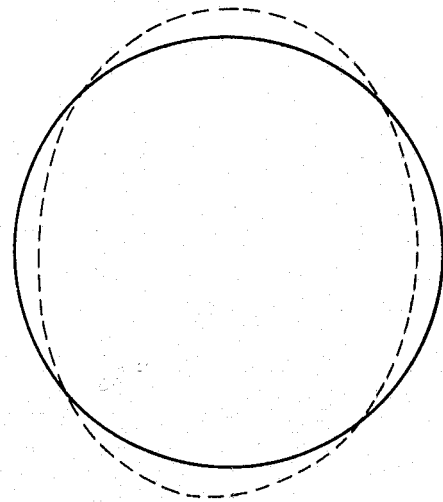
shapes could have been considered, this particular one has the desired 145 db (OAL) and has a high energy content in the low to intermediate frequency range, i.e., 31.5 to 250 Hz. Since excitation of the flexural shell modes contained in this frequency range gives the most significant contribution to internal stress levels, it is felt that the approach conservatively determines structural adequacy.

Analytical Results

The eigensolution gives 89 shell modes of vibration in the frequency range from 26.8 to 1320 Hz, see Table 3-17 for a list of the first 20 natural frequencies. The frequencies differ from those of preceding analysis because the structural analysis used a simplified model while the acoustic study utilized a very complex model of the outer housing. Calculated mode shapes, for particular cross sections along the vacuum housing are presented as a point of interest for the first three shell modes in Figures 3-50 to 3-52. Classical shell modes for a thin walled cylinder are very similar, thus giving confidence in the analytical results obtained. It is noted that a torsional mode occurs at approximately 73 Hz, but is not required in the response calculations. In order to determine the response to the acoustic spectrum shown in Figure 3-49, the first 20 shell modes have been used. As previously noted, the rationale for

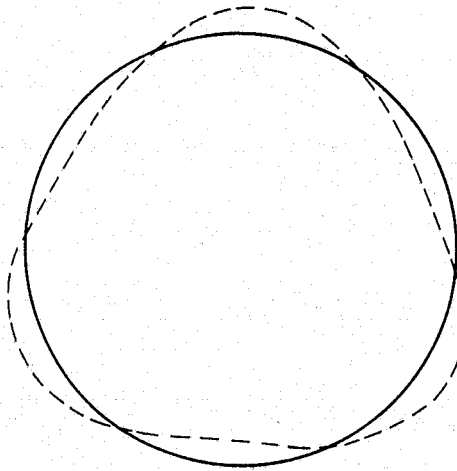
TABLE 3-17. SHELL NATURAL FREQUENCIES

<u>Number</u>	<u>Natural Frequency, Hz</u>
1	26.8
2	54.5
3	58.1
4	66.3
5	69.1
6	73.0
7	85.8
8	87.9
9	106.1
10	109.3
11	125.2
12	128.7
13	136.7
14	142.4
15	144.5
16	147.9
17	163.2
18	164.0
19	190.6
20	204.3



----- MODAL CONFIGURATION

Figure 3-50. First shell mode shape - axial view.



----- MODAL CONFIGURATION

Figure 3-51. Second shell mode shape - axial view.

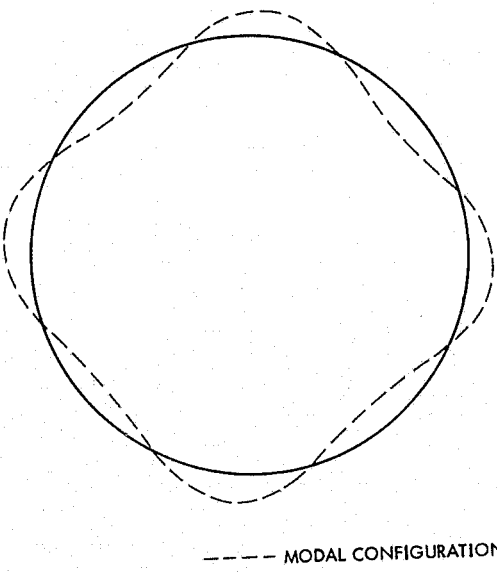


Figure 3-52. Third shell mode shape - axial view.

this approach is that excitation of the lower modes is the primary contribution to internal stresses and also the acoustic levels are higher in this frequency range. Another consideration is that in doing a finite element analysis the higher modes are not accurately determined. A structural modal damping factor of 5 percent is assumed for all modes of vibration.

The results of the acoustic response analysis show that the maximum calculated stress is 7.03×10^6 Pa (1.02×10^3 psi) (rms) which occurs in one of the circumferential ribs. It is of interest that the maximum stress calculated in the shell itself, i.e., in one of the quadrilateral plates of the analytical model, is only 6.9×10^5 Pa (0.1×10^3 psi) (rms). Assuming the vacuum housing to be made of aluminum - say 6061 - the endurance limit would be something between 6 and 10×10^7 Pa (9 and 14×10^3 psi). The computed stress levels, therefore, are not problematic from a fatigue viewpoint, thus the structural adequacy of the vacuum housing has been demonstrated for the 145 db (OAL) acoustic environment.

In addition to considering the vacuum housing structure, the analytical results predict the acceleration levels transmitted through the housing to the thermal isolator and thus the optics. Power spectral density plots in G^2/Hz

versus frequency (Hz) are presented in Figures 3-53 through 3-60 for the quarter points (90° increments) at the interface of the vacuum housing and thermal isolator. These plots represent the acceleration spectrum transmitted to the optics support structure. Integration under these curves gives a maximum of 0.723G (rms) radial acceleration and 0.083G (rms) tangential acceleration. A plot of the transmitted radial acceleration (rms) around the circumference of the interface is shown in Figure 3-61. While a more detailed analysis to determine the response of the optics and its supporting structure should be performed during the hardware development stage, no design problems are envisioned due to the low level of the transmitted acceleration. The optics and associated structure have in fact been sized on the basis of mechanical base acceleration inputs, which are significantly higher than those resulting from the acoustic environment (see Section 3.3.3.1).

3.3.4 SIRTF Telescope Mass Properties

A summary of the mass properties of the SIRTF telescope system is presented in Table 3-18. The Table provides a mass breakdown, axial cg coordinate calculation, and an estimate of the telescope's mass moment of inertia about a radial axis at the telescope/IPS interface.

Only the axial cg coordinate was calculated because of the symmetry of the system. Thus, the radial cg coordinates with respect to the telescope's optical axis have been assumed to be zero. In actuality, they will not be truly zero although it is believed that the radial coordinate will not exceed 0.5 cm (0.2 inch). The assumed reference plane is the IPS mounting surface.

The telescope inertia was also determined by calculation although this calculation was not as thorough and comprehensive as that performed for total mass and cg. This approach was taken because the inertia is completely dominated by both the large structure and the mr^2 term used to transform from the inertia about the cg to that about the telescope/IPS interface.

The estimated accuracy of mass and cg calculations is in the range of ± 5 percent to ± 10 percent. The inertia is estimated to have an accuracy within ± 30 percent.

SIRTF - RIB REINFORCED CYL.(200 IN.) SHUTTLE ACOUSTIC ENVIR. ~ 145DB

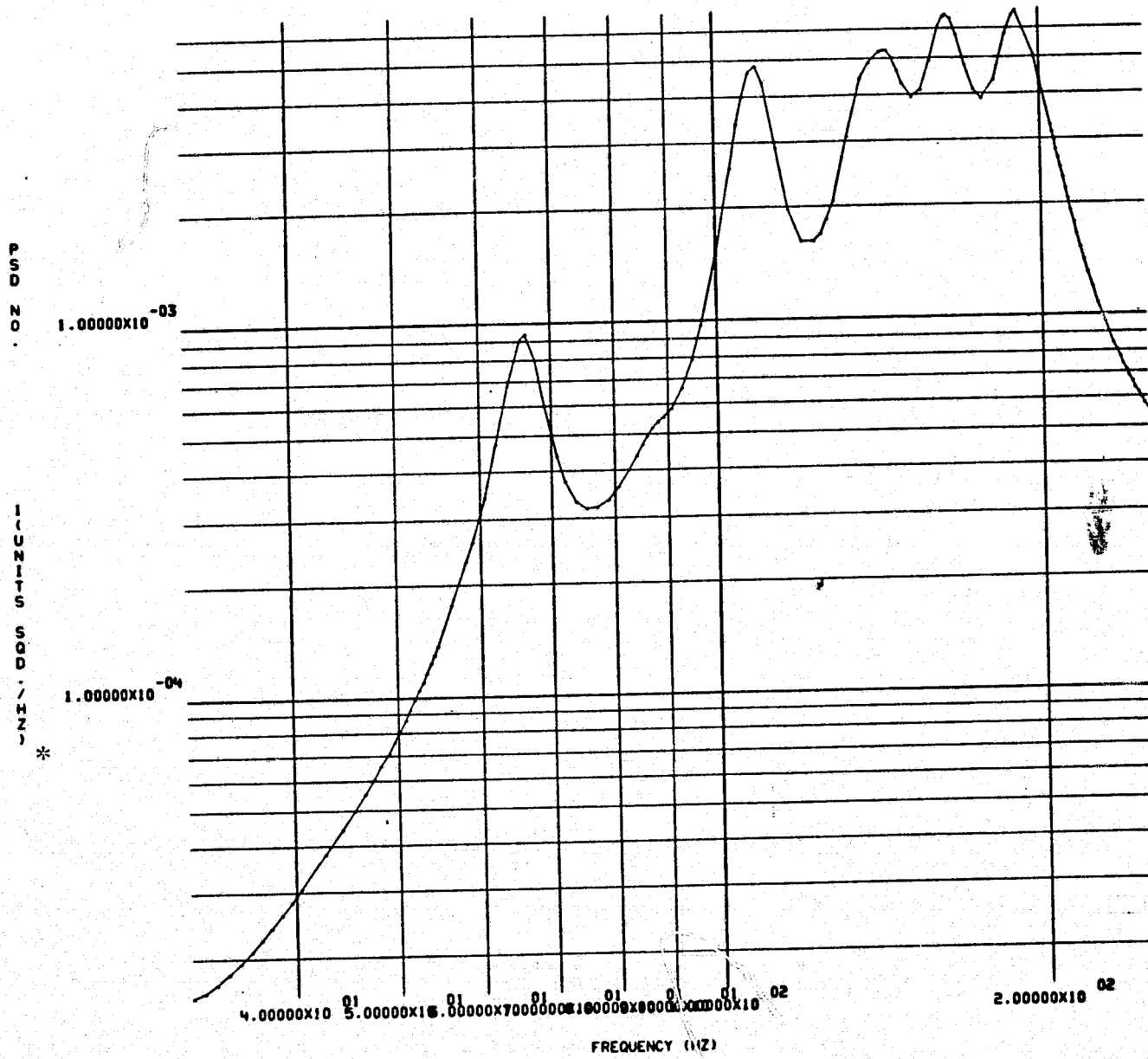


Figure 3-53. Radial acceleration spectrum -- Vacuum housing thermal isolator interface, $\theta = 0^\circ$

*PSD Units (G^2/Hz)

SIRTF - RIB REINFORCED CYL.(200 IN.) SHUTTLE ACOUSTIC ENVIR. - 14508

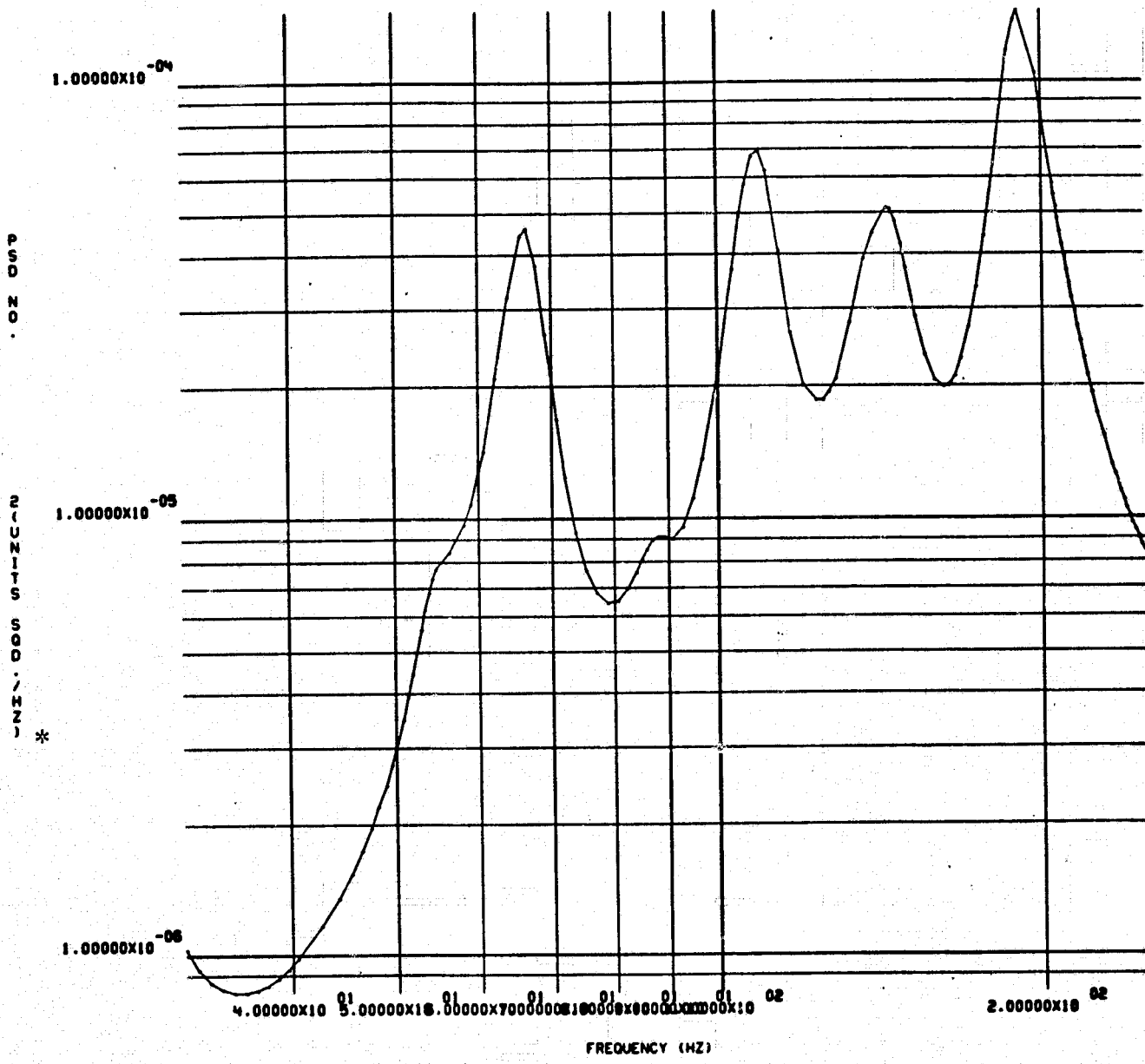


Figure 3-54. Axial acceleration spectrum — Vacuum housing thermal isolator interface, $\theta = 0^\circ$

*PSD Units (G^2/Hz)

SIRTF - RIB REINFORCED CYL.(200 IN.) SHUTTLE ACOUSTIC ENVIR. - 145dB

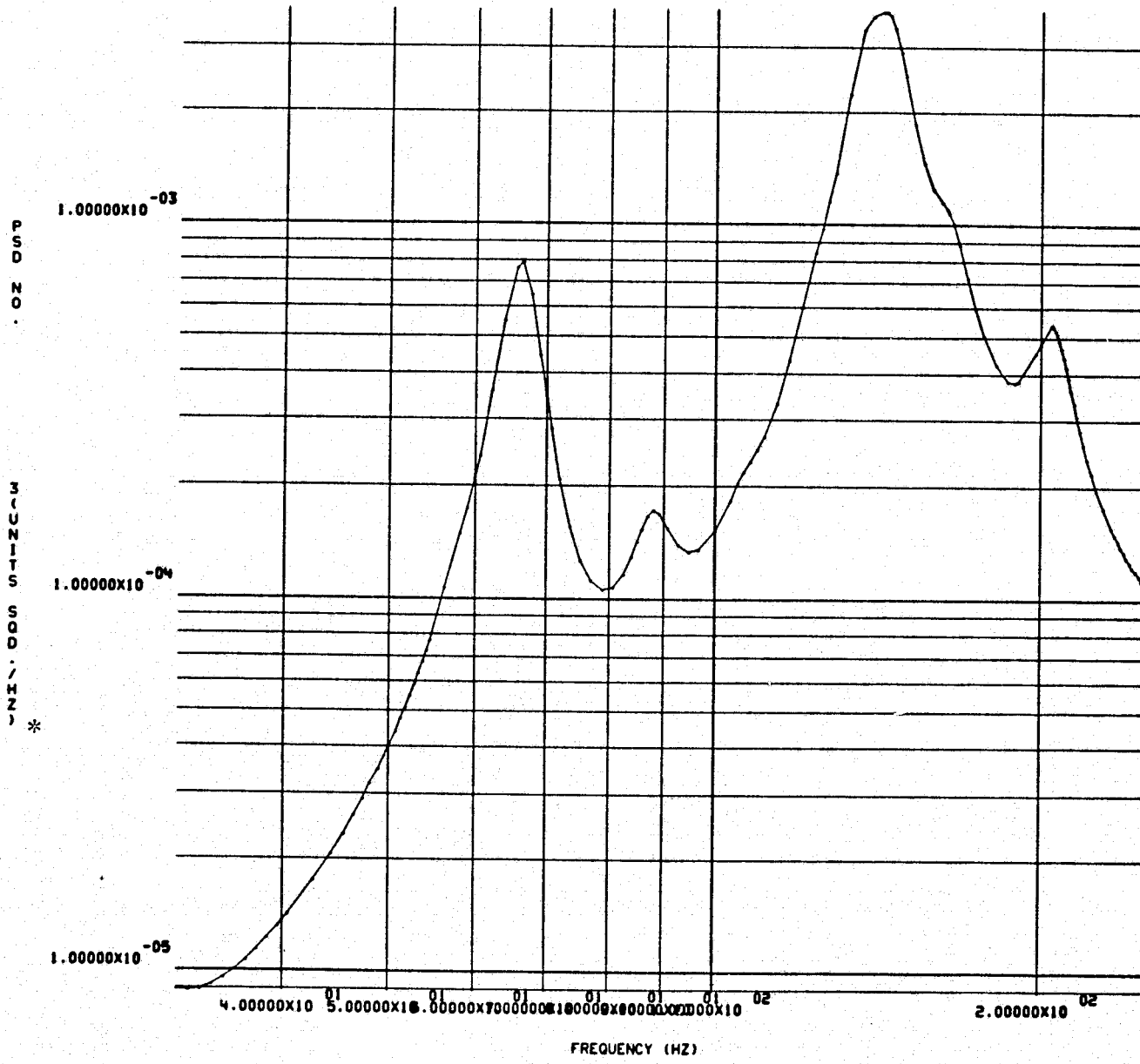


Figure 3-55. Radial acceleration spectrum — Vacuum housing thermal isolator interface, $\theta = 90^\circ$

*PSD Units (G^2/Hz)

SIRTF - RIB REINFORCED CYL.(200 IN.) SHUTTLE ACOUSTIC ENVIR. - 145DB

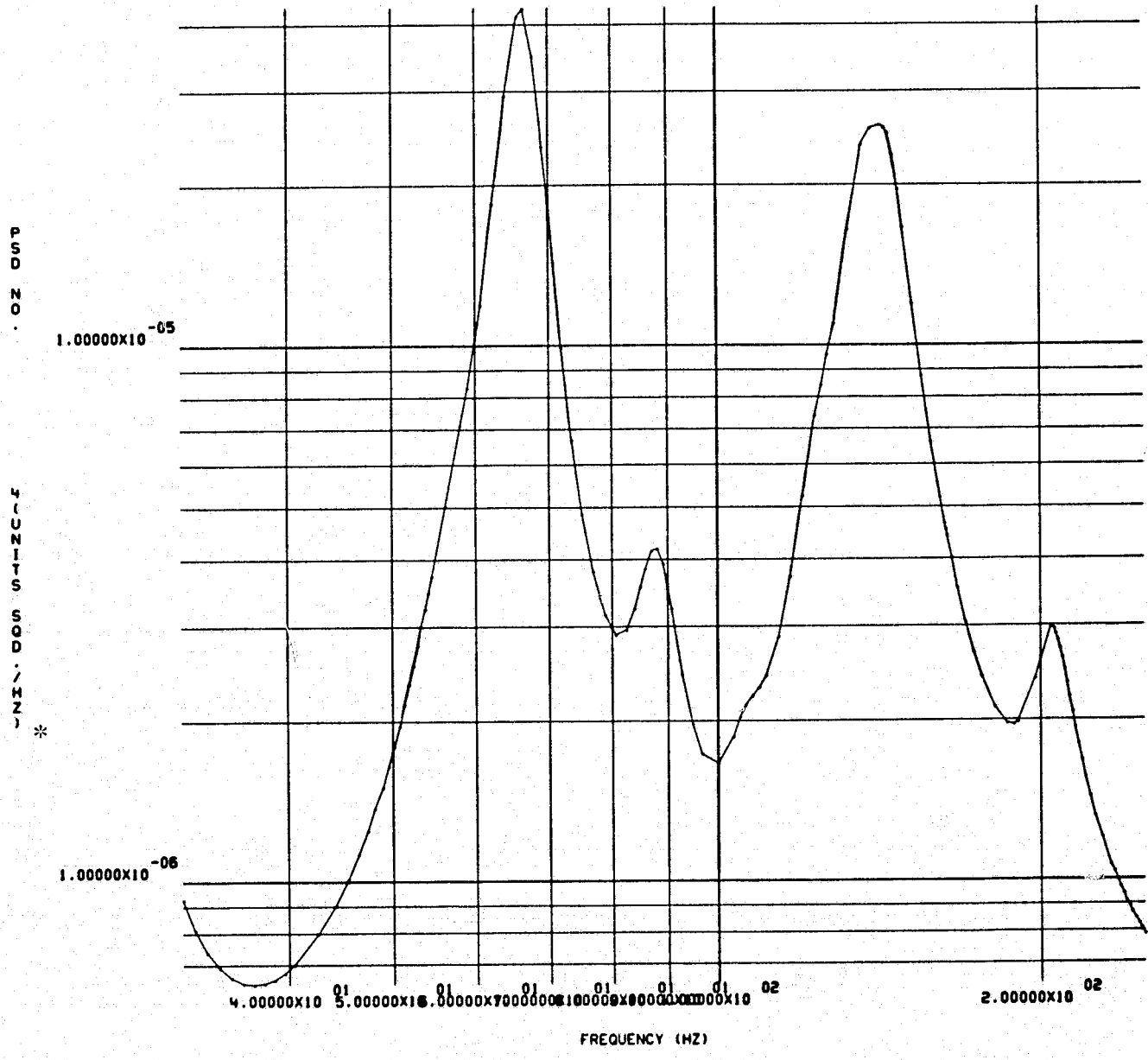


Figure 3-56. Axial acceleration spectrum - Vacuum housing thermal isolator interface, $\theta = 90^\circ$

*PSD Units (G^2/Hz)

SIRTF - RIB REINFORCED CYL.(200 IN.) SHUTTLE ACOUSTIC ENVIR. - 145DB

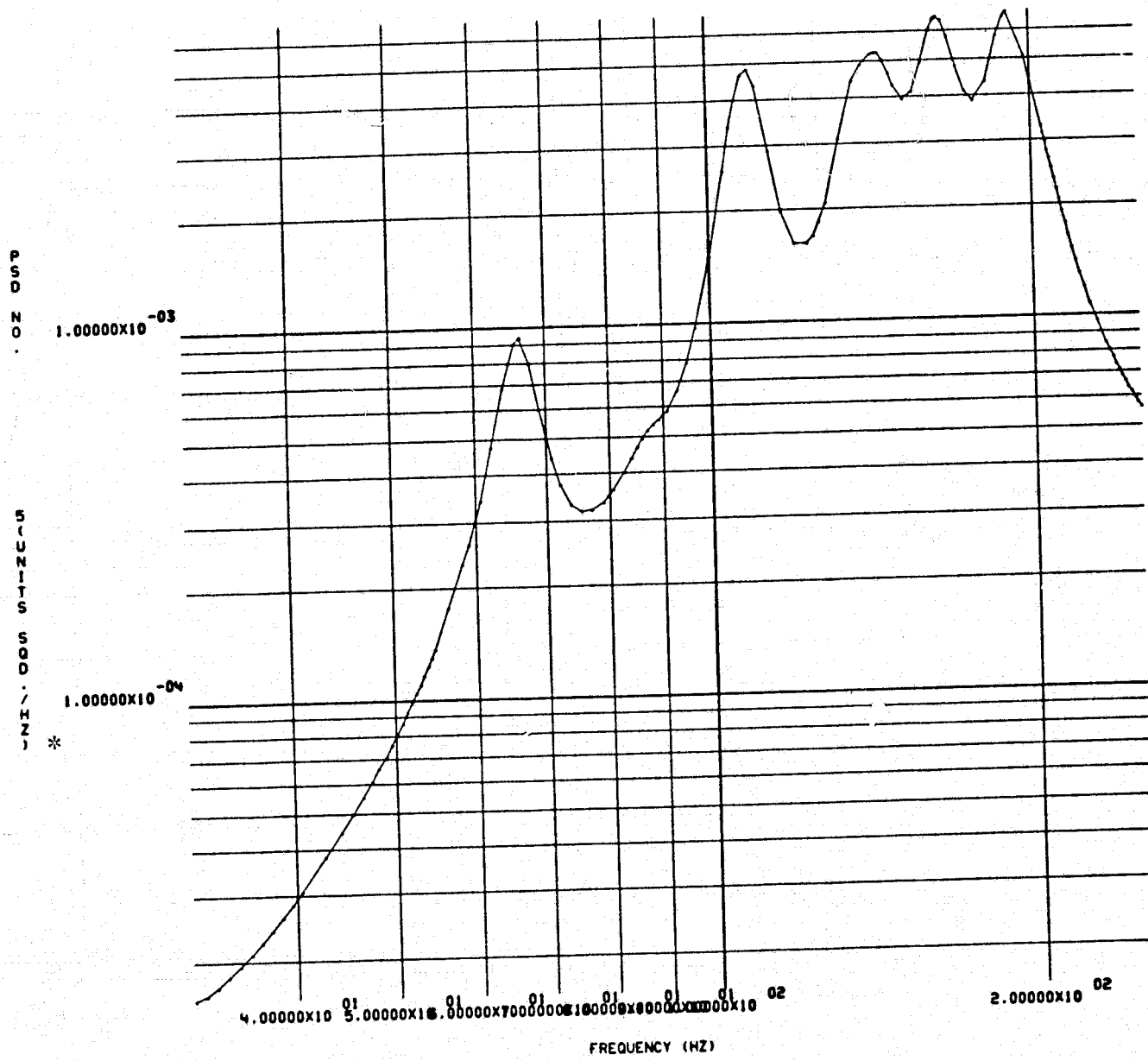


Figure 3-57. Radial acceleration spectrum — Vacuum housing thermal isolator interface, $\theta = 180^\circ$

*PSD Units (G^2/Hz)

SIRTF - RIB REINFORCED CYL.(200 IN.) SHUTTLE ACOUSTIC ENVIR. - 145DB

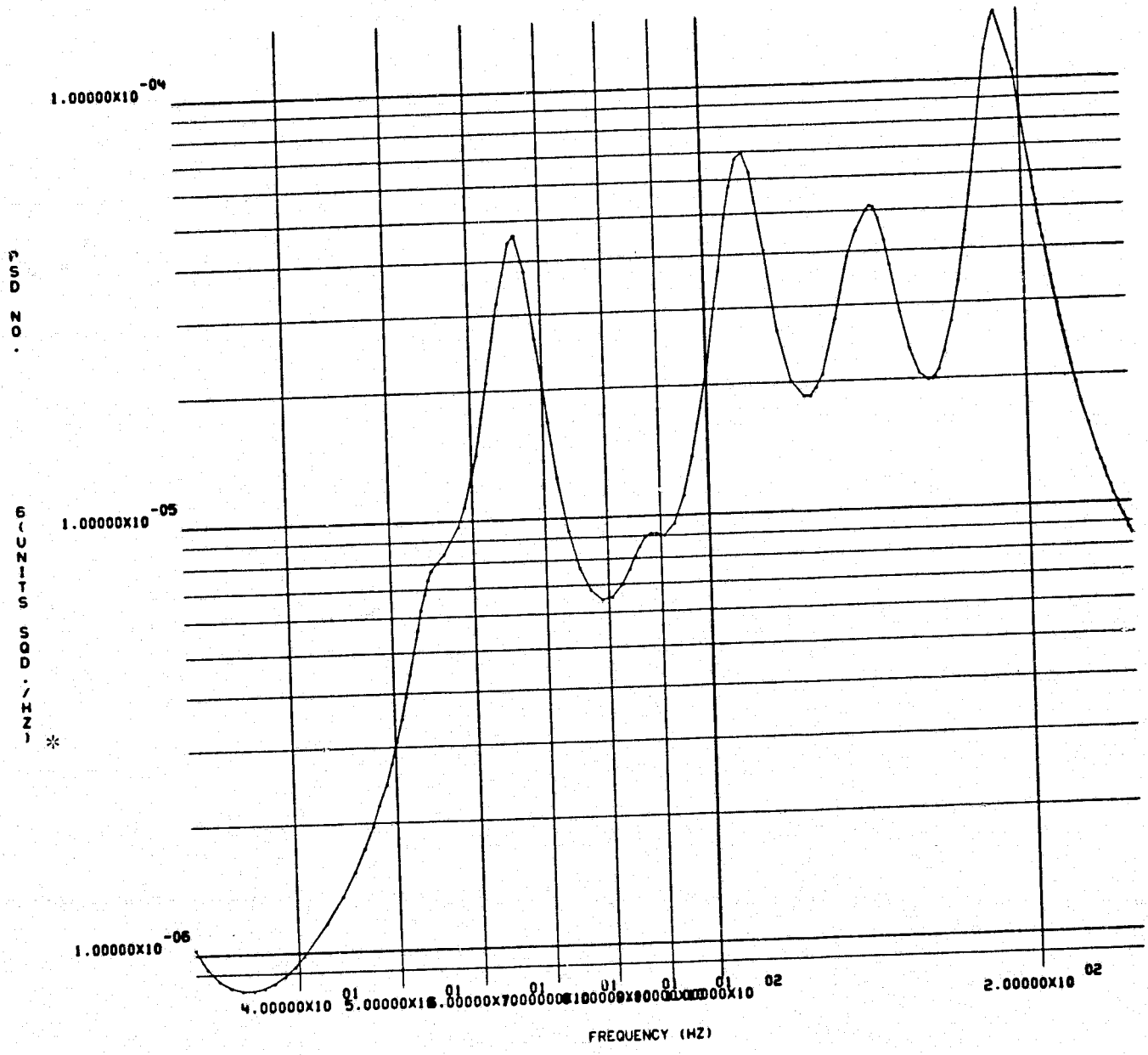


Figure 3-58. Axial acceleration spectrum - Vacuum housing thermal isolator interface, $\theta = 180^\circ$

*PSD Units (G^2/Hz)

SIRTF - RIB REINFORCED CYL.(200 IN.) SHUTTLE ACOUSTIC ENVIR. - 14508

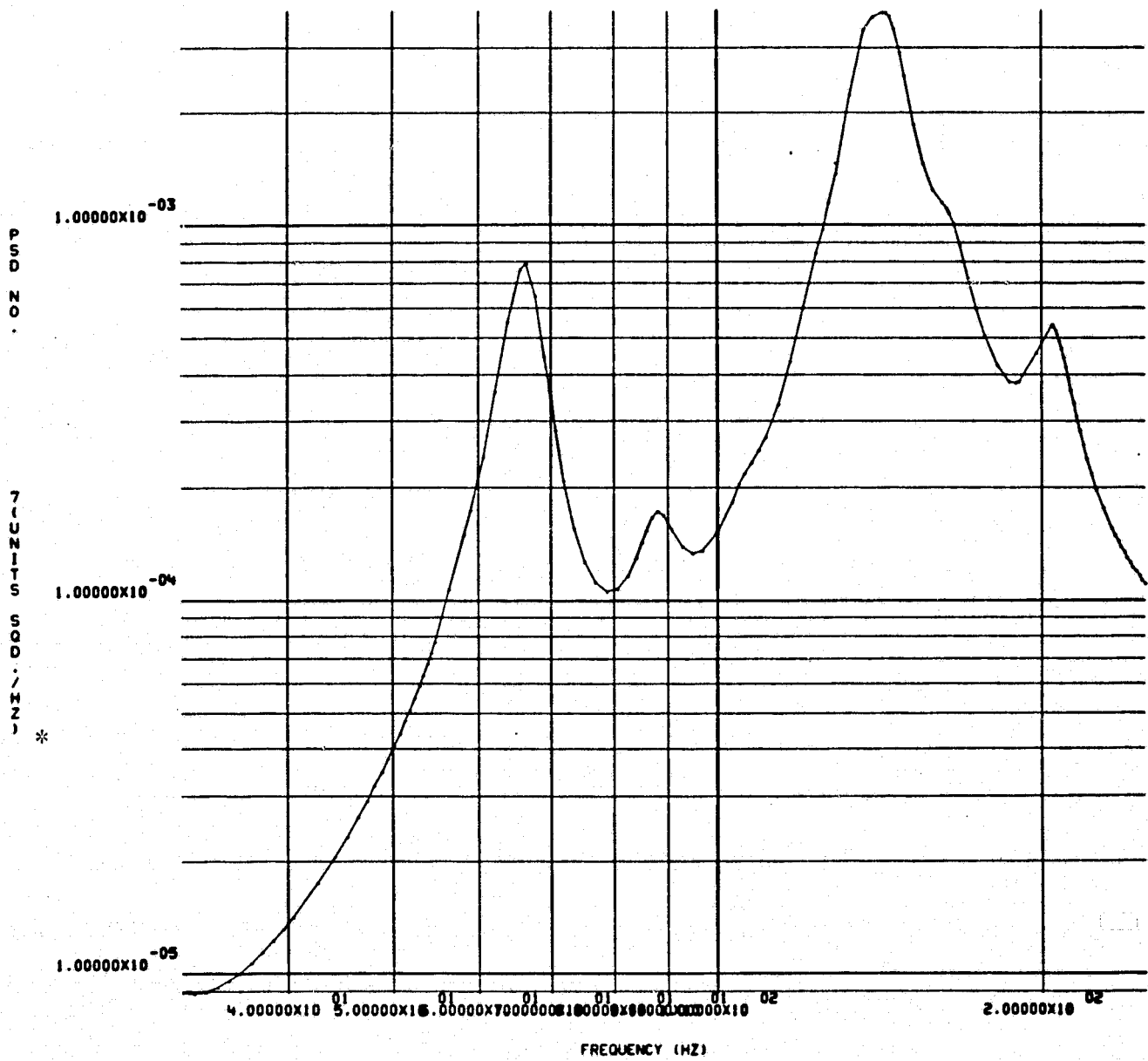


Figure 3-59. Radial acceleration spectrum — Vacuum housing thermal isolator interface, $\theta = 270^\circ$

* PSD Units (G^2/Hz)

SIRTF - RIB REINFORCED CYL.(200 IN.) SHUTTLE ACOUSTIC ENVIR. - 145DB

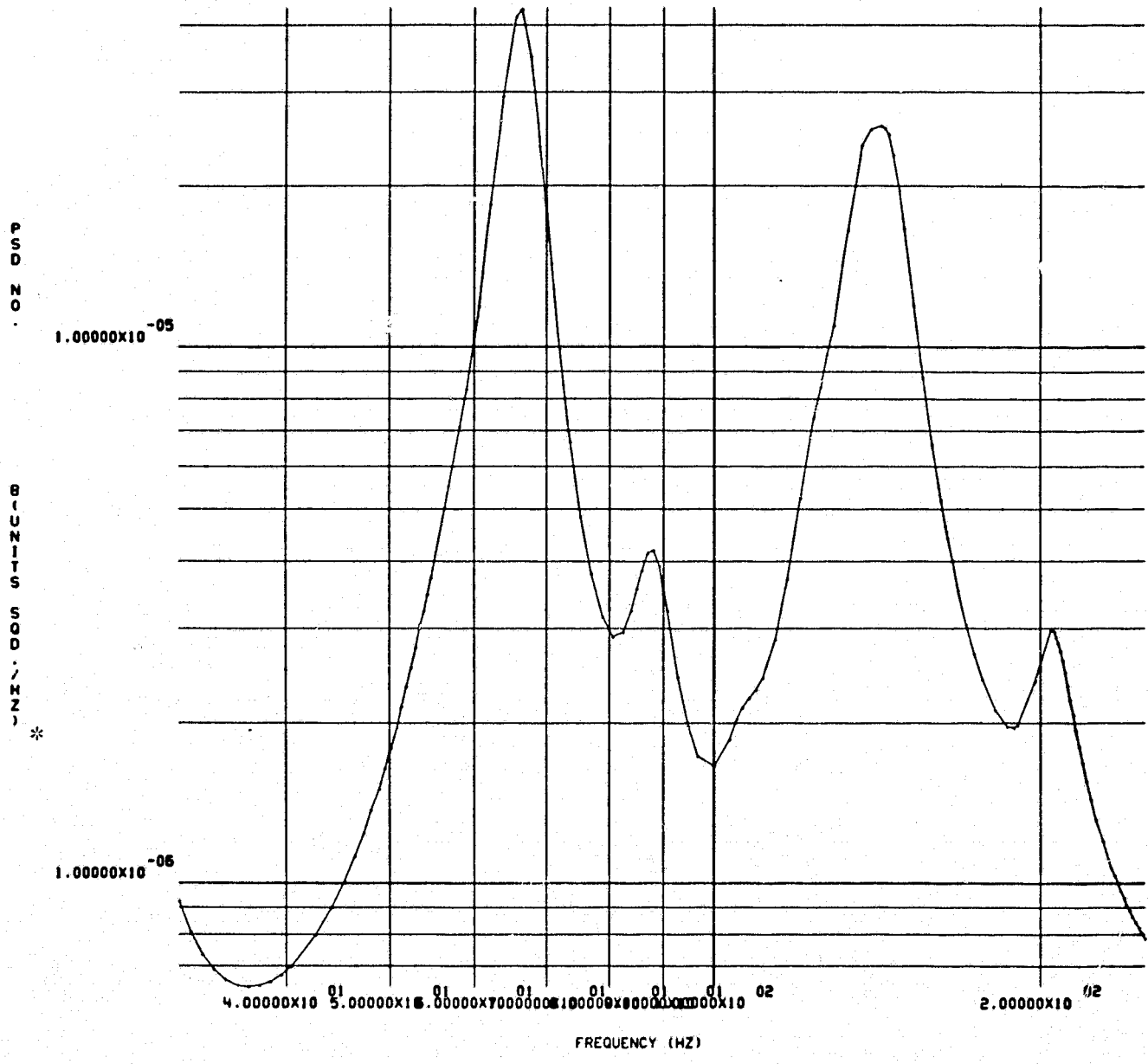


Figure 3-60. Axial acceleration spectrum — Vacuum housing thermal isolator interface, $\theta = 270^\circ$

*PSD Units (G^2/Hz)

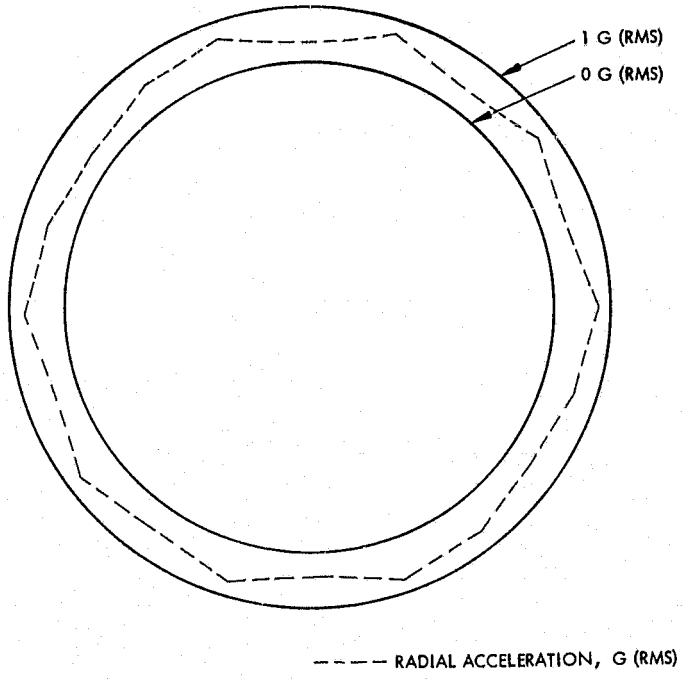


Figure 3-61. RMS radial acceleration level at interface.

TABLE 3-18. SIRTF TELESCOPE MASS PROPERTIES

	Mass, Mi		Axial cg* Coordinate, m	MiXi* Kg-m
	Kg	lbs		
Primary Optics				
Main Optical Support	37	81	1.99	73.6
Primary Mirror Ring	20	45	2.17	43.4
Primary Mirror Supports	14	30	2.21	30.9
Primary Mirror	90	197	2.36	212.4
Main Telescope Cylinder	69	152	3.33	229.8
1st Folding Mirror Support	43	94	4.88	209.8
Autofocus Drive and Support	8	18	4.96	39.7
1st Folding Mirror	8	18	4.96	39.7
Baffles	21	47	3.33	69.9
MIC Support	40	89	1.38	55.2
Secondary Optics				
Secondary Support	6	14	1.99	11.9
Secondary Mirror Ring	4	9	1.99	8.0
Secondary Mirror Mounts	5	12	1.99	10.0
Secondary Mirror	9	20	1.99	17.9
Steering/Chopping Mirror Support	15	33	2.60	39.0
Steering/Chopping Mirror Assy	20	45	3.45	69.0
MIC Selector	32	70	1.75	56.0
Thermal Isolator	219	482	1.38	302.2
Radiation Shields	148	326	2.60	384.8
MIC (including Star Tracker)	91	200	1.38	125.6
Outer Vacuum Housing	345	760	2.44	841.8
Plumbing/Heat Exchanges	21	47	2.30	48.3
Miscellaneous Parts	45	100	2.30	103.5
Sunshade	82	180		
(Stowed)			(4.60)	(377.2)
(Deployed)			(5.69)	(466.6)
	1392	3069	(2.44)	(3399.0)
			(2.51)	(3489.0)

Notes:

Telescope cg (sunshade stowed) = 2.44 m

Telescope cg (sunshade deployed) = 2.51 m

Cover assembly and support - 590 Kg (1300 lb_m)

Mass moment of inertia around telescope cg

(sun/earth shield deployed) - 8830 Kg - m² (6500 ft - lb_f - sec²)

At IPS mount

(sun/earth shield deployed) - 16900 Kg - m² (12400 ft - lb_f - sec²)

*CG and MiXi are referenced to the IPS mounting surface.

3.4 THERMAL ANALYSIS

To meet the SIRTF performance levels, the optics, inner barrel, and baffles of the SIRTF telescope must be cooled to between 18°K and 21°K. The temperatures are achieved by flowing supercritical helium through heat exchangers located in various positions throughout the telescope. The heat exchangers cool the components either by direct contact, or by means of conduction straps running between the heat exchanger and the component.

The general design approach of the telescope is similar to that used in storage dewars for low temperature cryogens. Helium from the storage dewar flows first to the inner telescope, where the low temperature must be maintained. The inner telescope is surrounded by radiation shields which are cooled in sequence by the gradually warming helium after it completes cooling the inner telescope. Super insulation between the radiation shields further reduces heat transfer from shield to shield.

The major sources of heat inside the telescope are the power dissipation in the Multiple Instrument Chamber (MIC) instruments and in the second folding mirror which is servo-driven for stabilization and space chopping. Heat also enters the telescope through the radiation shields, thermal isolators, and the aperture. The calculation of aperture loads for various conditions represented a major portion of the effort in the thermal area.

The conclusion reached based on the work done on this study is that the telescope can be maintained at the required temperature with a relatively small supply of supercritical helium; this allows the tanks to be mounted directly on the telescope, thus eliminating the potential problems associated with transfer of cryogen across the gimbals.

In addition to the material presented here, the SIRTF thermal analysis report (Reference 3-22) contains a listing of the program, and a description of the Shuttle thermal modeling which defined some external inputs to the telescope aperture shield as well as the impact on the aperture heat input of variation in aperture shield IR emissivity.

3.4.1 Thermal Model

SIRTF telescope cooling to 21°K is required to meet the specified sensitivity in the 5 to 30μ band and 18°K or lower for the 30μ to 200μ band. These and other considerations have led to the selection of supercritical helium as the cryogen for SIRTF (reference 3.2-2). The thermal requirements must be met for missions of from 7 to 30 days duration.

Design Approaches

The thermal design utilizes heat exchangers, superinsulation, various surface finishes, and the thermal isolators. The primary modes of heat transfer are conduction and radiation. The MIC and telescope are supported from the outer vacuum housing by three fiberglass isolators each having the form of a frustum of a cone. The radiation shields are attached at the intersections of the isolators. Heat exchangers are also attached at these points in order to cool the radiation shields as well as to intercept heat being conducted through the fiberglass isolators. The outer radiation shield is thermally isolated from the vacuum housing by an inch-thick blanket of multilayer insulation. The inner radiation shield is thermally isolated from the outer shield by a similar multilayer insulation blanket. A vacuum space then separates the MIC and telescope barrel from the inner radiation shield. The surface finishes of the inner radiation shield as well as the outer surface of the telescope barrel which supports the optics and baffles, and the MIC are polished aluminum. The polished aluminum radiatively decouples these components due to its low infrared emissivity.

The cooling of critical components is accomplished by direct contact heat exchangers. The heat exchangers are lengths of tubing bent to shape and brazed to heat sink plates, as has been done successfully with other telescopes. This approach allows for cooling at the critical components minimizing the conductive path because thermal conductivity of beryllium and aluminum is poor at low temperatures. Where this direct approach is not feasible (e.g., primary mirror), soft woven copper straps between the heat exchanger and components are used. This approach has further advantages in reducing cool-down times as well as preventing temperature gradients.

The heat exchangers are part of a continuous line through which the helium flows. The flow path is presented schematically in Figure 3-62. It can be seen from the figure that the helium flows first to the MIC, then to primary and secondary optics, then to the telescope barrel at the base of the first folding mirror spider, and finally to the radiation shields which surround the telescope assembly. A portion of the gas is expelled into the telescope barrel for purging purposes. This arrangement provides the lowest-temperature coolant for the most critical components and somewhat higher-temperature coolant for the less critical components and radiation shields.

The first folding mirror is conductively coupled to the telescope barrel by means of the spider which supports the mirror from the forward portion of the telescope barrel. The surface of the first folding mirror facing outward from the aperture is coated with vacuum deposited aluminum (VDA). This causes most of the incident aperture load to be reflected away, minimizing the aperture load absorbed by the first folding mirror assembly. The baffles, however, fully absorb their portion of incident aperture load. The heat exchanger on the telescope barrel allows for cooling of both the baffles and first folding mirror.

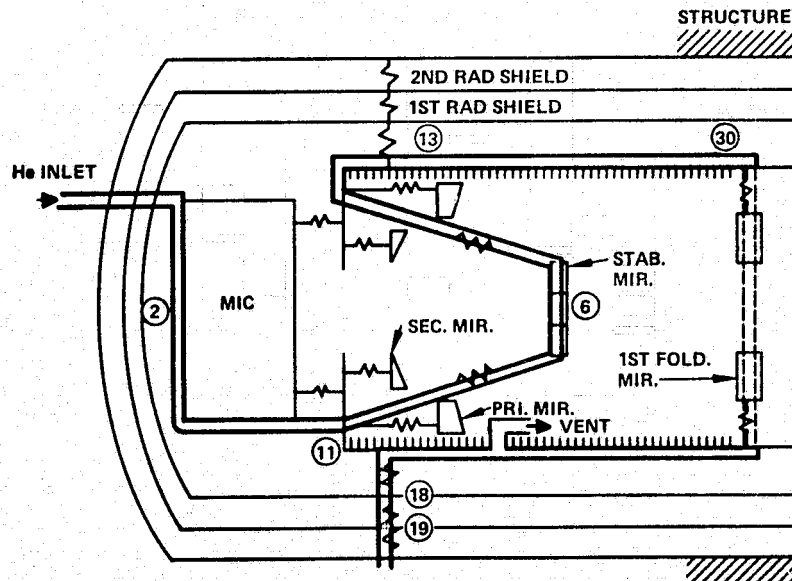


Figure 3-62. Proposed helium flow-path in SIRTF cryogenic system.

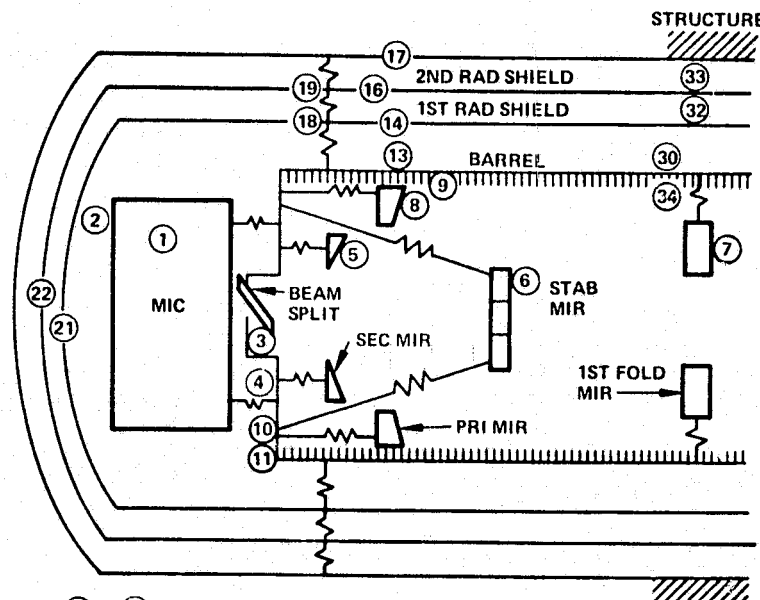
Model Characteristics

A thermal model was developed to compute the helium flow rates necessary to reach the desired temperatures. The driving assumptions are that the helium inlet temperature is 10°K , the vacuum housing is a boundary at 300°K , the MIC requires 1.5 watts of cooling, the secondary mirror requires 0.2 watts of cooling, and aperture loads vary from 0 to 9.5 watts.

The assumption of a 10°K helium inlet temperature is conservative. The helium inlet temperature is anticipated to be 6.5°K at the beginning of the mission reaching 10°K approximately 30 days later; hence the results presented are those expected at the end of a 30 day mission. The effect of inlet temperatures less than 10°K is to reduce the optics and telescope temperatures by an equal amount. This will allow the flow rate to be decreased, thus conserving helium. In addition, the MIC heat load of 1.5 watts is twice that estimated for a sample complement of instruments; the effect of reducing the load to 0.75 watts was studied and is presented in Table 3-22..

The computer model is based on a network of 36 nodes. The nodes are interconnected by conductances which were calculated from the SIRTF geometry. The heat exchangers will be designed so that the temperature of the helium leaving will be 1°K below the temperature of the component being cooled. The design of heat exchangers to accomplish this requires only the determination of the necessary length of tubing to be used as the heat exchanger. The conductive couplings were calculated using the thermal conductivity integrals because the thermal conductivities vary significantly over these temperature ranges. Within the optics only conductive couplings were considered as radiative couplings will be very small due to the low absolute temperatures. Only steady-state solutions were obtained under steady-state environmental conditions. Figure 3-63 presents the node locations in the model.

The material properties used were based on measured data and previous experience with similar telescopes. The properties used are listed in Table 3-19. Aluminum components were assumed to be made from 6061 aluminum alloy and the beryllium components from beryllium.



(23) - (29) HEAT EXCHANGERS
MISSING NODES WERE ON 3RD RADIATION SHIELD (PROBABLY UNNECESSARY)

Figure 3-63. Node locations.

TABLE 3-19. MATERIAL PROPERTIES

Silvered Teflon	Emissivity	0.75	
	Solar Absorptivity	0.10	
Vacuum Deposited Aluminum	Emissivity	0.025	New
		0.05	Degraded
	Solar Absorptivity	0.08	New
		0.125	Degraded
Polished Aluminum	Emissivity	0.06	
	Solar Absorptivity	0.20	
Multi-Layered Insulation	Conductivity	1.5×10^{-6} W/cm-°K	
Aluminum	Thermal Conductivity	$\int_4^T KdT = 2.04 \times 10^{-2} T^{1.698}$ W/cm	
Beryllium	Thermal Conductivity	$\int_4^T KdT = 1.21 T^{1.935}$ W/cm	
Fiberglass	Thermal Conductivity	$\int_4^T KdT = 8.1 \times 10^{-5} T^{1.741}$ W/cm	
Helium	Specific Heat ($T > 10^0$ K)	$5.2 \text{ J/gm - } ^\circ\text{K}$	

Because the solar absorptivity is likely to be degraded below the value achievable when new, the degraded value was used in all computations. The IR emissivity will substantially retain its new value, thus the new value was used throughout.

3.4.2 Aperture Load

The telescope aperture must be shielded from direct inputs from the sun, earth, and Shuttle because of the high radiative input levels of these sources. The SIRTF shade is designed to reflect incident energy away from the aperture. Protection from incoming energy is provided to within 45° of the LOS. In addition, the shade is designed to minimize the effects of diffuse reflectance and IR self-emission.

A number of designs that meet the shielding requirements were investigated. A 22.5° half-angle conical shade meets the shielding requirements but is quite large. Smaller alternatives were sought. A paraboloid is the smallest in size that is able to meet the shielding requirements. It, however, would be difficult to construct and make deployable. The final design is a shade constructed from three conical frustums as in Figure 3-33. The first frustum section is a 22.5 half-angle cone (LC1), the second a 12° half-angle cone (MC1), and the third a 6° half-angle cone (HC1). This design, as well as meeting the requirements, lends itself to being deployable. In addition, it is acceptable in size, being slightly larger than the parabola design but significantly smaller than the 22.5° cone design.

The analysis of the shade utilized a Monte Carlo ray tracing computer program, the Boeing Thermal Radiation Interchange Factor Program (see Appendix B, of Reference 3-22). Two shade models were constructed. One model included the sun, earth, Shuttle, and telescope, with the Shuttle in the X local vertical (XLV) orbital mode. This model was used to determine the radiant interchange between the shade and the sources, and hence the shade temperature. The second model consisted of the shade alone with a disc as the aperture and a disc sun. With this model, the aperture loading due to scattered solar energy, the earth within 30° of the line of sight (LOS), and shade IR self-emission were investigated. No specular energy was reflected into the aperture as per the design requirements. The diffuse component and sun angle from the LOS were varied to determine the effects on

aperture loads. The results of these analyses provided the radiant interchange terms required for the telescope thermal model as well as aperture loads.

Figure 3-64 presents the measured scattering data obtained from a sample vacuum deposited aluminum (VDA) surface on a fiberglass face sheet covering an aluminum honeycomb structure. The scattering is the percentage of energy reflected outside of a 2θ cone about the specular beam. (Scattering is largely independent of angle of incidence.) The Monte Carlo ray tracing program, used to generate the aperture loads due to diffuse solar scattering of 1 percent and 2 percent (Figure 3-65), is unable to deal with the measured scattering distribution and assumes a Lambertian distribution

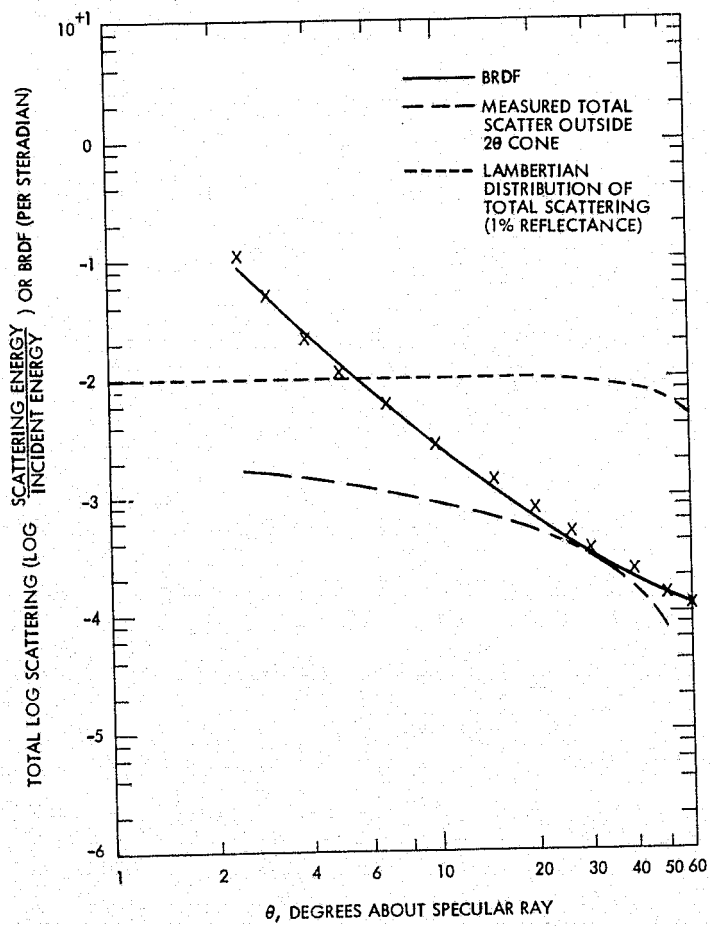


Figure 3-64. Scattering data.

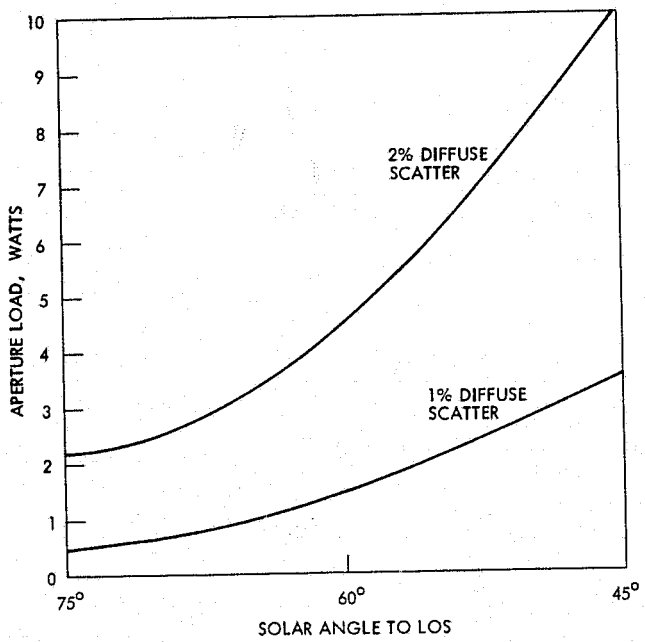


Figure 3-65. Solar aperture load.

which is also shown in Figure 3-64. The Lambertian distribution assumption causes the calculated aperture loads to be higher than would actually occur.

In the analysis all shade surfaces viewed by the aperture were considered to be VDA with a diffuse solar reflection component of 1 percent. This resulted in a maximum contribution to the total aperture load of 3.4 watts with the sun at 45° to the LOS. The measured scattering data in Figure 3-64 indicates a surface with a 2×10^{-3} diffuse solar scattering outside of a 2° half-angle cone. The 1 percent value was chosen based on previous work on thermal shielding as well as concerns arising from possible prelaunch handling problems and possible launch and in-orbit contamination. The 1 percent diffuse solar reflectance is a design requirement for the solar shade. Minimizing aperture loads from this source will require increasing the shade cone angles a few degrees and the overall shade length slightly. This change will prevent the energy scattered near the specular beam from entering the aperture.

Aperture loads due to the shade's IR emission can be substantial. The inner segment is the strongest source of aperture loading. Active cooling of the shade is not effective because the available cooling from the

residual helium is 80 watts which is far exceeded by the absorbed energy due to the sun, earth, and/or Shuttle. Applying the available helium residual cooling of 80 watts to the inner segment would decrease the aperture loading by 0.2 watt which is equivalent to an approximate temperature drop of 0.4°K in the temperature of the baffles. Thus the shade temperature must be made as low as possible by suitable choice of thermal control coatings on the exterior.

The inside of the shade is a vacuum deposited aluminum (VDA) surface for which a degraded solar absorptivity of 0.125 and an IR emissivity of 0.025 were used in the analysis. A freshly deposited surface has a solar absorptivity of 0.08 and an IR emissivity of 0.025. The temperature of the shade is controlled by covering the outside surface with silvered teflon which has a solar absorptivity of 0.10 and an IR emissivity of 0.75. This strongly radiatively couples the shade to space. The equilibrium temperature of the shade then varies depending on the relative locations of the heat sources and the shade.

In determining the shade steady state temperatures the solar input was orbit-averaged to 60 percent of its total value of 0.14 watt/cm^2 . The earth was taken as a 250°K blackbody, and the Shuttle's external temperature was taken to be 210°K . Table 3-20 presents the cases investigated which bound the maximum and minimum thermal IR loading into the aperture, as well as a nominal aperture load.

The maximum shade thermal emission aperture load (6.1W) occurs when the shade absorbs energy from the sun directly and solar energy reflected from the Shuttle as well as earth loads. The minimum (1.8W) occurs when the shade is not exposed to the sun.

Combining the maximum heat inputs from the thermal emission of the shade and 1 percent diffuse solar scattering with the sun at 45° to the LOS the total aperture load is 9.5 watts. The minimum aperture load is 1.8 watts due to the shade IR emission alone.

The maximum aperture load occurs only when the telescope is viewing between the earth and the sun at angles of 45° to the LOS. It is not anticipated that this environment will prevail for protracted periods. A nominal case was chosen. The nominal case includes the minimum shield

TABLE 3-20. APERTURE LOADS DUE TO IR EMISSION FROM SHADE

Shade Frustum	Maximum		Minimum		Nominal	
	Shade Temp. (°K)	Aperture Load (W)	Shade Temp. (°K)	Aperture Load (W)	Shade Temp. (°K)	Aperture Load (W)
Inner	288	3.9	208	1.0	232	1.6
Middle	256	1.5	196	0.5	220	0.9
Outer	242	0.7	119	0.3	210	0.5
Total	-	6.1	-	1.8	-	3.0

thermal emission load of 1.8 W. The nominal sun angle with the LOS was taken to be 75° causing the scattered energy to be 0.36W with a 1 percent solar diffuse scattering component. In addition the sun was orbit averaged at 60 percent of its total input. Under these conditions the average aperture load is 3.4W. Table 3-21 presents sources of aperture loads. The thermal analysis of the SIRTF telescope used a 3.4 W nominal aperture load.

With respect to the earth, the original specification requirement is that the telescope meet its performance requirements when the LOS is at an angle of 30° to the hard earth horizon. To maintain a reasonable size, however, the shade is designed to prevent off axis sources from illuminating the inner barrel when the sources are no closer than 45° to the LOS.

The effect of the earth's horizon at 30° to the LOS was investigated. It was found that under this condition the aperture load was increased by an additional 7.4 watts due to shade IR emission. When the albedo of 0.4 is

TABLE 3-21. APERTURE LOADS (W)

Source	Maximum	Nominal
IR	6.1	3.0
Solar	3.4	0.4
Total	9.5	3.4

also included the aperture load approaches 28 W. In order to obtain acceptable aperture loads in this environment an additional shade would be required or a mission constraint requiring that the earth's horizon come no closer than 45° to the LOS. This is the recommended approach.

3.4.3 Results

The thermal characteristics of the major configurations considered are presented in Table 3-22. The table presents significant cases in the evolution of the design. The first column is the first configuration considered while the columns on the right are for the present design. The trade-off between two or three radiation shields can be seen by comparing columns one and two. The major thermal impact of using two radiation shields instead of three is an increase of 1 K of the first folding mirror temperature, which will still be below the 18 K limit. It was therefore deemed thermally acceptable to use two shields. A mass savings of 75 kg (165 pounds) is realized. Column eight presents the temperature distributions for the present design for the nominal case: 3.4 W aperture load, 0.1 gm/sec (19 lbs/day) helium flow rate, 0.2 W dissipation by the stabilization mirror and 1.5 W dissipated by the MIC. Column five shows the temperature distribution for the present design with a 5 W aperture load and a helium flow rate of 0.25 gm/sec (48 lbs/day). Column six and seven show the temperature distribution for a 9.5 W aperture load varying the helium flow rate from 0.1 gm/sec (19 lbs/day) to 0.25 gm/sec (48 lbs/day). Table 3-23 shows the optics heat balance for the present design for a nominal case.

3.4.4 Conclusions

The thermal analysis indicates that the SIRTF telescope will maintain the desired thermal conditions at flow rates of 0.1 to 0.25 gm/sec if the telescope LOS is kept 45° or more from the sun or earth. The helium supplied by two 1300 liter (45 cubic feet) tanks is adequate to meet the flow rates required for the duration of the missions.

In a nominal aperture load environment, 0.1 gm/sec (19 lbs/day) of cryogen is adequate to meet the minimum temperature. For the sun at 45°

TABLE 3-22. MODEL RESULTS (TEMPERATURES IN °K)

Column Number	1	2	3	4	5	6	7	8*	9
Conditions									
He Flow (lb/day) (gm/s)	95 (0.5)		19 (0.1)		48 (0.25)		—	19 (0.1)	
Aperture Load (W)	5		3		5		9.5	3.4	
MIC Disp. (W)	1.5		—		1.5		1.5	—	
Stab. Mir. Disp. (W)	0.2		0.2		0.2		0.2	0.2	
Fwd Radiation Shield Supports	4 Titanium Wires		None		None		None	None	
# Radiation Shields	—		2		2		2	2	
Variable	3 rad. shields	2 rad. shields	MIC Disp. 1.5w	MIC Disp. 0.75	1.5w MIC Disp.	He Flow Rate 48 lbs/day 0.25 gm/s	He Flow Rate 19 lbs/day 0.1 gm/s	MIC Disp. 1.5w	MIC Disp. 0.75w
Component									
He Inlet	10.0	10.0	10.0	10.0	10.0	10.0	10.0	10.0	10.0
MIC	11.8	11.8	15.0	13.1	12.6	12.6	14.9	14.9	13.2
Beam Splitter	11.7	11.7	15.3	12.9	13.9	14.0	14.9	14.7	14.3
Stab. Mirror	11.8	11.7	16.1	13.5	13.9	14.1	15.5	15.3	14.5
Secondary Optics	11.8	11.6	15.4	13.2	13.9	14.0	14.9	14.7	14.3
1st Folding Mirror	16.3	17.3	22.1	20.5	16.6	19.4	23.3	18.1	17.5
Primary Optics	11.8	11.5	15.4	13.2	13.8	14.1	15.5	14.8	14.4
Baffle (Fwd.)	15.2	15.9	22.1	20.5	16.4	18.5	22.2	17.8	16.6
He Exhaust	42.5	50.0	89.1	98.6	50.0	51.0	97.3	92.1	92.0

*Nominal operating conditions.

TABLE 3-23. HEAT BALANCE NOMINAL CASE SIRTF

OPTICS HEAT BALANCE			
<u>Sources</u>		<u>Losses</u>	
MIC	1.5w	He Coolant	6.2w
Stab. Mirror	0.2w		
Aperture	3.4w		
Fiberglass Isolator	0.5w		
Radiation Shield	0.6w		
	<hr/>		<hr/>
	6.2w		6.2w

RADIATION SHIELDS HEAT BALANCE			
<u>Sources</u>		<u>Losses</u>	
Outer Rad Shield		He Coolant	85.1w
Fiberglass Insulator	18.7w		
Multi-layered Insulation	50.5w		
Central Rad Shield			
Fiberglass Insulator	1.2w		
Multi-layered Insulation	14.7w		
	<hr/>		<hr/>
	85.1w		85.1w

to the LOS and the earth fully loading the outside surface of the sun shade, the aperture load will be 9.5 W. With this aperture load, a helium flow rate of 0.25 gm/sec (48 lbs/day) is required to meet the minimum temperature of 18K for the 30 to 200 μ m experiments. The flow rate rises to 0.28 gm/sec for the 9.5 W aperture loading at the end of the flight.

During any mission the flow rate can be varied to meet changes in aperture loading and thermal requirements of the different experiments. By adjusting the cryogen flow rate, cryogen can be conserved extending the

available supply. For a tank capacity of 1300 liters (45 cubic feet) or 160 kg (350 pounds) of helium per tank, one tank will be sufficient for a 7 day mission under normal aperture loads utilizing 50 percent of its available cryogen at an average flow rate of 0.1 gm/sec (19 lbs/day). Two tanks will be sufficient for a 30 day mission averaging a helium flow rate of 0.1 gm/sec (19 lbs/day). This longer mission will utilize 80 percent of the available cryogen.

The first folding mirror is the critical element in the thermal design. It is most sensitive to aperture loads as it is directly heated by the aperture load. In addition, the first folding mirror is strongly coupled to the forward telescope barrel which is the primary heat sink for the absorbed aperture load. In order to further cool the first folding mirror, the forward portion of the telescope barrel needs to be more strongly coupled to the aft portion of the telescope barrel which is approximately 4.5°K cooler. This will be done with the addition of a high conducting sheath or straps (1100 aluminum or high purity copper) on the telescope barrel.

The initial cooldown of SIRTF on the pad in a period of one day is desirable. This can be achieved by first pre-cooling with liquid nitrogen (LN_2) and then final cooling with helium. The average thermal capacity of SIRTF from room temperature to 10 K is 1.3×10^7 joules/K. The time for cooldown will depend on flow rates; however, 10 gm/sec for both cryogens is adequate to achieve a one day cooldown. The thermal capacity of the optics between 10 K and 20 K is 3.0×10^4 joules/K. The maximum excursion rate for the optics in the 20 K to 10 K temperature range resulting from 1 watt heat load will be 0.12 C/hr. Hence, the optics temperatures will be stable with regard to transient heat inputs.

Figure 3-66 is a schematic of the SIRTF telescope and tanks, with a table showing valve positions at various times from pre-launch cooldown to re-entry. Initially, V_1 , V_2 , V_5 , and V_6 are open and helium flows to the tank(s) and the telescope. At T-4, all valves are closed except V_3 and V_8 which allow venting of the tank and telescope, and V_4 which is used to regulate the pressure in the tank. The vacuum pump and D_5 , D_6 , D_7 and D_8 disconnect when the T-4 umbilical is disconnected. There is no change until cover removal. The valves are located as close to the tank and telescope as

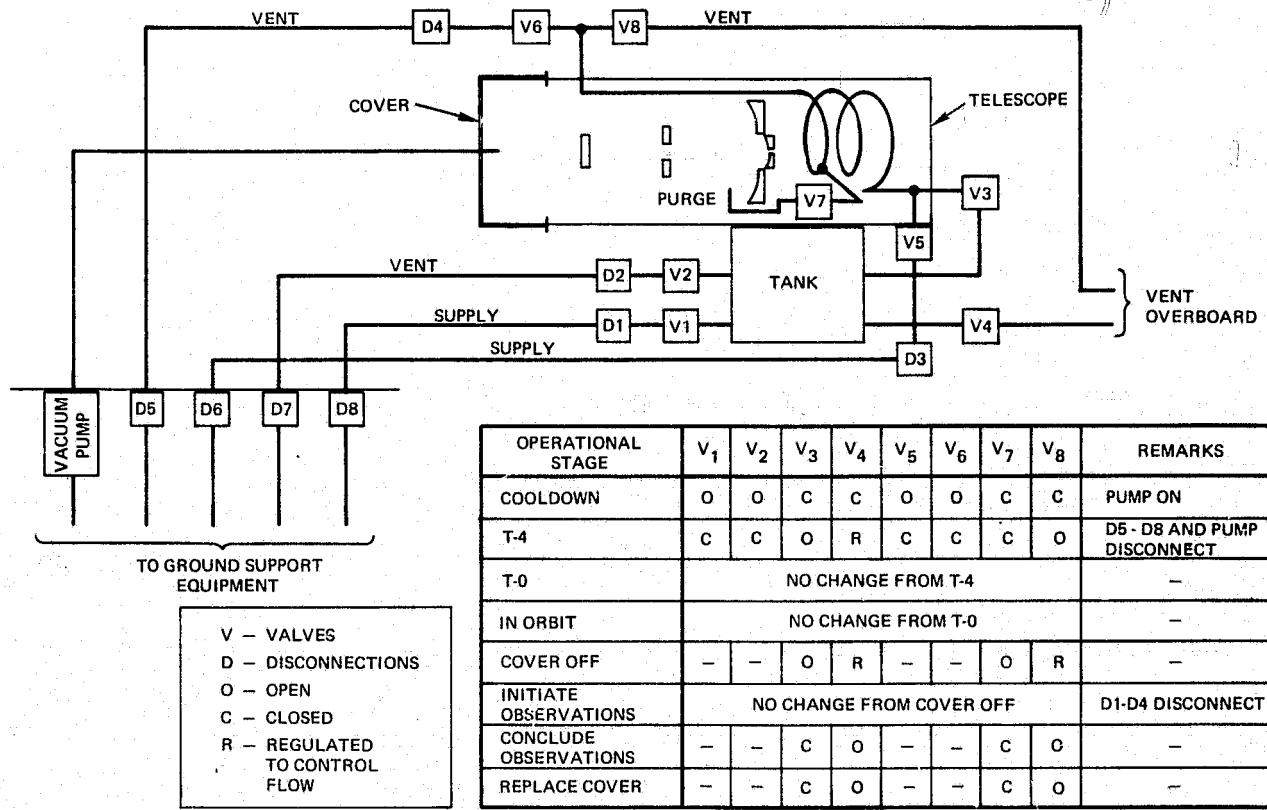


Figure 3-66. Schematic of SIRTF cooling and vacuum system.

possible, to reduce heat leaks. When the cover is removed, V₇ is opened to allow contaminant purging to begin, and V₈ is used to regulate the purging flow. When the telescope is raised to begin operations, D₁-D₄ disconnect. They are located near the tank and telescope so that no unnecessary line remains attached to the telescope. At the conclusion of observations, V₃ and V₇ are closed and venting continues through V₄ and V₈.

3.5 ACQUISITION, STABILIZATION AND POINTING

This section discusses the stabilization and pointing of the SIRTF telescope using the Spacelab Instrument Pointing System (IPS) as the SIRTF mount.* A general description of the salient features of SIRTF and the IPS is given, and the interface between the two systems is discussed in detail. The SIRTF stabilization subsystem includes a gyro-stabilized platform mounted on the telescope body, a laser optical link to the focal plane, a focal plane star tracker, and a two-axis steerable mirror. The mirror is servo-driven to provide a high degree of stability for the SIRTF image. The SIRTF internal stabilization subsystem is very similar to the Ames-developed video-inertial pointing system (reference 3-24).

A major conclusion of this study is thus that the SIRTF pointing and stabilization requirements will be met with SIRTF mounted on the IPS. Preliminary studies indicate that the telescope can be made sufficiently rigid so that the mass unbalance on the IPS does not cause impairment of performance due to telescope flexing. There remains, however, the serious limitation that the IPS cannot be performance tested on the ground prior to flight.

3.5.1 SIRTF-IPS System Concept

The general SIRTF-IPS installation in the Shuttle bay is shown in Figure 2-1 (page 2-2). The IPS gimbals are mounted on a platform supported by a standard Spacelab pallet. The gimbals support the telescope at its end point. In order to avoid damaging or misaligning the gimbal bearings and flexures during launch the telescope will be decoupled from the gimbals and supported along its length by a clamp-arm structure mounted on another pallet.

An illustration of the IPS gimbal configuration is given in Figure 3-67. The gimbals consist essentially of a universal joint mounted on a post. Angular travel about a pair of axes normal to the telescope line-of-sight (LOS) is

*The IPS configuration discussed here is that which was documented at the time of this report, i.e., as described in reference 2-4 and the Dornier Systems Technical notes released over the period August 1974 to March 1975. The IPS is currently undergoing redesign; when this redesign is documented, a supplementary report on the SIRTF-IPS interface will be prepared and issued.

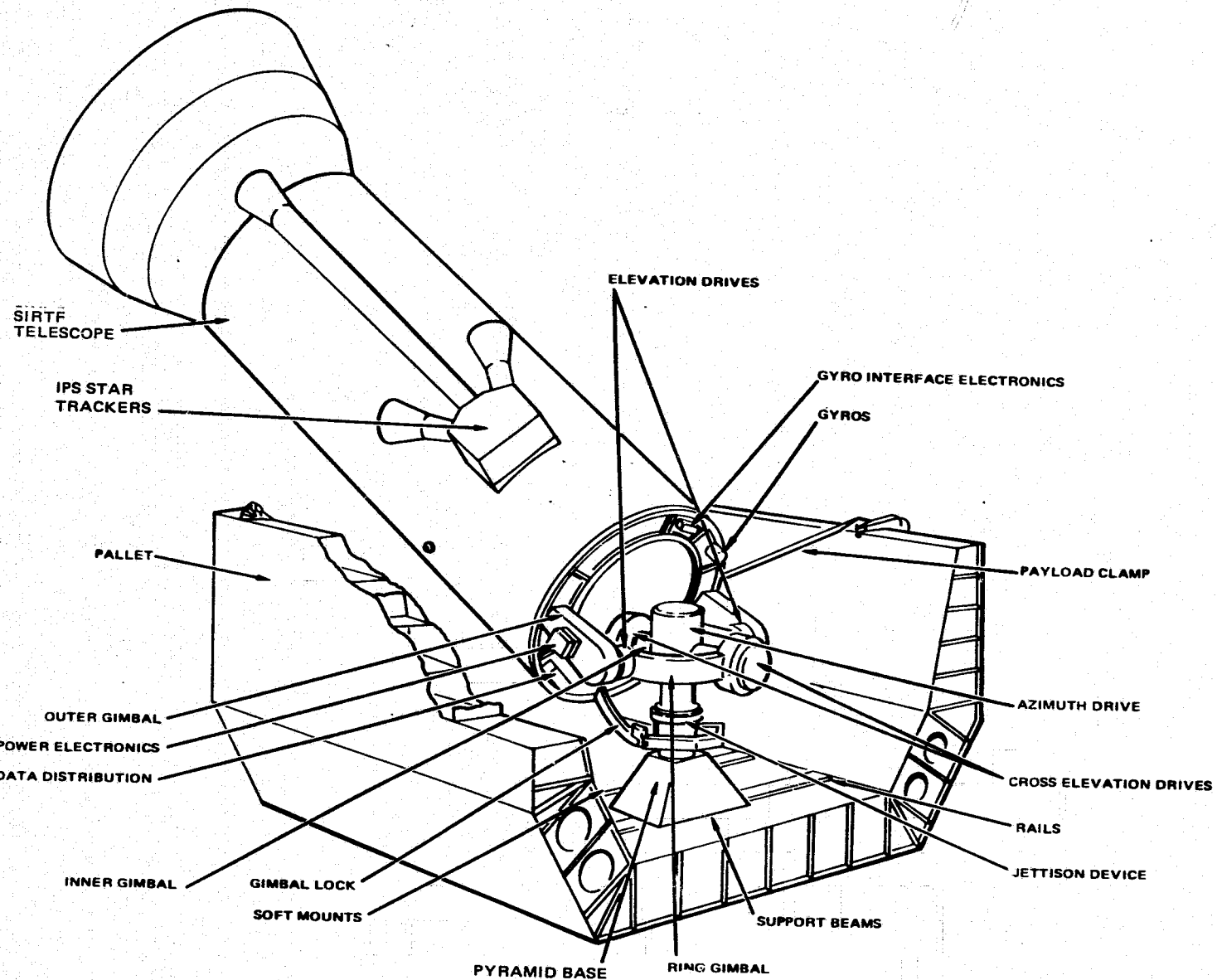


Figure 3-67. IPS gimbal configuration.

provided by the bearings of the universal joint. Capability for rolling the telescope about its LOS is provided by rotation of the universal joint about the post. The gimbal base is soft-mounted to the platform to partially isolate the gimbals from base-motion disturbances. The cables crossing the gimbals and the SIRTF gyro platform are not shown.

IPS Gimbal Configuration

A sketch indicating the angular coverage of the IPS gimbals is shown in Figure 3-68. The first gimbal (the gimbal mounted on the gimbal base) is designated as azimuth and provides $\pm 180^\circ$ of angular travel. The second or middle gimbal is designated as cross-elevation and provides $\pm 60^\circ$ of angular travel. The third gimbal (which supports the telescope) is designated as elevation and provides $\pm 90^\circ$ of angular coverage.

The elevation and cross-elevation gimbals provide angular motion of the telescope about a pair of axes orthogonal to the LOS. When it is required to rotate the telescope about its LOS the azimuth gimbal must also be moved. It should be noted that since the azimuth gimbal is not attached directly to the telescope it is necessary in general to move all three gimbals over large angles to accomplish the telescope roll.

A schematic showing the IPS bearing configuration is given in Figure 3-69. Each IPS gimbal axis utilizes both flexure pivots and conventional ball bearings. The flexure pivots are used for precision pointing over a small angular range. The ball bearings provide the required large angular coverage. A brake is used to hold the ball bearings in a fixed position so that precision stabilization can be accomplished using the flexure pivots only. The friction torque of the brake is adjusted to be slightly less than the spring torque produced by the flexure pivots at their point of maximum excursion. When large angular travel is commanded the flexure pivots will wind up to their limits at which point the brake will begin to slip.

There is considerable controversy at present as to whether the brakes are necessary or desirable. It is clear that in any operational mode where large gimbal travel is required the brakes create a difficult stabilization problem by injecting a large friction disturbance into the stabilization loops. (Subsequent to the completion of the study, we have been advised that the brakes will be deleted.)

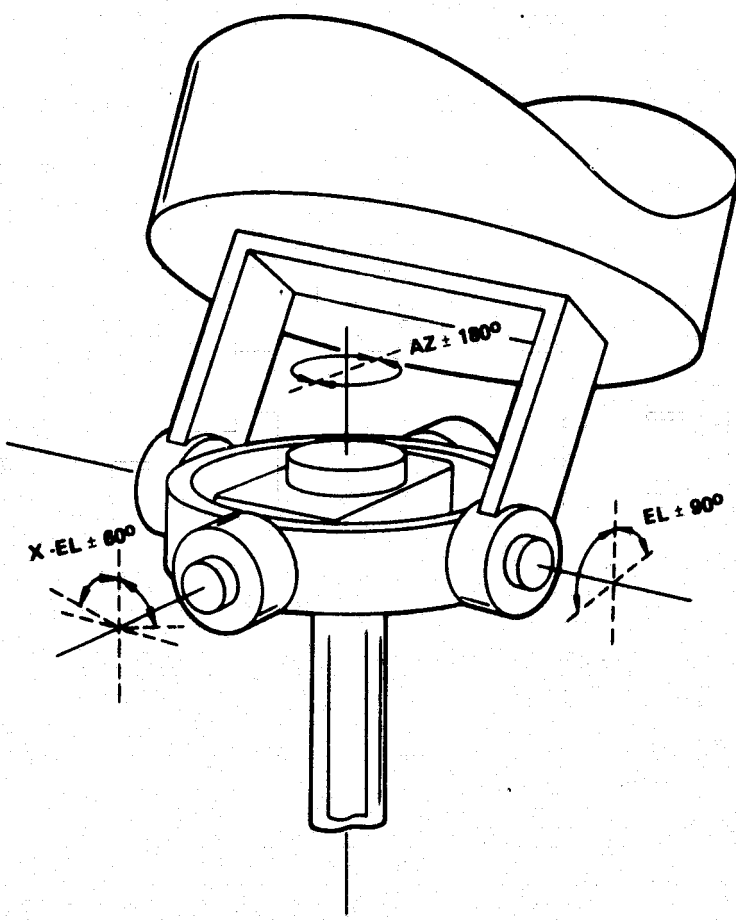


Figure 3-68. IPS angular coverage.

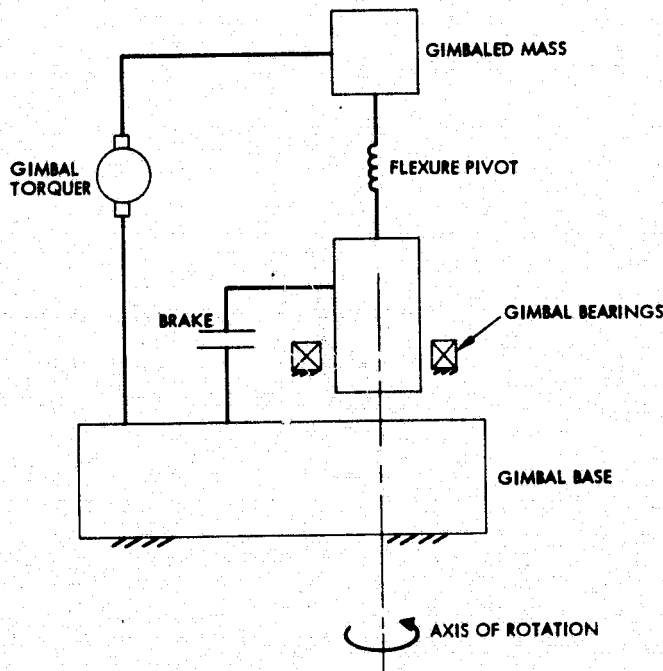


Figure 3-69. IPS gimbal suspension configuration.

The IPS gimbals are driven by brushless dc torque motors. Each gimbal axis is equipped with a pair of torquers to provide redundancy.

There are a number of reasons why an internal stabilization system is required as a final stage in addition to the IPS:

- The IPS pointing stability requirement is 1 arc sec rms; the SIRTF stability requirement is 0.25 arc sec rms.
- The IPS stabilization loops are relatively low bandwidths, and cannot respond to high frequency excitations.
- The SIRTF telescope focal plane can move by small amounts relative to the telescope outer housing.

Hence, the final control of the system must be exercised in the SIRTF focal plane. Several configurations have been developed; the two favored approaches are shown in Figures 3-70 and 3-71.

The mode of operation differs depending on the brightness of the guide star. For a bright guide star ($\sim M_v = 8$), the CCD array (Figure 3-70) or the star tracker (Figure 3-71) detects and tracks the guide star. Motion of the guide star generates an error signal in the electronics which is fed back to the stabilization mirror (second folding mirror - Figure 3-70; first folding mirror - Figure 3-71).

The remainder of the stabilization subsystem is used when the guide star is weaker ($M_v = 9$ to $M_v = 14$). Magnitudes as low as 14 are required to provide greater than 99 percent probability of having a guide star in the 30 arc min diameter star tracker field of view. At magnitudes of 9 to 14, the sensitivity of the star tracker is such that it must integrate for 0.1 sec or longer in order to achieve adequate signal-to-noise ratio. The long integration time does not permit stabilization of high frequency disturbances.

To solve this problem, a gyro-stabilized platform is used: The platform provides the short-term stable reference, and the gyro drifts are periodically corrected by data from the focal plane star tracker. This basically simple system is complicated by the fact that the gyros cannot be located in the SIRTF focal plane: There are no gyros designed to operate at cryogenic temperatures, and the heat load of a warm gyro platform would boil off large amounts of cryogen. Thus, the stable platform is used to

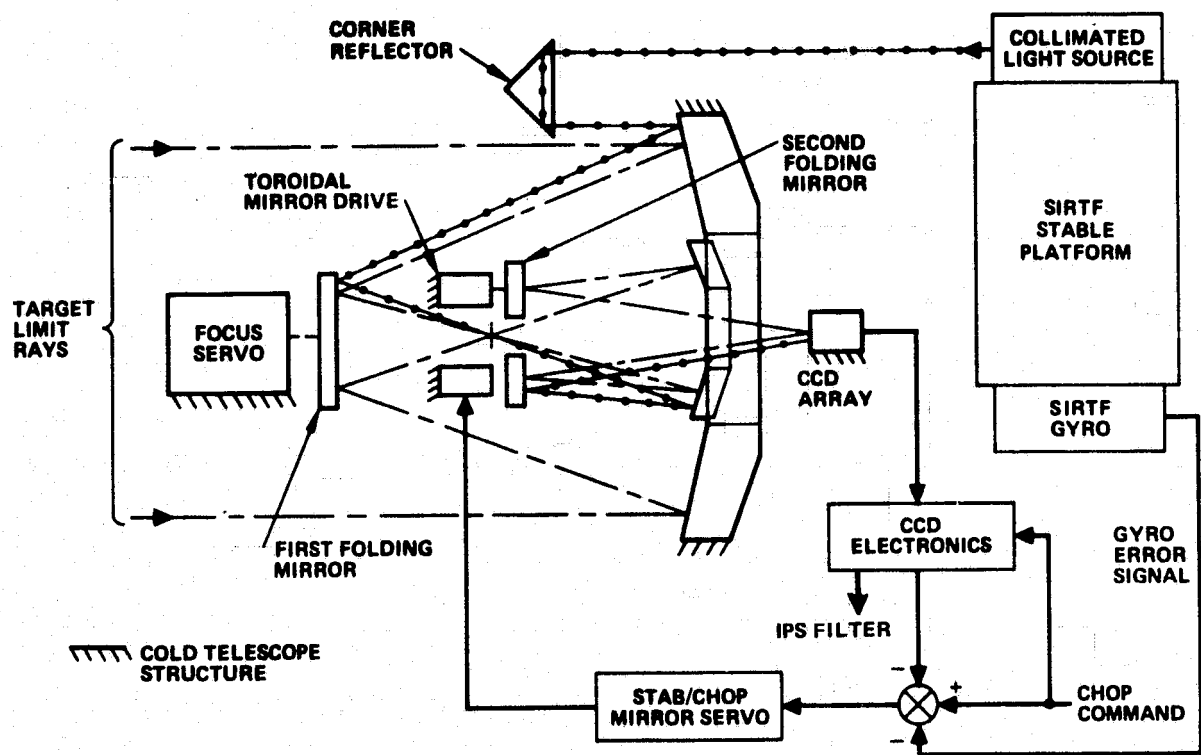


Figure 3-70. Optical stabilization loop using CCD array detector.

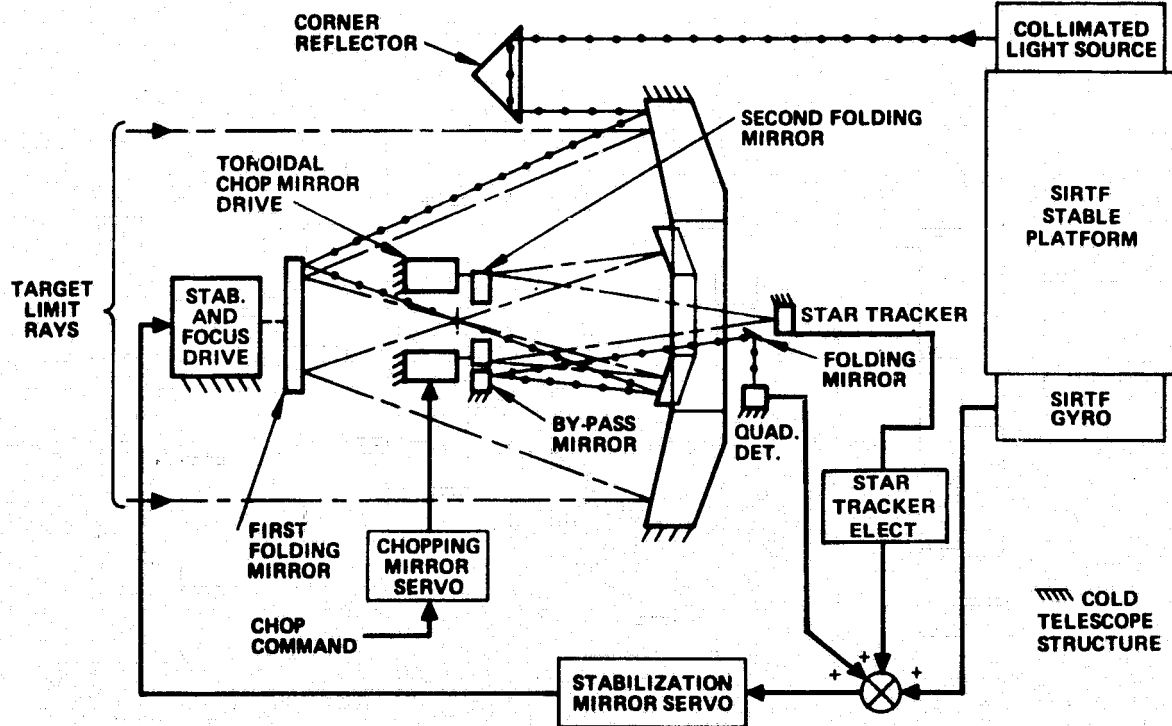


Figure 3-71. Optical stabilization loop using chopping bypass mirror and quadrant detector.

generate an artificial star which is directed to the focal plane and detected and tracked by the focal plane star tracker. A corner reflector directs the laser source onto a small area of the primary mirror. Cooled narrow-band optical filters and baffling are used to prevent other energy from entering through the corner reflector. In the system illustrated in Figure 3-70, the energy from the laser passes through the telescope and is detected by the CCD array star tracker. Flexing of the SIRTF telescope, or motion of the IPS and/or telescope appear as motions of the artificial star; error signals are generated and the steerable second folding mirror corrects the line of sight.

In the system of Figure 3-71, the laser beam does not fall on the second folding mirror, but on a fixed by-pass mirror which directs it to a quadrant detector located slightly off-axis. As the laser beam moves from the center of the quadrant detector, an error signal is generated and the steerable first folding mirror holds the line of sight stable.

The final step in stabilization is to use the gyro error signals directly to make an additional correction to the steerable mirror. It is expected that the platform can be stabilized to within 1 arc second. A further improvement in the LOS stabilization can be realized by using the platform gyro signals as additional inputs to the optical alignment mirror servos. These feed-forward signals cannot accomplish complete correction due to variations in the scale factors involved. It is usually possible to achieve a reduction on the order of 15/1 to 20/1 by use of a feed forward technique. This will bring the SIRTF LOS jitter to well within the required value of ± 0.25 arc second.

To insure that the IPS follows the SIRTF star tracker, the gyro error signal is also fed to the IPS and the IPS is slaved to the SIRTF star tracker.

The general scheme for slaving the telescope to the stable platform is shown (for one axis) in Figure 3-72. The SIRTF rate integrating gyros provide an inertial reference for the stable platform. The difference between the platform position and the IPS gimbal position is the platform gimbal angle $\theta_{PLATFORM}$. This angle is used as an error signal to drive the IPS gimbal slave loop. The slave loop will tend to align the IPS gimbal with the platform and thus drive the platform gimbal angle to zero. The IPS gyro is used in a rate mode to measure the inertial angular rate ω_{IPS} of the platform. This

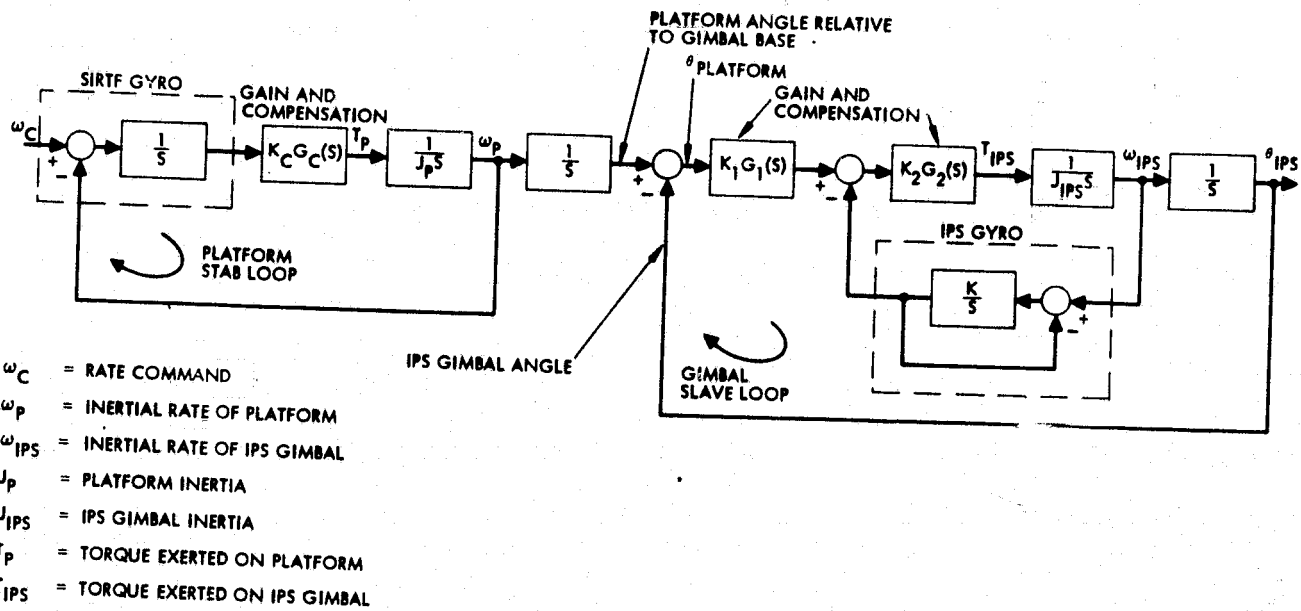


Figure 3-72. IPS gimbal slave loop configuration.

measured rate is fed back into the gimbal torquer thus producing a rate loop inside the slave loop. The rate loop adds damping to the servo and avoids the stability problems that might be encountered with Type II slave loop operation.

In evaluating the merits of the configurations of Figures 3-70 and 3-71, several considerations must be taken into account. The Figure 3-70 configuration, with the CCD star tracker, is a cleaner implementation if the CCD will perform the necessary functions. These include reading out the bright guide star or laser beam at high bandwidth, and the weak guide star at low bandwidth simultaneously with the laser beam readout. This is discussed further in Section 3.5.3 below.

The configuration of Figure 3-71 is simpler in that each component performs one function. However, the auto-alignment beam is reflected from a fixed mirror near the second folding mirror while the target energy is reflected from the moving mirror. Position transducers read the relative positions, but any errors which develop in the transducers cannot be removed by the servo system. Thus the approach pictured in Figure 3-70 is preferred. Table 3-24 summarizes the IPS and SIRTF stabilization performance.

Besides stabilization, the SIRTF telescope must provide space chopping, i. e., the beam of the telescope is alternately directed at the source and at a nearby patch of sky so that any fixed background irradiance can be subtracted out. In the Figure 3-70 configuration, the chop commands are fed into the servo loop and the second folding mirror carries out the chop command superimposed on the stabilization commands. In the Figure 3-71 configuration, the second folding mirror provides the chopping independent of the stabilization.

Control of stabilization during chopping can be exercised at three levels in the Figure 3-70 system, depending on the intensity of the guide star and the frequency of the chop:

1. The CCD array senses the position of the guide star at each end of the chop and corrects it during the dwell.
2. The CCD star tracker senses the time-averaged position of the guide star at each end of the chop and corrects the average position (over a few chopping periods).
3. The CCD star tracker senses the time-averaged position of the guide star at one end of the chop. The other end of the chop is not controlled.

All of these modes are within the capabilities of the system provided the data rates are high enough and/or the chop rates low enough. It is planned to implement level (2) initially for relatively low bandwidths; implementation of level (1) can be made as a later modification to the basic servo system if it is needed.

3.5.2 SIRTF - IPS Operational Sequence

The sequence of operations required to acquire a desired guide star with the SIRTF internal star tracker involves Shuttle, IPS, and SIRTF subsystems. The basic operations for acquisition of the first object are:

1. Align the Shuttle Inertial Measurement Unit (IMU) with respect to celestial coordinates by using the sun sensor and star tracker associated with the IMU. These components and subsystems are mounted on the Shuttle navigation base.

TABLE 3-24. SIRTF-IPS STABILIZATION PERFORMANCE

<u>IPS Gimbal Angular Coverage</u>	
Coarse Pointing:	
Elevation	$\pm 60^\circ$
Cross-Elevation	$\pm 90^\circ$
Azimuth	$\pm 180^\circ$
Fine Pointing:	
Elevation	$\pm 1^\circ$
Cross-Elevation	$\pm 1^\circ$
Azimuth	$\pm 1^\circ$
<u>IPS Gimbal Stabilization (bias + jitter)</u>	
Coarse Pointing:	
All axes	± 30 arc second RMS to ± 1 arc minute, RMS
Fine Pointing:	
Elevation	± 1 arc second, RMS
Cross-Elevation	± 1 arc second, RMS
Roll (about LOS)	± 30 arc seconds, RMS
<u>SIRTF Gyro-Platform Stabilization (bias + jitter)</u>	
1 arc second, RMS (orthogonal to LOS)	
<u>Overall LOS Stabilization*</u> (bias + jitter)	
1/4 arc second, RMS (orthogonal to LOS)	

*With autoalignment system and gyro feedforward signals.

2. Call up the pre-computed data stored in the onboard computer regarding the first guide star and command the Reaction Control System (RCS) to orient the Shuttle body axes to the correct spatial angles.
3. Prepare the SIRTF telescope for observation by releasing the telescope hold down clamps that lock the telescope to the Shuttle pallet, operate the mechanism that attaches the telescope and the IPS integration plate, and release the telescope cover.
4. Rotate the IPS gimbals to pre-computed angles by commanding a gimbal positioning servo loop, then extend the SIRTF telescope sun shade.
5. Transmit pre-stored guide star coordinates and magnitude data to the IPS star trackers, and command the star trackers to acquire the first set of guide stars.
6. Transmit pre-stored guide star coordinates and magnitudes to the SIRTF star tracker, and command the star tracker to acquire the guide star.

If it is desired to select a guide star not included in the precomputed and stored data, then onboard- or ground-generated commands may be utilized. Normally, the Shuttle pilot will command the IMU alignment and Shuttle orientation, the mission specialist will control or monitor the IPS gimbal orientation and star tracker acquisition, and the payload specialist will control or monitor the SIRTF star tracker acquisition and telescope pointing.

After the first guide star has been acquired, a simplified procedure may be used to acquire the second and subsequent guide stars as follows:

1. Call up the pre-computed and stored data regarding the second guide star, which will contain the data necessary to torque the IPS gyros so as to slew from the coordinates of the first guide star to those of the second. These data will include a torquing rate and torquing duration for each of the IPS gyros. This torquing can be done with adequate precision to insure that the second guide star will be within the central portion of the SIRTF field of view (FOV) at the end of the torquing sequence.
2. If through some operational error or transient equipment malfunction, the second guide star is not acquired, then repeat the torquing operation in the opposite direction so as to reacquire the first guide star. If this operation is not successful, then repeat the acquisition sequence originally used to locate the first guide star.

The significant parameters and precision of each subsystem and alignment sequence are tabulated in Table 3-25. Note that the structural bending and instability of the Shuttle between the navigation base and the IPS mounting point can produce errors as large as ± 2 deg. However, the $8^{\circ} \times 8^{\circ}$ FOV of the IPS wide angle star trackers is more than sufficient to assure acquiring the guide stars. Similarly, uncertainties in the SIRTF telescope structure can cause errors as large as ± 3 arc minutes between the IPS star tracker mounting base and the SIRTF telescope LOS. The SIRTF internal star tracker FOV of 30 arc minutes insures that the SIRTF star tracker can acquire its selected guide star. The optical stabilization subsystem in the SIRTF telescope will then align the LOS to within ± 0.4 arc second, 1σ .

3.5.3 Subsystem Studies

CCD Star Tracker

The mechanization of Figure 3-70 employs a CCD array. This detector has the large dynamic range, linearity, and fine resolution required to accurately measure the small stabilization error (± 0.25 arc second) at each end of a relatively large chopping command (up to 7.5 minutes of arc). The CCD detector has four equal horizontal fields as shown in Figure 3-73. One field is used for the reference beam readout, which is done at a high rate consistent with the chopping servo bandwidth requirements. The remaining fields are read out at a low rate consistent with the integration time required to obtain an adequate S/N ratio from the guide star signal. The advantages and disadvantages of the CCD approach are:

<u>Advantages</u>	<u>Disadvantages</u>
1. Only one two-axis drive is required.	The CCD array involves new technology with some unknowns
2. The target rays and reference beam travel identical paths through the telescope.	The large dynamic range and high accuracy requirements of the stab/chop servo may result in crosstalk or interference between the chopping and stabilization functions.
3. The CCD array provides a video output of the entire telescope 30 arc minute field.	

TABLE 3-25. STAR ACQUISITION ELEMENT CHARACTERISTICS

	Acquisition Sequence Element				
	IMU Alignment	Shuttle Orientation	Telescope Pointing	WFOV Star Trackers	SIRTF Star Tracker
Sensor	Sun, Star Trackers	IMU	Resolvers	WFOV Star Tracker	SIRTF Star Tracker
FOV	—	—	$\pm 60^\circ$, $\pm 90^\circ$, $\pm 180^\circ$	$8^\circ \times 8^\circ$	30 min
Error (3σ)	—	—	1 min	$\pm 9 \text{ sec}$	0.4 sec
BW	—	—	—	0.16 Hz	5 Hz
Controller	IMU	Flight Controller	IPS ACS	IPS ACS	SIRTF Stabilization Loop
Error (3σ)	—	0.25°	—	—	0.75 sec
Actuator	IMU Torquers	Shuttle RCS	IPS Torquers	IPS Torquers	Stabilization Mirror
Reference	Nav. Base	Nav. Base	Nav. Base	IPS Integration Plate	Inertial Space
Total Error (3σ)	0.1°	0.35°	0.35°	9 sec	—
SIRTF LOS Error (3σ)	—	—	$\sim 2^\circ$ (Orbiter Structure)	$\sim 3 \text{ min}$ (Telescope Structure)	1.1 sec

IMU — Inertial Measurement Unit
RCS — Reaction Control System
ACS — Attitude Control System

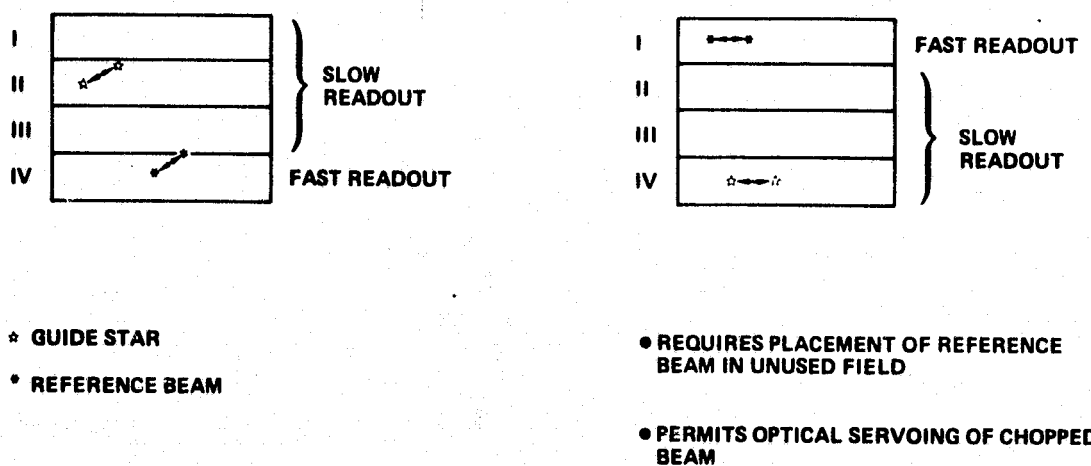


Figure 3-73. Four-field readout of CCD star tracker.

Reactionless Drive Mirror

A drawing of the second folding mirror and reactionless drive is included in Figure 3-74. A reactionless drive is required to avoid exciting telescope structural resonances which would otherwise occur when the mirror is commanded to chop over the wide frequency range from zero to 200 Hz. Both the mirror and reaction inertia are mounted with a pair of flexures to a cruciform shaped spider unit. The remaining pair of spider arms is attached to the telescope structure by a second identical pair of flexures. In this way, both the mirror and reaction inertia are flexure suspended for motion with respect to the base (cold telescope) about two orthogonal axes. Four moving coil electric driver assemblies, similar to a loud speaker cone driver, are attached between the mirror and reaction inertia at 90 degree intervals. Diametrically opposing pairs of drivers excited in opposition produce equal and opposite torques and forces on the mirror and reaction inertia. The net reaction torques and forces on the base are then cancelled. The specifications for the reactionless mirror drive are listed in Table 3-26.

Space Chopping Drive

The space chopping waveform is shown in Figure 3-75. Equal and opposite constant torques are applied to the mirror during acceleration and

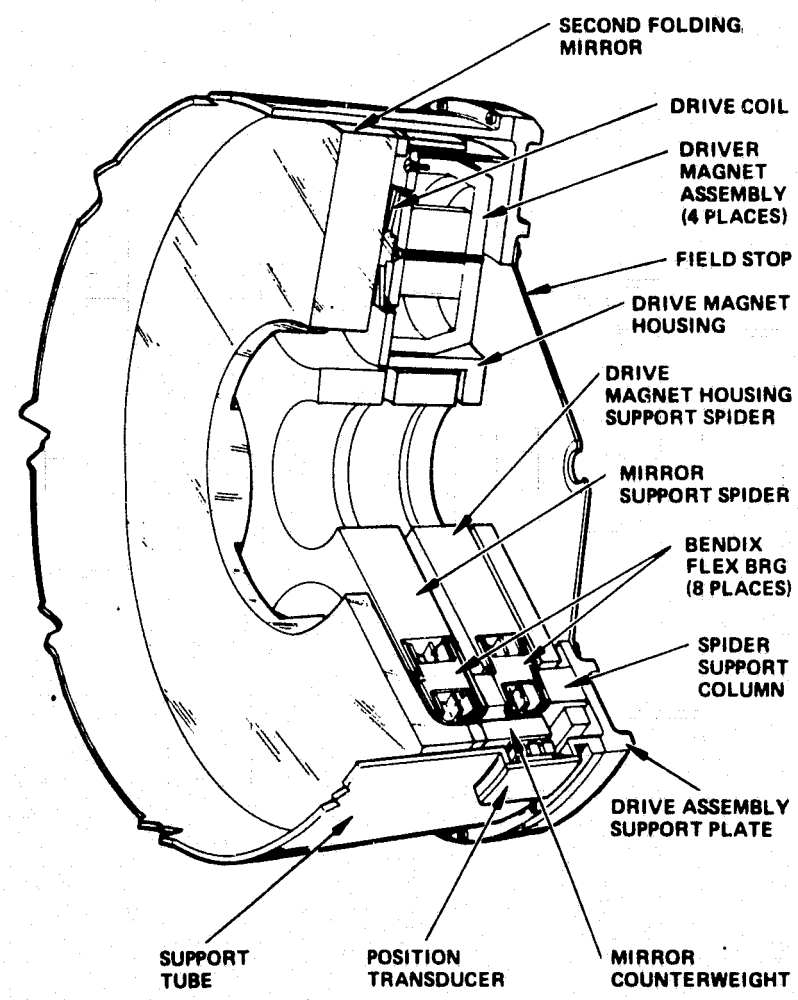


Figure 3-74. Reactionless two-axis drive
for second folding mirror.

TABLE 3-26. SECOND FOLDING MIRROR DRIVE SPECIFICATIONS

Type	Two axis reactionless
Torquers	Moving coil electric
Supports	Two axis Bendix type flexures
Angular Excursion	± 2 degrees, maximum
Bandwidth	500 Hz
Weight	15.5 kgm
Power Dissipated at 20°K	1.3 mw (1 arc minute chop at 20 Hz)

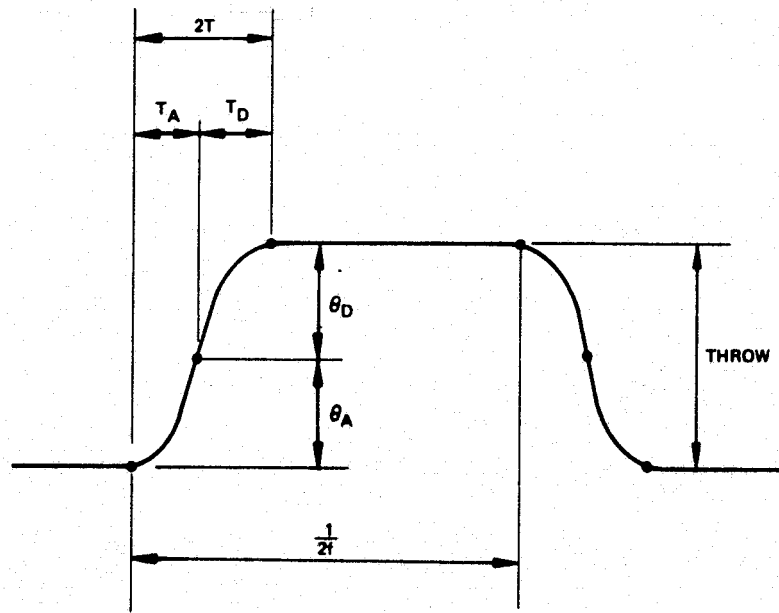


Figure 3-75. Space chopping waveform.

deceleration so that a symmetrical waveform is produced. The mirror throw is defined as the total angular excursion of the mirror. The dwell D is the fraction of the total time that the mirror spends at the end points of the throw. The dwell can be expressed as

$$D = \frac{\frac{1}{2f} - 2T}{\frac{1}{2f}} = 1 - 4 f T$$

where f is the chopping frequency and T is the time required to either accelerate or decelerate the mirror. The angle θ shown in Figure 3-75 is one half the mirror throw. The throw can also be expressed in image space using the relationship

$$\phi = \frac{180}{0.01665\pi} \theta$$

where ϕ is the peak-to-peak throw in image space expressed in arc minutes. The angle θ in the above equation is expressed in radians.

The relationship between the chopping frequency, chopping power, dwell, and throw in image space is

$$f^4 = \left(\frac{A^5}{KJ^2}\right) \frac{P(1-D)^3}{\phi^2}$$

where:

f = chopping frequency (Hz)

P = chopping power (watts)

D = dwell

ϕ = throw in image space (arc minute)

A = mirror diameter (cm)

J = mirror inertia ($N\cdot m\cdot sec^2$)

The constant K in the above equation is adjusted to accommodate the units. The numerical value of K is 0.703. The minimum chopping performance requirements are given in Table 3-27. The throw and frequency ranges listed in the table define rectangular areas on the graphs of Figures 3-76, 3-77, 3-78, and 3-79. Figures 3-76, 3-77, 3-78, and 3-79 are plots of the relationship between frequency, throw, and dwell for 10 mw, 30 mw, 100 mw, and 500 mw of chopping power, respectively. The portions of the rectangular areas that exceed the specified dwell curves are indicated by cross-hatched shading. The rectangular area defined by the throw range of 0 to 1 arc minute and the frequency range of 0 to 200 Hz exceeds the 90 percent dwell curve over a portion of the range in all cases and is not shown on the figures.

TABLE 3-27. CHOPPING PERFORMANCE REQUIREMENTS

Throw, arc min	Frequency, Hz	% of Cycle at Limits
0 to 1	0 to 200	90
1 to 4	0 to 20	90
	20 to 40	80
4 to 10	0 to 20	80
10 to 15	0 to 20	70

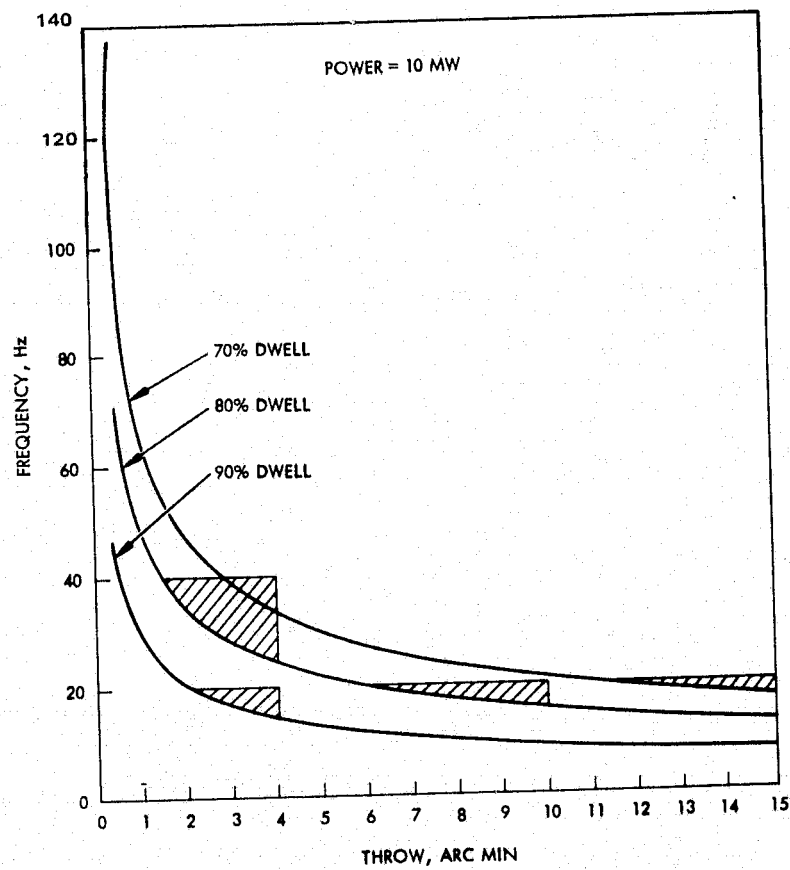


Figure 3-76. SIRTF chopping mirror performance - 10 mW.

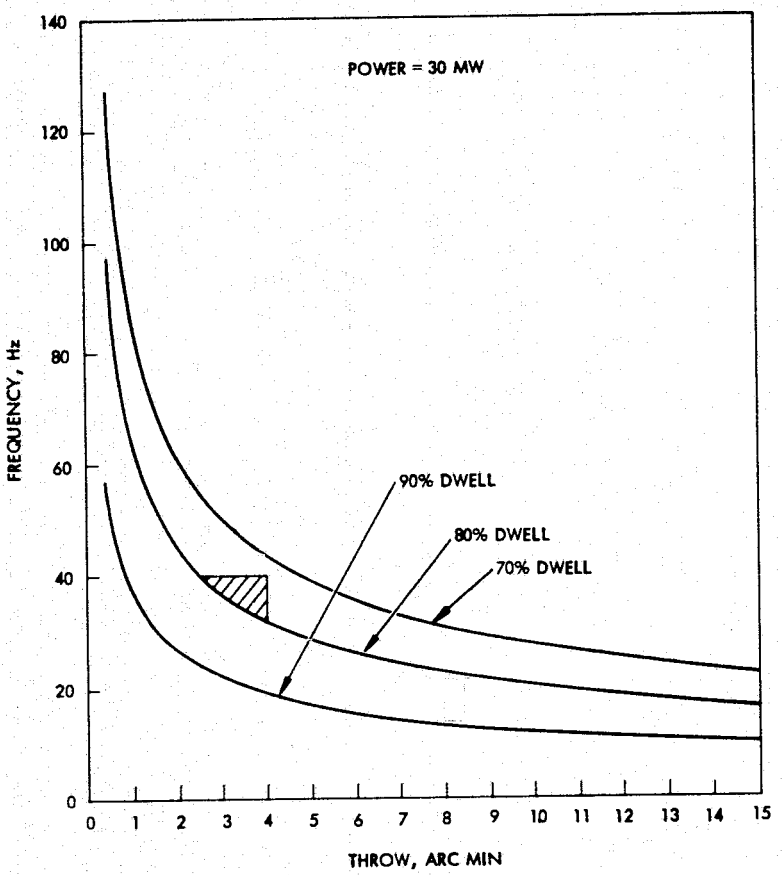


Figure 3-77. SIRTF chopping mirror performance - 30 mW.

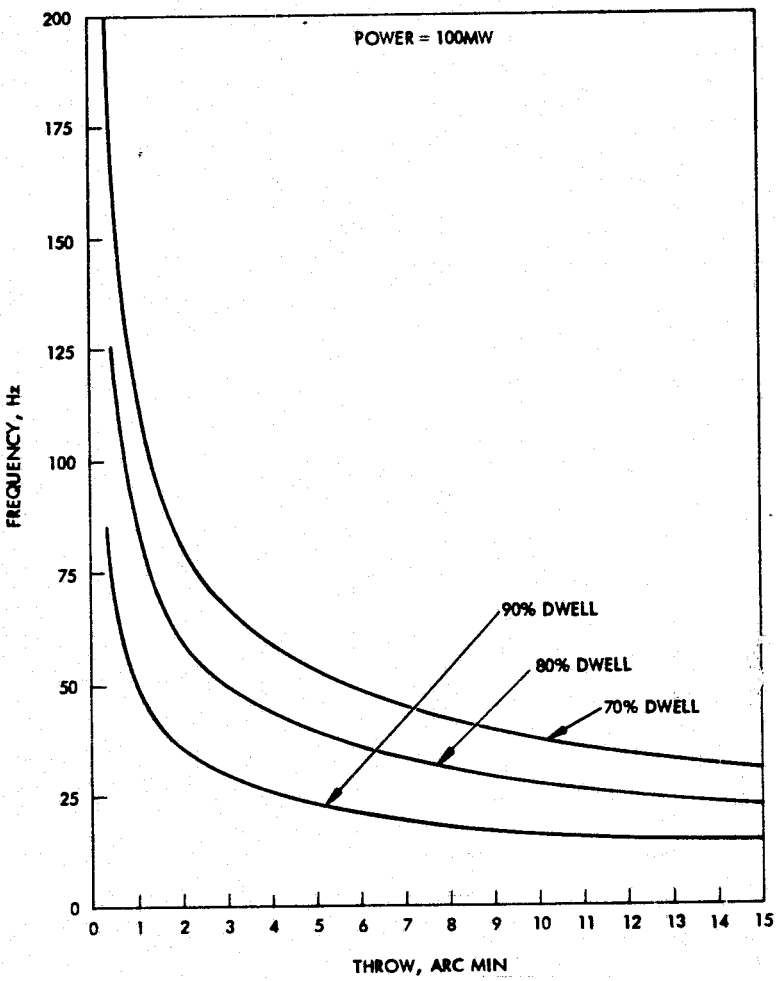


Figure 3-78. SIRTF chopping mirror performance - 100 mW.

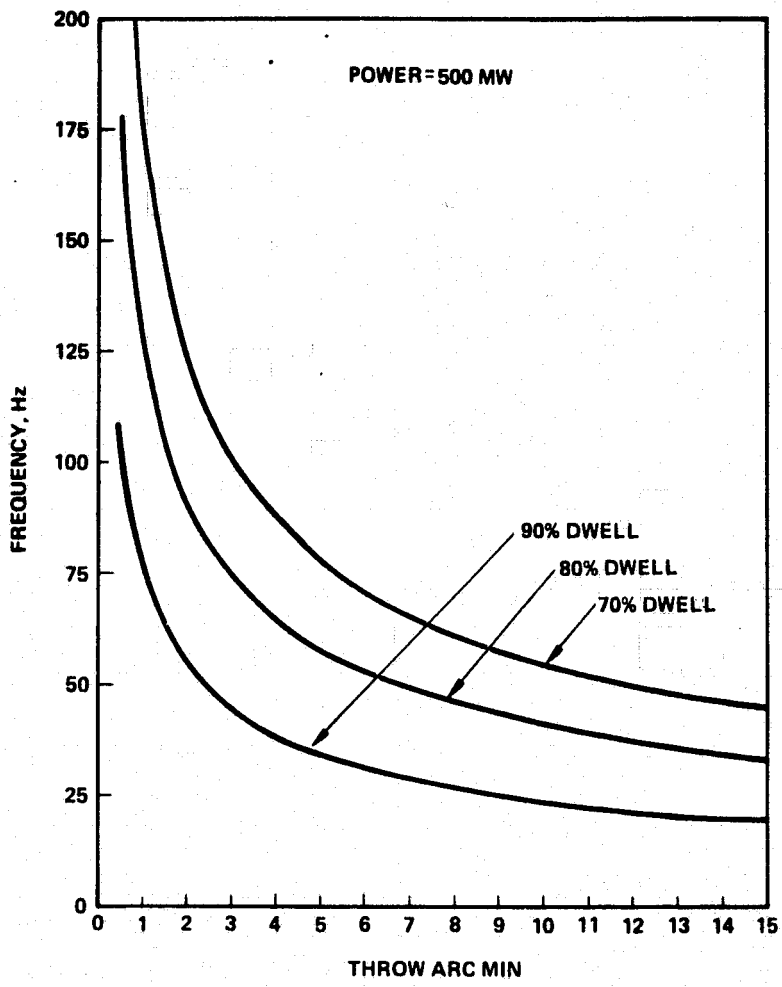


Figure 3-79. SIRTF chopping mirror performance - 500 mW.

However, the purpose of the very high frequency chop is to reject low-frequency excess noise; it can be rejected more efficiently by means of a chopper wheel mounted in the experimental instrument.

3.6 SIRTF TELESCOPE PERFORMANCE

The purpose of this section is to assemble the major SIRTF performance parameters in a single location in this report. Many of the parameters are discussed extensively in other sections of the report. The performance parameters of interest are those which directly affect the acquisition of scientific data. They fall broadly into two groups: spatial characteristics and radiometric parameters. The spatial characteristics include resolution, field of view, pointing accuracy and stability, and the space chopping parameters. Radiometric performance includes sensitivity limitations imposed by telescope temperature, shuttle contamination, residual atmosphere, and zodiacal emission.

3.6.1 Spatial Performance Parameters

The resolution and field of view of the SIRTF telescope are discussed first under static conditions; the effects of space chopping, and the pointing accuracy and stability discussion follows.

Resolution and Field of View

The resolution of the SIRTF telescope is evaluated at 5μ , in accordance with the performance specification (Reference 3-25). Figure 3-80 shows the point spread function. Due to the very high degree of correction of the optical system, the point spread function does not change as a function of position in the field of view. The dimensions and amplitudes of the various features of the diffraction spot are shown in Figure 3-80. Table 3-28 relates linear and angular dimensions of the SIRTF focal plane. The first dark ring encloses 53 percent of the energy in the diffraction blur; the second dark ring encloses 83 percent of the energy.

The telescope will be mounted on the Instrument Pointing System. The IPS provides the freedom for pointing over a 60 degree half-angle cone. The region near the tail is excluded since the tail will be a warm off-axis source radiating into the telescope. The limitations imposed by the tail are dependent on SIRTF placement in the bay and wavelength and sensitivity of operation. Figure 3-81 shows a 15° minimum angle between the LOS and the tail, corresponding to the situation for zodiacal-emission-limited performance at 10μ , which is the most restricted case.

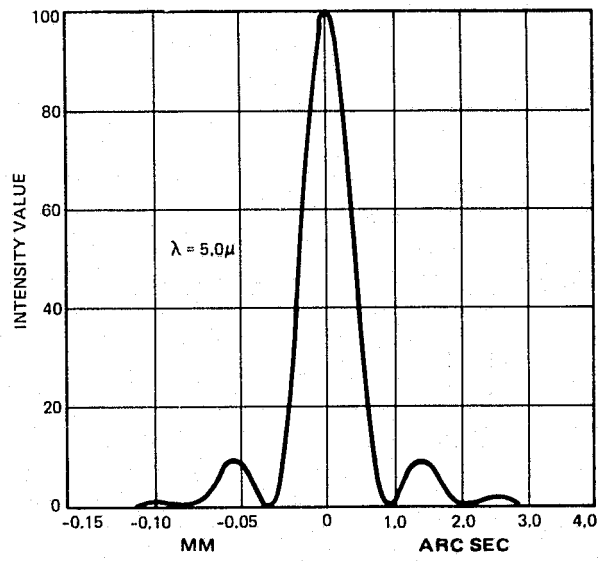
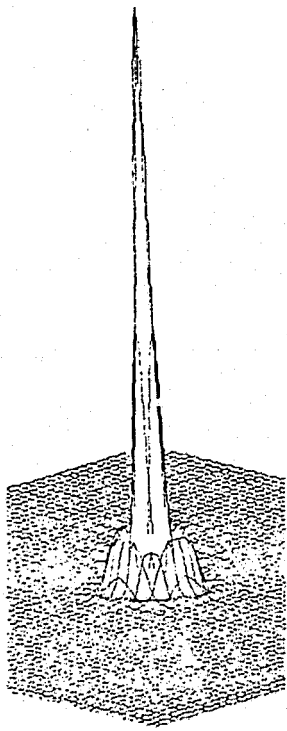


Figure 3-80. On-axis point spread function, $\lambda = 5$ micrometers.

TABLE 3-28. SIRTF FOCAL PLANE LINEAR AND ANGULAR DIMENSIONS

	Angular	Linear
IR FOV	15 arc min	34.76 mm
Dia 1st dark ring at		
5μ	1.9 arc sec	0.073 mm
50μ	19 arc sec	0.73 mm
500μ	3.2 arc min	7.3 mm
Dia 1st bright ring at		
5μ	3.8 arc sec	0.146 mm
50μ	38 arc sec	1.46 mm
500μ	6.3 arc min	14.6 mm
Scale Factors	1.2555 mr/cm 4.315 arc min/cm 258.9 arc sec/cm	

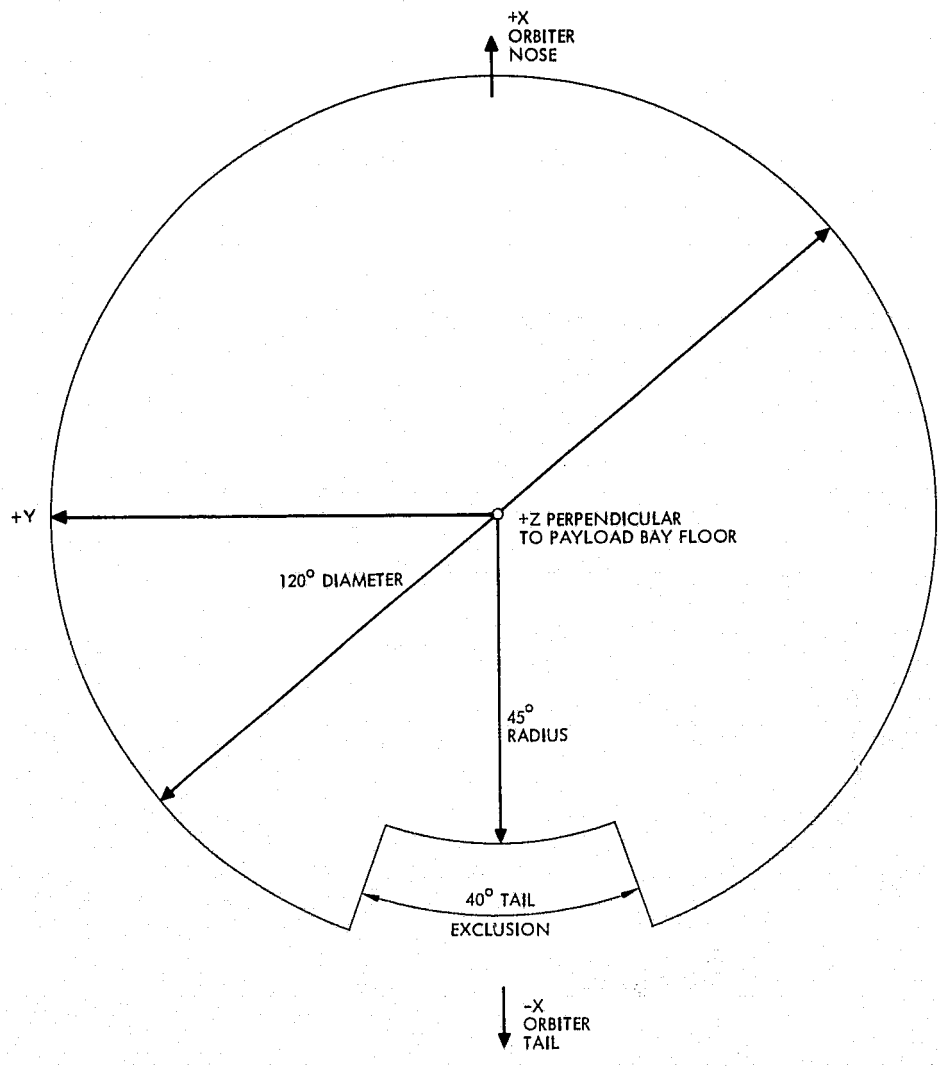


Figure 3-81. SIRTF telescope field-of-view coverage.

The ELMS cryogen tanks will restrict the freedom near the $\pm Y$ direction if full $\pm 90^\circ$ rotation of the telescope is required for polarization measurements. However, 90° rotation is available through the 60° half-angle cone. The current plan is to develop cryogen tanks specifically for SIRTF to remove this limitation.

Space Chopping

The second folding mirror can be driven to provide space chopping in two perpendicular directions to either side of the optical axis. The performance of the chopping mirror (throw, frequency, and dwell at the end positions) is a function of the power which can be absorbed by the cooling system at the second folding mirror. For a nominal 100 mW dissipated by the second folding mirror, the chop throws, frequencies, and dwells shown by the curves in Figure 3-82 can be obtained. The straight lines define the

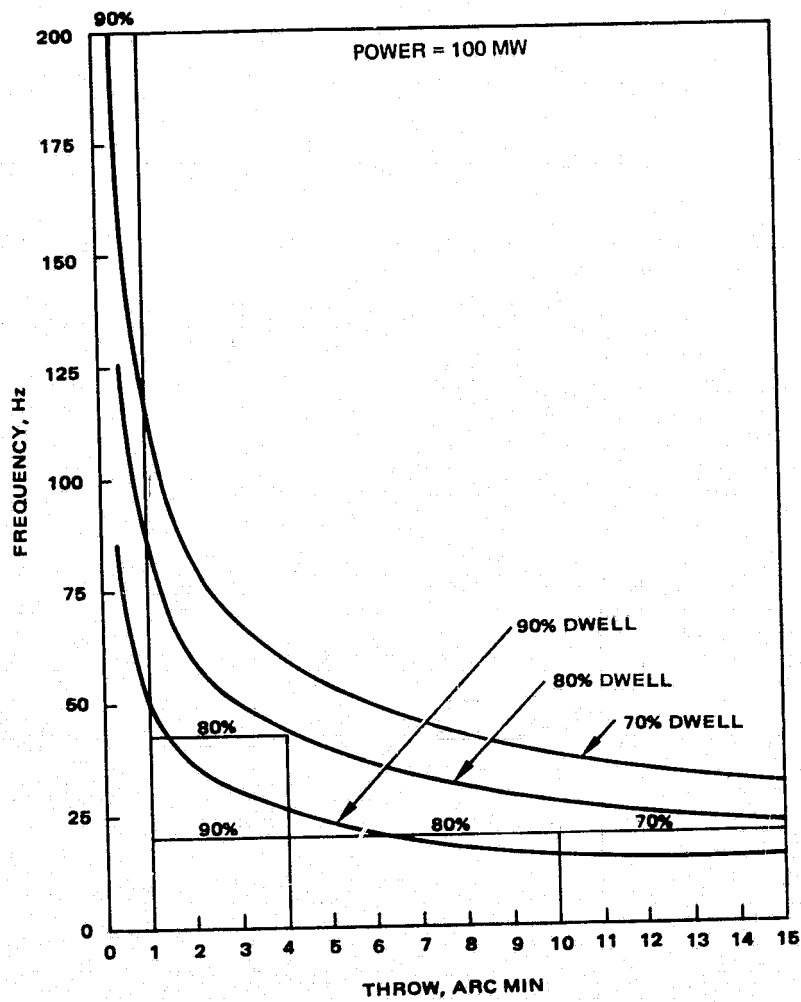


Figure 3-82. SIRTF chopping power requirements - 100 mw.

requirements which are also listed in Table 3-29. All requirements are met except the 200 Hz - 1 arc minute - 90 percent dwell requirement. This requirement was based on the need for chopping (and synchronously demodulating) certain detectors to escape excess noise limitations. It can equally well be met by including a cold chopper wheel or tuning fork in the particular instruments where it is required. Alternatively, operation of the second folding mirror at higher power levels for limited periods of time will be possible although the conditions have not been defined.

In Table 3-29 the throw is total (end-to-end) in object space, and the dwell is expressed as the fraction of the period that the image spends at its extreme positions.

Because the space chopping is controlled by the same servo that controls image motion compensation, the stability of the throw and of the dwell will be comparable to that of the stabilized stationary image, as discussed below.

Pointing and Stabilization

Prediction of the pointing and stabilization performance of SIRTF is uncertain due to lack of definition of Orbiter excitations and structural modes, and definition of IPS capabilities. These uncertainties mean that the forces and torques acting on the SIRTF telescope are not defined, and hence detailed analysis is not meaningful. However, estimates have been made.

TABLE 3-29. CHOPPING PERFORMANCE REQUIREMENTS

Throw, arc min	Frequency, Hz	% of Cycle at Limits
0 to 1	0 to 200	90
	0 to 20	90
1 to 4	20 to 40	80
	0 to 20	80
4 to 10	0 to 20	70
	0 to 20	70
10 to 15		

Assuming that the star tracker array data can be processed to provide centroid location to 1/10 the center-to-center spacing of elements, the pointing error will be on the order of 0.4 arc second. Table 3-30 gives the stabilization system errors, exclusive of the CCD pointing error. Thus automatic pointing will provide 0.4 arc second pointing error plus an additional 0.1 arc second of stabilization system bias and jitter. The payload specialist can correct the CCD pointing error for a given location certainly by as much as a factor of 3 to bring the total pointing error (bias plus jitter) to within 0.25 arc second rms. Whether the star used to guide on is on or off the telescope axis makes no difference in tracking accuracy. The 30 arc second roll stability of the IPS results in a linear angular error orthogonal to the line of sight at the edge of the field of view under 1/10 arc second. Hence no additional roll stabilization is required.

Scanning

SIRTF offers two methods of performing raster scans over restricted regions of the sky as required by the specification. For small fields, the second folding mirror can be driven while the telescope is held stabilized by the IPS. Figure 3-83 illustrates two fields that can be accommodated. These

TABLE 3-30. SIRTF STABILIZATION SYSTEM ERROR ESTIMATES

IPS Gimbal Stabilization (bias + jitter)

Coarse Pointing:

All axes ± 30 arc sec, RMS to ± 1 arc min,
 RMS

Fine Pointing:

Elevation ± 1 arc sec, RMS

Cross-Elevation ± 1 arc sec, RMS

Roll (about LOS) ± 3 arc sec, RMS

SIRTF Gyro-Platform Stabilization (bias + jitter)

1 arc sec, RMS (orthogonal to LOS)

Overall LOS Stabilization with autoalignment system and gyro feedforward signals (bias + jitter)

1/10 arc sec, RMS (orthogonal to LOS)

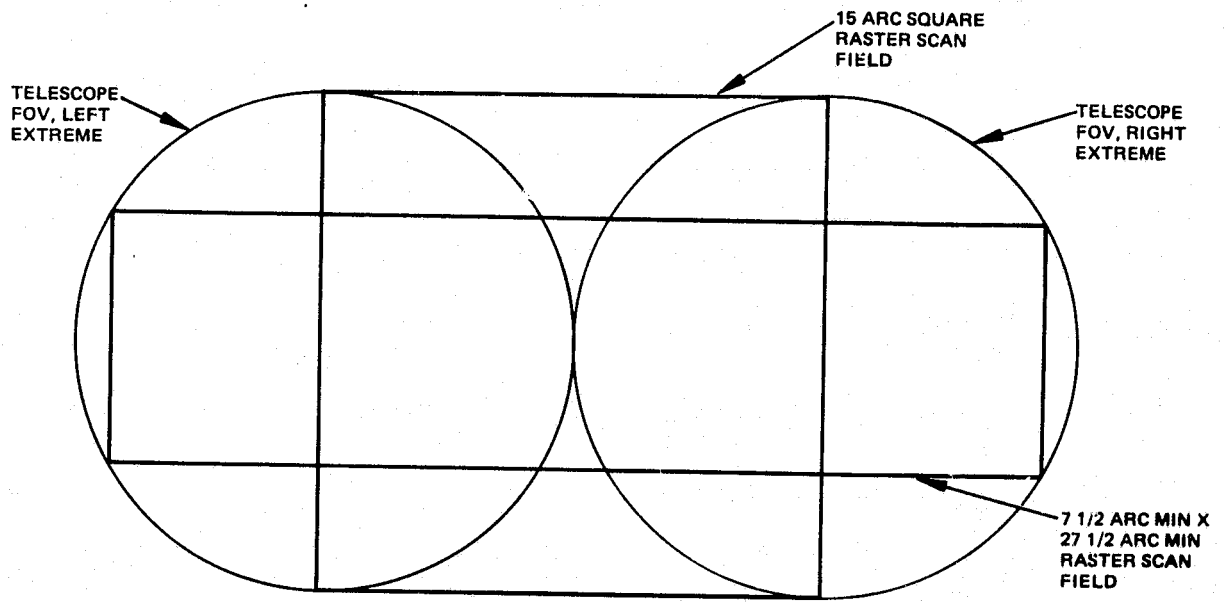


Figure 3-83. Example scan fields using second folding mirror scanning.

scan patterns can be executed with pointing accuracy and stability comparable to the static pointing case, since the gyro drifts will be small over a scan period (across and back). The guide star will be reacquired each time it returns to the field of view.

For larger scan patterns, the IPS gimbals will be used. The IPS is expected to maintain its 1 arc second stability over a ± 1 deg field. Providing that the IPS can maintain this level of stability in a dynamic (scanning) situation, the line of sight stability and pointing accuracy will be comparable to that in the static pointing case. Several guide stars, situated throughout the raster pattern, will be used to correct gyro drift over the scan period.

3.6.2 Radiometric Performance

The SIRTF specification called for a telescope design which would provide the levels of performance listed in Table 3-31. The required sensitivity is achieved by cooling the telescope to 18°K (to meet the 200μ

TABLE 3-31. SIRTF RADIOMETRIC PERFORMANCE SPECIFICATION

Wavelength Range	FOV diameter (arc min)	NEP (W $\sqrt{\text{Hz}} \cdot 10\mu$)
5 μ to 30 μ	1.0	10 ⁻¹⁷
5 to 30 μ	$8.3 \times 10^{-3} \lambda [\mu]$	10 ⁻¹⁸
30 μ to 200 μ	1.0	10 ⁻¹⁶

requirement) or 21°K (to meet the 30 μ requirement). The 1 arc minute FOV requirement dominates in the 5 μ to 12 μ band while the $8.3 \times 10^{-3} \lambda$ arc minute FOV requirement dominates from 12 μ to 30 μ . It became evident during the study, however, that the telescope will probably be limited by external phenomena: residual atmosphere above the Shuttle, zodiacal emission, and molecular and particulate contaminants ejected by the Shuttle. More extensive discussion of the contaminant environment is given in the referenced papers by Witteborn and Simpson; Section 3.6.3 provides data on a current model of the zodiacal emission in the infrared.

Figure 3-84 shows the situation with respect to the residual atmosphere.* The assumptions made in developing the atmospheric model are discussed fully in Reference 3-26 (Simpson and Witteborn). Bars on the individual lines indicate line strengths at 250, 300, 350, and 400 km altitude. For the short wavelength lines, the dashed lines indicate nighttime strengths and the solid ones, daytime strengths. The figure makes clear that the only interference will arise from the NO lines between 5 and 6 microns. Strictly

*The NEP's discussed and shown on graphs in this section are strictly based on photon fluctuations; i. e., they do not take into account the facts that (1) for photoconductive detectors, each photoelectron generates a hole-electron pair and hence the electrical noise is $\sqrt{2}$ times greater than the photon fluctuation noise; and (2) the quantum efficiency η . The actual performance of the given detector in the SIRTF focal plane will be $\sqrt{2}/\eta$ worse than illustrated here.

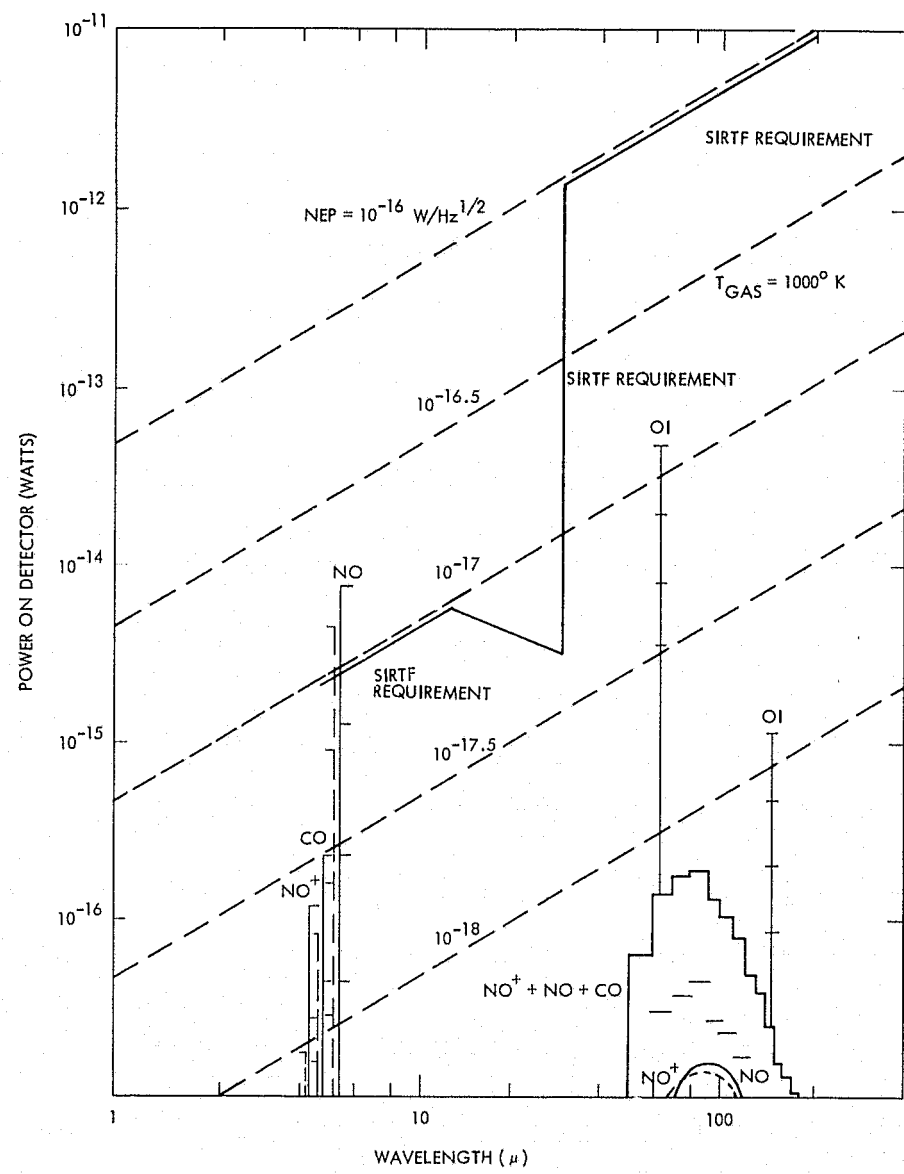


Figure 3-84. Photon fluctuation noise in the SIRTF focal plane caused by emission of atmospheric gases.

speaking, even these do not exceed the requirement, which is based on the average over a 10μ -wide band.

Figure 3-85 illustrates the situation with respect to Shuttle-generated contaminants. The column densities assumed in Figure 3-86 are 10^{12} molecules/cm² of H_2O and 2×10^{11} molecules/cm² of CO_2 . Other assumptions relevant to the radiance values (e.g., temperatures) are discussed in

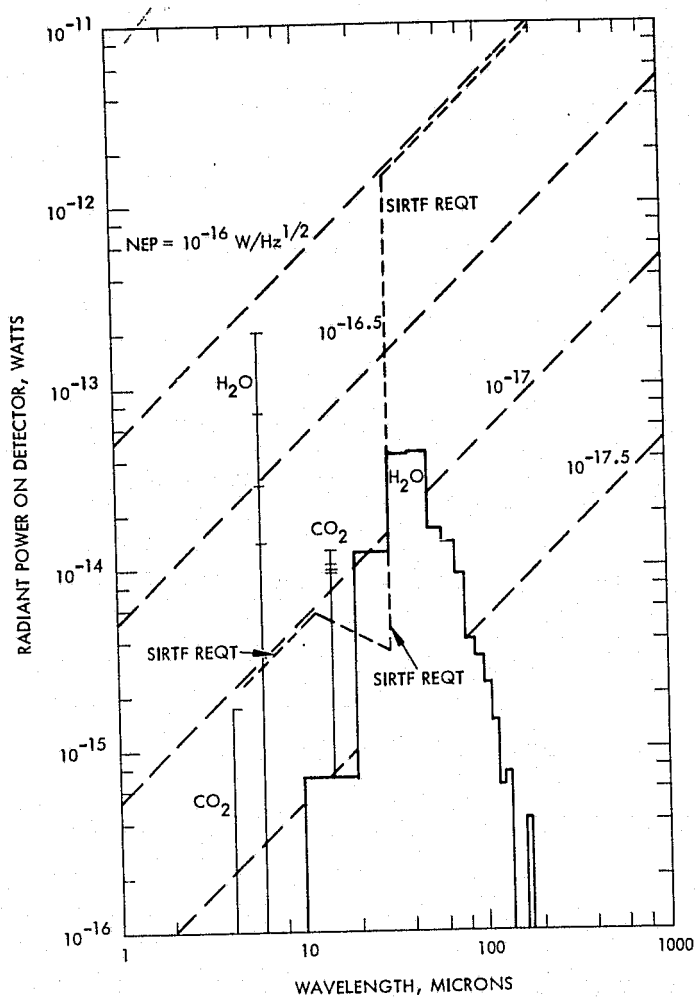


Figure 3-85. Radiant power on the 1 arc minute SIRTF detector due to water and carbon dioxide released by the Shuttle. (The SIRTF NEP requirement is shown for comparison. The $4.3 \mu\text{m}$ and $15 \mu\text{m}$ bands of CO_2 and the $6.3 \mu\text{m}$ band of H_2O are excited by collisions with molecules in the earth's atmosphere; marks are 250, 300, 350, and 400 km.)

Reference 3-26. As Figure 3-85 shows, one water and one carbon dioxide line exceed the SIRTF requirement level, although there is not enough energy in the lines to exceed the requirement over its 10μ band. The only band where contamination will limit telescope performance is 20μ to 30μ where the H_2O rotational lines exceed the NEP requirement by about a factor of 1.7.

The column density of water vapor will vary as a function of Shuttle operations, Shuttle orientation, and line of sight.

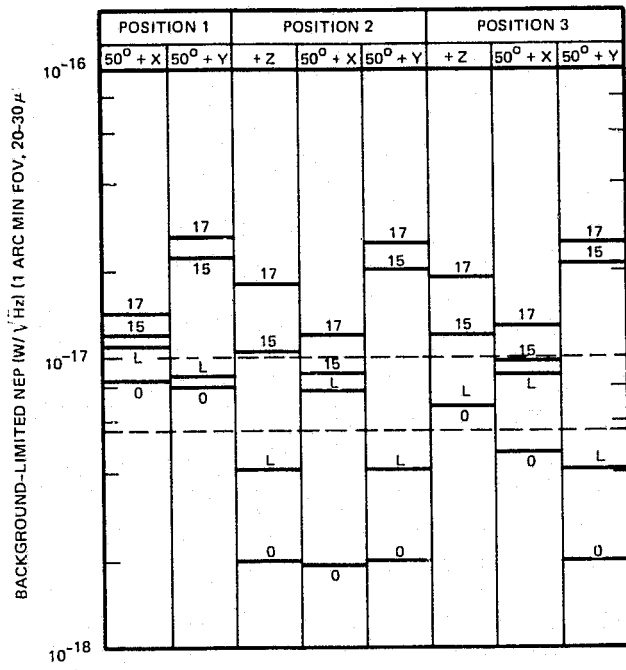
Figure 3-86 is a plot of the individual contributions to the 20 to 30μ water vapor rotation band background for various orientations of the Shuttle and the SIRTF line of sight. Definitions are as follows:

Position 1:

Top of Shuttle and payload bay facing sun.

Position 2:

Top of Shuttle and payload bay facing away from sun and earth.



POSITIONS AND LOS ORIENTATIONS ARE DEFINED IN TEXT

NEP LEVEL CODE: 0 = OFF GASSING AFTER 24 HOURS
 L = CABIN LEAKAGE PLUS OFF-GASSING
 15 = EVAPORATORS AT POSITION 15 PLUS
 OFF-GASSING PLUS LEAKAGE
 17 = EVAPORATORS AT POSITION 17 PLUS
 OFF-GASSING PLUS LEAKAGE

*NEP EQUIVALENT TO
 10^{-18} W/ $\text{Hz}^{1/2}$ FOR
 DIFFRACTION-LIMITED FOV

Figure 3-86. Water vapor rotation band radiation ($20-30\mu$) and SIRTF NEP.
 (Data from reference 3-27.)

Position 3: One side of Shuttle facing sun; payload bay is shaded.

LOS + Z: Straight up out of payload bay.

LOS $50^\circ + X$: Forward over cabin 50° from perpendicular to payload bay floor.

LOS $50^\circ + Y$: Over wings 50° from perpendicular to payload bay floor.

Note that Position 1, LOS + Z is looking directly at the sun and hence has been disregarded. In position 3, the $50^\circ + Y$ LOS is away from the sun.

The points made by Figure 3-86 are (1) for three cases with the evaporators off (position 2, + Z and $50^\circ + Y$, and position 3, $50^\circ + Y$) the NEP requirement will be met; (2) for all cases but one (position 1, $50^\circ + X$) an NEP of $1.0 \times 10^{-17} W/\sqrt{Hz}$ is obtained with the evaporators off; and (3) for three cases (position 2, + Z, and $50^\circ + X$, and position 3, $50^\circ + X$) an NEP of $1.0 \times 10^{-17} w/\sqrt{Hz}$ is obtained with the evaporators.

According to a study by Martin-Marietta for NASA-MSFC, (Reference 3-27) the water evaporators produce column densities, for some view angles, that may be in excess of the requirements. Since the evaporators are a prime concern, SIRTF planning includes tanks for water storage during periods that the evaporators are not required for heat rejection. These tanks can be emptied periodically at times when observations will not be impaired by a high level of molecular water and/or ice particles in the Shuttle vicinity. If water storage tanks are equally necessary for other astronomy payloads, it is suggested that they be made a standard optional Shuttle kit.

Another result of the Martin-Marietta study is that the water vapor column density produced by RCS engine firings is about 2-1/2 orders of magnitude higher than that shown in Figure 3-86, with the result that the limitation on sensitivity is 10 to 20 times worse than the requirement; i. e., in the low $10^{-16} W/\sqrt{Hz}$ region. This leads to the need for either (1) operation in the XLV (nose or tail down) gravity-gradient mode to reduce RCS firings to an absolute minimum; or (2) use of control moment gyros for Orbiter stabilization to eliminate the need for RCS firings during observation periods. As mentioned before, local vertical mode operation requires fine pointing by the IPS over large slew angles to provide the requisite long integration times.

Another contamination concern is purging of the fuel cells. Definition of the resulting column densities has not yet been published, but the location of the purge vents and their effect on the column density must be evaluated.

3.6.3 Zodiacal Emission Model

The thermal radiation from interplanetary dust acts as an LWIR source extended over the entire sky. The radiation is stronger in the ecliptic

plane and towards the sun. The variation in the anti-solar hemisphere is small since the radiation is dominated by particles relatively near the earth. There is little observational data to guide a theoretical description, but it is clear that zodiacal radiance limit telescope performance, across the 5 to 30μ band. The model proposed here, like others, suffers from the paucity of data about the chemical composition, and hence the optical properties, of the dust, and about its size and space density distribution.

Dust Material

The choice of dust materials used in this model is guided by observations of dust clouds associated with stars and with the dust released by comets into their tails. Cometary dust tails are thought to contribute part or all of the interplanetary dust. Spectral observations of these objects show a silicate feature at $10\mu\text{m}$. The picture is complicated by three factors: it appears that more than one kind of material is present; a given dust particle may not be homogeneous; and a certain proportion of metallic materials may be mixed in with the silicates. (Reference 3-28, 3-29, 3-30.) The detailed chemical composition is not determined from the observations but some understanding about the expected spectral distribution can be gained by assuming a material.

In order to calculate radiances from the model, the optical constants of the chosen material must be known. The simplest silicate is crystalline quartz but it is not a realistic choice. Stony meteorites which strike the earth contain minerals of the olivine family which have impurities mixed with the quartz. Andesite is an example and it is used in the present model. The optical constants are given in Reference 3-31. Andesite has a visible absorption coefficient of 380 cm^{-1} which makes an $18\mu\text{m}$ particle absorb 50 percent. The effect of this visible absorptance on the model will be discussed below.

Particle Size and Number Density Distribution

The dust particle size and number density distributions provide the basis for the zodiacal emission calculations. No ideal source of data exists on the interplanetary dust. Visible zodiacal radiance has been thoroughly studied, but it is not possible to derive unambiguous size and density distributions from the radiance data. Studies of comet radiance similarly indicate

more than one possible distribution depending on conditions during tail ejection.

Direct satellite observations (microphonics or diaphragm rupture) provide the best data, although care must be taken to avoid systematic microphonics, which contaminated some early measurements. The size distribution is plotted in Figure 3-87, which shows data from references 3-32 and 3-33. Also shown are micrometeorite counts on moon rocks (Schneider), which lie below the other estimates. For large particle radii, photographic studies of meteorites were used. Two curves are drawn through the data and used in the calculations. One is through the center and one is along an upper envelope.

The total particle density was assumed to be inversely proportional to the distance from the sun as measured by Pioneer 10, Reference 3-34.

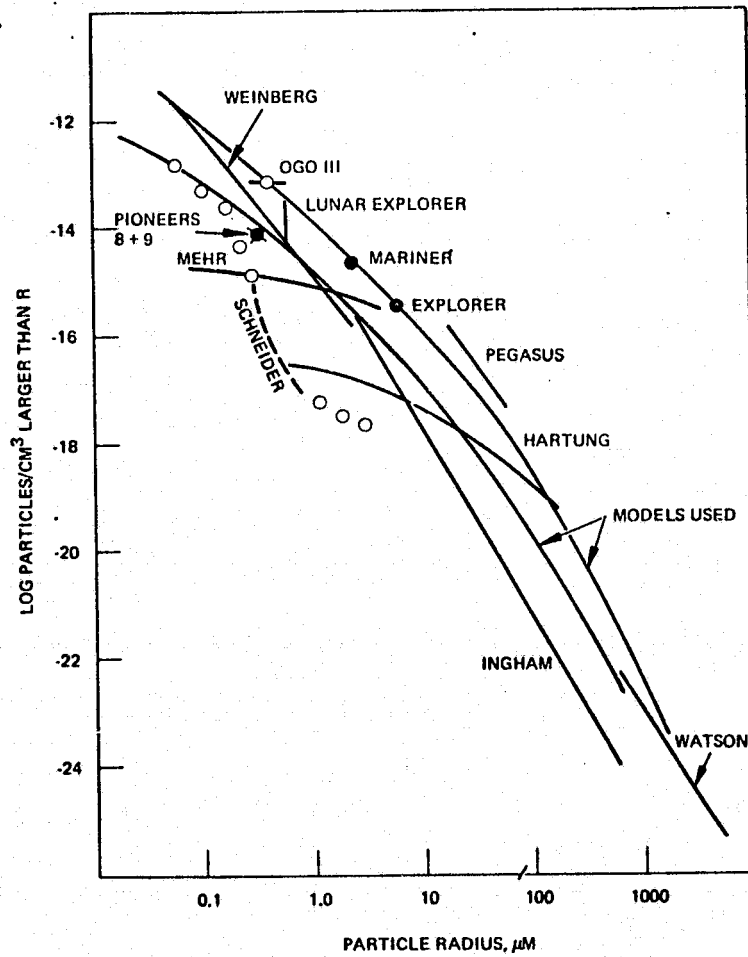


Figure 3-87. Particle size distribution.

Mathematical Statement of the Problem

The spectral radiance of zodiacal dust from a volume dV (Figure 3-88) can be expressed as

$$N(\lambda) = \int_{1 \text{ A.U.}}^{\infty} \int_0^{\infty} D(a, r) CE(\lambda, a) \frac{B(\lambda, T_a)}{\pi} da ds$$

where $N(\lambda)$ is the spectral radiance in $\text{watts}/\text{cm}^2 - \mu\text{m} - \text{sr}$ at wavelength λ ,

$D(a, r)$ is the number of particles per cm^3 at distance r from the sun with a radius between a and $a + da$,

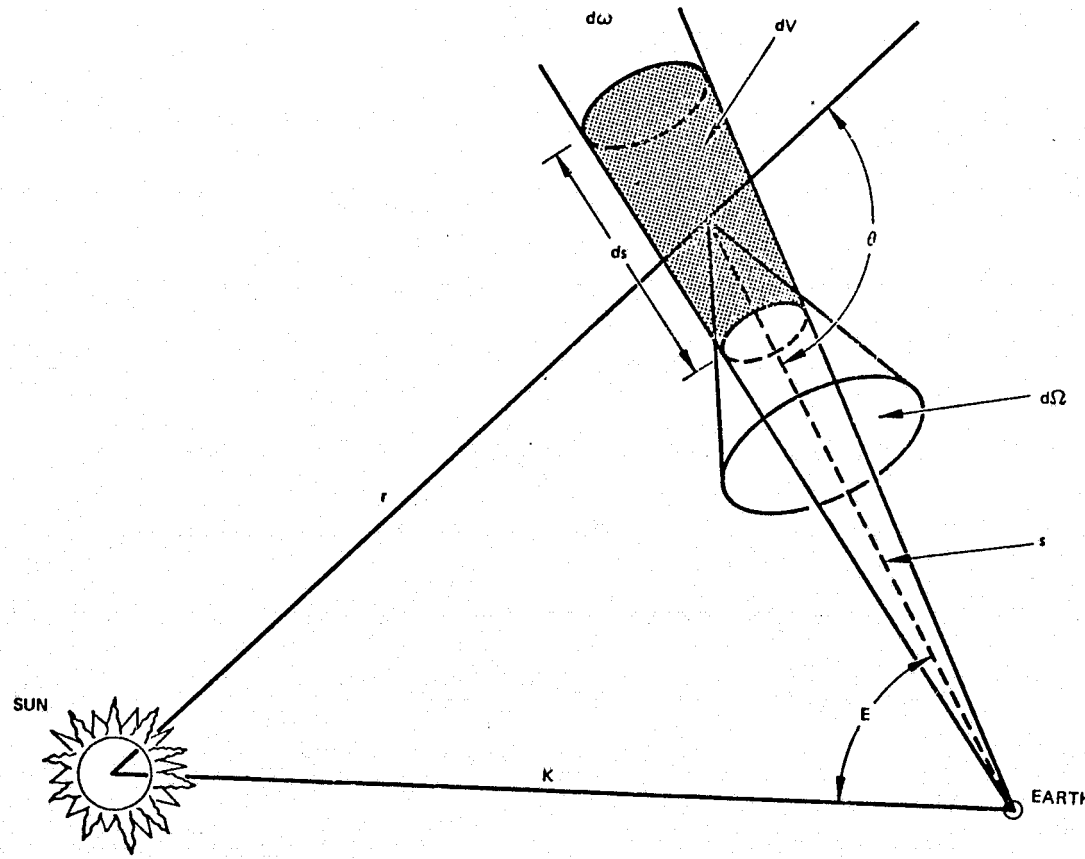


Figure 3-88. Geometry of integration scheme. (Drawing is in the plane of the ecliptic.)

$B(\lambda, T_a)$ is the Planck radiation function for a particle with a temperature T_a in watts/cm² - μm and
 $CE(\lambda, a)$ is the emission cross section of a particle with radius a at a wavelength λ such that the spectral radiant intensity J in watt - sr - μm emitted from the particle is given by

$$J(a, \lambda) = CE(\lambda, a) \frac{B(\lambda, T_a)}{\pi} \text{ and}$$

ds is along the line of sight.

The temperature T_a of a particle with radius a is given in the relation expressing the balance between the energy absorbed by the particle from the sun and the energy re-emitted thermally when the particle is in equilibrium. The relation is

$$\int_0^{\infty} CE(a, \lambda) B(\lambda, T_a) d\lambda = \frac{R_o^2}{2r^2} \int_0^{\infty} CA(a, \lambda) B(\lambda, T_o) d\lambda$$

where

T_o is the temperature of the sun,

R_o is the radius of the sun,

r is the distance from the sun to the particle and

$CA(\lambda, a)$ is the absorption cross section such that

$$CA(\lambda, a) = CE(\lambda, a)$$

for any given wavelength.

In addition, the visible radiance from the interplanetary dust as predicted by this model will be calculated to determine whether it is constant with visible observations. It is given by

$$N(\lambda) = \int_{1 \text{ A.U.}}^{\infty} \int_0^{\infty} \frac{B_o R_o^2 K^2}{r^3 (2\pi)^2} D(a, r) |S(\theta)|^2 da ds$$

where the terms have their previous meaning and

$$K = 1.5 \times 10^{13} \text{ cm}$$

$S(\theta)$ is the scattering amplitude function (Reference 3-35).

Because the average particle size is on the order of the wavelength of light being scattered or absorbed, Mie theory must be used to express $CE(\lambda, a)$ and $S(\theta)$.

Mie Theory Approximations

Three realms of $2\pi a/\lambda$ are defined. The particles are assumed to be smooth homogeneous spheres.

Realm 1: $2\pi a/\lambda \leq 1$

$$CE(\lambda, a) = \frac{8\pi a^3}{\lambda} \left[\frac{2nk}{(n^2 - k^2 - 2)^2 + 4n^2 k^2} \right]$$

Here n and k are the real and imaginary parts of the index of refraction (Reference 3-35).

Realm 2: $\frac{2\pi a}{\lambda} > 1$ and $a < \frac{3}{4\alpha_\lambda}$

where $\alpha_\lambda = \frac{4\pi k}{\lambda}$, the absorption coefficient.

This realm contains particles which have a circumference greater than the wavelength and an absorption coefficient low enough at that wavelength so that not all energy is absorbed (i.e., they are not opaque at that radius). The condition $a < \frac{3}{4\alpha_\lambda}$ for translucence is due to Kaiser (Reference 3-36) in addition, this simplification requires that the reflectivity at that wavelength is negligible. In this case the cross section is (References 3-35 and 3-36).

$$CE = \frac{4\pi}{3} a^3 \alpha(\lambda)$$

This condition is met for silicates, i.e., at wavelengths where the quartz is translucent, the reflectivity is simultaneously low.

Realm 3: $2\pi a/\lambda > 1$ and $a > \frac{3}{4\alpha_\lambda}$

i.e., the particles are opaque. The cross section in this case is given (for spherical particles) by Reference 3-36)

$$CE = \left[1 - \int_0^{\pi/2} \frac{1}{2} \left(|r_1|^2 + |r_2|^2 \right) d(\cos^2 \phi) \right] \pi a^2$$

where

r_1 and r_2 are the Fresnel reflection coefficients in the two directions of polarization and $90-\phi$ is the angle of incidence on the particle.

Roughly speaking, CE in this case is $1-R$, the reflectivity. Hence, if R is large as it can become in the reststrahlen bands, the emission cross section becomes small.

The approximation for $S(\theta)$ is made in two steps. First assume the particles are opaque enough so that only reflected radiation contributes to the energy. Then,

$$|S(\theta)|^2 = \left(\frac{1}{4} \frac{2\pi}{\lambda} \right)^2 \left(|r_1|^2 + |r_2|^2 \right)$$

Second, assuming that the reflectivity and absorption are small, a refracted component of energy is added which passes through the particles

$$|S(\theta)|^2 = \frac{4\mu^2 k^2 a^2}{(4\mu^2 + \theta^2)^2} \left(\frac{1 - |r_1|^2 + |r_2|^2}{2} \right)$$

Both approximations assume $2\pi a/\lambda \gg 1$ which is true for most particles in the visible. These approximations must be applied consistently as discussed below.

Results and Discussion

The visible results are discussed first because they place some constraints on the particle size and density distributions. In particular, in the expansion of the equations, the integral

$$\int_0^{\infty} a^2 D(a, r) da$$

appears as a scale factor to the radiance. It represents the total scattering area summed over all particles. Because the number of particles with sizes between a and $a + da$ is proportional to a^{-3} for the size distribution used here, the integral is dominated by the smallest particles. The size distribution extends down to a radius of $0.1 \mu m$. Figure 3-89 shows the results for the lower size-density distribution chosen in Figure 3-87.

The curves for reflected and refracted energy are averages over the two planes of polarization. However, only the reflected energy shows significant polarization. Note first that reflection by itself does not produce enough energy to equal the visible observations. It might come close if the higher density curve were used from Figure 3-87 but that would require that no component of refracted energy be present and the absorption coefficient necessary to make the smallest particles opaque would be unrealistically high.

Given that refracted energy is present even if it is only from the smallest particles, then Figure 3-89 shows that the refracted energy dominates. At elongations between 10 and 90 degrees, the refracted component lies two to six times below the visible data but cannot produce much energy at large elongation angles due to the nature of refraction in a spherical particle. The model assumes that only one pass through the particle occurs; so, in fact, internal reflections may be important when the high angles of incidence are

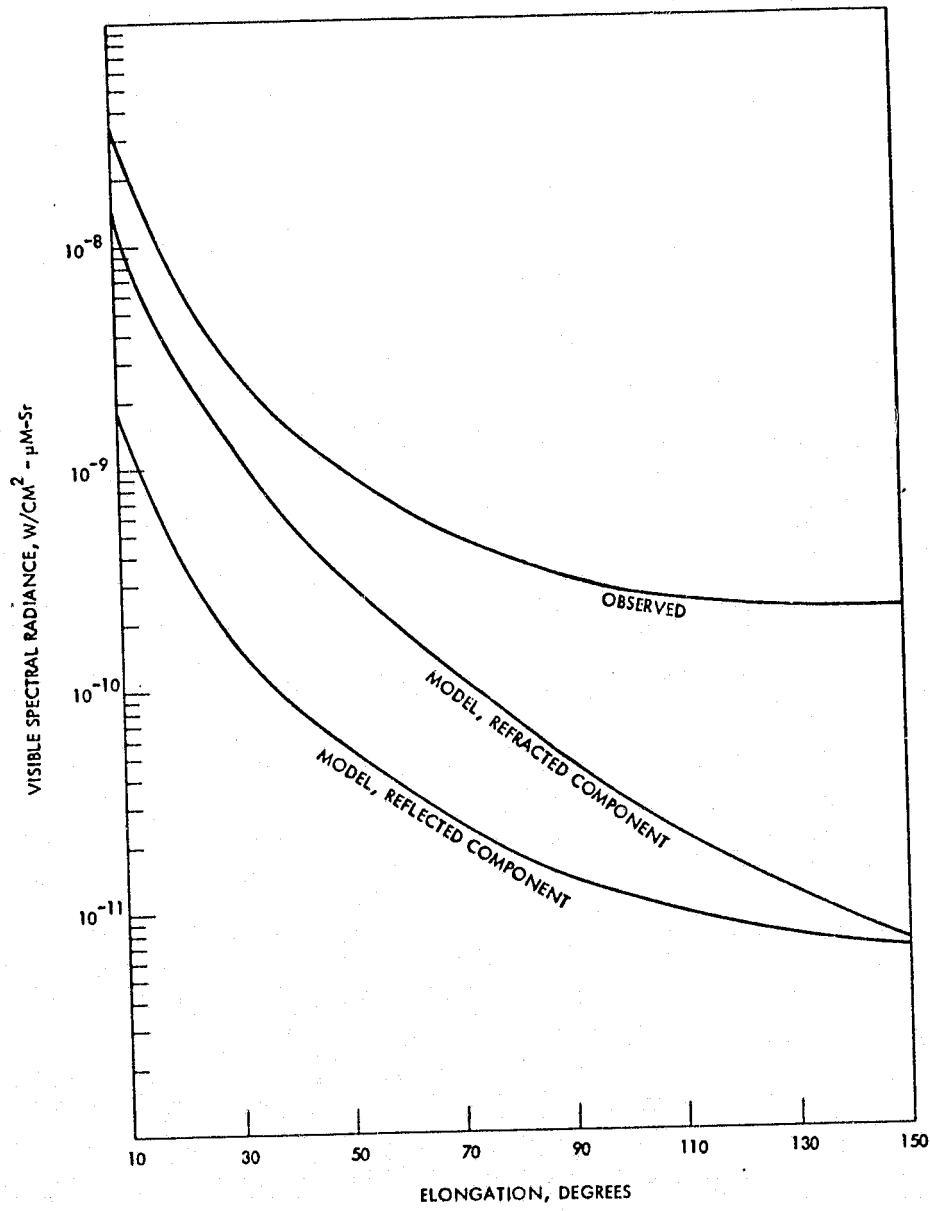


Figure 3-89. Visible zodiacal radiance for assumptions of only a refracted and only a reflected component. (Average particle density model from Figure 3-88.)

encountered for a single pass through the particle at large elongations. An average albedo in this model was about 0.2.

In addition the reflected component could be larger at large elongations if the index of refraction in the visible and, hence, the reflectivity were larger than for andesite.

Two conclusions are drawn about the material and density distributions from the visible model. First, the visible continuum opacity of andesite does not affect the scattering of the visible light in the model because the small particles dominate. Second, the density distribution at least for the smaller particles should lie between the two chosen in Figure 3-87.

Figures 3-90, 3-91, and 3-92 are plots of the infrared spectral radiance produced in the model presented here. Figure 3-90 shows the effects of additional continuum opacity; it is not large. It further shows the effects of the choice of particle size and density distributions. Figure 3-91 shows the effect of elongation on spectral distribution and Figure 3-92 shows the spectral radiance as a function of elongation.

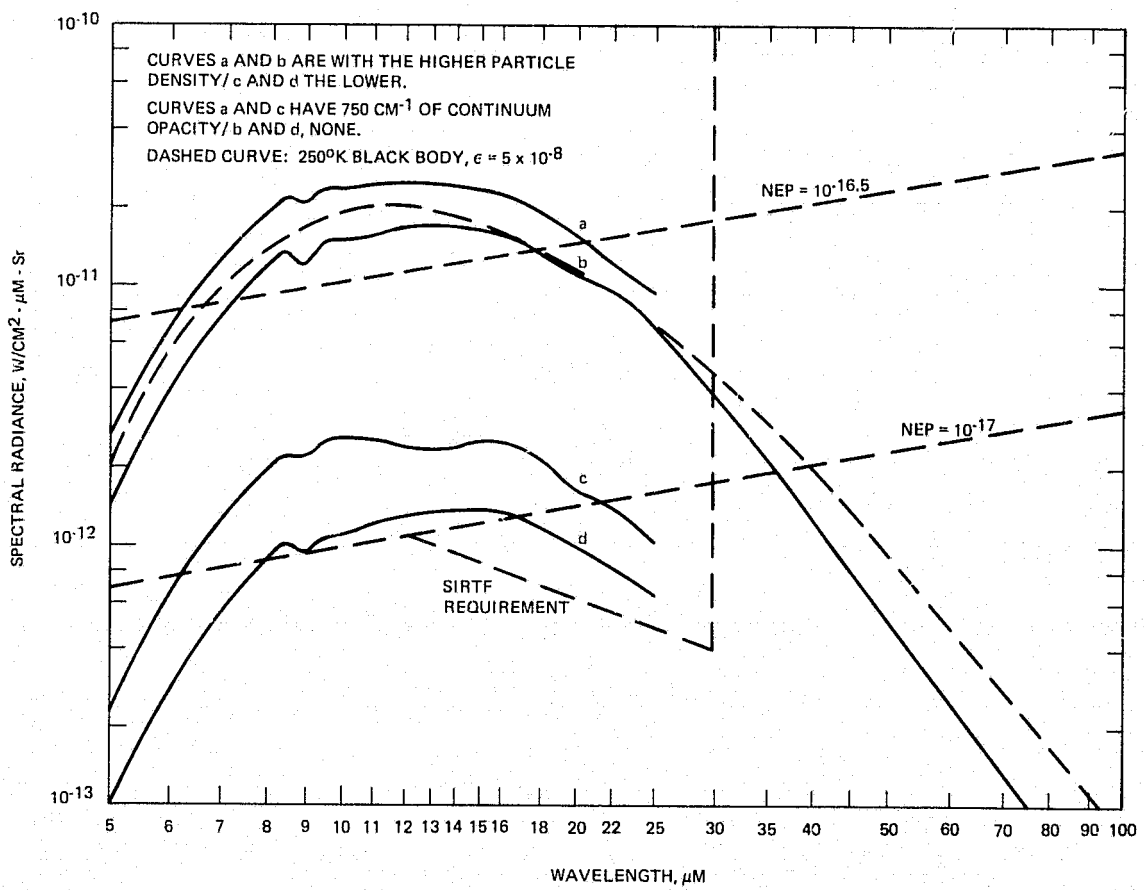


Figure 3-90. Infrared zodiacal radiance in the plane of ecliptic at 90° elongation.

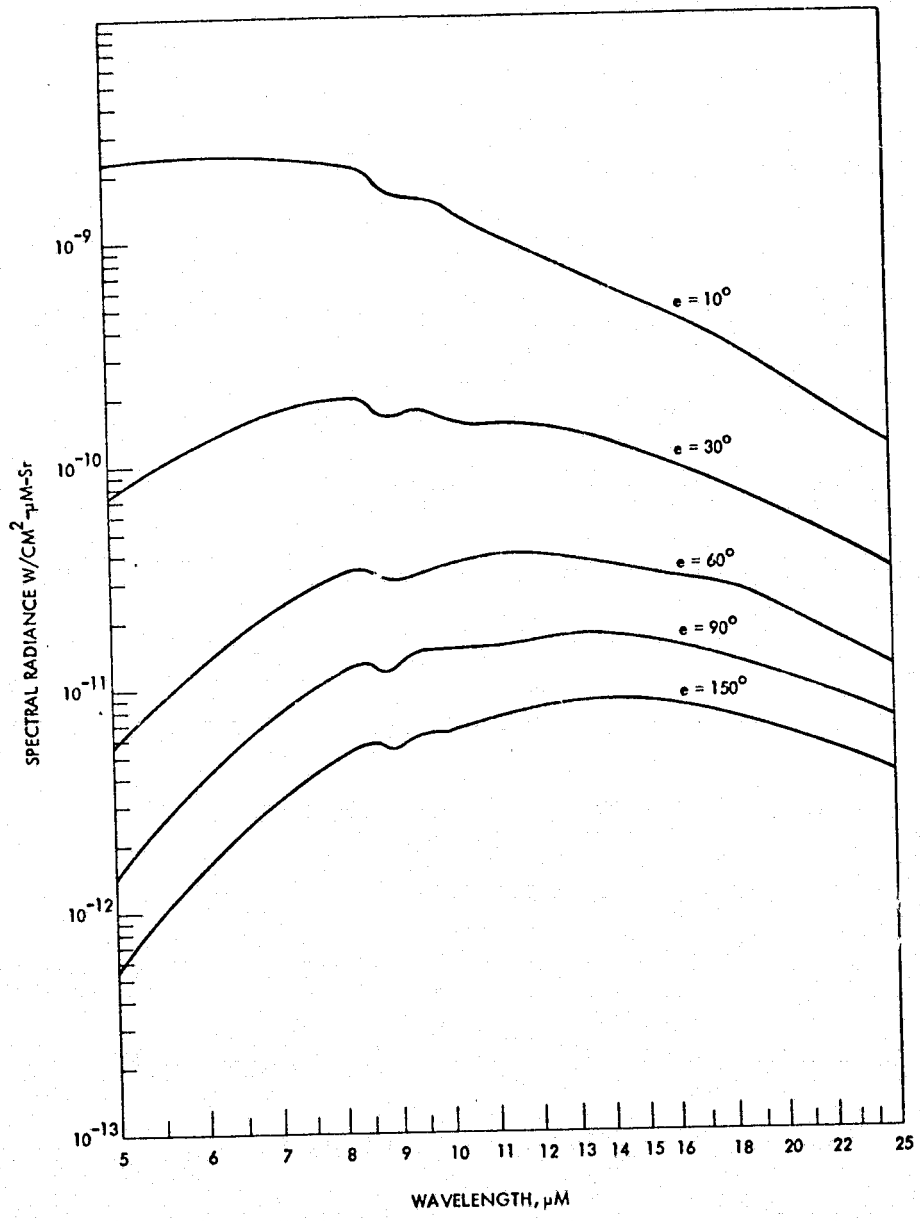


Figure 3-91. Infrared zodiacal radiance for five elongations for curve b in Figure 3-90.

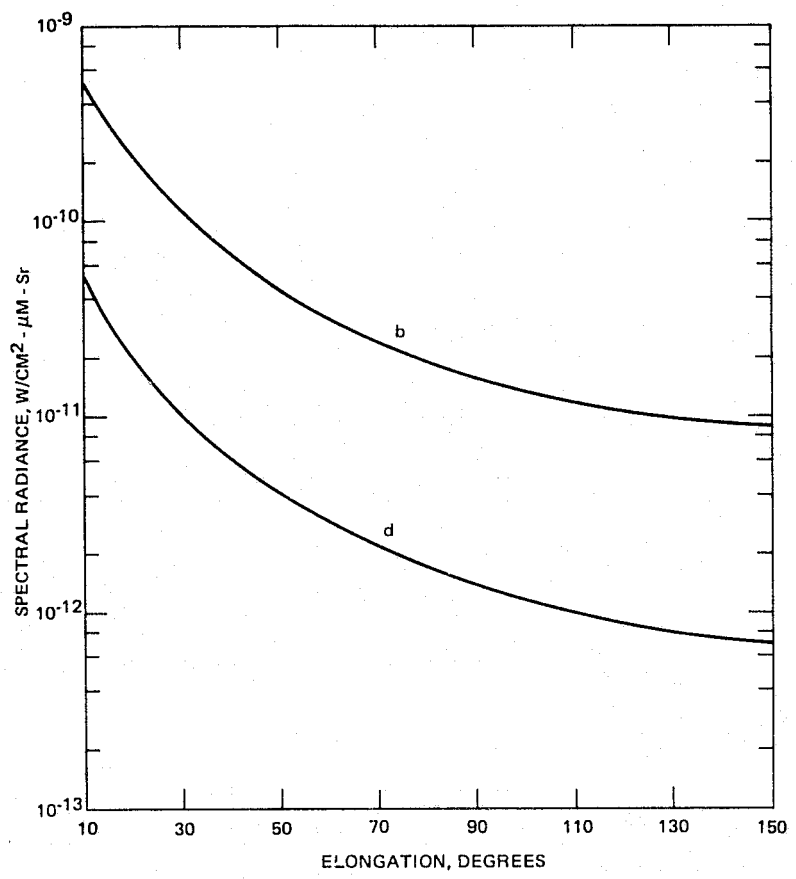


Figure 3-92. Infrared zodiacal radiance as a function of elongation for curves b and d in Figure 3-90 at a wavelength of 15 μm .

The most obvious feature of the radiance curves in Figure 3-90 is the lack of spectral lines. The broad curves are essentially a mixture of blackbody curves of different temperatures. A small dip in the spectral curve at 9 μm is due to the SiO_2 reststrahlen band. The energy is coming primarily from particles with sizes in the 10 μm size which have emittances characteristics of large opaque particles (i.e., realm 3, $\text{CE} \approx 1$ - reflectivity is only 35 percent for andesite in the 9 μm SiO_2 reststrahlen band, the dip is not pronounced and is more washed out by the upper curves of each pair due to the added continuum opacity of 750 cm^{-1} . The difference between the two curves is attributable to the difference in the two size-density distributions used. A preferred curve lies between the two sets.

The α/ϵ values are essentially equal to one for particles larger than 25 μm with temperatures around 275°K at 1 AU. Smaller particles have α/ϵ less than one because the visible opacity is much less than the infrared opacity and the particles are optically thin to visible radiation. The temperatures range down to 160°K for the 0.4 μm particles.

Figure 3-92 shows that the curves represent cooler dust on the average at larger elongations.

Figure 3-90 also shows the SIRTF NEP requirement, as well as several other lines of constant NEP. It shows that SIRTF will be background limited by zodiacal emission over the 5 to 30 μ band. In particular the zodiacal emission is predicted to be at least a factor of 50 higher than the emission from the 10^{12} molecules/cm² column density of water vapor discussed above.

3.6.4 Radiation Effects on Detectors

SIRTF will operate in a natural radiation environment consisting of trapped electrons and protons. The effects of these particle radiations on potential detector candidates to be used in the Multiple Instrument Chamber (MIC) of SIRTF were studied. The work task was basically threefold; first, the radiation levels incident on the SIRTF and the particle fluxes transmitted through the baseline sensor shielding were defined. Second, a survey of candidate detector data was performed in order to establish clear environment operating conditions. Third, the effects of the transmitted radiation on the candidate MIC detectors were evaluated in order to assess their operability and survivability. The results are summarized here; Reference 3-37 gives the complete data.

The average false alarm rates generated in the detectors were relatively low outside the Van Allen belts and South Atlantic Anomaly. The peak transmitted fluxes experienced in the South Atlantic Anomaly cause the highest event rates, but by keeping the detector size small the false alarm rate can be kept to a relatively low level to avoid significant excess noise increase, and hence, degradation in detector performance (D* or NEP).

Pulse suppression circuits can be used to gate out the single false alarms as long as the event rate is not too high and the voltage pulses decay fast enough to avoid pulse pile-up. Additional high atomic number material shielding (e.g., tungsten or tantalum) around the detectors in the MIC is effective in reducing the bremsstrahlung false alarm rates which are mainly caused by photons whose energies are less than 0.3 MEV. Approximately 1.68 gm/cm² (1mm) of tantalum is required to reduce the bremsstrahlung levels by an order of magnitude. Shielding to reduce the higher energy proton event rate takes large amounts of material and is not practical.

A distribution of pulse amplitudes will be generated in the detectors since there are a spectrum of incident proton and bremsstrahlung photon energies and detector chord lengths vary depending on detector size. The average voltage pulse heights are expected to be observable above the baseline noise levels for most of the detector-preamplifier candidates evaluated. The shielding inherent in the SIRTF-MIC structure reduces by a large fraction the number of lower energy protons and bremsstrahlung photons incident on the detectors. These lower energy particles ($E_p < 1-10$ MEV, $E_\gamma < 0.03$ MEV) generate smaller pulses which are below the clear environment noise threshold for pulse suppression or gating. Additional tantalum shielding as discussed above is effective in further reducing the number of smaller pulses generated by bremsstrahlung-induced secondary electrons.

No permanent damage is expected for any of the detector candidates up to the estimated maximum dose level of 12.6 Rad(Si) for a 30-day period.

The radiation environments that SIRTF will have to operate and survive in are based on the mission duration and orbital parameters given in SIRTF specification 2-24483 (Reference 3-25) and SIRTF/Orbiter/Spacelab Tradeoff Report (Reference 3-38). The primary radiation environments at nominally circular orbit altitudes of 300 km and higher over a range of orbital inclinations (from 28.5° to 57° from Kennedy Space Center, and 56° to 104° from Vandenberg Air Force Base) will consist of electrons and protons within the Van Allen belts.

Four potential orbits for the SIRTF system were studied with regard to radiation background levels. The orbits are all circular with the following altitudes and inclinations:

<u>Orbit</u>	<u>Altitude (KM)</u>	<u>Inclination ($^{\circ}$)</u>
1	300	28.5
2	300	70.0
3	600	28.5
4	600	70.0

The radiations of concern are the cosmic ray protons, the trapped electrons and protons in the earth's magnetic field at relatively low altitudes (predominantly in the South Atlantic Anomaly), and the bremsstrahlung radiation generated by the electrons penetrating the SIRTF structures and shields. The latest NASA radiation maps (see Reference 3-39) and computer codes (ORBIT, ORP, and MODEL) were used to compute particle fluxes as a function of time (alternatively, position) over a 24-hour period for each of the four orbits.

Figure 3-93 shows the predicted event rate outside the Van Allen belts and South Atlantic Anomaly. Event rates are below one per second for all detector types and all expected detector sizes. While each experimenter will be free to make his own decision, for most experiments no pulse suppression circuits are expected to be necessary.

Figures 3-94 and 3-95 show the same data for protons in the South Atlantic Anomaly. The event rates range above 10 per second at 300 km altitudes, and above 100 per second at 600 km altitude. Thus pulse suppression circuits will be needed, or data-taking may have to be temporarily discontinued. Event rates in the smaller detectors (at shorter wavelengths) will still be low.

Figures 3-96 and 3-97 reflect the fact that electron fluxes are confined mainly to the horns of the Van Allen belts, so that the 300 km, 28.5° orbit encounters low fluxes; event rates range up to a few per second. Figure 3-97 shows conditions for the other orbits which encounter higher fluxes ($\sim 300/\text{sec}$) at the long wavelengths. High-atomic number shielding is

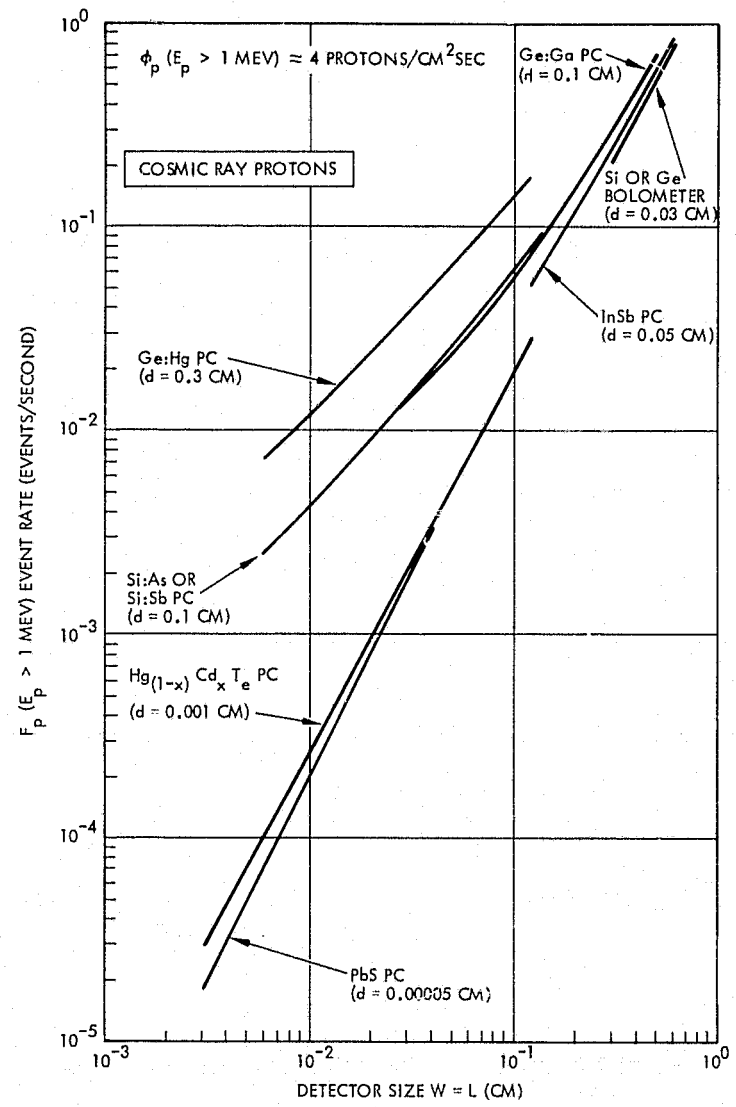


Figure 3-93. Detector event rate as a function of detector size.
(Between peak, cosmic ray proton background.)

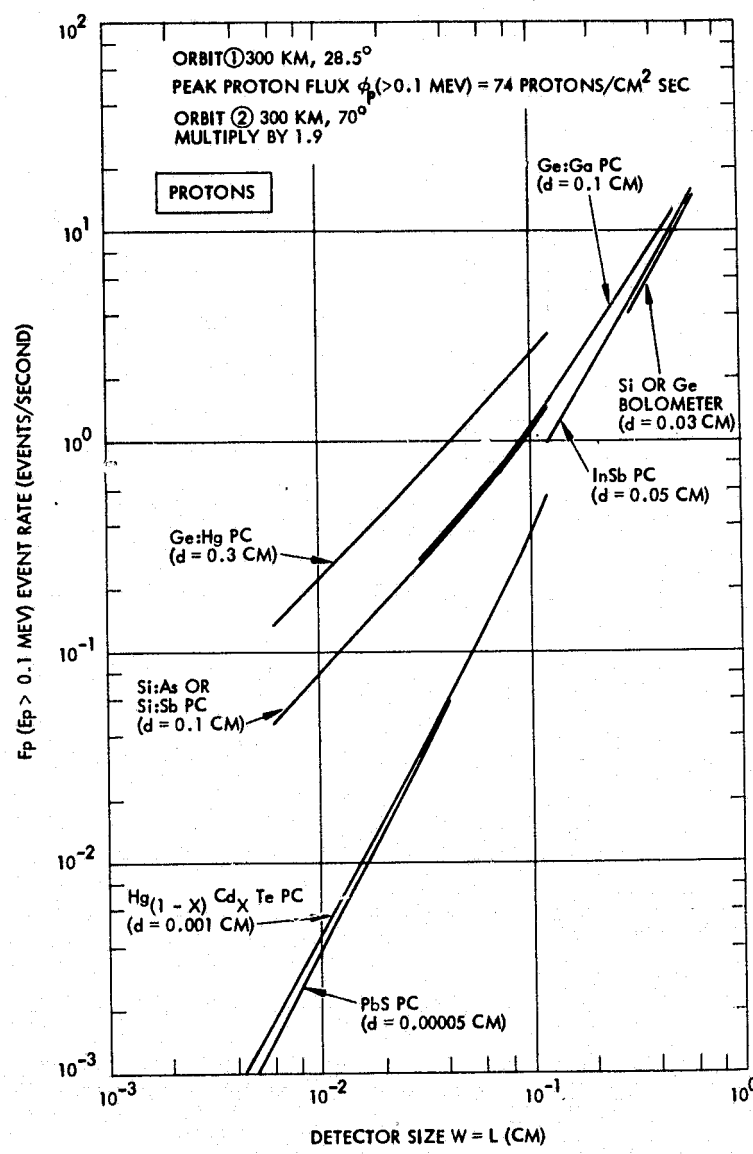


Figure 3-94. Comparison of detector event rates (peak) as a function of detector size.

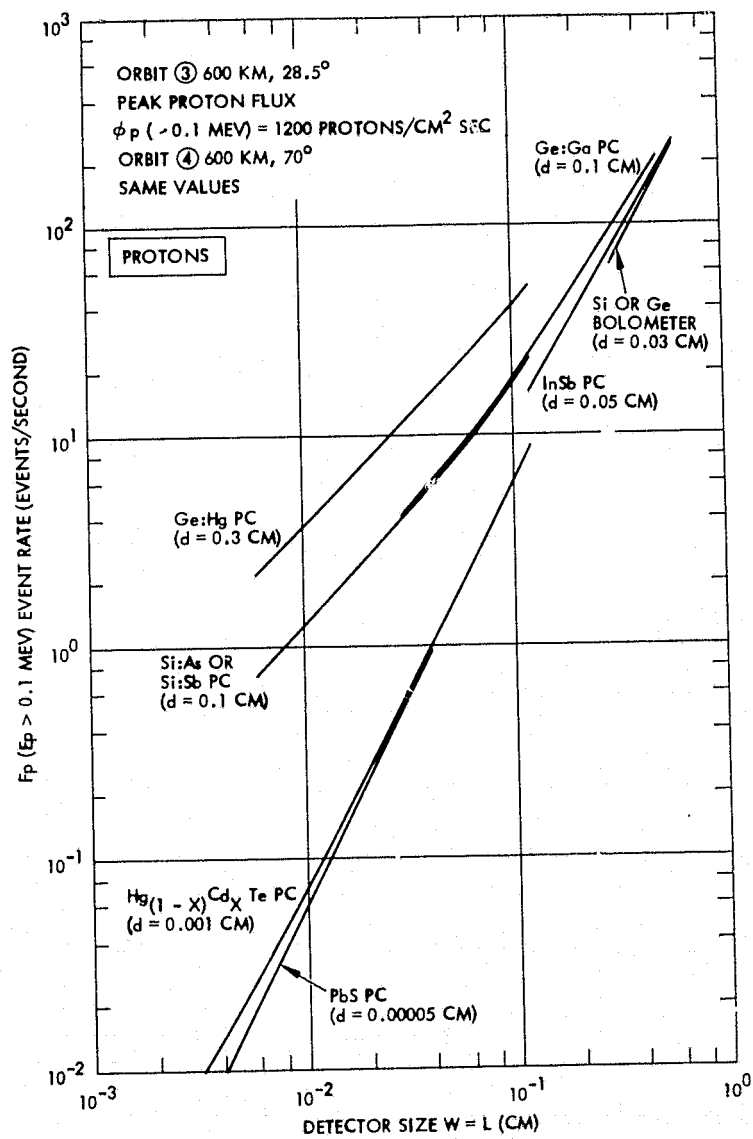


Figure 3-95. Comparison of detector event rates (peak) as a function of detector size.

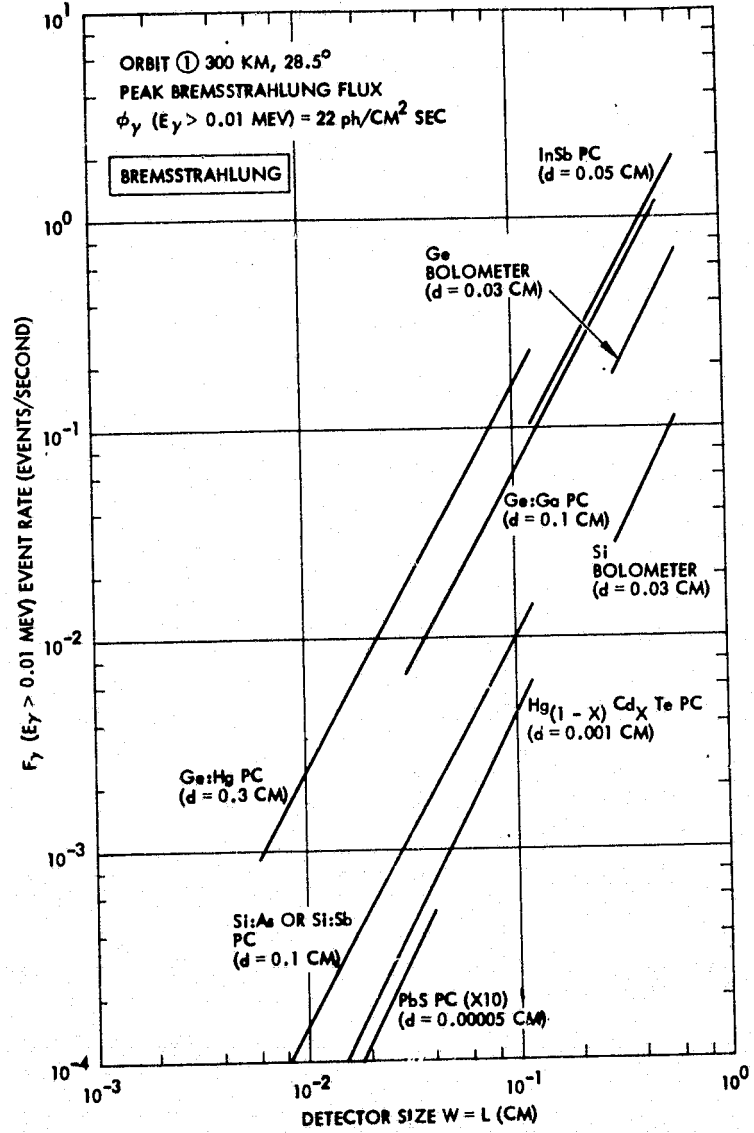


Figure 3-96. Comparison of detector event rates (peak) as a function of detector size.

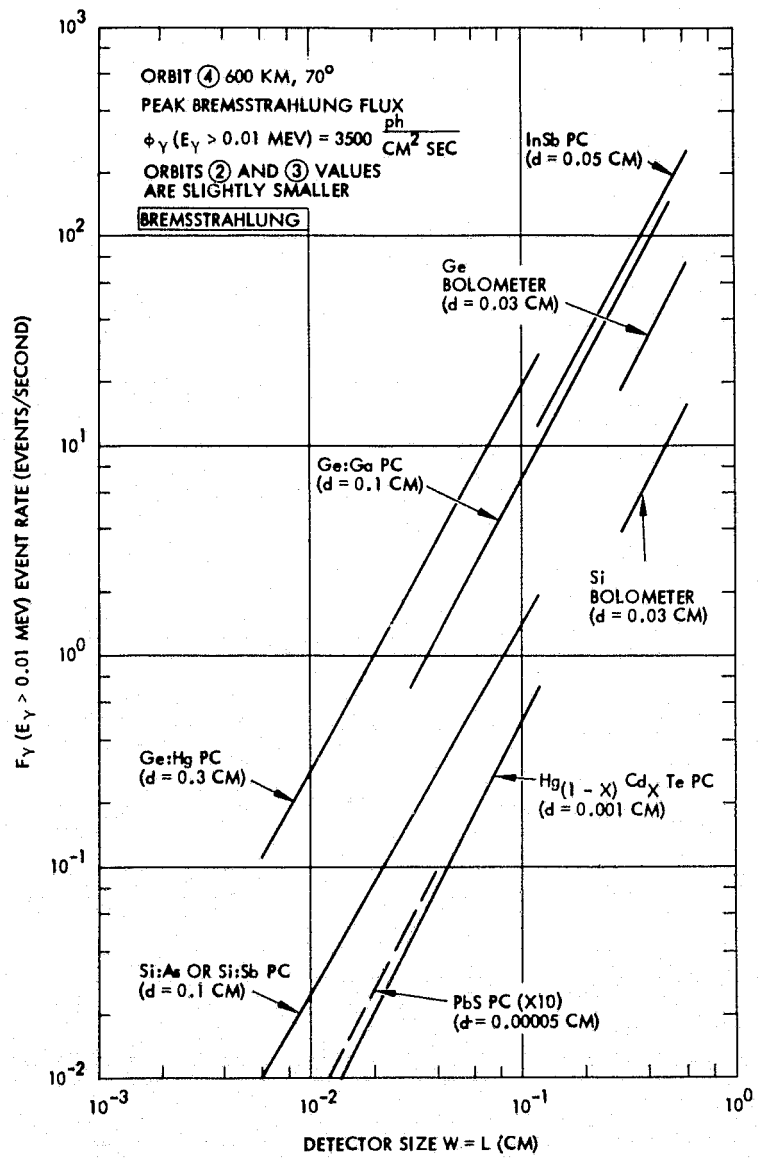


Figure 3-97. Comparison of detector event rates (peak) as a function of detector size.

effective against Bremsstrahlung, and a few millimeters of tantalum will reduce the event rate by two orders of magnitude.

The conclusions are thus that only the large, long wavelength detectors will experience event rates that can interfere with data taking, and that the 300 km, 28.5° inclination orbit is the best in terms of nuclear radiation effects.

REFERENCES FOR SECTION 3

- 3-1. Arnold, F., et. al.; "Infrared Spectral Reflectance of Plume Species on Cooled Low Scatter Mirrors," Air Force Rocket Propulsion Laboratory, Edwards, California, AFPL-TR-73-52, September 1973.
- 3-2. Wood, B. E., et. al; "Spectral Absolute Reflectance Measurements of CO₂ Frosts in the 0.5 to 12.0 Micron Region," ASTM/IES/AIAA Fifth Space Simulation Conference, Paper No. 41, 1970.
- 3-3. Wood, B. E., et. al.; "Infrared Reflectance of Water Frosts Condensed on Liquid-Nitrogen-Cooled Surfaces in Vacuum," ARO Inc., Arnold Air Force Station, Tennessee, AEDC-TR-70-215, December 1970.
- 3-4. Viehmann, W., et. al.; "Effects of Surface Contamination on the Infrared Emissivity and Visible-Light Scatter of Highly Reflective Surfaces at Cryogenic Temperatures," Goddard Space Flight Center, Greenbelt, Maryland, NASA TN D-6585, February, 1972.
- 3-5. Young, R. P.; "AEDC Mirror Scattering Measurements," ARO Inc., Arnold Air Force Station, Tennessee, Presented at the Twenty-First Midcourse Measurements Meeting, November 1973.
- 3-6. Scheele, S. R.; "Scattering Characteristics of Mirrors and the Associated Inverse Scattering Problem," Hughes Aircraft Company, Culver City, California, M73-62, November 1973.
- 3-7. Loveridge, R.; "Scattering Measurements of Four Mirrors and One Black Anodized Aperture Stop," Hughes Aircraft Company, Culver City, California, IDC 27789/425, February 1973.
- 3-8. A. L. Goldsmith, T. E. Waterman, H. J. Hirschorn, "Handbook of Thermo Physical Properties," Revised Edition, the MacMillan Company, New York, 1961.
- 3-9. T. F. Durham, R. M. McClintock, R. P. Reed, "Cryogenic Materials Data Handbook," Part II, G-L, Cryogenic Engineering Laboratory, Boulder, Colorado.
- 3-10. "Beryllium Mirror Technology State-of-the-Art Report," December 1972, R. A. Paguin and W. R. Goggin, Perkin-Elmer IS 11393.
- 3-11. "Thermal Expansion of Technical Solids at Low Temperatures," R. J. Correcini and J. J. Gniewek, NES Monograph 29, 19 May 1961.
- 3-12. SPIE 19th Annual Technical Symposium, August 18-22, 1975, Town and Country Hotel, San Diego, California, Papers MO-105, MO-109, and MO-118.
- 3-12A. R. M. Shemenski, et. al., "Kanigen Plating on Beryllium" Special Technical Report, Batelle Memorial Institute, Columbus, Ohio and Perkin-Elmer Corporation, Norwalk, Conn. April 1968.
- 3-13. Hughes Aircraft Company IDC 7212.2/73 dated 23 September 1975, "Approximate Sizing of the Thickness of the SIRTF Telescope Mirrors," from D. L. Pollet to S. G. McCarthy.

- 3-14. L. G. Cook, R. S. Kebo and A. D. Warren, "Shuttle Infrared Telescope Facility: Optical Performance Analysis Report," (Data Item ID1-2. a.), Hughes Aircraft Company, August 1975.
- 3-15. D. L. Pollett, "Shuttle Infrared Telescope Facility: Mechanical Design Tradeoff Report," (Data Item ID1-1. i.), Hughes Aircraft Company, to be published.
- 3-16. S. Temoshenko and S. Woinowsky-Krieger, Theory of Plates and Shells, McGraw-Hill Book Co., New York, 1959.
- 3-17. W. Griffel, Plate Formulas, Frederick Ungar Publishing Co., New York, 1968.
- 3-18. Optical Telescope Technology, Workshop Held at Marshall Space Flight Center, Huntsville, Alabama, April 29 - May 1, 1969, NASA SP-233, pg. 219-239.
- 3-19. "MRI/STARDYNE 3 Static and Dynamic Structural Analysis Systems User Information Manual," Publication Number 86603500, Control Data Corporation, 1974.
- 3-20. "MRI/STARDYNE Static and Dynamic Structural Analysis System Theoretical Manual," Publication Number 86616300, Control Data Corporation, 1974.
- 3-21. "Payload Effects on Shuttle Orbiter Payload Bay Internal Acoustic Environment," F. J. On and J. P. Young, Memorandum Report Number 751-35, Goddard Space Flight Center, August 4, 1975.
- 3-22. Shuttle Infrared Telescope Facility, Thermal Analysis Report (Data Item ID1-2.d) Hughes Aircraft Company, October 1975.
- 3-23. Shuttle Infrared Telescope Facility, Preliminary System Tradeoff Report (Data Item I. D1-1.a), Hughes Aircraft Company, October 1974.
- 3-24. J. P. Murphy, K. R. Lorell, and C. D. Swift, "A Computer-Aided Telescope Pointing System Utilizing a Video Star Tracker". NASA TMX-62, 505, 1976.
- 3-25. "Performance Requirements for Space Shuttle Infrared Telescope Facility (SIRTF)" Specification 2-4483, NASA-Ames Research Center, Moffett Field, California, July 15, 1974.
- 3-26. Simpson, J. P., and Witteborn, F. C., "The Effect of the Shuttle Contaminant Environment on a Sensitive Infrared Telescope" To be published, 1976
- 3-27. Bareiss, L. E., et al., Payload/Orbiter Contamination Control Requirement Study Final Report, Martin Marietta Aerospace Corporation, Denver, CO, 1974.

3-28. Rieke, G. H., Low, F. J., Lee, T. A., and Wisniewski, W.; "Infrared Observations of Comet Kouhoutek", Proceedings Comet Kouhoutek Workshop, Marshall Space Flight Center (1974).

3-29. Aannestad, P. A., Astrophysical Journal, 200, pp. 30-41, August, 1975.

3-30. Ney, E. P., Icarus, 23, p. 551, 1974.

3-31. Pollack, J. B., Toon, O. B., and Khare, B. N., Icarus, 19, pp. 372-389, 1973.

3-32. Schneider, E., Proceedings of the Lunar Science Conference IV, Houston, Texas, Vol. 3, p. 3255-3276, March 5-8, 1973.

3-33. Berg, O. E., Gerloff, U., Journal of Geophysical Research, Space Physics, 75, p. 6932, 1970.

3-34. Soberman, R. K., Neste, S. L., Lichtenfeld, K., Journal of Geophysical Research, 79, p. 3685, 1974.

3-35. Van de Hulst, H. C., Light Scattering by Small Particles, John Wiley and Sons, Inc., New York, 1957.

3-36. Kaiser, C. B., The Thermal Emission of Interplanetary Dust Cloud Models, PhD. Dissertation, Univ. of Chicago 1968, Univ. Microfilms 68-12, 409.

3-37. Shuttle Infrared Telescope Facility: Radiation Effects Analysis Report (Data Item ID1-2.9) Hughes Aircraft Company, December 1975.

3-38. "SIRTF/Orbiter/Spacelab Tradeoff Report: Orbiter/Spacelab Capabilities with Respect to SIRTF Requirements, Data Item ID1.-1.l., May 1975, Grumman Aerospace Corporation.

3-39. M. J. Teague, et al., NASA Radiation Models, NSSDC documents 72-11, 13; 74-3, 10, 13, dated 1973-1975.

4. MAJOR SYSTEM TRADES

Tradeoffs between two or more design approaches were carried out at all levels of the SIRTF Design Study. Tradeoffs which chiefly affect only one subsystem are discussed in the appropriate section of this report or in the detail reports. The tradeoffs discussed here are those which impact two or more major subsystems.

Section 4.1 compares double-folded Gregorian and Cassegrainian telescopes. Image quality over the field and over the space chopping angles is more uniform in the Gregorian (in which the second folding mirror is tilted) than in the Cassegrainian (in which the secondary mirror is tilted). Off-axis rejection for static backgrounds is somewhat better for the fully baffled Cassegrainian than for the Gregorian; however, the advantage of the smaller central obscuration in the Cassegrainian is lost due to obscuration by the baffle on the secondary mirror. Performance characteristics of a longer Cassegrain without the secondary mirror baffle and of a comparably-sized Gregorian are also shown for comparison. Off-axis rejection during space chopping is shown to be better in the Gregorian, due to suppression of diffraction at the edge of the field and hence a more uniform focal plane background.

Section 4.2 is a discussion of the SIRTF aperture diameter. Reduction of the diffraction blur is the reason for wanting the larger aperture. Shuttle, Spacelab, and IPS limitations are examined to determine the constraints. All limitations lie in the range 1.6 to 1.8 m, which is compatible with the maximum 1.6 m diameter primary mirror blanks available in beryllium.

Section 4.3 is a short discussion of various focal plane star tracker sensors. The CCD sensor provides all the desired functions in a compact device. Operation at SIRTF temperatures, however, remains to be demonstrated.

Section 4.4 summarizes a study of the relative merits of SIRTF and a large ambient telescope. The ambient telescope has a resolution advantage of about 2, but far poorer sensitivity due to both steady backgrounds and scan modulation.

Section 4.5 discusses the relative merits of the IPS and a dedicated gimbal-servo system for the SIRTF. While a dedicated gimbal-servo would have a number of advantages, the IPS performance will be satisfactory, and will afford substantial cost savings.

Section 4.6 discusses various configurations for the SIRTF cryogenic supply.

4.1 GREGORIAN VS. CASSEGRAINIAN TELESCOPE

The choice of basic telescope design has an effect on most of the major optical performance parameters. The performance requirements of SIRTF (notably good resolution over a moderately large field, maintenance of resolution during space chopping, and a high degree of rejection of radiation from out-of-field sources) dictate a sophisticated design regardless of the basic telescope adopted. Hence, a tradeoff study was carried out at the beginning of the SIRTF program to analyze the relative merits of the two major telescope types appropriate to the mission, namely the Cassegrainian and Gregorian.

The discussion is divided into two main areas: optical performance (diffraction and geometrical aberration effects on blur diameter) and out-of-field rejection. Reference 4-1 reports in detail on the study.

4.1.1 Optical Performance

The first iteration of the study was made with a classical Cassegrainian (parabola-hyperbola). Because of the performance limitations of this design due to coma, later iterations used a Ritchey-Chretien version of the

Cassegrainian. For the Gregorian a modified doubled-folded version (ellipse-ellipse) was used throughout. The SIRTF optical performance requirements which affect the tradeoff study are listed in Table 4-1.

The parameters of the Cassegrainian telescope whose performance was evaluated initially are listed in Table 4-2. The obscuration is set by a sky baffle which is needed to achieve the out of field of view rejection requirements (see Section 4.1.2). The telescope is diffraction-limited at 5 μm over the 15 arc minute diameter field of view.

If the secondary mirror is tilted to displace the field of view, the image quality is no longer diffraction-limited. This is illustrated in Figure 4-1, which shows how the blur diameter increases as a function of the field of view displacement angle. (If the telescope were diffraction-limited when the field of view was displaced, the solid lines in Figure 4-1 would be horizontal.) The parameters are the diameters of the circles enclosing 70 percent, 80 percent, and 90 percent of the energy incident on the focal plane. The geometrical blur, which is also shown in Figure 4-1, is nearly linear with field displacement angle. Because the dominant geometrical

TABLE 4-1. SIRTF OPTICAL PERFORMANCE REQUIREMENTS

Aperture diameter (effective)	1 m
Focal ratio	f/3 to f/30
Field of view (diameter)	15 arc min
Back focal length (minimum)	60 cm
Space chopping displacement	± 7.5 arc min
Resolution (over field of view at all chopping angles)	diffraction limited at 5 μm
Out of field rejection (maintains NEP requirements)	
Earth	30 deg
Sun	45 deg

TABLE 4-2. CLASSICAL CASSEGRAINIAN TELESCOPE PARAMETERS

Telescope f-number	f/16
Primary mirror f-number	f/2
Aperture stop location	Secondary
Secondary magnification	8
Back focal length	0.8 m
Linear obscuration	0.41
Entrance pupil diameter	1.25 m
Effective collecting area	0.785 m ²
Field of view (diameter)	15 arc min

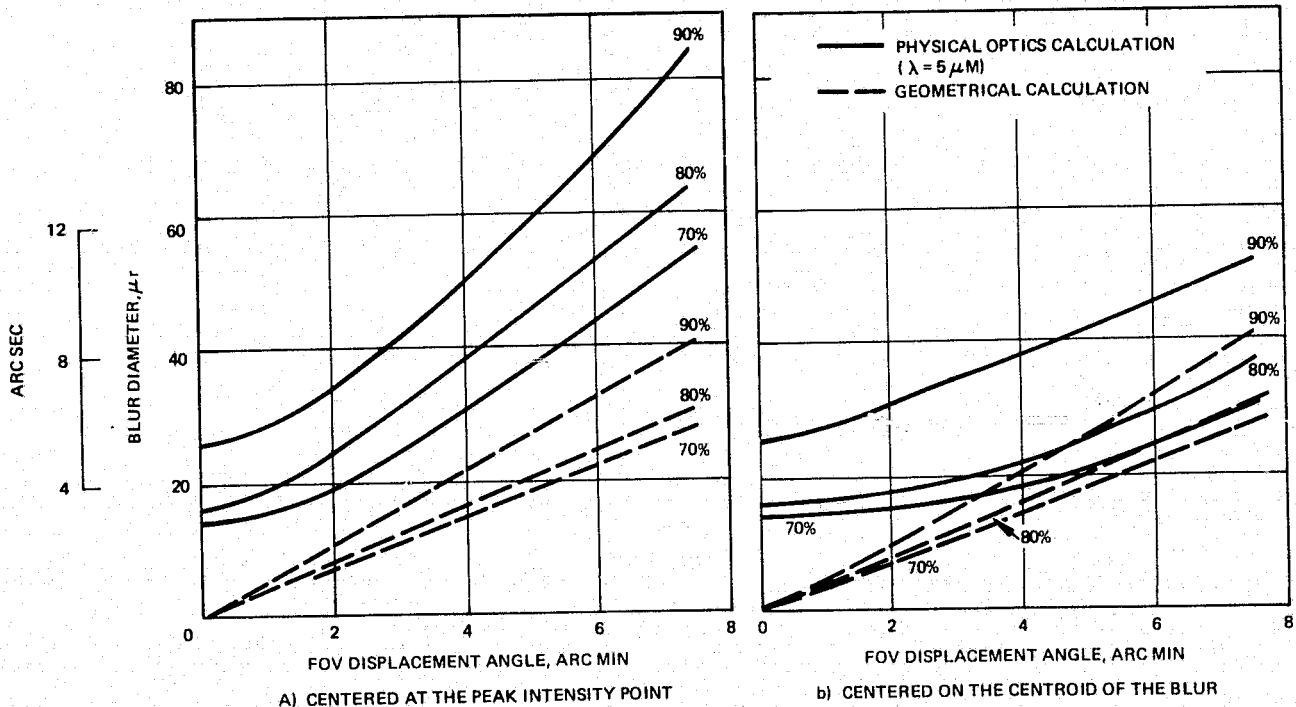


Figure 4-1. Variation of radial energy distribution with field of view displacement for different percent encircled energies. (The telescope characteristics are given in Table 4-2 and the secondary mirror is scanned.)

aberration is coma, there are substantial differences in the encircling circle diameter when it is centered on the peak intensity point (Figure 4-1a) and when it is centered on the centroid of the blur energy (Figure 4-1b). In any case, the requirement for diffraction-limited performance at $5 \mu\text{m}$ is not met.

The next step in the study was to look at the effect of primary mirror f/number on the blur size with the telescope f/number held constant.

Table 4-3 summarizes the parameters of the three telescopes investigated. As with the first Cassegrainian studied (which is number 1 in Table 4-3), the central obscuration is imposed by the baffle on the secondary mirror, not the secondary mirror itself.

TABLE 4-3. OPTICAL CHARACTERISTICS OF THREE CASSEGRAINIAN TELESCOPES

	<u>1</u>	<u>2</u>	<u>3</u>
Telescope f/number	16		
Primary f/number	2	3	4
Secondary magnification	8	5.33	4
secondary mirror			
Aperture stop			
Entrance pupil diameter		1.24 m	
Linear obscuration		0.41	
Effective diameter		1m	
Secondary diameter	0.182m	0.237m	0.287m
Back focal length	0.8m	0.8m	0.8m
15 arc min			
Field of view			
Secondary mirror tilt, degrees required to displace the FOV by 7.5 arc min	0.425	0.326	0.269

Figure 4-2 shows the variation of 80 percent encircled energy diameter as a function of primary mirror f/number over the range of telescopes 1, 2 and 3. As can be seen, the telescope is not diffraction limited at the 7.5 arc minute displacement angle even for an f/4 primary. (The 70-percent energy blur is just diffraction limited at f/4; the 90 percent blur is about 1.5 times the diffraction blur.)

Because coma is the dominant geometrical aberration in the Cassegrainian telescope, it was decided to examine the performance of a modified Ritchey-Chretien telescope. The approach used was to modify the conic constant of the primary to minimize coma, and at the same time to modify the conic constant of the secondary to maintain third-order spherical aberration correction.

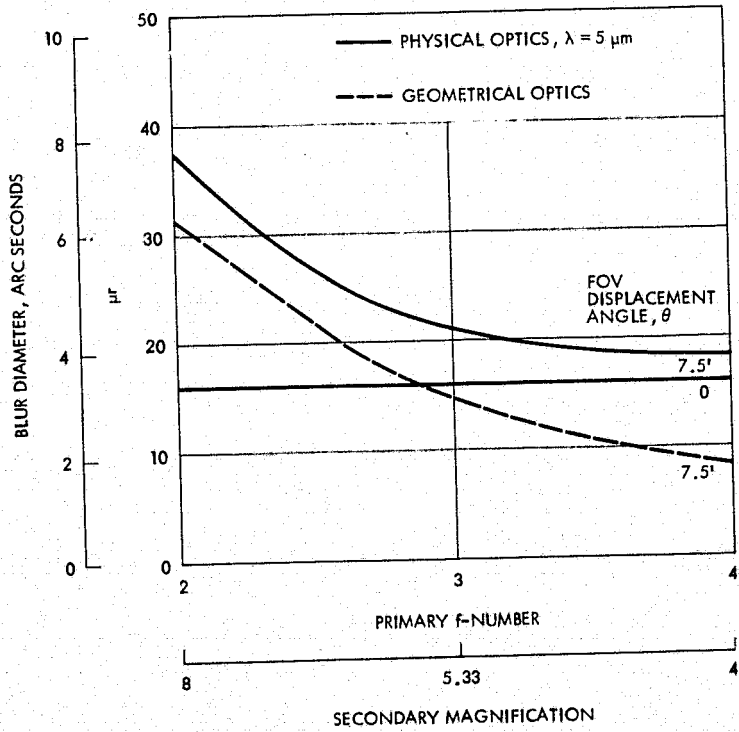


Figure 4-2. Variation of 80-percent blur diameters (centered on centroid) as a function of primary f-number and secondary magnification for the telescopes summarized in Table 4-3 for the point in the center of the displaced FOV.

Telescope designs which were studied have the same major parameters (see Table 4-4) as the initial telescope; however, the method of evaluation was changed.

The image points at which the telescopes have been investigated are fixed in the image plane (see Figure 4-3). In this figure, points B, C and D

TABLE 4-4. RITCHIEY-CHRETIEN TELESCOPE OPTICAL CHARACTERISTICS

Telescope f-number	16
Primary mirror f-number	2
Secondary magnification	8
Telescope back focal length, m	0.8
Entrance pupil diameter, m	1.24
Linear obscuration	0.41
Effective collecting area, m ²	0.785
Total field of view, arc min	15

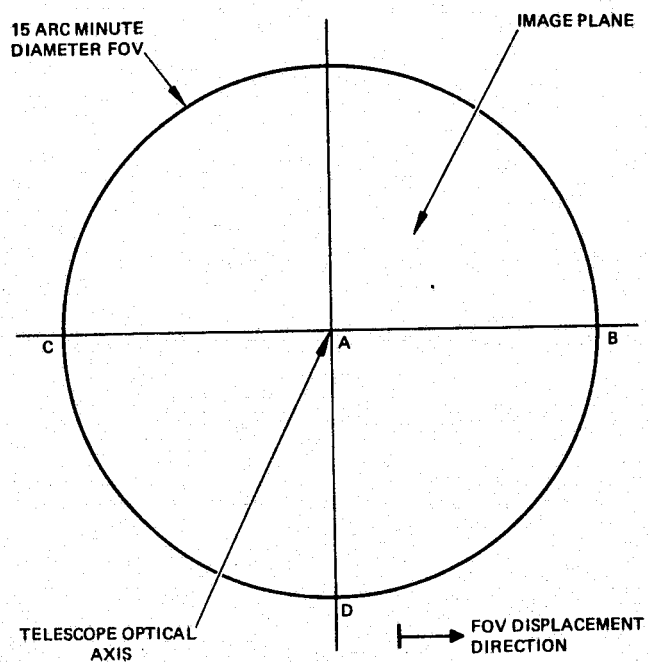


Figure 4-3. Image points at which the telescopes are evaluated.

are on the edge of a 15 arc minute diameter FOV centered on A which is on the telescope optical axis. The actual field of view viewed by points A, B, C and D has been evaluated for field of view displacement angles of up to 7.5 arc minutes, the field of view being displaced by tilting the secondary mirror. The measure of coma used in this investigation is the total geometrical extent of the comatic blur from the chief ray intercept with the image plane to the edge of the blur (Figure 4-4). This is different from the radial energy distributions taken about the centroid of the physical optics blur which was the criterion of image quality used in the earlier discussion as illustrated in Figure 4-1.

Figure 4-5 summarizes the results. Figure 4-5a shows the growth of coma in the Cassegrainian telescope analyzed earlier as a function of field of view displacement angle. The coma, initially zero, grows linearly with field angle and equally at all points in the field. The dashed line, the measure of coma perpendicular to the scan direction at point D, remains zero independent of field angle.

Skipping Figure 4-5b for the moment, Figure 4-5c shows the situation where the on-axis coma is corrected completely. Point A (and point D in the scan direction) shows no coma as a function of field angle. Points B and C show equal coma in opposite senses, although for all points the coma is independent of field displacement.

Between $K = -1$ and $K = -1.17$, a range of compromise is possible. One such is shown in Figure 4-5b, where the zero field displacement

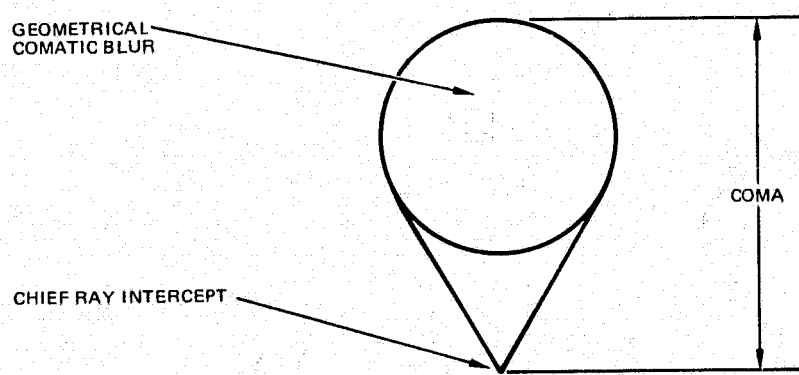


Figure 4-4. The measure of coma used in the evaluation of Figure 4-5.

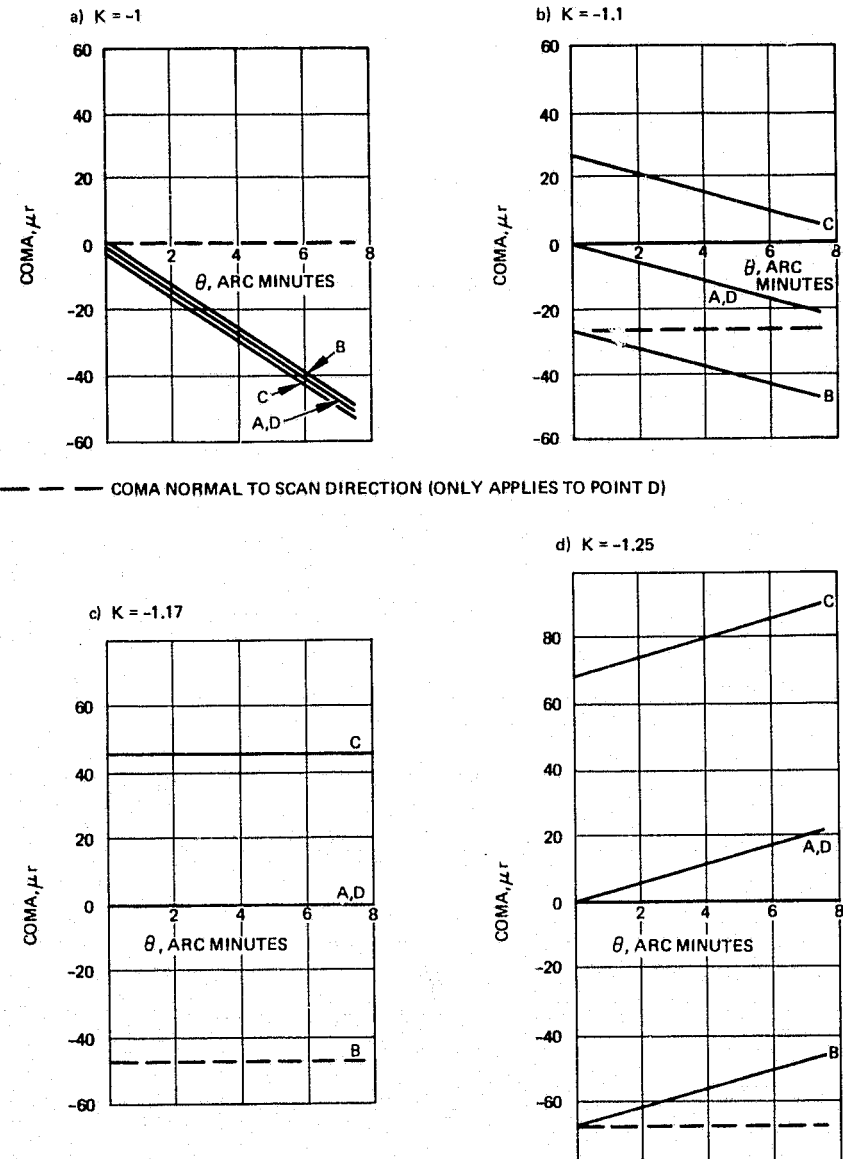


Figure 4-5. Variation in coma as a function of displacement angle, θ , for different values of the primary mirror conic constant, K . (90 percent-energy diffraction-limited blur at $5 \mu\text{m}$ is $27 \mu\text{rad}$.)

aberration of points B and C is smaller than in Figure 4-5c, and the rate of growth of coma with the field displacement is more gradual than in Figure 4-5a. However, the coma at the point (or points) in the field experiencing the largest aberrations is always about the same (on the order of 50 μ rad).

An intermediate value of conic constant is undesirable for another reason. A typical measurement will consist of a symmetrical chop around the optical axis with a minimum aperture mask over the detector. If the detector is located at point B, the size of the image will be different on the two sides of the optical axis. Hence, either a large mask corresponding to maximum coma must be used, or the intensity of the target will appear to be modulated.

Figure 4-5d confirms that beyond $K = -1.17$, the coma is increased for both zero and finite displacements of the field. Hence, the Ritchey-Chretien design offers improvement only over a limited fixed field of view (~3 arc min), or a limited displacement angle (~3 arc min) but not for both over the full SIRTF requirement range.

The alternate approach to tilting the secondary mirror to achieve space chopping is to tilt a flat mirror lying behind the secondary mirror. This is implemented very easily in the Gregorian by tilting the second folding mirror. It is also possible in either Gregorian or Cassegrainian configuration to mount mirrors near the focal plane; however, this is less desirable due to the substantial heat load introduced in the MIC.

It is shown in Reference 4-1 that the aberration introduced by tilting a flat mirror is defocusing of the image. Figure 4-6 illustrates the geometry. The solid lines and unprimed points are untilted positions; the dashed lines and primed points are the tilted positions. For a fixed set of telescope parameters, the defocus decreases as the space chopping mirror moves further from the focal plane, specifically

$$\Delta\phi = \frac{D}{2R} \theta^2$$

where $\Delta\phi$ is the fractional increase in geometrical angular blur, D is the entrance diameter, R is the distance from the chopping mirror to the focal plane, and θ is the field of view displacement angle.

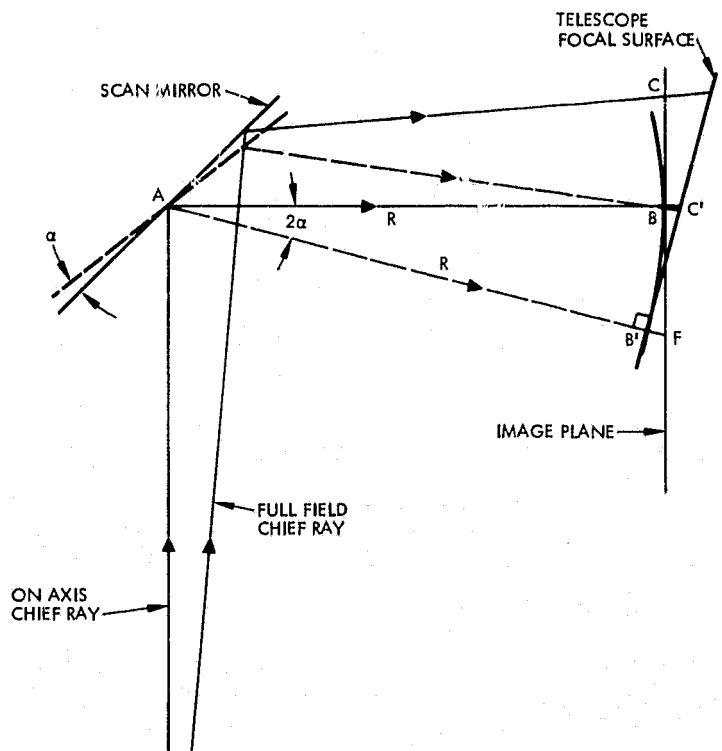


Figure 4-6. Effects of defocus at the image plane due to tilting the scan mirror through an angle, α .

Figure 4-7 shows the through-focus variation in blur radius for various encircled energy contours and field angles. For the SIRTF telescope

$$\Delta f = R(1 - \cos 2\alpha)$$

$$\approx \frac{f^2}{2R} \theta^2$$

$$= 0,094 \text{ mm}$$

where f is the focal length, Δf , the defocus, and α , the scan mirror tilt angle.

When the total field of view is angularly displaced by an amount equal to the semi-field of view, the defocus at C (the worst point in the displaced FOV) is approximately $CD = -3\Delta f$. For this FOV displacement angle, the defocus therefore extends from $-3\Delta f$ to Δf across the displaced field of view. Improvement is obtained by defocusing the telescope by an amount equal to

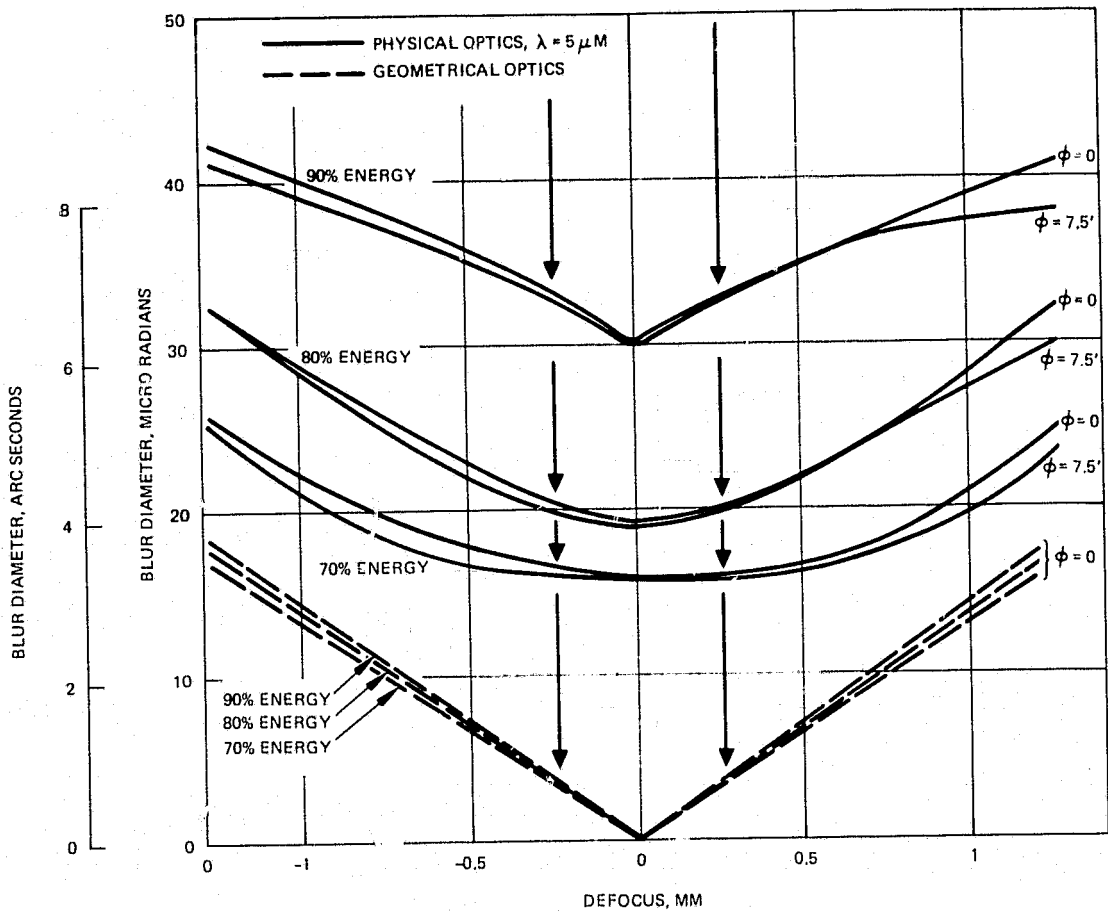


Figure 4-7. Through-focus variation in blur radius for 70, 80, and 90 percent energies, and for field angles, θ , of 0 and 7.5 arc minutes. (Arrows indicate blur diameter variations for SIRTF Gregorian design 7.5 arc min field displacement.)

Δf so that the defocus range extends from $-2\Delta f$ to $2\Delta f$, thus minimizing the defocus across the displaced FOV. The arrows on Figure 4-7 show the defocus and blur diameter in the Gregorian design when the FOV is displaced the full 7.5 arc min. The blur grows from 19 to 20 microradians diameter. This is in contrast to the result of tilting the secondary in the Cassegrainian (Figure 4-1) where the displacement for 80 percent energy blur diameter of 20 arc sec is limited to 1 or 3 arc min depending on whether the calculation is around the peak or the centroid.

If the tilting mirror is used in the Cassegrainian, its distance from the focal plane will be 1/2 to 1/3 the distance of the Gregorian second folding mirror from the focal plane. Thus the defocus will be 2 to 3 times greater (0.4 to 0.6 mm). However, the performance is substantially better tilting a flat rather than the secondary.

The above discussion pertains to the SIRTF specification requirement for diffraction-limited performance at 5 μ m over the full field of view and the full chopping throw. For wavelengths beyond 10 μ m where the 90 percent diffraction blur is 54 μ rad, the difference in performance of the systems is small. Similarly, for the small displacements (≤ 1 arc min) and small fields (≤ 1 arc min) generally used at short wavelengths, the coma does not seriously affect the blur diameter.

4.1.2 Off-Axis Rejection

For the off-axis rejection portion of the tradeoff study, the ground rules were as follows:

1. Aperture: 0.785 m² clear aperture
2. Baffle Tube: long enough to prevent illumination of the primary at source angles greater than 30 degrees off-axis
3. A conical shade prevents illumination of the aperture at source angles greater than 45 degrees off-axis
4. A thickness of 12.7 cm (5 in) is assumed for the telescope wall structure and insulation
5. Mirror surfaces are bare beryllium.

The wall thickness assumption affects the shade dimensions, since the shade must be retractable and therefore must slide over the outer diameter of the telescope.

Various Cassegrainian designs were considered, including those with primary mirror f-number and total system f-number combinations of f/2 - f/8, f/2 - f/16, f/3 - f/8, f/3 - f/16, and f/3 - f/30. The f/2 - f/16 system was chosen for comparison to the Gregorian for the following reasons: it can be baffled most successfully of all the systems, its secondary mirror diameter is small, and the telescope length is the shortest. The pertinent

dimensions are those of system A in Figure 4-8. The area obscuration of system A is 20.5 percent, which is caused by the baffle on the secondary mirror.

Because of the interest in a small central obscuration to reduce the energy in the diffraction rings, the effect of removing the shield at the secondary mirror was investigated. In order to eliminate scattering of radiation from directly illuminated baffles by the secondary mirror, the telescope must be lengthened, so that no baffles visible to this mirror are directly illuminated. This configuration is shown in Figure 4-8, system B. It has the same optical dimensions as System A, but has no secondary shield. This increases the collecting area. The other choice, a system with the same collecting area as system A and no secondary shield, was not analyzed since the reduced aperture diameter results in a 9-percent increase in diffraction dimensions.

The double-folded Gregorian analyzed in system C in Figure 4-9, with 20.2 percent of the collecting area obscured. The fact that the area obscurations of A and C are almost identical is coincidental. The major scattering path is scattering by the folding mirror from directly illuminated baffles. By extending the telescope length (system D in Figure 4-9), this

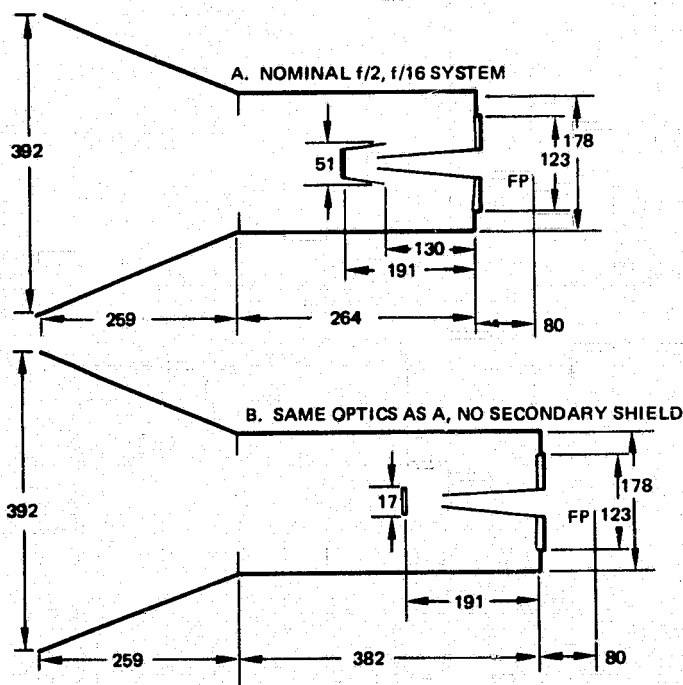


Figure 4-8. Cassegrainian systems (dimensions in cm).

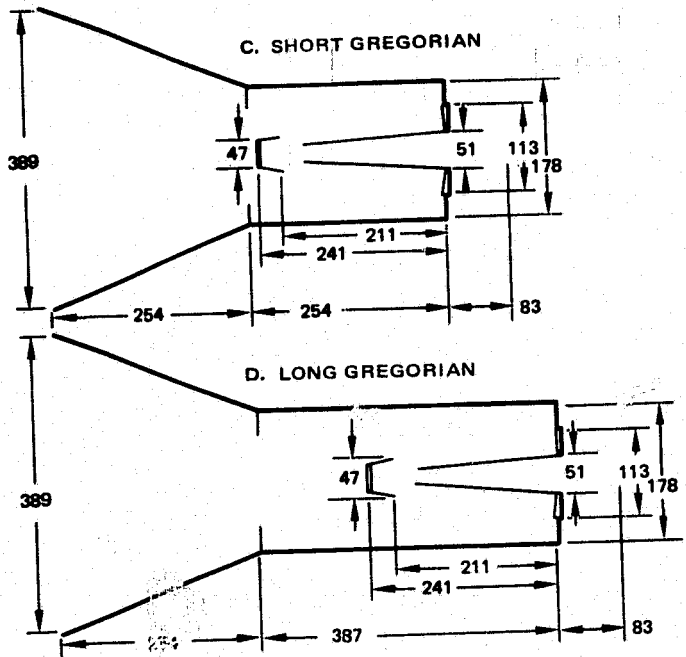


Figure 4-9. Double-folded Gregorian systems.

path is eliminated, resulting in lower scattered irradiance. The optical and dimensional data for these four systems are listed in Table 4-5.

Figure 4-10 shows the off-axis rejection of the four systems as a function of angle between the earth horizon and the telescope line of sight for a 300 km telescope altitude. The off-axis rejection requirement derived from the telescope NEP requirement is shown.

To understand the reasons behind the curves in Figure 4-10, the phenomena contributing to background from out-of-field sources must be considered. There are two: (1) scattering of energy off the baffle tube and then off a mirror at an angle which is within the field of view bundle, and (2) diffraction by the telescope apertures. The diffracted energy is concentrated in a ring at the edge of the field of view. Thus, the background photon flux due to out of field sources is not the same at the center and at the edge of the field of view. This is true for both Cassegrainian and Gregorian.

The Cassegrainian with the baffle on the secondary mirror more effectively rejects scattered radiation at source angles near 30 degrees. There is no direct scattering path from the illuminated baffles on the baffle tube to the secondary mirror. In contrast, there are scattering paths from

TABLE 4-5. DIMENSIONAL DATA FOR SYSTEMS CONSIDERED

System	F/2-F/16 Cassegrainian		F/7.67 Gregorian	
	A	B	C	D
Shield length (cm)	259	259	254	254
Telescope length (cm)	264	382	254	387
Back focal length (cm)	80	80	83	83
Shield diameter (cm)	392	392	389	389
Telescope diameter (cm)	178	178	178	178
Primary mirror dia, (cm)	123	123	113	113
Aperture dia, (cm)	112	112	112	112
Obscuration dia, (cm)	51	17	51	51
Obscuration (% area)	20.5	2.3	20.2	20.2
Collecting area (cm ²)	7,839	9,667	8,006	8,006
Equivalent focal length (cm)	1,796	1,796	770	770

illuminated baffles to the first folding mirror in the Gregorian, which are eliminated by lengthening the telescope tube (system D). Thus, Figure 4-10 shows the Cassegrainian A to be about an order of magnitude better than Gregorian C at 30 degrees. As the angle increases, the Gregorian improves rapidly because the illuminated baffle area which can be seen by the first folding mirror decreases. At large angles the Gregorian is better because the first folding mirror subtends a smaller angle at the primary than does the Cassegrainian secondary.

At the edges of the field of view, diffraction adds to the scattered background. In the Cassegrainian the added flux due to diffraction amounts to about 10 percent of the scattered flux; in the Gregorian the increase is about 2 percent. Thus in the static (non-space-chopped) case, the Cassegrainian provides better off-axis rejection.

Photon flux values for the Cassegrainian with no secondary shield and the long Gregorian are shown for comparison. The advantage of a small central obscuration is offset by a factor of 30 worse off-axis rejection

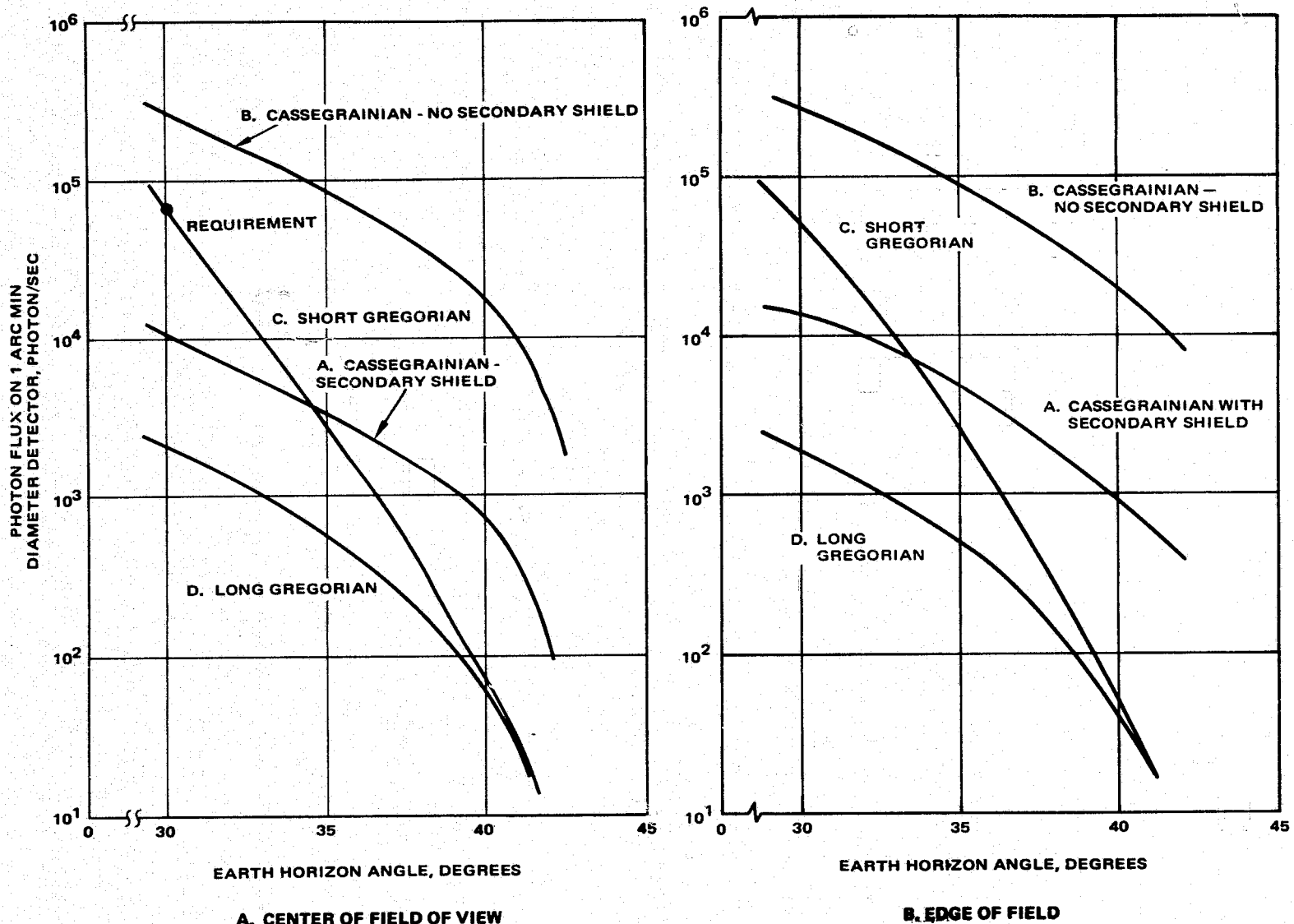


Figure 4-10. Steady-state photon flux in focal plane with space chopping mirror centered (300 km altitude).

performance and a 1.2 m longer telescope. If the telescope were not lengthened, the off-axis rejection would be substantially worse.

The long Gregorian, comparable in size to the long Cassegrainian, provides the best off-axis rejection of any of the systems at all field positions and earth-LOS angles.

The reduced diffracted energy causes a reduction in the background difference in the Gregorian as compared to the Cassegrainian. Figure 4-11 illustrates the effects for space chopping perpendicular to the horizon. Both long and short Gregorians are better than either Cassegrainian, by a small factor for a detector at the center of the field of view, and by an order of magnitude for a detector at the edge of the field. The value of the improvement depends on the particular application; no requirement has been established for SIRTF focal plane background difference during space chopping.

For space chopping parallel to the horizon, the variation in flux was determined to be less than 10 photons/sec and hence was not calculated exactly.

4.1.3 Conclusions

The conclusions derived from the tradeoff study are:

- The Gregorian, with space chopping by the second folding mirror, exhibits very nearly uniform image quality at all field positions and throw angles. The Cassegrainian exhibits substantial image growth due to coma at field positions and/or space chopping throw angles above 3 to 4 arc min.
- A well-baffled Cassegrainian provides better suppression of out-of-field source energy at small angles. The baffling required to achieve this suppression produces a central obscuration comparable to that of the Gregorian.
- The Gregorian designs provides a lower background difference during space chopping perpendicular to a source than do the Cassegrainians.

Based on this study, the Gregorian was chosen as the baseline for the SIRTF preliminary design. The conclusions only slightly favor the Gregorian, especially because subsequent discussions with the SIRTSAG indicate that in most cases measurements at short wavelength will be made with small space chopping throws. Thus the better image quality during space chopping at

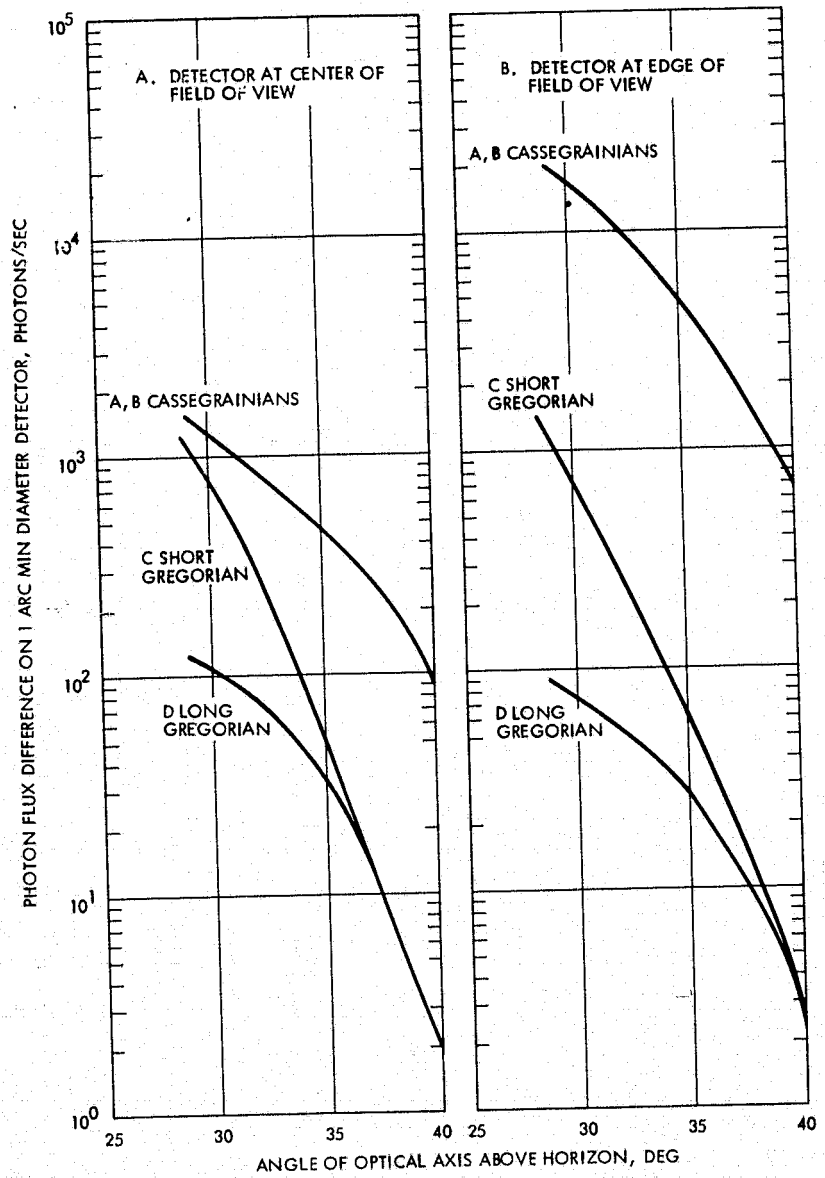


Figure 4-11. Variation in photon flux on detector (scan modulation). (Flux with scan mirror on axis minus flux with scan mirror at full throw.)

large angles will rarely be used. To the extent this holds true, the relative merits of the two telescopes become very nearly equal.

Further work is indicated in evaluating the importance of the three conclusions listed above in terms of predicted usage of the telescope.

4.2 APERTURE DIAMETER

As a facility-class instrument, SIRTF was initially specified as a 1.0 meter diameter aperture telescope. Quite early in the study, it was decided to use $(\pi/4) m^2$ clear aperture area as a standard. Thus the primary mirror diameters varied as a function of central obscuration ratio; for the design finally adopted, the clear aperture is 1.16 m diameter and the primary mirror is 1.23 m diameter. As part of the study, the impact of aperture diameter on other system parameters and on Spacelab and Shuttle constraints was investigated.

The major driver toward making the telescope larger is to increase the resolution by decreasing the diameter of the diffraction blur. Although sky surveys in the infrared have not been made to anywhere near the SIRTF sensitivity level, extrapolation from surveys that have been made indicates that SIRTF will be confusion-limited in the galactic plane and possibly outside it. That is, there will be several stars within a very few resolution elements over certain portions of the sky.

The dependence of diffraction blur characteristics on primary mirror diameter is well known. Figure 4-12 illustrates the relationship by a plot of the diameter of the first dark ring and first bright ring for primary mirror diameters of 1.0 to 2.5 meters. The diameter of the first dark ring ranges from 2.3 to 0.94 arc seconds; that of the first bright ring from 4.6 to 1.9 arc seconds.

Changing the primary mirror diameter and scaling the telescope (maintaining constant f/no) produces substantial changes in weight. Figure 4-13 illustrates the relationship. The masses of Tables 2-5 and 2-6 were used as a baseline. The ballast masses were subtracted out since it is expected that they will be unnecessary. The telescope, telescope support structure, aperture cover assembly and cover support structure masses

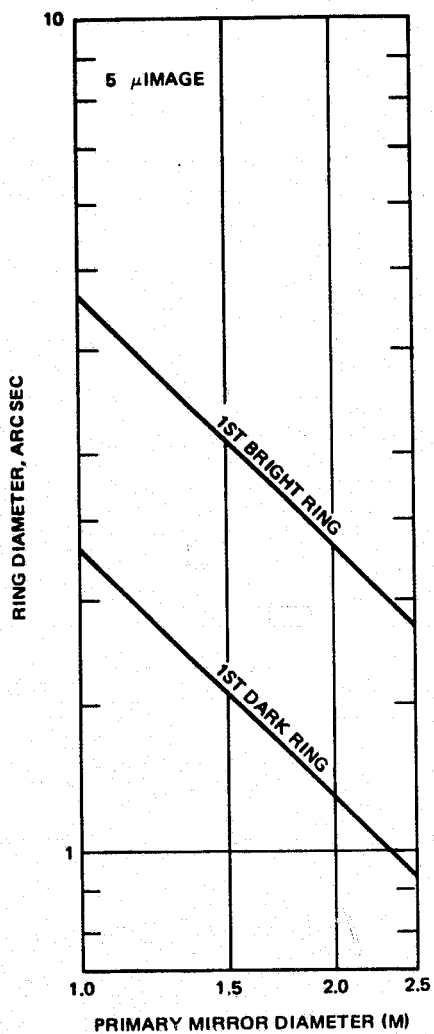


Figure 4-12. Diffraction blur parameters as a function of primary mirror diameter.

were considered variable, while all other masses were considered independent of primary mirror diameter.

Based on the experience of previous detailed studies, the variable masses were assumed to vary with primary mirror diameter:

$$M \propto d^p$$

where $2 \leq p \leq 2.2$. Figure 4-13 shows the relationship of the total SIRTF system mass to primary mirror diameter. For 7-day missions, the total

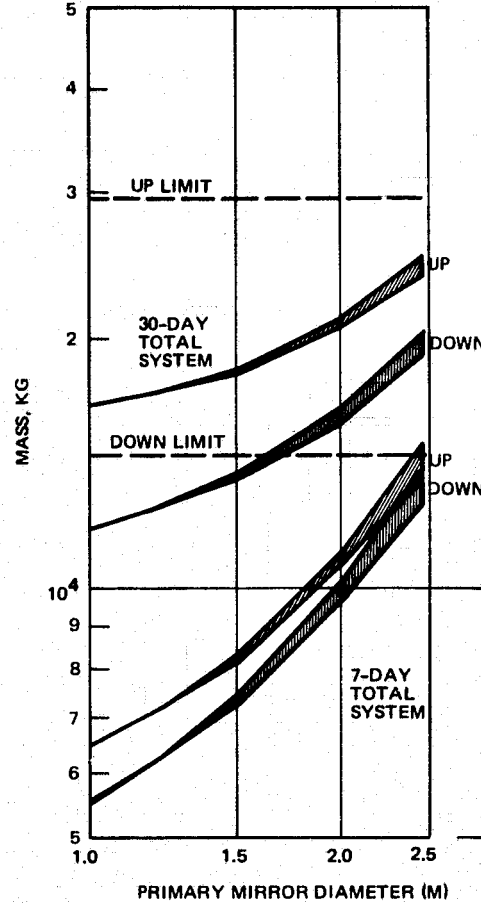


Figure 4-13. Total SIRTF system weight as a function of primary mirror diameter.

system masses are below the limits for all diameters considered. For 30-day missions, due to the large mass of expendables which must be carried to support the Shuttle, crew, and telescope, the down weight limit is exceeded for a primary mirror diameter greater than about 1.65 m. (Reference 4-2.)

The Spacelab pallets also impose load limitations. Figure 4-14 shows the mass of the SIRTF system components mounted on the two-pallet train as a function of primary mirror diameter. The load limit of the two-pallet train is 5500 kg, which restricts the primary mirror diameter to about 1.9 m for 7-day missions and about 1.8 m for 30-day missions. (Reference 4-3.) In comparison with Figure 4-13, the pallet represents a limit for the 7-day mission; for the 30-day mission, the limit is imposed by the Shuttle down weight. It is understood that the Spacelab pallet load limits are preliminary and modifications may change the conclusions. No data is available on the load limit of a strengthened two-pallet train.

A third consideration is the moment of inertia of the telescope mounted on the IPS. There is no firm limitation on the moment at the present time.

Figure 4-14. Pallet train load as a function of primary mirror diameter.

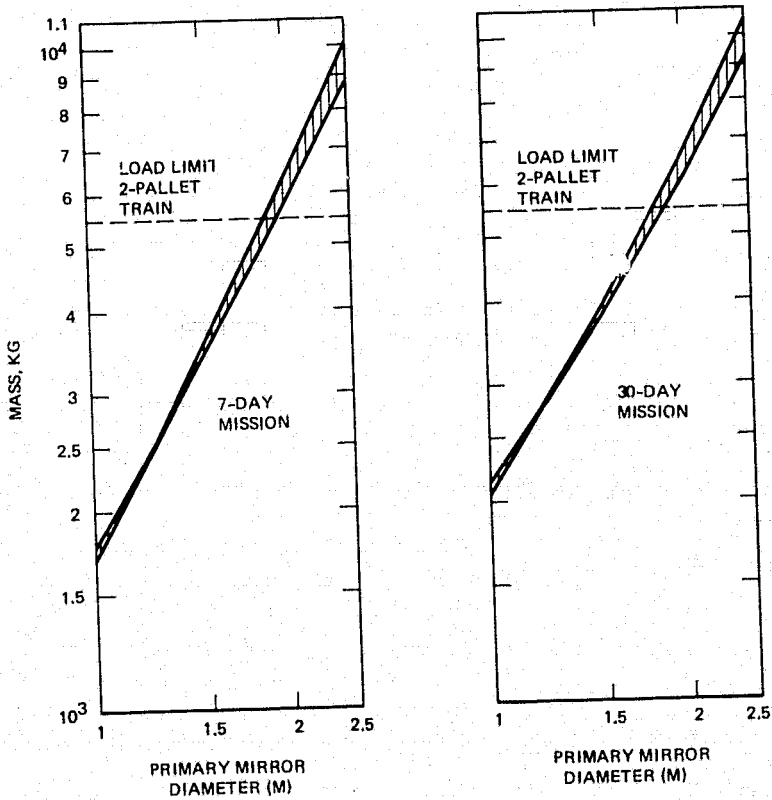


Figure 4-15 shows that the nominal SIRTF design has an inertia which exceeds that of the IPS nominal large payload by 20 percent and 31 percent for one and two cryogen tanks mounted on the telescope (Reference 4-4). (The case with the cryogen tank or tanks mounted on the pallet is also illustrated; in this case, the inertia exceeds that of the IPS nominal large payload by 9 percent.)

In the absence of more detailed information, it is assumed that the major effect of increasing inertia is to reduce the telescope angular acceleration and velocity during slewing, and to increase the time constant of the stabilization loop. The first effect impacts observing efficiency most strongly, and cannot be evaluated with the information currently available. The second does not appear to be important since the SIRTF internal stabilization system will provide the high frequency stabilization of the line of sight. More study is clearly needed when the IPS is more fully defined.

Notice that the IPS itself does not impose a load-carrying limit because it is decoupled from the telescope assembly during launch and landing.

The final consideration is in cost of fabrication of the SIRTF telescope. A step increase in cost exists at 1.6 m primary mirror diameter based on the availability of beryllium blanks. Current tooling exists for forming blanks of about 1.7 m diameter and allowing for edges effects; this results in a 1.6 m diameter mirror. The cost of tooling for larger blanks has not been formally estimated, but it is expected that the cost of tooling would be a substantial fraction of the SIRTF program cost. In addition, the quality of the initial blanks is unknown so that extensive testing and possibly revision of manufacturing processes would be needed. It is therefore not recommended that primary mirrors larger than 1.6 m be considered.

Within the range of 1.0 m to 1.6 m, two cost data points were developed during the study, one at the nominal 1.2 m diameter and another at 1.6 m diameter. The cost figures are discussed in Section 6.3.

The conclusion of the trade study is thus that SIRTF should be built with the largest possible primary mirror which is (1) smaller than 1.6 m in diameter and (2) consistent with Shuttle and Spacelab constraints. On the basis of current information, it appears that the Shuttle limit is also 1.6 m (down weight of 30-day mission configuration). These limits must be

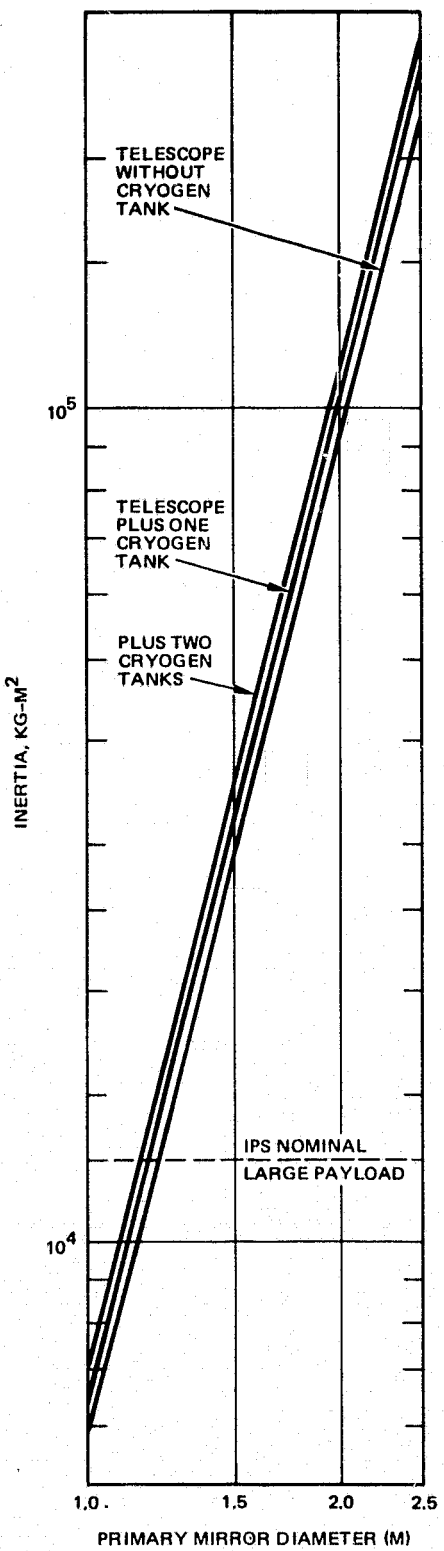


Figure 4-15. Moment of inertia of SIRTF telescope as a function of primary mirror diameter.

re-evaluated when the Spacelab characteristics and capabilities are firmly established.

4.3 CCD VS. VIDEO STAR TRACKER

The SIRTF specification includes requirements for focal plane star tracking and a visible-light image of the data telescope field of view. This requirement can be fulfilled (within certain limitations) by either a charge-coupled device or an image intensifier star tracker. The selection will be based on sensitivity, ability to track two or more stars simultaneously, ability to track during space-chopping, capability of producing an image of the field while tracking, and operability at or near MIC temperatures. Since little is known about this last criterion, which impacts the entire question, the discussion here is preliminary. Tests currently in preparation at Jet Propulsion Laboratory will give at least a first data set on the CCD Star Tracker performance at reduced temperature.

The star tracking requirement established by the SIRTSAG was that the star tracker shall be capable of locating and guiding an object throughout the celestial sphere with a probability of success of 0.99. Two stars must be tracked simultaneously in order to maintain X-Y and roll alignment. Star counts indicate that at high galactic latitudes, 0.99 probability of two stars in the field of view requires $M_V = 13.3$ sensitivity for a 30 arc minute diameter field. $M_V = 14$ was adopted as the SIRTF sensitivity requirement.

Table 4-6 indicates the major considerations behind selection of the CCD focal plane star tracker. All three devices provide tracking of multiple stars, and a video signal representing the focal plane star field in the visible. The Image Dissector is basically designed to track a single star; tracking of multiple stars and/or producing a video signal reduces the error signal data rate.

All three sensors have comparable resolutions and data for tracking multiple stars.

Both tubes require large electrical or magnetic fields for deflection and/or focusing. Interference of these fields with low-level signals in the focal plane instrument detection and preamps is a cause of concern. In addition, the filament of the SIT represents a substantial heat-input into the MIC.

TABLE 4-6. COMPARISON OF STAR TRACKER SENSORS

	SIT	I.D.	CCD
Multiple star tracking	Yes	Time Shared	Yes
Video output	Yes	Time Shared	Yes
Resolution	1/525	1/500	1/400
Data Rate (Single $M_V = 145$ stars)	30 Hz	15 Hz	10 sps
Electric/Magnetic fields	Yes	Yes	No
Focal plane	Yes	Yes	No
Heat source in focal plane	Yes	No	No
Off-axis tracking non-linearity	Yes	Yes	No
Non-uniformity of response	Yes	Yes	Yes

The tubes suffer from non-linearity and non-repeatability of position in the off-axis tracking mode. In contrast, the CCD with its fixed geometry tracks equally accurately at all points in the field of view. Tracking accuracy in all three sensors is limited by non-uniformity of response when stabilizing to a fraction of a resolution element; current CCDs exhibit worse effects than the tubes although improvements are expected in the SIRTF time frame.

None of the devices have been used extensively at the MIC ambient temperature ($\sim 10^{\circ}\text{K}$). Isolation of the star tracker from the MIC and operation at a higher temperature is possible. The CCD is preferred in this respect because of its small mass and hence small heat load on the MIC. Tests currently (summer 1976) under way at JPL will characterize the performance of CCDs at low temperatures.

Methods of calibration and stored detector element performance parameters are being developed to combat the non-uniformity of response problems. Assuming success of these efforts, the CCDs represent the most favorable selection of star tracker.

4.4 SIRTF VS. LARGE AMBIENT IR TELESCOPE

As part of the processes of evaluating SIRTF, a comparison was made between SIRTF and a large ambient temperature Shuttle-borne telescope. The comparison encompassed performance, problem areas (chiefly thermal design), and a cost comparison. Rather than starting from scratch, it was agreed that the LIRTS telescope as defined by Engins MATRA would be used to represent the ambient telescope (Reference 4-5).

Although the Matra study was used as a starting point, additional work was done:

- A mechanical layout was made and the telescope mass properties were calculated.
- A rudimentary thermal model was developed to show that a small amount of active temperature control could alleviate the critical thermal problems.

These are discussed in the material which follows.

Table 4-7 presents the major parameters of the LIRTS telescope. Two columns of values are shown: the requirements or design goals at the start of the study and the final values resulting from the study. Dashed lines indicate that values for those parameters are not given in the report.

The most significant point in Table 4-7 is that the standard pallet limits the diameter of LIRTS to 2.3 m, rather than the 3.0 m design goal. Since one of the SIRTF ground rules has been that it will use standard Spacelab equipment whenever possible, the same assumption was made for this comparison. Designing special pallets relieves some significant constraints in both SIRTF and LIRTS; however, the comparison has not been made under these conditions.

A second point with regard to Table 4-7 is that an imposed study ground rule was that cooling be entirely passive. Hughes' brief study of the thermal problem showed the promise of a small amount of active cooling in solving the thermal problems: the limitation to passive cooling should be removed.

Figure 4-16 is a conceptual layout of the LIRTS telescope made by Hughes. It shows a 2.3 m aperture, f/15 Cassegrain telescope with the

TABLE 4-7. LIRTS PARAMETER SUMMARY

	Requirement/ Design Goal	MATRA Study Output
Telescope type	Cassegrain	Ritchey-Chretien
Primary f/no	---	2.2
Obscuration (linear)	---	0.15
System f/no	15	14.7
Entrance aperture	3m	Standard pallet limits to 2.3m
Resolution	Diff limited at 30μ (first dark ring: 5 sec dia)	---
FOV	---	40 min curved focal surface, $R = 1.45m$
Spectral range	30μ to 1000μ	30μ to 1800μ
NEP ($\text{W} / \sqrt{\text{Hz}} - 3\mu$) at 30μ	1×10^{-15}	Mid 10^{-15}
Cooling	Passive	Passive
Space chopping	Wobbling secondary 30 min, 30 Hz	Wobbling secondary 30 min, 30 Hz
Pointing accuracy	5 sec (3σ)	---
Pointing stability	2 sec (3σ)	---

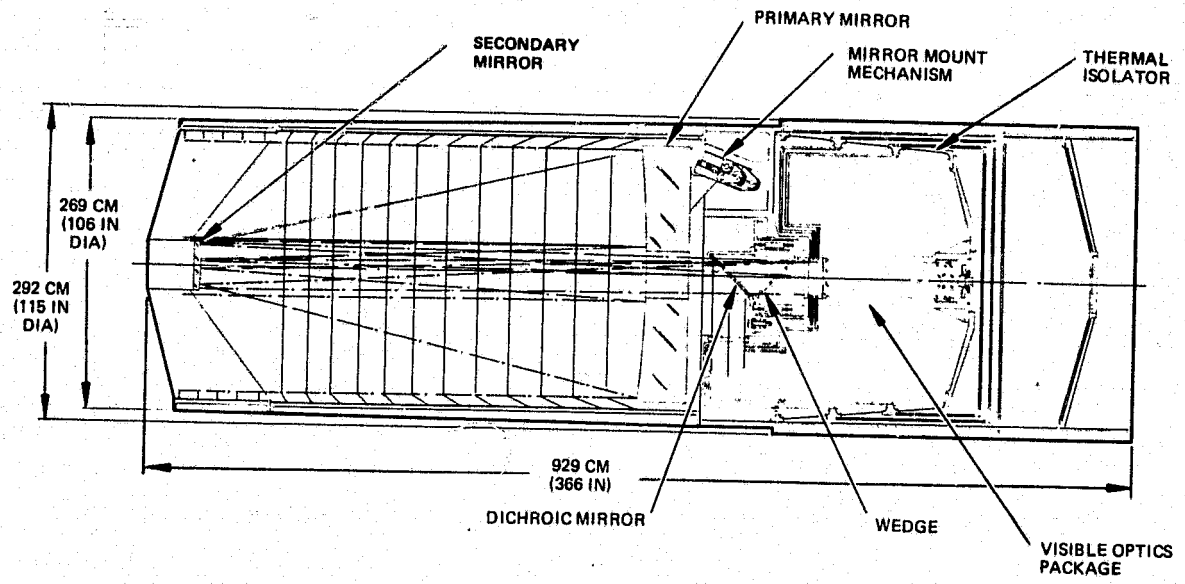


Figure 4-16. LIRTS sensor - Hughes conceptual layout.

SIRTF dichroic beam splitter, star tracker, and instrument chamber configurations. The telescope walls are essentially single thickness (no multi-layer insulation). The Multiple Instrument Chamber is mounted on a conical thermal isolator with two radiation shields to maintain the detectors and focal plane instruments at cryogenic temperatures. The dichroic beamsplitter is located in the warm volume; the infrared energy enters the MIC through windows located in front of the various instrument positions.

In evaluating the LIRTS performance, the primary mirror is the critical component. There are three requirements:

- Low Average Temperature: The photon fluctuations noise level is directly related to the temperature of the primary mirror.
- Low Gradient: Since the beam moves on the primary mirror during space chopping, the gradient must be small so that scan noise does not limit the sensitivity.
- Low Time Derivative: In order to carry out integration of signals from weak sources, the temperature of the primary must be stable in time.

The last two items are closely interconnected through a process called telescope wobbling which is widely used in ground-based telescopes. In wobbling,

the telescope is pointed at a star and space chopping is done with the left beam (i.e., the telescope alternately looks at the star with its chop mirror on-axis and at a nearby piece of clear sky with its chop mirror in the left position). The telescope is then moved so that it views the star with its chop mirror in the left position and another piece of sky when the chop mirror is on axis. By subtracting the average sky signals from the average star signals, an accurate measure of the star intensity is obtained, with both sky and telescope contributions subtracted out to first order, and partially to third order.

To improve the likelihood that wobbling will produce an acceptable S/N ratio, there are essentially two ways to approach the thermal design: either minimize the absolute temperature (so that the primary mirror contributions are lower than other noise sources) or minimize the gradients. The elements of the two approaches can be summarized as follows:

<u>Approach</u>	<u>Minimize Gradients</u>	<u>Minimize Temperature</u>
Thermal capacity	High	Low
Coupling	Low	High
Thermal time constant	»Mission	«Mission

Tied directly into selection of the thermal approach is the selection of the primary mirror material. Table 4-8 summarizes the primary mirror material tradeoff.

Beryllium is immediately rejected due to the unavailability of blanks larger than about 1.6 m diameter. This limitation is actually a cost limitation in that tooling does not exist and would have to be manufactured, and several blanks would probably have to be made before the necessary uniformity is achieved. Since the cost of the tooling and blanks is estimated to be a substantial fraction of the cost of the whole program, this is a real limitation.

Aluminum is rejected due to its poor temporal stability characteristics and surface quality problems. This leaves the low-expansion materials with their poor thermal conductivity (and hence long-term gradients) and high weight.

TABLE 4-8 LIRTS PRIMARY MIRROR TRADE

	Cervit, ULE, Zerodur	Aluminum	Beryllium
Blank size	OK	OK	<input checked="" type="checkbox"/> NO
Experience	Vast	Adequate	<input type="checkbox"/> Adequate
Polishability	Excellent	Good (nickel plated)	<input type="checkbox"/> OK
Thermal expansion	Low	High	<input type="checkbox"/> High
Thermal conduction	Low	High	<input type="checkbox"/> High
Temporal stability	Good	<input checked="" type="checkbox"/> Poor	<input type="checkbox"/> Good
Weight	Heaviest (limits aperture on standard pallet)	Medium	<input type="checkbox"/> Lightest

Indicates chief reason for rejection by Matra.

The first approach analyzed by MATRA was the low primary mirror temperature approach. The initial temperature is assumed to be 300°K; the equilibrium temperature in orbit is 230°K. A mirror front surface emissivity of 2 to 4 percent was assumed. Two cases were looked at:

1. A mirror with enough mass to be structurally stable.
2. A mirror that would reach the equilibrium temperature after 1 day in orbit (thus allowing 6 days of observation in a 7-day mission).

The results are summarized in Table 4-9.

A mirror which will reach equilibrium in 1 day is one 0.43 cm thick, whereas a mirror which is structurally sound is 8.7 cm thick and will have

TABLE 4-9. LOW TEMPERATURE MIRROR TRADE

	Fast Cooling	Stable Mirror
Final Temperature	230°K	273°K
Period	1 day	6 days
Density	1.0 gm/cm ²	20 gm/cm ²
Primary mirror thickness	0.43 cm	8.7 cm

reached a temperature of only 273°K after 6 days in orbit. Adding radiative coupling through a black back plate reduced the temperature after 6 days to the range 243°K to 258°K ; i.e., equilibrium was still not reached. Hence the low temperature mirror approach was dropped and most of the work in the study was directed toward developing a design which was well insulated and for which the gradients and time derivatives of temperature were minimized.

A typical result of the insulated design developed by MATRA is shown in Figure 4-17 for $\lambda = 30\mu$. The thermal model showed a gradient of $1.7 \times 10^{-1} \text{ K}$ across the primary mirror after 2 days in orbit. (The gradient does not change much over the rest of the 7-day mission, although the temperature continues to drop.) To obtain an NEP value, read the intersections of the arrows and the 1-second integration (solid line). (The integration lines rise toward the left because for larger chop throws, the aberrations increase the blur; hence, the detector size; hence, the noise.) This indicates an NEP of about $3 \times 10^{-15} \text{ W}/\sqrt{\text{Hz}}$, and that space chopping throws are limited to about

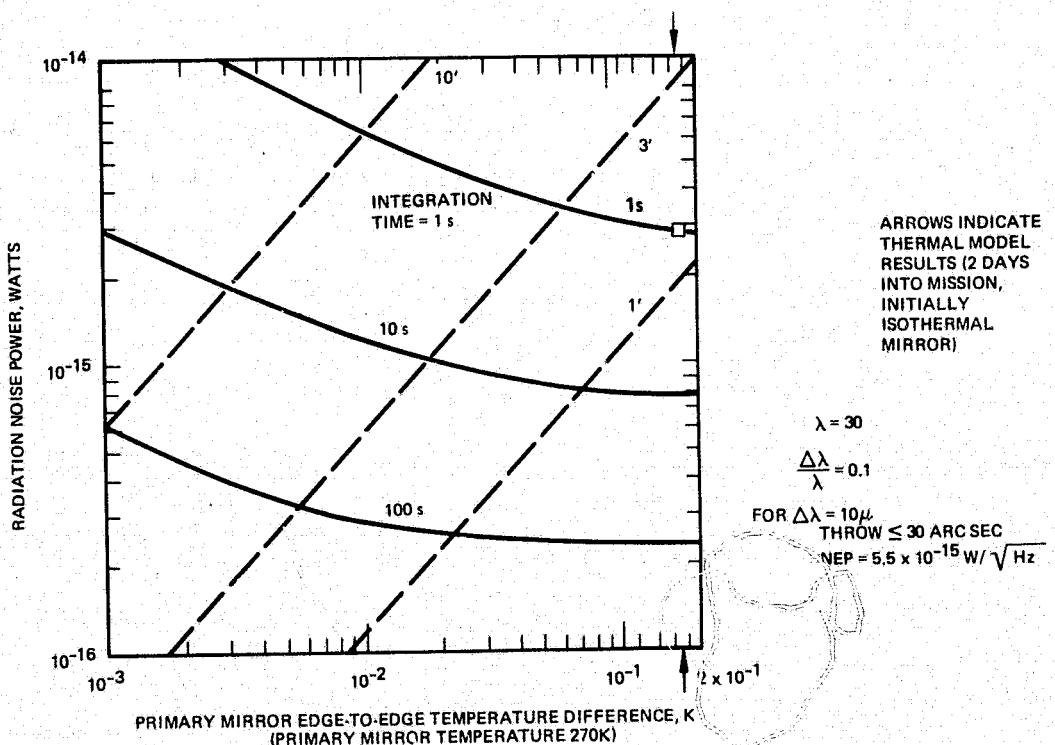


Figure 4-17. Typical LIRTS performance curves.

1.5 arc minute, if the chopping noise is not to exceed the photon fluctuation noise. Since the primary mirror ΔT is about 6 K/day or 0.08 K/20 min (20 minutes is about the maximum period available for integration in orbit), integrations on the order of 100's of seconds can be carried out, and sensitivity in the $1 \times 10^{-16} \text{ W}/\sqrt{\text{Hz}}$ region can be obtained.

Figure 4-18 provides a comparison of NEPs for LIRTS and SIRTF. The assumptions which affect the comparison are listed on the figure. The spectral bandwidth is the SIRTF specification value, $10 \mu\text{m}$; quantum efficiency of 1 is assumed for the diffraction-limited sized detectors used in both telescopes. LIRTS is assumed to be at its lowest temperature during a typical mission (270K). SIRTF is at the temperature required to meet the specifications at $200 \mu\text{m}$ with a 1 arc minute diameter detector (not the

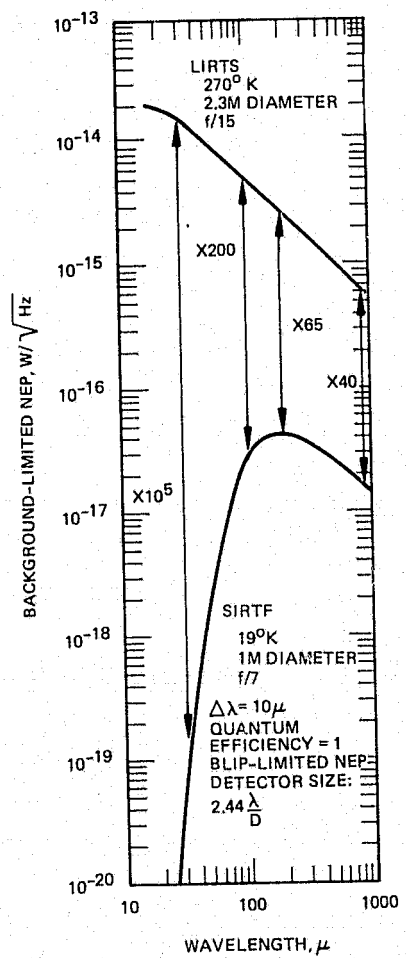


Figure 4-18. SIRTF and LIRTS NEP comparison.

diffraction-limited detector used for the Figure 4-18 comparison). The ratios of NEP sensitivities at 20 μm , 100 μm , 200 μm and 1000 μm are shown.

A better measure of a telescope's ability to detect faint sources is its noise-equivalent flux density per root hertz, measured at the entrance aperture. This is shown in Figure 4-19 for the same telescope parameters. The larger diameter and smaller obscuration of LIRTS reduces the sensitivity advantage of SIRTF by a factor of about 9. It is clear that under these conditions, SIRTF still is significantly more sensitive at wavelengths less than 100 μm . SIRTF can achieve a further sensitivity advantage at the longer wavelengths by increasing the cryogen flow and reducing the telescope temperature to the 10 K range. Thus, for sensitivity, SIRTF can provide a significant advantage at all wavelengths.

The LIRTS can achieve decreased noise below 30 μm by improving the optics so that it is diffraction limited down to 5 μm , but this improvement is

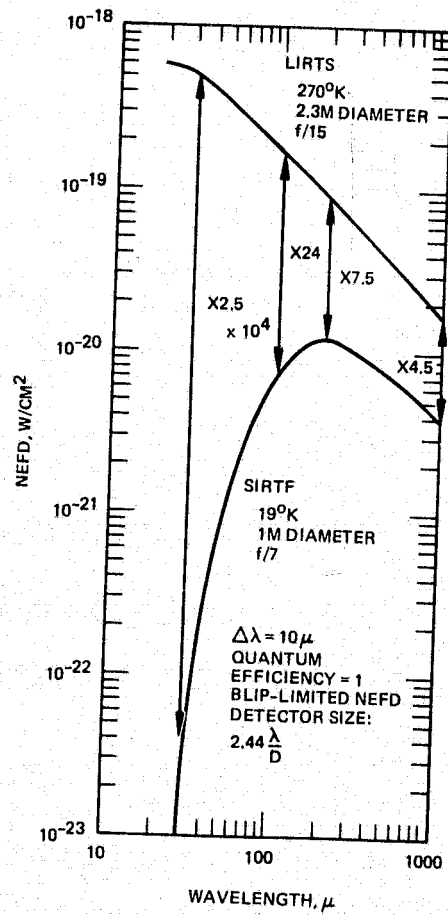


Figure 4-19. SIRTF and LIRTS NEFD comparison.

only a factor of 4 in a region where the SIRTF advantage is on the order of 10^4 . Costs are comparable as discussed in Section 6. The advantage of LIRTS in having increased spatial resolution represents a trade-off in the science area. The two telescopes are complementary in their capabilities: one provides the ability to study fainter objects and the other can resolve brighter objects at smaller angles.

4.5 DEDICATED GIMBAL VS. IPS

At the time the SIRTF contract was started, only very preliminary work had been completed on the IPS, and its status and potential capabilities were not clear. In order to insure that a complete SIRTF system was feasible, design of a SIRTF-dedicated gimbal mount was included in the study effort. Appendix D provides a description of this dedicated gimbal preliminary design.

As the IPS design matured, the SIRTF contract emphasis was redirected toward use of the IPS with SIRTF, such that it is now the baseline as described in Section 2.

In comparing the merits of the two systems, the following points stand out:

1. The IPS provides pointing accuracy and stability for SIRTF to levels where the requirements on the fine stabilization system are reasonable.
2. The inside-out gimbal design approach of the IPS provides maximum volume for mounting cryogen tanks on the telescope.
3. There is a substantial cost savings through use of the IPS (See Section 6).

The design approach for the dedicated gimbal assumed use of rotary joints (currently under development by Hughes for NASA-Ames) for transfer of cryogen from pallet-mounted tanks to the telescope. The yoke-type gimbal interferes with but does not rule out the mounting of large cryogen tanks on the telescope. As is well known, a yoke gimbal has some structural advantages over an inside-out gimbal. These are briefly enumerated below.

Driven Inertia

When the telescope is supported about its center of mass rather than at its end, the driven inertia is reduced by a factor of 3 to 4. The size and power requirements for the gimbal torquers are correspondingly reduced.

Sensitivity to Linear Vibration

Center of gravity gimbaling minimizes rotational disturbances of the telescope caused by linear vibration of the pallet.

Structural Problems

When the telescope is mounted about its center of mass, its unsupported length is minimized. The problems relating to structural bending are therefore also minimized, and the resonant frequencies of the telescope are made as high as possible. The reduction in sensitivity to linear vibration and in structural problems might make possible the elimination of the second folding mirror stabilization function. The telescope would be flexure mounted within the coarse gimbals, and fine pointed by movement of the entire telescope.

Disturbances Due to LOS Roll Commands

A final advantage of the dedicated gimbal design is that the innermost gimbal of the three-axis system provides the roll capability. The telescope can therefore be rolled 90 degrees about its line-of-sight (LOS) for polarization measurement purposes without moving the two outer gimbals and causing unnecessary LOS disturbances. The IPS gimbal configuration requires that all three gimbals be moved over large angles to produce LOS roll.

In addition, the yoke design permits the gimbal to be tested on the earth without an external support system. The use of pulleys, cables, springs, or other devices for supporting the telescope in a 1-g environment will alter the structural properties of the telescope such that ground testing of the IPS-telescope combination will not provide complete assurance that

operation in space will be satisfactory. Analysis and simulation will therefore be heavily relied upon. It has been assumed that the IPS will be tested on Shuttle flights before SIRTF uses it, and therefore no cost or mission effects have been estimated. Further discussion will be found in Reference 4-7.

4.6 CRYOGEN TRANSFER

An examination has been made of several possible methods for supplying super-critical helium (SHe) to the telescope. Four configurations were investigated in the study:

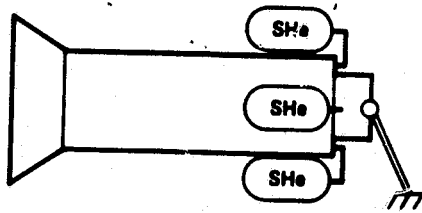
1. Storage of full flight supply on gimbal prior to launch.
2. Transfer of cryogen to the telescope periodically during flight.
3. Coils of flexible cryogen line providing continuous flow to the telescope during flight.
4. Rigid piping with on-axis rotary joints providing continuous flow to the telescope during flight.

The four configurations are shown schematically in Figure 4-20, and a performance summary is given in Table 4-10. Configuration (2) was eliminated from further consideration upon indication that sufficient on-gimbal area was available for at least one large storage tank (7 to 14 day supply).

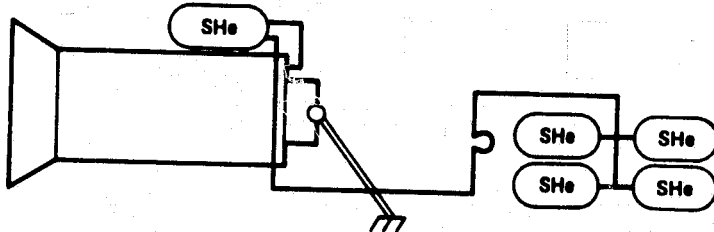
Configuration (1) appears capable of mounting up to three large tanks on gimbal while configurations (3) and (4) can utilize four tanks, so that all contemplated mission lengths can be met. Each tank can be connected to the telescope by a short length of rigid double-wall line. It should be noted that all configurations discussed here use double-walled line with super insulation in the annulus to reduce line heat leak.

Coils of flex line are used in configuration (3) to provide rotational capability. Three coils of 2.4 foot nominal diameter are required to stay within the limitation of a one-foot minimum bend radius and to clear the gimbal structure. An additional loop of flex line is needed to accommodate gimbal translation for any off-gimbal design. This requires an additional four feet. Flexible line has an inherently higher heat leak and pressure loss

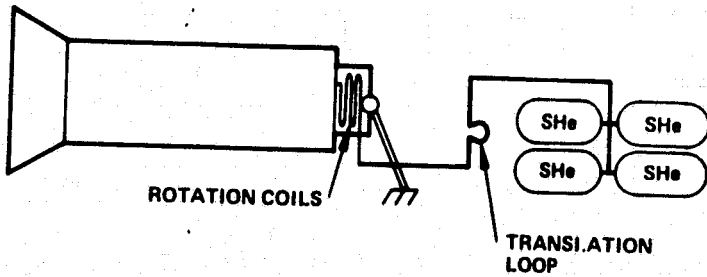
1. STORAGE OF FULL FLIGHT SUPPLY ON GIMBAL PRIOR TO LAUNCH



2. TRANSFER OF CRYOGEN TO TELESCOPE PERIODICALLY DURING FLIGHT (~ONCE EVERY 24 HOURS)



3. COILS OF FLEXIBLE CRYOGEN LINE PROVIDING CONTINUOUS FLOW TO THE TELESCOPE DURING FLIGHT



4. RIGID PIPING WITH ON-AXIS ROTARY JOINTS PROVIDING CONTINUOUS FLOW TO THE TELESCOPE DURING FLIGHT

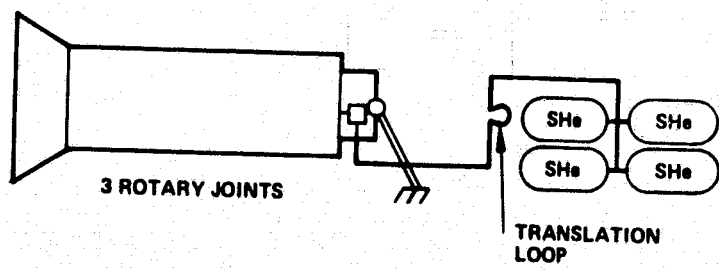


Figure 4-20. Cryogen supply trade study approaches.

TABLE 4-10. CRYOGEN SUPPLY TRADE RESULTS

Configuration	Line Size	Line Length	Weight	Heat Leak(W)	Δ Helium Temperature Tank-Telescope(K)
1. Tanks on Telescope	ID: 0.3 cm (1/8 in) OD: 1.3 cm (1/2 in)	4.6m (15 ft)	0.68 kg (1.5 lb)	0.9	0.5
2. Periodic Transfer		Not considered - high risk - can mount large tank on gimbal			
3. Continuous, Flex Line	ID: 0.3 cm (1/8 in) OD: 1.3 cm (1/2 in)	12m (39 ft)	3.5 kg (7.8 lb)	5.7	3.2
4. Continuous, Rigid Line	ID: 0.3 cm (1/8 in) OD: 1.3 cm (1/2 in)	4.9m (16 ft)	1.4 kg (3 lb)	2.3	1.2

than rigid line of the same diameter. For the 39 feet of 1/8 inch ID line required in configuration (3) the pressure drop is 4 psi. Should this be considered excessive, the use of 3/16 inch ID line would reduce the pressure drop to less than 1 psi. The larger line would present a penalty in terms of heat leak and disturbance torque acting on the gimbals.

Configuration (4) makes use of three rotary joints for three-axis rotation. In order to accommodate gimbal translation, an additional loop in the cryogen line is required as indicated in Figure 4-20.

A summary of cryogen supply requirements for the four configurations is given in Table 4-10. At the present time, it appears that configuration (1) is preferred. Configuration (4) is also feasible, but required an auxiliary drive system and would be complicated to interface with the IPS.

REFERENCES FOR SECTION 4

- 4-1 Shuttle Infrared Telescope Facility, Optics Design Tradeoff Report, Hughes Aircraft Company, October 1974.
- 4-2 Space Shuttle System Payload Accommodations, Level II Program Definition and Requirements. JSC 07700, Volume XIV, Revision D. NASA, Johnson Space Center, November 26, 1975, pp 3-9, 3-13.
- 4-3 Spacelab Payload Accommodation Handbook, ESTEC Reference No. SLP/2104, European Space Research Organization, May 1975, p 4-13.
- 4-4 Ibid, p. 4-61.

- 4-5 "A Large Infrared Telescope for Spacelab: Preliminary Analysis, Phase I Summary," Engins Marta, Space Division, February 24, 1975..
- 4-6 Shuttle Infrared Telescope Facility, Apodization Study, Special Report, Hughes Aircraft Company, September 1975.
- 4-7 Shuttle Infrared Telescope Facility, Initial IPS Evaluation for SIRTF Pointing and Stabilization (Data Item ID1-4.c.), January 1975.

5. SIRTF OPERATIONS

This section describes the SIRTF integration and launch support, flight operations, and post-flight support. The section on launch support includes a description of the cryogenic servicing operation, since it is the major non-standard support operation. The section on flight operations includes discussion of the Payload Operations Control Center (POCC).

5.1 INTEGRATION AND LAUNCH SUPPORT

Integration and launch support covers the period from the conclusion of SIRTF calibration in the cryogenic test chamber, through integration into Spacelab and the Shuttle, and up to launch. This entire period is shown as taking place at Kennedy Space Center; this is necessitated by the fact that SIRTF will be clamped to a two-pallet train, which cannot be carried in the C5-A aircraft. For flights subsequent to the first, SIRTF may or may not be cycled through the calibration facility, depending on the instrument package and observing plan. If SIRTF is to be calibrated, the integration starts upon return from the calibration chamber; if SIRTF is not to be calibrated, integration can commence immediately upon completion of routine maintenance, and refurbishment if needed.

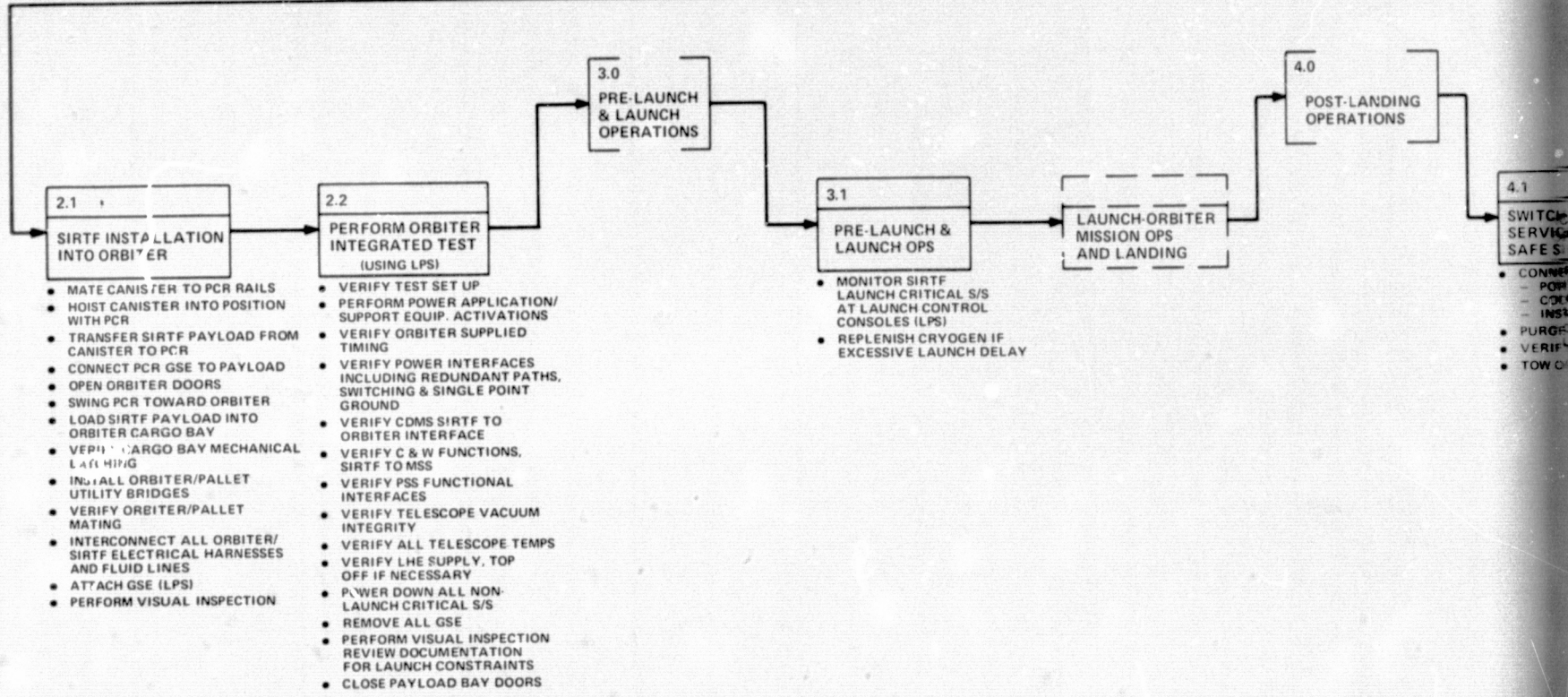
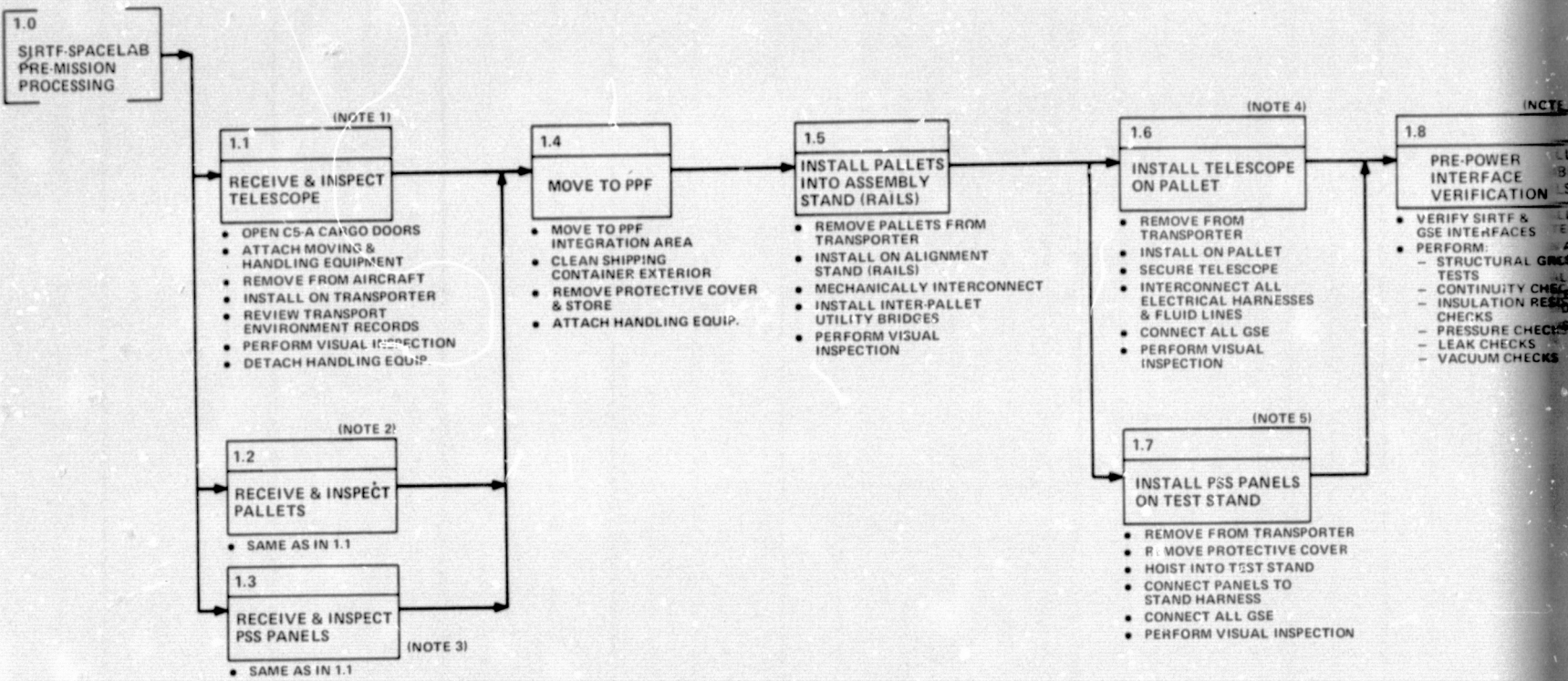
A Task Flow has been prepared (see Figure 5-1) which shows the SIRTF delivery to, integration with, and removal from the Shuttle.

Table 5-1 lists acronyms used in the flow chart.

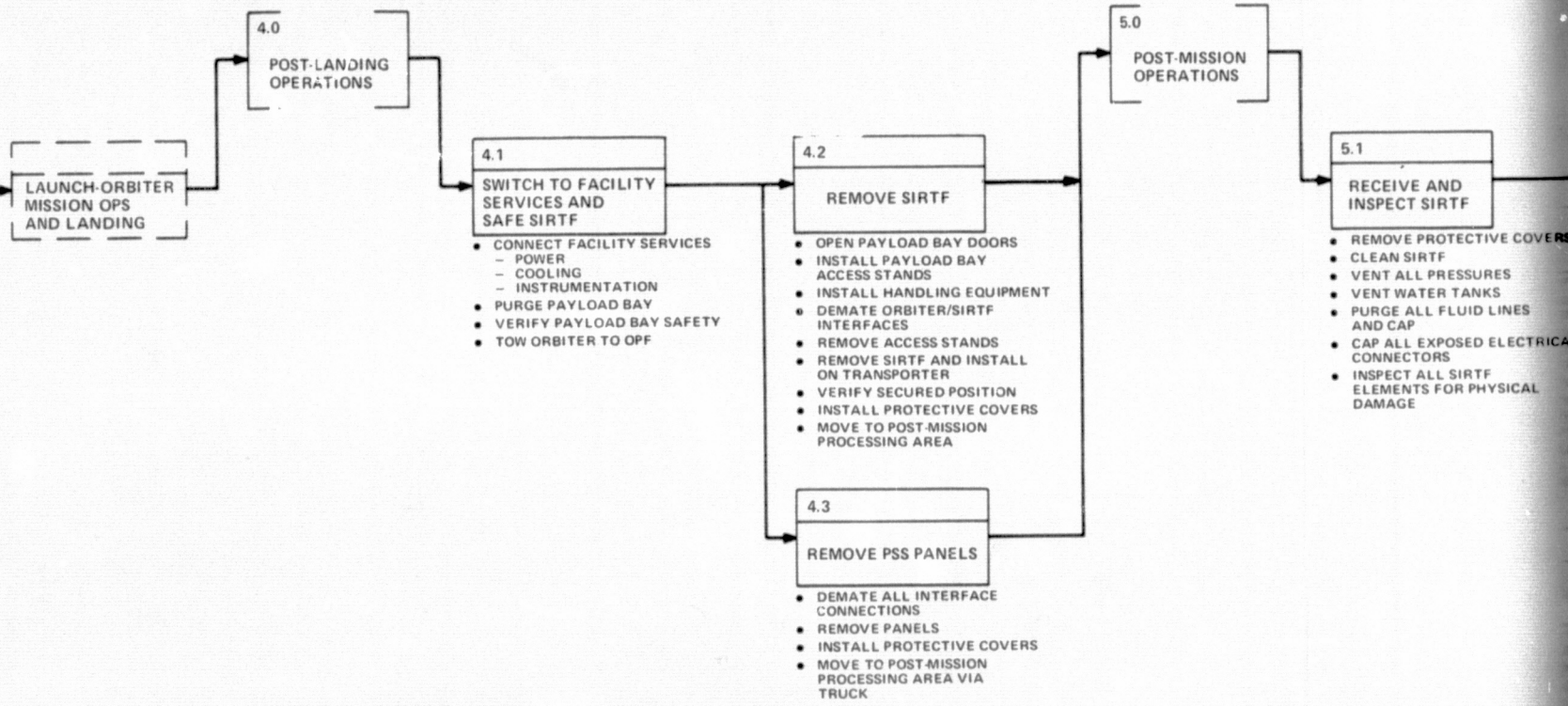
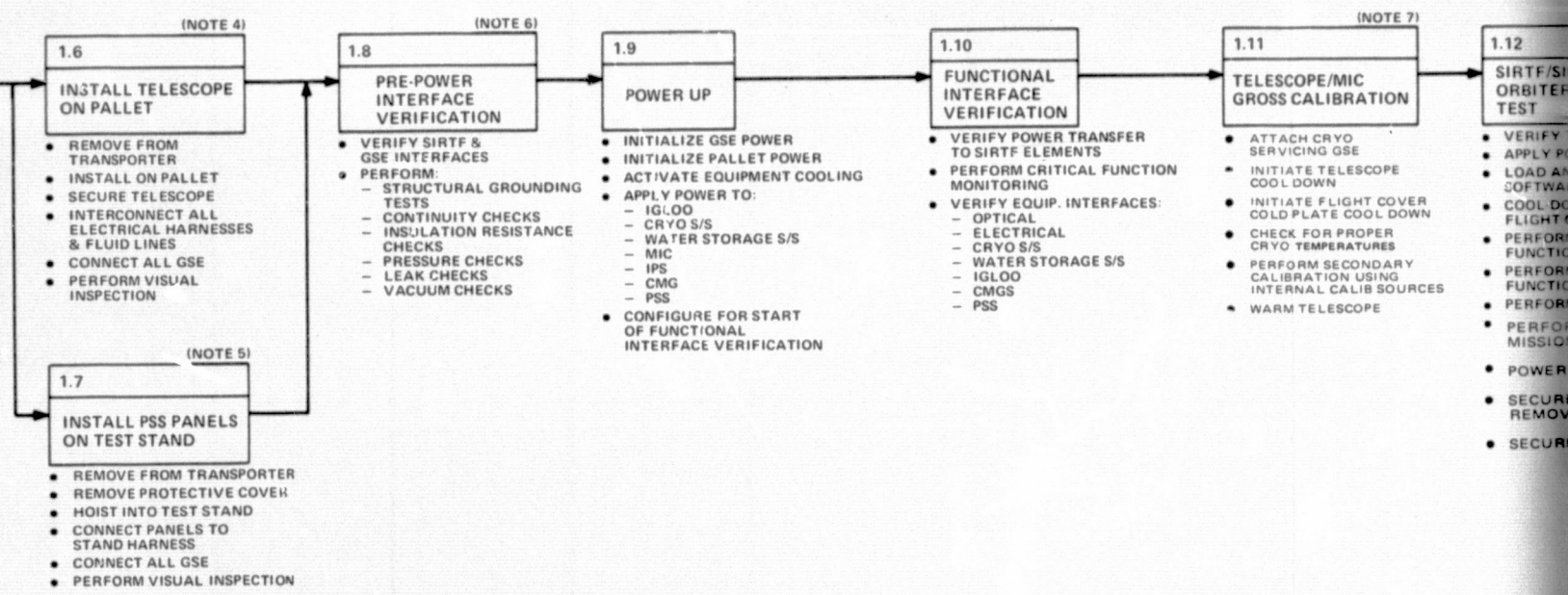
The launch site integration flow can be broken down into six main tasks, labelled 1 through 6 in Figure 5-1. Under the first task, the SIRTF and Spacelab are delivered and pre-mission processing occurs at the launch site. Boxes 1.1 through 1.15 in Figure 5-1 show how the SIRTF is integrated with Spacelab and moved to the Payload Processing Facility (PPF) for the

TABLE 5-1. LIST OF ACRONYMS FOR FIGURE 5-1

CDMS	Command and Data Management System
CMG	Control Moment Gyro
IOG	Inside-out Gimbal
IPS	Instrument Pointing System
LPS	Launch Processing System
MIC	Multiple Instrument Chamber
MSS	Mission Specialist Station
OPF	Orbiter Processing Facility
PCR	Payload Changeout Room
PPF	Payload Processing Facility
PSS	Payload Specialist Station
VAB	Vehicle Assembly Building



FOLDOUT FRAME



REPRODUCIBILITY OF THE
ORIGINAL PAGE IS POOR

FOLDOUT FRAME 2

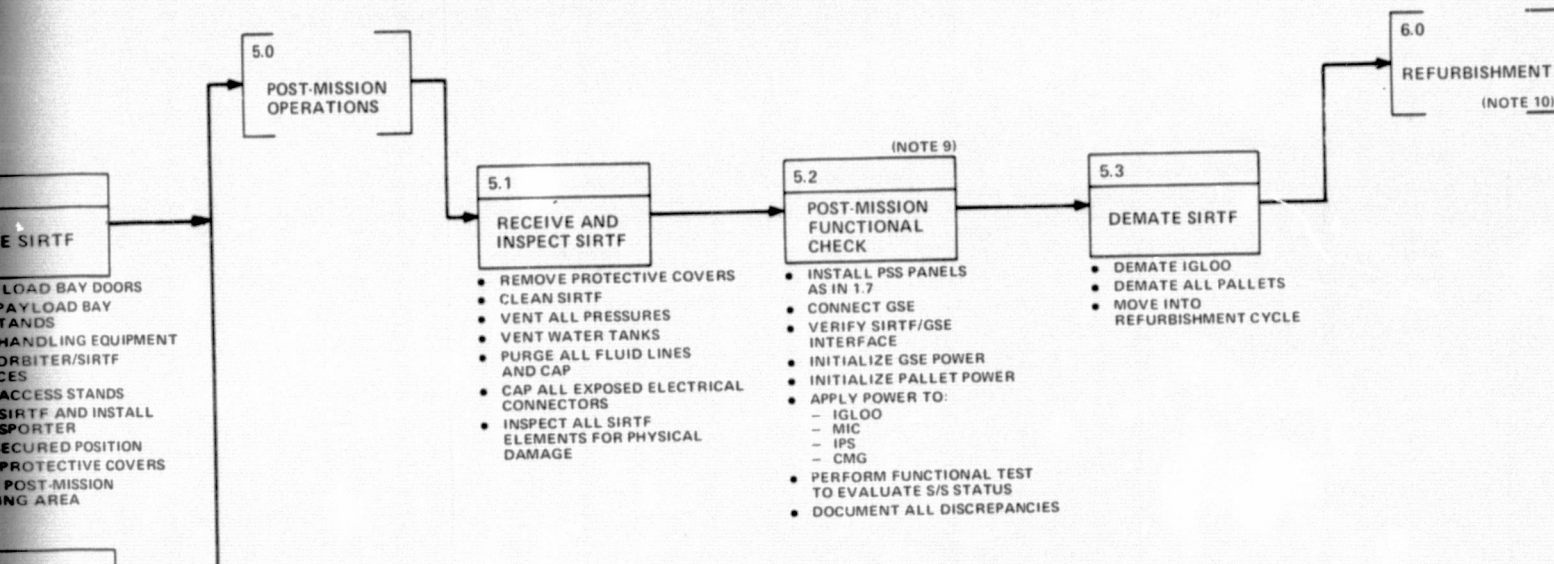
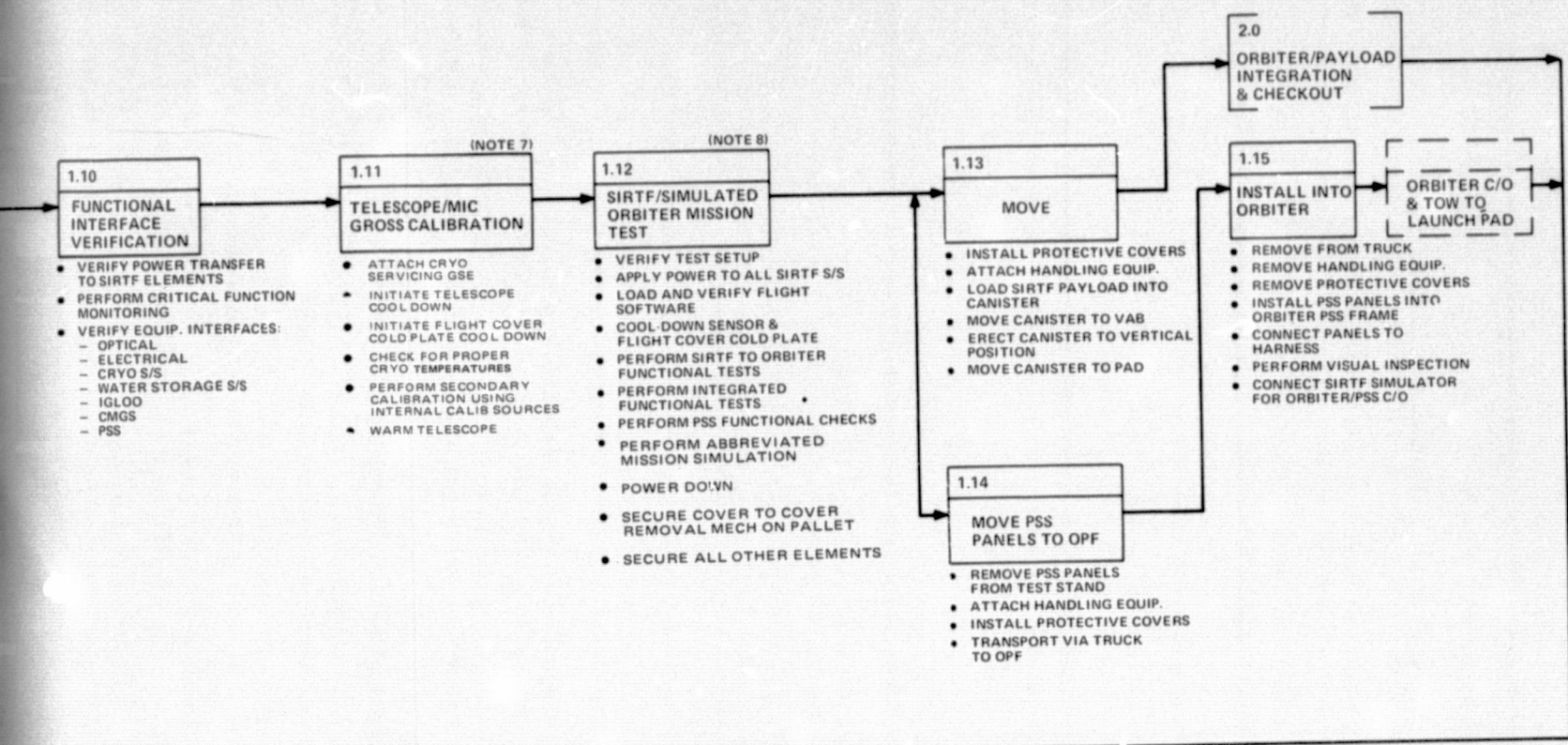


Figure 5-1. SIRTF launch site integration flow.

FOLDOUT FRAM

gross calibration of the telescope and MIC and the SIRTF/simulated Orbiter mission test. After the completion of these tests, the SIRTF-Spacelab is moved to the launch pad via the Vehicle Assembly Building (VAB). This is the start of the second major task, wherein the SIRTF-Spacelab is installed and integrated with the Shuttle Orbiter (see Boxes 2.1 and 2.2). Tasks 3 and 4 involve the pre-launch, launch, and post-landing operations. Removal of the SIRTF-Spacelab from the Shuttle Orbiter constitutes the fifth major task of the integration flow and is shown in Boxes 4.1 through 4.3. After the SIRTF-Spacelab and any SIRTF-peculiar Payload Specialists Station (PSS) panels are removed from the Shuttle Orbiter, tasks 5 and 6 take place. The final two major tasks (Post-Mission Operations and Refurbishment) are shown in order to complete the SIRTF launch site integration flow. Post-flight support will be discussed in Section 5.4.

Although there are some inconsistencies in details, in general operations 1.1 through 1.5 correspond to Level III integration; 1.6 through 1.11 correspond to Level II integration; and 1.12 through 2.2 correspond to Level I integration. Level IV integration is not shown on the integration flow.

The integration plan is currently built around launch pad integration of SIRTF into the Orbiter. The only reason for this is the fact that power is not available between the OPF and the launch pad, and continuous monitoring of the cryogen tank is necessary for safety reasons because of the very remote chance of a thermal leak developing and causing an explosion. If this monitoring can be provided, SIRTF-Orbiter integration will be moved to the OPF.

There are several references to vacuum checks in the course of integration. The telescope will be maintained in an evacuated condition throughout integration by means of a small vacuum pump. Monitoring of the vacuum will essentially be continuous; the vacuum checks in Figure 5-1 are critical points for vacuum integrity.

PRECEDING PAGE BLANK NOT FILMED

The following items are keyed to the Notes called out in Figure 5-1:

1. The pallet dimensions of approximately 4.6m by 3.0m (15 ft by 10 ft) require its installation into the C5-A delivery aircraft turned sideways from its normal Orbiter position. The C5-A entrance is limited to under 3.3m (13 ft.). As a result the telescope, which exceeds the pallet envelope, cannot be installed on the pallet during shipment and will require its own shipping pallet. Utility bridges are installed at KSC. The other SIRTF elements may be installed and shipped with the pallet since they fit within the pallet envelope. The Igloo arrives connected to its pallet with equipment installed. This functional flow assumes that the aircraft shipping transporters are not designed to be used for intra-plant moves. Therefore, the arriving SIRTF elements are installed on a launch site transporter.
2. Assume that pallets will contain:
 - Cryogen supply system (if not on telescope)
 - Water storage system
 - Interconnecting pipes and electrical cables
 - IPS
 - Igloo
 - Inter-pallet utility bridges
 - Vacuum system
3. The PSS main frame is the common Orbiter frame. Therefore, the PSS arrives as individual replaceable panels.
4. IPS/Telescope alignment will be carried out at this time. It is assumed that all GSE have been previously checked out.
5. It is assumed that the PSS panels are installed in a GSE test stand which simulates the Orbiter harness PSS interface. This is required in order to perform a functional checkout of SIRTF. It is assumed that all GSE has been previously checked out.
6. The SIRTF elements have been previously checked out during telescope integration at the Contractor facilities.
7. The cool-down sequence and calibration is assumed as follows: Prior to the start of SIRTF test, the cryo tanks are filled. The telescope cover has optical ports for calibration check.
8. All SIRTF testing is performed on an evacuated and cooled telescope. Electrical and data line integration takes place at this time (Subtask 1.12). A similar integrated functional test is again performed during Task 2.2, when the SIRTF-Spacelab is integrated with the actual Shuttle Orbiter. The cryogenic GSE, after the simulated Orbiter mission test, is moved to the PCR (see Task 2.1).

During the electrical and data line tests, after integration with Spacelab the following end items are checked out:

- On-board computer
- Mission software
- Star catalog data
- Star tracker sensors
- Payload specialist station (PSS) panels
- Mission specialist station (MSS) panels
- Remote access unit (RAU)
- Caution and warning (C&S) system
- Uplink and downlink communication with the POCC.

The checkout procedures for demonstrating acceptable performance of the above end items are as follows:

A. Computer Operations Checkout

1. Verify computer turn-on sequence from PSS panels.
2. Perform computer auto-check (sum and parity).
3. Perform noise check.
4. Dump previously loaded mission software and star catalog data.
5. Load and verify next mission software and star catalog.
6. Perform timing signal accuracy check, if internally timed, or verify Orbiter simulated clock.

B. Star Tracker Checkout

1. Simulate star tracker sensor operation with star simulator.
2. Verify star tracker operation on PSS panels.

C. Remote Access Unit (RAU) Checkout

1. Simulate the RAU inputs from the various data sources.
2. Verify response on PSS panels and caution and warning (C&W) signals on mission specialist station (MSS) simulated panels.

D. Communication Checkout

1. Inject an uplink command using a simulated Orbiter communication interface unit (CIU) and verify on PSS and MSS panels, and at POCC.
2. Receive a downlink signal at the CIU and verify SIRTF static status (both housekeeping and scientific data). (SIRTF does not have its own transmitter receiver, but uses the Orbiter's telemetry system.)

E. Experiment Checkout

1. Verify temperatures
2. Inject test signals
3. Monitor outputs

F. SIRTF Stabilization Subsystem Checkout

1. Inject chopping commands
2. Monitor response

Discussion of post-flight operations is presented in Section 5.4.

5.2 CRYOGENIC SERVICING

5.2.1 General Approach

As stated in the introduction, cryogenic servicing of the SIRTF storage tank and telescope will be described in more detail than the other elements of the integration procedure, because the requirements are less widely known than other integration procedures. The general approach will be to use the procedures developed for servicing the supercritical helium tank for the Lunar Module descent stage engine pressurization.

The cryogen subsystem requirements lead to two major decisions with respect to launch support operations. First, because the Orbiter will be powered down during transport from the Orbiter Processing Facility (OPF) to the launch pad, pressure and temperature monitoring of the cryogenic tanks cannot be maintained continuously. The monitoring is advisable because the helium tanks represent a serious although remote safety problem;

if a heat leak develops, the helium may be subjected to thermal runaway and, under certain conditions, the tank can explode. Thus it is planned that SIRTF will be integrated into the Orbiter in the Payload Changeout Room (PCR) after the Orbiter has been erected on the launch pad.

The second major decision is that the SIRTF telescope and cryogen tank will be loaded in the Payload Processing Facility (PPF) prior to transfer to the PCR. This is because some 70 to 80 hours of service time are required to service the cryogenic tanks, and a similar period of time (in parallel) is required to cool down the telescope. The time frame presently allocated at the pad for servicing is 6 hours (Reference 5-1). Thus cryogenic servicing must precede installation of SIRTF into the payload bay. It is thus necessary that the payload cannister, used with the PCR for installation of payloads, provide facilities for monitoring status during transfer from the PPF to the PCR.

After installation of SIRTF into the Orbiter, a launch delay of approximately 12 hours or more will require reservicing of the cryo tank for the 7-day mission, and a launch delay of approximately 48 hours or more will require reservicing of the cryotanks for the 30-day mission. This is because supplying cryogen to telescope and vapor shield during launch hold will reduce the amount of cryogen available for the mission. If the delay occurs prior to disconnect of the T-4 umbilical, cryogen is transferred through the lines. If the hold occurs after T-4 disconnect, the lines must be reconnected. The payload bay doors need not be opened in either case. The quoted time elements of 12 or 48 hours, respectively, for the 7-day or 30-day mission, represent a realistic 6 to 7 percent margin for the cryogenic supply system.

5.2.2 Cryogenic Servicing Timeline

The basic servicing steps are given in Table 5-2. The major steps are discussed below. The procedure was developed and used repeatedly by Grumman in servicing the Lunar Module supercritical helium tank; no substantial deviations from the Lunar Module procedures are recommended.

TABLE 5-2. SIRTF CRYOGENIC HELIUM SERVICING TIME LINE

Step	Function	Hours Required
(a)	GSE leak check, pump-down of GSE vacuum including lines, liquid helium dewar fill, leak test GSE, purging and sampling of GSE	40 (30-day) 30 (7-day)
(b)	Connect GSE to T-4 umbilical; purge with gaseous helium; sample	4
(c)	SIRTF cryogenic tanks initial fill for cold soaking	4
(d)	Cold soak	24
(e)	Refill LHe dewar; fill LN ₂ cart (parallel with operation (d))	(8)
(f)	Final liquid of SIRTF tanks	4
(g)	Top-off to desired density	
(h)	Disconnect GSE, cap flight coupling halves	2
(i)	Final helium leak check of flight items	2
	Total Services Servicing Time:	70 - 80

Inerting (a) and (b)

Preceding the cryogenic operations, the whole ground and flight system is inerted by ambient temperature helium.

Final Fill with Liquid Helium

At the end of the cold soak cycle, another liquid fill is initiated. The steps are similar to those described previously with one exception: Before opening the fill line to the tank, the supply line between the dewar and the fluid distribution systems is prechilled by venting helium through the bypass valve of the fluid distribution system. Temperature monitoring within the GSE indicates when the line prechill is complete. Subsequently, the tank vent valve is opened, the by-pass valve closed, and the tank fill valve opened. Thus, refill operation of the tank is achieved without unnecessarily introducing warm helium into the flight tank. Completion of the tank refill operation is again signalled by the indication of liquid present in the vent line.

Purging is maintained until gas samples indicate sufficiently low (generally less than 50 ppm) contamination levels.

Cold Soaking

To assure stabilized temperature conditions in the flight tank by the time the GSE is disconnected, prechilling of the flight tank always precedes the final fill operation. This consists of filling of the flight tank to overflow condition, and subsequently maintaining at least some cold fluid in the tank for a minimum of 22 hours duration.

The initial liquid loading operation for cold soaking is carried out as follows: All valves providing a continuous flow passage for helium between the storage and transfer dewar are commanded to the open position. Slight over-pressure (0.4 to 0.5 atmosphere) is applied on the dewar which initiates the mass transfer into the flight tank. Substantial pressure oscillation is noticeable during the first 10 to 15 minutes of transfer, caused by sudden volumetric expansion of liquid helium when it contacts warm metal parts. The transfer is completed when the liquid indicators in the fluid distribution subassembly signal liquid helium present in the vent line.

This operation takes approximately 1 hour. Subsequently, both the fill and vent line valves of the fluid distribution system are closed and the tank is allowed to cold soak for a minimum of 22 hours. During this time, helium temperature within the tank is maintained between 5°K and 9°K through partial venting of the tank when the higher temperature is reached.

Topping-Off to Higher-Than-Liquid Densities

During the final liquid fill operation, just described, preparations are made to ready the conditioning unit subassembly for the final step of the loading operation: Topping-off, that is, to drive the liquid helium within the flight tank into the supercritical regime, with associated attainment of the desired higher-than-liquid helium density. Once the final liquid fill is completed, the following steps accomplish the topping-off operation in less than

2 minutes to 0.13 gram per cubic centimeter (8.2 pounds per cubic foot) and less than 4 minutes to 0.14 grams per cubic centimeter (8.8 pounds per cubic foot):

- Flow from the liquid helium dewar is stopped.
- The vent valve is closed in the fluid distribution subassembly.
- High-pressure helium gas flow is initiated through the conditioning unit subassembly until the desired tank pressure is reached. Approximately 5 atmospheres pressure in the flight tank yields the 0.13 gram per cubic centimeter (8.2 pounds per cubic foot) density condition.
- The flight tank is disconnected at the fill and vent couplings.

Access to the cryogenic tanks within the payload bay (after installation in the Orbiter) will be provided by securing the fill and vent flight coupling halves of each cryogenic tank into the prelaunch payload service panel. This will require flexible connections between flight tank(s) and the service panel. Reservicing in launch position would consist essentially of reconnecting the GSE to the T-4 umbilical and at steps (e), (f), and (g) of the Table 5-2 time line. Contaminant sampling may be averted through maintenance of positive helium pressure on the already-verified GSE system while it is being moved to the Shuttle/Orbiter service structure.

Servicing in launch position (orbiter X-axis vertical) necessitates that the parts be located to allow fill and vent in either orientation. This will result in a slight reduction in fill factor component to single orientation tanks, but this is not serious due to the ample capacity.

Automation of the GSE does not seem to be justified beyond that employed on the Apollo-LM system. Actually, except for line connections, the servicing steps are made through remote control valve operations. Engineering supervision will likely be present throughout the loading operations, as was the case on the LM. There is, however, no reason why the whole loading operation could not be made fully automatic, using a sequencer reacting to the stimuli generated by the liquid level indicators and/or pressure and temperature signals of the GSE.

In summary, close reliance on the Apollo-LM servicing technique and system is recommended, using the LM conditioning unit subassemblies

with commercially available dewars and new fluid distribution system(s) as described in Section 2.4.2.

5.3 FLIGHT OPERATIONS

SIRTF flight operations concepts have been developed around the basic four-man Orbiter crew as defined in Vol. XIV (Reference 4-2); Commander, Pilot, Mission Specialists, and Payload Specialist. The crew will be supported by personnel located at the Payload Operations Control Center, and at remote sites in direct communication with the POCC. Direction of SIRTF observation will be from a principal investigator representing the mission scientists at a remote site (Ames Research Center). The duties of all personnel follow the general guidelines as given in Vol. XIV. Flight crew duties are discussed in Section 5.3.1, and POCC operations in 5.3.2. Section 5.3.3 presents an initial formulation of a malfunction operational plan.

Because of the complexity of SIRTF, MIC instrument and subsystem controls, it is planned that missions will be preplanned, and will follow the observing program. Hence much of the flight crew operations will be a matter of monitoring and adjusting a largely automatic series of operations. Qualified flight crews are essential, however, to detect malfunctions or faulty data taking, and to take over operations when the preplanned observing program cannot be followed, working with the mission scientists on the ground. The crew will have the ability to override and rearrange the planned sequence and/or substitute preprogrammed sequence (i.e., search rasters).

5.3.1 Flight Crew Duties

As stated above, the SIRTF crew for both 7-day and 30-day missions will be the basic four-man Orbiter crew: Commander, Pilot, Mission Specialist, and Payload Specialist. Because it reflects their relative involvement in SIRTF operation, it will be most convenient to discuss their duties in reverse order.

Payload Specialist

The payload specialist is responsible for attainment of the SIRTF flight objectives. He will be proficient in both SIRTF operations and the operations of the focal plane instruments mounted for the flight. This means a detailed knowledge of the telescope, cryogen system, instrument pointing system (IPS), focal plane instruments, individual instrument data processors, the overall MIC data processor, and the software packages for on-board data processing. He will understand the observational goals of the various instruments and the effects of contamination of various types and levels on the observations. He will be capable of assisting the ground-based mission scientists in planning meaningful observation programs if the prepared observing program cannot be used. SIRTF is generally compatible with other astronomy payloads, so it is envisioned that the Payload Specialist will be an astronomer with the necessary additional specific training, or possibly an infrared measurements specialist with a strong astronomy background, if the other payloads are also infrared astronomy payloads.

Mission Specialist

The mission specialist will be proficient in SIRTF operations, and will have detailed knowledge of SIRTF and SIRTF support subsystems operations and requirements, including the cryogenic supply, IPS, water storage system, Spacelab Command and Data Management System (CDMS), Orbiter Avionics system. He will be responsible for coordination of overall Orbiter operations in the areas of flight planning and consumables usage as they affect SIRTF operations. He may, if requested, assist in the management of SIRTF operations and/or act in specific cases as the Payload Specialist.

In view of his training requirements and mission responsibilities, it is expected that the Mission Specialist will be a career astronaut.

Pilot and Commander

Besides their Orbiter flight duties, which are not discussed here, it is expected that the Pilot and Commander will have a high level of proficiency and knowledge of SIRTF support systems and operations. These will include

electrical power (EPS), thermal control, water, storage, command and data management, avionics and payload communications. They will be responsible for on-orbit management and operation of these support systems. They may support or perform specific payload operations if requested.

Figure 5-2 is a flow chart representing typical PS and MS duties for three major time phases: before, during, and after the flight. Their responsibilities include the setting up of a series of initial conditions for Orbiter attitude throughout the mission. Several months of pre-flight training will be followed by a pre-flight briefing period and mission specific familiarization at the launch site. After a week to a month in orbit, flight debriefing will be followed by routine post-flight activities. Since the pre- and post-flight activities are treated elsewhere, they have been only briefly sketched for orientation of the overall mission. The activities between lift-off and touch-down are treated in more detail.

The PS and MS launch and descent duties for SIRTF are minimal; the major responsibilities in orbit will begin with the initialization of SIRTF, followed by observing sequences and maintenance and concluding with de-orbit preparations. The workload will be long but not extremely strenuous, probably 13 hours per 24-hour period. When automatic controls are functioning smoothly, SIRTF may be left to run automatically while the crew is asleep.

Because it is planned that SIRTF operates according to a pre-programmed observing sequence, the routine monitoring of observations can be done by either the payload specialist or the mission specialist. When anomalies are noted or problems occur, it may then be necessary to call on one or the other (most likely the payload specialist) for his expert knowledge. Manual intervention in the observing program by the PS or MS is possible at any time.

Analysis of PS and MS duties provides a convenient way to assess SIRTF efficiency. For the various operational phases, the following estimates apply:

Block No.

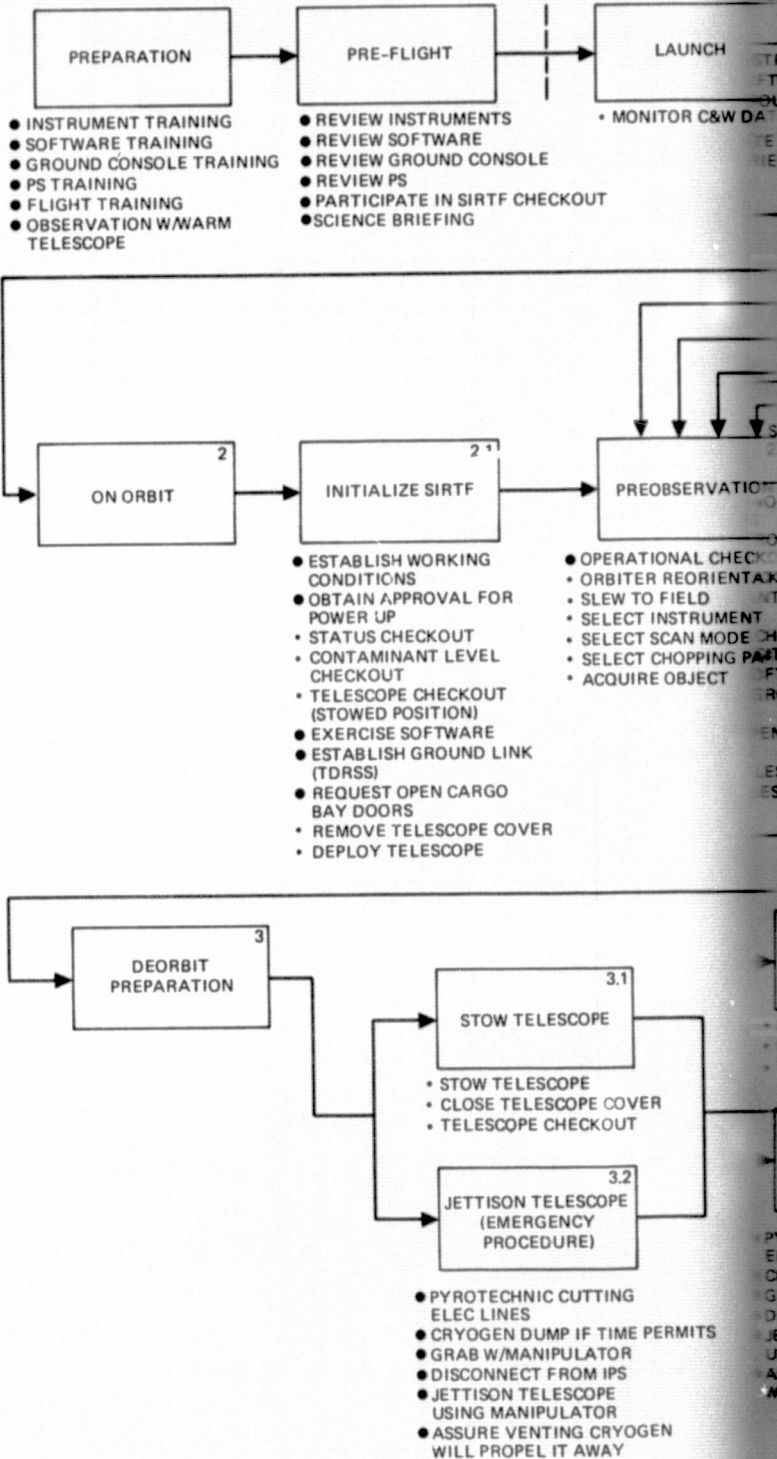
- (2.1) Initialize SIRTF. Order of 1-hour actual operations, but contamination restrictions may delay this for 24 hours.
- (2.2) Pre-observations. Order of 5 minutes per target.
- (2.3) Observations. Order of 20 minutes per target.
- (2.4) Ground contact. Order of 5 minutes per rev; continuous contact is possible, but may not be economical or necessary.
- (2.5) Maintenance. Order of 10 minutes for 12-hour of operation.
- (3) De-orbit preparation. Order of 2-hours.

Based upon the above assumptions, approximately 60 percent of the total flight time may be used for observation on a 7-day mission, and 70 percent on a 30-day mission.

5.3.2 POCC Operations

Figure 5-3, representing the duties of the ground-based scientists at the Payload Operations Control Center (POCC), is presented in a format similar to that of Figure 5-2. The numbering system is consistent, in that the same block numbers represent like time periods on each figure.

The ground-based scientists may be intimately familiar with a single instrument or familiar with all instruments. Generally, there will be experimenter teams for various science objectives and there may be teams for specific instruments. A single principal investigator for each mission will speak for all science teams, although team members may serve as contact during use of some instruments. The scientists will be familiar with the science center consoles and with the SIRTF-related Orbiter consoles. Their primary involvement at the instrument/data level will necessitate a thorough involvement with SIRTF for considerable periods prior to missions.



FOLDOUT FRAME

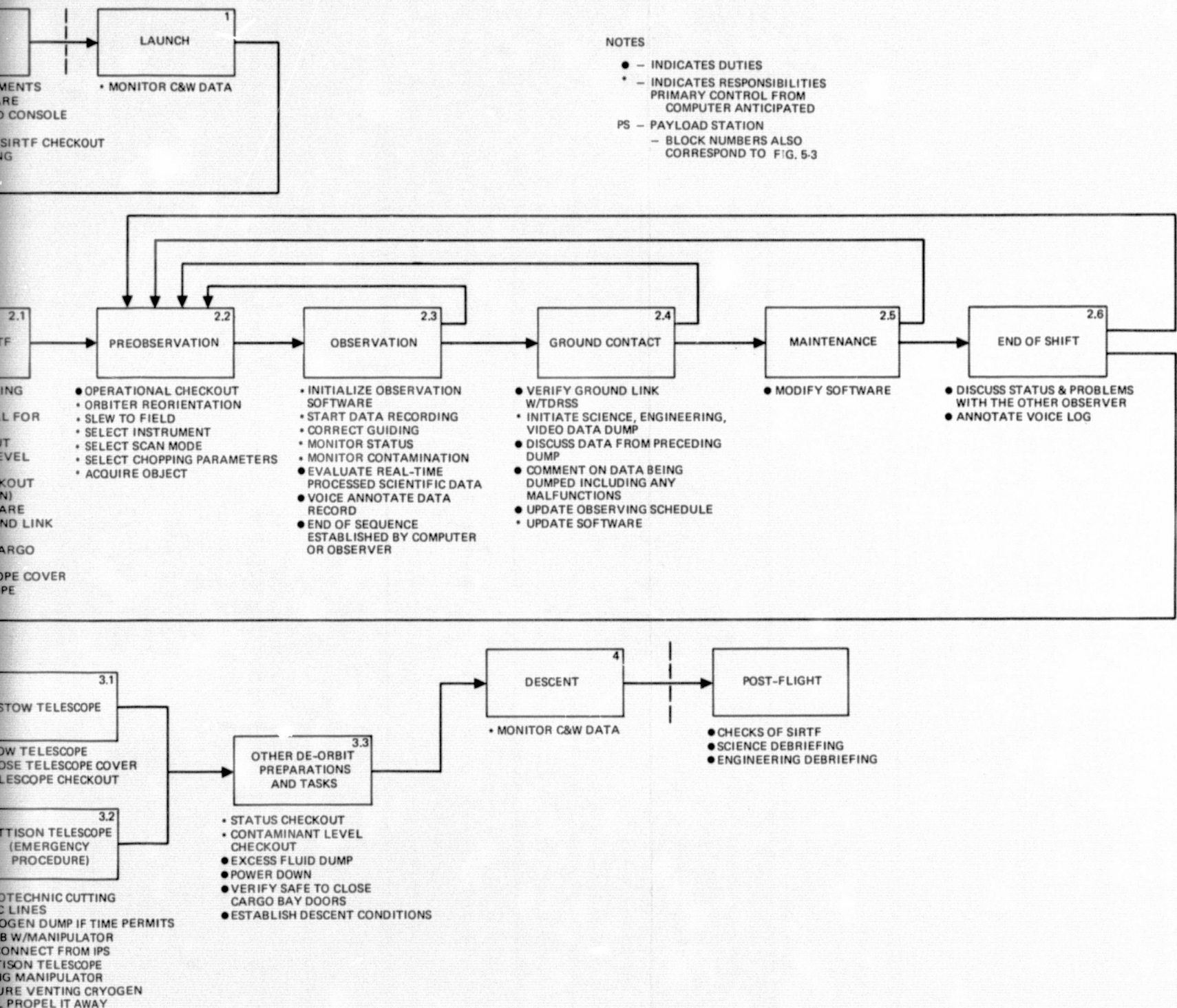
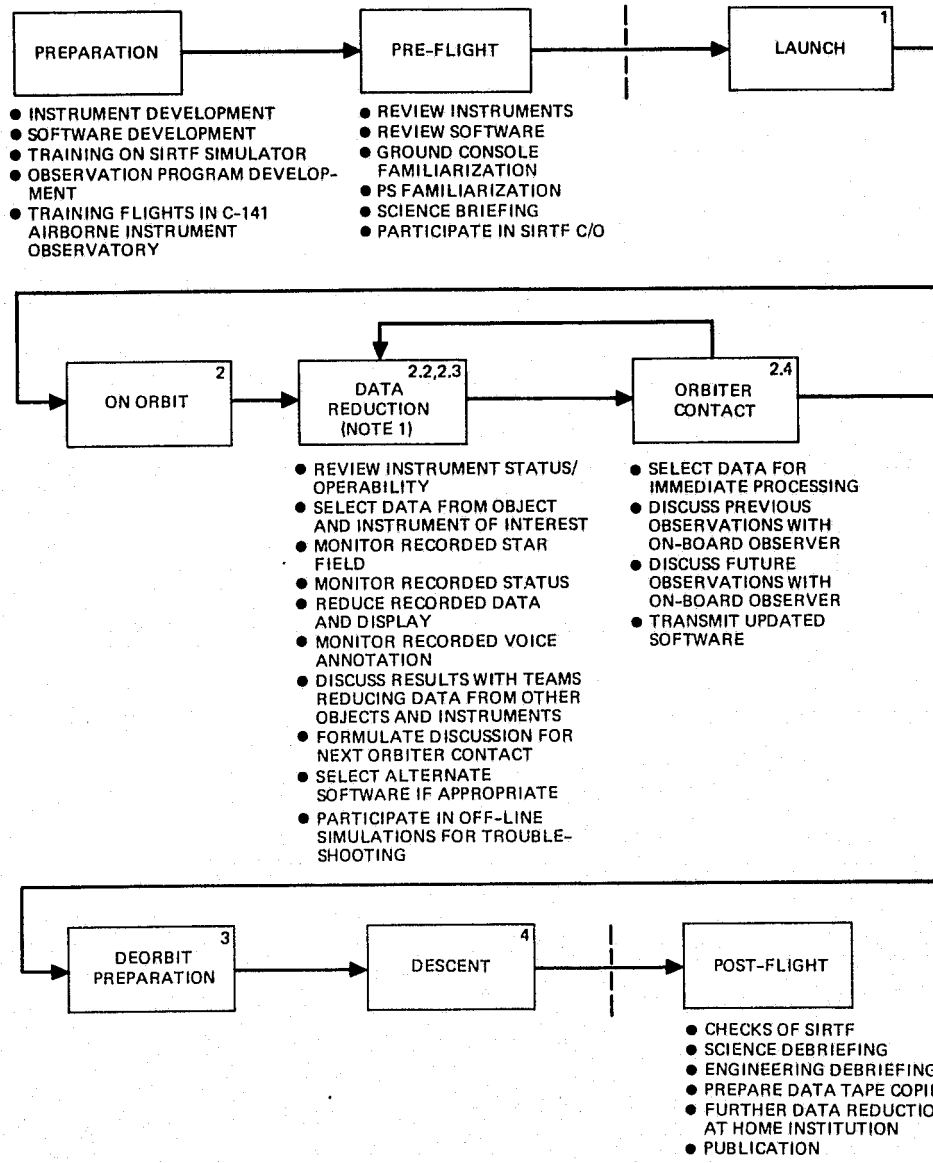


Figure 5-2. Payload and mission specialist SIRTF duties.



NOTES

1. ALL DATA REDUCTION FROM MAGNETIC TAPE DATA TRANSMITTED DOWN FROM PREVIOUS REV.
2. BLOCK NUMBERS ALSO CORRESPOND TO FIG. 5-3
PS - PAYLOAD STATION

Figure 5-3. Ground-based scientist SIRTF duties.

While TDRSS will allow essentially continuous (80 percent) communication with SIRTF, the need for continuous communication is not expected to arise often. Normal operation is expected to consist of short periods of contact (Block 2.4 of Figure 5-3) interleaved with long periods of data gathering by SIRTF and data analysis by the ground-based scientists

(Blocks 2.2 and 2.3 of Figure 5-3). For efficient ground station operation, it is expected that the scientists will be able to select the quantities essential for primary evaluation from the compressed downlink data train; the necessary decoding and sorting capability at the POCC to supply the scientists with appropriate quick-look data is assumed to exist.

Figure 5-4 illustrates the planned flow of commands and data. TDRSS is the prime mode for data transfer, command, and voice. The TDRSS data passes through the White Sands station to the POCC at Johnson Space Center, and finally to Ames Research Center. Tapes of data as recorded at White Sands are sent to Ames. At JSC, the data tapes are stripped, annotated and pertinent Orbiter data (e.g., state vector) are added. Reduction of the data to scientifically useful form is done at the Science Operations Center at Ames.

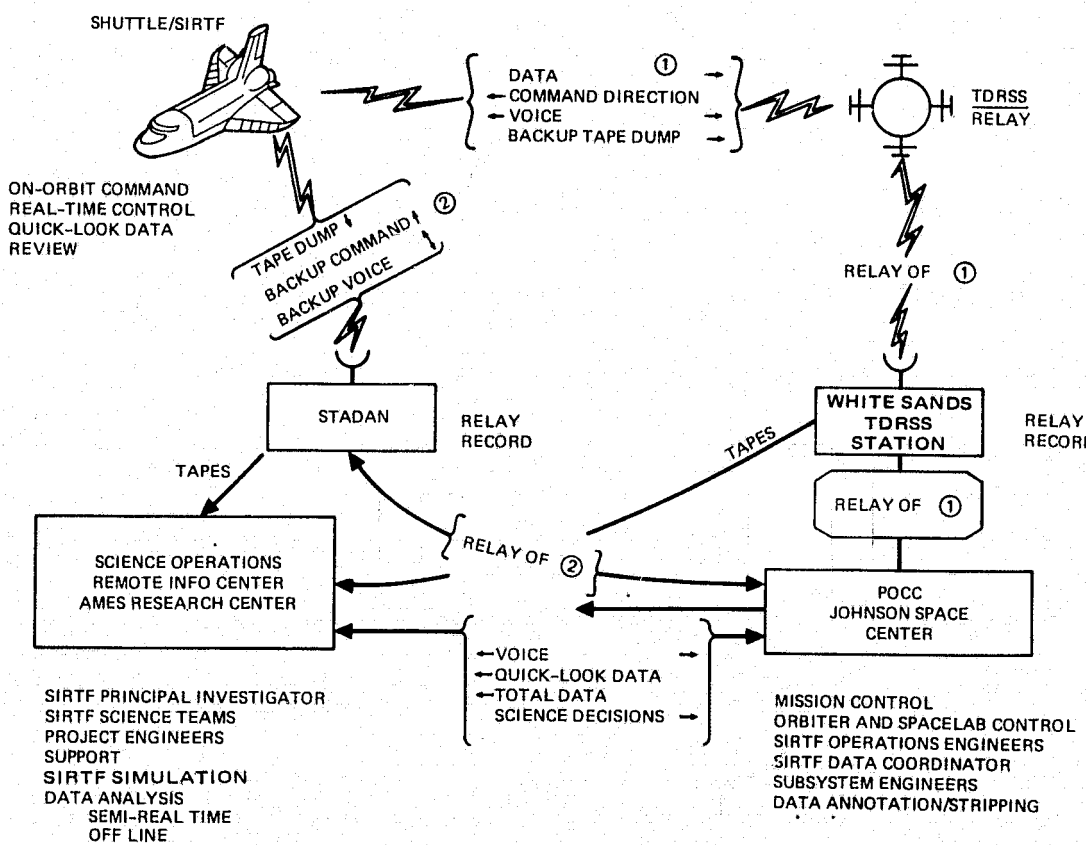


Figure 5-4. SIRTF on-orbit operations.

All POCC will also have facilities for generating quick-look data from selected portions of the total data. This will be transferred to Ames. Science decisions are relayed from Ames through JSC and to the Payload Specialist via White Sands and TDRSS.

NASA's STADAN stations will act in pickup mode for all the TDRSS functions discussed above. Relay records will be sent to Ames from the STADAN stations; however, the primary data mode will be through the POCC. The STADAN stations will be the primary mode for tape dumps when data is accumulated due to TDRSS outages. Alternatively, after short outages, the tapes can be dumped through TDRSS.

5.3.3 Mission Philosophy for Partial Malfunctions

In order to develop a back-up mission philosophy for partial malfunctions, several significant mission rules must be considered and agreed upon. As the SIRTF Program evolves, these mission rules may be altered and new ones introduced. During the SIRTF Program, mission philosophy will be continually evaluated at conferences attended by representatives from the NASA Centers, the SIRTF contractors, and the participating astronomers.

For this task, the following significant mission rules are being proposed and will be used as the criteria for developing back-up mission philosophy in the presence of a partial malfunction.

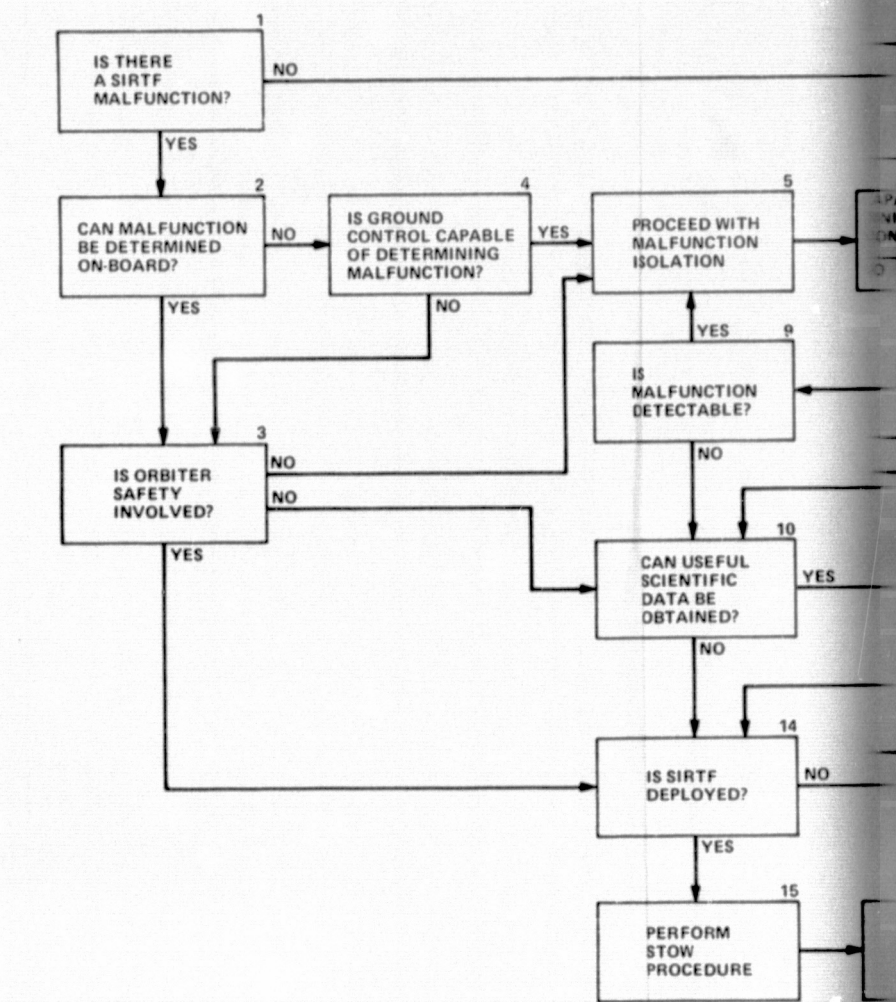
- Under all conditions, if Shuttle Orbiter or crew safety is involved, the SIRTF mission will be aborted and the Orbiter will return to earth.
- If useful scientific data can be obtained, the SIRTF mission will continue with an alternate operation.
- If the partial malfunction cannot be corrected, but useful scientific data can be obtained, then the SIRTF mission will continue.
- If only one instrument in the MIC is operating satisfactorily, the SIRTF mission will continue.
- If the SIRTF cannot be stowed in the normal manner, the EVA hand crank stowing will be used. If this fails, the wires will be guillotined and the payload detached from the Orbiter so that it can be drift into space; the IPS performs this separation.

- If the partial malfunction cannot be determined on-board or by ground control, and Orbiter safety is not involved, the mission will continue as long as useful data is being obtained (on-board crew and ground personnel will continue to attempt to isolate the cause of the partial malfunction).

In order to show how the mission rules are utilized in developing a back-up philosophy in the presence of a partial malfunction, the SIRTF Malfunction Decision Tree (Figure 5-5) was created. This decision tree is general enough to handle most partial malfunctions that can be considered at this time.

Referring to Figure 5-5, the flow of alternate questions and decisions starts with the question of the presence of a SIRTF malfunction, Block 1. If the malfunction can be determined on-board (Block 2), the next question (Block 3) is whether Orbiter safety is involved. For the case where safety of the Orbiter is involved, the return trip to earth is only held up if the SIRTF is deployed. Blocks 16 through 19 consider the case where the SIRTF cannot be stowed. If the malfunction cannot be determined on-board, ground control will be asked to determine the partial malfunction. If neither the ground nor the on-board crew is able to determine the malfunction, the flow goes back to Block 3 to ascertain whether Orbiter safety is involved. If Orbiter safety is not involved, isolation of the malfunction will be attempted (Block 5). If the malfunction cannot be corrected (Block 7) but useful scientific data is obtained, then the mission will continue. Where the malfunction can be corrected (Block 7) in the Orbiter's cargo-bay, the Mission Specialist (MS) will first use the Remote Manipulator System (RMS) to perform the correction. Where manual assistance beyond the capability of the RMS is required, the MS will perform an extra-vehicular activity (EVA) to correct the partial malfunction on the payload.

As an example, assume a partial malfunction in the form of severely limited travel of the SIRTF telescope about the vertical position. Also assume it is not possible to stow SIRTF. Since in this case immediate Orbiter safety would not be involved and very likely some useful scientific data could be obtained, the mission would therefore continue under the mission rules that have been proposed. It is obvious that each partial malfunction must be examined carefully to determine where it fits on the malfunction



FOLDOUT FRAME

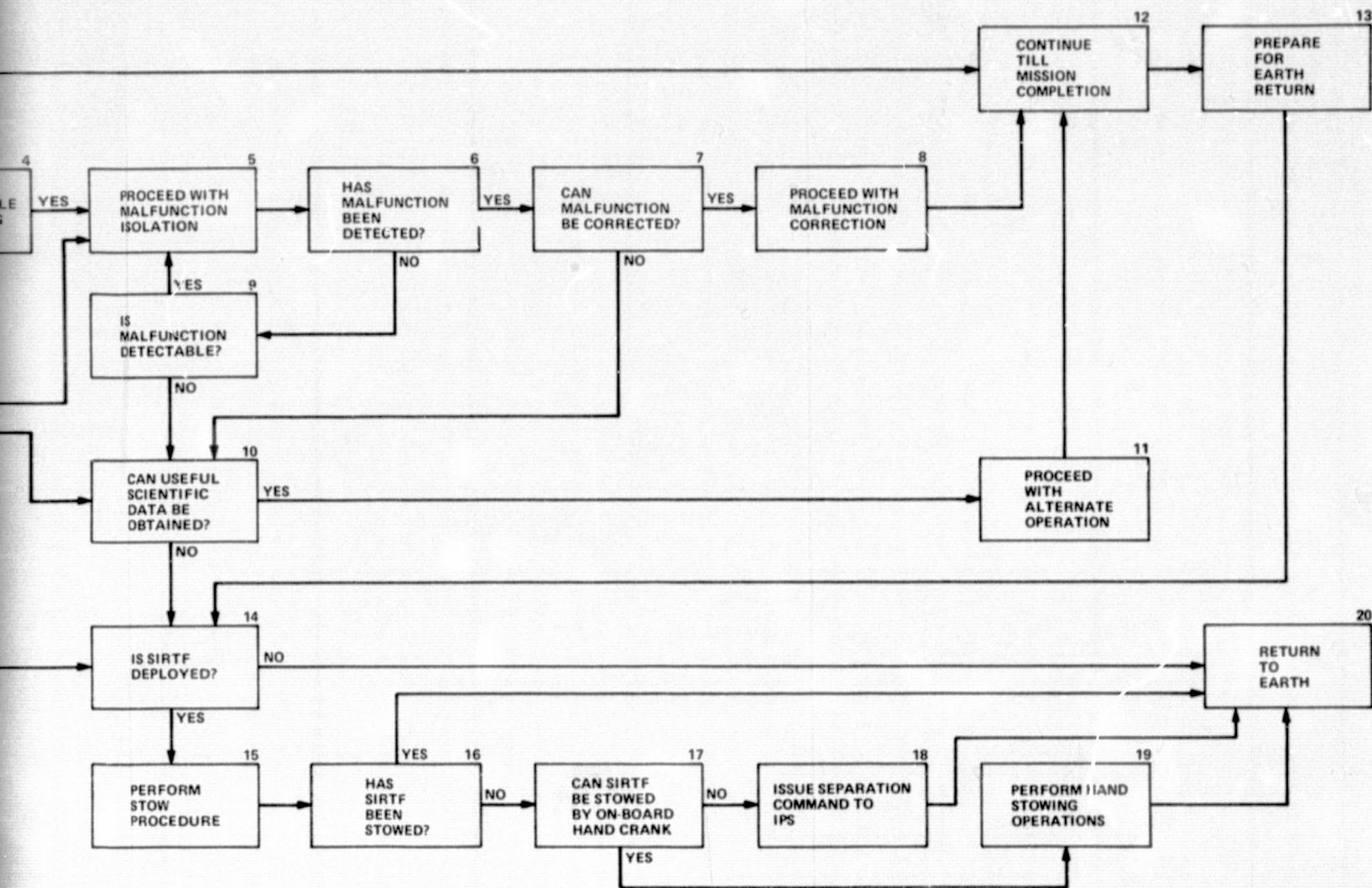


Figure 5-5. SIRTF malfunction decision tree.

decision tree. Another area that must be investigated thoroughly for further definition is the concept of what constitutes useful scientific data. Each instrument/experiment will establish a minimum success criterion before launch, as will the whole payload.

5.4 POST-FLIGHT OPERATIONS

Post-flight operations are shown in boxes 4, 5 and 6 of Figure 5-1. These include post-landing operations, post-mission operations, and refurbishment if necessary.

With respect to Block 4-1, there are no requirements, under normal conditions, for rapid connection to facility services for SIRTF or its specialized support systems. No immediate servicing of the helium storage tanks will be necessary. Although it is understood that with an adiabatic payload such as SIRTF the payload bay temperature may reach 82°C (180°F) and remain in that vicinity for some time, this will have no effect on the SIRTF inner structure since the insulation provides a thermal time constant much longer than the 3 hours between Orbiter landing and the start of the purge gas flow. Electronics which are extreme to the SIRTF thermal structure will have to be signed to withstand the 180°F environment.

The following notes apply to Boxes 5.2 and 6.0:

- These tests are performed on a warm telescope to provide a functional indication of SIRTF elements requiring refurbishment or replacement. It is assumed that any physically damaged elements are not critical to this functional test. For immediate re-cycle after the functional check of Box 5.2, the SIRTF elements could go directly to pre-power interface verification (Box 1.8).
- All SIRTF demated elements are returned for refurbishment. It is probable, considering a two-flight-per-year program, that most of the SIRTF elements will not be removed from the pallet.

It is also expected that all SIRTF Elements will either:

- Be refurbished in the launch site facility and enter the loop at Function 1.4, or
- Go back to contractor for major repair and then re-enter at Function 1.1.

The question of how to deal with the multi-launch requirements and re-qualification has not been resolved. One approach is to design for multi-launch life, build in self-test devices, and fly these subsystems until the self-test indicates sub-standard operation. A second approach is to perform limited tests after each flight to determine the operational status of each subsystem. The third is to develop qualified long-life components and subsystems which could then be flown on a large number of missions with a high expectation of success. It is expected that one of the first two approaches, or a combination of them, will be satisfactory, and least costly.

REFERENCE FOR SECTION 5

5-1. Shuttle Ground Operations Plan, K-SM-09, Kennedy Space Center,
31 May 1974.

6. SIRTF DEVELOPMENT PLAN

As part of the SIRTF contract effort, Hughes prepared a development plan and an estimate of the cost of developing SIRTF. As a supplement to the development plan, a technology development program was formulated, to be carried out in the period between the conclusion of the preliminary design study and the start of the hardware contract.

An additional task, which was added as part of the large ambient IR telescope tradeoff (see Section 4.6), was to prepare a technology program, development program, and cost estimate for the ambient telescope. This material is also presented in this section. Estimates for LIRTS have been prepared by the European study group; however, it was believed to be valuable to have a direct comparison of SIRTF and a LIRTS-type telescope based on the same assumptions. Where design approaches advocated by Hughes and the European differed, the Hughes approaches were used.

6.1 BASIS OF PLANS AND ESTIMATES

The SIRTF and ambient telescope schedules and estimates were based on a start date for the hardware implementation phase of 1 January 1979 and an end date (first flight) of September 1982. The hardware program will be preceded by a group of technology programs and design studies starting in Fiscal Year 1977 and continuing through Fiscal year 1978.

For the purposes of the cost estimate, the program elements for SIRTF and the ambient telescope are as follows:

- Program Management and Controls
- Design
- Fabrication

- Assembly
- Unit Test
- Telescope Integration
- System Test
- Chamber Test with SubMIC installed
- MIC Integration
- Chamber Test with MIC installed
- Telescope-Spacelab-Integration and Checkout
- Telescope-Spacelab-Shuttle Integration and Checkout
- Standby from Final Checkout to Launch

In addition, the following were estimated on a per-flight minimum effort basis:

- Flight Support
- Refurbishment

The flight support and refurbishment do not include either astronomer support or scientific data reduction.

Although the MIC is not part of SIRTF, Hughes estimated the cost of the MIC and MIC instruments in order to give a complete program cost picture. Effort in this area includes:

- Design
- Fabrication
- Instrument Test
- Integration of Instruments with MIC
- Chamber test of MIC with instruments installed

During the refurbishment cycle, instruments may be reworked or replaced. This involves:

- Integration of (new or reworked) instruments with MIC
- Chamber test of MIC with instruments installed

6.1.1 Subsystems and Components

Table 6-1 lists the major subsystems and components which were included in the cost estimates. The following items are specifically excluded from the SIRTF pricing:

- Storage tanks for waste water and associated collection, expulsion, and control equipment.
- Supplementary control systems such as Control Moment Gyros, Reaction Wheels, etc., and associated control equipment.
- All Spacelab and Shuttle-provided equipment.

6.1.2 Documentation

The documentation will be minimum level appropriate to one-of-a-kind fabrication for a reusable system. The cost estimate is based on:

- Hughes Grade B Drawings for flight equipment
- Hughes Grade C Drawings for ground equipment
- Informal (typewritten and Xeroxed) reports

Drawings will be prepared using English (not metric) units. Hughes Grade B Drawings conform to MIL-D-1000 Form 2 requirements in all respects except legibility (microfilm reproduction through six generations). Hughes Grade C Drawings deviate from MIL-D-1000 Form 2 in the following areas:

- Drawing numbers
- Part number identification marking
- Order of precedence for standards and specifications
- Standard and specification callouts
- Vendor items (specification and source control drawings)
- Inspection and test requirements
- Summary parts list
- Legibility

Subcontractor developed items will be documented in drawings using subcontractor format generally in conformance with MIL-D-1000 Form 2 for flight equipment. A lower grade subcontractor format will be used for ground equipment.

TABLE 6-1. SIRTF SUBSYSTEMS, ASSEMBLIES AND MAJOR COMPONENTS

TELESCOPE
Optics
Primary Mirror
Secondary Mirror
First Folding Mirror
Second Folding Mirror
Beamsplitter/Compensation Plate
Star Tracker Optics Set
Corner Cube/ Filters
Baffles
Mechanical/ Thermal
Telescope
Vacuum Shell
Thermal Isolators
Primary Mirror Mount
Secondary Mirror Mount
SUBMIC Structure
SUBMIC Instrument Selector
SUBMIC Detectors
SIRTF Calibration Sources
Heat Exchangers
Cryogen Distribution and Control System
Vacuum System
Sunshade
Sunshade Drive and Control
Flight Cover
Chopping and Internal Stabilization
Chop/Stabilization Mirror Drive (Second Folding Mirror)
Focus Mirror Drive (First Folding Mirror)
Laser Source
Top/Bottom Field Selector
CCD Star Tracker
Video Inertial Pointing Mini-Computer
IPS-SIRTF INTEGRATION KIT
Gyro-stabilized Platform
Telescope Mounting Hardware
Computer Interface Unit

(Continued next page)

(Table 6-1, concluded)

DEDICATED GIMBAL/SERVO (Alternate to IPS)

- Base**
- Coarse Gimbal Set**
 - Coarse Gimbal Torquers
 - Coarse Gimbal Bearings
 - Coarse Gimbal Shaft Encoders
- Coarse Loop Servo**
- Fine Gimbal Set**
 - Fine Gimbal Actuator
 - Flexure Suspension
- Fine Loop Servo**
- Gyro Set**
- Wide FOV Star Tracker**
- Cover Support/Retraction Mechanism**
- Clamp and Lock Mechanism**

CRYOGEN STORAGE SYSTEM

- Cryogen Tank(s) (up to three)**
- Temperature/Pressure Monitor and Controls**
- Tank Support/Restraints**
- Cryogen line to Shuttle Umbilical with Disconnect at Tank**

DATA AND COMMAND SYSTEM

- MIC Interface Unit**
- SIRTF Interface Unit**

INSTRUMENTS AND MIC

- MIC Structure**
- MIC Selector Mirror**
- Star Tracker Optics Set**
- CCD Star Tracker**
- VIP Mini-Computer**
- Scientist's Instruments (up to six)**

GROUND SUPPORT EQUIPMENT

- Cryogen Servicing Equipment**
- Cryogen Transfer Lines**
 - (Servicing Equipment to Shuttle Umbilical)
- Shuttle Umbilical Interface**
- Preflight Test Console**
- Flight Control Console (at KSC and ARC)**
- Ground Transportation and Handling Equipment**
- Control Console Simulator (at Ames Research Center)**
- Test Cover**

In addition to the standard reports and documentation (which was not explicitly defined), the contractor will complete a Shuttle Safety Compliance Document estimated at 200 pages, and will compile an Experimenter's Handbook to guide astronomers in the design of focal plane instruments and in the aspects of SIRTF operations that affect science.

6.1.3 Qualification

For purposes of qualification, SIRTF Subsystems are divided into two groups: those in which a failure may impair the safety-of-flight of the Shuttle (safety-of-flight items), and those in which safety-of-flight is not impaired. As SIRTF is presently envisioned, the following subsystems fall in the safety-of-flight category; the method of insuring safety of these items is listed to the right:

(1) Cryogen storage tanks, lines and control system (pressure)	Test
(2) Telescope/tank structural integrity in acoustic environment	Analysis
(3) Attachment/locking device integrity	Test
(4) Venting not in excess of Orbiter vent capability	Analysis
(5) Jettison capability (IPS)	Test
(6) Caution and Warning System	Functional Test
(7) Telescope motion limit to avoid contact with orbiter (may be gas function)	Test or Analysis

Non-standard safety-of-flight items are to be subjected to testing or analysis as indicated above. Definition of the test or analysis program is the responsibility of the subsystem development organization.

All subsystems which do not affect safety-of-flight will be qualified for structural integrity by environmental testing to the levels defined by Volume XIV (Reference 6-1). Testing will be performed on the flight article (a qualification model will not be built).

6.1.4 Quality

The philosophy behind the estimate for quality assurance is summarized in the following points:

1. Quality control will be under Hughes supervision. NASA's monitoring of the quality program will be exercised through review of Hughes quality control documentation; there will be no in process inspection by NASA in-plant representatives.
2. Subcontractor quality control will be monitored by Hughes; direct participation by delegated Hughes personnel is not planned. Hughes can monitor, witness, and have full access to the subcontractor quality operations and documentation to assure compliance with the quality assurance plan. This includes all quality activities, such as meetings, manufacturing inspection, test operations, parts, materials, process controls, and Material Review Board actions.
3. High reliability parts will be used to the fullest extent possible. Locations of non-high-reliability parts will be controlled and catalogued for future replacement.
4. Qualification testing is not a quality control function; see Qualification paragraph.

6.1.5 Reliability

Reliability analysis will be limited to mission success estimates for the first few flights. Goals for SIRTF are:

1. First flight: specific goals are to demonstrate operability, confirm science data flow.
2. Second flight: 80 percent probability of 100 percent success, 90 percent probability of 50 percent scientific success.
3. Third and subsequent flights: TBD

6.2 SIRTF DEVELOPMENT SCHEDULE AND COST

Figures 6-1 and 6-2 present the SIRTF hardware development plan and cost breakdown. The schedule and costs are shown for program start at the beginning of Calendar Year 1979; however, the schedule may be moved forward or back as required. Because of the uncertainty in the start date of the hardware program, the cost estimates have been expressed in Fiscal Year 1976 dollars. The costs in real dollars will be substantially higher; applying the SAMSO 1975 inflation model to the program cost shown in Figure 6-2

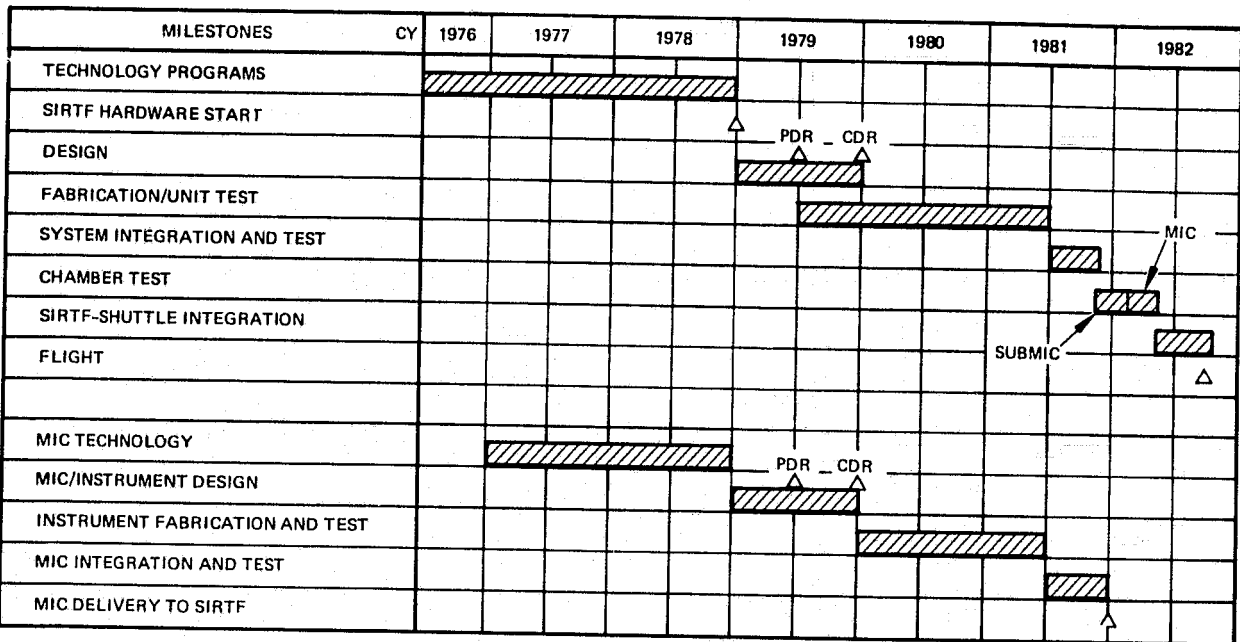


Figure 6-1. SIRTF hardware development program schedule.

	CALENDAR YEAR				
	1979	1980	1981	1982	TOTAL
OPTICS	339	1,367	-	-	1,706
MECHANICAL	2,216	2,891	1,042		6,149
GIMBAL/SERVO	1,485	2,908	1,105	36	5,534
IPS INTEGRATION KIT	1,052	1,210	160		2,422
DATA SYSTEMS	400	1,026	905	189	2,520
TELESCOPE INTEGRATION AND TEST/GSE	124	702	478	221	1,525
CRYOGENIC TANKS	1,196	1,015	1,090		3,301
SHUTTLE INTEGRATION AND LAUNCH SUPPORT	680	1,578	1,534	511	4,303
QUALITY (SHUTTLE-AMES GUIDELINES)	188	462	363	91	1,104
SYSTEM ENGINEERING	1,009	1,009	863	507	3,388
PROGRAM MANAGEMENT	647	647	647	646	2,587
TOTAL IPS MOUNTED	7,851	11,907	7,082	2,165	29,005
TOTAL DEDICATED GIMBAL/SERVO	8,284	13,605	8,027	2,201	32,112

Figure 6-2. SIRTF hardware development program cost estimate (thousands of Fiscal Year 1976 dollars).

increases it to about \$38 million. The figures assume that the technology programs of Section 6.5 are completed before initiation of the hardware program but the costs shown in Figure 6-2 do not include the costs of the technology programs.

These cost figures also do not include scientific instrument development, fabrication and test, scientific data reduction, and telescope performance testing in major facilities such as AEDC. NASA/ARC has arrived at an estimate of \$8.6 million in Fiscal Year 1976 dollars for these items to be added to the costs given in Figure 6-2.

A consideration that arose during the study was whether it would be better to requalify the ELMS cryogen tanks or to procure tanks of a new design. If NASA/ARC decides that new tanks are preferred, a cost delta of \$1.7 million would accrue over the tank cost estimated by Hughes/Grumman. NASA/ARC obtained this estimate partly by discussion with a tank manufacturer, and the figure is based on tanks that are smaller in volume and larger in number than were considered in the study. The advantages of a new tank design are (1) larger design margins can be used, thus avoiding the difficulty experienced with the ELMS tanks; and (2) by making the tanks smaller, the clearance constraints are reduced and a larger telescope could be considered if it is deemed desirable. A more complicated control system is required for the greater number of tanks and this expense has been included in the estimate.

Cost estimates for both an IPS-mounted and a dedicated gimbal/servo version of SIRTF are shown in Figure 6-2. The IPS-mounted total is the sum of all the rows above except the gimbal/servo, whereas the dedicated gimbal/servo total is the sum of all rows above except the IPS integration kit. The IPS integration kit includes the internal stabilization subsystem (gyro platform, laser, stabilization mirror mount, and associated equipment), as well as the mechanical mounting interface and alignment equipment. The dedicated gimbal/servo includes all stabilization equipment required. A cost of \$1.7 millions was estimated for a refurbishment cycle, not including the cost of new instruments.

Since the cost estimates for 1979 assume a January start, the cost estimates can be interpreted equally well on a fiscal year basis if the program starts on 1 October 1978 rather than January 1979.

6.3 COST DRIVERS

The major cost drivers that were identified in the SIRTF preliminary design study are reflected in the proposed technology development tasks (Section 6.5). These are chiefly associated with the scientific instruments (including the multiple instrument chamber). Experience has shown that a good understanding of the physical and operational requirements of the science is essential to a strong project baseline. The more complete the science definition, the better the cost limitation can be met without having to accept performance reduction.

Cooling of the instruments to temperature below the telescope reservoir temperature is another area that could adversely affect cost if it were not defined until during the design phase.

It does not appear that contaminants in the Shuttle environment will appreciably affect the cost of building SIRTF. However, if the environment is not carefully measured as a function of Shuttle operation mode, SIRTF operations could be limited by insufficient planning data and the operational cost could therefore be quite high for early missions. In other words, the scientific return for an investment in a Shuttle flight would be much smaller than optimum.

The recommended work on beryllium mirrors probably does not represent a potential impact on SIRTF cost unless some unexpected effect is found. In this case, if it were to be discovered late in the fabrication program, the cost would be very much higher than if the development work is done before SIRTF starts. If the IRAS (Infrared Astronomy Satellite) project, which is planned for development through Fiscal Year 1979, uses beryllium mirrors, this may eliminate concern for SIRTF.

The chopping mirror mechanism at cryogenic temperature has a status similar to that of the beryllium mirror development. If the development work is done before project starts, potential cost effects can be avoided.

The stabilization subsystem is another area of technology extension that has been identified for SIRTF. The work already under way and planned for the interim period (section 6.5) should result in an excellent background for project implementation.

Finally, other areas that will have major effects on cost are the Shuttle/Spacelab developments themselves. As the capabilities of the STS and the mission support equipment are better defined, it is essential that the effects on SIRTF performance and cost be assessed. It is our understanding that Ames plans to pursue this effort vigorously.

6.4 COST REDUCTION OPTIONS

Most of the cost tradeoffs have been described in the appropriate technical sections of this report, and the cost-reducing features that were acceptable to the SIRTSAG have been included. However, some discussion of options is worthwhile.

The cost presented in Section 6.2 includes a 30-day mission capability. Although a detailed estimate has not been made, it appears that at least two million dollars could be saved if the basic design is restricted to a 7-day mission. Somewhat less would be saved if a 14-day mission capability were included at the start. Adding the longer duration capability later in the program would result in higher total cost because of both redesign and inflation. Alternatively, about a million dollars might be deferred if the basic design included a 30-day duration but only the cryogen tanks and service equipment for a 7-day mission were included at the start.

The question of telescope aperture size versus cost has been raised outside the SIRTSAG. We find that the only design, fabrication or test cost strongly affected by telescope aperture size, assuming an IPS mount that is independent of telescope size, is that of the optics. It can be seen in Figure 6-2 that the optics represent only about 6 percent of the total cost, so reducing the size cannot be expected to make dramatic savings. The SIRTSAG expressed interest in what maximum size telescope could be provided, and so the trade described in Section 4.2.1 was performed. The cost delta for increasing the aperture diameter to 1.6m (the maximum possible without serious development cost for beryllium mirror blanks) has been estimated to be \$3 million. The larger telescope will be close to the weight, size, clearance, and center-of-gravity limits placed by the STS, and therefore the more precise interface definition and design coordination will cost an additional \$3 million.

Another option would be to delay software implementation of fully-automatic control operation, on-orbit (section 2.3.2.2) and to depend heavily on the crew for insertion of new target coordinates, acquisition of guide stars, and control of data taking. This might have a deleterious effect on operational efficiency, thus increasing operational costs per data point. However, some periods of this sort of operation should be expected during early missions so the full effect would not be apparent until the second year of operation and the automatic software might be phased into the program by that time.

Several cost-saving options may be possible on the science side, but these will have to be considered by the scientists themselves.

The only SIRTF performance requirement that might reasonably be relaxed to save cost are those associated with the space chopper throw versus frequency and the requirement for pointing using $m_v = 14$ magnitude stars. Relaxation in these areas will not be a major cost saving based on present knowledge.

6.5 SIRTF TECHNOLOGY DEVELOPMENT

The technology background for SIRTF has largely been developed under previous military programs. Hence the technology development falls in two categories. The first category is that of cost/risk items, where technology development prior to SIRTF hardware program start will reduce cost and/or risk by defining precisely the procedures for designing, fabricating, and/or testing a key item. The second category is that of enhancing technology whereby performance or capabilities of SIRTF may be improved, or its efficiency increased.

The technology programs are presented here as separate entities, preceding the SIRTF hardware contract (Figure 6-1). Because the technology is all of the engineering development type, some or all of the items could be included in an extended design phase during the hardware program. Instead of preliminary design review six months after hardware program start, and critical design review 6 months later, critical design review could be moved to 2 years after program start and the various technology programs carried out in parallel during the extra year between preliminary and critical design reviews.

Table 6-2 lists the various elements of the SIRTF technology development program organized by major areas. Program elements are described and the responsible organization identified. Program status and plans are summarized briefly.

This table shows that a substantial fraction of the SIRTF technology programs are underway under NASA/ARC sponsorship. The detector development being sponsored under the study by NASA-Goddard, and JPL's development of a CCD Star Tracker are contributing technology developments in two important areas. Major technology programs which remain for Fiscal Year 1977 and 1978 funding are the MIC and MIC instrument preliminary design, the stabilization system simulation, cryogenic mirror space chopping breadboard, and testing of a large beryllium mirror at cryogenic temperatures. Completion of these programs will provide a solid technological base for the SIRTF hardware development.

6.6 LARGE AMBIENT TELESCOPE DEVELOPMENT

The ambient telescope technology plan was limited to identifying similarities and differences from the SIRTF program. Similarly, schedule differences were identified. The cost estimate was, however, generated independently.

The technology development tasks for an ambient telescope are very similar in the areas of the Multiple Instrument Chamber and its instruments, and the stabilization subsystem. The one difference in the stabilization subsystem is that the chopping and stabilization mirror need not operate at cryogenic temperatures. The major technology program not common to SIRTF is the primary mirror isothermalization design. This program will require conceptual designs, probably involving active cooling, analysis, the building of a test unit, and thermal testing. This program would be carried out during Fiscal Years 1977 and 1978, so that a proven design approach is available for the hardware program.

The cost estimate for the ambient telescope is shown in Figure 6-3. Costs were estimated only for an IPS-mounted telescope, since a dedicated

TABLE 6-2. SIRTF TECHNOLOGY DEVELOPMENT PROGRAM

Task	Description	Category/ Priority	Organization	Status	Plans
Cryogenics					
Joule Thomson (J-T) Expander	Develop Joule-Thomson expander to produce 1.2°K liquid helium from supercritical helium supply	I/2	Garrett-AiResearch	First of three units built, delivered to JPL	Improved units, redesigned as indicated by test results to be fabricated and tested in FY 77
	Initial tests of J-T Expander	I/2	JPL	First unit tested; 1.8°K cold end temperature achieved	Complete verification of performance prediction; test compatibility with various IR detectors
	Test J-T Expander	I/2	NASA-Ames	Test apparatus being assembled	Selection and optimization of J-T control techniques; assessment of system compatibility. Tests completed 12/76
Rotary Joint	Design and build a low heat leak, low torque rotary joint for 6-10°K supercritical helium supply line	I/4	Hughes	Started 5/76	Deliver unit 12/76
	Test rotary joint	I/4	NASA-Ames	Test apparatus being designed	Tests completed 3/77
Cryogenic Cross-Contamination	Develop means for testing material outgassing rates, optical contamination rates and cross-contamination between focal-plane instruments	I/1	NASA-Ames	Test apparatus ready	Testing and definition of material performance FY 77-78. Test scientists' instruments in FY 78
³ He Cryostat	Develop and demonstrate a ³ He cryostat capable of providing several milliwatts of cooling at 0.3°K in space	II/2	NASA-Ames	Plan submitted to NASA headquarters	Select phase separation device for zero-g and demonstrate in inverted position in FY 77. Complete 6/79

(Continued next page)

(Table 6-2, continued)

Task	Description	Category/ Priority	Organization	Status	Plans
Cryogenics (continued)					
Superfluid He Cryostat	Develop He II dewar for zero-g cooling of detectors	I/2	JPL	Program in progress	Results for IRAS application FY 77
Optics					
Beryllium Mirrors	Demonstrate figuring of Be mirrors for low-temperature performance	I/3	NASA-Ames, Contractor to be selected	Plan not defined	FY 78
Mirror Overcoating	Develop or demonstrate an overcoating that will protect silver deposited on Be without IR absorption	I/1	NASA-Ames, Contractor to be selected	Plan not defined	FY 77
Mirror Mount	Develop mounting technique for large Be mirror on aluminum telescope structure	I/4	NASA-Ames, Contractor to be selected	Plan not defined	FY 78
Contamination					
Contamination Prevention	Develop techniques for protection of cryogenically-cooled optics from contamination by atmospheric constituents	I/2	NASA-Ames	Experimental setup being assembled. Analytical study of purge gas effectiveness completed 6/75	Measure deposition rates on 4°K surfaces from expected environment including STS sources. Demonstrate effectiveness of purge gas (cryogen exhaust) by 1/77. Test in-flight warmup techniques by 8/77. Complete by 6/78.
Contaminant Prediction	Predict gaseous and particulate contamination levels in field of view in STS environment	I/1	NASA-Ames	Summary report being prepared	Report released 4/76. Monitoring of STS materials, design and operations plans will continue through FY 79

(Continued next page)

(Table 6-2, continued)

Task	Description	Category/ Priority	Organization	Status	Plans
Contamination (continued) Contaminant Measurement	Provide means for obtaining contaminant column density, particle occurrence and total IR background as functions of STS operation mode	I/1	NASA-Ames, Contractor to be selected	Preliminary study completed 12/75 by Perkin-Elmer	Additional study to be completed 12/76. Flight planned for Orbital Flight Test early CY 80. Contract activity FY 77
MIC					
Far IR Detectors	Develop and test improved Ge:Ga material and contacts for 50-120 band detectors*	II/5	Santa Barbara Research	Effort started 2/76	Deliver detectors, test results 10/76
	Develop and test improved Ge:Be detectors for 30-50 band*	II/5	Santa Barbara Research	Planned	Deliver detectors, test results 12/76
Instrument Preliminary Designs	Develop preliminary designs of focal plane instruments	I/1	NASA-Ames, Contractor to be selected	Plan awaiting NASA Headquarters agreement	FY 77
MIC Preliminary Design	Develop preliminary design of multiple instrument chamber: mechanical, thermal, and data processing	I/1	NASA-Ames, Contractor to be selected	Plan only	FY 77
Stabilization					
CCD Star Tracker	Develop CCD star tracker. Test CCD chip at cryogenic temperatures	I/2	JPL	Basic JPL stellar sensor designed	CCD focal plane sensor delivered to ARC 6/76. Cold tests CCD complete FY 77. Preliminary SIRTF design complete FY 77

*Currently sponsored under IRAS study contract

(Continued next page)

(Table 6-2, continued)

Task	Description	Category/ Priority	Organization	Status	Plans
<u>Stabilization</u> (continued)					
Video Inertial Pointing (VIP) Subsystem	Develop the Video Inertial Pointing Subsystem for SIRTF	I/1	NASA-Ames/Stanford University	First phase, develop- ment of hardware and software, com- pleted FY 76	Expand to include CCD sensor FY 77. Bread- board with CCD focal plane sensor FY 78
Stabilization System Simulation	Computer simulation of combined IPS and SIRTF Stabilization Systems	I/1	NASA-Ames	Planning started	FY 77
Second Folding Mirror Chopping	Breadboard cryogenic chop mirror unit; test	I/3	NASA-Ames, Contractor to be selected	Plan not defined	FY 78
System					
Scaled Gregorian Test	Design, build, test 30 cm uncooled Gregorian telescope to verify astronomical performance	I/1	NASA-Ames	Effort started 1/76	Complete telescope 11/76
	Ground and airborne tests	I/1	NASA-Ames	Test plan written	Tests complete 4/77
	Support design effort	I/1	Hughes	Effort started 1/76	Continue through 6/76
Mechanical					
MIC Selector	Develop precise repeat- able alignment of rotating selector (dichroic beam splitter) at cryogenic tempera- tures. Demonstrate operation without con- taminating instruments	I/3	NASA-Ames, Contractor to be selected	Plan not defined	FY 78

(Continued next page)

(Table 6-2, concluded)

Task	Description	Category/ Priority	Organization	Status	Plans
Mechanical (continued) Autofocus Subsystem	Breadboard laser link, mirror drive and CCD sensor to demonstrate focus and collimation technique for cooled telescope	I/3.	NASA-Ames, Contractor to be selected	Plan not defined	FY 78

PRIORITY DEFINITIONS

1. Mandatory before starting SIRTF design.
2. One of several alternate approaches, one must be developed before SIRTF design start.
3. Very important technology, can save cost in program.
4. Early development will improve capability to perform program.
5. Essential for later SIRTF missions for full performance.

CATEGORY DEFINITIONS

I Cost/Risk

II Enhancing Technology

	CALENDAR YEAR				
	1978	1979	1980	1981	TOTAL
OPTICS*	339	2,385			2,724
MECHANICAL†	2,662	3,712	1,120		7,494
IPS INTEGRATION KIT	1,052	1,210	160		2,442
DATA SYSTEMS	400	1,026	905	190	2,521
TELESCOPE INTEGRATION AND TEST/GSE	119	570	398	195	1,282
SHUTTLE INTERFACE AND LAUNCH SUPPORT (GAC)	680	1,578	1,534	511	4,303
QUALITY (SHUTTLE-AMES GUIDELINES)	126	363	257	52	798
SYSTEM ENGINEERING	1,009	1,009	863	507	3,389
PROGRAM MANAGEMENT	647	647	647	647	2,587
TOTAL IPS MOUNTED	7,034	12,500	5,884	2,101	27,519

*LIGHT WEIGHT CERVIT (OR EQUIVALENT) PRIMARY. ADD ~ \$3.5 MILLION AND ~ 1 YEAR FOR ACTIVE FIGURE CONTROLLED ALUMINUM PRIMARY

†ASSUMES SOLUTION TO ISOTHERMALIZATION PROBLEM IS DEVELOPED DURING 1976 - 1978

Figure 6-3. Ambient telescope hardware development program cost estimate (thousands of Fiscal Year 1976 dollars).

gimbal/servo for the ambient telescope was not studied. A 2.5 meter aperture was assumed, although costs do not vary substantially over the 2.3 meter to 2.6 meter range covered by the study.

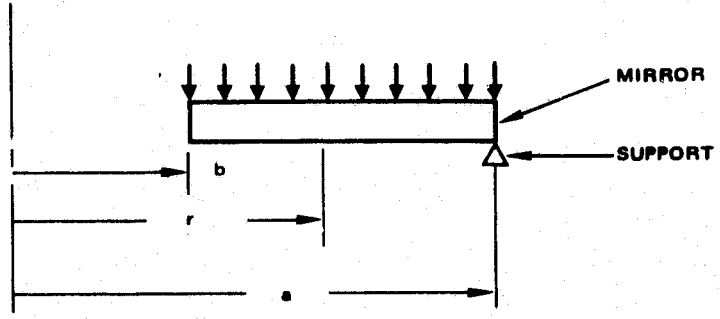
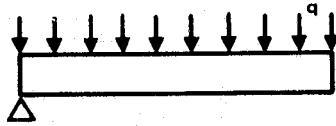
For the hardware program, the same schedule can be met for an ambient telescope as for SIRTF if a Cervit primary mirror proves satisfactory. The alternate is an aluminum mirror with active figure control. This technology is established but will result in an addition of 1 year to the project schedule and an additional cost estimated at \$3.5 million. To the estimate in Figure 6-3 must be added the costs for scientific instruments, data reduction and testing facility use that NASA/ARC estimated for SIRTF approximately \$8.6 million.

REFERENCE FOR SECTION 6

**6-1 Space Shuttle System Payload Accommodations, Level II Program
Definition and Requirements Volume XIV, Revision D, JSC-07700.
NASA-JSC, November 26, 1975.**

APPENDIX A. UNIFORMLY LOADED ANNULAR PLATE SIMPLY SUPPORTED ALONG THE OUTER DIAMETER

DEFINITION OF GEOMETRICAL FACTORS



The differential equation of the deflection surface w_0 is given by
 (eq. 57, p. 53, Ref. A-1)

$$\frac{d}{dr} \left[\frac{1}{r} \frac{d}{dr} \left(r \frac{dw_0}{dr} \right) \right] = \frac{Q}{D} \quad (1)$$

where r = radius (polar coordinates)

Q = shearing force per unit length of the cylindrical section of radius.

$$D = \frac{Eh^3}{12(1-\nu^2)}$$

E = Elastic Modulus

h = plate thickness

ν = poisson's ratio

The shear Q is related to load intensity q by

$$2\pi r Q = qA = \pi q (r^2 - b^2)$$

hence,

$$Q = \frac{q}{2} \left(r - \frac{b^2}{r} \right) \quad (2)$$

The solution to equation (1) must satisfy the boundary conditions

$$(w)_{r=a} = 0 \quad (3)$$

$$(M_r)_{r=a} = (M_r)_{r=b} = 0 \quad (4)$$

where M_r is the radial bending moment and is given by (eq. 52, p. 52, Ref. 1).

$$M_r = -D \left\{ \frac{d^2 w_o}{dr^2} + \frac{\nu}{r} \frac{dw_o}{dr} \right\} \quad (5)$$

Substitution of (2) into (1) and performing the required integration yields

$$w = \frac{q}{2D} \left[\frac{r^4}{32} - \frac{b^2 r^2}{4} \left(\log \left(\frac{r}{a} \right) - \frac{1}{2} \right) + \frac{b^2 r^2}{8} \right] + C_1 \frac{r^2}{4} + C_2 \log \left(\frac{r}{a} \right) + C_3 \quad (6)$$

Applying the boundary condition given by (3) yields

$$C_3 = -\frac{a^2}{4} \left\{ \frac{a^2}{8} + b^2 + C_1 \right\} \quad (7)$$

Performing the required differentiations of (6) and substituting into (5) yields

$$M_r = -\frac{q}{2} \left\{ \frac{r^2}{8} (3+\nu) - \frac{b^2}{2} (1+\nu) \log \left(\frac{r}{a} \right) - \frac{b^2}{4} (1-\nu) + \frac{C_1}{2} (1+\nu) - \frac{C_2}{r^2} (1-\nu) \right\} \quad (8)$$

Applying the boundary conditions given by (4) yields

$$C_1 = \frac{2}{(1+\nu)} \left[-\frac{(a^2 + b^2)}{8} (3+\nu) - \frac{b^4}{(a^2-b^2)} \left(\frac{1+\nu}{2}\right) \log \left(\frac{b}{a}\right) + \frac{b^2}{4} (1-\nu) \right] \quad (9)$$

$$C_2 = -\frac{a^2 b^2}{(a^2-b^2)(1-\nu)} \left[\frac{(a^2-b^2)}{8} (3+\nu) + \frac{b^2}{2} (1+\nu) \log \left(\frac{b}{a}\right) \right] \quad (10)$$

In some instances, a normalized form of (6), (7), (9), and (10) is more convenient.

$$\text{Let } t = \frac{b}{a} \text{ and } \rho = \frac{r}{a}$$

$$\text{then } w = \frac{q a^4}{2D} \left\{ \frac{\rho^4}{32} - \frac{t^2 \rho^2}{4} \left[\log \rho - \frac{1}{2} \right] + \frac{t^2 \rho^2}{8} \right. \\ \left. + J_1 \frac{\rho^2}{4} + J_2 \log \rho + J_3 \right\} \quad (11)$$

$$\text{where } J_1 = \frac{2}{(1+\nu)} \left\{ -\frac{(1+t^2)}{8} (3+\nu) - \frac{t^4}{(1-t^2)} \left(\frac{1+\nu}{2}\right) \log t \right. \\ \left. + \frac{t^2}{4} (1-\nu^2) \right\} \quad (12)$$

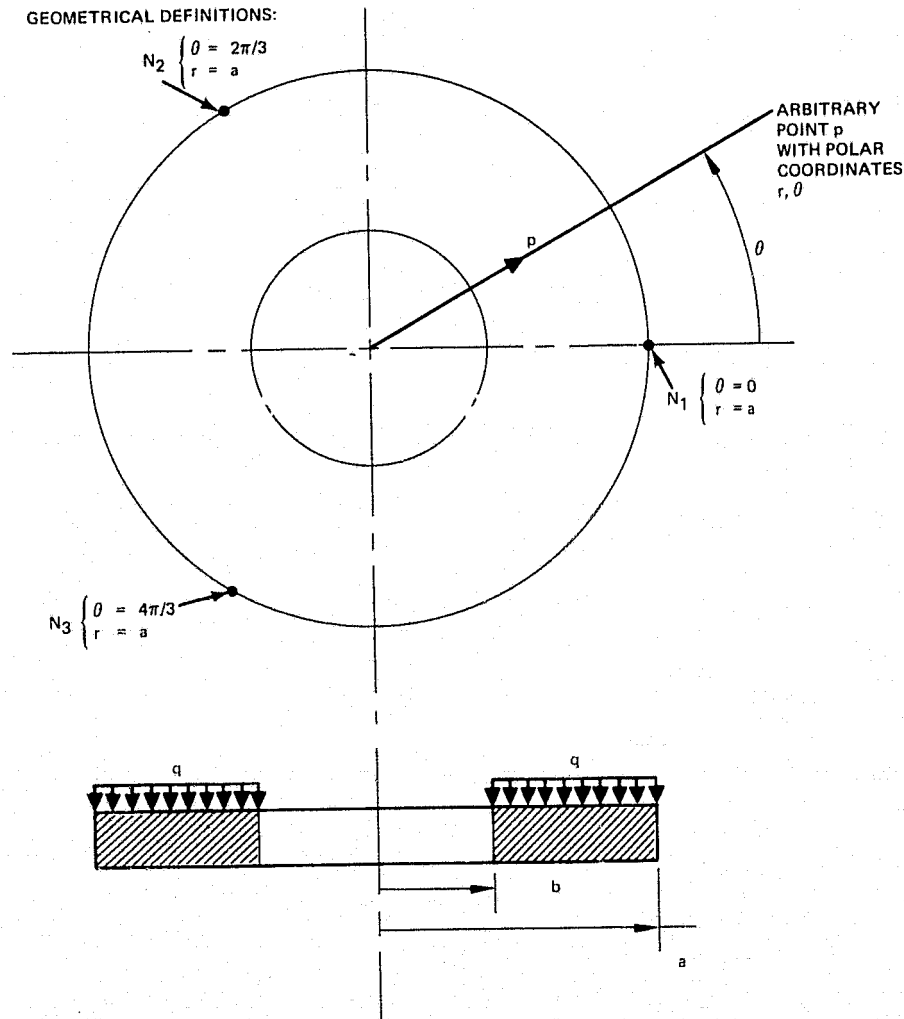
$$J_2 = \frac{-t^2}{(1-t^2)(1-\nu)} \left\{ \frac{(1-t^2)}{8} (3+\nu) + \frac{t^2}{2} (1+\nu) \log t \right\} \quad (13)$$

$$J_3 = -\frac{1}{32} - \frac{t^2}{4} - \frac{J_1}{4} \quad (14)$$

REFERENCE FOR APPENDIX A

A-1. S. Timoshenko and S. Woinowsky-Krieger. Theory of Plates and Shells, Second Edition, McGraw Hill Book Company, New York, 1959.

APPENDIX B. UNIFORMLY LOADED ANNULAR PLATE SIMPLY SUPPORTED AT THREE EQUALLY SPACED POINTS ON THE OUTER DIAMETER



The deflection surface, w , is given by (p. 293, Ref. 1),

$$w = w_0 + w_1 \quad (1)$$

where w_0 is the deflection of a plate simply supported along the entire boundary (see Appendix A for derivation) and w_1 satisfies the homogeneous differential equation,

$$\left(\frac{\partial}{\partial r^2} + \frac{1}{r} \frac{\partial}{\partial r} + \frac{1}{r^2} \frac{\partial^2}{\partial \theta^2} \right) \left(\frac{\partial^2 w_1}{\partial r^2} + \frac{1}{r} \frac{\partial w_1}{\partial r} + \frac{1}{r^2} \frac{\partial^2 w_1}{\partial \theta^2} \right) = 0 \quad (2)$$

where r, θ are the polar coordinates of an arbitrary point on the surface.

The solution to (2) can be expressed in the form of an infinite series (pp. 284 - 285, Ref. 1).

$$\begin{aligned} w_1 = & A_0 + B_0 \log r + C_0 r^2 + D_0 r^2 \log r \\ & + A_1 r \cos \theta + B_1 r^{-1} \cos \theta + C_1 r^3 \cos \theta + D_1 r \log r \cos \theta \\ & + A'_1 r \sin \theta + B'_1 r^{-1} \sin \theta + C'_1 r^3 \sin \theta + D'_1 r \log r \sin \theta \\ & + \sum_{m=2}^{\infty} \{A_m r^m + B_m r^{-m} + C_m r^{m+2} + D_m r^{-m+2}\} \cos m\theta \\ & + \sum_{m=2}^{\infty} \{A'_m r^m + B'_m r^{-m} + C'_m r^{m+2} + D'_m r^{-m+2}\} \sin m\theta \end{aligned} \quad (3)$$

The solution (1) must satisfy the following boundary conditions

$$\begin{aligned} (w)_{r=a} &= (w)_{r=a} = (w)_{r=a} = 0 \\ \theta=0 &\quad \theta=\frac{2\pi}{3} \quad \theta=\frac{4\pi}{3} \end{aligned}$$

Because $w_0 = 0$ for $r=a$, the above become

$$(w_1)_{r=a} = (w_1)_{r=a} = (w_1)_{r=a} \quad \begin{matrix} \theta=0 \\ \theta=\frac{2\pi}{3} \\ \theta=\frac{4\pi}{3} \end{matrix} \quad (4)$$

Also, the radial bending moment, M_r , must vanish for $r=b$ and $r=a$, or

$$(M_r)_{r=a} = (M_r)_{r=b} = 0 \quad (5)$$

The final two boundary conditions are established by the net shear

V. (See p. 293, Ref. B-1).

$$(V)_{r=b} = 0 \quad (6)$$

$$(V)_{r=a} = - \sum_{i=1}^{3N} \frac{i}{\pi a} \left\{ \frac{1}{2} + \sum_{m=1}^{\infty} \cos m\theta_i \right\} \quad (7)$$

where $\theta_i = \theta - \gamma_i$

γ_i = i th support angular coordinate

N_i = Reaction of i th support.

By symmetry,

$$N_i = \frac{q}{3} \pi (a^2 - b^2)$$

$$\text{Also, } \gamma_1 = 0, \gamma_2 = \frac{2\pi}{3}, \gamma_3 = \frac{4\pi}{3}.$$

Substituting into (7) and simplifying yields

$$(V)_{r=a} = \frac{q}{2} \left(\frac{b^2}{a} - a \right) + q \left(\frac{b^2}{a} - a \right) \sum_{m=3, 6, 9}^{\infty} \cos m\theta \quad (8)$$

The radial bending moment M_r is given by (e.g. 192, p. 283, Ref. 1).

$$M_r = -D \left\{ \frac{\partial^2 w}{\partial r^2} + v \left[\frac{1}{r} \frac{\partial w}{\partial r} + \frac{1}{r^2} \frac{\partial^2 w}{\partial r^2} \right] \right\} \quad (9)$$

Because w_0 already satisfies (5) (see Appendix A), the constants of (3) must satisfy (5) separately. Performing the necessary differentiations on (3) and substituting into (9) yields

$$\begin{aligned} M_{r_{w_1}} &= -B_o r^{-2} (1-v) + 2 (1+v) C_o + D_o [(3+v)+2(1+v) \log r] \\ &+ 2(1-v) B_1 r^{-3} \cos \theta + 2 (3+v) C_1 r \cos \theta + (1+v) D_1 r^{-1} \cos \theta \\ &+ 2(1-v) B'_1 r^{-3} \sin \theta + 2(3+v) C'_1 r \sin \theta + (1+v) D'_1 r^{-1} \sin \theta \\ &+ \sum_{m=2}^{\infty} \{m(m-1)(1-v) A_m r^{m-2} + m(m+1)(1-v) B_m r^{-m-2} \\ &\quad + (m+1) [m(1-v)+2(1+v)] C_m r^m \\ &\quad + (m-1) [m(1-v)-2(1+v)] D_m r^{-m}\} \cos m\theta \\ &+ \sum_{m=2}^{\infty} \{m(m-1)(1-v) A'_m r^{m-2} + (m+1)(1-v) B'_m r^{-m-2} \\ &\quad + (m+1) [m(1-v)+2(1+v)] C'_m r^m \\ &\quad + (m-1) [m(1-v)-2(1+v)] D'_m r^{-m}\} \sin m\theta \end{aligned} \quad (10)$$

The net shear V is given by (eq. j, p. 284, Ref. 1)

$$V = Q_r - \frac{1}{r} \frac{\partial M_{rt}}{\partial \theta} \quad (11)$$

where $Q_r = -D \frac{\partial}{\partial r} \left\{ \frac{\partial^2 w}{\partial y^2} + \frac{1}{r} \frac{\partial w}{\partial r} + \frac{1}{r^2} \frac{\partial^2 w}{\partial \theta^2} \right\}$

$$M_{rt} = (1-v)D \left\{ \frac{1}{r} \frac{\partial^2 w}{\partial r \partial \theta} - \frac{1}{r^2} \frac{\partial w}{\partial \theta} \right\}$$

Performing the required integrations on (3) of this section and (6) of Appendix A, and substituting the results into (11) yields

$$V = \frac{q}{2} \left\{ \frac{b^2}{r} - r \right\} + D \left\{ -2(3+v)C_1 \cos \theta - 2(3+v)C'_1 \sin \theta \right.$$

$$\left. -2(1-v)B_1 r^{-4} \cos \theta - 2(1-v)B'_1 r^{-4} \sin \theta - 4D_o r^{-1} \right.$$

$$+ (3-v)D_1 r^{-2} \cos \theta + (3-v)D'_1 r^{-2} \sin \theta$$

$$+ \sum_{m=2}^{\infty} \left[m^2(m-1)(1-v)A_m r^{m-3} - m^2(m+1)(1-v)B_m r^{-m-3} \right.$$

$$+ m(m+1) \left[\overline{m}(1-v)-4 \right] C_m r^{m-1}$$

$$- m(m-1) \left[\overline{m}(1-v)+4 \right] D_m r^{-m-1} \left. \right] \cos m\theta$$

$$+ \sum_{m=2}^{\infty} \left[m^2(m-1)(1-v)A'_m r^{m-3} - m^2(m+1)(1-v)B'_m r^{-m-3} \right.$$

$$+ m(m+1) \left[\overline{m}(1-v)-4 \right] C'_m r^{m-1}$$

$$- m(m-1) \left[\overline{m}(1-v)+4 \right] D'_m r^{-m-1} \left. \right] \sin m\theta \}$$

(12)

Applying the boundary conditions expressed by (5), (6) and (8) to (10) and (12) yields

$$B_0 = C_0 = D_0 = 0$$

$$C_1 = B_1 = D_1 = 0$$

$$C'_1 = B'_1 = D'_1 = 0$$

$$A'_m = B'_m = C'_m = D'_m = 0$$

if $M \neq 3, 6, 9 \dots$

$$A_m = B_m = C_m = D_m = 0$$

if $M = 3, 6, 9 \dots$

$$A_m = \frac{1}{m(m+1)(1-\nu)} \{ -(m+1)(3+\nu)b^{2m+2}C_m - (m-1)(m+1)(1-\nu)b^2D_m \}$$

$$B_m = \frac{1}{m(m-1)(1-\nu)} \{ -(m+1)(m-1)(1-\nu)b^2C_m + (m-1)(3+\nu)b^{-2m+2}D_m \}$$

$$C_m = \frac{q}{D} (t^2-1)a^2b^{-m} \frac{K_m}{(m+1)} \{ \left[\begin{matrix} m(1-\nu)-2(1+\nu) \\ \end{matrix} \right] t^m + (3+\nu)t^{-m+2} - (m+1)(1-\nu)t^{m+2} \} \quad (13)$$

$$D_m = \frac{q}{D} (t^2-1)a^2b^m \frac{K_m}{(m-1)} \{ - \left[\begin{matrix} m(1-\nu)+2(1+\nu) \\ \end{matrix} \right] t^{-m} + (3+\nu)t^{m+2} + (m-1)(1-\nu)t^{-m+2} \}$$

$$\text{where } K_m = m^{-1} \{ 2m^2(t^2-1)^2(1-v)^2 - 2(3+v)^2 t^2(t^{2m} + t^{-2m}) \\ + 16(1+v)(t^4+1) + 4(1-v)^2 t^2 \}^{-1} \quad (14)$$

and $t = (b/a)$.

But, using the first two equations of (13),

$$\begin{aligned} & \{ A_m r^m + B_m r^{-m} + C_m r^{m+2} + D_m r^{-m+2} \} \\ &= \left\{ - \left(\frac{m+1}{m} \right) \left(\frac{\rho}{t} \right)^m - \frac{(3+v)}{m(1-v)} \left(\frac{\rho}{t} \right)^{-m} + \left(\frac{\rho}{t} \right)^{m+2} \right\} t^2 a^2 b^m C_m \\ &+ \left\{ \frac{(3+v)}{m(1-v)} \left(\frac{\rho}{t} \right)^m - \frac{(m-1)}{m} \left(\frac{\rho}{t} \right)^{-m} + \left(\frac{\rho}{t} \right)^{-m+2} \right\} t^2 a^2 b^{-m} D_m \end{aligned} \quad (15)$$

$$\text{where } \rho = \frac{r}{a}$$

by letting

$$F_m = \frac{K_m}{(m+1)} \{ [m(1-v) - 2(1+v)] t^m + (3+v) t^{-m+2} - (m+1)(1-v) t^{m+2} \} \quad (16)$$

$$G_m = \frac{K_m}{(m-1)} \{ -[m(1-v) + 2(1+v)] t^{-m} + (3+v) t^{m+2} + (m-1)(1-v) t^{-m+2} \}$$

and substituting into (13), (15), and (3), there results

$$w_1 = A_0 + A_1 r \cos\theta + A'_1 r \sin\theta$$

$$+ \frac{qa^4(t^4-t^2)}{D} \left\{ \sum_{m=3,6,9}^{\infty} \left[-\frac{m+1}{m} \frac{\rho^m}{t} - \frac{(3+\nu)}{m(1-\nu)} \frac{\rho^{-m}}{t} + \frac{\rho^{m+2}}{t} \right] F_m \cos m\theta \right. \\ \left. + \sum_{m=3,6,9}^{\infty} \left[-\frac{(m-1)}{m} \frac{\rho^{-m}}{t} + \frac{(3+\nu)}{m(1-\nu)} \frac{\rho^m}{t} + \frac{\rho^{-m+2}}{t} \right] G_m \cos m\theta \right\} \quad (17)$$

Applying the boundary conditions expressed by (4) to (17) results in

$$A_1 = A'_1 = 0$$

$$A_0 = + \frac{qa^4(t^4-t^2)}{D} \sum_{m=3,6,9}^{\infty} \left[H_m F_m + I_m G_m \right]$$

...

$$\text{where } H_m = + \frac{(m+1)}{m} t^{-m} + \frac{(3+\nu)}{m(1-\nu)} t^m - t^{-m-2} \quad (18)$$

$$I_m = + \frac{(m-1)}{m} t^m - \frac{(3+\nu)}{m(1-\nu)} t^{-m} - t^{m-2}$$

Using (17) and (18) of this section and (11) of Appendix A, equation

(1) becomes

$$w = \frac{qa^4}{D} \left\{ \frac{4}{64} - \frac{t^2 p^2}{8} (\log \rho - 1) + J_1 \frac{\rho^2}{8} + \frac{J_2}{2} \log \rho + \frac{J_3}{2} \right. \\ + (t^4 - t^2) \left[\sum_{m=3,6,9}^{\infty} (H_m F_m + I_m G_m) \right. \\ \left. \dots \right. \\ \left. + \sum_{m=3,6,9}^{\infty} \left(-\frac{(m+1)}{m} \frac{\rho^m}{t} - \frac{(3+\nu)}{m(1-\nu)} \frac{\rho^{-m}}{t} + \frac{\rho^{m+2}}{t} \right) F_m \cos m\theta \right. \\ \left. + \sum_{m=3,6,9}^{\infty} \left(-\frac{(m-1)}{m} \frac{\rho^{-m}}{t} + \frac{(3+\nu)}{m(1-\nu)} \frac{\rho^m}{t} + \frac{\rho^{-m+2}}{t} \right) G_m \cos m\theta \right\} \quad (19)$$

where J_1, J_2, J_3 are given by (12), (13), (14) of Appendix A and F_m , G_m, H_m, I_m , are given by (16) and (18) of this section. Denoting the terms contained in {} by X_m , (19) becomes

$$w = \frac{qa^4}{D} X_m \quad (20)$$

The slope in the radial direction, ϕ_r , is given by

$$\phi_r = - \left(\frac{\partial w}{\partial r} \right)_\theta$$

Performing the differentiation on (20) yields

$$\phi = \frac{qa^3}{D} Y_m \quad (21)$$

$$\text{where } Y_m = \frac{-\rho^3}{16} + \frac{t^2 \rho}{8} (2 \log \rho - 1) - J_1 \frac{\rho}{4} - \frac{J_2}{2\rho}$$

$$+ (t^3 - t) \left\{ \sum_{m=3,6,9,}^{\infty} \left[(m+1) \left(\frac{\rho}{t} \right)^{m-1} - \frac{(3+\nu)}{(1-\nu)} \left(\frac{\rho}{t} \right)^{-m-1} - (m+2) \left(\frac{\rho}{t} \right)^{m+1} \right] F_m \cos m\theta \right. \\ \left. \dots \right. \\ + \sum_{m=3,6,9,}^{\infty} \left[-(m-1) \left(\frac{\rho}{t} \right)^{-m-1} - \frac{(3+\nu)}{(1-\nu)} \left(\frac{\rho}{t} \right)^{m-1} + (m-2) \left(\frac{\rho}{t} \right)^{-m+1} \right] G_m \cos m\theta \left. \right\}$$

The slope in the θ direction is given by

$$\phi_\theta = - \frac{1}{r} \frac{\partial w}{\partial \theta} \Big|_r$$

Performing the differentiation on (20) yields

$$\phi_\theta = \frac{qa^3}{D} Z_m \quad (22)$$

$$\begin{aligned}
 \text{where } Z_m &= (t^3 - t) \left\{ \sum_{m=3,6,9}^{\infty} \left[-(m+1) \left(\frac{\rho}{t} \right)^{m-1} - \frac{(3+\nu)}{(1-\nu)} \left(\frac{\rho}{t} \right)^{-m-1} \right. \right. \\
 &\quad \cdots \\
 &\quad \left. + m \left(\frac{\rho}{t} \right)^{m+1} \right] F_m \sin m\theta \\
 &\quad + \sum_{m=3,6,9}^{\infty} \left[-(m-1) \left(\frac{\rho}{t} \right)^{-m-1} + \frac{(3+\nu)}{(1-\nu)} \left(\frac{\rho}{t} \right)^{m-1} + m \left(\frac{\rho}{t} \right)^{-m+1} \right] \\
 &\quad \cdots \\
 &\quad \left. G_m \sin m\theta \right\}
 \end{aligned}$$

REFERENCE FOR APPENDIX B

B-1. S. Temoshenko and S. Woinowsky-Krieger. Theory of Plates and Shells, Second Edition, McGraw Hill Book Company, New York, 1959.

REPRODUCIBILITY OF THE
ORIGINAL PAGE IS POOR

APPENDIX C. THERMAL ANALYSIS MODEL

The SIRTF thermal model is a nodal network consisting of 36 nodes. The node locations are listed in Table C-1. The node locations selected to obtain realistic temperature distributions and to accurately model the thermal paths from points of thermal loading to points of thermal cooling. The model is constructed such that various configurations can be investigated without creating another model. Due to this, nodes 14, 20, 26, 31 do not appear in the model network listing. The model is programmed directly for computer solution as this provides much more flexibility in modeling and efficiency in computer usage than when using a standard thermal analyzer program. The model is programmed for the Hughes Decsystem-10.

The couplings consist of two types: Those due to radiation and those due to conduction. Convection was not considered; the telescope will be in vacuum and the heat exchangers were treated under the condition that the heat exchanger exhaust gas temperature is 1°K below that of the node being cooled. The radiation couplings were represented by the relationship:

$$Q_{12} = A_1 F_e F_{12} (T_1^4 - T_2^4)$$

1

where

A_1	=	Area of node 1
F_e	=	Effective emissivity between node 1 and 2
F_{12}	=	View factor between node 1 and 2
T_1	=	Temperature node 1
T_2	=	Temperature node 2

MODEL NODE LOCATIONS

TABLE C-1

1	MIC
2	MIC Housing
3	Mirror (Beam Splitter)
4	Mounting Flange
5	Mirror (Secondary)
6	Mirror (Stabilization)
7	Mirror (1st Folding)
8	Mirror (Primary)
9	Baffles
10	Primary Mirror Support
11	Telescope Support
12	Telescope Support/4th Fiberglass Isolator (Three Shield Model)
13	Telescope Barrel Aft
14	Inner Telescope Radiation Shield (Three Shield Model)
15	Central Telescope Radiation Shield

(Continued next page)

TABLE C-1 (continued)

16	Outer Telescope Radiation Shield
17	Vacuum Jacket
18	Fiberglass Support Isolator Joint (Central)
19	Fiberglass Support Isolator Joint (Outer)
20	MIC Inner Radiation Shield (Three Shield Model)
21	MIC Central Radiation Shield
22	MIC Outer Radiation Shield
23	Inlet Helium
24	Heat Exchanger (MIC Housing)
25	Heat Exchanger (Interface of Telescope MIC and Fiberglass Isolator)
26	Heat Exchanger (Spare)
27	Heat Exchanger (Stabilization Mirror)
28	Heat Exchanger (Telescope Barrel Fwd)
29	Heat Exchanger (Telescope Barrel Aft)
30	Telescope Barrel Fwd
31	Fwd Inner Radiation Shield (Three-Shield Model)
32	Fwd Central Radiation Shield
33	Fwd Outer Radiation Shield
34	Fwd Baffle
35	Heat Exchanger (Central Telescope Radiation Shield)
36	Heat Exchanger (Outer Telescope Radiation Shield)

The conductive couplings were represented by the relationship

$$Q_{12} = \frac{A_1}{L_{12}} \left(\int_{T_1}^{T_2} K dT - \int_{T_2}^{T_1} K dT \right) \quad 2$$

where

A_1 = Cross sectional area

L = Length between node 1 and 2

K = Conductivity

T = Temperature

Thermal conductivity integrals were used for all materials due to the large conductivity variation over the SIRTF operating temperature range. The thermal conductivity integrals for aluminum 6061, beryllium, and fiberglass were plotted as a function of temperature. The equations for the conductivity integrals were then determined for each material, and the equations were then used in the model (see Table 3-19).

The program variables are presented in Table C-2. It should be noted that not all variables in the program listing were used. This is due to the fact that this program is a general format. It can be applied to many thermal analysis problems by changing the thermal network and its specifications. The program uses the forward differencing technique to analyze the network. It continues this until the change in temperatures between iterations becomes less than a predetermined value. At this point the temperature solutions to the network are printed. An additional parameter, which acts as an iteration counter, prevents excessive iterations. When this parameter is surpassed it causes the temperatures at that point to be printed and execution to cease. A listing of the program is supplied in reference 3-22.

TABLE C-2
MODEL VARIABLES

T	-	Node Temperatures ($^{\circ}$ K)
H	-	Node Heat Inputs (Watts)
Q	-	Heat Flow Paths Resulting from Conductance (Watts)
SQ	-	Node Heat Flow Paths Summation (Watts)
CM	-	Network Stabilization Constants
AA	-	Thermal Conductivity Integral for 6061 Aluminum (W/cm)
CC	-	Thermal Conductivity Integral for Beryllium (W/cm)
BB	-	Thermal Conductivity Integral for Fiberglass (W/cm)
DTMP	-	Forward Differencing Step
ERRT	-	Stabilization Criterion ΔT
FM	-	Mass Flow of Helium (GM/SEC)
ITER	-	A Counter to Prevent Excessive Iterations
LIMIT	-	Iteration Limit

REFERENCE FOR APPENDIX C

C-1. V.J. Johnson, Editor "A Compendium of the Properties of Materials at Low Temperatures," Part II, Solids, October 1960.

APPENDIX D

DEDICATED GIMBAL ASSEMBLY FOR SIRTF

D-1. INTRODUCTION

This appendix describes a three-axis dedicated gimbal assembly which provides an alternative to the European Instrument Pointing System (IPS), and can be used with Shuttle payloads other than SIRTF*.

Section D-2 gives a brief description of the telescope and its associated equipment. Section D-3 provides a detailed description of the mechanical configuration of the dedicated gimbal assembly. Section D-4 presents the results of a preliminary structural analysis of the dedicated gimbal design. Section D-5 describes the overall configuration of the dedicated gimbal servo system.

Table D-1 lists the specifications pertaining to gimbal performance, pointing, and line-of-sight stabilization for the SIRTF telescope and dedicated gimbal assembly.

The dedicated gimbal design relies on proven technology and offers a number of advantages compared to the IPS. Of primary importance is the fact that the gimbals are mass-balanced around all three axes of rotation. This provides the following operational and structural advantages.

*Because this work was done early in the program, the SIRTF telescope configuration used is the one current at that time. The subsequent changes do not affect the validity of the general configuration or conclusions.

Table D-1. SIRTF SPECIFICATIONS WITH DEDICATED GIMBAL SYSTEM

Parameter	Numerical Values		Comments
Gimbal Configuration	Cross-elevation	Outer	See Figure D-5 for illustration. All gimbals are balanced about their axes of rotation.
	Elevation	Middle	
	LOS Roll	Inner	
Gimbal Angular Coverage	Cross-elevation	± 60 deg	Elevation gimbal rotates 90 deg forward to stow.
	Elevation	± 60 deg	
	LOS Roll	>90 deg	
Gimbal Scan (Raster)	Height and width	0 deg to 1 deg (1 min increments)	Scan specifications refer to inertial space.
	line spacing	0.1 min to 30 min (adjustable increments from 2 sec to 2 min)	
	Scan Rate	-10 deg/min to +10 deg/min (0.1 deg/min increments)	
Gimbal Slewling	Slew Rate	>2 deg/sec	Slew rate pertains to either elevation or cross-elevation gimbals.
Gimbal Acceleration Capability	Cross-elevation	10 mrad/sec ²	These values are based on estimated gimbal inertias.
	Elevation	10 mrad/sec ²	
	LOS Roll	70 mrad/sec ²	
System Weight		6693 Kg	Total including telescope, gimbals, CMG's, cryogen tanks, cover, and pallets.
Gimbal Stabilization	Cross-elevation	30 sec, RMS	Bias and Jitter
	Elevation	30 sec, RMS	
	LOS Roll	30 sec, RMS	
SIRTF Gyro Platform Stabilization		1 sec, RMS about each platform axis	Bias and Jitter
Overall LOS Stabilization		<1/4 sec, RMS about each axis orthogonal to LOS	Bias and Jitter (with internal alignment mirror and platform gyro feed-forward signals)
Image Roll Stabilization about LOS		30 sec, RMS	
LOS Drift		<0.1 sec/sec	Low-frequency drive

Earth Testing

The balanced design permits the gimbals to be tested on the earth without an external support system. The use of pulleys, cables, springs, or other devices for supporting the telescope in a 1-g environment would probably alter the structural properties of the telescope such that ground testing would be insufficient to insure satisfactory performance in space.

Minimization of Driven Inertia

When the telescope is supported about its center of mass rather than at its end, the driven inertia is reduced by a factor of 3 to 4. The size and power requirements for the gimbal torquers are correspondingly reduced.

Minimization of Sensitivity to Linear Vibration

Center of gravity gimbaling minimizes rotational disturbances of the telescope caused by linear vibration of the pallet.

Minimization of Structural Problems

When the telescope is mounted about its center of mass its unsupported length is minimized. The problems relating to structural bending are therefore also minimized, and the resonant frequencies of the telescope are made as high as possible.

The structural problems relating to the attachment of the telescope to the gimbals are also minimized when the gimbal ring surrounds the telescope at its center of mass.

Minimization of LOS Stabilization Disturbances Due to LOS Roll Commands

A final advantage of the dedicated gimbal design is that the innermost gimbal of the three-axis system provides the roll capability. The telescope can therefore be rolled 90 degrees about its line-of-sight (LOS) for polarization purposes without moving the two outer gimbals and causing unnecessary

LOS disturbances. The IPS gimbal configuration requires that all three gimbals be moved over large distances to produce LOS roll.

A disadvantage of the yoke design used in the gimbal described here is that a substantial portion of the volume surrounding the telescope is occupied by the yoke. Relatively small cryogen tanks must be used if they are to be mounted on the telescope (between the yoke and the sunshade). Off-gimbal mounting of the tanks is also a possibility, and is discussed here as the baseline configuration.

D-2. SIRTF SYSTEM DESCRIPTION

The general configuration of the SIRTF telescope and its associated equipment is shown in Figure D-1. The following discussion provides a brief description of the major subsystems. A more complete description is presented in Reference D-1.

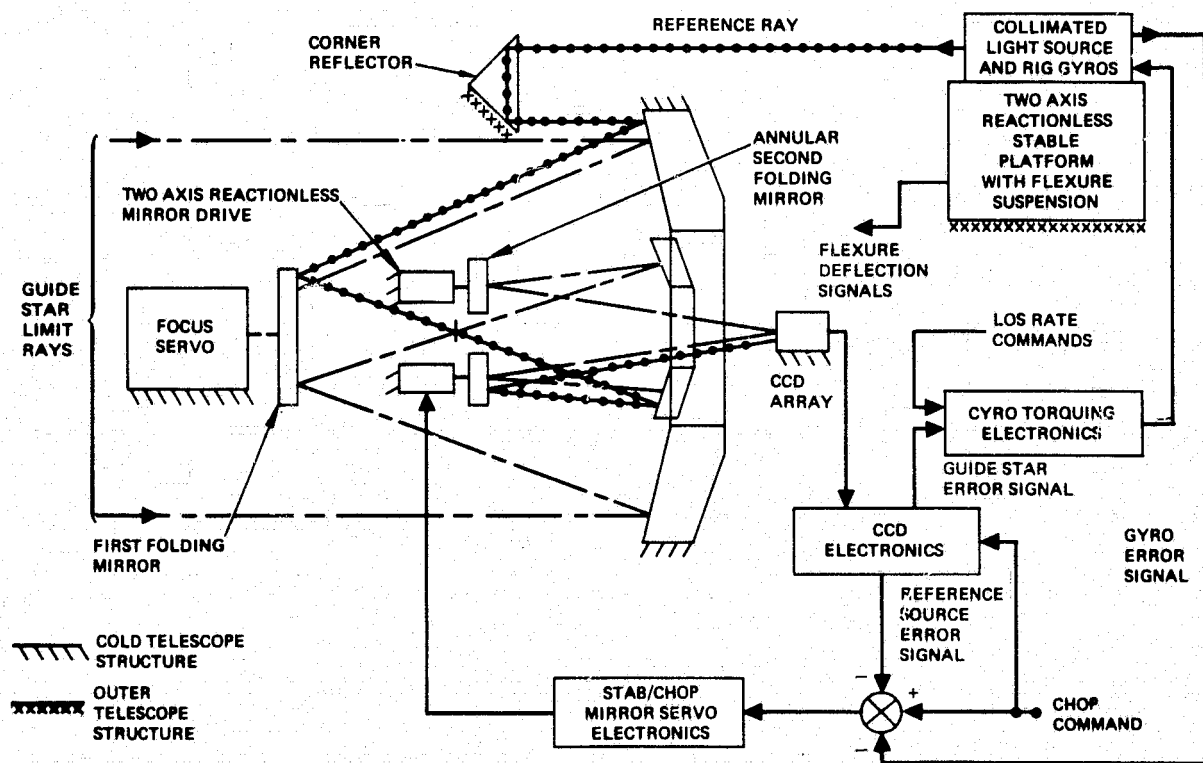


Figure D-1. SIRTF system configuration.

Telescope

The SIRTF instrument is a cryogenically-cooled, Gregorian telescope having a 1-meter aperture. In order to provide thermal isolation the telescope structure consists of two concentric cylindrical shells attached by a fiberglass cone structure. The supporting gimbal is attached to the outer telescope shell, and the optics are supported by the inner shell.

Because of its double shell configuration, dictated by thermal considerations, the overall telescope structure cannot be made highly rigid. However, preliminary analysis of a 40-node model of the telescope indicates that all telescope resonances will be above 30 Hz.

Internal Alignment Mirror

The telescope is provided with an internal, two-axis, LOS steering mirror that performs the following functions:

1. Corrects for optical misalignments and jitter due to structural motion of the inner telescope shell with respect to the outer and thermally induced shifts.
2. Provides stabilization of the LOS relative to the gyro reference.
3. Implements the space chopping function.

A reactionless drive is proposed for the mirror in order to avoid exciting telescope structural resonances that could occur when the mirror is commanded to chop over the wide frequency range from zero to 200 Hz.

Both the mirror and its reaction inertia are mounted with flexure pivots to a cruciform-shaped spider structure. Four moving coil electric driver assemblies, similar to a loudspeaker cone driver, are attached between the mirror and reaction inertia at 90-degree intervals. Diametrically opposing pairs of drivers excited in opposition produce equal and opposite torques and

forces on the mirror and reaction inertia. The reaction torques and forces on the base (cold telescope structure) are therefore cancelled.

Gyro-Stabilized Platform and Laser Reference

A precision, gyro-stabilized platform is mounted on the outer telescope shell. The platform is supported by flexure pivots and is controlled by wide bandwidth stabilization servos.

An alignment laser source is mounted on the platform. This inertially stabilized source injects an alignment beam into the telescope as shown in Figure D-1. The alignment beam travels through the telescope optics and is focused on an error detector (CCD array). The internal LOS steering mirror is servoed so as to bring the telescope LOS into the desired position relative to the alignment reference beam. Space chopping is implemented by commanding the internal alignment mirror as shown in Figure D-1.

CCD Array and Star Tracking

A charge coupled device (CCD) array is used for both optical alignment purposes and for providing guide star position information. The CCD array output is processed by the CCD electronics as shown in Figure D-1, and gyro torquing signals are derived. The torquing signals drive the gyros to the desired angular orientation relative to the selected guide stars. A detailed discussion of the star tracking process is given in Reference D-2.

There is some doubt as to whether the CCD array can provide sufficient frequency response for following the space chopping commands. If the CCD array does not have adequate bandwidth it will be necessary to mount a separate set of position transducers on the LOS steering mirror for implementing the wide-bandwidth chopping servo. The chopping servo will

then be a wide-bandwidth position loop enclosed within a lower-bandwidth optical alignment loop.

Coarse Gimbal Assembly

Large angular coverage for the telescope is provided by the coarse gimbal assembly. The coarse gimbals are described in Section D-3. The coarse gimbals are controlled by slaving them to the SIRTF stable platform. The slave loops are implemented by using the deflection angles of the platform flexures as error signals to drive the coarse gimbals into alignment with the platform.

D-3. DEDICATED GIMBAL MECHANICAL CONFIGURATION

Figure D-2 shows the stowed position of the telescope in the Shuttle bay, and Figure D-3 shows the telescope in its operational position. In the stowed position the telescope is supported at its forward end by the telescope cover. The cover moves longitudinally to fit over the telescope end and rotates to lock firmly onto the telescope barrel.

Figure D-4 shows the angular coverage provided by the gimbals. The telescope can sweep out a cone having an angle of 60 degrees measured from the vertical. The elevation gimbal provides 90 degrees of motion from the vertical to permit the telescope to stow in a horizontal position.

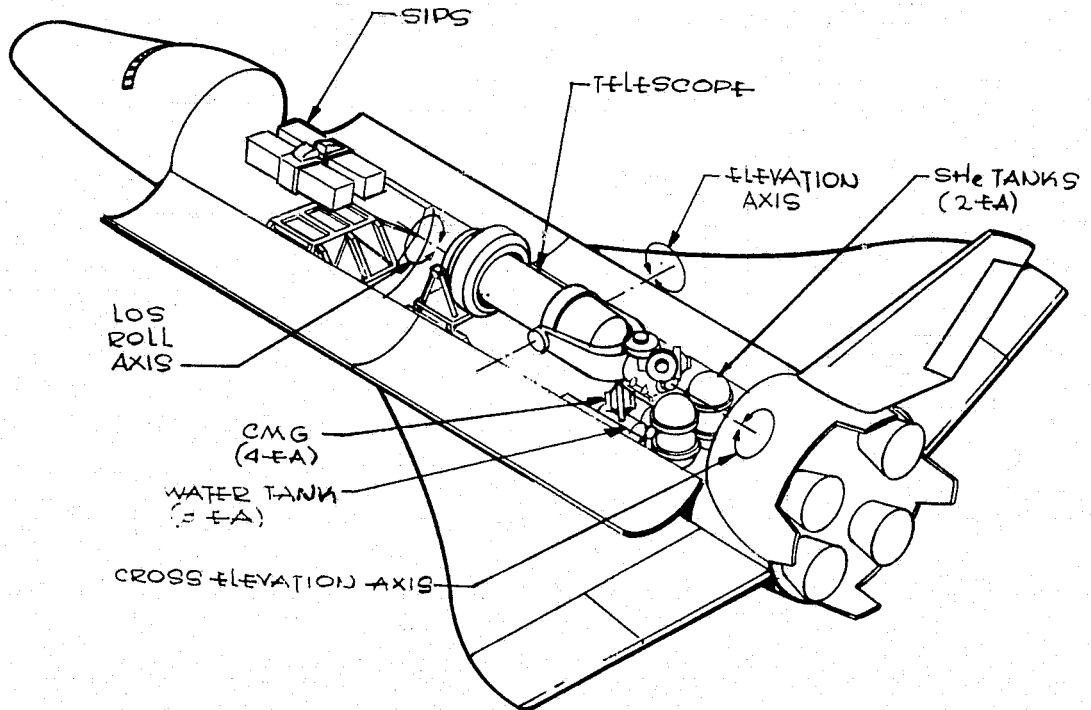


Figure D-2. Telescope in stowed position.

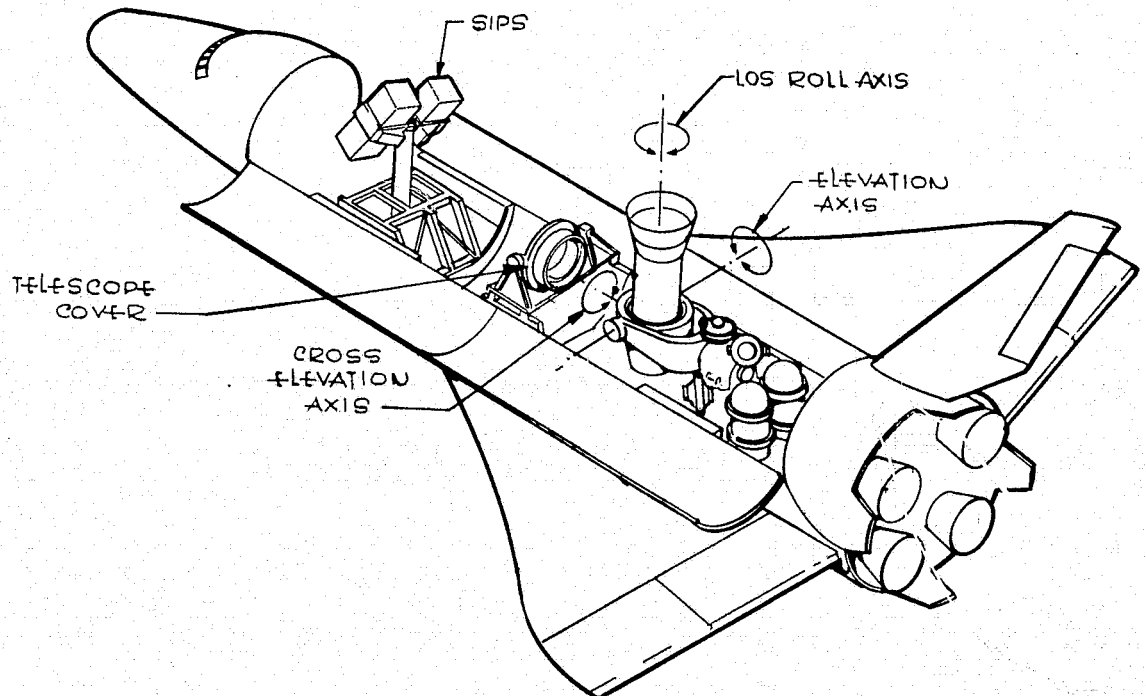


Figure D-3. Telescope in deployed position.

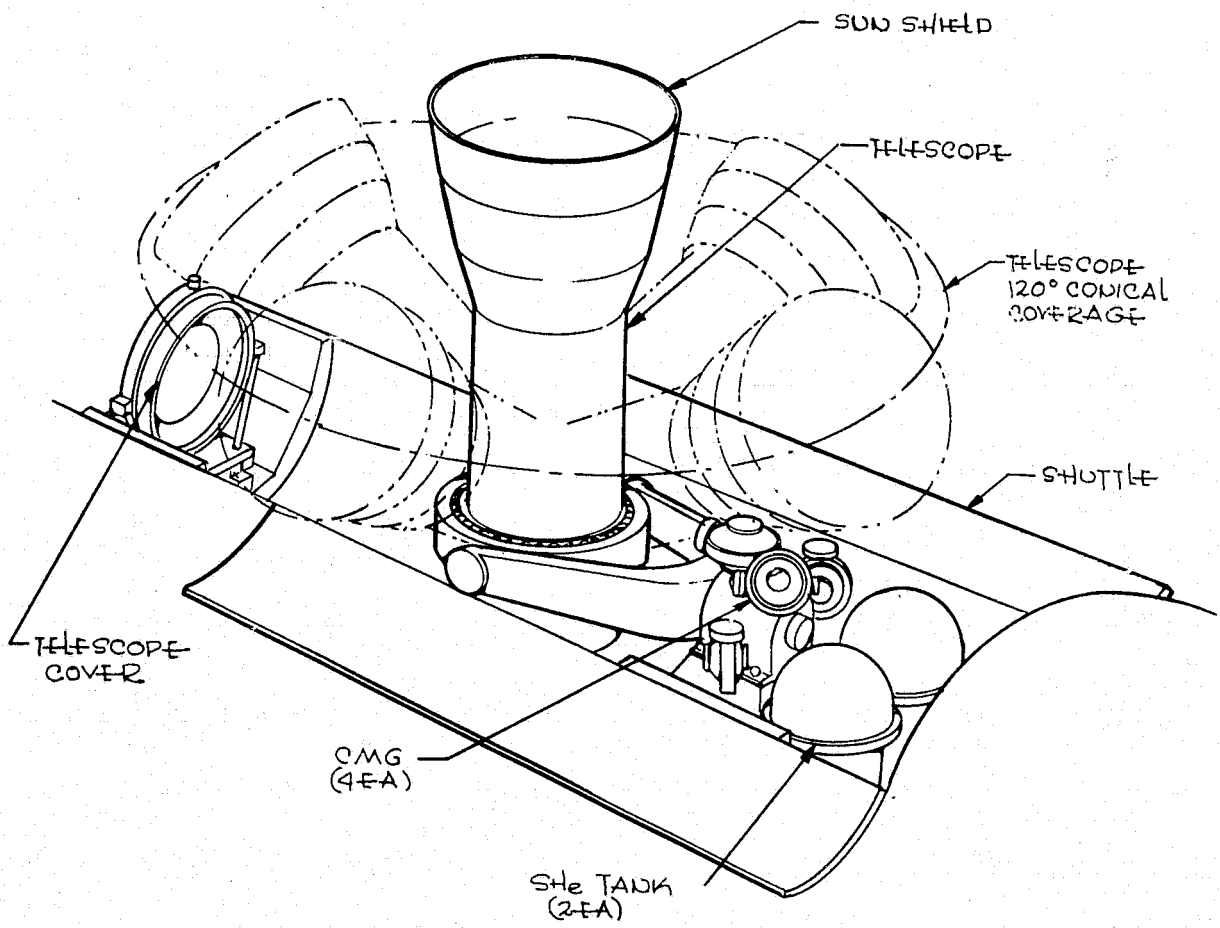


Figure D-4. Telescope angular coverage.

The arrangement of the gimbal axes of rotation is shown in Figure D-5.

The gimbal base is a pedestal mounted on the Shuttle pallet. The outer gimbal is a yoke that turns about the cross-elevation axis. The middle gimbal is a ring that surrounds the telescope and provides motion about the elevation axis. Roll about the telescope LOS is produced by rotating the telescope within the elevation gimbal ring.

An outline and mounting drawing of the telescope and dedicated gimbal assembly is shown in Figure D-6. Although control moment gyros (CMG's) are

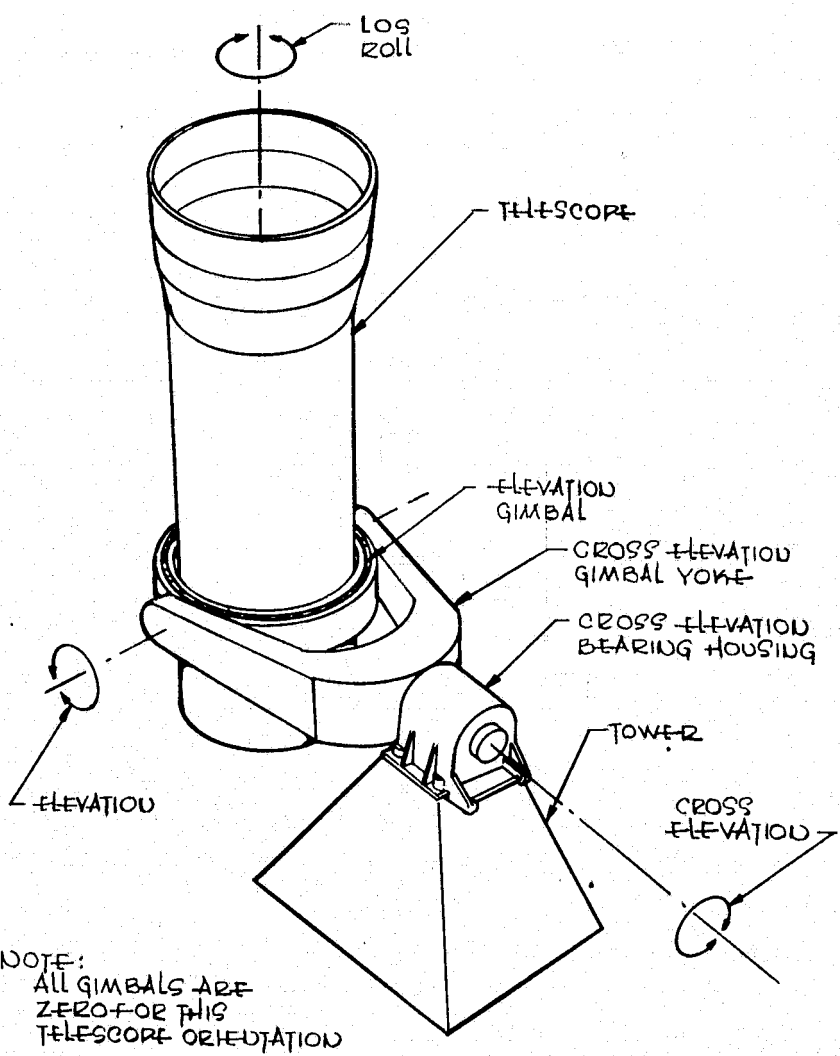
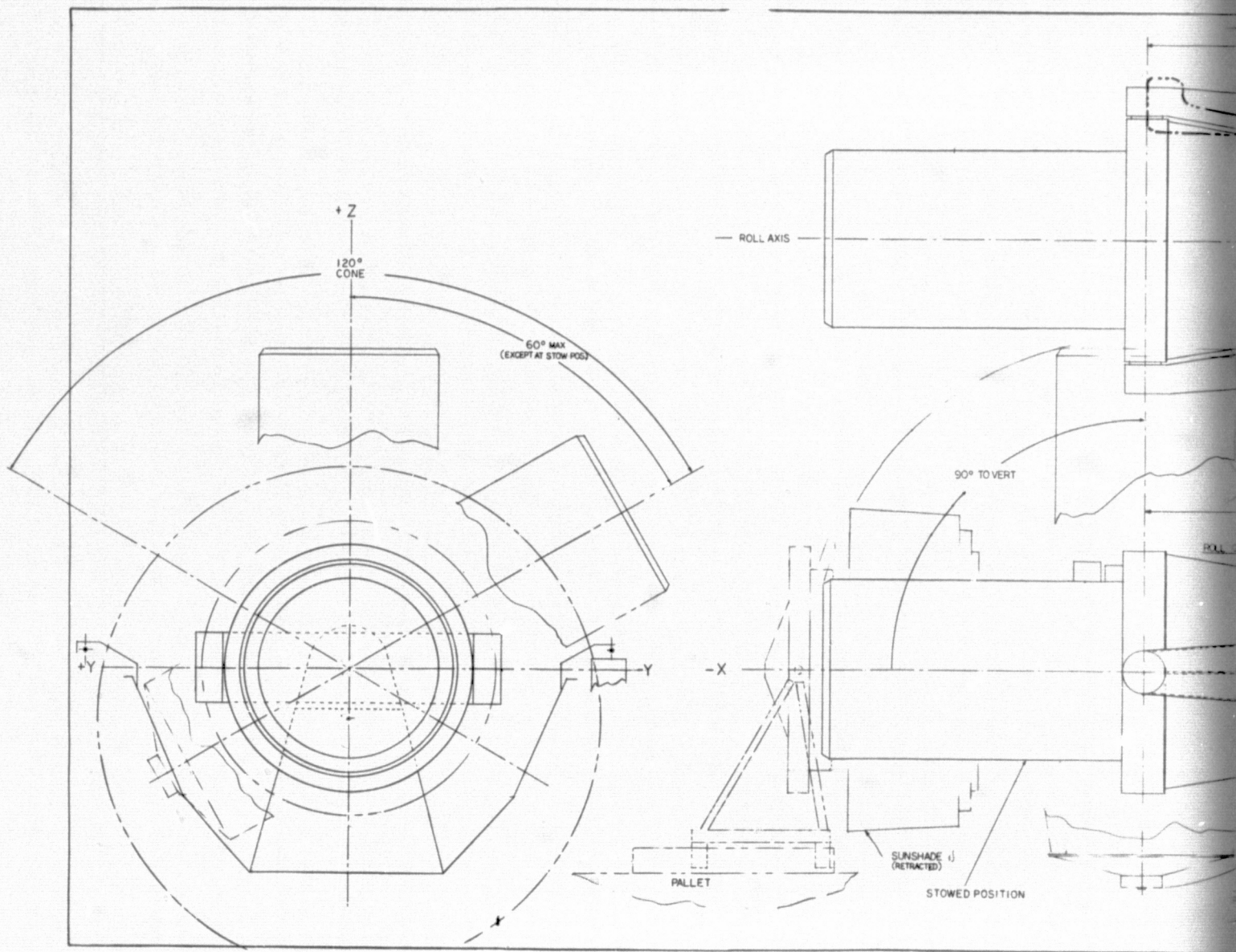
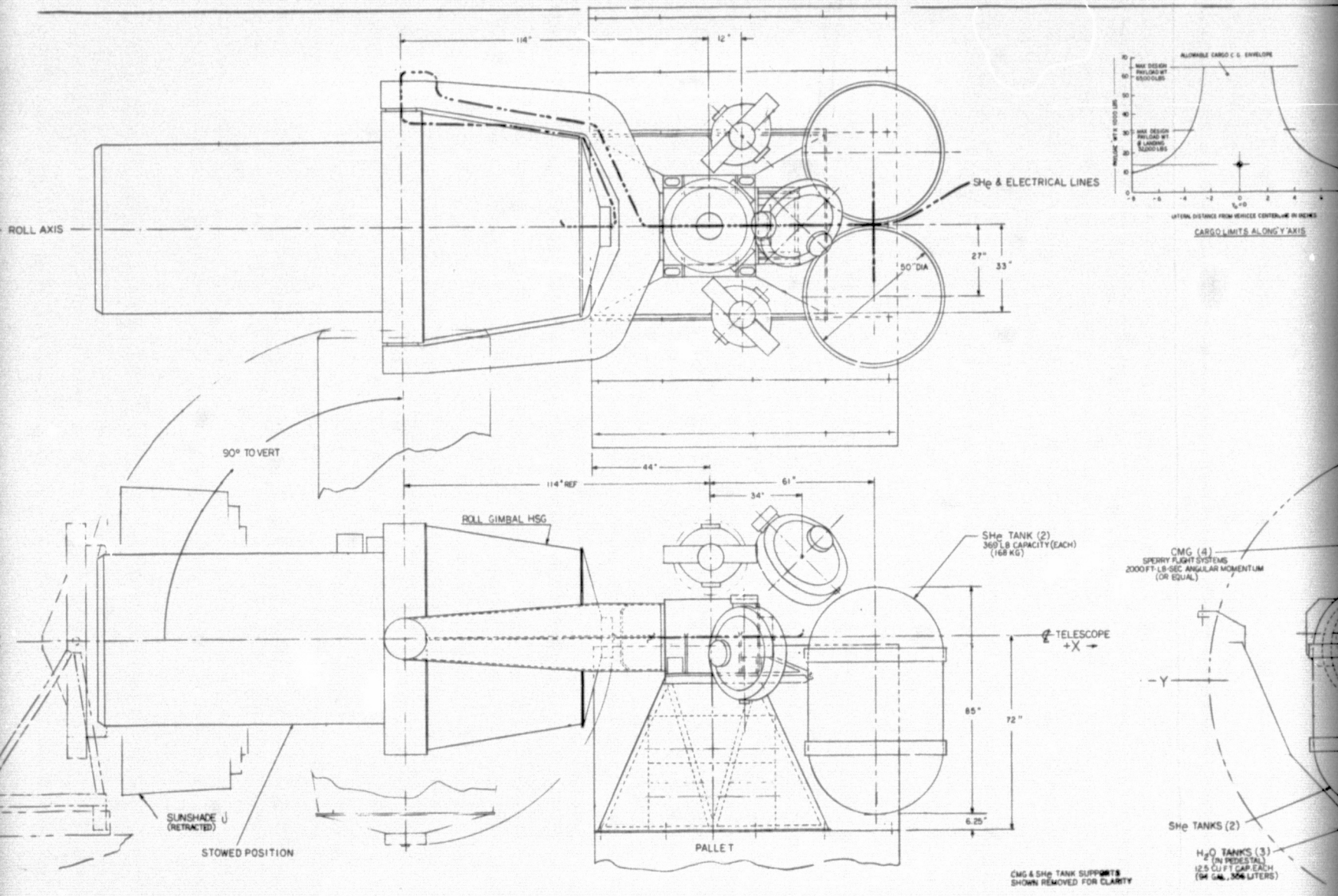


Figure D-5. Layout of the SIRTS gimbal system.

not part of the baseline system, provision is made for mounting a set of four CMG's on the gimbal pedestal. The CMG's can be used for precision attitude control of the Shuttle during SIRTF active viewing periods. The advantage of the CMG's is that they do not produce combustion products which can degrade the viewing and contaminate the optical surfaces.



FOLDOUT FRAME |



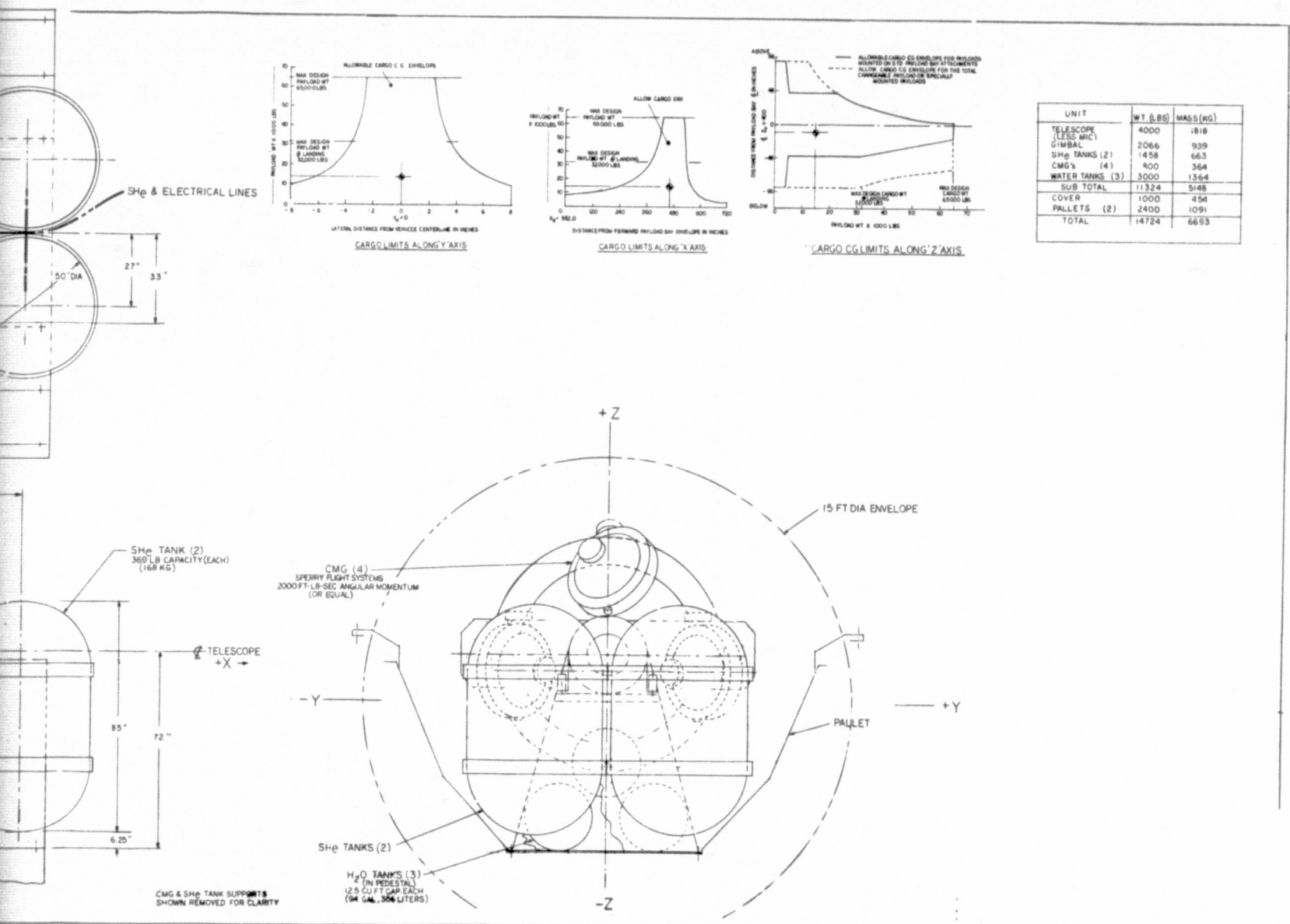


Figure D-6. SIRTF telescope.

FOLDOUT FRAME 3

D-11

REPRODUCIBILITY OF THE ORIGINAL PAGE IS POOR

A detailed drawing of the cross-elevation gimbal drive is shown in Figure D-7. The cross-elevation yoke turns on steel race bearings of approximately 67 cm diameter. The cross-elevation gimbal is driven by a dc pancake torquer. Cryogen is fed across the gimbal junction by means of a rotary joint located on the axis of rotation.

The elevation gimbal details are shown in Figures D-8 and D-9. The elevation torquer and resolver are mounted on opposite sides of the telescope. The elevation gimbal is supported by steel race bearings having a diameter of approximately 27 cm. Cryogen is transferred across the gimbal junction by a rotary joint.

The roll bearings permit the telescope to rotate about the LOS within the elevation gimbal ring. The roll bearings have aluminum races and are approximately 196 cm in diameter. The position of the roll bearings can be seen in Figure D-8 or Figure D-9.

The roll torquer is located at the rear end of the telescope as shown in Figure D-10. This torquer is connected between the telescope outer shell rear structure and the external roll gimbal housing. The roll gimbal housing is a thin shell that attaches to the elevation gimbal ring and envelopes the rear end of the telescope as shown in Figure D-6.

The roll torquer is provided with a set of small bearings as indicated in Figure D-10. The rotary joint for bringing cryogen into the telescope is located at the rear of the telescope on the roll axis.

A listing of the gimbal torquers is given in Table D-2. The torquers are of the brushless, pancake type and are built by Magtech. The manufacturer's numbers listed in the table pertain to the conventional brush version

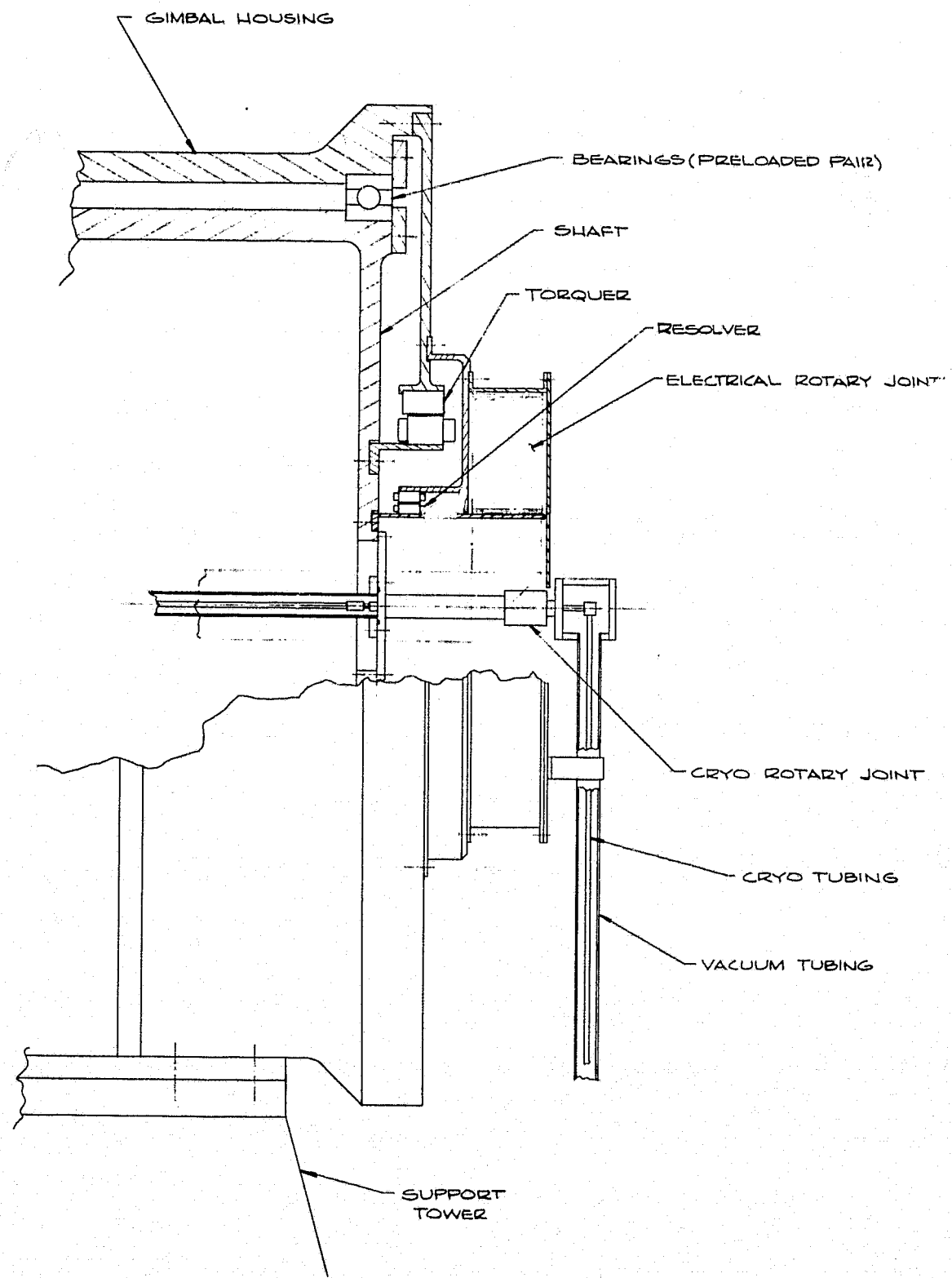


Figure D-7. Cross elevation gimbled, drive and rotary joints.

D-15

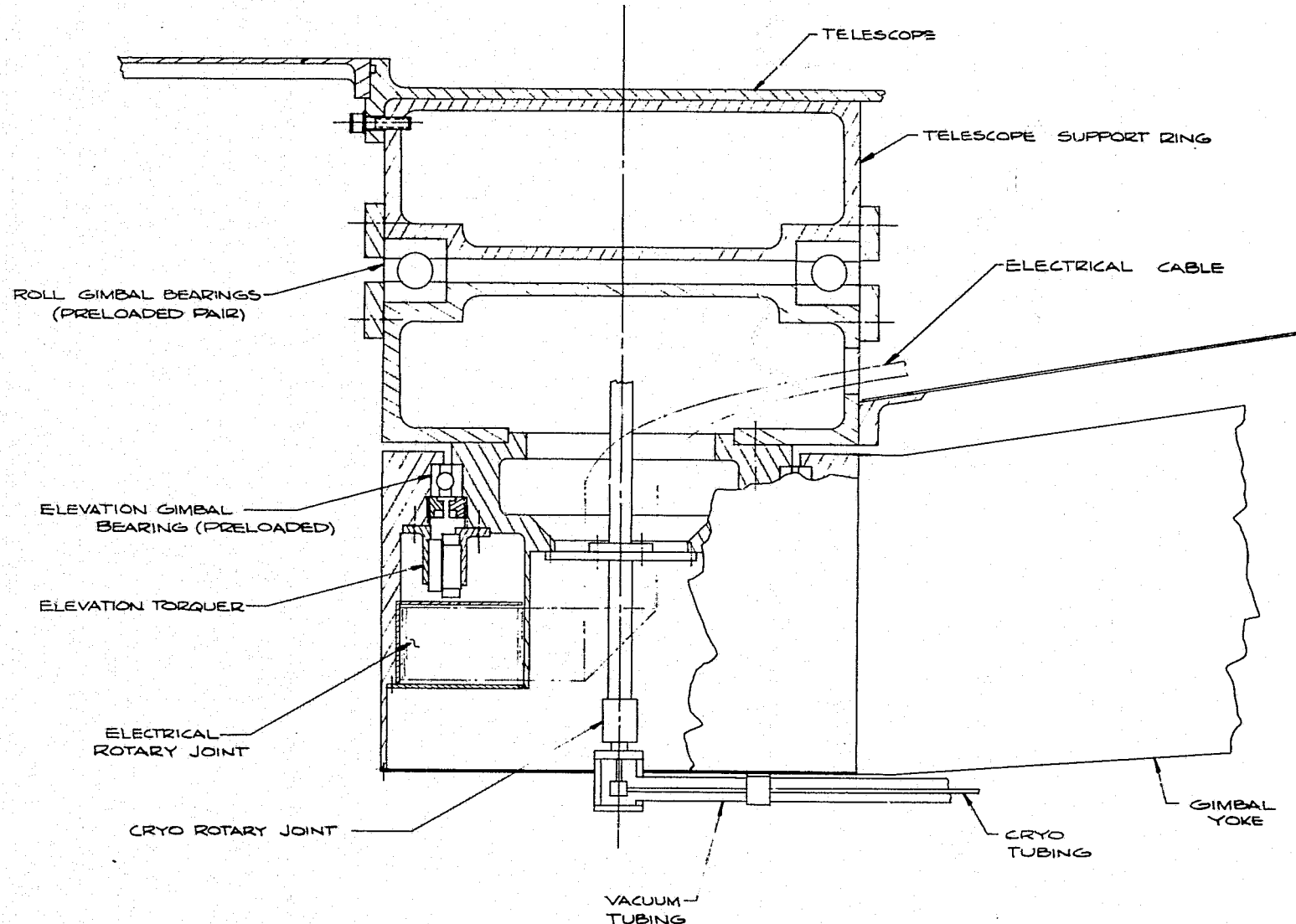


Figure D-8. Elevation gimbal (torquer side).

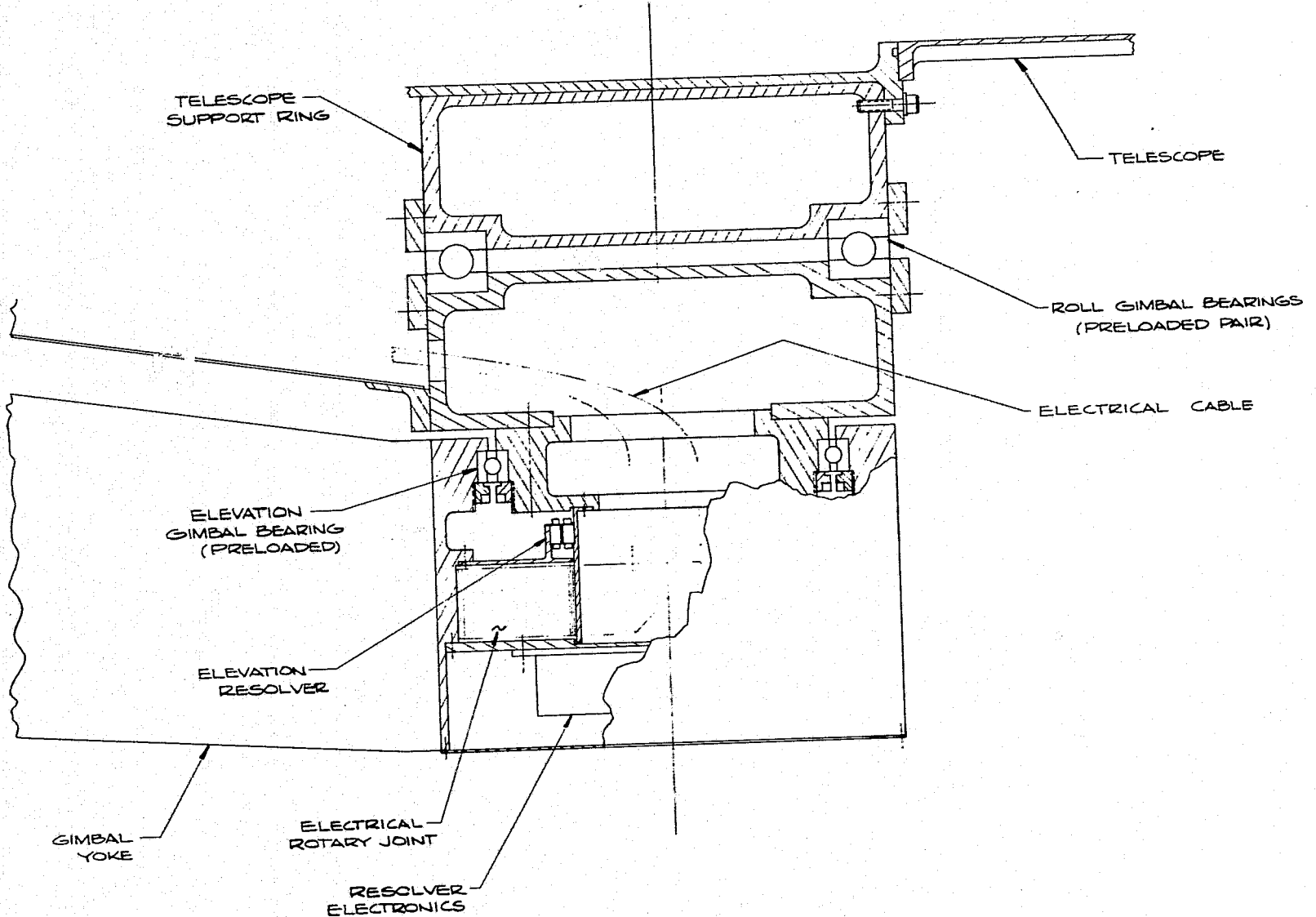


Figure D-9. Elevation gimbal (resolver side).

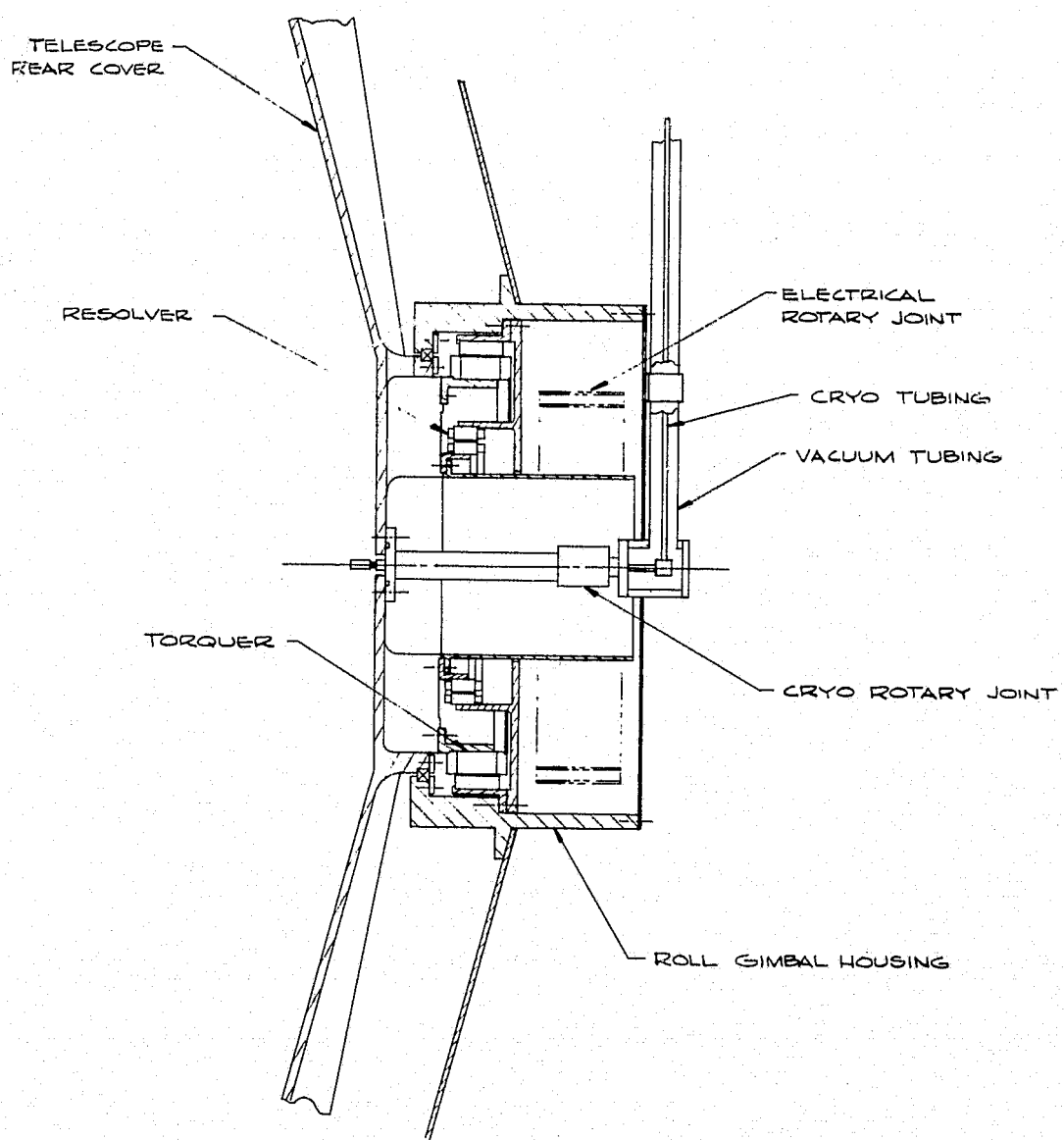


Figure D-10. Roll gimbal.

TABLE D-2. DEDICATED GIMBAL TORQUER SUMMARY

Gimbal Axis	Magtech Number	Maximum Torque (lb ft)	Driven Inertia (lb ft sec ²)
X-EL	14000D-180	50	4330
EL	23040-270	37.5	3935
ROLL	12040-200	29	404

of the torquers. Equivalent brushless units can be obtained from the manufacturer.

The elevation and cross-elevation torquers are sized to permit the gimbals to start from rest at one gimbal limit, travel over the entire range of 120 degrees, and come to rest at the other gimbal limit all in 30 seconds.

A weight summary for the telescope, dedicated gimbals, and associated equipment is given in Table D-3.

TABLE D-3. SIRTF WEIGHT SUMMARY

Unit	Wt. (lbs)	Mass (kg)
Telescope (less MIC)	4000	1818
Gimbals	2066	939
SHe Tanks (2)	1458	663
CMG's (4)	800*	364*
Water Tanks (3)	3000	1364
Sub Total	11324	5148
Cover	1000	454
Pallets (2)	2400	1091
Total	13924	6329

*Not included in total.

D-4. DEDICATED GIMBAL STRUCTURAL ANALYSIS

A static and dynamic structural analysis has been performed using the MRI/STARDYNE structural analysis system. The dynamic analysis consisted of a modal extraction yielding the first 10 natural frequencies and associated mode shapes.

The results of the dynamic analysis are summarized in Table D-4. This table lists the first 10 natural modes and modal frequencies. A mode shape description is also given. A detailed discussion of the analysis and a graphical presentation of the mode shapes are given in Reference D-3.

Table D-4 indicates that the lowest modal frequency excited by the elevation drive is 6.2 Hz. The elevation gimbal servo will therefore have a bandwidth of about 1 to 2 Hz. The cross-elevation gimbal servo can have a bandwidth on the order of 4 Hz because the lowest modal frequency excited by the cross-elevation drive is 24.2 Hz.

There is a possibility of improving the gimbal servo bandwidths by using a constrained-layer damping technique for the cross-elevation gimbal yoke as shown in Figure D-11. Preliminary analytical studies, following the procedure outlined in DuPont's "Engineering Design Sheet for Constrained-Layer Damping of Beams," suggest that the dynamic amplification factor for the cross-elevation gimbal yoke could be reduced by 20 db. The damping technique involves bonding a visco-elastic damping material between the gimbal yoke and a constraining layer of beryllium or aluminum.

The improved structural damping should make it possible to increase the open-loop crossover frequencies of the gimbal servos without changing the basic resonant frequencies of the structure.

TABLE D-4. RESULTS OF MODAL EXTRACTION FOR SIRTF GIMBAL SYSTEM

Mode Shape Number	Mode Shape Frequency	Mode Shape Description	Excitation of Modes by Gimbal Drives		
			LOS	Elevation	Cross Elevation
1	5.6 Hz	Lateral translation and LOS rotation of telescope due to cross-elevation gimbal flexure	Yes	No	No
2	6.2 Hz	Vertical translation and elevation rotation of telescope due to cross-elevation gimbal flexure	No	Yes	No
3	14.0 Hz	Elevation rotation of telescope due to elevation gimbal flexure	No	Yes	No
4	21.1 Hz	Lateral translation and LOS rotation of telescope due to elevation and cross-elevation gimbal flexure	Yes	No	No
5	22.3 Hz	Longitudinal translation of telescope due to elevation and cross-elevation gimbal flexure	No	No	No
6	24.2 Hz	Cross elevation rotation of telescope due to cross-elevation gimbal flexure	No	No	Yes
7	83.6 Hz	Lateral translation and LOS rotation of telescope due to elevation and cross-elevation gimbal and tower flexure	Yes	No	No
8	111 Hz	Vertical translation and elevation rotation of telescope due to elevation and cross-elevation gimbal and tower flexure	No	Yes	No
9	118 Hz	Cross elevation rotation of telescope due to cross-elevation gimbal flexure	No	No	Yes
10	120 Hz	Vertical translation and elevation rotation of telescope due to elevation and cross-elevation gimbal and tower flexure	No	Yes	No

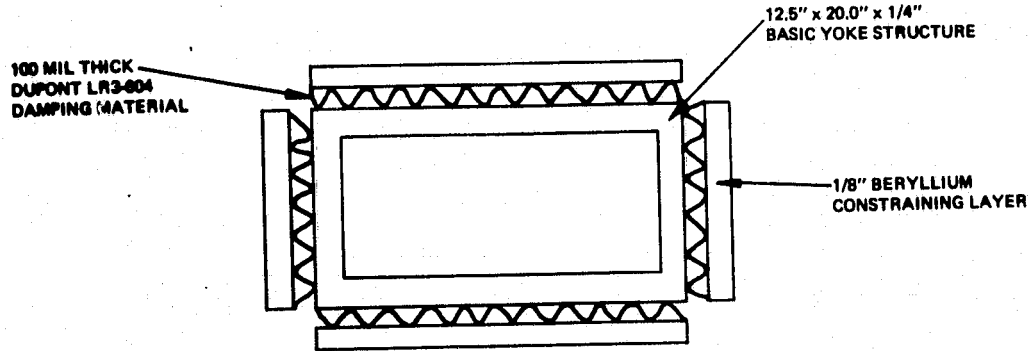


Figure D-11. Cross elevation yoke cross section showing proposed damping treatment.

D-5. SERVO SYSTEM CONFIGURATION

The purpose of this section is to describe the gimbal kinematics and servo configuration for the dedicated gimbal system. See Section D-6 for a general introduction to the nomenclature.

Gimbal Configuration and Nomenclature

Since many gimbal angles and coordinate systems must be considered, the kinematic description is greatly facilitated by the adoption of an organized system of notation. The nomenclature defined here has the advantages of being both mnemonic and easy to write.

The various bodies that constitute the gimbal system are identified by capital letters as follows:

Body A	Shuttle
Body B	Coarse outer gimbal (X-EL)
Body C	Coarse middle gimbal (EL)
Body D	Coarse inner gimbal (LOS ROLL)
Body E	Gyro-stabilized platform

A sketch of the gimbal system showing the various gimbaled bodies is shown in Figure D-12.

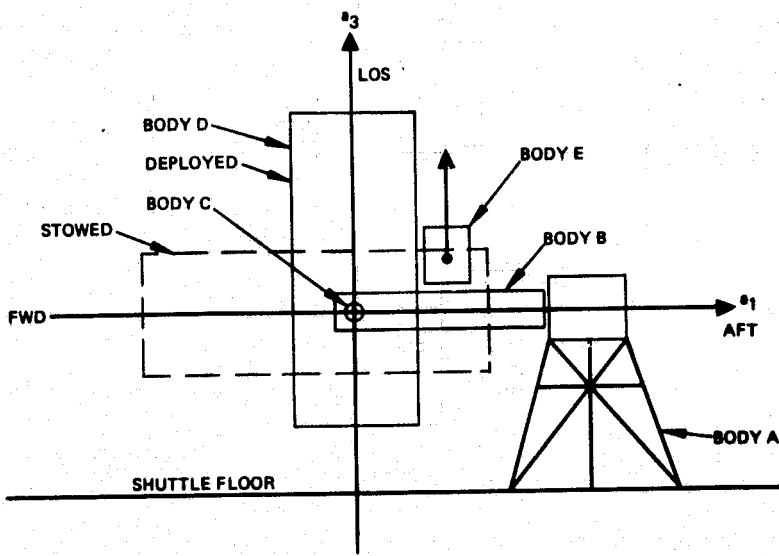


Figure D-12. Identification of SIRTF gimbaled bodies.

Each body has a set of body-fixed coordinate axes that constitute an orthogonal and dextral coordinate system. The axes are denoted by appropriate lower case letters with subscripts.

Body	Body Axes
A	a_1, a_2, a_3
B	b_1, b_2, b_3
C	c_1, c_2, c_3
D	d_1, d_2, d_3
E	e_1, e_2, e_3

The gimbal angles for the coarse gimbal assembly are

θ = coarse outer gimbal angle (X-EL)

ϵ = coarse middle gimbal angle (EL)

ϕ = coarse inner gimbal angle (LOS ROLL)

The deflection angles for the gyro platform suspension are

δ_1 = deflection angle about d_1 axis

δ_2 = deflection angle about d_2 axis

The gimbal angles and body axes are defined pictorially in Figure D-13.

The Shuttle axes a_1 , a_2 , a_3 have the orientation shown in Figure D-13(a). These axes have the directions of aft, right wing, and up, respectively. The longitudinal axis of the telescope is axis d_3 . When all gimbal angles are zero the telescope points upward relative to the Shuttle. The telescope is stowed with $\epsilon = -90$ degrees (looking forward).

A more concise definition of the gimbal angles and axes is given by the Program of Figure D-14. This figure employs the pictorial representation of coordinate systems described in Section D-6 of this appendix. The symbols δ_1 and δ_2 represent the deflection angles of the gyro platform suspension. Since these angles are small, the order in which they appear in Figure D-14 is immaterial.

The inertial angular rates for each body are denoted by the symbol ω with appropriate subscripts to identify both the body and the axis of rotation.

ω_{Aa1} , ω_{Aa2} , ω_{Aa3} = inertial angular rates of Body A about a_1 , a_2 , a_3 axes, respectively.

ω_{Bb1} , ω_{Bb2} , ω_{Bb3} = inertial angular rates of Body B about b_1 , b_2 , b_3 axes, respectively.

ω_{Cc1} , ω_{Cc2} , ω_{Cc3} = inertial angular rates of Body C about c_1 , c_2 , c_3 axes, respectively.

ω_{Dd1} , ω_{Dd2} , ω_{Dd3} = inertial angular rates of Body D about d_1 , d_2 , d_3 axes, respectively.

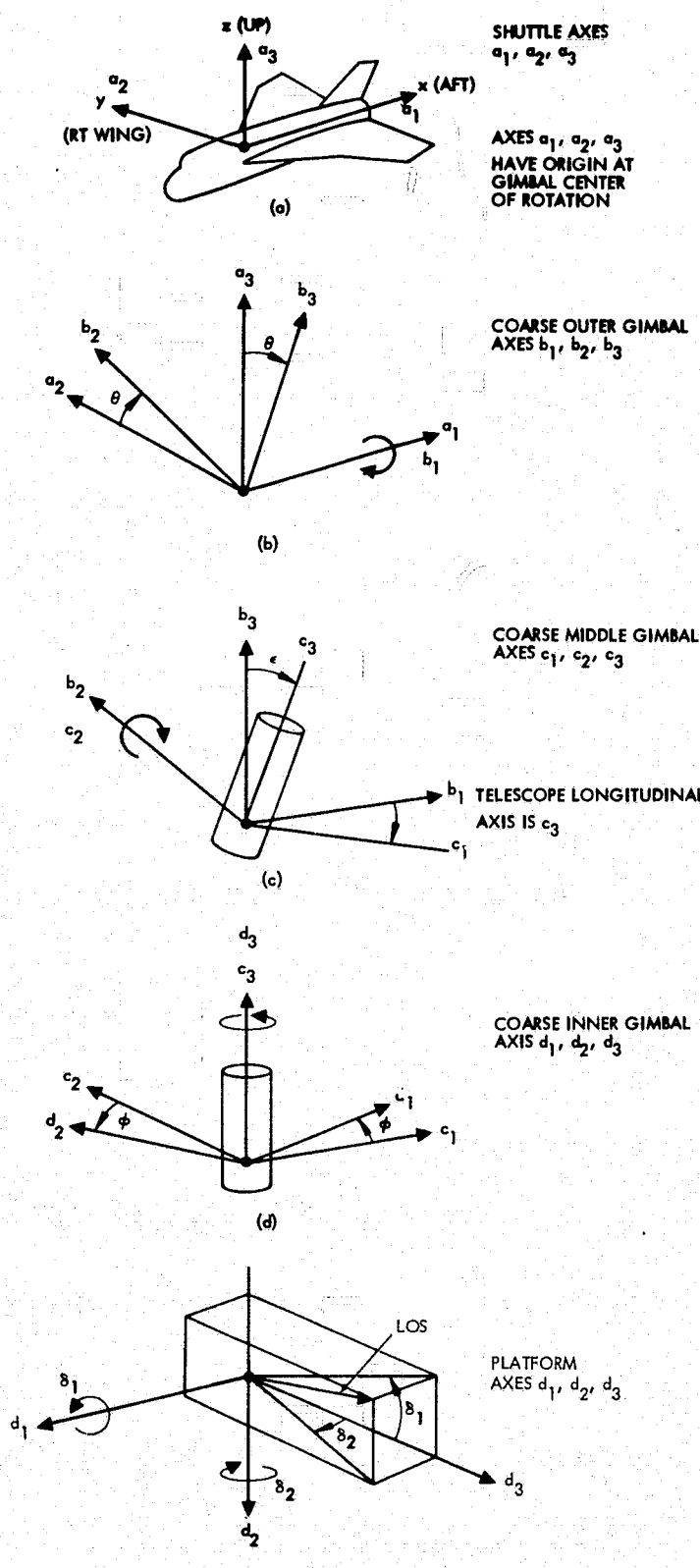


Figure D-13. Coordinate system definition.

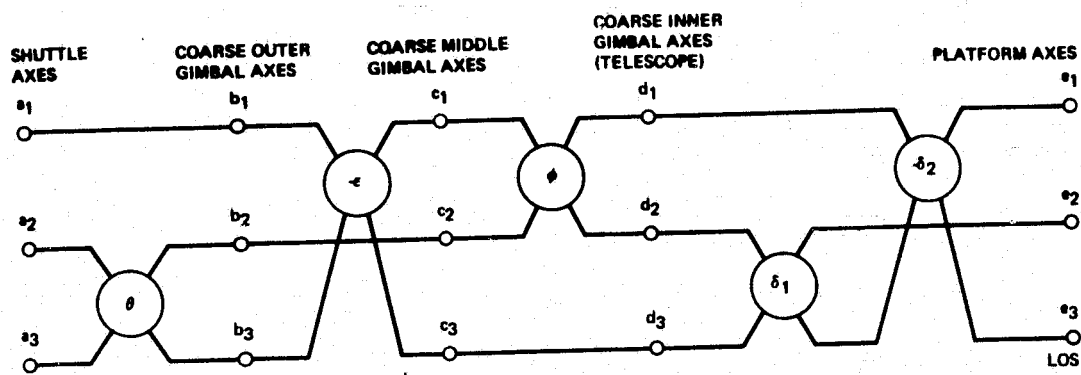


Figure D-14. Gimbal angle Program.

$\omega_{Ed1}, \omega_{Ed2}, \omega_{Ed3}$ = inertial angular rates of Body E about d_1, d_2, d_3 axes, respectively

$\omega_{Eel}, \omega_{Ee2}, \omega_{Ee3}$ = inertial angular rates of Body E about e_1, e_2, e_3 axes, respectively.

The torques acting on the gimbaled bodies are denoted by the letter T with appropriate subscripts to identify both the body and the axis about which the torque is applied.

$T_{Bbl}, T_{Bb2}, T_{Bb3}$ = torques acting on Body B about b_1, b_2, b_3 axes, respectively.

$T_{Ccl}, T_{Cc2}, T_{Cc3}$ = torques acting on Body C about c_1, c_2, c_3 axes, respectively.

$T_{Ddl}, T_{Dd2}, T_{Dd3}$ = torques acting on Body D about d_1, d_2, d_3 axes, respectively.

$T_{Ed1}, T_{Ed2}, T_{Ed3}$ = torques acting on Body E about e_1, e_2, e_3 axes, respectively.

The moments of inertia of the gimbaled bodies are denoted by capital letters with appropriate numerical subscripts.

B_1, B_2, B_3 = moments of inertia of Body B, about b_1, b_2, b_3 axes, respectively.

C_1, C_2, C_3 = moments of inertia of Body C about c_1, c_2, c_3 axes, respectively.

D_1, D_2, D_3 = moments of inertia of Body D about d_1, d_2, d_3 axes, respectively.

E_1, E_2, E_3 = moments of inertia of Body E about d_1, d_2, d_3 axes, respectively.

Angular Rate Relationships for Gimbal

The derivatives of the gimbal angles can be expressed as the differences of various inertial rates as follows:

$$\begin{aligned}\dot{\theta} &= \omega_{Bbl} - \omega_{Aal} \\ \dot{\epsilon} &= \omega_{Cc2} - \omega_{Bb2} \\ \dot{\phi} &= \omega_{Dd3} - \omega_{Cc3}\end{aligned}\tag{1}$$

The relationships of Equations (1) imply that axes a_1 and b_1 are coincident with the cross-elevation gimbal axis, axes b_2 and c_2 are coincident with the elevation gimbal axis, and axes c_3 and d_3 are coincident with the LOS roll gimbal axis.

Similar expressions can be written to express the derivatives of the gyro platform suspension angles.

$$\begin{aligned}\dot{\delta}_1 &= \omega_{Ed1} - \omega_{Dd1} \\ \dot{\delta}_2 &= \omega_{Ed2} - \omega_{Dd2}\end{aligned}\tag{2}$$

The relationships expressed by Equations (1) and (2) are included in Figure D-15 which shows the angular rate relationships for the gimbal assembly.

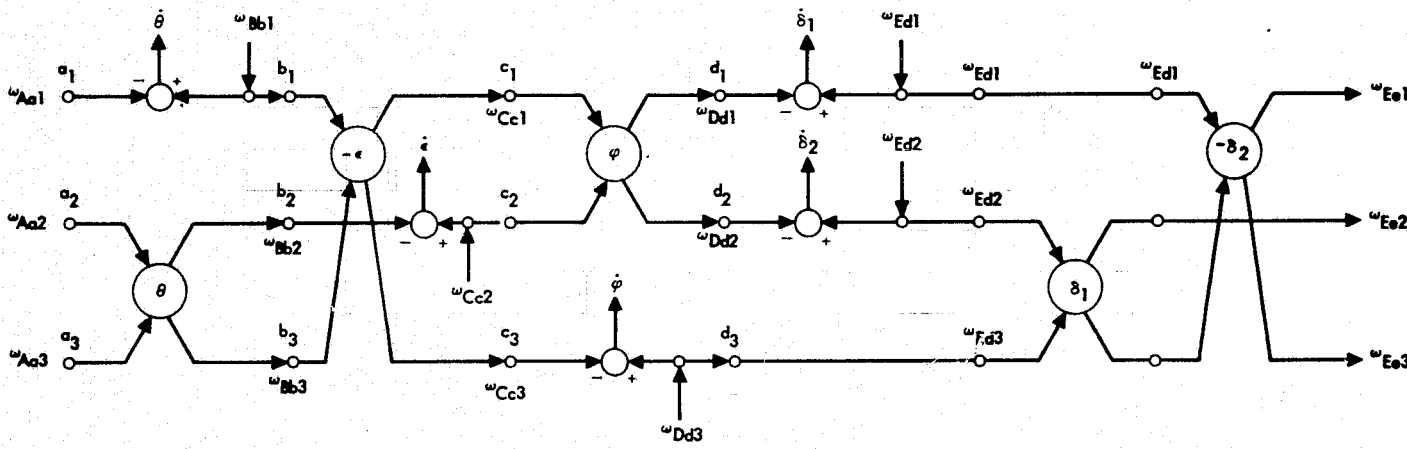


Figure D-15. Angular rate relationships for gimbal system.

The inputs shown in the figure are the Shuttle inertial rates (ω_{Aa1} , ω_{Aa2} , ω_{Aa3}), the rates produced by the coarse gimbal torquers (ω_{Bb1} , ω_{Cc2} , ω_{Dd3}), and the rates produced by the gyro platform torquers (ω_{Ed1} , and ω_{Ed2}). The outputs of Figure D-15 are the inertial rates of the gyro platform (ω_{Ee1} , ω_{Ee2} , ω_{Ee3}). Since the LOS is held in coincidence with axis e_3 by the internal alignment mirror, the rates ω_{Ee2} and ω_{Ee3} are the inertial rates of the LOS.

Gyro Platform Dynamics

Since the platform deflection angles δ_1 and δ_2 are small, the right side of Figure D-15 can be replaced by the small angle approximation of Figure D-16.

The rotational dynamics of the platform are expressed by the Euler equations listed below. These equations are written in terms of the axes d_1 , d_2 , and d_3 . In order to be strictly correct these equations should express

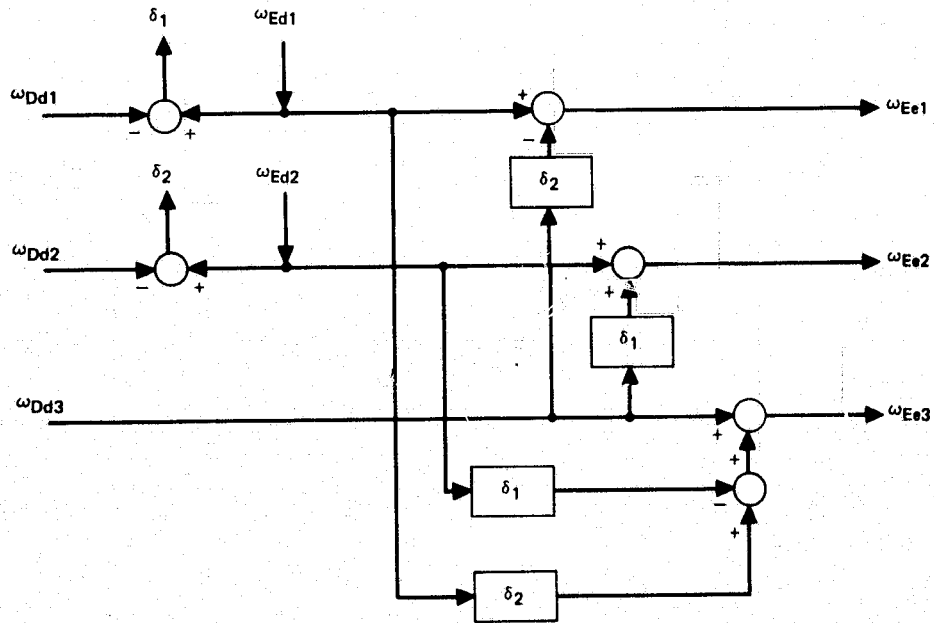


Figure D-16. Simplified angular rate relationships for gyro platform.

the dynamics of the platform (Body E) in terms of the platform body axes e_1 , e_2 , and e_3 . Since the platform deflection angles δ_1 and δ_2 are small, however, the equations can be written approximately in terms of the axes d_1 , d_2 , and d_3 .

$$T_{Ed1} = E_1 \dot{\omega}_{Ed1} + (E_3 - E_2) \omega_{Ed3} \omega_{Ed2}$$

$$T_{Ed2} = E_2 \dot{\omega}_{Ed2} + (E_1 - E_3) \omega_{Ed1} \omega_{Ed3} \quad (3)$$

$$T_{Ed3} = E_3 \dot{\omega}_{Ed3} + (E_2 - E_1) \omega_{Ed2} \omega_{Ed1}$$

The platform is driven by a set of four linear, electromagnetic actuators which produce forces denoted by F_1 , F_2 , F_3 , and F_4 . The force configuration relative to the d_1 , d_2 , d_3 coordinate system is shown in Figure D-17. The forces F_1 and F_2 acting at a distance r from the center of rotation provide a force couple or torque about the d_1 axis. Forces F_3 and F_4 similarly produce a couple about the d_2 axis.

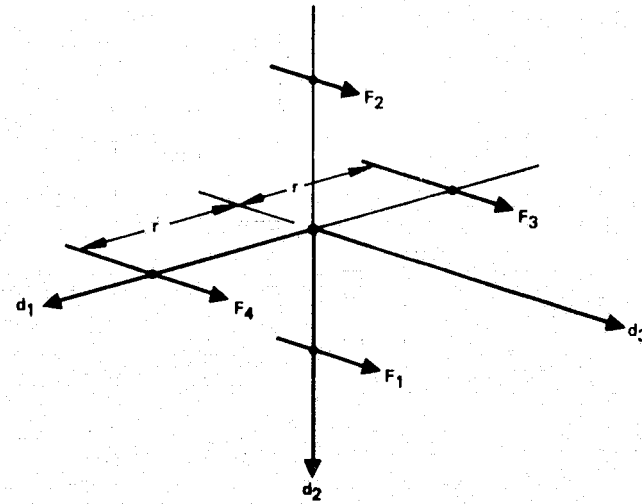


Figure D-17. Platform actuator configuration.

The combination of the angular rate relationships of Figure D-16, the force configuration of Figure D-17, and the Euler equations for the platform (Equations (3)) give the dynamic model of the platform shown in Figure D-18. The symbols K_{d1} and K_{d2} in Figure D-18 represent the spring stiffnesses of the platform about the d_1 and d_2 axes, respectively.

Overall Stabilization System Configuration

An overall model for the SIRTF stabilization employing the dedicated gimbal assembly is shown in Figure D-19. This model incorporates Figures D-15 and D-16. In addition the various servo loops that drive the coarse gimbals and the platform are indicated.

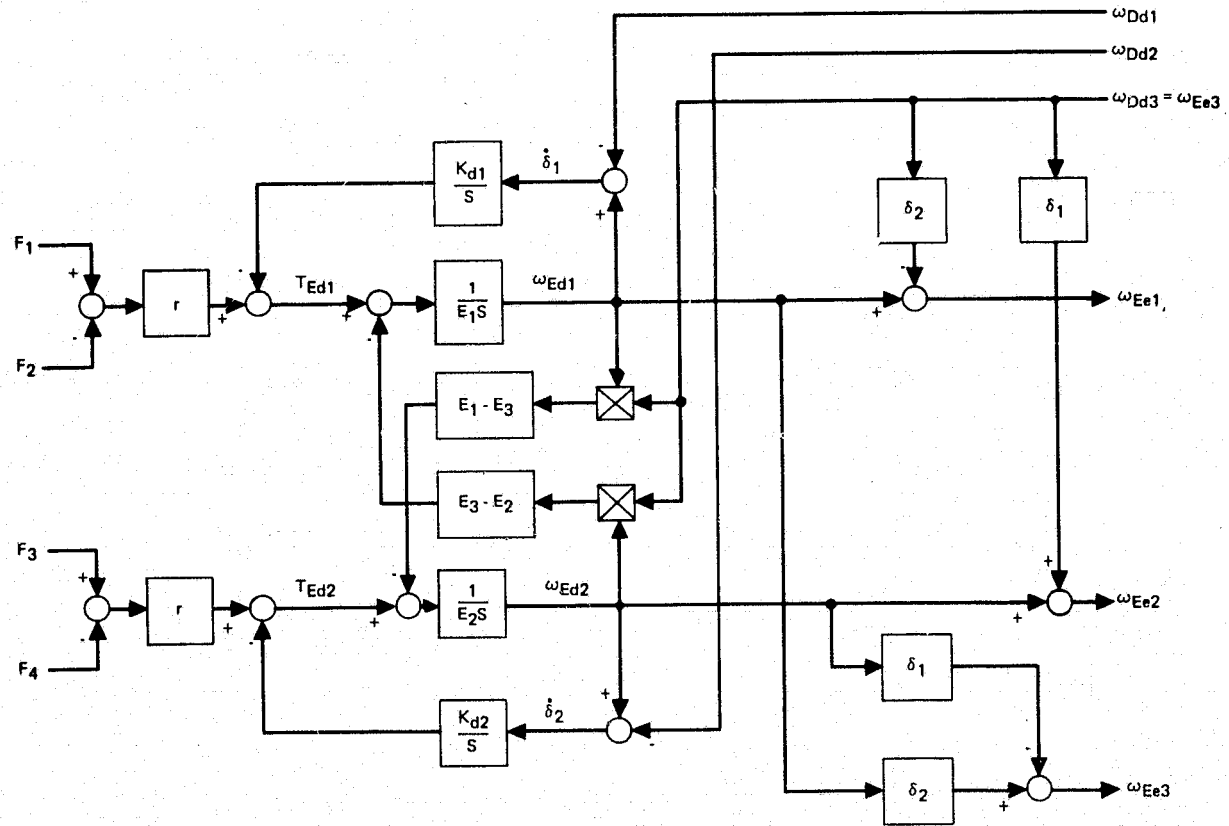


Figure D-18. Dynamic model for gyro platform.

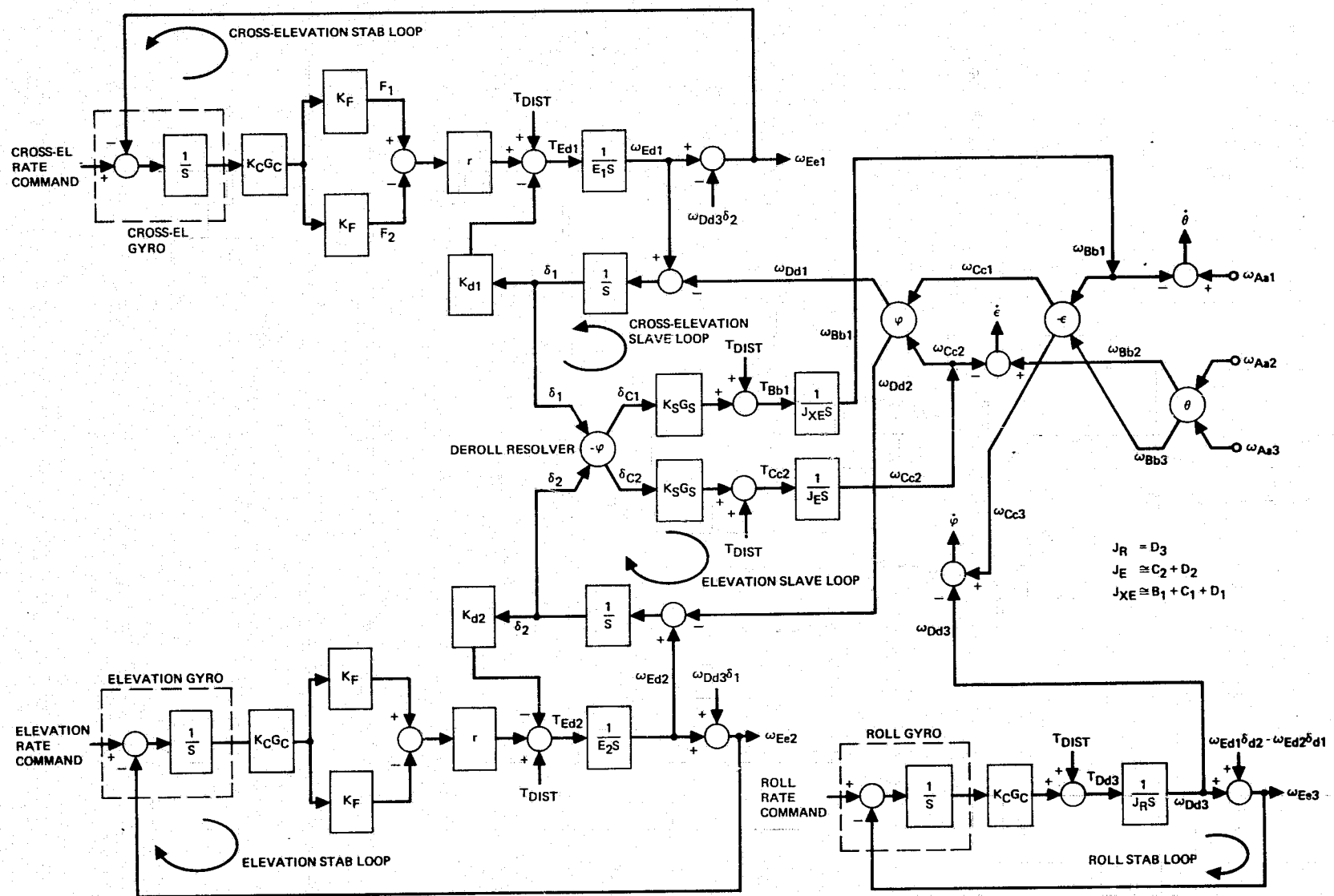


Figure D-19. Dynamic model of SIRTF stabilization system.

The platform is stabilized by the elevation and cross-elevation stabilization servos which derive their error signals from the corresponding platform gyros. The roll gimbal is stabilized by the roll stabilization servo. This servo derives its error signal from the roll gyro also mounted on the platform.

The elevation and cross-elevation coarse gimbals are controlled by slaving them to the gyro platform. If the roll gimbal angle were zero, then the platform angle δ_1 would serve as an error signal for the cross-elevation slave loop. Similarly, the platform angle δ_2 would provide the error signal for the elevation slave loop. The slave loops would tend to align the coarse gimbals with the platform and thus drive the platform angles δ_1 and δ_2 to zero.

Since, in general, the roll angle ϕ will have a nonzero value, it is necessary to deroll the slaving signals using a deroll resolver as shown in Figure D-19. The derolled slaving signals δ_{c1} and δ_{c2} are the deflection angles of the platform measured about the c_1 and c_2 axes.

In order to simplify Figure D-19, the disturbance torques that affect the various servo loops are indicated by the general symbol T_{DIST} . The disturbance torques include friction torques, gyroscopic cross-coupling torques, and residual mass unbalance torques.

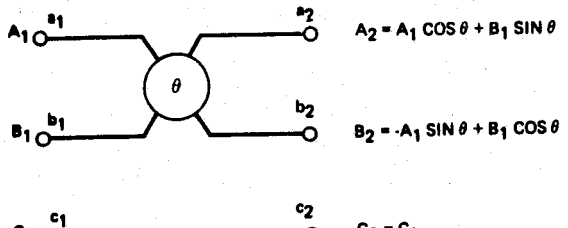
The servo electronic gain and compensation is denoted by $K_c G_c$ in the stabilization loops and by $K_s G_s$ in the slave loops. The symbol K_f which appears in the elevation and cross-elevation stabilization loops is a constant force coefficient associated with the linear platform drivers.

D-6. THE PICTORIAL METHOD OF COORDINATE SYSTEM TRANSFORMATIONS

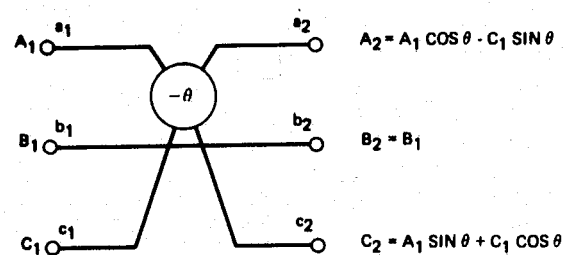
The mathematical description and analysis of the stabilization system require the extensive use of coordinate transformations. If all coordinate systems are orthogonal and dextral, the transformation of a vector from one set of coordinate axes to a second set of rotated coordinate axes can be represented pictorially by Pio's method. This technique is illustrated in Figure D-20. The symbols a_1 , b_1 , c_1 in Figure D-20 denote the original coordinate axes, and a_2 , b_2 , c_2 denote the rotated coordinate axes. The angle θ is the angle of rotation between the two coordinate systems. Parts (a), (b), and (c) of Figure D-20 represent rotations about the first, second, and third coordinate axes, respectively.

The vector components in the original coordinate system are denoted by A_1 , B_1 , C_1 , and the components in the rotated coordinate system are denoted by A_2 , B_2 , C_2 . The relationships between the two sets of vector components in each case are given in the figure.

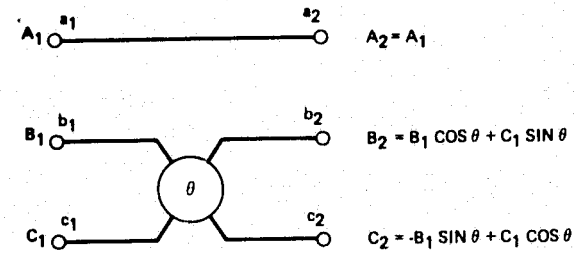
Each of the pictorial representations in Figure D-20 is equivalent to a 3×3 transformation matrix. A spatially-ordered sequence of coordinate transformations can be represented by connecting diagrams of the form shown in Figure D-20 in series. Any number of sequential coordinate transformations can be handled in this manner.



(a) ROTATION ABOUT FIRST COORDINATE AXIS



(b) ROTATION ABOUT SECOND COORDINATE AXIS



(c) ROTATION ABOUT THIRD COORDINATE AXIS

Figure D-20. Pictorial representation of coordinate transformations.

REFERENCES FOR APPENDIX D

- D-1. C. E. Kaplow/E. C. Welch, "Shuttle Infrared Telescope Facility (SIRTF) Acquisition/Stabilization/Auto-Alignment Tradeoff Report," Part A: IPS Mounted, Data Item ID1-1.c., Hughes Aircraft Co., Culver City, Calif., August 1975.
- D-2. James P. Murphy, Kenneth R. Lorell, and Charles D. Swift, "A Computer-Aided Telescope Pointing System Utilizing a Video Star Tracker," NASA Technical Memorandum NASA TM X-73, 079, Ames Research Center, Moffet Field, California, December 1975.
- D-3. R. E. Holman "Structural Analysis of the SIRTF Gimbal System," Special Report (Data Item I. D. 4.c.), Hughes Aircraft Co., Culver City, Calif., October 1975.
- D-4. C. E. Kaplow, "Initial IPS Evaluation for SIRTF Pointing and Stabilization," Data Item ID1-4.c., Hughes Aircraft Co., Culver City, Calif., January 1975.

BIBLIOGRAPHY

<u>Category</u>	<u>Title</u>	<u>Author/Organization</u>	<u>Date</u>	<u>Report No.</u>
General	Preliminary System Tradeoff Report	Hughes	October 1974	ID1-1. a.
	First Review Meeting (Viewgraph Book)	Hughes	November 1974	ID1. d.
	Second Review Meeting (Viewgraph Book)	Hughes	April 1975	ID1. d.
	Third Review Meeting (Viewgraph Book)	Hughes	July 1975	ID1. d.
	A Cooled Infrared Telescope for the Space Shuttle - (SIRTF)	Ames	January 1976	AIAA-76-174
	A Large Cooled Infrared Telescope Facility for Spacelab	Ames/Hughes	August 1975	AAS-75-234
	Orbiter/Spacelab Capabilities with Respect to SIRTF Requirements	Grumman/Hughes	May 1975	ID1-1. f.
Optics	SIRTF Interfaces	Grumman/Hughes	January 1976	ID1-10. b.
	Optics Design Tradeoff Report	Hughes	October 1974	ID1-1. b.
	Optical Performance Analysis Report	Hughes	August 1975	ID1-2. a.
	Optical Engineering Analysis Report	Hughes	January 1976	ID1-2. b.
Mechanical/ Thermal	Apodization Study Special Report	Hughes	September 1975	ID1-4. c.
	Mechanical Design Tradeoff Report	Hughes	To Be Published	ID1-1. i.
	Structural Analysis Report	Hughes	November 1975	ID1-2. c.
	Effects of Acoustic Environment	Hughes	October 1975	ID1-4. e.
	Thermal Analysis Report	Hughes	October 1975	ID1-2. d.
Gimbal/Servo	Cryogenic Servicing	Grumman/Hughes	May 1975	ID1-2. f.
	Initial IPS Evaluation for SIRTF Pointing and Stabilization	Hughes	January 1975	ID1-4. c.
	Acquisition/Stabilization/Auto-Alignment Tradeoff Report			
	Part A. IPS-Mounted	Hughes	August 1975	ID1-1. c.
	Part B. Dedicated Gimbal	Hughes	May 1976	ID1-1. c.
	Structural Analysis of the SIRTF Gimbal System	Hughes	October 1975	ID1-4. c.
	A Computer-Aided Telescope Pointing System Utilizing a Video Star Tracker	Ames	1976	NASA TMX-62, 505
Data Processing	Data Processing, Control, and Display Tradeoff Report	Hughes	January 1976	ID1-1. f, 1. j, 1. k
Special Reports	Radiation Effects Analysis Report	Hughes	December 1975	ID1-2. g.
	Particle Sighting Study Special Report	Hughes	September 1975	ID1-4. 2
	SIRTF Integration	Grumman/Hughes	January 1976	ID1-4. e.
	A Radiometer for Monitoring Column Densities of Infrared-Active Molecules	Ames	1975	NASA SP-379
Contamination	The Effect of the Shuttle Contaminant Environment on a Sensitive Infrared Telescope	Ames	To Be Published	
	Infrared Emission from the Atmosphere Above 200 KM	Ames	October 1975	NASA TND-8138